Brno University of Technology

Faculty of Chemistry

# Additive Fabrication of Functional Patterns by Inkjet Material Printing: Physico-chemical Aspects of Ink Formulation and Substrate Interactions

Habilitation thesis

Ing. Petr Dzik, Ph.D.

Brno 2016

BRNO UNIVERSITY OF TECHNOLOGY
FACULTY OF CHEMISTRY

# Additive Fabrication of Functional Patterns by Inkjet Material Printing: Physico-chemical Aspects of Ink Formulation and Substrate Interactions.

Habilitation thesis

Ing. Petr Dzik, Ph.D.

Brno 2016

*Chtěl bych upřímně poděkovat všem mým blízkým, kteří mě v mém úsilí podporovali a vytvořili mi pevné rodinné zázemí. Děkuji Michalu Veselému za důvěru, poskytnutí příležitosti „být u toho“ a předání cenných zkušeností. Dále děkuji dlouhé řadě skvělých kolegů z fakulty za vytvoření příznivého pracovního prostředí.*

*Věnováno Lence, Magdaleně a Karolíně.*

## Abstract

This thesis summarizes the outputs of the author's research and publication activites devoted to the topic of functional materials deposition by meant of inkjet printing. The results disclosed in this thesis represent a complete account of the author research activities for the past 8 years. First, the present state of the art is discussed from the technological point of view, i.e. the methods and techniques are being reviewed rather than particular materials. Then the general research aims are explained and their importance is substantiated. Further separate chapter gives the summary of the methodology used throughout the entire thesis and three following subchapters are dedicated to the presentation of selected results as well as their discussion in the context to relevant papers published recently. The three chapters focus on the three major groups of material classified according to their electrical properties (insulating, semiconductive and conductive species). Finally, all papers included in the thesis are listed in chapter 9.

All included results explicitly indicate that the direct patterning performed by piezoelectric inkjet printing proved to be an attractive method for depositing liquid formulations onto solid supports. As far as the insulating species are concerned, we managed to formulate reliable inks based on soluble redox indicators allowing highly reproducible testing of photocatalytic activity. Inkjet printing also proved to be an elegant and efficient method for the fabrication of metallic conductor patterns. The greatest deal of attention has been paid to the patterning of transition metal oxide semiconductors. Functional inks containing blended colloidal systems (either sol-gel or crystalline nanoparticulate, sometimes with optional silicon based binders) were successfully developed and utilized for the fabrication of titania, zinc oxide and tungsten oxide functional coatings. The additive fabrication of complex functional structures was successfully accomplished and is illustrated on the example of interdigitated electrochemical cell.

Keywords:
Material printing, inkjet printing, photocatalysis, electrocatalysis, direct patterning, additive manufacturing, printed electronics

## Content

# 1 Introduction

The performance of oxide nanomaterials as functional device components is often subject to interfaces which emerge upon materials integration. Examples for the use of fully integrated and interface-determined nanoparticle systems can be found in different rapidly developing fields like solar-to-chemical conversion, sensing and printed electronics. For light conversion into chemicals and energy the spatial and directional arrangement of the light harvesting entities plays a critical role. Additional performance determining factors are related to the separation and transport of photo-generated charge carriers, the chemical conversion at catalytic sites and mass transfer from or to reactive sites. However, the immobilization and integration of the materials components into devices is just as important as their individual optimization.

Mixing chemically different nanoparticles by colloidal processing in combination with the utilization of the attractive interaction between the dissimilar components may lead to functional interfaces between the dissimilar components which can add new functionalities to the entire particle ensemble. The ability to introduce chemical heterogeneity in nanoparticle mixtures at different length scales opens the opportunity region to deliberately transform particle interfaces into heterojunctions which in turn are key to a number of applications that rely on the separation and surface chemistry of photogenerated charge carriers.

Recently, especially in the domain of electronic component fabrication, the dominant position of subtractive processes based on sequential etching through resists masks has been challenged by a new additive approach. The so-called material printing techniques [1] are based on sequential laying of patterned functional layers by means of modified conventional printing techniques and they seem to be a promising tool for the micro-fabrication of planar structures with features in the micrometer range. While such resolution is not capable to replace the nanometer-scale lithographic processes used for the fabrication of memory chips and processors, there is still a wide range of less integrated devices and structures which may be fabricated in this way effectively. Actually, the concept isn't new at all, but the approach has been limited to the fabrication of metallic conductive tracks by screen printing for the past 50 years. During the past decade, the concept of material printing broadened significantly and the portfolio of applicable techniques now includes off-set, gravure, flexo, and inkjet printing. Following this boom, the idea of fully printed electronics[2] has been successfully transferred from lab to mass production. However, the approach proved to be also useful in the material[3] and life sciences[4] domains.

While essentially all traditional printing techniques can be adopted for printing of functional patterns, inkjet printing [5] occupies a prominent position. Despite quite narrow viscosity and particle size limits, it is most suitable for lab-scale rapid prototyping as no hardware printing form is required, i.e. patterns designed as computer files can be printed directly. Moreover, up-scaling is easily accomplished by switching to a bigger printer. Inkjet printing has been successfully used for the deposition of a variety of functional liquids, such as conducting polymers [6-8], dispersions of catalyst nanoparticles [9], etc. Numerous biochemical applications have been reported, such as tissue scaffolds [10-11] or cellular patterns [12-13]. Moreover, many components such as capacitors [14], transistors [15], electronic filters [16], and even complete multi-component devices such as OLEDs[17], solar cells[18] and photoelectrochemical cells [19] have been successfully fabricated.

Material printing tends to be compared (and sometimes confused) with 3D printing. While some of the material science related challenges are common to both the technologies, there are other

important differences. 3D printing uses a few construction materials to build spatial objects characterized by their form rather than by any additional functionality. Material printing generally also produces tree-dimensional objects, but their footprint is always much greater than their height and the main topic of interest is their advanced functionality.

The results disclosed in this thesis represent a complete account of the author research activities for the past 8 years. First, the present state of the art is discussed from the technological point of view, i.e. the methods and techniques are being reviewed rather than particular materials. Then, in chapter 3, the general research aims are explained. Chapter 4 contains a subchapter giving the summary of methodology used throughout the entire thesis and 3 subchapters dedicated to the presentation of selected results as well as their discussion in the context to relevant papers published recently. The three chapters focus on the three major groups of material classified according to their electrical properties (insulating, semiconductive and conductive species). Finally, all papers included in the thesis are listed in chapter 9.

## 2 Inkjet Printing from the Viewpoint of Physical Chemistry

A functional coating can generally originate from precursors delivered to the substrate either in the gaseous or liquid phase. The former way has evolve into a wide portfolio of various CVD methods offering a great level of control over the deposition conditions but requiring sophisticated instruments and featuring somewhat limited substrate sizes. The latter represents usually a simpler alternative and is capable of coating substrates several meters in size. Many different wet coating techniques have been developed, such as dip-, spin-, or spray-coating, doctor blade or roller spreading.[20] Continuous roll-to-roll processes are applied on mass industrial scale for various manufacturing tasks[21], and gained further attention with the boom of printed electronics[22].

There are two significant methods of thin layer preparation from liquid precursors which are worth mentioning because of their simplicity and general widespread utilization: Spin-coating method uses centrifugal force to form a film of liquid precursor: a sufficient volume of precursor is placed onto the support which is then rotated at a high speed. The liquid is spread by centrifugal force and a wet film of precursor is formed. The thickness of the resulting wet film depends mainly on the angular velocity of substrate rotation, precursor viscosity, precursor concentration and solvent evaporation rate [23]. In contrary, dip coating is based on dipping the substrate into liquid precursor and pulling it out at constant speed[24]. Again, viscosity, concentration, solvent volatility and speed of pulling influence the resulting film thickness. The faster we pull, the thicker the film is.

Both these methods are widely used, yet they are burdened by several significant disadvantages, as summarized in Table 1. Firstly, the coated area is rather limited. In the case of spin coating, this limitation is due to the centrifugal force. Substrates larger than a few centimeters simply can not be rotated at several thousands rpm. The area of dip coated substrates is usually also limited to centimeter scale, although devices handling large substrates up to meter size are known. Secondly, the efficiency of precursor use is extremely poor. In both spin- and dip-coating, most of the precursor is wasted, and only few percents are actually used to build up the film. Moreover, dip-coating gives us substrates coated from both sides, which is not always desired. Thirdly, both these methods are very sensitive to surface defects. A surface defect can produce traces and streaks and degrade large areas of coated substrate. At last, these classic methods on their own are not capable of selective deposition ("patterning"), i.e. the whole area of substrate is coated.

***Table 1*** *Comparison of deposition techniques (adopted from [17], modified)*

| | Spin | Dip | Inkjet |
|---|---|---|---|
| Precursor use efficiency | ~95 % wasted | ~95 % wasted | ~5 % wasted (print head cleaning an purging) |
| Coated area | ~ cm | ~ dm | ~ m |
| Sensitivity to surface deffects | high | high | low |
| Patterning possibility | none | none | excellent |

Because of these problems and limitations, a more robust method of liquid precursor application has been searched for and, as accounted in the introduction section, material printing seems to be a promising alternative. Of the numerous printing techniques potentially applicable for this purpose, inkjet printing seems to be especially promising representative of the novel material

printing approach. The technique shares the basic principles of conventional inkjet printing[25], i.e., tiny droplets of a low-viscosity liquid are precisely deposited onto a substrate by means of a thermal or a piezoelectric printhead. Obviously, in the case of material printing, the "ink" is a specially formulated liquid used for transporting a functional component onto the substrate surface[26]

## 2.1 The Art of Ink Formulation – Getting Control over Dispersions

The ink surface tension, substrate surface energy, and ink viscosity are the most prominent factors influencing droplet formation and layer merging during the inkjet printing of a functional liquid onto a non-porous non-absorbing substrate. Apart from these ink properties, the substrate temperature also plays a very important role because it is the main factor influencing the solvent evaporation rate. Lower temperatures result in slow drying, mottling, and dust accumulation, while higher temperatures lead to premature solvent evaporation and banding pattern formation because of imperfect printed bands merging. These rules seem to be valid generally, irrespective of the ink composition. Therefore, the volatile phase of the inks should preferably contain 2-4 solvents differing significantly in their volatility, which contributes to the gradual drying and seamless merging of the printed bands.[27] Moreover, a humectant that prevents the ink from drying in the printhead nozzles should be always present, too.

The final surface topologies of the printouts depend on complex interactions between the drop-shaping forces and the surface properties of the substrate used. Several distinctive phases have been identified during drop-spreading on solid non-absorbing substrates: a kinematic phase, a spreading phase, a relaxation phase, and a wetting phase[28]. The drop dynamics and film formation can be predicted to a certain degree by theoretical descriptors such as the Weber number ($We = \delta \cdot v^2 \cdot d/\sigma$), Ohnesorge number ($Oh = \eta/\sqrt{(d \cdot \sigma \cdot \delta)}$), Z number ($Z = \sqrt{(d \cdot \sigma \cdot \delta)}/\eta$), and Reynolds number ($Re = \delta \cdot v^2 \cdot d/\eta$), where $\delta$ is the density, $v$ is the drop velocity, $d$ is the diameter of the nozzle, $\sigma$ is the surface tension, and $\eta$ is the viscosity of the liquid. While some theories predict a stable drop formation in drop-on-demand systems when $Z > 2$,[29] others determined that a printable fluid should have a $Z$ value between 1 and 10.[30] It is also known that the lower limit is governed by the viscosity of the fluid and its printing ability, while the upper limit is determined by the point at which multiple drops are formed instead of a single droplet[31].

However, apart from the volatile fraction, the ink needs to contain the functional non-volatile fraction which is actually going to build-up the printed layer and/or pattern. Several distinct approaches to this task can be easily identified:

The first and simplest way is the formation of a true analytical solution of the functional compound in the solvent. This works fine in the case of polymers with film-forming properties[32]. However, low molecular compounds would crystallize upon the solvent evaporation and thus prevent the formations of homogeneous continuous layer.

The second option is based on the sol-gel process, i.e., soluble metal salts and/or metal alkoxides are complexed by suitable chelates, pre-crosslinked by partial hydrolysis, and the resulting metastable colloidal sols are then coated onto a substrate, gelled, and converted into dense or porous oxide layers[33]. Thermal calcination is the most common way to achieve this conversion, but low temperature alternatives are available[34]. The process can be made very simple and the liquids formulated so mild that a modified office inkjet printer[35] could be used. Thick multilayer coatings can be printed with the help of polymeric anti-cracking agent[36]. Alcohol based sols are

generally well compatible with macromolecular templates allowing for a controlled porosity formation[37]. Reverse micelle templates[38] were also successfully adapted for inkjet printing.

Much experimental attention has also been paid to explore the third possible approach leading to printed solid functional patterns. This route is based on the synthesis of stable colloidal suspensions of nanocrystalline solids followed by the delivery of this suspension onto a substrate by means of inkjet printing. This approach seems to be the most challenging with respect to particle stabilization issues but offers the greatest freedom in functional material choice. Bernacka-Wojcik and coworkers recently demonstrated[39] a disposable biosensor integrating an inkjet printed photodetector fabricated by printing a commercial dispersion of titania nanoparticles. A similar approach was adopted by Yang et al.[40] to produce an oxygen demand sensing photoanode and by Arin et al.[41] who fabricated photocatalytically active $TiO_2$ films by inkjet printing of nanoparticle suspensions obtained from microwave-assisted hydrothermal synthesis. Fine nanodispersions originating from hydrothermal processes[42-43] seems to be especially well suited for the formulation of such inks.

The obvious issue inherently associated with this second approach is the adhesion of the deposited material to the substrate. The loosely aggregated nanoparticles left after solvent evaporation only have a very limited adhesion to the substrate and need to be fixed in some way. The above-referenced examples employed the most common solution to this problem, i.e., sintering by heat treatment at 300-500 °C. However, more sophisticated solutions have been reported. Cold-setting processes yielding stable layers are very attractive for the fabrication of photoelectrochemical functional or auxiliary coatings on the surface of heat-sensitive substrates. This is especially true in the case of dye-sensitized solar cells[44], where the adoption of cheap flexible polymer supports is considered a necessary condition for commercial success. A great deal of attention has therefore been paid to this problem, and several interesting processes have been reported so far e.g. a mechanical processing of the printed nanoparticulate layer [45] or a rapid photonic sintering[46] which would not damage even heat-sensitive common polymeric foils.

An interesting modification of the nanoparticulate suspension approach represents the so called brick-and-mortar strategy[47] based on the mixing of prefabricated nanocrystalline “bricks” with “mortar” consisting of a suitable binder followed by preferably cold fixing. Several different materials have been proposed as binders and various processes may be adopted for their fixing. For example amorphous silica[48] or graphene[49] binders are fixed by mere solvent drying or more sophisticated systems utilize alkoxide [50] or organo-silicate[51] binders fixed by UV-curing.

## 2.2 The Art of Printing – Quality and Functionality of Printed Particle Systems

With the traditional inkjet printing systems utilizing piezoelectric heads, we generally observe that the feature size that can be printed is closely related to the size of the droplet that can be ejected. However, this is only a part of the story, since substrate-ink interactions also play an important role. Anyway, a typical present inkjet system designed for material printing can be expected to employ nozzles of 10-50 μm diameter delivering droplet volumes in the range 1–100 pL.[52] The desire to access ever finer feature sizes has resulted in the development of subfemtoliter inkjet printing systems based on electrohydrodynamic (EHD) jet printing[53].

The piezoelectric element pulsing frequency is found to exert a strong influence on the formation of ink droplets and so is the voltage waveform (i.e., the voltage pulse profile) delivered to the piezoelectric element.[54] The authors found that with increasing frequency, the droplets formed

reduced in size (and size variability), which would be expected to decrease the size of the minimum feature printed. However, this decrease was accompanied by an increase in the impact velocity of the droplet on the substrate, which in turn is expected to degrade the quality of the print. Obviously, the placement accuracy of the drop is governed by the width of the jet and the resolution provided by the moving stage. The diameter of the jet has been found to be proportional to the square root of the nozzle size and inversely proportional to the electric field[55].

Stroboscopic camera providing a magnified, slowed-down view of the nozzle plate is an valuable tool for evaluating the ink behaviour upon the ejection from the printhead nozzle. Reliable jetting without satellite droplets formation takes place when the liquid rheological properties (viscosity and surface tension) well match the waveform pattern. Image data from stroboscopic camera can thus provide important feedback for waveform optimization enabling printing fluids of a wide range of viscosities.[56]

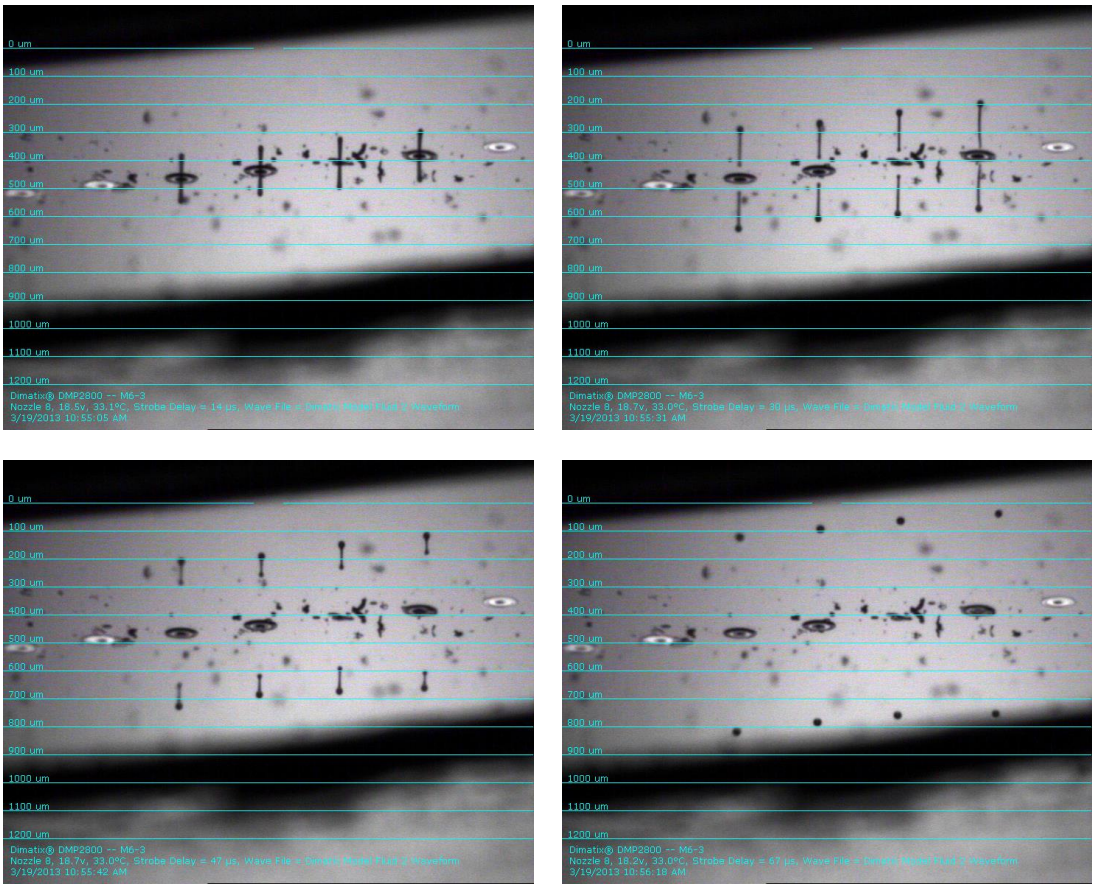

**Fig. 1** *Stills from a stroboscope slowed-down video can be used for the analysis of droplet formation characteristics and for the optimization of the voltage waveform. In this case, the satellite droplets formation has been effectively suppressed and a single droplet leaves every four tested nozzles.*

Print quality is further influenced by various dynamic phenomena observed during drop landing on substrate, such as splashing, spreading, receding, bouncing and crown formation[57]. As mentioned earlier, Rioboo et al. [28] have in detail analyzed the process and identified several distinctive phases of drop spreading: kinematic phase, spreading phase, relaxation phase and finally equilibrium wetting phase, driven by surface energies (see below). Various artefacts spoiling the resulting print quality can result from these processes. Perhaps the most well-known is the coffee-ring effect, which has been observed, described and explained actually independently

to inkjet issues.[58] Although several different approaches have been attempted for its control or elimination[59], it still poses a major challenge in the design for inkjet material printing[60-61]. Quite surprisingly, several recent papers reported intentional use of the ring structures for obtaining special morphologies.[62-63] Another phenomenon spoiling the printed patterns is the so called fishbone effect. It takes place upon the oblique collision of two continuous liquid jets and leads to the formation of a thin oval liquid sheet bounded by a thicker rim which disintegrates into ligaments and droplets. [64]

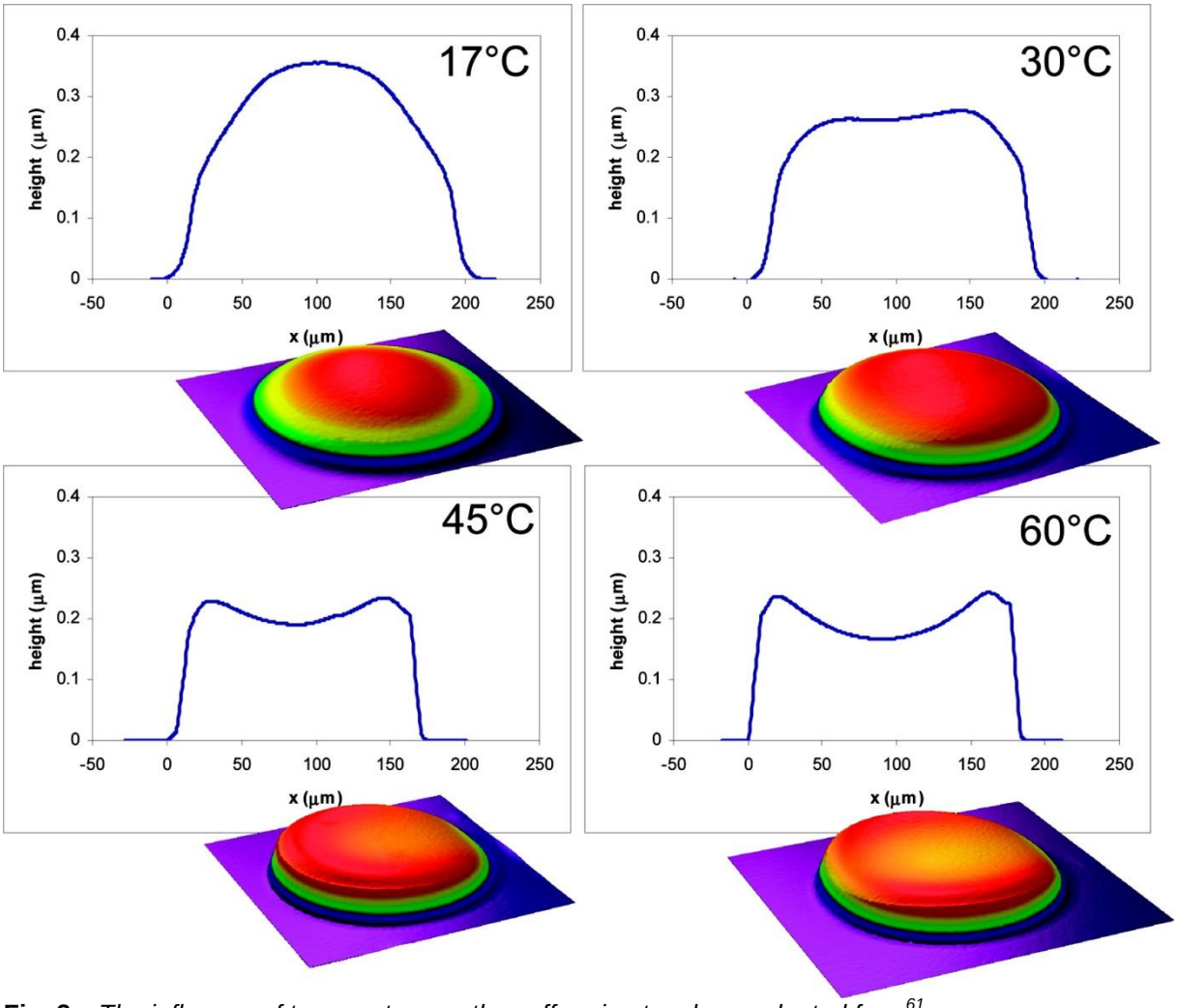


**Fig. 2** *The influence of temperature on the coffee ring topology, adopted from*[61]

The final drop spreading phase, i.e. the equilibrium wetting phase, seems to play a crucial role in the formation of printed patterns and their final quality. Generally, during inkjet printing on a nonporous, non-absorbing surface, the surface tension of printed ink and the surface energy of the substrate must closely match in order to ensure optimal wetting and smooth, well defined wet layer formation [65]. If the printed liquid is wetting the surface too much, excessive positive dot-gain or even pattern bleeding [57] may occur. Conversely, poor wetting of substrate by the printed ink results in spontaneous shrinking of the printed ink (negative dot-gain), or the formation of a bumpy surface resembling an orange peel texture [66-68]. The following figures briefly illustrate these

phenomena on the examples of UV curable acrylate ink and gold electrical conductor lines obtained from printed gold resinate[69] ink.


**Fig. 3** *Influence of substrate treatment on the print quality illustrated by the behavior of acrylate UV ink printed on FTO substrate: a) FTO surface after baking is excessively wetted by the printed ink with significant positive dotgain and irregular ink bleeding, b) application of the dewetting agent suppresses ink spreading but ink is actually dewetting the surface too much, resulting into slight negative dotgain, c) treatment by the dewetting agent plus dodecylbenzene sulfonate produces just the right degree of wetting with excellent definition of pattern edges.*


**Fig. 4** *The influence of substrate treatment on print quality illustrated on the example of 200 µm gold line originating from printed gold resinate: left - alumina surface right after baking is excessively wetted by the printed ink with significant positive dotgain resulting into line broadening and resolution decrease, middle - treatment by 1 vol.% solution: the dewetting agent reduces ink spreading and provides excellent definition of pattern edge, right – treatment by 5 vol.% solution: the dewetting agent results in poor wetting and gold layer separation.*

## 3 General Goals of the Research Work Included in the Thesis

Understanding the formation and exploring the photochemical relevance of solid-solid interfaces in blended nanoparticle ensembles including the identification of related synergistic effects are vital to the development of particle-based photovoltaic and photochemically active devices. Procedures for the controlled aggregation of dissimilar metal oxides in colloidal dispersion and/or sol-gel formulations needs to be implemented into the rational formulation of functional inks to be employed for state-of-the art inkjet printing.

In the discussed research, we have been essentially undertaking a strategic structure/ microstructure-photoactivity study to identify for printed metal oxide nanoparticle systems the key parameters that determine compositional heterogeneity from the nano- up to the micrometer scale. The knowledge based formulation of functional inks prepared from pure and blended metal oxide with optional organosilicon based binders has actually enabled the realization of printed nanoparticle structures with remarkable level of control over hetero interfaces across different length scales. We have been using the printing technique to selectively engineer submicron sized patches of different motifs on different substrates and with high concentrations of interfaces joining chemically different oxides, i.e. photocatalytically active heterojunctions. These novel structures of immobilized nanoparticle patterns may find application as device concepts of solar-to-energy conversion and sensors since they should be able to sort and sustain photoinduced surface reactions in a spatially resolved way and on the length scale of nano- to micrometers.

The primary objectives of the presented research work thus were:

1. rationally develop functional inks containing blended colloidal systems (either sol-gel or crystalline nanoparticulate, sometimes with optional silicon based binders) that allow for nanoparticle aggregation at different stages of the printing process;

2. explore the effect of the colloidal system mixing and demixing during printing and to understand the impact of curing parameters on microstructure evolution and functional performances resulting therefrom; Intermediate process steps that are associated with the emergence of defects and impurities that are detrimental to light induced charge separation will be identified;

3. demonstrate that the forced assembly of the solid fraction of the colloidal system via inkjet printing in combination with the naturally occurring arrangement of nanoparticles upon formation of compositionally heterogeneous mesostructures provides a rich playground towards the hierarchical organization of composite nanoparticle systems.

4. pattern 2-dimensional substrates with spatially organized structural features, such as patches and crossings of printed nanoparticle tracks with photocatalytic hot spot regions, the activity of which can be imaged at different length scales up to the sub mm range. Characterize heterojunctions of particle systems across different length scales and probe photoactivity or even photocatalytic activity on 2-dimensional substrates;

# 4 Selected Results and their Discussion

The following chapters represent an account on our "success stories", i.e. we disclose a brief summary of the most interesting aspects of our recent work related to the discussed topic. The addressed issued are discussed in the context with relevant references preceding our work, but their number is rather limited in order to keep the text concise. For a more complete discussion and additional references, please see the full-text papers listed in the end of the thesis.

## 4.1 Outline of the Used Methodology

Inkjet direct patterning as such has constitute the main research activity. However, it needs to be preceded by necessary preparative operations (substrates conditioning, inks filtering and stability checks etc.) and detailed analyses would follow after printing each sample batch. Simultaneously, the patterns to be printed need to be generated in suitable software and exported into the printer driving software.

As far as the preparative stage is concerned, the staff of Photochemistry Lab has gained extensive experience with the technique. Various substrate cleaning and activating techniques (thermal annealing, sonication, plasmatic treatment) have been previously implemented and are routinely performed in the lab. Should more demanding request on process cleanliness take place, a cleanroom workplace is available right at the faculty laboratory building.

Printing of all functional and auxiliary layers has been performed with an experimental inkjet printer Fujifilm Dimatix 2831. The printer features disposable 16-nozzle piezoelectric jetting printhead coupled with a 2 mL polyethylene inktank. It is capable of printing A4 size substrate with resolution of up to 5080 DPI, i.e. 5 μm. Both substrate and printhead can be heated in order to speed up solvent evaporation and reduce ink viscosity, respectively. A stroboscopic camera provides still images or slow-down video for the observation of drop formation process, while another fiducial camera is used for precise substrate positioning and aligning of subsequently print layers. The printer has been successfully employed for the deposition of a wide variety of functional and auxiliary layers and during the past years has de facto become the industrial standard tool for ink development and testing[2].

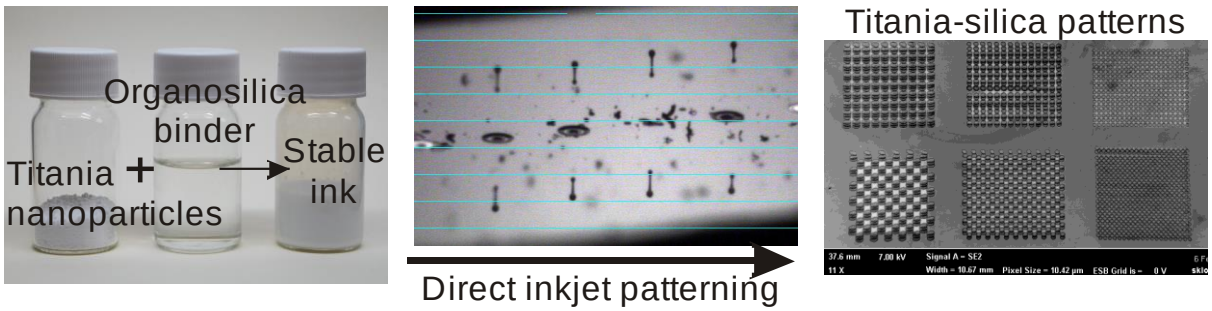


**Fig. 5** *Schematic outline of the key experimental activities: inks are formulated on the basis of blended colloidal systems (either sol-gel or crystalline nanoparticulate, sometimes with optional silicon based binders) and the resulting metastable colloids are patterned by inkjet printing*

Compared to the other research tasks, the printed patter design is a rather trivial issue which is again routinely performed by the Photochemistry Lab team. Usually vector patterns drawn in Corel Draw are used for printing most geometries. For special demands (which actually happen

occasionally in conjunction with special projects) a single droplet level control can be achieved by manipulating bitmap pattern files at the individual pixel level.

The described activities together have contributed to achieving the results summarized on the following pages. The key specialty, novelty and scientific progress of our work is represented by the ability of inducing a forced assembled structure inherently associated with the printing process. While the prepared mixtures of various studied materials will naturally arrange at the sub-micron scale upon printed layer drying, we have been able to combine this primary spontaneously created structure with a hierarchically higher-level forced structure created by overprinting of various patterns. The exact description of the strategy for the sub-micron-scale forced assembly goes beyond the scope of this summary but it would certainly include features like multilayer assemblies, charge-transporting mesh structures adjacent to thick layers of bulk heterojunction composites, employment of shaped conductive substrates (interdigitated arrays), gap structures, active "hot spots" created by line crossing etc.

Moreover, a significant fraction of our research activities has been devoted to the investigation of the physico-chemical transformations taking place in the dry solid printed layer. Several different approaches have been utilized and are reported below. A special attention has been paid to investigation of layer consolidation by means of organosilicate binders. We have shown recently that the organosilicate matrix can be mineralized by both thermal oxidation or UV curing. However, there are many other optional processes (e.g. plasma treatment or flash sintering) which may prove useful for this task and bring interesting performance.

The analytical techniques employed in our research have primarily included various microscopic and imaging techniques involving, but not limited to SEM, AFM, optical, interference and confocal microscopy. Mechanical profilometry and profilometric mapping proved to be especially useful for the visualization of sub-milimeter printed structures and these analytical techniques are readily available at the FCH labs. The processes accompanying the binder mineralization will be investigated by spectral methods such as FTIR, XPS etc. For the purpose of catalytic functionality investigation, several standard activity testing methods have been successfully implemented and several others were designed or adopted and modified[70-73].

## 4.2 Conductive Species

Although complex multilayered printed devices were demonstrated multiple times, the relatively simple task of conductive track fabrication remains one of the most explored applications of material printing. In the conventional technology of copper plated "printed circuit boards", industrial scale processes use *screen-printing* of thick inks based on micron-sized particles or optical resist patterning and etching when finer tracks are needed. Similarly, small batches may be produced by contact copying of masks *printed* on photographic film onto pre-sensitized boards.

The direct printing of conductive tracks by means of a printing press and conductive ink, using a digital pattern outline has been addressed by numerous studies yielding some very promising results. However, the advance from screen-printing of thick metal dispersions followed by thermal sintering to direct patterning by inkjet requires nanoparticulate dispersions with well controlled rheology and particle stabilization. Inks of stabilized silver nanoparticles proved to deliver good performance [74-77]. Water based gold nanoparticle ink has been reported recently [78] to produce tracks of resistivity approaching that of bulk gold. Stabilized palladium nanoparticle inks

have been printed for use as activator for electroless deposition of conductive nickel tracks [79]. Palladium nanodispersions were successfully synthetized and printed by the author of this thesis.[80]

An alternative approach is based on the deposition of a soluble metal precursor, and reduction to metal. Silver nitrate has been successfully used for the fabrication of conductive tracks [81]. Silver carboxylates represent an organometallic option of this process, allowing for photo-thermal curing [82]. Similarly, aqueous Pd(II) solution was printed onto polyimide film, followed by reduction to metallic palladium which served as activator for subsequent electroless copper plating [83].

We approached this problem through a rather less popular chemical path and utilized soluble resonates and metal precursor. Metal resinates originate from the reaction of sulfurized natural resins with metal salts, e.g. yielding a mixture of gold mercaptoterpenes in the form of thick pastes soluble in non-polar solvents [69]. The chemical structure of a resinate solution is variable and no exact formula can be given. The metal content can be determined by suitable analytical methods [84]. While their traditional application was limited to ceramic decoration, later resinates found numerous uses in the electronic industry for fabrication of conductors, resistors, heating elements, actuators, etc. [85].

The method proved to be effective and thus we were able to develop a complete fabrication process for printing and fixing of gold conductive tracks on various substrates. It has been used for example for the fabrication of cells for measuring conductance of very low conductive electrolytes. Further applications may involve various capacitive sensors [86-87] and photoelectrochemical cells [88]. Due to the materials used in this study, the printed electrodes are curable at high temperature if contaminating deposits are to be removed, e.g. when biological samples had been measured[89].

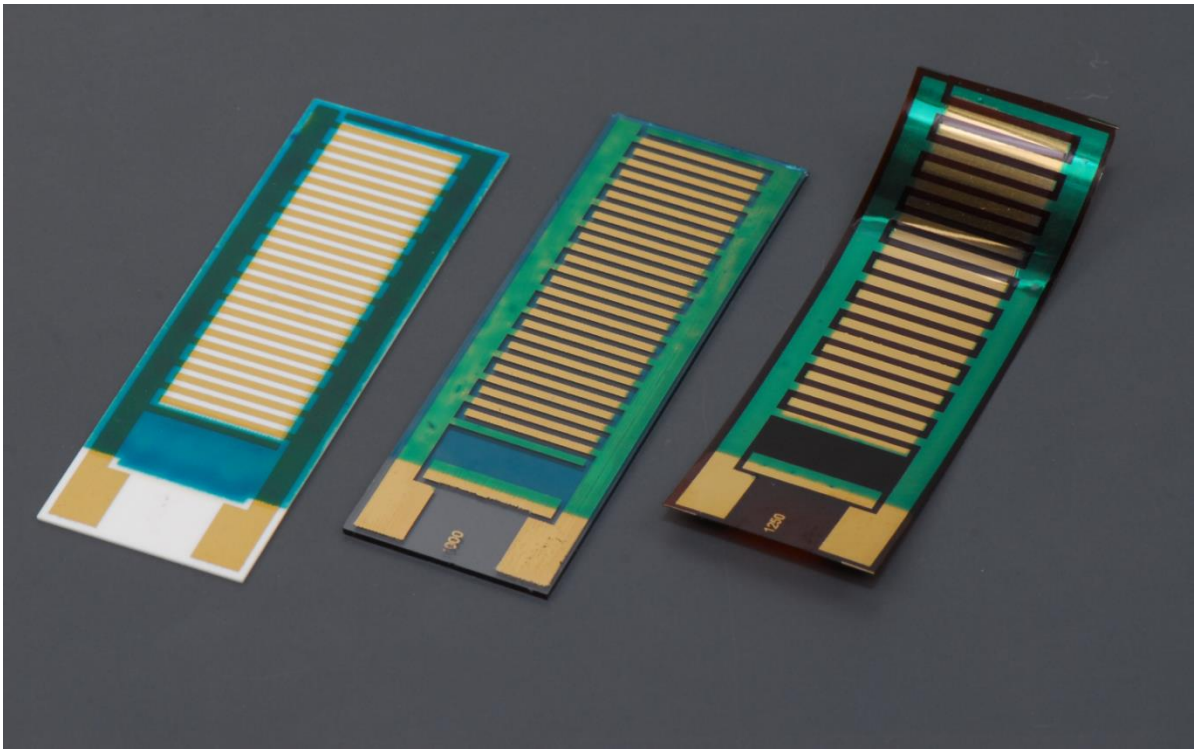

**Fig. 6** *Conductivity gold IDE cells printed on alumina (left), glass (middle) and Kapton (right) substrates.Cyan insulating masking frame is overprinted in order to eliminate border effects.*

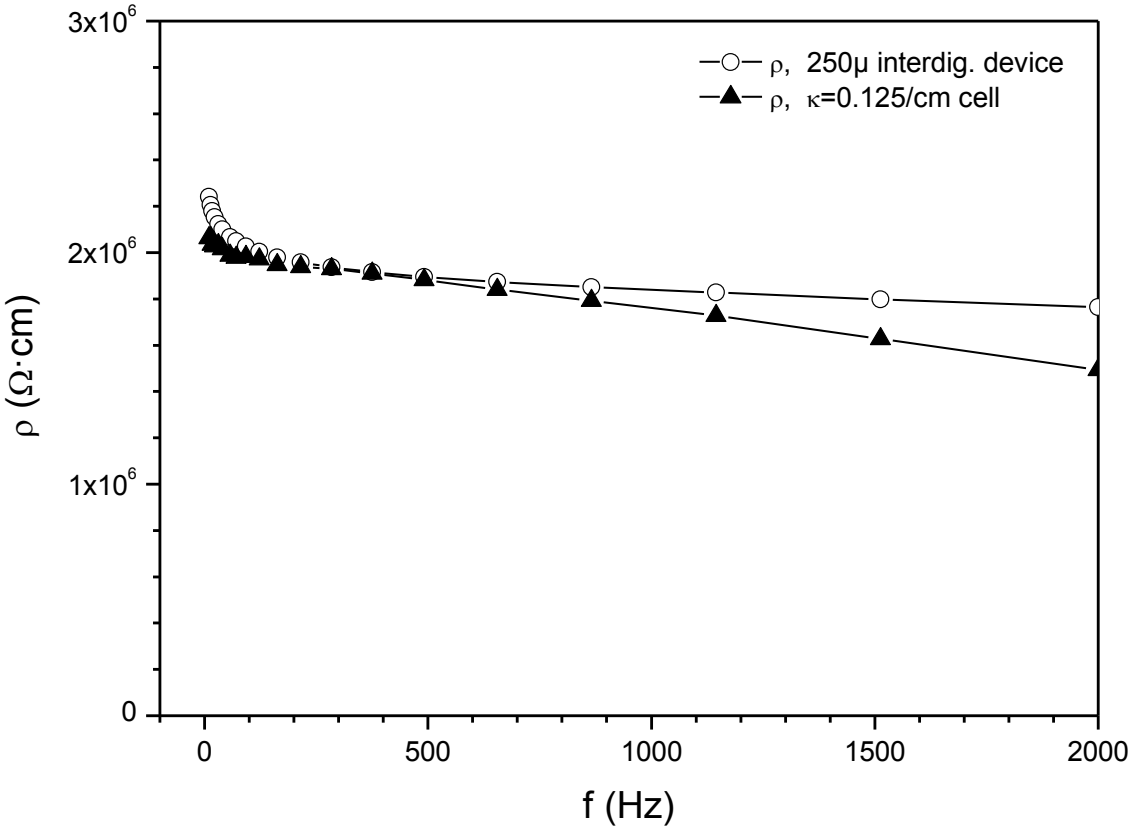


**Fig. 7** *Impedance spectroscopy of ultrapure water using an interdigitated device made by printing Au on alumina with 250 µm finger width a spacing (open circles) or a conventional parallel plate cell with κ = 0.125 cm$^{-1}$ (filled triangles). The amplitude of the perturbing signal was 0.01 V rms.*

As shown in a recent exhaustive review [3], printing gold patterns remains a challenging tasks with a only a few successful studies reported so far. Yet, inkjet printing proved to be an elegant and efficient method for the fabrication of gold conductor narrow spaced interdigitated planar devices (electrochemichal cells) in our study. With modern high speed flatbed printers readily available, the technique is also suited for industrial scale production. While interdigitated electrode systems have been routinely fabricated by screen-printing for the past 50 years, the here proposed fully digital printing workflow eliminates the need for physical printing forms, saves expensive gold resinate ink and allows an unlimited freedom in the design of the electrode patterns. The benefits of the presented approach become even more prominent during the fabrication of single prototypes or small batches of large-scale devices, where the dead volume of conventional coating devices would prohibitively increase the production costs.

### 4.3 Semiconducting Species

Transition metals oxides form a group of n-type semiconducting materials with a plenty of special properties enabling a huge range of applications. The range of interesting properties is further widened by virtually endless possibilities of doping and structural modifications. Apart from the naturally inherent semiconductive properties[90], these materials feature highly interesting ferromagnetic[91], charge transport [92], sensing[93], emissive[94], and electrochemical activity[95].

Metal oxide semiconductors and their related photocatalytic processes have been the subjects of intensive research for the past four decades. The primary discovery of the photoelectrochemical splitting of water on titanium dioxide electrodes[96] has gradually evolved into a broad technological field of applied photocatalysis. This technology may have the potential to address some of the most urgent technological challenges,[97] especially if solar light is employed as the irradiation source[98].

Basically, any photocatalytic process is initiated by the photogeneration of electron-hole pairs in a semiconductor crystal lattice, which results from the absorption of UV (or even visible light in the case of a narrow band gap semiconductor) quanta of energy equal to or higher than the corresponding band gap. The electrons and holes can either recombine, dissipating the absorbed energy as heat, or remain separated and available for redox reactions with electron-donor or acceptor species adsorbed at the semiconductor surface or localized in the electrical double layer surrounding the particle[99].

Titanium dioxide is definitely the most popular and promising material among transition metal semiconductors for photocatalytic applications. $TiO_2$ is both widely commercially available and also easy to prepare by various methods that yield different titania grades. It has been successfully used for the design of many commercial devices that decompose hazardous substances in our living environment based on the strong oxidizing power of its photogenerated holes and its high photostability. So far, we have witnessed the proposal and successful application of photocatalytic phenomena for water purification[100] and disinfection[101], toxic waste treatment[102], air purification and deodorizing[103], and self-cleaning[104], self-disinfecting[105], and superhydrophilic antifogging[106] surfaces.

While photocatalytic processes utilizing the slurried form of a catalyst deliver excellent performances because of their inherently high surface area, a photocatalyst immobilized onto a suitable support is usually the preferred form for practical applications. Upon immobilization, the free surface of the catalyst inevitably decreases, resulting into a loss of catalytic performance because of limited mass transport. Conversely, immobilized systems are not burdened by the need for catalyst recovery, which could otherwise prohibitively increase the operational costs. Both the gas phase deposition and the wet coating method have been successfully adopted for the preparation of immobilized photocatalyst layers[107].

Sol-gel is one of the most successful techniques for preparing nanosized metallic oxide materials with high photocatalytic activities[108]. By tailoring the chemical structure of primary precursor and carefully controlling the processing parameters, nanocrystalline products with very high level of chemical purity can be achieved. In sol-gel processes, $TiO_2$ is usually prepared by the reactions of hydrolysis and polycondensation of titanium alkoxides, Ti(OR)n to form oxopolymers, which are then transformed into an tridimensional network.

In one of our early papers[109], we demonstrated the benefits of using inkjet printing technology for the preparation of $TiO_2$ thin layers and report about some important properties of prepared printed layers of photocatalytically active $TiO_2$. By utilizing the well known sol-gel chemistry used so far mostly for spin- and dip coated layers of $TiO_2$, together with the wide deposition possibilities offered by inkjet printing, we were able to prepare transparent, photocatalytic layers of $TiO_2$ of variable thickness in a very effective and clean way with minimum waste. These layers were also successfully employed for several model pollutant degradation studies[70-73, 110]

While the previous work dealing with inkjet printed titania film focused on direct patterning of various shapes onto substrate, our work was targeted to the fabrication of smooth compact films applicable as self-cleaning surfaces. We managed to prepare samples up to 25 $cm^2$ large. The structure of prepared layers greatly depends on the printing conditions: If the sol ejection rate is faster then solvent evaporation, a smooth compact layer is produced. On the other hand, when the solvent evaporation rate is grater than sol ejection, we obtain optically rough and highly structured layer.

Slowly printed layers have a structured surface at the microscale with the "islet-like" pattern giving them a semi-opaque pearl appearance. Their photocatalytic performance is slightly lower compared to rapidly printed layers. Rapidly printed layers have better optical properties – they are perfectly smooth, even and mirror-like glossy. Their photocatalytic performance is better than the performance of the slowly printed layers probably due to greater roughness at the nanoscale, while the even thickness and smooth surface resulting into a more efficient absorption of UV radiation may also contribute.

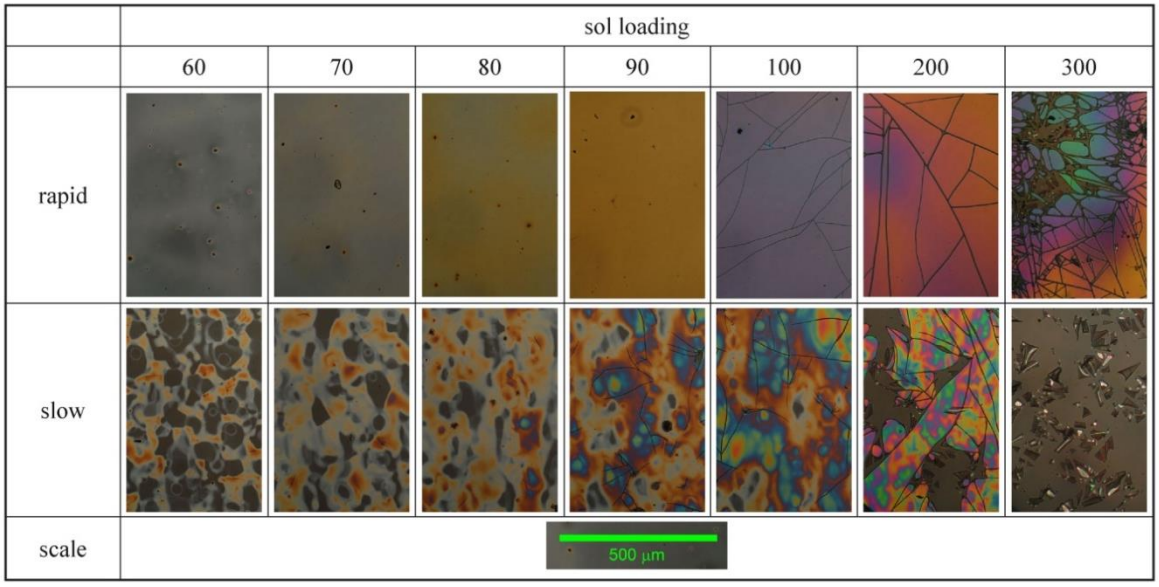


**Fig. 8** *Side-by-side comparison of the "slowly" and "rapidly" printed sample series.*

The photocatalytic activity of $TiO_2$ film depends strongly on the crystal phase structures, thickness and porosity of the thin films. A highly porous surface structure is therefore a very imperative among these factors because it offers amuch larger number of catalytic sites than a dense surface. Porous inorganic $TiO_2$-anatase films can be obtained using templating macromolecular agents[111] or conventional alkoxide sol–gel route with the addition of surfactants[112]. The templates permit to retain the initial polymer morphology up to the final porous structure. Polyethylene glycol is especially suitable for modifying the porous structure of coatings due to its complete decomposition at relatively low temperature.

Printed transparent $TiO_2$ thin films with supressed cracking were successfully prepared using PEG (average molar weigh 1500 g/mol) in a titanium isopropoxide sol–gel system. The PEG plays a key role in stopping the generation of cracks in the layers during the annealing step at a high temperature. Sol coating on the substrate was performed again by inkjet printing with a modified office inkjet printer. We discovered that the PEG concentration of 4 g/L is sufficient for

suppressing the formation all cracks in the layers. When we compared the samples with and without PEG, we found out that with increasing amount of PEG the contact angle is decreasing and so is the value of its initial rate of droplet spreading. It is probably caused by increasing of the roughness with higher PEG concentration. Sample PEG 4 showed the best photocatalytic efficiency. When we compared different sol loading we discovered that the best sample is with 100% sol loading. In the case of thinner layers, the absorption of incident radiation was probably not complete and therefore no general trends were identified.

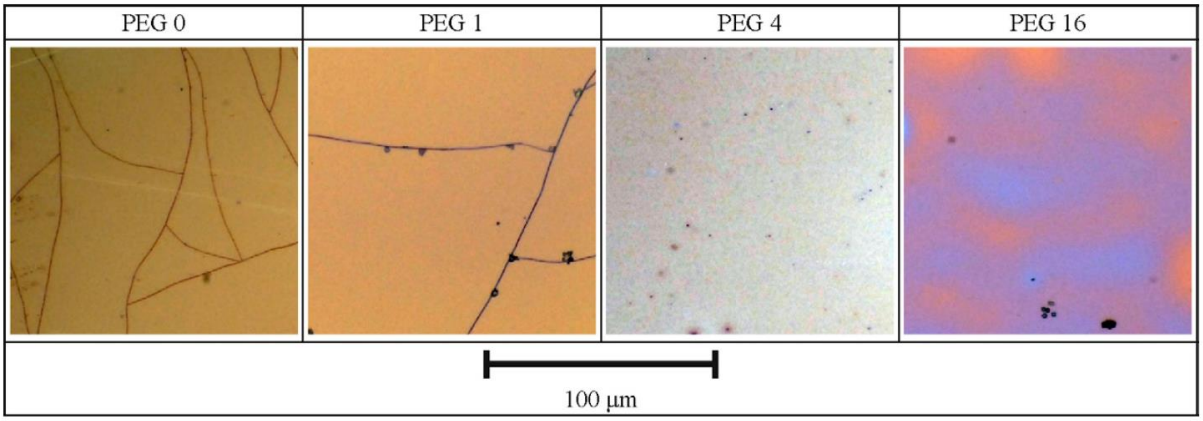


**Fig. 9** *The influence of PEG content (wt.% addition to the sol-gel formulation) on the cracking intensity.*

A special type of titania templating can be induced by the incorporation of the reverse micelles in the sol-gel composition used for coating[38]. We successfully adopted this aproach and developed inkjettable composition based on titanium isopropoxide encapsulated into reverse micelles of Triton X-102 nonionic surfactant suspended in xylen nonpolar continuous phase.[113] The solvent choice and viscosity adjustment issues crucial for the reliable jetting performance were investigated in detail and so were the layer morphology and material properties.

Xylene was found as the suitable optimal non-polar solvent for the reverse micelle sol preparation owing to its low volatility and good surface tension. The printed layers possess smooth, homogeneous and transparent surface with low amount of defects. The photoelectrochemical functionality and photocatalytic efficiency of the inkjet printed $TiO_2$ layers have also been discussed. The photocatalytic degradation of stearic acid revealed strong dependence of photocatalytic activity on the layers thickness. On the contrary, no influence of the layer thickness to photoinduced hydrophilicity has been noticed. It was proved that prepared $TiO_2$/ITO electrodes ($TiO_2$ thin layers on ITO glass used as photoanode) are stable and possess good photoinduced properties. The obtained electrochemical curves of layers reflect the ability to react on UV light signal by generation of the charge carriers. The electrochemical measurements confirmed the high potential of photoelectrochemistry for detection of the semiconductor oxides photoactivity. This study clearly proved the possibility of production of transparent functional thin layers deposited on various substrates by inkjet printing from the liquid sol utilizing the reverse micelles system. Titania layers fabricated in this way were later successfully used as self-cleaning layers, photoanodes and high refraction optical coatings[114-117].

Easy incorporation of doping agents is another worth noting benefit of the sol-gel process[118]. The compatibility of such approach with inkjet printing deposition was clearly demonstrated in a dedicated paper[119]. A series of experiments with different printing conditions was carried out and

the optimum printing settings were indeed determined. Consequently, iron and silver dopants were incorporated into the sol. The influence of doping on the photocatalytic activity of $TiO_2$ as well as the shift of absorption edge towards high wavelengths was investigated.

Iron and silver doped titanium dioxide was synthesized by the sol-gel process employing PEG as the anticracking agent and conveniently deposited by inkjet material printing. The solvent type and concentration in the printing formulation was optimized and the concentration of PEG was set to 4 g/L providing a good compromise between the intensity of its effect and the viscosity increase inevitably accompanying its introduction into the printing formulation. Full rheological characterization was performed and the jetting performance was theoretically evaluated by means of Z-number rheologic model. Empirical jetting behavior confirmed the positive expectations and all formulation showed flawless printability. The Z-number was practically identical for all studied formulations, therefore printed catalyst samples of equal quality were possible to prepare and the influence of added amount of iron and silver on the final physical properties as well as photocatalytic activity were investigated. These samples were compared with pure $TiO_2$ fabricated in the same way.

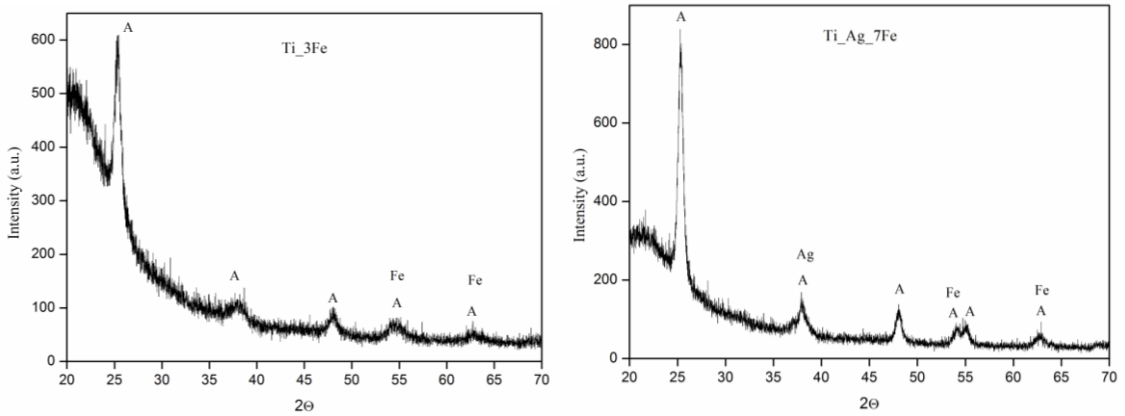


**Fig. 10** *XRD spectra of printed titania layers confirming pure anatas phase (marked by A) and the presence of doping agents Ag and Fe.*

Once well performing jettable compositions were ready, different printing conditions were tested and the quality of created thin films was studied. Temperature of 30°C, droplet pitch 30 μm and two overprinted layers were eventually evaluated as the best conditions. These were eventually used for for the fabrication of the doped samples set investigated in this study. After firing the printed layers at 450 °C, homogeneous compact layers with grain size around 10 nm were obtained.

We observed that structure of the film was only slightly changed with the silver addition. In this case we could observe higher grains. In the case of iron we did not see any differences. From XRD analysis we found out that pure anatase phase was present in all samples. Band gap energy of non-doped titania was determined at 3.20 eV which is a typical value for pure anatase. Subsequently, we observed that with increasing amount of Fe band the gap energy decreased. This decrease of band gap indicates that shift of absorption edge to higher wavelength occurred however it did not lead to increasing of photocatalytic activity. We were not able to measure $E_g$ for silver doped titania because of a uniform dark grey colour of prepared powders resulting into a high absorption of light and very small reflection with no pronounced peaks nor edges.

While the sol-gel route to the design of inkjettable formulations undoubtedly confirmed it viability, there may be situation at which nanocrystalline suspensions may prove more suitable. In another paper[120] we report the influence of different hydrothermal conditions on the physical properties and photocatalytic activity of prepared $TiO_2$. Hydrothermally prepared titania slurries were deposited onto soda-lime glass substrates by material printing and effect of layers thickness was investigated.

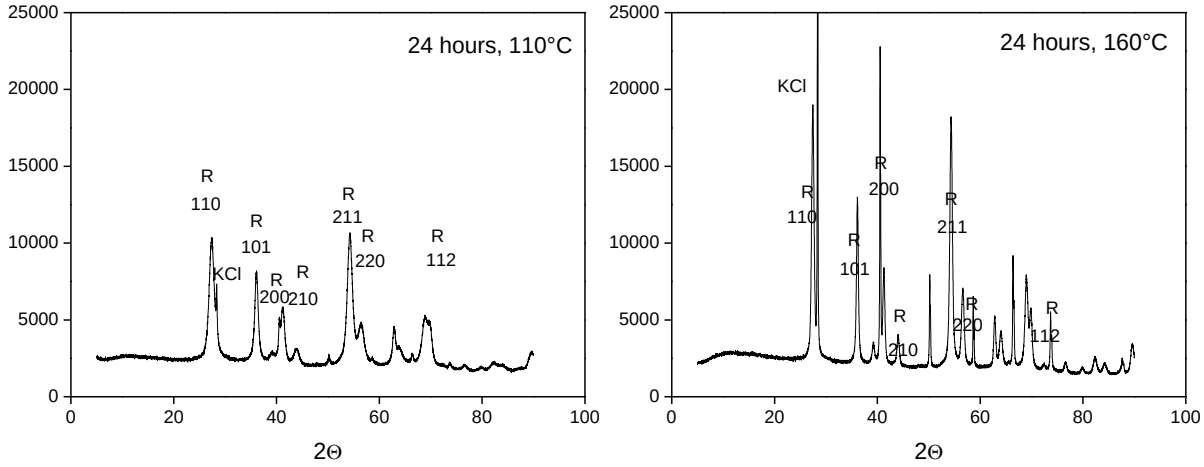


**Fig. 11** *XRD spectra of raw $TiO_2$ powders obtained from slurries synthesized at 110 °C (left) and 160 °C (right)*

In this study, $TiO_2$ colloidal dispersions were conveniently synthesized by the hydrothermal process. TEM analysis shows that particle size decreased with increasing time of synthesis. In all cases, pure rutile was prepared that implies that neither time nor temperature of hydrothermally treatment have significant influence on the final crystalline phase. Phase depends mainly on the pH used and it was the same in all samples in this study. Using a less acidic pH level (2-3) would probably result into the formation of a mixture of anatase and rutile or pure anatase. Another process parameter which could lead to the creation of rutile phase is possibly insufficient washing of the primary slurry. From the band gap energy analysis we found out that all prepared $TiO_2$ samples were direct semiconductors.

The obvious issue inherently associated with the building of nanoparticular layers from suspension is the problem of adhesion of the deposited material to the substrate. Naturally, the aggregated nanoparticles left after solvent evaporation have only very limited adhesion to the substrate and need to be fixed in some way in order to improve this property. The above referenced examples employed the most common solution of this problem, i.e. heat sintering at 300-500 °C. However, more sophisticated solutions have been reported. Cold-setting processes yielding stable titania layers are very attractive for the fabrication of photoelectrochemical functional or auxiliary coatings on the surface of heat sensitive substrates. This is especially true in the case of dye-sensitized solar cells, where the adoption of cheap flexible polymer supports is considered as a necessary condition for commercial success. A great deal of research attention has been therefore paid to this problem and several interesting processes have been reported so far. The key involved mechanisms of titania layer building and fixing include e.g. UV-curing of titanium alkoxide binder[50], the incorporation of mineral binder such as amorphous silica[48], atomic layer deposition over a mesoporous template[121], low temperature CVD fed with custom molecular precursor[122], titanium alkoxide decomposition in supercritical carbon dioxide[123], or cold isostatic pressing of standard P-25 grade of titania[45].

In a recent paper[124], we informed about our development of a hybrid titania-silica cold-setting sol that can be deposited onto a wide variety of surfaces without the need of high-temperature fixing and that is suitable for material printing deposition. We employed a low-temperature modification of the so called brick-and-mortar strategy[47] based on mixing prefabricated nanocrystalline titania "bricks" with "mortar" consisting of amorphous silica binder.

Detailed characterization of physicochemical properties of studied samples indicates excellent mechanical and optical properties, making the reported material well suited for the fabrication of transparent self cleaning coatings both on mineral and organic substrates. The obvious issue of a polymeric substrate resisting to photocatalytic degradation could be easily solved by the introduction of a pure silica barrier layer. The observed photocatalytic activity is superior to commercial CVD originating products even in the case of the thinnest layer used in this study. Coting originated in this way also exhibited interesting biocidic activity.[125]

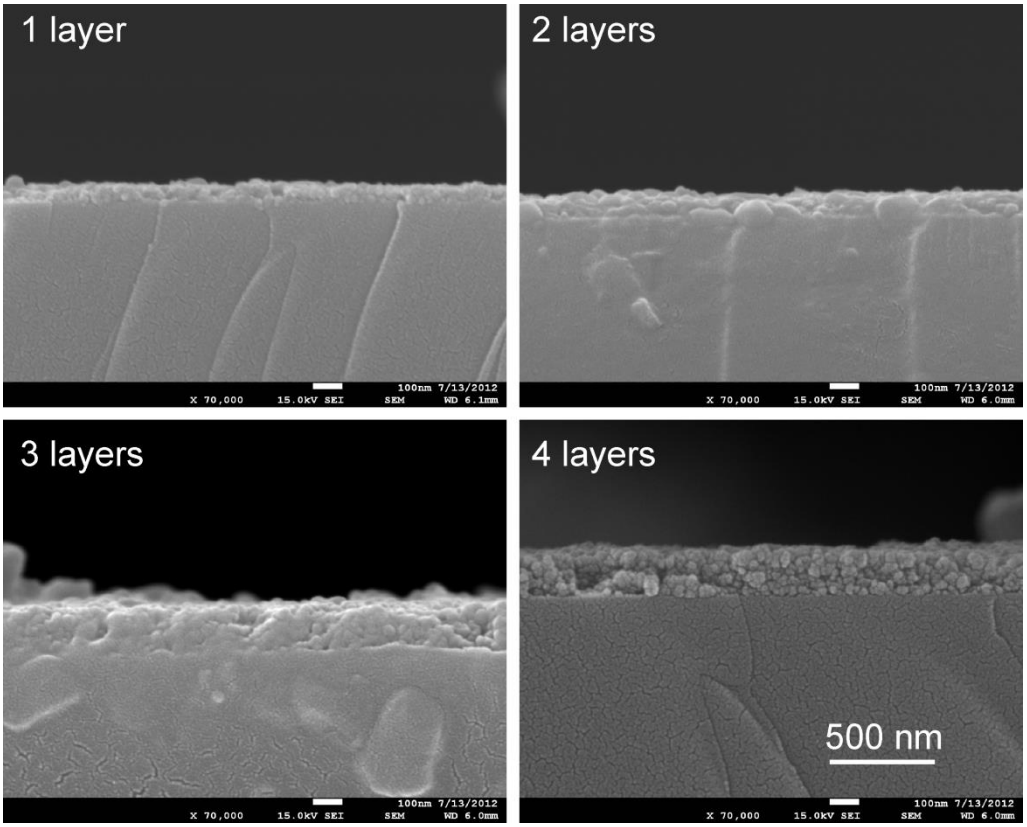


**Fig. 12** *SEM cross section images of studied samples. Various layer thickness can be conveniently achieved by multiple overprinting.*

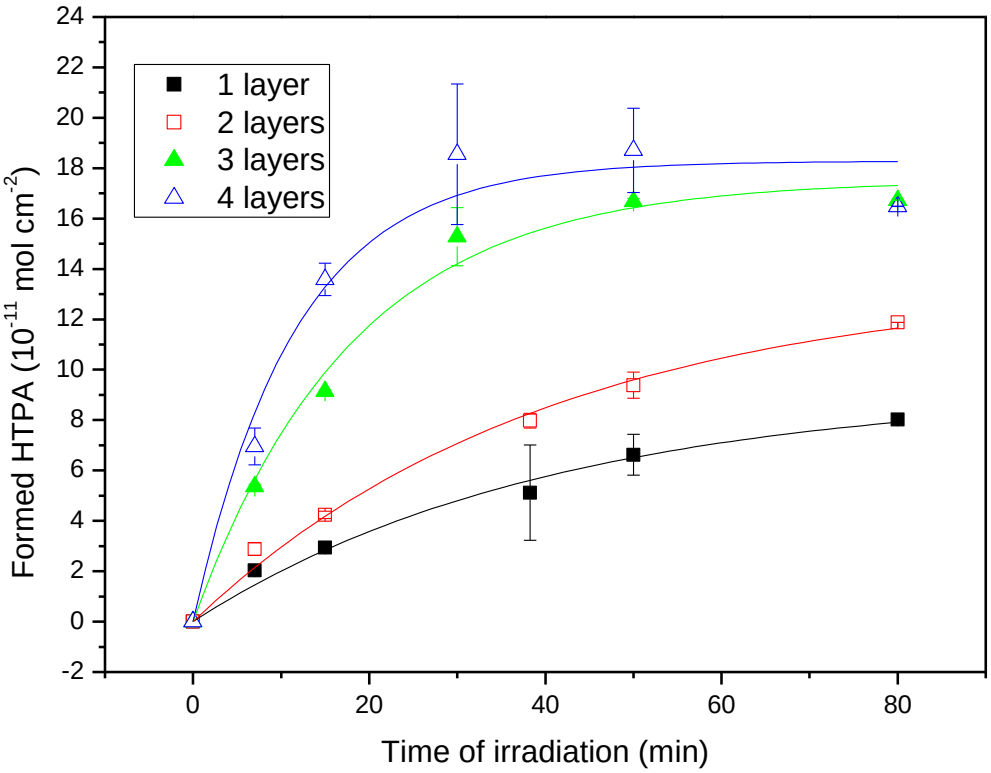


**Fig. 13** *Oxidative activity of printed photocatalytic coating expressed in moles of hydroxyterephtalic acid produced upon UV-A irradiation density of 2 mW/cm$^2$.*

Similar approach has been employed recently for the fabrication of cold setting titania-silica coatings with improved electrical properties[126]. A hybrid organo-silica sol was used as a binder for reinforcing of commercial titanium dioxide nanoparticles (Evonic P25) deposited on glass substrates. The organo-silica binder was prepared by the sol-gel process and mixtures of titania nanoparticles with the binder in various ratios were deposited by materials printing technique. Patterns with both positive and negative features down to 100 μm size and variable thickness were reliably printed by Fujifilm Dimatix inkjet printer. All prepared films well adhered onto substrates, however further post-printing treatment proved to be necessary in order to improve their reactivity. The influence of UV radiation as well as of thermal sintering on the final electrochemical and photocatalytic properties was investigated. A mixture containing 63 wt % of titania delivered a balanced compromise of mechanical stability, generated photocurrent density and photocatalytic activity. Although the heat treated samples yielded generally higher photocurrent, higher photocatalytic activity towards model aqueous pollutant was observed in the case of UV cured samples because of their superhydrophilic properties. While heat sintering remains the superior processing method for inorganic substrates, UV-curing provides a sound treatment option for heat sensitive ones.

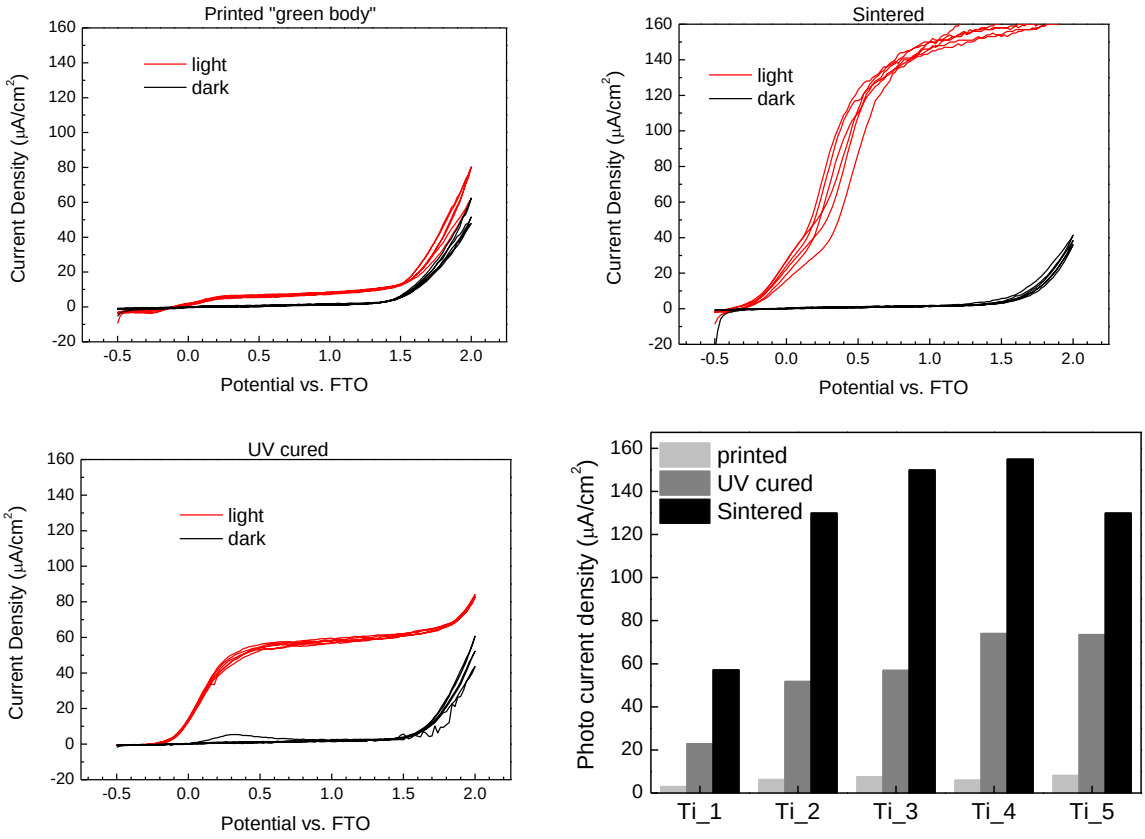


**Fig. 14** *Comparison of generated photocurrents for a printed nanaparticulate titania electrode bonded by an organosilica binder. Printed "green body" electrode (top left), thermally sintered (top right), UV cured (bottom left) and the summary of photocurrent density (μA/cm²) at 1 V potential for all the studied sample sets (bottom right).*

Zinc oxide is another representative on the oxidic semiconductor family with very interesting properties. Its use for conventional photocatalysis is somewhat limited by its tendency to photocorrosion. Anyway, with carefully designed reaction systems, ZnO proved to be useful catalytic material as well[127-128]. Similarly to titania, zinc oxide printing can be performed with inks based on the sol-gel chemistry or on colloidal dispersions of prefabricated crystalline nanoparticles, optionally with a suitable binder.

In a recent paper, we reported on the TiO2/ITO and ZnO/ITO electrodes prepared by piezoelectric ink-jet printing of inks based on the sol-gel chemistry were stable and possessed very good photo-induced functional properties[129]. The obtained electrochemical characteristics reflected the ability to react immediately on the UV light signal by generation the charge carriers. The measurements also confirmed a high potential of the photo-electrochemistry tests for evaluation the role of the used ionic liquids (IL) as electrolytes. The electrochemical system with ILs behaved almost perfectly according to the experimental Walden rule[130]. We believe that the change of polarity decrease with growing alkyl chain results in a rapid change in the photo-electrochemical behaviour for both types of semiconductor layers. The alkyl chain obviously decreased the molar conductivity of the molecule due to decreasing the polarity/mass ratio and increasing the value of the dynamic viscosity, and these properties were clearly reflected in the shape of the recorded polarization curves.

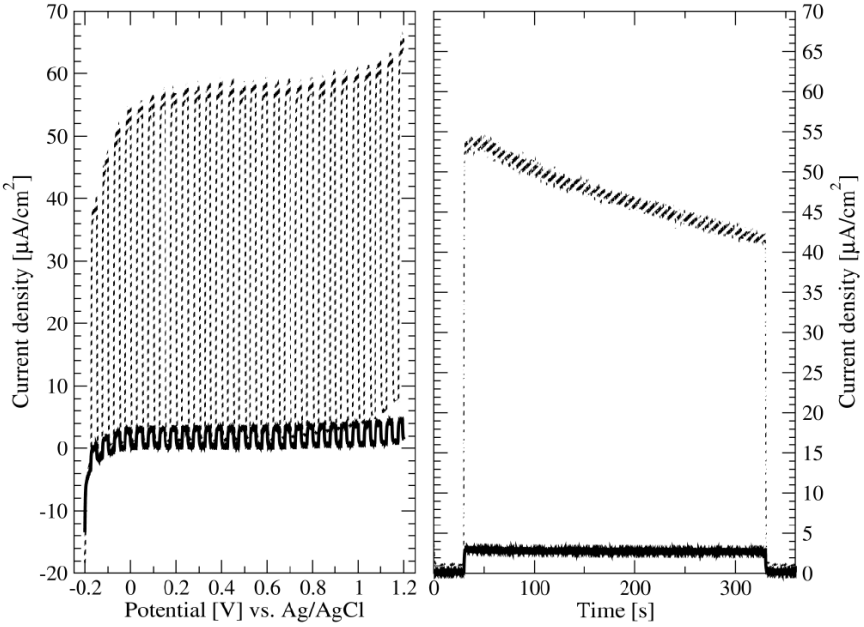


**Fig. 15** *Records from linear sweep voltammetry under chopper irradiation(left) and amperometry with continuous one (right) comparing the photocurrent densities generated by $TiO_2$ (thick line) and ZnO (thin line) electrodes.*

ZnO inks were also successfully formulated as prefabricated nanoparticular dispersions.[131] Thin transparent films were prepared by dip-coating and inkjet-printing of few-layer ZnO nanosheets on glass plates. The advantage of the ZnO nanosheets is the possibility to fabricate transparent and oriented surfaces with exposed high energy facets {001}. The manner of the nanosheets arrangement affected the morphology of the films from very smooth, nonporous dip-coated films to rather rough inkjet-printed films with a surface area in the range of *ca.* 100-160 $m^2g^{-1}$. The 4-chlorophenol photocatalytic degradation rate constants of the nanosheets-based films were approximately 1.5 to 1.7 times larger when compared with the ZnO films with a nanocolumn morphology or with the ZnO films prepared by the sol-gel technique. We attribute the high photocatalytic activity of the ZnO nanosheets to their surface arrangement with the exposed facets {001} towards the oxidized substrate.

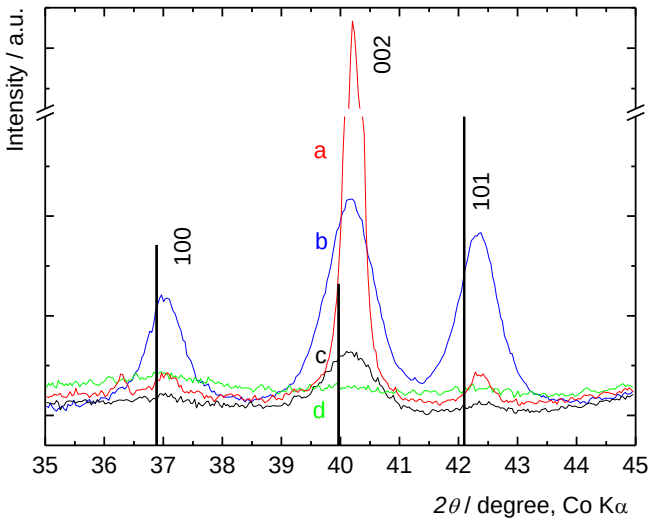


**Fig. 16** *XRD patterns of (a) nanocolumns, (b) inkjet-printed 5 layer film, (c) dip-coated 9 layer film, and (d) sol-gel film.*

Tungsten (VI) is widely studied functional inorganic semiconductor material[132] with some very special properties, notably exceptional electrochromic behavior[133]. It enables attractive application in energy efficient systems (e.g. smart windows), sensors, displays, storage units, electric and photo catalysts and solar cells. The $WO_3$ layers are mostly made by expensive vacuum deposition methods, while our recent contribution we reported inkjet printing of sol-gel derived tungsten solution on glass and transparent conductive oxide.[134] We used the peroxo sol-gel synthesis to prepare the peroxopolytungstic acid sols which were then further modified with different solvents in order to get suitable jetting solution for inkjet printing. Furthermore, we describe the rheological and structural properties of $WO_3$ sols, dynamics of WO3 droplets and the morphology and quality, of $WO_3$ printouts. The functionality of transparent $WO_3$ layers is demonstrated in an electrochromic device.

Most often used methods for $WO_3$ coating fabrication include various chemical vapor deposition arrangements, sputtering or electrodeposition. CVD and RF sputtering are inherently "dry" deposition methods, whereas electrodeposition is a wet method. Also important is the flexibility of RF sputtering deposition conditions, which enables large area deposition of thin films under various conditions. All of these methods give uniform and homogenous layers exhibiting good chromogenic performance with regards to stability, coloration and bleaching kinetics, transmission modulation and coloration effi-ciency. However, electrodeposition is the only low cost conventional procedure with the ability to produce amorphous or nanocrystalline coating over a large area at room temperature. In comparison, inkjet printing is relatively cost efficient, enables selective deposition over a large area, flexibility, and allows the use of different functional materials.

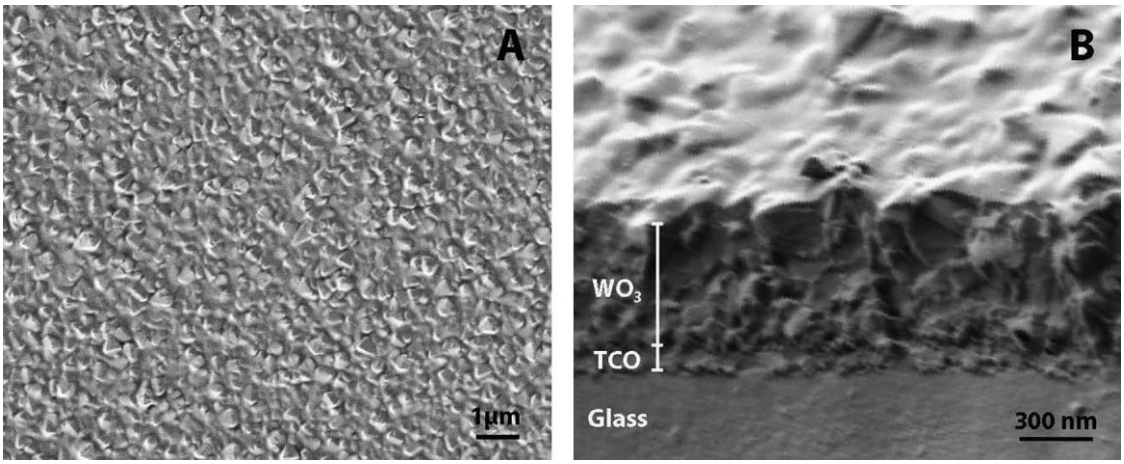


**Fig. 17** *SEM images of a $WO_3$ layer printed on a TCO substrate,surface (A) andcrosssection(B).*

## 4.4 Insulating Species

The number of functional non-conductors which are possible to deposit by inkjet printing is huge and so is the number of potential applications. Below we briefly describe two selected cases which may be of interest to a wider audience. Both were extensively used in our lab for the purpose of evaluating the photocatalytic activity of self-cleaning glass.

Recently, the benefits of photocatalytic activity testing by means of redox indicator inks have been convincingly demonstrated[135]. We adopted this approach and the experiment was performed in a special dedicated photochemical reactor developed by the authors. It consists of a simple housing holding a sample of photocatalytic self-cleaning glass over a collimating lens terminated

optical fibre. This "plate reactor" was further equipped with two LEDs positioned opposite the collimating lens. One of them, emitting at 650 nm, served as the light source for measurement of absorbance with a RedTide USB650 UV-VIS spectrophotometer (Ocean Optics), while the second diode (UVLUX320-HL-3, Roithner LaserTechnik) emitting at 337 nm, served as the actinic radiation source for $TiO_2$ excitation. Irradiance was set to 0.5 $mW \cdot cm^{-2}$. The investigated sample of self-cleaning glass coated with a layer indicator ink[136] containing 2,6-dichloroindophenol, placed in the reactor and the absorbance drop was measured in 5 s increments at 650 nm. While a wire-bar application of the indicator ink is suggested in the referenced paper, we employed the inkjet printing method.

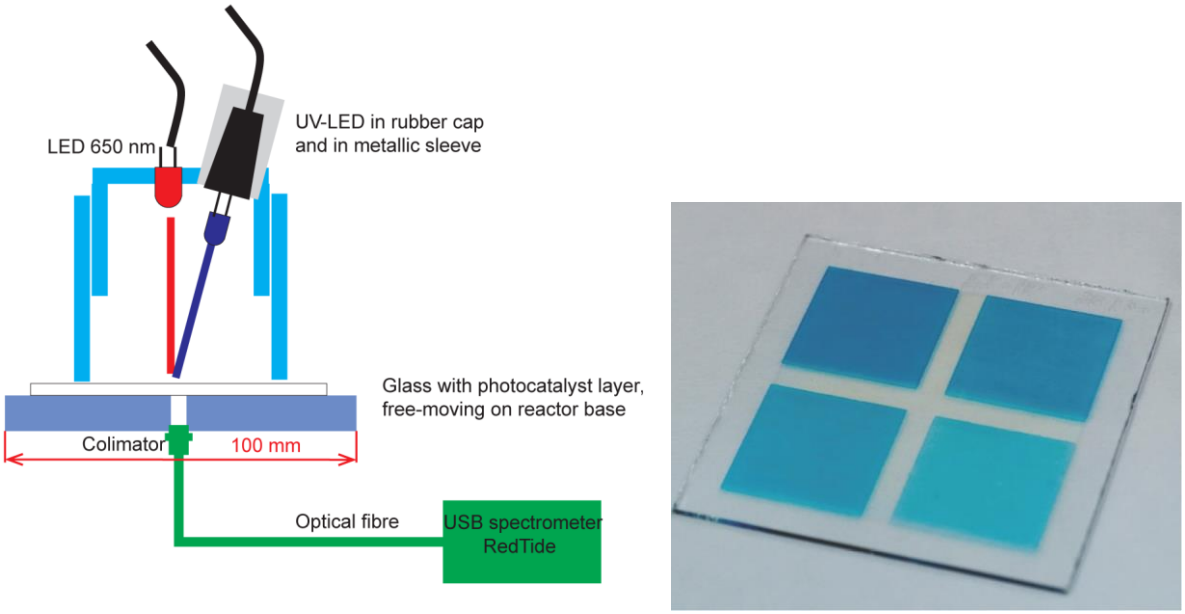


**Fig. 18** *Photochemical reactor for photocatalytic degradation of redox dye ink (left) and a glass slide coated with a photocatalyst overprinted by patches of DCIP inkof various thickness (right)*

Degradation of a dye 2,6-dichloroindophenol to its colourless form is explained as reduction to its leuco-form accompanied by the oxidation of a suitable hole scavenger. [137-138] We discovered that the dependence of relative absorbance on time is linear so it means that photochemical degradation of DCIP ink runs according to the zero order kinetics.[114] The oxidation reaction of the DCIP ink is a complicated process affected namely by glycerol concentration in the polymer layer. The degradation reaction rate can be characterized by its formal rate constant. An experiment with the blank sample (without the photocatalyst) was also carried out and the resulting final value of direct photolysis rate constant of the ink was subtracted from the final measurement rate constant values to obtain the net formal rate constant corresponding to photocatalytic efficiency of tested lyers.

Stearic acid is another attractive model compound because of its similarity to many of the waxy, hydrophobic solids that adhere to glass in the real world. The kinetics of its removal is zero-order, i.e., independent of how much is deposited, except for very thin films.[139] The destruction of stearic acid can be indirectly measured via monitoring the amount of generated $CO_2$ using gas chromatography[140] or FTIR[141], through the change in thickness of the stearic acid film using ellipsometry[142], but the generally preferred and simplest method is by monitoring the disappearance of the infrared absorption[143] of the stearic acid film as a function of time.

We employed the last mentioned approach and integral absorbance values of the printed stearic acid layer in the range of 3200–2600 $cm^{-1}$ were recorded by FTIR spectrometer.In most cases, the observed kinetic profiles obey to the formal first order kinetics, which is consistent with the results reported by other authors.[144-146]

Yet, the kinetic profile of stearic acid degradation is affected by several aspects. It depends on homogeneity, roughness, thickness of photocatalyst and thickness of stearic acid. In the case of a very thin stearic acid layer on a superhydrophilic photocatalyst, the clusters of stearic acid are likely to be formed. Only in this particular case, the degradation rate can be described by the first order kinetics. If the stearic acid is thick and uniform, the degradation rate would obey the zero order kinetics since we can expect a linear decrease of the fatty acid layer thickness. However, the stearic acid degradation kinetics observed on real samples is not unambiguous and usually is between zero and first order kinetics[139].

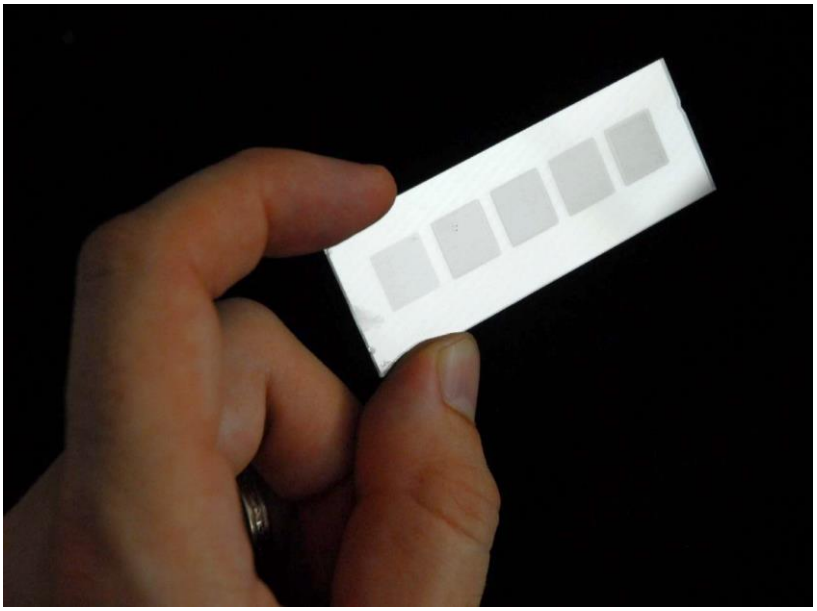

**Fig. 19** *A glass slide coated with a photocatalyst overprinted by patches of stearic acid of various thickness.*

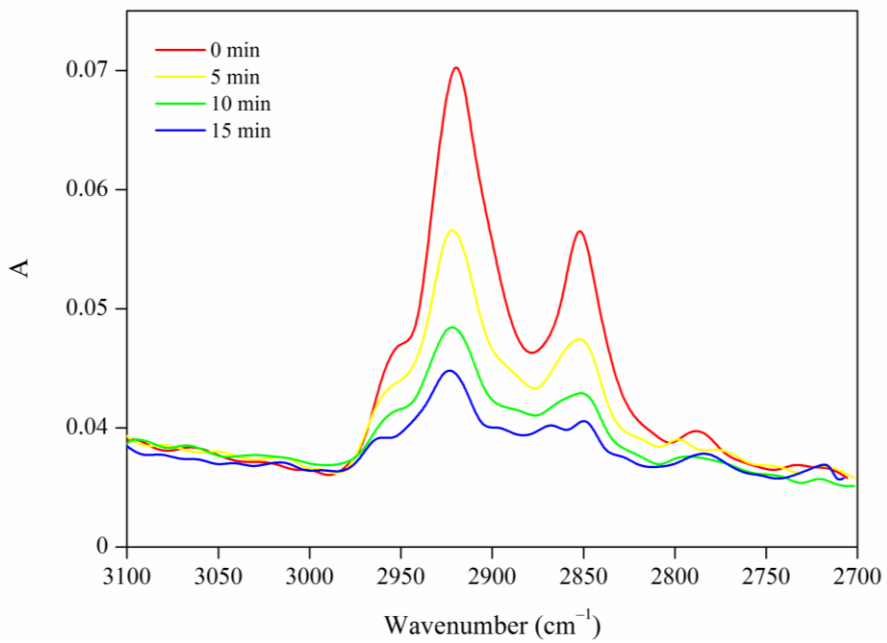


**Fig. 20** *Changes in FTIR transmittance spectra of stearic acid printed onto a photocatalyst layer*

## 5 Examples of a Complex Printed Functional Structures – Printed Electrochemical Cell

The following paragraphs further expand the concept presented above. Printable materials mentioned so far, i.e. conductive, semiconductive and insulating materials, are all used together to make a fully printable functional electrochemical device.

The photocatalytic activity of any immobilized semiconductor photocatalyst can be boosted by the application of external electrical bias.[147] The strategy is based on enhancing the electron–hole separation and consequently increasing the quantum yield of the pollutant degradation by the application of electrical bias, which is possible when the photocatalyst is deposited on an electrically conducting substrate[148-150]. However, in the resulting electrochemical cell, *iR* drop is one of the factors limiting high current throughput at moderate bias. If the treatment of low ionic strength media (drinking water) is envisaged, means for minimizing the *iR* drop must be secured.

One way is to use a parallel plate reactor with two opposite electrodes and a small space between them where the electrolyte is passed through[151]. However, the pressure build-up is considerable in a module consisting of many such cells. This drawback can be avoided by using a planar electrochemical cell with two interdigitated electrodes (IDE). The working electrode consists of an electrical conductor covered by a semiconducting metal oxide (e.g. titanium dioxide). The counter electrode material is not critical as long as sufficient electrical conductivity and corrosion resistance is provided and interdigital geometry is respected. Such a design ensures two key functions: (1) it suppresses the main obstacle to efficient use of absorbed photons, i.e. the recombination of photogenerated charge carriers, by applying external electrical bias to the semiconducting photocatalyst and (2) it avoids the reduction of the generated photocurrent due to *iR* drop, even in electrolytes of low ionic strength. These features make the device an interesting candidate for electrophotocatalytic purification of drinking water.

Material printing seems to be a promising microfabrication method well applicable for the production of planar layered devices, including interdigitated cells. In a recent paper, we adopt the principle of planar electrochemical cells to the versatile method of ink-jet printing allowing for rapid processing and essentially unlimited upscaling, and reported on the design and technology of planar interdigitated photoelectrochemical cells.[152] We employed a mixed subtractive and additive approach and deposited all the functional and auxiliary layers solely by inkjet printing.

Thus planar, interdigitated photoelectrochemical cells were made by ink jet printing. The electrode fingers had widths from 200 to 2000 μm and were revealed by printing a positive protective polymer mask on FTO ($F:SnO_2$) covered glass slides and subsequent etching. One finger family was covered by $TiO_2$, made by using an ink containing the precursor inside inverted micelles and annealing in air. The device was finalized by printing a masking frame around its edges defining the active area. The same UV curable ink and curing procedure was employed for this task.

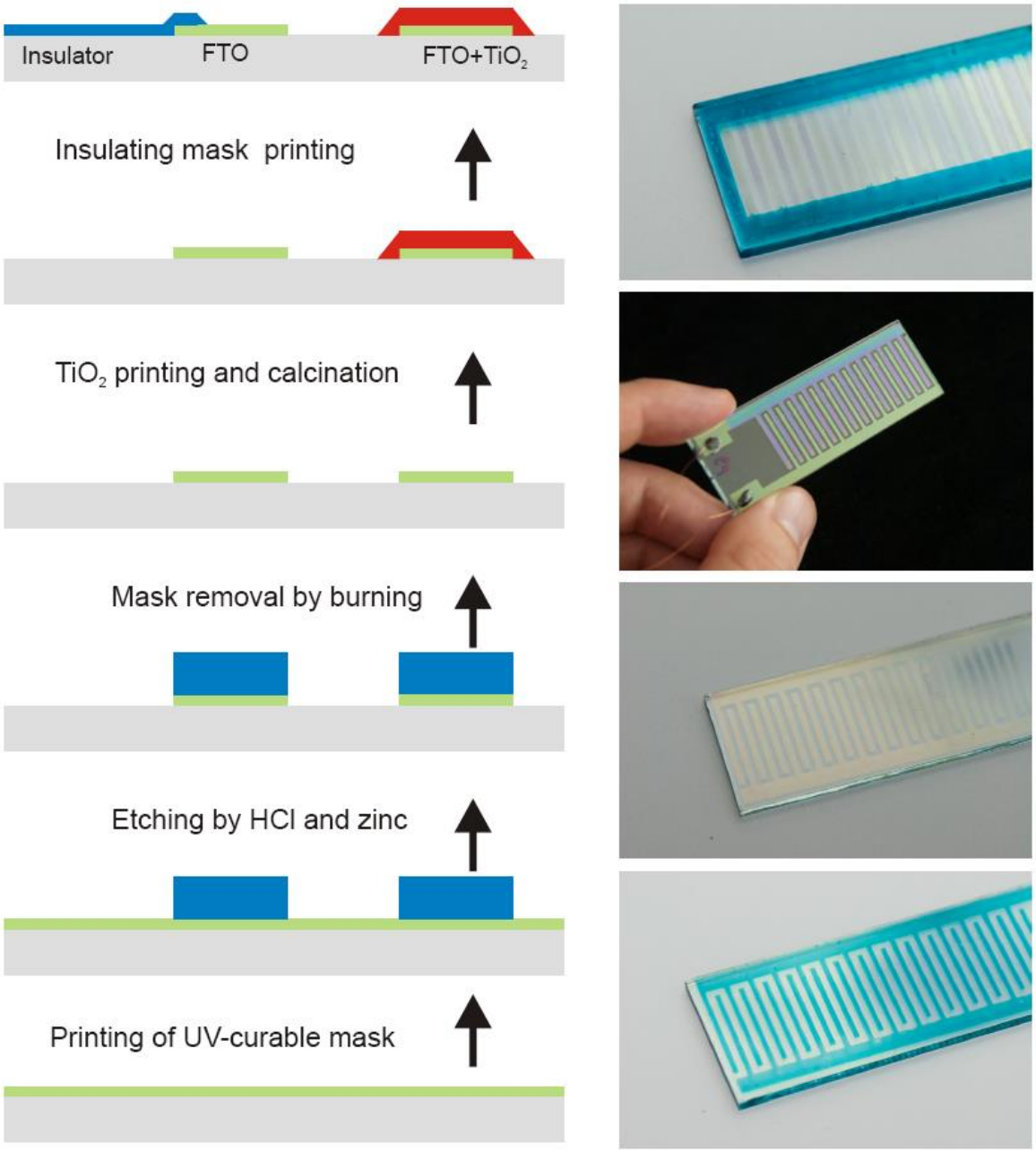


**Fig. 21** *IDE cell fabrication procedure.*

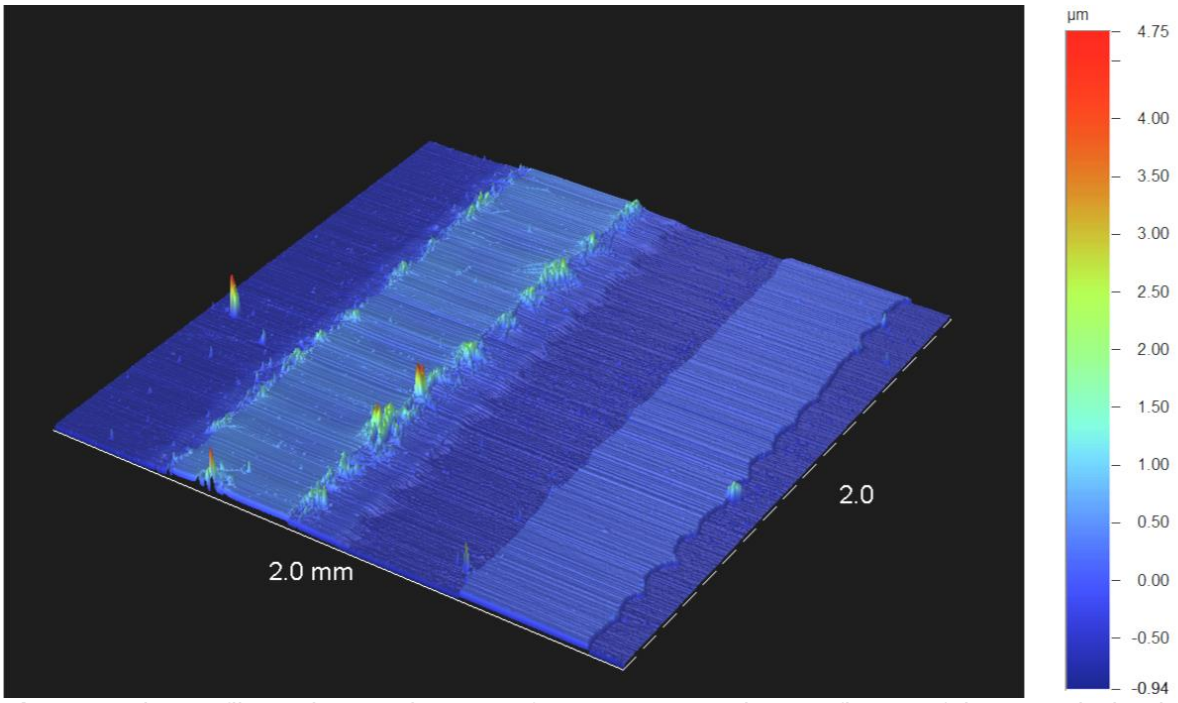


**Fig. 22** *Stylus profilometric scanning map of a segment covering two fingers of the C8-3 device (500-500-500-500 µm, 300 nm titania), where the one on the left is FTO covered by TiO2 and the one on the right FTO.*

A typical photoelectrochemical response of one of the finger devices under continuous UV irradiation and in the dark is depicted at Fig. 23. Three complete cyclic scans were recorded in this measurement in order to confirm the stability and the repeatability. The "UV curve" describes the profile of the total photocurrent delivered by the device, corresponding to the number of free charge carriers generated in the semiconductor and drawn into the external circuit by the applied voltage. The photocurrent steeply increases in the 0-0.5 V range, and then reaches a plateau where the current density is essentially independent on the voltage.

The positive effect of interdigitated electrode design on the cell performance can be illustrated by comparing the response curves in various electrolytes (Fig. 24). Generally, in a conventional electrochemical cell, with decreasing electrolyte conductivity the photocurrent-voltage characteristic should become flatter. However, with the interdigitated design, the ohmic drop is (partially) compensated and therefore the observed current is well conserved – while a photocurrent of 80 µA at 1V bias in sodium sulfate solution of specific conductivity of 4450 µS/cm is flowing, still 70 µA are obtained in a more diluted solution of conductivity 266 µS/cm, and 65 µA in an even more diluted solution of conductivity 30 µS/cm.

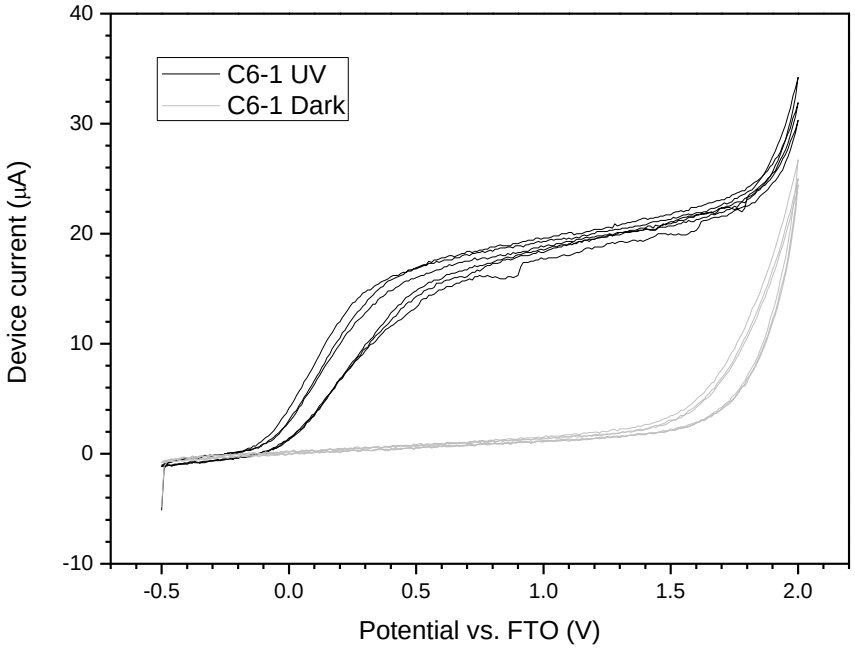


**Fig. 23** *Typical i-V response curve of a printed IDE device (C7-1, 1000-1000-1000-1000 μm, 100 nm titania) under continuous irradiation in 0.1 molar sodium sulfate.*

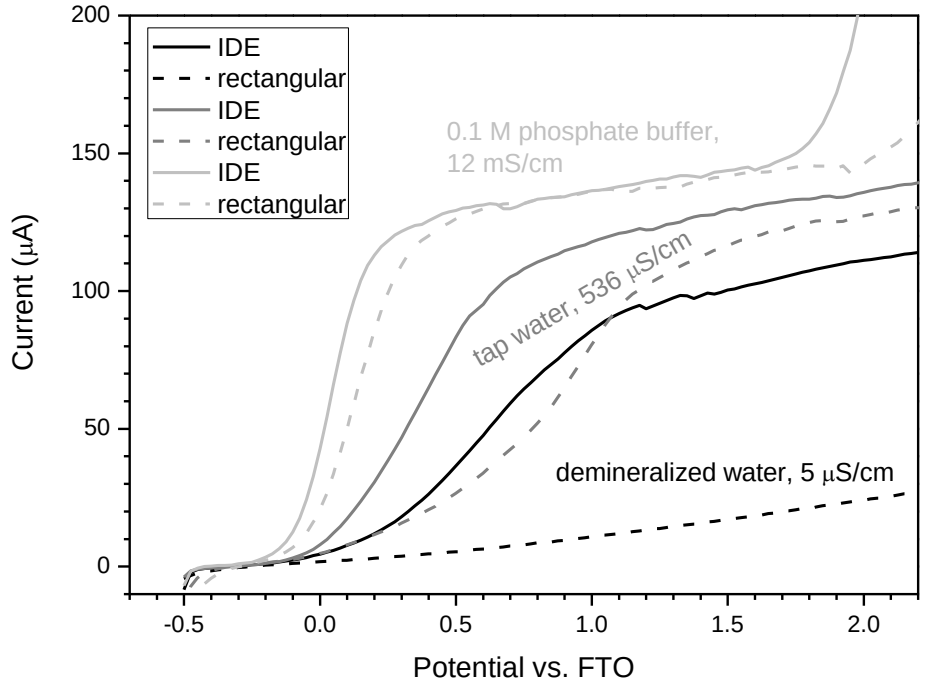


**Fig. 24** *Comparison of i-V response curves of electrodes with rectangular and interdigitated geometries in different electrolytes under continuous irradiation*

An example of photodegradation of a solution of terephthalic acid under UVA irradiation and assisted by electrical bias, using a 1000-1000-1000-1000 device with 200 nm thick $TiO_2$ fingers is shown at Fig. 25Fig. 25 . During the course of the experiment, the fluorescence due to an intermediary product (OH-substituted) increased and would eventually decrease down to zero as the fluorescent intermediate is further oxidised. The fluorescence at 425 nm plotted as a function

of time reflects the initial reaction rate. While the blank checks show essentially no reaction, we can observe a doubling of the reaction rate (with respect to the unbiased case) when an external bias of 1 V was applied. From the initial slopes of the traces, the production rates, $v$, can be calculated taking into account the total volume of the solution. These production rates, considering Farday's law of electrolysis, are related to the electrical charge passed (photocurrent, $i_{photo}$). The Faradaic efficiency, $f$, of the process is calculated using $f = vF / i_{photo}$. The value of 0.009 obtained for the experiment shown in Fig. 9 is satisfactory given the fact that a very low concentration of electroactive species ($1.10^{-5}$ M) was used. Polychromatic light centered at 365 nm was used for this experiment. The IPCE (incident photon-to-current efficiency) was 0.13 at 365 nm for 200 nm thick electrodes. Values of $f$ were found close to values obtained for the degradation of phthalic acid in a parallel plate reactor[153]. While the datasets of the irradiated samples were measured continuously in 10 s intervals, the dark ones needed to be measured discontinuously only a few times during the reaction duration because a single radiation source was used for both catalyst activation and fluorescent probe excitation.

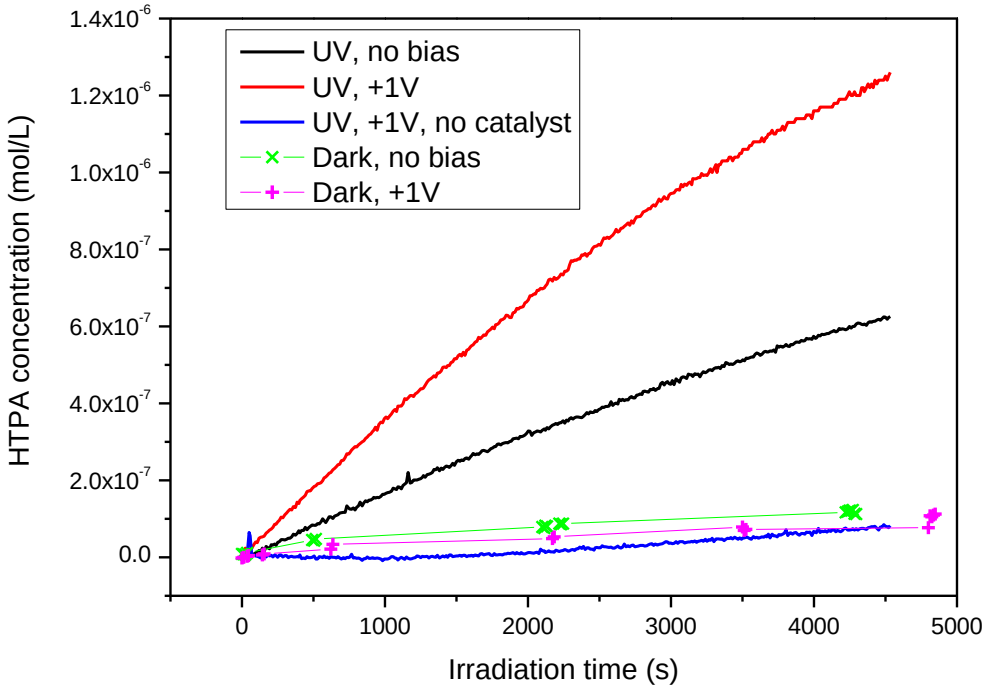


**Fig. 25** *Concentration profiles of HTPA under various experimental conditions*

# 6 Conclusion

This thesis represents a complete account of the author research activities for the past 8 years. The results of all relevant papers were briefly discussed and all the papers are disclosed in chapter 9 of this thesis.

Direct patterning performed by piezoelectric inkjet printing proved to be an attractive method for depositing liquid formulations onto solid supports. It provides clean, efficient and highly repeatable way of coating. Moreover, it is easy to up-scale to coat large substrates by means of industrial large-format printers and at the same time it brings the possibility to produce 2D patterns with micrometer accuracy. These features make direct inkjet patterning one of the prominent deposition techniques for the quickly expanding field of printed electronics.

As far as the insulating species are concerned, two cases dealing with the deposition of indicator inks were discussed. Both are relevant to generally applicable testing of photocatalytic activity of transparent coatings on glass. Stearic acid as well as DCIP were suggested previously as useful indicators. We managed to formulate reliable inks a demonstrated complete systems with dedicated photoreactors allowing highly reproducible testing of photocatalytic activity.

Inkjet printing also proved to be an elegant and efficient method for the fabrication of gold conductor patterns. With modern high speed flatbed printers readily available, the technique is also suited for industrial scale production. While interdigitated electrode systems have been routinely fabricated by screen-printing for the past 50 years, the here proposed fully digital printing workflow eliminates the need for physical printing forms, saves expensive precious metal ink and allows an unlimited freedom in the design of the electrode patterns. The benefits of the presented approach become even more prominent during the fabrication of single prototypes or small batches of large-scale devices, where the dead volume of conventional coating devices would prohibitively increase the production costs.

The greatest deal of attention has been paid to the patterning of transition metal oxide semiconductors. Direct patterning performed by piezoelectric inkjet printing proved to be an attractive method for depositing liquid formulations onto solid supports. Functional inks containing blended colloidal systems (either sol-gel or crystalline nanoparticulate, sometimes with optional silicon based binders) were successfully developed and utilized for the fabrication of titania, zinc oxide and tungsten oxide functional coatings.

Apart from the inkjet material printing of individual materials forming single layers, the fabrication of complex functional structures has been achieved, which is illustrated on the example of planar interdigitated photoelectrochemical cells.

The papers reporting on this research have been published in leading leading high-impact journals and so far have received 52 citations which accounts for the recognition of the work by other researchers.

## 7 List of Papers Included in the Thesis

1. DZIK, P.; VESELÝ, M.; BLAŠKOVÁ, M.; KRÁLOVÁ, M.; NEUMANN-SPALLART, M. Inkjet printed interdigitated cells for photoelectrochemical oxidation of diluted aqueous pollutants. JOURNAL OF APPLIED ELECTROCHEMISTRY, 2015, vol. 45, no. 12, p. 1265-1276. ISSN: 0021-891X.

2. DZIK, P.; VESELÝ, M.; KRÁLOVÁ, M.; NEUMANN-SPALLART, M. Ink- jet printed planar electrochemical cells. APPLIED CATALYSIS B- ENVIRONMENTAL, 2015, vol. 2015, no. 178, p. 186-191. ISSN: 0926-3373.

3. KRÁLOVÁ, M.; DZIK, P.; KAŠPÁREK, V.; VESELÝ, M.; CIHLÁŘ, J. Cold- setting Inkjet Printed Titania Patterns Reinforced by Organosilicate Binder. MOLECULES, 2015, vol. 20, no. 9, p. 16582-16603. ISSN: 1420-3049.

4. VESELÝ, M.; DZIK, P.; VESELÁ, M.; KETE, M.; LAVRENČIČ-ŠTANGAR, U. Photocatalytic and Antimicrobial Activity of Printed Hybrid Titania/ Silica Layers. JOURNAL OF NANOSCIENCE AND NANOTECHNOLOGY, 2015, vol. 15, no. 9, p. 6550-6558. ISSN: 1533-4880.

5. SCHMIEDOVÁ, V.; DZIK, P.; VESELÝ, M.; ZMEŠKAL, O.; MOROZOVÁ, M.; KLUSOŇ, P. Optical properties of titania coatings prepared by inkjet direct patterning of the reverse micelles sol- gel composition. MOLECULES, 2015, vol. 20, no. 8, p. 14552-14564. ISSN: 1420-3049.

6. DZIK, P.; VESELÝ, M.; KETE, M.; PAVLICA, E.; LAVRENČIČ-ŠTANGAR, U.; NEUMANN-SPALLART, M. Properties and Application Perspective of Hybrid Titania-silica Patterns Fabricated by Inkjet Printing. ACS APPL MATER INTER, 2015, vol. 30, no. 7, p. 1-15. ISSN: 1944-8244.

7. KRÁLOVÁ, M.; DZIK, P.; VESELÝ, M.; CIHLÁŘ, J. Preparation and characterization of doped titanium dioxide printed layers. CATALYSIS TODAY, 2014, vol. 230, no. 4, p. 188-196. ISSN: 0920-5861.

8. DYTRYCH, P.; KLUSOŇ, P.; DZIK, P.; VESELÝ, M.; MOROZOVÁ, M.; SEDLÁKOVÁ, Z.; ŠOLCOVÁ, O. Photo- electrochemical properties of ZnO and TiO2 layers in ionic liquid environment. CATALYSIS TODAY, 2014, vol. 2014, no. 230, p. 152-157. ISSN: 0920-5861.

9. VIDMAR, T.; TOPIČ, M.; DZIK, P.; OPARA KRAŠOVEC, U. Inkjet printing of sol– gel derived tungsten oxide inks. SOLAR ENERGY MATERIALS AND SOLAR CELLS, 2014, vol. 2014, no. 125, p. 87-95. ISSN: 0927-0248.

10. HYNEK, J.; KALOUSEK, V.; ZOUZELKA, R.; BEZDICKA, P.; DZIK, P.; RATHOUSKY, J.; DEMEL, J.; LANG, K. High photocatalytic activity of transparent films composed of ZnO nanosheets. Langmuir, 2013, vol. 30, no. 1, p. 380-386. ISSN: 0743-7463.

11. ČERNÁ, M.; VESELÝ, M.; DZIK, P.; GUILLARD, C.; PUZENAT, E.; LEPIČOVÁ, M. Fabrication, characterization and photocatalytic activity of TiO2 layers prepared by inkjet

printing of stabilized nanocrystalline suspensions. APPLIED CATALYSIS B-ENVIRONMENTAL, 2013, vol. 138- 139, no. 0, p. 84-94. ISSN: 0926-3373.

12. MOROZOVA, M.; KLUSON, P.; DZIK, P.; VESELY, M.; BAUDYS, M.; KRYSA, J.; SOLCOVA O. The influence of various deposition techniques on the photoelectrochemical properties of the titanium dioxide thin film. JOURNAL OF SOL- GEL SCIENCE AND TECHNOLOGY, 2013, vol. 65, no. 3, p. 452-458. ISSN: 0928-0707.

13. MOROZOVÁ, M.; KLUSOŇ, P.; KRÝSA, J.; VESELÝ, M.; DZIK, P.; ŠOLCOVÁ, O. Electrochemical Properties of TiO2 Electrode Prepared by Various Methods. Procedia Engineering, 2012, vol. 2012, no. 42, p. 573-580. ISSN: 1877-7058.

14. DZIK, P.; MOROZOVÁ, M.; KLUSOŇ, P.; VESELÝ, M. Photocatalytic and Self-cleaning Properties of Titania Coatings Prepared by Inkjet Direct Patterning of a Reverse Micelles Sol- gel Composition. JOURNAL OF ADVANCED OXIDATION TECHNOLOGIES, 2012, vol. 15, no. 1, p. 89-97. ISSN: 1203-8407.

15. MOROZOVÁ, M.; KLUSOŇ, P.; KRÝSA, J.; DZIK, P.; VESELÝ, M.; ŠOLCOVÁ, O. Thin TiO2 films prepared by inkjet printing of the reverse micelles sol- gel composition. Sensors and Actuators B: Chemical, 2011, vol. 160, no. 1, p. 371-378. ISSN: 0925-4005.

16. ČERNÁ, M.; GUILLARD, C.; PUZENAT, E.; VESELÝ, M.; DZIK, P. Hydrothermal synthesis of TiO2: influence of process conditions on photocatalytic activity. International Journal of Chemical and Environmental Engeneering, 2011, vol. 2, no. 4, p. 255-260. ISSN: 2078-0737.

17. KLAPETEK, P.; VALTR, M.; NEČAS, D.; SALYK, O.; DZIK, P. Atomic force microscopy analysis of nanoparticles in non- ideal conditions. Nanoscale Research Letters, 2011, vol. 6, no. 8, p. 1-9. ISSN: 1931-7573.

18. ČERNÁ, M.; VESELÝ, M.; DZIK, P. Physical and chemical properties of titanium dioxide printed layers. CATALYSIS TODAY, 2011, vol. 161, no. 1, p. 97-104. ISSN: 0920-5861.

19. DZIK, P.; VESELÝ, M.; CHOMOUCKÁ, J. Thin Layers of Photocatalytic TiO2 Prepared by Inkjet Printing of a Solgel Precursor. JOURNAL OF ADVANCED OXIDATION TECHNOLOGIES, 2010, vol. 13, no. 2, p. 172-183. ISSN: 1203-8407.

20. CHOMOUCKÁ, J.; DRBOHLAVOVÁ, J.; DZIK, P.; VESELÁ, M.; VESELÝ, M. The Study of TiO2 Thin Films Photocatalytic Degradation of Yeast and Dye Pollutants. Chemické listy, 2008, vol. 102, no. 15, p. s1037 (s1038 p.) ISSN: 1213-7103.

21. CHOMOUCKÁ, J.; DZIK, P.; VESELÝ, M.; DRBOHLAVOVÁ, J. Photocatalytic Degradation of Formic Acid on TiO2 Thin Layers. Chemické listy, 2008, vol. 102, no. 15, p. s986 (s988 p.) ISSN: 1213-7103.

22. DZIK, P.; VESELÝ, M.; CHOMOUCKÁ, J. Thin Layers of TiO2 Prepared by Inkjet Printing. Chemické listy (S), 2008, vol. 102, no. 15, p. s995 (s998 p.) ISSN: 1803-2389.

23. VESELÝ, M.; DZIK, P.; VESELÁ, M.; DRBOHLAVOVÁ, J.; CHOMOUCKÁ, J. Kinetics of oxidative processes on inkjet- printed thin layers of titanium dioxide. Chemické listy, 2008, vol. 102, no. 15, p. 1029-1032. ISSN: 1213-7103.

24. VESELÁ, M.; VESELÝ, M.; DZIK, P.; CHOMOUCKÁ, J.; ŠUPINOVÁ, L. Fungicidal effect of printed titanium dioxide layers. Chemické listy, 2008, vol. 102, no. 15, p. 505-506. ISSN: 1213-7103.

# 8 References


1. Khan, S.; Lorenzelli, L.; Dahiya, R. S., Technologies for Printing Sensors and Electronics Over Large Flexible Substrates: A Review. *IEEE Sens. J.* **2015,** *15* (6), 3164-3185.
2. Sternkiker, C.; Sowade, E.; Mitra, K. Y.; Zichner, R.; Baumann, R. R., Upscaling of the Inkjet Printing Process for the Manufacturing of Passive Electronic Devices. *Ieee Transactions on Electron Devices* **2016,** *63* (1), 426-431.
3. Choi, H. W.; Zhou, T.; Singh, M.; Jabbour, G. E., Recent developments and directions in printed nanomaterials. *Nanoscale* **2015,** *7* (8), 3338-3355.
4. Barbulovic-Nad, I.; Lucente, M.; Sun, Y.; Zhang, M. J.; Wheeler, A. R.; Bussmann, M., Bio-microarray fabrication techniques - A review. *Crit. Rev. Biotechnol.* **2006,** *26* (4), 237-259.
5. Martin, G. D.; Hoath, S. D.; Hutchings, I. M.; Iop In *Inkjet printing - the physics of manipulating liquid jets and drops*, Conference on Engineering in Physics - Synergy for Success, London, ENGLAND, Oct 05; London, ENGLAND, **2006**.
6. Ballarin, B.; Fraleoni-Morgera, A.; Frascaro, D.; Marazzita, S.; Piana, C.; Setti, L., Thermal inkjet microdeposition of PEDOT : PSS on ITO-coated glass and characterization of the obtained film. *Synth. Met.* **2004,** *146* (2), 201-205.
7. Morrin, A.; Ngamna, O.; O'Malley, E.; Kent, N.; Moulton, S. E.; Wallace, G. G.; Smyth, M. R.; Killard, A. J., The fabrication and characterization of inkjet-printed polyaniline nanoparticle films. *Electrochimica Acta* **2008,** *53* (16), 5092-5099.
8. Yoshioka, Y.; Jabbour, G. E., Desktop inkjet printer as a tool to print conducting polymers. *Synthetic Metals* **2006,** *156* (11-13), 779-783.
9. Taylor, A. D.; Kim, E. Y.; Humes, V. P.; Kizuka, J.; Thompson, L. T., Inkjet printing of carbon supported platinum 3-D catalyst layers for use in fuel cells. *J. Power Sources* **2007,** *171* (1), 101-106.
10. Radulescu, D.; Dhar, S.; Young, C. M.; Taylor, D. W.; Trost, H. J.; Hayes, D. J.; Evans, G. R. In *Tissue engineering scaffolds for nerve regeneration manufactured by ink-jet technology*, Symposium on Next Generation Biomaterals, Pittsburgh, PA, Sep 25-28; Pittsburgh, PA, **2005**; pp 534-539.
11. Zhang, C. H.; Wen, X. J.; Vyavahare, N. R.; Boland, T., Synthesis and characterization of biodegradable elastomeric polyurethane scaffolds fabricated by the inkjet technique. *Biomaterials* **2008,** *29* (28), 3781-3791.
12. Xu, T.; Gregory, C. A.; Molnar, P.; Cui, X.; Jalota, S.; Bhaduri, S. B.; Boland, T., Viability and electrophysiology of neural cell structures generated by the inkjet printing method. *Biomaterials* **2006,** *27* (19), 3580-3588.
13. Xu, T.; Jin, J.; Gregory, C.; Hickman, J. J.; Boland, T., Inkjet printing of viable mammalian cells. *Biomaterials* **2005,** *26* (1), 93-99.
14. Liu, Y.; Cui, T. H.; Varahramyan, K., All-polymer capacitor fabricated with inkjet printing technique. *Solid-State Electronics* **2003,** *47* (9), 1543-1548.
15. Kawase, T.; Shimoda, T.; Newsome, C.; Sirringhaus, H.; Friend, R. H. In *Inkjet printing of polymer thin film transistors*, 5th International Conference on Nano-Molecular Electronics (ICNME2002), Kobe, Japan, Dec 10-12; Kobe, Japan, **2002**; pp 279-287.

16. Chen, B.; Cui, T. H.; Liu, Y.; Varahramyan, K., All-polymer RC filter circuits fabricated with inkjet printing technology. *Solid-State Electronics* **2003,** *47* (5), 841-847.

17. Bharathan, J.; Yang, Y., Polymer electroluminescent devices processed by inkjet printing: I. Polymer light-emitting logo. *Applied Physics Letters* **1998,** *72* (21), 2660-2662.

18. Jung, J.; Kim, D.; Lim, J.; Lee, C.; Yoon, S. C., Highly Efficient Inkjet-Printed Organic Photovoltaic Cells. *Japanese Journal of Applied Physics* **2010,** *49* (5).

19. Dzik, P.; Veselý, M.; Králová, M.; Neumann-Spallart, M., Ink-jet printed planar electrochemical cells. *Appl. Catal., B* (0).

20. Putz, J.; Aegerter, M. A., Versatile wet deposition techniques for functional oxide coatings on glass. *Glass Sci. Technol.* **2004,** *77* (5), 229-238.

21. Giessmann, A., *Coating Substrates and Textiles - A Practical Guide to Coating and Laminating*. Springer-Verlag Berlin Heidelberg: **2015**; p 246.

22. Krebs, F. C., Fabrication and processing of polymer solar cells: A review of printing and coating techniques. *Sol. Energy Mater. Sol. Cells* **2009,** *93* (4), 394-412.

23. Schubert, D. W.; Dunkel, T., Spin coating from a molecular point of view: its concentration regimes, influence of molar mass and distribution. *Mater. Res. Innovations* **2003,** *7* (5), 314-321.

24. Malek, M. F.; Mamat, M. H.; Zahidi, M. M.; Sahdan, M. Z.; Mahmood, M. R., Factors Affecting the Properties of Zinc Oxide Thin Films Prepared by Dip-Coating Method: A Review. *Nanosynthesis and Nanodevice* **2013,** *667*, 193-199.

25. Heinzl, J.; Hertz, C. H., INK-JET PRINTING. *Adv. Imaging Electron Phys.* **1985,** *65*, 91-171.

26. Tekin, E.; Smith, P. J.; Schubert, U. S., Inkjet printing as a deposition and patterning tool for polymers and inorganic particles. *Soft Matter* **2012,** *4* (4), 703-713.

27. Creagh, L. T.; Schoeppler, M. W.; Is, *Ink jet tools for precision fabrication*. **2005**; p 6-7.

28. Rioboo, R.; Marengo, M.; Tropea, C., Time evolution of liquid drop impact onto solid, dry surfaces. *Exp. Fluids* **2002,** *33* (1), 112-124.

29. Fromm, J. E., NUMERICAL-CALCULATION OF THE FLUID-DYNAMICS OF DROP-ON-DEMAND JETS. *IBM J. Res. Dev.* **1984,** *28* (3), 322-333.

30. Reis, N.; Derby, B. In *Ink jet deposition of ceramic suspensions: Modelling and experiments of droplet formation*, Symposium on Materials Development for Direct Write Technologies, San Francisco, Ca, 2000, Apr 24-26; San Francisco, Ca, **2000**; pp 65-70.

31. Jang, D.; Kim, D.; Moon, J., Influence of Fluid Physical Properties on Ink-Jet Printability. *Langmuir* **2009,** *25* (5), 2629-2635.

32. Wang, M. W.; Pang, D. C.; Tseng, Y. E.; Tseng, C. C., The study of light guide plate fabricated by inkjet printing technique. *Journal of the Taiwan Institute of Chemical Engineers* **2014,** *45* (3), 1049-1055.

33. Attia, S. M.; Wang, J.; Wu, G. M.; Shen, J.; Ma, J. H., Review on sol-gel derived coatings: Process, techniques and optical applications. *J. Mater. Sci. Technol.* **2002,** *18* (3), 211-218.

34. Bartkova, H.; Kluson, P.; Bartek, L.; Drobek, M.; Cajthaml, T.; Krysa, J., Photoelectrochemical and photocatalytic properties of titanium (IV) oxide nanoparticulate layers. *Thin Solid Films* **2007,** *515* (24), 8455-8460.

35. Zori, M. H.; Soleimani-Gorgani, A., Ink-jet printing of micro-emulsion TiO2 nano-particles ink on the surface of glass. *J. Eur. Ceram. Soc.* **2012,** *32* (16), 4271-4277.

36. Černá, M.; Veselý, M.; Dzik, P., Physical and chemical properties of titanium dioxide printed layers. *Catal. Today* **2011,** *161* (1), 97-104.

37. Arconada, N.; Duran, A.; Suarez, S.; Portela, R.; Coronado, J. M.; Sanchez, B.; Castro, Y., Synthesis and photocatalytic properties of dense and porous TiO2-anatase thin films prepared by sol-gel. *Appl. Catal., B* **2009,** *86* (1-2), 1-7.

38. Morozova, M.; Kluson, P.; Krysa, J.; Zlamal, M.; Solcova, O.; Kment, S.; Steck, T., Role of the template molecular structure on the photo-electrochemical functionality of the sol-gel titania thin films. *J. Sol-Gel Sci. Technol.* **2009,** *52* (3), 398-407.

39. Bernacka-Wojcik, I.; Senadeera, R.; Wojcik, P. J.; Silva, L. B.; Doria, G.; Baptista, P.; Aguas, H.; Fortunato, E.; Martins, R., Inkjet printed and "doctor blade" TiO2 photodetectors for DNA biosensors. *Biosens. Bioelectron.* **2010,** *25* (5), 1229-1234.

40. Yang, M.; Li, L. H.; Zhang, S. Q.; Li, G. Y.; Zhao, H. J., Preparation, characterisation and sensing application of inkjet-printed nanostructured TiO2 photoanode. *Sens. Actuators, B* **2010,** *147* (2), 622-628.

41. Arin, M.; Lommens, P.; Hopkins, S. C.; Pollefeyt, G.; Van der Eycken, J.; Ricart, S.; Granados, X.; Glowacki, B. A.; Van Driessche, I., Deposition of photocatalytically active TiO2 films by inkjet printing of TiO2 nanoparticle suspensions obtained from microwave-assisted hydrothermal synthesis. *Nanotechnology* **2012,** *23* (16), 165603-165613.

42. Makwana, N. M.; Tighe, C. J.; Gruar, R. I.; McMillan, P. F.; Darr, J. A., Pilot plant scale continuous hydrothermal synthesis of nano-titania; effect of size on photocatalytic activity. *Mater. Sci. Semicond. Process.* **2016,** *42*, 131-137.

43. M., C.; C., G.; E., P.; M., V.; P., D., Hydrothermal synthesis of TiO2: influence of process conditions on photocatalytic activity. *International journal of chemical and environmental engineering* **2011,** *2*, 255-260.

44. Burgues-Ceballos, I.; Stella, M.; Lacharmoise, P.; Martinez-Ferrero, E., Towards industrialization of polymer solar cells: material processing for upscaling. *J. Mater. Chem. A* **2014,** *2* (42), 17711-17722.

45. Weerasinghe, H. C.; Sirimanne, P. M.; Simon, G. P.; Cheng, Y. B., Cold isostatic pressing technique for producing highly efficient flexible dye-sensitised solar cells on plastic substrates. *Prog. Photovoltaics* **2012,** *20* (3), 321-332.

46. Drahi, E.; Blayac, S.; Borbely, A.; Benaben, P., Impact of ink synthesis on processing of inkjet-printed silicon nanoparticle thin films: A comparison of Rapid Thermal Annealing and photonic sintering. *Thin Solid Films* **2015,** *574*, 169-176.

47. Szeifert, J. M.; Fattakhova-Rohlfing, D.; Rathousky, J.; Bein, T., Multilayered High Surface Area "Brick and Mortar" Mesoporous Titania Films as Efficient Anodes in Dye-Sensitized Solar Cells. *Chem. Mater.* **2012,** *24* (4), 659-663.

48. Shibata, H.; Sakai, H.; Rangsunvigit, P.; Hirano, T.; Abe, M., Preparation and photocatalytic activity of titania particulate film with silica as binder. *Surf. Coat. Int., Part B* **2003,** *86* (2), 125-130.

49. Neo, C. Y.; Ouyang, J., Graphene oxide as auxiliary binder for TiO2 nanoparticle coating to more effectively fabricate dye-sensitized solar cells. *J. Power Sources* **2013,** *222*, 161-168.

50. Oh, Y.; Lee, S. N.; Kim, H. K.; Kim, J., UV-Assisted Chemical Sintering of Inkjet-Printed TiO2 Photoelectrodes for Low-Temperature Flexible Dye-Sensitized Solar Cells. *J. Electrochem. Soc.* **2012,** *159* (10), H777-H781.

51. Gregori, D.; Benchenaa, I.; Chaput, F.; Therias, S.; Gardette, J. L.; Leonard, D.; Guillard, C.; Parola, S., Mechanically stable and photocatalytically active TiO2/SiO2 hybrid films on flexible organic substrates. *J. Mater. Chem. A* **2014,** *2* (47), 20096-20104.

52. Singh, M.; Haverinen, H. M.; Dhagat, P.; Jabbour, G. E., Inkjet printing-process and its applications. *Advanced Materrials* **2010,** *22* (6), 673-685.

53. Park, J.-U.; Hardy, M.; Kang, S. J.; Barton, K.; Adair, K.; Mukhopadhyay, D. K.; Lee, C. Y.; Strano, M. S.; Alleyne, A. G.; Georgiadis, J. G.; Ferreira, P. M.; Rogers, J. A., High-resolution electrohydrodynamic jet printing. *Nature Materials* **2007,** *6* (10), 782-789.

54. Lee, M. W.; An, S.; Kim, N. Y.; Seo, J. H.; Huh, J.-Y.; Kim, H. Y.; Yoon, S. S., Effects of pulsing frequency on characteristics of electrohydrodynamic inkjet using micro-Al and nano-Ag particles. *Exp. Therm Fluid Sci.* **2013,** *46*, 103-110.

55. Choi, H. K.; Park, J.-U.; Park, O. O.; Ferreira, P. M.; Georgiadis, J. G.; Rogers, J. A., Scaling laws for jet pulsations associated with high-resolution electrohydrodynamic printing. *Appl. Phys. Lett.* **2008,** *92* (12).

56. Liu, Y.-F.; Tsai, M.-H.; Pai, Y.-F.; Hwang, W.-S., Control of droplet formation by operating waveform for inks with various viscosities in piezoelectric inkjet printing. *Applied Physics a-Materials Science & Processing* **2013,** *111* (2), 509-516.

57. Sousa, S. C. L.; Mendes, A. D.; Fiadeiro, P. T.; Ramos, A. M. M., Dynamic Interactions of Pigment-Based Inks on Chemically Modified Papers and Their Influence on Inkjet Print Quality. *Industrial & Engineering Chemistry Research* **2014,** *53* (12), 4660-4668.

58. Deegan, R. D.; Bakajin, O.; Dupont, T. F.; Huber, G.; Nagel, S. R.; Witten, T. A., Capillary flow as the cause of ring stains from dried liquid drops. *Nature* **1997,** *389* (6653), 827-829.

59. Sun, J.; Kuang, M.; Song, Y., Control and Application of "Coffee Ring" Effect in Inkjet Printing. *Progress in Chemistry* **2015,** *27* (8), 979-985.

60. Wang, T. M.; Roberts, M. A.; Kinloch, I. A.; Derby, B., Inkjet printed carbon nanotube networks: the influence of drop spacing and drying on electrical properties. *Journal of Physics D-Applied Physics* **2012,** *45* (31).

61. Soltman, D.; Subramanian, V., Inkjet-printed line morphologies and temperature control of the coffee ring effect. *Langmuir* **2008,** *24* (5), 2224-2231.

62. Chung, S.; Ul Karim, M. A.; Spencer, M.; Kwon, H.-J.; Grigoropoulos, C. P.; Alon, E.; Subramanian, V., Exploitation of the coffee-ring effect to realize mechanically enhanced inkjet-printed microelectromechanical relays with U-bar-shaped cantilevers. *Appl. Phys. Lett.* **2014,** *105* (26).

63. Graddage, N.; Chu, T.-Y.; Ding, H.; Py, C.; Dadvand, A.; Tao, Y., Inkjet printed thin and uniform dielectrics for capacitors and organic thin film transistors enabled by the coffee ring effect. *Org. Electron.* **2016,** *29*, 114-119.

64. Jung, S.; Hoath, S. D.; Martin, G. D.; Hutchings, I. M., A New Method to Assess the Jetting Behavior of Drop-on-Demand Ink Jet Fluids. *J. Imaging Sci. Technol.* **2011,** *55* (1).

65. Chow, E.; Herrmann, J.; Barton, C. S.; Raguse, B.; Wieczorek, L., Inkjet-printed gold nanoparticle chemiresistors: Influence of film morphology and ionic strength on the detection of organics dissolved in aqueous solution. *Anal. Chim. Acta* **2009,** *632* (1), 135-142.

66. Roper, J. A.; Urscheler, R.; Salminen, P.; Moore, E.; Tappi, Optimization of formulation parameters to reduce misting and orange peel formation on metered film coaters. *Metered Size Press Forum Ii - 1998 Tappi Proceedings* **1998**, 37-55.

67. KigleBoeckler, G., Measuring gloss and reflection properties of surfaces. *Tappi J.* **1996,** *79* (9), 194-198.

68. Matsuta, M., NEW, PORTABLE ORANGE PEEL METER FOR PAINT COATINGS. *J. Coat. Technol.* **1987,** *59* (754), 61-64.

69. Stclair, W. E.; Minor, J. C.; Lawrence, R. V., FUSED METAL RESINATES FROM ALDEHYDE-MODIFIED ROSIN. *Ind. Eng. Chem.* **1954,** *46* (9), 1973-1976.

70. Chomoucká, J.; Dzik, P.; Veselý, M.; Drbohlavová, J.; Puzenat, E.; Guilard, C., Photocatalytic degradation of formic acid on TiO2 thin layers. *Chem. Listy* **2008,** *102* (15 SPEC. ISS.), s986-s988.

71. Chomoucká, J.; Drbohlavová, J.; Dzik, P.; Veselá, M.; Veselý, M., P01 the study of TiO2 thin films photocatalytic activity on degradation of yeast and dye pollutants. *Chem. Listy* **2008,** *102* (15 SPEC. ISS.), s1037-s1038.

72. Veselá, M.; Veselý, M.; Dzik, P.; Chomoucká, J.; Šupinová, L., Fungicidal effect of printed titanium dioxide layers. *Chem. Listy* **2008,** *102* (15 SPEC. ISS.), s505-s506.

73. Veselý, M.; Dzik, P.; Veselá, M.; Drbohlavová, J.; Chomoucká, J., L18 kinetics of oxidative processes on inkjet-printed thin layers of titanium dioxide. *Chem. Listy* **2008,** *102* (15 SPEC. ISS.), s1029-s1032.

74. Kim, D.; Jeong, S.; Lee, S.; Park, B. K.; Moon, J., Organic thin film transistor using silver electrodes by the ink-jet printing technology. *Thin Solid Films* **2007,** *515* (19), 7692-7696.

75. Shim, I.-K.; Lee, Y. I.; Lee, K. J.; Joung, J., An organometallic route to highly monodispersed silver nanoparticles and their application to ink-jet printing. *Mater. Chem. Phys.* **2008,** *110* (2-3), 316-321.

76. Eom, S. H.; Senthilarasu, S.; Uthirakumar, P.; Hong, C. H.; Lee, Y. S.; Lim, J. S.; Yoon, S. C.; Lee, C. J.; Lee, S. H., Preparation and characterization of nano-scale ZnO as a buffer layer for inkjet printing of silver cathode in polymer solar cells. *Sol. Energy Mater. Sol. Cells* **2008,** *92* (5), 564-570.

77. Ryu, B. H.; Choi, Y.; Park, H. S.; Byun, J. H.; Kong, K.; Lee, J. O.; Chang, H., Synthesis of highly concentrated silver nanosol and its application to inkjet printing. *Colloids and Surfaces a-Physicochemical and Engineering Aspects* **2005,** *270*, 345-351.

78. Cui, W.; Lu, W.; Zhang, Y.; Lin, G.; Wei, T.; Jiang, L., Gold nanoparticle ink suitable for electric-conductive pattern fabrication using in ink-jet printing technology. *Colloids and Surfaces a-Physicochemical and Engineering Aspects* **2010,** *358* (1-3), 35-41.

79. Tseng, C.-C.; Chang, C.-P.; Sung, Y.; Chen, Y.-C.; Ger, M.-D., A novel method to produce Pd nanoparticle ink for ink-jet printing technology. *Colloids and Surfaces a-Physicochemical and Engineering Aspects* **2009,** *339* (1-3), 206-210.

80. Klapetek, P.; Valtr, M.; Necas, D.; Salyk, O.; Dzik, P., Atomic force microscopy analysis of nanoparticles in non-ideal conditions. *Nanoscale Research Letters* **2011,** *6*.

81. Wu, J.-T.; Hsu, S. L.-C.; Tsai, M.-H.; Hwang, W.-S., Conductive silver patterns via ethylene glycol vapor reduction of ink-jet printed silver nitrate tracks on a polyimide substrate. *Thin Solid Films* **2009,** *517* (20), 5913-5917.

82. Jahn, S. F.; Jakob, A.; Blaudeck, T.; Schmidt, P.; Lang, H.; Baumann, R. R., Inkjet printing of conductive patterns with an aqueous solution of AgO2C(CH2OCH2)(3)H without any additional stabilizing ligands. *Thin Solid Films* **2010,** *518* (12), 3218-3222.

83. Busato, S.; Belloli, A.; Ermanni, P., Inkjet printing of palladium catalyst patterns on polyimide film for electroless copper plating. *Sens. Actuators, B* **2007,** *123* (2), 840-846.

84. Prinsen, P., THIN RESISTIVE THICK-FILM LAYERS BASED ON PRECIOUS METAL RESINATE-GLASS SYSTEMS. *Electrocomponent Science and Technology* **1978,** *5* (1), 41-43.

85. Takechi, S.; Abe, N., DIRECT PATTERNING USING METALLOORGANICS AND ITS APPLICATION TO MASK REPAIR. *Polym. Eng. Sci.* **1992,** *32* (21), 1605-1609.

86. Jung, H.-W.; Chang, Y. W.; Lee, G.-Y.; Cho, S.; Kang, M.-J.; Pyun, J.-C., A capacitive biosensor based on an interdigitated electrode with nanoislands. *Anal. Chim. Acta* **2014,** *844*, 27-34.

87. Guadarrama-Santana, A.; Garcia-Valenzuela, A.; Perez-Jimenez, F.; Polo-Parada, L., Interdigitated capacitance sensors in the mm scale with sub-femtoFarad resolution suitable for monitoring processes in liquid films. *Revista Mexicana De Fisica* **2014,** *60* (6), 451-459.

88. Neumann-Spallart, M., Photoelectrochemistry on a planar, interdigitated electrochemical cell. *Electrochim. Acta* **2011,** *56* (24), 8752-8757.

89. Fu, Y.; Callaway, Z.; Lum, J.; Wang, R.; Lin, J.; Li, Y., Exploiting Enzyme Catalysis in Ultra-Low Ion Strength Media for Impedance Biosensing of Avian Influenza Virus Using a Bare Interdigitated Electrode. *Anal. Chem.* **2014,** *86* (4), 1965-1971.

90. Zhao, Y.; Zhang, J.; Liu, S.; Gao, Y.; Yang, X.; Leck, K. S.; Abiyasa, A. P.; Divayana, Y.; Mutlugun, E.; Tan, S. T.; Xiong, Q.; Demir, H. V.; Sun, X. W., Transition metal oxides on organic semiconductors. *Org. Electron.* **2014,** *15* (4), 871-877.

91. Jeong, Y. H.; Han, S. J.; Park, J. H.; Lee, Y. H., A critical examination of room temperature ferromagnetism in transition metal-doped oxide semiconductors. *J. Magn. Magn. Mater.* **2004,** *272*, 1976-1980.

92. Li, H.; Duan, L.; Qiu, Y., Mechanisms of Charge Transport in Transition Metal Oxide Doped Organic Semiconductors. *J. Phys. Chem. C* **2014,** *118* (51), 29636-29642.

93. Mann, D. P.; Pratt, K. F. E.; Paraskeva, T.; Parkin, I. P.; Williams, D. E., Transition metal exchanged zeolite layers for selectivity enhancement of metal-oxide semiconductor gas sensors. *IEEE Sens. J.* **2007,** *7* (3-4), 551-556.

94. Mizokawa, T., Photoemission study of layered transition-metal oxides and oxide-based diluted magnetic semiconductors. *J. Phys. Chem. Solids* **2004,** *65* (8-9), 1409-1415.

95. Schembry, H.; Hepel, M., Nanostructured transition-metal oxide semiconductor photoanodes. *Abstracts of Papers of the American Chemical Society* **2012,** *244*.

96. Fujishima, A.; Honda, K., Electrochemical Photolysis of Water at a Semiconductor Electrode. *Nature* **1972,** *238* (5358), 37-38.

97. Chen, X.; Shaohua, S.; Guo, L.; Mao, S. S., Semiconductor-based photocatalytic hydrogen generation. *Chem. Rev.* **2010,** *110* (11), 6503-70.

98. Pelaez, M.; Nolan, N. T.; Pillai, S. C.; Seery, M. K.; Falaras, P.; Kontos, A. G.; Dunlop, P. S. M.; Hamilton, J. W. J.; Byrne, J. A.; O'Shea, K.; Entezari, M. H.; Dionysiou, D. D., A review on the visible light active titanium dioxide photocatalysts for environmental applications. *Appl. Catal., B* **2012,** *125* (0), 331-349.

99. Fujishima, A.; Hashimoto, K.; Watanabe, T., *TiO2 photocatalysis : fundamentals and applications*. Bkc: Tokyo, **1999**.

100. Silva, C. P.; Otero, M.; Esteves, V., Processes for the elimination of estrogenic steroid hormones from water: a review. In *Environmental Pollution*, 2012 Elsevier Ltd: England, **2012**, pp 38-58.

101. Mahmood, M.; Baruah, S.; Anal, A.; Dutta, J., Heterogeneous photocatalysis for removal of microbes from water. *Environ. Chem. Lett.* **2012,** *10* (2), 145-151.

102. Vinu, R.; Madras, G., Environmental remediation by photocatalysis. *J. Indian Inst. Sci.* **2010,** *90* (2), 189-230.

103. Park, S.; Kim, H. R.; Bang, H.; Fujimori, K.; Kim, B. S.; Kim, S. H.; Kim, I. S., Fabrication and deodorizing efficiency of nanostructured core-sheath TiO2 nanofibers. *J. Appl. Polym. Sci.* **2012,** *125* (4), 2929-2935.

104. Wang, C. Y.; Tang, H. J.; Pang, S. H.; Qiu, J. X.; Tao, Y., Enhancing sunlight photocatalytic efficiency of self-cleaning glass by coating ZnFe2O4-TiO2 film. *Rare Metal Materials and Engineering* **2008,** *37*, 548-551.

105. Dunlop, P. S. M.; Sheeran, C. P.; Byrne, J. A.; McMahon, M. A. S.; Boyle, M. A.; McGuigan, K. G., Inactivation of clinically relevant pathogens by photocatalytic coatings. *J. Photochem. Photobiol., A* **2010,** *216* (2–3), 303-310.

106. Gan, W. Y.; Lam, S. W.; Chiang, K.; Amal, R.; Zhao, H. J.; Brungs, M. P., Novel TiO2 thin film with non-UV activated superwetting and antifogging behaviours. *J. Mater. Chem.* **2007,** *17* (10), 952-954.

107. Sobczyk-Guzenda, A.; Pietrzyk, B.; Szymanowski, H.; Gazicki-Lipman, M.; Jakubowski, W., Photocatalytic activity of thin TiO2 films deposited using sol–gel and plasma enhanced chemical vapor deposition methods. *Ceram. Int.* **2013,** *39* (3), 2787–2794.

108. Macwan, D. P.; Dave, P. N.; Chaturvedi, S., A review on nano-TiO2 sol-gel type syntheses and its applications. *J. Mater. Sci.* **2011,** *46* (11), 3669-3686.

109. Dzik, P.; Vesely, M.; Chomoucka, J., Thin Layers of Photocatalytic TiO2 Prepared by Inkjet Printing of a Solgel Precursor. *J. Adv. Oxid. Technol.* **2010,** *13* (2), 172-183.

110. Dzik, P.; Chomoucká, J.; Veselý, M., Thin layers of TiO2 prepared by inkjet printing. *Chem. Listy* **2008,** *102* (15 SPEC. ISS.), s995-s998.

111. Samsudin, E. M.; Abd Hamid, S. B.; Juan, J. C.; Basirun, W. J., Influence of triblock copolymer (pluronic F127) on enhancing the physico-chemical properties and photocatalytic response of mesoporous TiO2. *Appl. Surf. Sci.* **2015,** *355*, 959-968.

112. Kluson, P.; Kacer, P., Preliminary specification of the structure of photoactive TiO2 by the surfactant-mediated sol-gel method. *Chem. Listy* **2000,** *94* (7), 432-436.

113. Morozova, M.; Kluson, P.; Krysa, J.; Dzik, P.; Vesely, M.; Solcova, O., Thin TiO 2 films prepared by inkjet printing of the reverse micelles sol-gel composition. *Sens. Actuators, B* **2011,** *160* (1), 371-378.

114. Dzik, P.; Morozová, M.; Klusoň, P.; Veselý, M., Photocatalytic and self-cleaning properties of titania coatings prepared by inkjet direct patterning of a reverse micelles sol-gel composition. *J. Adv. Oxid. Technol.* **2012,** *15* (1), 89-97.

115. Morozova, M.; Kluson, P.; Krysa, J.; Vesely, M.; Dzik, P.; Solcova, O. In *Electrochemical properties of TiO2 electrode prepared by various methods*, Procedia Engineering, Prague, Prague, **2012**; pp 573-580.

116. Schmiedova, V.; Dzik, P.; Vesely, M.; Zmeskal, O.; Morozova, M.; Kluson, P., Optical Properties of Titania Coatings Prepared by Inkjet Direct Patterning of a Reverse Micelles Sol-Gel Composition. *Molecules* **2015,** *20* (8), 14552.

117. Morozova, M.; Kluson, P.; Dzik, P.; Vesely, M.; Baudys, M.; Krysa, J.; Solcova, O., The influence of various deposition techniques on the photoelectrochemical properties of the titanium dioxide thin film. *J. Sol-Gel Sci. Technol.* **2013,** *65* (3), 452-458.

118. Akpan, U. G.; Hameed, B. H., The advancements in sol-gel method of doped-TiO2 photocatalysts. *Applied Catalysis a-General* **2010,** *375* (1), 1-11.

119. Kralova, M.; Dzik, P.; Vesely, M.; Cihlar, J., Preparation and characterization of doped titanium dioxide printed layers. *Catal. Today* **2014,** *230*, 188-196.

120. černá, M.; Veselý, M.; Dzik, P.; Guillard, C.; Puzenat, E.; Lepičová, M., Fabrication, characterization and photocatalytic activity of TiO2 layers prepared by inkjet printing of stabilized nanocrystalline suspensions. *Appl. Catal., B* **2013,** *138-139*, 84-94.

121. Chandiran, A. K.; Yella, A.; Stefik, M.; Heiniger, L. P.; Comte, P.; Nazeeruddin, M. K.; Gratzel, M., Low-Temperature Crystalline Titanium Dioxide by Atomic Layer Deposition for Dye-Sensitized Solar Cells. *ACS Appl. Mater. Interfaces* **2013,** *5* (8), 3487-3493.

122. Gilmer, D. C.; Gladfelter, W. L.; Colombo, D. G.; Taylor, C. J.; Roberts, J.; Campbell, S. A.; Kim, H. S.; Wilk, G. D.; Gribelyuk, M. A., Low temperature chemical vapor deposition of titanium dioxide thin films using tetranitratotitanium(IV). In *Chemical Aspects of Electronic Ceramics Processing*, Kumta, P. N.; Hepp, A. F.; Beach, D. B.; Arkles, B.; Sullivan, J. J., Eds. **1998**, pp 45-50.

123. Uchida, H.; Otsubo, A.; Itatani, K.; Koda, S., Low-temperature deposition of polycrystalline titanium oxide thin film on Si substrate using supercritical carbon dioxide fluid. *Jpn. J. Appl. Phys., Part 1* **2005,** *44* (4A), 1901-1906.

124. Dzik, P.; Veselý, M.; Kete, M.; Pavlica, E.; Štangar, U. L.; Neumann-Spallart, M., Properties and Application Perspective of Hybrid Titania-Silica Patterns Fabricated by Inkjet Printing. *ACS Appl. Mater. Interfaces* **2015,** *7* (30), 16177-16190.

125. Vesely, M.; Dzik, P.; Vesela, M.; Kete, M.; Stangar, U. L., Photocatalytic and Antimicrobial Activity of Printed Hybrid Titania/Silica Layers. *Journal of Nanoscience and Nanotechnology* **2015,** *15* (9), 6550-6558.

126. Králová, M.; Dzik, P.; Kašpárek, V.; Veselý, M.; Cihlář, J., Cold-Setting Inkjet Printed Titania Patterns Reinforced by Organosilicate Binder. *Molecules* **2015,** *20* (9), 16582.

127. Han, C.; Yang, M.-Q.; Weng, B.; Xu, Y.-J., Improving the photocatalytic activity and anti-photocorrosion of semiconductor ZnO by coupling with versatile carbon. *PCCP* **2014,** *16* (32), 16891-16903.

128. Vu, T. T.; del Rio, L.; Valdes-Solis, T.; Marban, G., Fabrication of wire mesh-supported ZnO photocatalysts protected against photocorrosion. *Appl. Catal., B* **2013,** *140*, 189-198.

129. Dytrych, P.; Kluson, P.; Dzik, P.; Vesely, M.; Morozova, M.; Sedlakova, Z.; Solcovaa, O., Photo-electrochemical properties of ZnO and TiO2 layers in ionic liquid environment. *Catal. Today* **2014,** *230*, 152-157.

130. Constantin, V.; Adya, A. K.; Popescu, A.-M., Density, transport properties and electrochemical potential windows for the 2-hydroxy-N,N,N-trimethylethanaminium chlorides based ionic liquids at several temperatures. *Fluid Phase Equilib.* **2015,** *395*, 58-66.

131. Hynek, J.; Kalousek, V.; Zouzelka, R.; Bezdicka, P.; Dzik, P.; Rathousky, J.; Demel, J.; Lang, K., High Photocatalytic Activity of Transparent Films Composed of ZnO Nanosheets. *Langmuir* **2014,** *30* (1), 380-386.

132. Bignozzi, C. A.; Caramori, S.; Cristino, V.; Argazzi, R.; Meda, L.; Tacca, A., Nanostructured photoelectrodes based on WO3: applications to photooxidation of aqueous electrolytes. *Chem. Soc. Rev.* **2013,** *42* (6), 2228-2246.

133. Li, C.; Hsieh, J. H.; Hung, M.-T.; Huang, B. Q., Electrochromic study on amorphous tungsten oxide films by sputtering. *Thin Solid Films* **2015,** *587*, 75-82.

134. Vidmar, T.; Topic, M.; Dzik, P.; Krasovec, U. O., Inkjet printing of sol-gel derived tungsten oxide inks. *Sol. Energy Mater. Sol. Cells* **2014,** *125*, 87-95.

135. Mills, A.; Hepburn, J.; McFarlane, M., A Novel, Fast-Responding, Indicator Ink for Thin Film Photocatalytic Surfaces. *ACS Appl. Mater. Interfaces* **2009,** *1* (6), 1163-1165.

136. Mills, A.; McGrady, M.; Wang, J.; Hepburn, J., A Rapid Method of Assessing the Photocatalytic Activity of Thin Films Using an Ink Based on the Redox Dye 2,6-Dichloroindophenol. *International Journal of Photoenergy* **2008,** *2008*, 6.

137. Mills, A.; McGrady, M., A study of new photocatalyst indicator inks. *Journal of Photochemistry and Photobiology A: Chemistry* **2008,** *193* (2–3), 228-236.

138. Mills, A.; McGrady, M.; Wang, J.; Hepburn, J., A rapid method of assessing the photocatalytic activity of thin TiO2 films using an ink based on the redox dye 2,6-dichloroindophenol. *Int. J. Photoenergy* **2008**, No pp. given.

139. Ollis, D., Kinetics of photocatalyzed film removal on self-cleaning surfaces: Simple configurations and useful models. *Appl. Catal., B* **2010,** *99* (3–4), 478-484.

140. Hidaka, H.; Yamada, S.; Suenaga, S.; Zhao, J.; Serpone, N.; Pelizzetti, E., Photodegradation of surfactants: Part vi complete photocatalytic degradation of anionic, cationic and nonionic surfactants in aqueous semiconductor dispersions. *J. Mol. Catal.* **1990,** *59* (3), 279-290.

141. Mills, A.; Wang, J., Simultaneous monitoring of the destruction of stearic acid and generation of carbon dioxide by self-cleaning semiconductor photocatalytic films. *J. Photochem. Photobiol., A* **2006,** *182* (2), 181-186.

142. Remillard, J. T.; McBride, J. R.; Nietering, K. E.; Drews, A. R.; Zhang, X., Real Time in Situ Spectroscopic Ellipsometry Studies of the Photocatalytic Oxidation of Stearic Acid on Titania Films. *The Journal of Physical Chemistry B* **2000,** *104* (18), 4440-4447.

143. Paz, Y.; Luo, Z.; Rabenberg, L.; Heller, A., Photooxidative self-cleaning transparent titanium dioxide films on glass. *J. Mater. Res.* **1995,** *10* (11), 2842-2848.

144. Limage, H.; Tichelaar, F. D.; Closset, R.; Delvaux, S.; Cloots, R.; Lucas, S., Study of the effect of a silver nanoparticle seeding layer on the crystallisation temperature, photoinduced hydrophylic and catalytic properties of TiO2 thin films deposited on glass by magnetron sputtering. *Surf. Coat. Technol.* **2011,** *205* (13–14), 3774-3778.

145. Peruchon, L.; Puzenat, E.; Girard-Egrot, A.; Blum, L.; Herrmann, J. M.; Guillard, C., Characterization of self-cleaning glasses using Langmuir–Blodgett technique to control thickness of stearic acid multilayers: Importance of spectral emission to define standard test. *J. Photochem. Photobiol., A* **2008,** *197* (2–3), 170-176.

146. Piispanen, M.; Hupa, L., Comparison of self-cleaning properties of three titania coatings on float glass. *Appl. Surf. Sci.* **2011,** *258* (3), 1126-1131.

147. Neumann-Spallart, M., Aspects of photocatalysis on semiconductors: Photoelectrocatalysis. *Chimia* **2007,** *61* (12), 806-809.

148. Waldner, G.; Bruger, A.; Gaikwad, N. S.; Neumann-Spallart, M., WO3 thin films for photoelectrochemical purification of water. *Chemosphere* **2007,** *67* (4), 779-784.

149. Fernandez-Ibanez, P.; Malato, S.; Enea, O., Photoelectrochemical reactors for the solar decontamination of water. *Catal. Today* **1999,** *54* (2-3), 329-339.

150. Butterfield, I. M.; Christensen, P. A.; Hamnett, A.; Shaw, K. E.; Walker, G. M.; Walker, S. A.; Howarth, C. R., Applied studies on immobilized titanium dioxide films as catalysts for the photoelectrochemical detoxification of water. *J. Appl. Electrochem.* **1997,** *27* (4), 385-395.

151. Shinde, P. S.; Patil, P. S.; Bhosale, P. N.; Bruger, A.; Nauer, G.; Neumann-Spallart, M.; Bhosale, C. H., UVA and solar light assisted photoelectrocatalytic degradation of AO7 dye in water using spray deposited TiO2 thin films. *Appl. Catal., B* **2009,** *89* (1-2), 288-294.

152. Dzik, P.; Veselý, M.; Králová, M.; Neumann-Spallart, M., Ink-jet printed planar electrochemical cells. *Appl. Catal., B* **2015,** *178* (0), 186-191.

153. Neumann-Spallart, M.; Shinde, S. S.; Mahadik, M.; Bhosale, C. H., Photoelectrochemical degradation of selected aromatic molecules. *Electrochim. Acta* **2013,** *111*, 830-836.

# 9 Articles

Original research articles the results of which have been discussed in this thesis are listed in chapter 7. At the following pages, all these papers are disclosed for the reader's convenience.

J Appl Electrochem
DOI 10.1007/s10800-015-0893-1

RESEARCH ARTICLE

# Inkjet-printed interdigitated cells for photoelectrochemical oxidation of diluted aqueous pollutants

**Petr Dzik[1,2] · Michal Veselý[1,2] · Martina Blašková[1] · Marcela Králová[2] · Michael Neumann-Spallart[3]**

Received: 18 June 2015 / Accepted: 28 September 2015


**Abstract** Planar, interdigitated photoelectrochemical cells were made by inkjet printing. The electrode fingers had widths ranging from 200 to 1500 µm and were revealed by printing a positive protective polymer mask on fluorine-doped tin oxide-coated glass slides and subsequent etching. One finger family was overprinted by an ink-jettable sol–gel composition based on titanium propoxide which was then converted into $TiO_2$ by annealing in air. An incident photon to current conversion efficiency of 0.19 was obtained at 360 nm for 200-nm-thick films. The influence of electrode geometry and titania thickness on the electrochemical properties of resulting cells is discussed in detail. Due to the interdigitated layout, photoelectrochemical response was not suffering from *iR* drop down to low electrolyte ionic strengths. The printed cells were used in photoelectrocatalytic degradation experiments of aqueous solutions of benzoic acid by broadband ultraviolet irradiation (UVA) and electric bias of 1 V and delivered considerable acceleration of the degradation process compared to the plain photocatalytic mode.

✉ Petr Dzik
petr@dzik.cz

[1] Faculty of Chemistry, Brno University of Technology, Purkynova 118, 612 00 Brno, Czech Republic

[2] Central European Institute of Technology, Brno University of Technology, Technicka 3058/10, 616 00 Brno, Czech Republic

[3] Groupe d'Étude de la Matière Condensée (GEMaC), CNRS/Université de Versailles, 45, avenue des États-Unis, 78035 Versailles Cedex, France

**Keywords** Interdigitated cell · Advanced oxidation process · Material printing · Inkjet · Electrochemistry · Water treatment · Photoelectrocatalysis

## 1 Introduction

Photocatalytic systems employing slurried powders of $TiO_2$ are able to deliver excellent performance due to their very high-catalyst surface area [1]. However, catalyst immobilization inevitably results in the decrease of active catalyst surface area which is accompanied by a loss of catalytic performance due to limited mass transport [2]. Yet, immobilized $TiO_2$ is the preferred form of photocatalyst for industrial applications, because with an immobilized catalyst there is no need for separation of the catalyst from the liquid phase and continuous reactors are thus easier to design.

The enhancement of photocatalytic activity of an immobilized semiconductor photocatalyst by the application of external electrical bias has been convincingly demonstrated [3]. The strategy is based on promoting photogenerated electron–hole pair separation by applying an electrical potential which results in an increase of the quantum yield of the pollutant degradation. This is only possible when the photocatalyst is deposited on an electrically conducting substrate [4–6] working as photoanode. The most straightforward fabrication route for metal oxide-coated photoanodes is the anodic oxidation process [7] which is capable of providing oxide coating with various topology and doping options [8–13], but oxide-coated photoanodes can be deposited by many other methods which are upscalable, among them sol–gel-based ones (dip-coating, spin-coating) [14] and spray pyrolysis [15].

Published online: 05 October 2015

However, when using conventional reactor design and electrolytes of low conductivity, *iR* drop is one of the factors limiting high-current throughput at moderate bias. Supporting electrolyte may be added to increase the electrical conductivity in traditional electrochemical cells, but if the treatment of inevitably low ionic strength media (drinking water) is envisaged, other means for minimizing the *iR* drop must be secured.

The *iR* drop may be reduced by the use of a parallel plate reactor with two opposite electrodes and a small space between them where the electrolyte is passed through [16]. However, this configuration is prone to the pressure build-up in a module consisting of many such cells. This drawback can be avoided by placing both electrodes onto a single substrate and shaping them into a close mutual proximity with a very long boundary, i.e., creating interdigitated electrodes (IDE). The working electrode consists of an electrical conductor covered by semiconducting titanium dioxide. The counter electrode material is not critical as long as sufficient electrical conductivity and corrosion resistance is provided, and interdigital geometry is respected. Such a design ensures two key functions: (1) it suppresses the main obstacle for efficient use of absorbed photons, i.e., the recombination of photogenerated charge carriers, by applying external electrical bias to the semiconducting photocatalyst and (2) it avoids the reduction of the generated photocurrent due to *iR* drop, even in electrolytes of low ionic strength. These features qualify the device as an interesting candidate for photoelectrocatalytic purification of drinking water. Decomposition of model pollutants has been observed on centimeter-scale prototype devices fabricated by conventional lithographic techniques using optical copying through contact masks for resist patterning [17]. Although the lithographic approach allows for very fine patterns to be fabricated, it is unsuitable for the fabrication of large foot-print cell modules.

Recently, major developments in the technology of electronic component fabrication have taken place. The dominant position of subtractive fabrication processes based on sequential etching through temporary resists masks has been challenged by a new additive approach. The so-called material printing techniques [18] seem to be a promising microfabrication method well applicable for the production of planar structures with a low level of integration. The technique is based on sequential laying of patterned functional layers by means of modified conventional printing techniques. Strictly speaking, material printing has been around for several decades, but limited to screen printing [19–21] which has been widely applied in the electronic industry. During the past decade, the concept of material printing has been significantly broadened, and the portfolio of applicable techniques has included offset, gravure, flexo, and inkjet printing.

While generally all traditional printing techniques can be adopted for printing functional layers and patterns, inkjet printing [22] occupies a prominent position. Despite its quite narrow viscosity and particle size limits, it seems to be the most suitable technique for lab scale prototype development as no hardware printing form is necessary, i.e., patterns designed on a printer driving computer can be printed directly without the need for physical printing form manufacturing. Moreover, upscaling is very smooth and easy, because industrial inkjet printers with several meters working width are readily available [23–25], so transfer from prototype level to a small series level is reduced to switching to a bigger printer.

In this paper, we report on further improvement in the design and fabrication technology of planar-interdigitated photoelectrochemical cells fabricated by inkjet printing. The concept of fully printed electrochemical cell introduced recently [26] is further expanded, and more design variables are discussed in this paper. The adoption of inkjet printing provided a great freedom in the design of the cells, and thus samples of various geometries and active layer thickness could be easily fabricated and their electrochemical properties were investigated. Cell functionality is demonstrated by the photoelectrocatalytic oxidation of benzoic acid.

## 2 Experimental

### 2.1 Cell fabrication procedure

FTO glass sheets (Sigma-Aldrich, 11 Ω/□) were cut down to 26 × 76 mm slides, sonicated in Neodisher LM cleaning agent, rinsed in ethanol, fired at 450 °C, rinsed in 1 vol% ethanolic solution of an aliphatic hydrocarbon-based hydrophobization agent (Toko Waterstop, Tokowax, Switzerland), rinsed in 1 vol% aqueous solution of sodium dodecylbenzene sulfonate (Enaspol Inc., Czech republic), and dried with a stream of nitrogen.

Printing of all functional and auxiliary layers was performed with an experimental inkjet printer Fujifilm Dimatix 2831. The printer has been successfully employed for the deposition of a wide variety of functional and auxiliary layers [27–34], and during the past years *de facto* has become the industrial standard tool for ink development and testing.

Generally, the following procedure was repeated for each printing step: the prepared printing formulations were sonicated for 5 min and then loaded into syringes. 0.45-μm membrane filters (Pall Corporation, USA) and blunt needles were attached to the syringe luer ports. The printing formulations were filtered and filled into the Dimatix ink tanks. Dimatix "10 pL" printing heads were attached to the

tanks, which were then mounted into the Dimatix printer. The IDE base pattern as well as the patterns for other layers was drawn as vector graphics and exported to 1-bit BMP files to be used for driving the printer.

The sequence of processing steps is outlined in Fig. 1. First, the base pattern serving as the current collecting IDE was revealed by printing a positive protective polymer mask on the FTO glass slides using a UV-curable ink (Svang Cyan, Grapo Ltd., Czech Republic), cured off-line under a mercury vapor medium pressure lamp (25 J/cm$^2$), and baked on a hot plate at 250 °C for 10 min (Fig. 1). Next, the unmasked FTO was subject to a three-step process in order to remove the naked FTO, while preserving those areas covered by the protective printed mask. First, most of the FTO was removed by electroreduction in a 0.05 molar solution of oxalic acid. Then, the remaining isolated FTO islands were etched off by gentle rubbing against the surface of a zinc plate immersed in 15 % aqueous HCl. Finally, the slide was rinsed in 4 % aqueous HF for 2 min. After the etching operation was finished, the mask was removed by firing at 450 °C for 30 min.

The second layer, i.e., the titania working electrode, was printed using a previously developed ink-jettable sol–gel composition [35]. The thickness after calcination was 50 nm per single layer. It was possible to print 2 layers of sol in wet-to-wet manner followed by single calcination (heating rate 3 °C per min, 30 min at 450 °C) yielding 100 nm titania layers without any cracking in one deposition cycle. Attempts to print more sol layers followed by single calcination resulted in cracked and/or peeling layers. Therefore, thicker layers were prepared by repeating the complete cycle of printing double sol layers and calcination.

The device was finalized (Fig. 2) by printing a masking frame around its edges defining the active area employing the same UV-curable ink and curing procedure. Proper aligning of the titania active layer and the insulator mask was achieved by means of the Dimatix fiducial camera, which enables sample observation and print origin alignment with 5 μm accuracy.

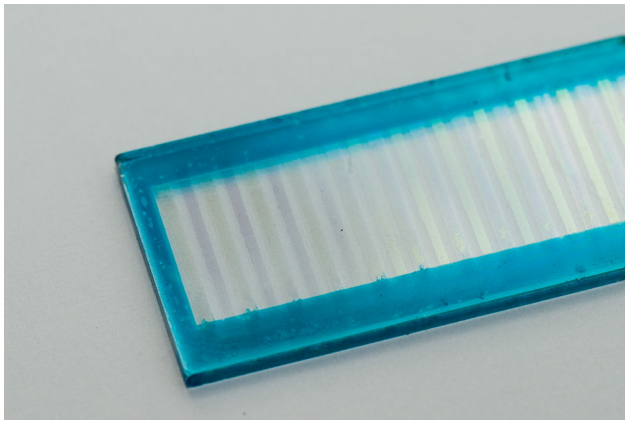

**Fig. 2** Finished cell

## 2.2 Investigation of IDE device properties

Layer quality was monitored by a Nikon Eclipse E200 optical microscope equipped with a polarized light unit and a Nikon D5000 digital camera and Nikon Camera Control Pro 2 software. SEM imaging and elemental analysis were performed on a ZEISS EVO LS 10 scanning electronic microscope. The same machine was used for layer thickness estimation by observing sample cross sections. Phase composition of calcined titania layers was confirmed by a Panalytical Empyrean XRD system, and their diffuse reflectance UV–Vis spectra were recorded by an Ocean Optics Redtide spectrophotometer with a reflectance fiber probe. Layer thickness was investigated by a Dektak XT stylus profilometer.

Photoelectrochemical characterization was performed using a two-electrode setup with the titania-overprinted FTO finger family as the working electrode and the opposite naked FTO finger family as the counter electrode.

**Fig. 1** Device fabrication scheme: Onto a FTO (*green*)-coated glass slide, a UV-curable mask (*violet*) is printed. Naked FTO is removed by etching and the mask over the remaining FTO is stripped off by burning at 450 °C. The exposed interdigitated FTO pattern is overprinted by titania ink (*orange*) and finally an insulating masking frame is printed. (Color figure online)

This setup was fitted into a custom-build 15 × 40 × 70 mm quartz cuvette. The cuvette was fitted onto an optical bench equipped with a Sylvania Lynx-S 11 W BL368 fluorescent UVA lamp. The lamp emission was monitored by a Gigahertz Optic X97 Irradiance Meter with a UV-3701 probe, and the irradiance was set to 2 mW $cm^{-2}$ (integral irradiance in the 320–400 nm range) by adjusting the lamp to cuvette distance. A magnetic stirrer was placed beneath the cuvette and a magnetic flea inside the cuvette provided efficient electrolyte mixing.

Current–potential and current–time measurements were performed with a custom computer-controlled power source meter built on the basis of the National Instruments Labview platform (NI cDAQ-9172 interface with NI9219 and NI9263 convertors), supplying linear voltage sweeps and measuring currents down to sub-μA range. For chopped response curves, the lamp was manually obscured and revealed at 5-s interval. Photoelectrocatalytic experiments were conducted with the same cell and light source.

For the estimation of IPCE (incident photon to current conversion efficiency) at various wavelengths, photocurrent measurements were conducted under potentiostatic control. An O-ring of 8-mm inner diameter confined a 10 μl drop of electrolyte into which an SCE reference electrode with attached Pt-wire functioning as counter electrode was dipped. Backside illumination (through the glass substrate) was provided by LEDs mounted below the sample (Fig. 3). Photocurrents were related to the photocurrents generated in a Hamamatsu S1337-1010BQ-calibrated photodiode positioned at the same location in separate runs, thus allowing for the calculation of IPCEs.

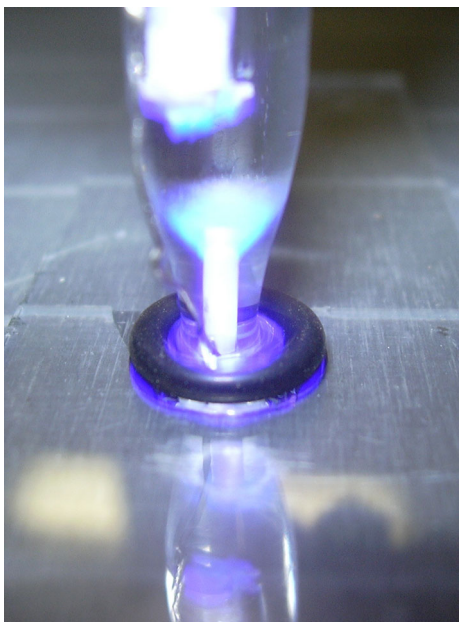

**Fig. 3** Setup used for the IPCE estimation

### 2.3 Photoelectrocatalysis

Recently, several aromatic fluorescent probes were suggested as model compounds for monitoring the oxidative activity of valence band holes generated in the immobilized photocatalyst, such as terephthalic acid [36] and coumarin [37]. Upon oxidation, presumably resulting from the attack of a hydroxyl radical or a valence band hole, the aromatic compound is oxidized into its hydroxylated derivative, which gives a strong fluorescence signal in the 400–500 nm spectral range. This approach simplified the experimental setup, because a single-radiation source could be used for both the activation of the photocatalyst and for the excitation of the fluorescent probe generated during the course of the reaction.

In this study, benzoic acid was employed as a model compound for photoelectrocatalytic degradation experiments. Its concentration can be determined by HPLC [38] which also allows to identify the degradation intermediates and monitor their concentration. Benzoic acid is also suitable as a fluorescent probe, because its dominant oxidation products, i.e., monohydroxybenzoic acid isomers, give an appreciable fluorescent signal around 410 nm [39, 40]. This makes in situ automated recording of oxidation intermediate concentration profiles possible by means of fiber optics spectrometers. With the same instrumentation, absorbance changes accompanying benzoic acid degradation were monitored. Neither the fluorescence measurement of the reaction intermediates nor the absorbance measurement of benzoic acid is selective, as the absorption and emission bands overlap to a large extent. Nevertheless, absorbance is a useful indicator of the remaining concentration of chromophores present in the reaction mixture.

Fluorescence emitted by the oxidized intermediates was collected by a quartz collimating lens mounted in the lateral wall of the cell holder and projected into an optical fiber attached to an Ocean Optics Maya 2000 spectrometer. Calibration was performed using salicylic acid standard (Sigma-Aldrich). Absorbance changes following the degradation of benzoic acid were measured by a transmission dip probe coupled to an Ocean Optics PX-2 pulsed xenon light source and a USB-650 Red Tide UV–vis spectrometer. The spectrometer driving software allowed for a convenient automated recording of the both fluorescence intensity and absorbance. Chronoamperometric measurements were performed during the course of the reaction with the custom-built ammeter. Samples for HPLC were collected at regular time intervals and their total volume did not exceed 10 vol% of the reaction batch volume. The analysis was performed using a Dionex-Ultimate 3000 High Performance Liquid Chromatograph with an Eclipse Plus C18 column. A mixture of $5 \times 10^{-6}$ mol $dm^{-3}$ sulfuric acid and methanol in the ratio

70:30 was used as a mobile phase with a flow rate 0.5 $cm^3$ $s^{-1}$ at a column temperature 30 °C. The peak for benzoic acid appeared at the retention time of 5.89 min at the wavelength of 230 nm.

## 3 Results and discussion

Devices with electrode finger widths ranging from 200 to 1000 μm were conveniently fabricated. Apart from regularly spaced devices, several other layouts were also fabricated and their properties were investigated, including reduced gap devices or devices with different finger widths of working and counter electrodes. Moreover, the thickness of the titania working electrode layer was varied in the 100–500 nm range (Table 1).

### 3.1 Physical properties of devices

Optical microscopy images of the transparent layers tended to be faint and had low contrast. Profilometric scanning provided information about the thickness, roughness, and homogeneity of deposited layers. Figure 4 depicts the record of a stylus profilometric mapping across 2 fingers of a 500-500-500-500 μm device fabricated with 3 cycles of titania deposition. The thickness of the FTO finger (app. 550 nm) and of the FTO + titania layer (app. 300 nm) can be exactly determined, and the overlap of the wider titania strip is also clearly visible. Figures 5 and 6 illustrate the optical properties and phase composition of the reverse micelles originated titania layers, respectively. Strong interference coloring observed visually expresses itself in the typical periodic peaks in the diffuse reflectance spectra. The phase composition was investigated by XRD, and the presence of anatase and cassiterite ($SnO_2$) phases was confirmed. Further details about the properties of this particular type of titania coating and comparison with titania coatings made by other methods can be found in our previous communication [41–43].

### 3.2 Electrical properties

The photoelectrochemical performance of the cell, i.e., the photocurrent as a function of applied voltage, is the key property for the evaluation of the IDE device quality and suitability for oxidation of organic molecules dissolved in water. Photocurrent analysis enables to investigate the influence of process variables and also checks for fabrication errors (shorts, layer separation, etc.). Some of the key variables are discussed below.

The irradiation intensity, wavelength, and incidence (from the electrolyte side or from the substrate side) determine the amount of photons reaching the semiconductor and being absorbed by it and the corresponding rate of electron–hole pair generation. This parameter was not altered in this study, and the irradiation was set to 20 $W/m^2$ UVA broadband irradiation incident on the photocatalyst (front) side.

The photocurrent–voltage characteristics also depend on the electrical resistance of the circuit, which is determined by the electrode design and electrolyte choice. Since an interdigitated design has been employed in this study, the concept of the (conductivity) cell constants, κ, of the interdigitated finger device [44] may be applied to evaluate the influence of electrode design on the observed photocurrents. It was observed that κ values were close to the ones calculated following Olthuis et al. [44]. A structure of 200-μm-wide fingers and spaces was already fine enough to obtain a κ value below 0.01 $cm^{-1}$. Other cells reported in this study, i.e., cells with 500- and 1000-μm-wide fingers, featured cell constants of 0.0136 and 0.0271 $cm^{-1}$, respectively. Thus, decreasing specific conductivity of a diluted electrolyte can be compensated by the lower cell constant of cells with finer fingers.

**Table 1** Outline of fabricated devices

| Sample code | Device properties | | |
|---|---|---|---|
| | IDE pattern | Working electrode coverage (%) | $TiO_2$ thickness |
| (C1–6)-x | 1000-1000-1000-1000 preliminary testing and process optimization | 25 | $x = 1, 2, 3, 4, 5$ deposition cycles |
| C7-x | 1000-1000-1000-1000 | 25 | 100 nm per single cycle |
| C8-x | 500-500-500-500 | 25 | |
| C9-x | 1500-500-500-500 | 50 | |
| C10-x | 1000-500-1000-500 | 33 | |
| C11-x | 200-200-200-200-200 | 25 | |

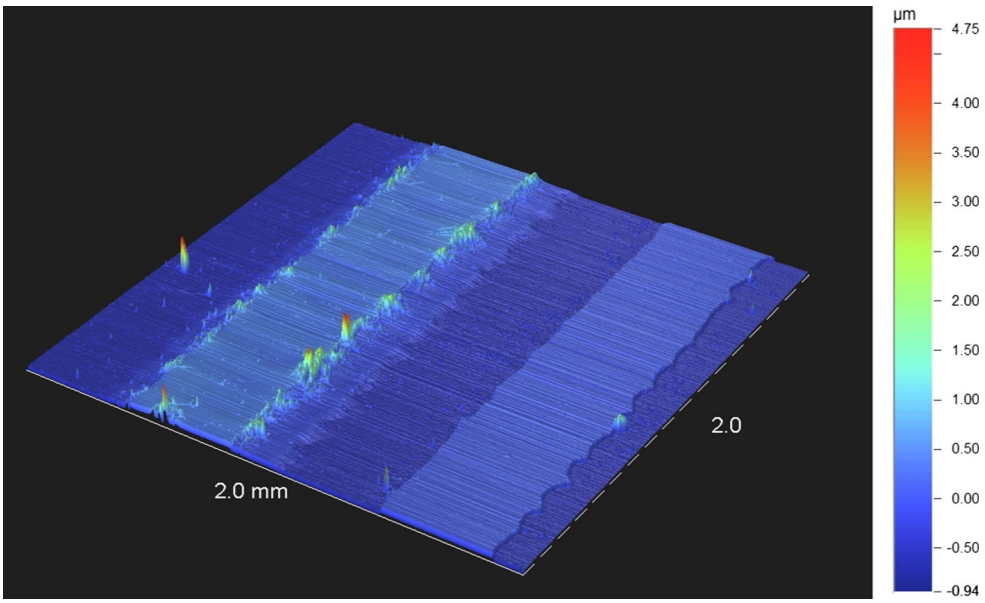


**Fig. 4** Stylus profilometric scanning map of a segment covering two fingers of the C8-3 device (500-500-500-500 µm, 300 nm titania), where the one on the *left* is FTO covered by TiO2 and the one on the *right* FTO

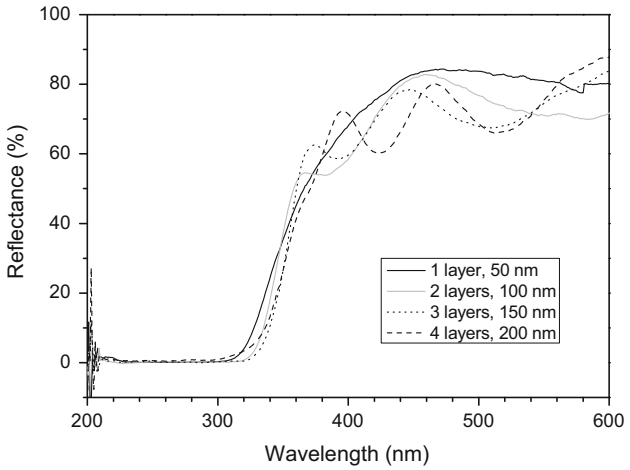


**Fig. 5** Diffuse reflectance spectra of printed titania on glass

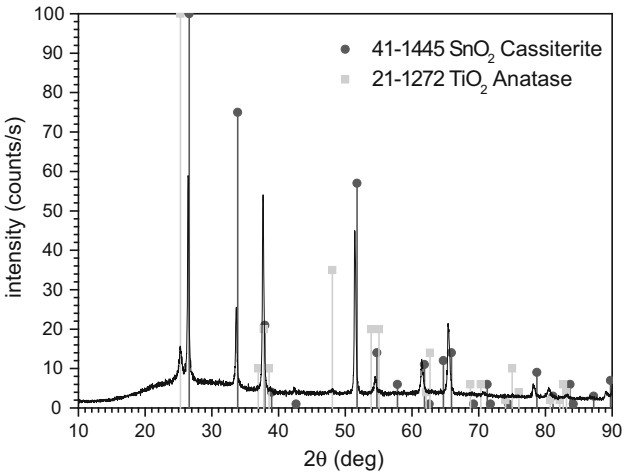


**Fig. 6** XRD diagram of a 200-nm-thick film on FTO/glass with peaks assigned to anatase and cassiterite

A typical photoelectrochemical response of one of the finger devices under continuous UV irradiation and in the dark is depicted in Fig. 7. Three complete cyclic scans were recorded in this measurement in order to confirm the stability and the repeatability. The "UV curve" describes the profile of the total photocurrent delivered by the device, corresponding to the number of free charge carriers generated in the semiconductor and drawn into the external circuit by the applied voltage. The photocurrent steeply increases in the 0–0.5 V range, and then reaches a plateau where the current density is essentially independent on the voltage.

In the plateau region (1.4 V vs. SCE), IPCE values reached 0.19 at 360 nm for a 200-nm-thick film (Fig. 8). The figure also features a Tauc plot revealing the position of the band gap.

The influence of titania thickness on the photocurrent density is depicted in Fig. 9 under regular chopping, allowing the simultaneous recording of the i–V response in the dark and under illumination. The plateau region of all the curves is very well developed and clearly indicates the linear additive trend of photocurrent with the number of deposition cycles.

Generally, the observed photocurrent is proportional to incident radiation flux and independent on electrolyte concentration. It can be calculated exactly from the IPCE-wavelength relation (Fig. 8) and the emission spectrum of any light source received at the surface of the device [3].

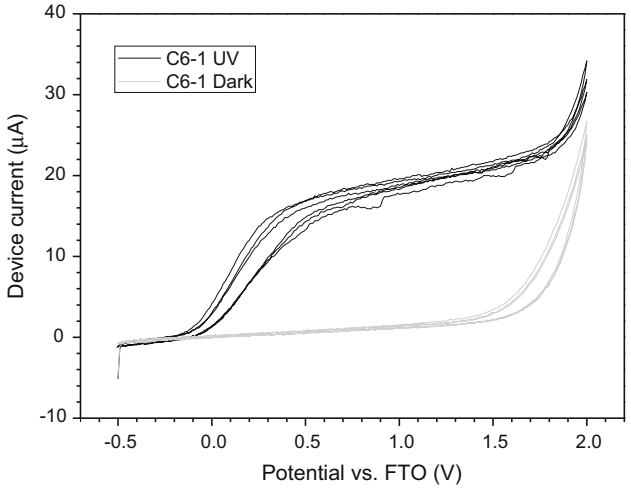


**Fig. 7** Typical *i–V* response curve of a printed IDE device (C7-1, 1000-1000-1000-1000 μm, 100 nm titania) under continuous irradiation in 0.1 molar sodium sulfate

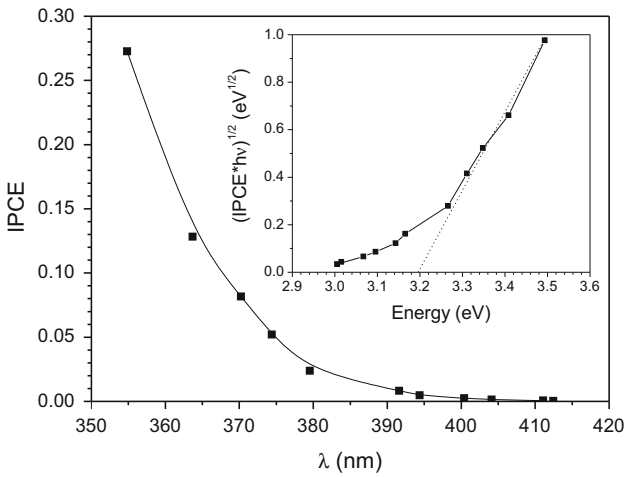


**Fig. 8** IPCE as a function of wavelength of an electrode (glass/FTO/200 nm $TiO_2$) at 1.4 V versus SCE under backside illumination. *Inset* Tauc plot of the IPCE data

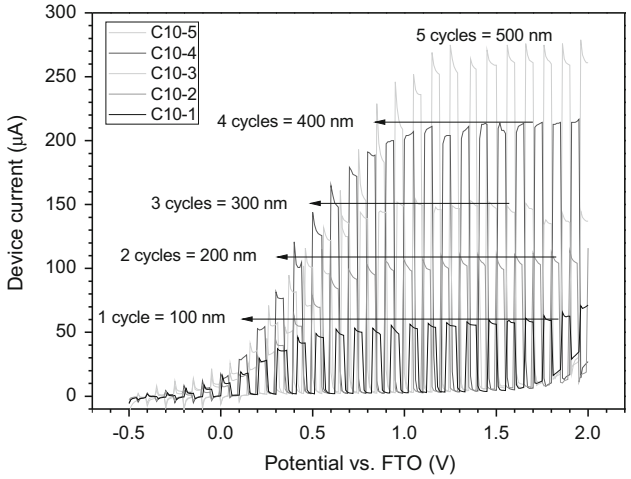


**Fig. 9** *i–V* response curves of 1000 μm devices for different titania thicknesses under chopped irradiation

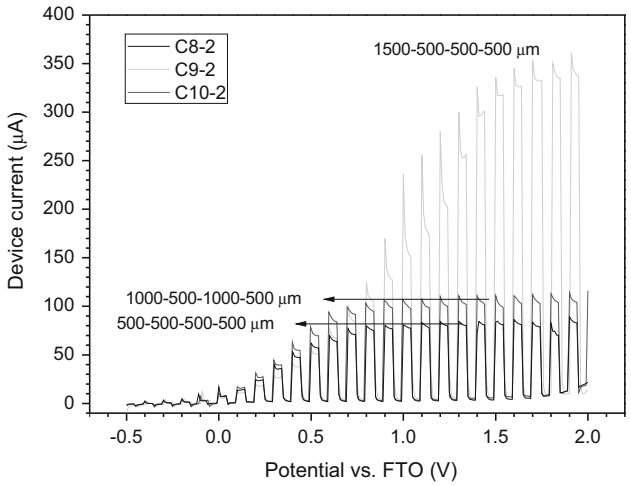


**Fig. 10** Comparison of *i–V* response curves for various IDE cell geometries, 200-nm-thick $TiO_2$ films

The current also depends on the area of the working electrode related to the total device area (the coverage). Figure 10 illustrates this by a comparative plot of response curves from samples C8, C9, and C10 having a working electrode ($TiO_2$) coverage of 25, 33, and 50 %, respectively. Although the general trend of increasing current with increasing coverage is respected, the absolute values do not correlate well, i.e., the photocurrent delivered by C9 (50 % working electrode coverage) is more than twice as high as the photocurrent of C8 (25 % coverage). This effect can be attributed to the isotropic nature of the etching bath which creates significant undercuts removing FTO even under the printed mask. Therefore, the real working electrode coverage of finer fingered devices tends to be more reduced than the area of wider fingered devices. The effect is even more obvious upon the comparison of two sample series with the same surface coverage by titania but different finger densities, e.g., the C7 and C8 samples (Fig. 11). The photocurrents generated by the finer fingered series were consistently smaller than the wider fingered one, despite the fact that the active area should be equal. In order to overcome this problem, mask files used for the fabrication of further sample series were modified to compensate for this phenomenon.

The positive effect of IDE design on the cell performance can be illustrated by comparing the response curves in various electrolytes (Fig. 12). Generally, in a conventional electrochemical cell, with decreasing electrolyte conductivity, the photocurrent–voltage characteristic should become flatter. However, with the interdigitated design, the

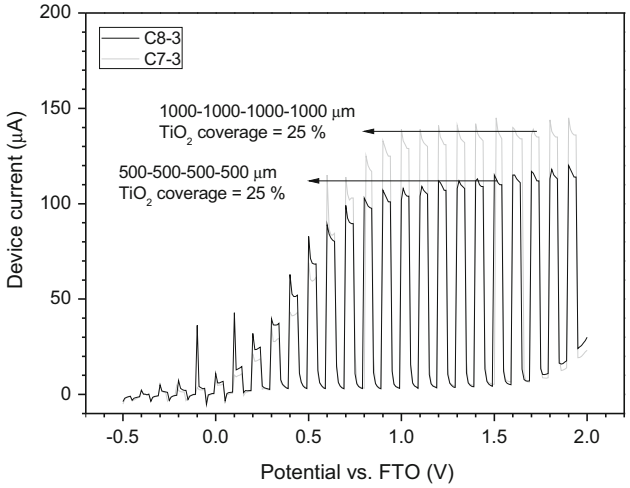


**Fig. 11** The photocurrent response curves of original (not compensated for undercutting) C7 and C8 series. 300-nm-thick $TiO_2$ films

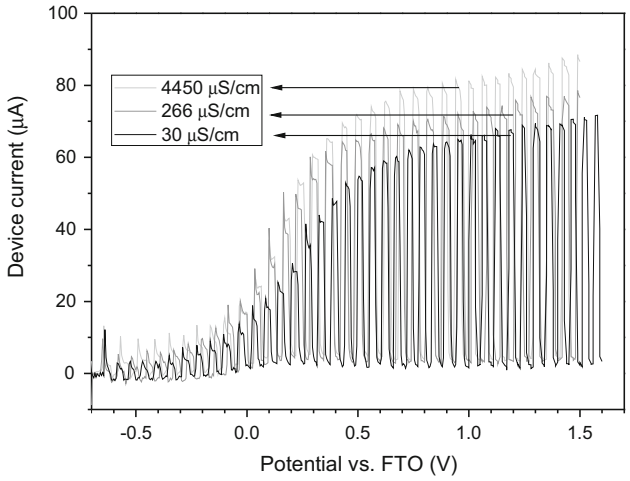


**Fig. 12** *i–V* response curve of the C3 device (100-nm thick) in electrolytes of various conductivities under chopped irradiation

ohmic drop is (partially) compensated and therefore the observed current is well conserved. While a photocurrent of 80 μA at 1 V bias in sodium sulfate solution of specific conductivity of 4450 μS/cm is flowing, 70 μA are obtained in a more diluted solution of conductivity 266 μS/cm, and still 65 μA are observed in an even more diluted solution of conductivity 30 μS/cm.

Plots in Fig. 13 further illustrate the positive effect of IDE electrode geometry on the magnitude of photocurrent generated at moderate bias and low-conductivity electrolytes. The behavior of two devices with the same working electrode (interdigitated titania photoanode) but different counter electrodes is compared: the "IDE" curve was recorded with the originally fabricated FTO digitated counter electrode, while the "rectangular" curve was recorded with a separate narrow rectangular strip of FTO

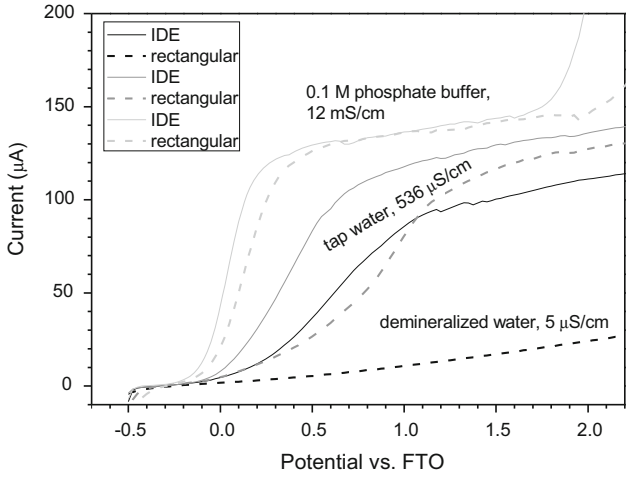


**Fig. 13** Comparison of *i–V* response curves of electrodes with rectangular and interdigitated geometries in different electrolytes under continuous irradiation

glass used as the counter electrode. The FTO strip was fixed perpendicular along the edge of the IDE device, and its exposed conductive area was identical to the area of the IDE used in the previous measurement. While there is essentially no difference in the shape of the two curves in phosphate buffer, the curves start to divert in tap water and significant differences can be observed in the case of demineralized water. The curves clearly manifest that the IDE device is able to deliver more current at moderate potentials in low-conductivity electrolytes, because the *iR* drop is effectively compensated.

The above-presented photocurrent response curves provide important insight into the cell properties and relation between the cell design and performance. The goal of the cell design is to maximize the delivered photocurrent, because this is the first and necessary (although not sufficient) step determining the rate of all following redox processes.

### 3.3 Photoelectrocatalysis

The following redox processes take place at an illuminated n-semiconductor/electrolyte interface, when conduction band electrons are channeled to a counter electrode due to applied reverse bias:

$$h^+_{vb} + H_2O \rightarrow HO\cdot + H^+ \quad (1)$$

$$h^+_{vb} + OH^- \rightarrow HO\cdot \quad (2)$$

where $h^+_{vb}$ is a valence band hole.

In the absence of an oxidizable solute, *R*, over a number of steps, water is oxidized to oxygen—in summary:

$$h^+_{vb} + 1/2\ H_2O \rightarrow H^+ + 1/4\ O_2 \quad (3)$$

If an oxidizable solute, R, is present in the electrolyte, the following reactions also occur:

$$h_{vb}^{+} + R \rightarrow R^{+} \quad (4)$$

$$HO\cdot + R \rightarrow R_{ox} \quad (5)$$

The total current is then composed of two sources: the oxidizable solute oxidation rate and the water oxidation rate [16], where the former increases with its concentration, $c_{ox}$. The Faradaic efficiency, $f$, reflecting the competition between reactions 3, 4, and 5 is a convenient measure for the description of the net efficiency of the initial oxidation step and is suitable for comparison of results obtained under various conditions:

$$f = V(dc_{ox}/dt)F/i_{photo}, \quad (6)$$

where $V$ is the total volume of the batch reactor and $F$ is Faraday's constant.

The oxidized species, $R^{+}$ or $R_{ox}$, undergo further electron transfer reactions and all intermediates may eventually be fully mineralized through a series of oxidative cleavage reactions into water and carbon dioxide.

A comparative example of photocatalytic and photoelectrocatalytic degradation of a $10^{-4}$ molar solution of benzoic acid under UVA irradiation and assisted by electrical bias of 1 V, using the 1000-1000-1000-1000 device with 200-nm-thick $TiO_2$ fingers is shown in Fig. 14 Although the exact mechanism is still being debated [45, 46], the net oxidative effect is evident and can be easily monitored by various methods.

Figure 14 depicts the observed concentration profiles using polychromatic light centered at 365 nm and 1 V bias. The Faradaic efficiency, $f$, of the *initial* process is calculated from Eq. 6. The value of 0.09, close to that obtained for the degradation of benzoic acid in a parallel plate reactor [16], is satisfactory given the fact that a low concentration of electroactive species ($1 \times 10^{-4}$ M) was used. The initial increase in hydroxybenzoic acid concentration was about one half of the decrease in benzoic acid concentration; it may, therefore, be concluded that part of the intermediate, in close proximity or adsorbed on the electrode, undergoes further oxidation reactions before being released into the solution.

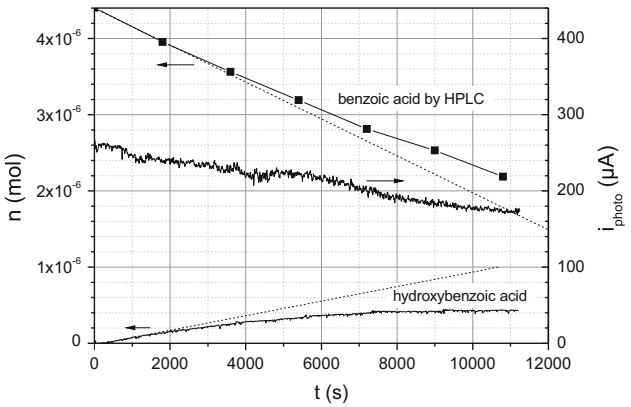


**Fig. 14** Concentration profiles of benzoic and hydroxybenzoic acid during a photoelectrocatalytic (1 V bias) experiment using a 1000-1000-1000-1000 IDE with 500-nm-thick $TiO_2$ fingers under UVA radiation. $1 \times 10^{-4}$ M benzoic acid in 35 ml stirred, air-saturated solution

In another experiment, without electrical bias, the decrease of the concentration of the parent molecule was only one third of that obtained under 1 V bias, thus proving the advantage of an immobilized catalyst deposited on an electrically conducting substrate allowing for application of electrical bias.

### 3.4 Application perspective

The benefits of electro-assisted photocatalysis have been convincingly accounted for on the theoretical basis [3], practically demonstrated by the presented results as well as reported in a number of studies involving various aqueous pollutants [47–52]. These studies have shown that in a direct comparison with competing advanced oxidation techniques, electro-assisted photocatalysis provides several important advantages: it requires no additives, mineralization proceeds to $CO_2$, the catalyst is immobilized on the electrode, and therefore there is no need for catalyst separation after the treatment and, as presented in the results and references above, significant acceleration of the process due to recombination suppression by applying electrical bias.

For a practical industrial employment, the stability of the cell is of a paramount importance. Some of the described devices which were used for repeated long-term electrochemical experiments have actually shown two types of wear, especially after degradation experiments with more concentrated organic acids. The degradation of the UV-curable polymeric masking frame was visually the most prominent, starting by gradual swelling of the mask followed by partial separation. The masking frame can be easily restored by overprinting with the same material on the studied sample set, but replacement with fully inorganic mask based on insulating inorganic pigment nanoparticles is currently being investigated. The second type of wear also occurred during experiments with acidic electrolytes. The FTO counter electrode gradually darkened, and the device photocurrent decayed. As the Pourbaix diagrams indicate [53], tin oxide is reduced to tin at negative potential and low pH solutions. Indeed, an XRD analysis confirmed the reduction of FTO to metallic tin which gets apparently further corroded by the acidic electrolyte. In order to protect the FTO cathode, a thin layer of

gold was electroplated, and the restoration and stabilization of the device performance were observed.

The present size of the reported devices allows for treatment of ca. 50 mL batches. Naturally, significant upscaling is inevitable in order to bring the concept to a plant scale. From the fabrication technology point of view, this can be easily accomplished. Multiple interdigitated cells can be easily connected in a serial/parallel fashion to match the characteristics of the bias voltage source just in the same way as conventional planar cells have been arranged [54]. The size of the individual cells can be adjusted in a wide range of sizes as the deposition technique does not represent any hurdle since flatbed or roll inkjet printers suitable for material printing and working with meter-sized substrates are readily available [55, 56]. Obviously, producing the cells on flexible substrates through roll-to-roll processing would bring further reduction in cost and contribute to the ease of handling, installation, and recycling. Recently, several promising alternatives for printing the base conductor [57–59] as well as the active titania layer [60] have been proposed. Although these processes generally require thermal sintering, several cold-setting options [61–63] have been reported recently enabling printing on plastic substrates as well.

## 4 Conclusion

Inkjet material printing was successfully employed for the fabrication of planar-interdigitated photoelectrochemical cells. It proved to be an elegant method for sol delivery to the substrate, providing complete control over the deposition process parameters together with an excellent efficiency of precursor use. A mixed subtractive and additive approach was adopted. The fully digital printing workflow eliminated the need for physical printing forms, saved valuable ink, and allowed unlimited freedom in the design of the electrode patterns.

The process of FTO patterning by etching with the help of a protecting printed mask can be easily adopted for pattering of other materials as well. Although the resolution of printed masks cannot compete with the well-established resist technologies as it is limited to micrometer resolution, it may be well suited for the fabrication of large foot-print devices requiring a low degree of integration (solar cells, electroluminescent modules, etc.). The absence of a resist development step makes the fabrication process environment friendly. Moreover, it does not require any special material or equipment as it can be performed with ordinary flatbed or roll printers and UV-curable inks. Inkjet-printed etching masks allow for very fast design changes and thus reduce time and cost for process optimization.

Planar arrangement of working and counter electrodes is a promising approach to the design of photoelectrochemical cells intended for high-current throughput at moderate bias. With transparent substrates, the back-irradiated configuration is an interesting option. Devices with finger width (w) and space width (s) ranging from 200 to 1000 μm were fabricated. The benefits of finer fingers are clearly demonstrated, resulting in lower cell constants which are beneficial for the suppression of *iR* drop in electrolytes of low conductivities. With the present technology, 200 μm fingers seem to be fine enough for work with electrolytes with ionic strength typical for drinking water.

Comparative photocatalytic and photoelectrocatalytic experiments with benzoic acid as model contaminant proved the beneficial role of external electrical bias in suppressing photogenerated electron–hole recombination in the semiconducting photocatalyst, leading to efficient charge separation and thus acceleration of benzoic acid oxidation.

**Acknowledgments** The authors thank the Ministry of Education, Youth and Sports of the Czech Republic for support through projects CZ.1.07/2.3.00/30.0005 and LD14131.

## References

1. van Grieken R, Marugan J, Sordo C, Pablos C (2009) Comparison of the photocatalytic disinfection of E. coli suspensions in slurry, wall and fixed-bed reactors. Catal Today 144(1–2):48–54. doi:10.1016/j.cattod.2008.11.017
2. Tasbihi M, Ngah CR, Aziz N, Mansor A, Abdullah AZ, Teong LK, Mohamed AR (2007) Lifetime and regeneration studies of various supported TiO2 photocatalysts for the degradation of phenol under UV-C light in a batch reactor. Ind Eng Chem Res 46(26):9006–9014. doi:10.1021/ie070284x
3. Neumann-Spallart M (2007) Aspects of photocatalysis on semiconductors: photoelectrocatalysis. Chimia 61(12):806–809. doi:10.2533/chimia.2007.806
4. Waldner G, Bruger A, Gaikwad NS, Neumann-Spallart M (2007) WO3 thin films for photoelectrochemical purification of water. Chemosphere 67(4):779–784. doi:10.1016/j.chemosphere.2006.10.024
5. Fernandez-Ibanez P, Malato S, Enea O (1999) Photoelectrochemical reactors for the solar decontamination of water. Catal Today 54(2–3):329–339. doi:10.1016/s0920-5861(99)00194-7
6. Butterfield IM, Christensen PA, Hamnett A, Shaw KE, Walker GM, Walker SA, Howarth CR (1997) Applied studies on immobilized titanium dioxide films as catalysts for the photoelectrochemical detoxification of water. J Appl Electrochem 27(4):385–395. doi:10.1023/a:1018453402332
7. Dikici T, Erol M, Toparli M, Celik E (2014) Characterization and photocatalytic properties of nanoporous titanium dioxide layer fabricated on pure titanium substrates by the anodic oxidation process. Ceram Int 40(1):1587–1591. doi:10.1016/j.ceramint.2013.07.046
8. Momeni MM, Ghayeb Y, Ghonchegi Z (2015) Visible light activity of sulfur-doped TiO2 nanostructure photoelectrodes prepared by single-step electrochemical anodizing process.

J Solid State Electrochem 19(5):1359–1366. doi:10.1007/s10008-015-2758-2
9. Momeni MM, Ghayeb Y, Ghonchegi Z (2015) Fabrication and characterization of copper doped TiO2 nanotube arrays by in situ electrochemical method as efficient visible-light photocatalyst. Ceram Int 41(7):8735–8741. doi:10.1016/j.ceramint.2015.03.094
10. Momeni MM, Ghayeb Y (2015) Fabrication, characterization and photoelectrochemical behavior of Fe–TiO2 nanotubes composite photoanodes for solar water splitting. J Electroanal Chem 751:43–48. doi:10.1016/j.jelechem.2015.05.035
11. Momeni M, Ghayeb Y (2015) Synthesis and characterization of iron-doped titania nanohoneycomb and nanoporous semiconductors by electrochemical anodizing method as good visible light active photocatalysts. J Mater Sci 26(7):5509–5517. doi:10.1007/s10854-015-3108-y
12. Momeni M, Ghayeb Y, Davarzadeh M (2015) Electrochemical construction of different titania–tungsten trioxide nanotubular composite and their photocatalytic activity for pollutant degradation: a recyclable photocatalysts. J Mater Sci 26(3):1560–1567. doi:10.1007/s10854-014-2575-x
13. Momeni MM, Ghayeb Y (2015) Photoelectrochemical water splitting on chromium-doped titanium dioxide nanotube photoanodes prepared by single-step anodizing. J Alloys Compd 637:393–400. doi:10.1016/j.jallcom.2015.02.137
14. Macwan DP, Dave PN, Chaturvedi S (2011) A review on nano-TiO2 sol-gel type syntheses and its applications. J Mater Sci 46(11):3669–3686. doi:10.1007/s10853-011-5378-y
15. Bettini LG, Dozzi MV, Della Foglia F, Chiarello GL, Selli E, Lenardi C, Piseri P, Milani P (2015) Mixed-phase nanocrystalline TiO2 photocatalysts produced by flame spray pyrolysis. Appl Catal B 178:226–232. doi:10.1016/j.apcatb.2014.09.013
16. Neumann-Spallart M, Shinde SS, Mahadik M, Bhosale CH (2013) Photoelectrochemical degradation of selected aromatic molecules. Electrochim Acta 111:830–836. doi:10.1016/j.electacta.2013.08.080
17. Neumann-Spallart M (2011) Photoelectrochemistry on a planar, interdigitated electrochemical cell. Electrochim Acta 56(24):8752–8757. doi:10.1016/j.electacta.2011.07.089
18. Krebs FC (2009) Fabrication and processing of polymer solar cells: a review of printing and coating techniques. Sol Energy Mater Sol Cells 93(4):394–412. doi:10.1016/j.solmat.2008.10.004
19. Alonso-Lomillo MA, Dominguez-Renedo O, Arcos-Martinez MJ (2010) Screen-printed biosensors in microbiology; a review. Talanta 82(5):1629–1636. doi:10.1016/j.talanta.2010.08.033
20. Li M, Li Y-T, Li D-W, Long Y-T (2012) Recent developments and applications of screen-printed electrodes in environmental assays—a review. Anal Chim Acta 734:31–44. doi:10.1016/j.aca.2012.05.018
21. Riegel S, Mutter F, Lauermann T, Terheiden B, Hahn G (2012) Review on screen printed metallization on p-type silicon. Proc Third Metallization Workshop Metallization Cryst Silicon Sol Cells 21:14–23. doi:10.1016/j.egypro.2012.05.003
22. Martin GD, Hoath SD, Hutchings IM (2006) Inkjet printing—the physics of manipulating liquid jets and drops. In: Conference on engineering in physics—synergy for success, London, England. doi:10.1088/1742-6596/105/1/012001
23. Calvert P (2001) Inkjet printing for materials and devices. Chem Mater 13(10):3299–3305. doi:10.1021/cm0101632
24. Sirringhaus H, Shimoda T (2003) Inkjet printing of functional materials. MRS Bull 28(11):802–806. doi:10.1557/mrs2003.228
25. Tekin E, Smith PJ, Schubert US (2012) Inkjet printing as a deposition and patterning tool for polymers and inorganic particles. Soft Matter 4(4):703–713. doi:10.1039/B711984D
26. Dzik P, Veselý M, Králová M, Neumann-Spallart M (2015) Ink-jet printed planar electrochemical cells. Appl Catal B 178:186–191. doi:10.1016/j.apcatb.2014.09.030
27. Tang W, Feng LR, Zhao JQ, Cui QY, Chen SJ, Guo XJ (2014) Inkjet printed fine silver electrodes for all-solution-processed low-voltage organic thin film transistors. J Mater Chem C 2(11):1995–2000. doi:10.1039/c3tc32134g
28. Wang MW, Pang DC, Tseng YE, Tseng CC (2014) The study of light guide plate fabricated by inkjet printing technique. J Taiwan Inst Chem Eng 45(3):1049–1055. doi:10.1016/j.jtice.2013.08.021
29. Tarapata G, Marzecki M (2013) Methodology and technological aspects of the flexible substrate preparation for Ink-jet Printing technology. In: Romaniuk RS (ed) Photonics applications in astronomy, communications, industry, and high-energy physics experiments, vol 8903. Proceedings of SPIE. doi:89032m10.1117/12.2041890
30. Kwon JT, Eom SH, Moon BS, Shin JK, Kim KS, Lee SH, Lee YS (2012) Studies on printing inks containing poly 2-methoxy-5-(2-ethylhexyl-oxyl)-1,4-phenylenevinylene as an emissive material for the fabrication of polymer light-emitting diodes by inkjet printing. Bull Korean Chem Soc 33(2):464–468. doi:10.5012/bkcs.2012.33.2.464
31. Dzik P, Morozová M, Klusoň P, Veselý M (2012) Photocatalytic and self-cleaning properties of titania coatings prepared by inkjet direct patterning of a reverse micelles sol-gel composition. J Adv Oxid Technol 15(1):89–97
32. Swartz JD, Deravi LF, Wright DW (2010) Bottom-up synthesis of biologically active multilayer films using inkjet-printed templates. Adv Funct Mater 20(9):1488–1492. doi:10.1002/adfm.200902169
33. Sowade E, Hammerschmidt J, Blaudeck T, Baumann RR, Polster D, Baumgartel T, Graaf H, von Borczyskowski C, Wagner R, Cichos F, Sist (2009) Inkjet printing of polymer microspheres. In: Nip 25: digital fabrication 2009, Technical program and proceedings
34. Deravi LF, Swartz JD, Wright DW (2008) Piezoelectric inkjet printing of biomimetic surfaces for enzyme encapsulation. In: Nip24/digital fabrication 2008: 24th international conference on digital printing technologies, technical program and proceedings
35. Černá M, Veselý M, Dzik P (2011) Physical and chemical properties of titanium dioxide printed layers. Catal Today 161(1):97–104. doi:10.1016/j.cattod.2010.11.019
36. Cernigoj U, Kete M, Stangar UL (2010) Development of a fluorescence-based method for evaluation of self-cleaning properties of photocatalytic layers. Catal Today 151(1–2):46–52. doi:10.1016/j.cattod.2010.03.043
37. Ishibashi K, Fujishima A, Watanabe T, Hashimoto K (2000) Detection of active oxidative species in TiO2 photocatalysis using the fluorescence technique. Electrochem Commun 2(3):207–210. doi:10.1016/s1388-2481(00)00006-0
38. Chan AHC, Chan CK, Barford JP, Porter JF (2003) Solar photocatalytic thin film cascade reactor for treatment of benzoic acid containing wastewater. Water Res 37(5):1125–1135. doi:10.1016/s0043-1354(02)00465-7
39. Karim MM, Lee HS, Kim YS, Bae HS, Lee SH (2006) Analysis of salicylic acid based on the fluorescence enhancement of the As(III)-salicylic acid system. Anal Chim Acta 576(1):136–139. doi:10.1016/j.aca.2006.02.004
40. Pozdnyakov IP, Pigliucci A, Tkachenko N, Plyusnin VF, Vauthey E, Lemmetyinen H (2009) The photophysics of salicylic acid derivatives in aqueous solution. J Phys Org Chem 22(5):449–454. doi:10.1002/poc.1489
41. Morozova M, Kluson P, Dzik P, Vesely M, Baudys M, Krysa J, Solcova O (2013) The influence of various deposition techniques on the photoelectrochemical properties of the titanium dioxide thin film. J Sol Gel Sci Technol 65(3):452–458. doi:10.1007/s10971-012-2957-6
42. Kralova M, Dzik P, Vesely M, Cihlar J (2013) Preparation and characterization of doped titanium dioxide printed layers. Catal Today 230:188–196

43. Schmiedova V, Dzik P, Vesely M, Zmeskal O, Morozova M, Kluson P (2015) Optical properties of titania coatings prepared by inkjet direct patterning of a reverse micelles sol-gel composition. Molecules 20(8):14552
44. Olthuis W, Streekstra W, Bergveld P (1995) Theoretical and experimental-determination of cell constants of planar-interdigitated electrolyte conductivity sensors. Sens Actuators B 24(1–3):252–256. doi:10.1016/0925-4005(95)85053-8
45. Herrmann JM (1999) Heterogeneous photocatalysis: fundamentals and applications to the removal of various types of aqueous pollutants. Catal Today 53(1):115–129. doi:10.1016/s0920-5861(99)00107-8
46. Lawless D, Serpone N, Meisel D (1991) Role of OH· radicals and trapped holes in photocatalysis—a pulse-radiolysis study. J Phys Chem 95(13):5166–5170. doi:10.1021/j100166a047
47. Tantis I, Bousiakou L, Frontistis Z, Mantzavinos D, Konstantinou I, Antonopoulou M, Karikas G-A, Lianos P (2015) Photocatalytic and photoelectrocatalytic degradation of the drug omeprazole on nanocrystalline titania films in alkaline media: effect of applied electrical bias on degradation and transformation products. J Hazard Mater 294:57–63. doi:10.1016/j.jhazmat.2015.03.042
48. Tantis I, Stathatos E, Mantzavinos D, Lianos P (2015) Photoelectrocatalytic degradation of potential water pollutants in the presence of NaCl using nanocrystalline titania films. J Chem Technol Biotechnol 90(7):1338–1344. doi:10.1002/jctb.4549
49. Tantis I, Bousiakou L, Karikas G-A, Lianos P (2015) Photocatalytic and photoelectrocatalytic degradation of the antibacterial agent ciprofloxacin. Photochem Photobiol Sci 14(3):603–607. doi:10.1039/c4pp00377b
50. Olya ME, Pirkarami A (2013) Cost-effective photoelectrocatalytic treatment of dyes in a batch reactor equipped with solar cells. Sep Purif Technol 118:557–566. doi:10.1016/j.seppur.2013.07.038
51. Mumjitha M, Raj V (2015) Electrochemical synthesis, structural features and photoelectrocatalytic activity of TiO2-SiO2 ceramic coatings on dye degradation. Mater Sci Eng B 198:62–73. doi:10.1016/j.mseb.2015.03.020
52. Li G, Liu X, An J, Yang H, Zhang S, Wong P-K, An T, Zhao H (2015) Photocatalytic and photoelectrocatalytic degradation and mineralization of small biological compounds amino acids at TiO2 photoanodes. Catal Today 245:46–53. doi:10.1016/j.cattod.2014.05.040
53. Pourbaix M (1974) Atlas of electrochemical equilibria in aqueous solutions, 2nd edn. National Association of Corrosion Engineers, Houston
54. Shinde PS, Patil PS, Bhosale PN, Bruger A, Nauer G, Neumann-Spallart M, Bhosale CH (2009) UVA and solar light assisted photoelectrocatalytic degradation of AO7 dye in water using spray deposited TiO2 thin films. Appl Catal B 89(1–2):288–294. doi:10.1016/j.apcatb.2009.02.025
55. Burgues-Ceballos I, Stella M, Lacharmoise P, Martinez-Ferrero E (2014) Towards industrialization of polymer solar cells: material processing for upscaling. J Mater Chem A 2(42):17711–17722. doi:10.1039/c4ta03780d
56. Toivola M, Peltola T, Miettunen K, Halme J, Lund P (2010) Thin film nano solar cells-from device optimization to upscaling. J Nanosci Nanotechnol 10(2):1078–1084. doi:10.1166/jnn.2010.1872
57. M-s Hwang, B-y Jeong, Moon J, Chun S-K, Kim J (2011) Inkjet-printing of indium tin oxide (ITO) films for transparent conducting electrodes. Mater Sci Eng B 176(14):1128–1131. doi:10.1016/j.mseb.2011.05.053
58. Song JW, Yoon YH, Kim J, Han CS, Choi BS, Kim JH, Sid (2007) Direct fabrication and patterning of transparent conductive carbon nanotube film using inkjet printing. In: SID International Symposium, Digest of Technical Papers, SID; Soc. Information Display: Long Beach, 2007; pp 1613–1616. doi: 10.1889/1.2785629
59. Jeong J-A, Kim H-K (2010) Characteristics of inkjet-printed nano indium tin oxide particles for transparent conducting electrodes. Curr Appl Phys 10(4):E105–E108. doi:10.1016/j.cap.2010.06.009
60. Černá M, Veselý M, Dzik P, Guillard C, Puzenat E, Lepičová M (2013) Fabrication, characterization and photocatalytic activity of TiO2 layers prepared by inkjet printing of stabilized nanocrystalline suspensions. Appl Catal B 138–139:84–94. doi:10.1016/j.apcatb.2013.02.035
61. Uchida H, Otsubo A, Itatani K, Koda S (2005) Low-temperature deposition of polycrystalline titanium oxide thin film on Si substrate using supercritical carbon dioxide fluid. Jpn J Appl Phys Part 1 44(4A):1901–1906. doi:10.1143/jjap.44.1901
62. Bazargan MH, Byranvand MM, Kharat AN (2012) Preparation and characterization of low temperature sintering nanocrystalline TiO2 prepared via the sol-gel method using titanium(IV) butoxide applicable to flexible dye sensitized solar cells. Int J Mater Res 103(3):347–351. doi:10.3139/146.110644
63. Dzik P, Veselý M, Kete M, Pavlica E, Štangar UL, Neumann-Spallart M (2015) Properties and application perspective of hybrid titania-silica patterns fabricated by inkjet printing. ACS Appl Mater Interfaces 7(30):16177–16190. doi:10.1021/acsami.5b03494

Applied Catalysis B: Environmental 178 (2015) 186–191

Contents lists available at ScienceDirect

Applied Catalysis B: Environmental

journal homepage: www.elsevier.com/locate/apcatb

# Ink-jet printed planar electrochemical cells

Petr Dzik[a,b,*], Michal Veselý[a,b], Marcela Králová[b], Michael Neumann-Spallart[c]

[a] Faculty of Chemistry, Brno University of Technology, Purkynova 118, 612 00 Brno, Czech Republic
[b] Central European Institute of Technology, Brno University of Technology, Technicka 3058/10, 616 00 Brno, Czech Republic
[c] Groupe d'Étude de la Matière Condensée (GEMaC), CNRS/Université de Versailles, 45, avenue des États-Unis, 78035 Versailles CEDEX, France

ARTICLE INFO

*Article history:*
Received 10 July 2014
Received in revised form 28 August 2014
Accepted 13 September 2014
Available online 27 September 2014

ABSTRACT

Planar, interdigitated photoelectrochemical cells were made by ink jet printing. The electrode fingers had widths from 200 to 2000 μm and were revealed by printing a positive protective polymer mask on FTO ($F:SnO_2$) covered glass slides and subsequent etching. One finger family was covered by $TiO_2$, made by using an ink containing the precursor inside inverted micelles and annealing in air. Due to the interdigitated layout, photoelectrochemical response was not suffering from *iR* drop down to low electrolyte ionic strengths. The photoelectro-catalytic degradation of an aqueous solution of terephthalic acid by UVA illumination and electric bias of 1 V was demonstrated by monitoring the fluorescence of the OH-substituted molecule.



## 1. Introduction

Photocatalytic systems based on slurried powder of $TiO_2$ offer excellent performance due to their very high catalyst surface area [1]. Upon immobilization, the free surface of catalyst inevitably decreases, resulting in a loss of catalytic performance due to limited mass transport [2]. Nevertheless, immobilized $TiO_2$ is the preferred form of photocatalyst for practical application, since the need of separating a suspended powder from the fluid to be purified can prohibitively complicate any process at the industrial scale.

The photocatalytic activity of any immobilized semiconductor photocatalyst can be boosted by the application of external electrical bias [3]. The strategy is based on enhancing the electron–hole separation and consequently increasing the quantum yield of the pollutant degradation by the application of electrical bias, which is possible when the photocatalyst is deposited on an electrically conducting substrate [4–6]. However, in the resulting electrochemical cell, *iR* drop is one of the factors limiting high current throughput at moderate bias. If the treatment of low ionic strength media (drinking water) is envisaged, means for minimizing the *iR* drop must be secured.

One way is to use a parallel plate reactor with two opposite electrodes and a small space between them where the electrolyte is passed through [7]. However, the pressure build-up is considerable in a module consisting of many such cells. This drawback can be avoided by using a planar electrochemical cell with two interdigitated electrodes (IDE). The working electrode consists of an electrical conductor covered by a semiconducting metal oxide (e.g. titanium dioxide). The counter electrode material is not critical as long as sufficient electrical conductivity and corrosion resistance is provided and interdigital geometry is respected. Such a design ensures two key functions: (1) it suppresses the main obstacle to efficient use of absorbed photons, i.e. the recombination of photogenerated charge carriers, by applying external electrical bias to the semiconducting photocatalyst and (2) it avoids the reduction of the generated photocurrent due to *iR* drop, even in electrolytes of low ionic strength. These features make the device an interesting candidate for electrophotocatalytic purification of drinking water. Decomposition of model pollutants has been observed on centimeter-scale prototype devices fabricated by standard lithographic techniques using optical copying through contact masks for resist patterning [8].

Material printing seems to be a promising microfabrication method well applicable for the production of planar layered devices, including interdigitated cells. The technique is based on sequential laying of patterned functional layers by means of modified conventional printing techniques [9]. While generally all traditional printing techniques can be adopted for printing functional layers and patterns, inkjet printing [10] occupies quite a prominent position. Despite its quite narrow viscosity and particle size limits, it seems to be the most suitable technique for lab scale prototype development as no hardware printing form is necessary, i.e., patterns designed on a printer driving computer can be printed directly without the need for physical printing form manufacturing. Moreover, up-scaling is very smooth and easy, because industrial inkjet printers with several meters working width are readily

* Corresponding author. Tel.: +420 541149411.
*E-mail address:* petr@dzik.cz (P. Dzik).

http://dx.doi.org/10.1016/j.apcatb.2014.09.030
0926-3373/

available [11–13], so transfer from prototype level to a small series level is reduced to switching to a bigger printer.

In this paper, we adopt the principle of planar electrochemical cells to the versatile method of ink-jet printing allowing for rapid processing and essentially unlimited upscaling, and report on the design and technology of planar interdigitated photoelectrochemical cells. We employed a mixed subtractive and additive approach and deposited all the functional and auxiliary layers solely by inkjet printing. The adoption of inkjet printing provided a great freedom in the design of the cells and thus samples of various geometries were easily fabricated. The fabrication procedure is described in this paper in detail, together with the physical, electrochemical and photocatalytic properties of selected cell types.

## 2. Experimental

### 2.1. Sample fabrication

Commercial FTO ($F:SnO_2$) coated glass (Sigma–Aldrich) was used as the substrate on which cells were fabricated by a combination of material removal and addition. FTO glass sheets were cut down to 26 × 76 mm slides and cleaned by sonication in Neodisher LM cleaning agent, rinsed in ethanol and fired at 450 °C to burn out any remaining contaminants and activate the surface. In order to adjust the surface energy and wetting behaviour of the printed ink, cooled slides were rinsed in 1 vol% ethanolic solution of an aliphatic hydrocarbon based hydrophobization agent (Toko Waterstop, Tokowax, Switzerland), dried with a stream of nitrogen, rinsed in 1 vol% aqueous solution of sodium dodecylbenzene sulfonate (Enaspol Inc., Czech republic) and dried again.

Printing of all functional and auxiliary layers was performed with an experimental inkjet printer Fujifilm Dimatix 2831. The printer features a disposable 16-nozzle piezoelectric jetting printhead coupled with a 2 mL polyethylene ink tank. It is capable of printing on A4 size substrates with a resolution of up to 5080 dpi, i.e. 5 μm. Both substrate and printhead can be heated in order to speed up solvent evaporation and reduce ink viscosity, respectively. A stroboscopic camera provides still images or slow-down video for the observation of drop formation process, while another fiducial camera is used for precise substrate positioning and aligning of subsequently print layers. The printer has been successfully employed for the deposition of a wide variety of functional and auxiliary layers [14–21] and during the past years has *de facto* become the industrial standard tool for ink development and testing.

Generally, the following procedure was repeated for each printing step: the prepared printing formulations (see below) were sonicated for 5 min and then loaded into syringes. 0.45 μm membrane filters (Pall Corporation, USA) and blunt needles were attached to the syringe luer ports. The printing formulations were filtered and filled into the Dimatix ink tanks. Dimatix 10 pL printing heads were attached to the tanks and sequentially mounted into the Dimatix printer. The drop formation characteristics of all formulations were checked by means of a built-in stroboscopic camera and interaction of the printed material with the substrate was observed by an optical microscope. The interdigitated electrode base pattern as well as the patterns for other layers were drawn as vector graphics and exported to 1-bit BMP files to be used for driving the printer. The electrode fingers had widths ranging from 200 to 2000 μm.

First, the FTO base pattern serving as the current collecting interdigitated electrode was revealed by printing a positive protective polymer mask on the FTO glass slides and subsequent etching. The polymer mask was printed by a commercial UV-curable ink (Svang Cyan, Grapo Ltd., Czech Republic), cured off-line under a mercury vapor medium pressure lamp (25 J/cm$^2$), and baked on a hot plate at 250 °C for 10 min. Next, the FTO slide was etched in a mixture of zinc powder and 15% aqueous HCl in order to remove the naked FTO while preserving those areas covered by the protective printed mask. After the etching operation was finished, the mask was lifted by burning in a furnace at 450 °C for 30 min.

The second layer, i.e. the titania working electrode, was printed using our previously developed reverse micelles sol–gel composition [18]. However, this time sol concentration was adjusted (0.6 mol of Ti/dm$^3$) in order to gain easier control over the resulting thickness and cracking. With this adjustment, the final thickness of the titania layer after calcination was 50 nm per single layer. We found that it was possible to print 2 layers of sol in wet-to-wet manner followed by single calcination (heating rate 3 °C per min, 30 min at 450 °C) yielding 100 nm titania layers without any cracking in one deposition cycle. Attempts to print more sol layers followed by single calcination resulted in cracked and/or peeling layers. Therefore, thicker layers need to be prepared by repeating the complete cycle of printing double sol layers and calcination.

The device was finalized by printing a masking frame around its edges defining the active area. The same UV curable ink and curing procedure was employed for this task. Proper aligning of the titania active layer and the insulator mask was achieved by means of the Dimatix fiducial camera, which enables sample observation and print origin alignment with 5 μm accuracy. Fig. 1 summarizes the cell production procedure.

In this manner, devices with electrode finger widths ranging from 200 to 2000 μm were conveniently fabricated. Apart from regularly spaced devices, several other lay-outs were also fabricated and their properties investigated, including reduced gap devices or devices with different finger widths of working and counter electrodes. Moreover, the thickness of the titania working electrode layer was varied in the 100–500 nm range.

### 2.2. Investigation of IDE device properties

Printed layer quality was monitored by a Nikon Eclipse E200 optical microscope equipped with a polarized light unit and a Nikon D5000 digital camera and a Nikon Camera Control Pro 2 software. SEM imaging and elemental analysis was performed on a ZEISS EVO LS 10 scanning electronic microscope. The same machine was used for layer thickness estimation by observing sample cross sections. Phase composition of calcined titania layers was confirmed by a Panalytical Empyrean XRD system and its diffuse reflectance UV-Vis spectra were recorded by an Ocean Optics Redtide spectrophotometer with a reflectance fiber probe. Layer thickness was investigated by a Dektak XT stylus profilometer.

Photoelectrochemical characterization was performed using a two-electrode setup with the titania overprinted FTO finger family as the working electrode and the opposite naked FTO finger family as the counter electrode. This setup was fitted into a custom-build 15 × 40 × 70 mm quartz cuvette. The cuvette was filled with 0.1 M sodium sulfate solution (15 mS cm$^{-1}$) and fitted onto an optical bench equipped with a Sylvania Lynx-L 18 W fluorescent UV-A lamp. The lamp emission was monitored by a Gigahertz Optic X97 Irradiance Meter with a UV-3701 probe and the irradiance was set to 5 mW cm$^{-2}$ by adjusting the lamp to cuvette distance. A magnetic stirrer was placed beneath the cuvette and a magnetic flea inside the cuvette provided efficient electrolyte mixing. Electrochemical measurements were performed with a computer controlled electrometer in combination with a National Instruments Labview platform supplying a linear voltage gradient of 5 mV s$^{-1}$ from −0.5 to 2 V. For chopped response curves, the lamp was manually obscured and revealed at 5 s intervals.

Electrophotocatalytic experiments were conducted with the same cell and light source as the electrochemical response curves were measured with. Recently, terephtalic acid was suggested as a model compound for monitoring the oxidative activity of valence

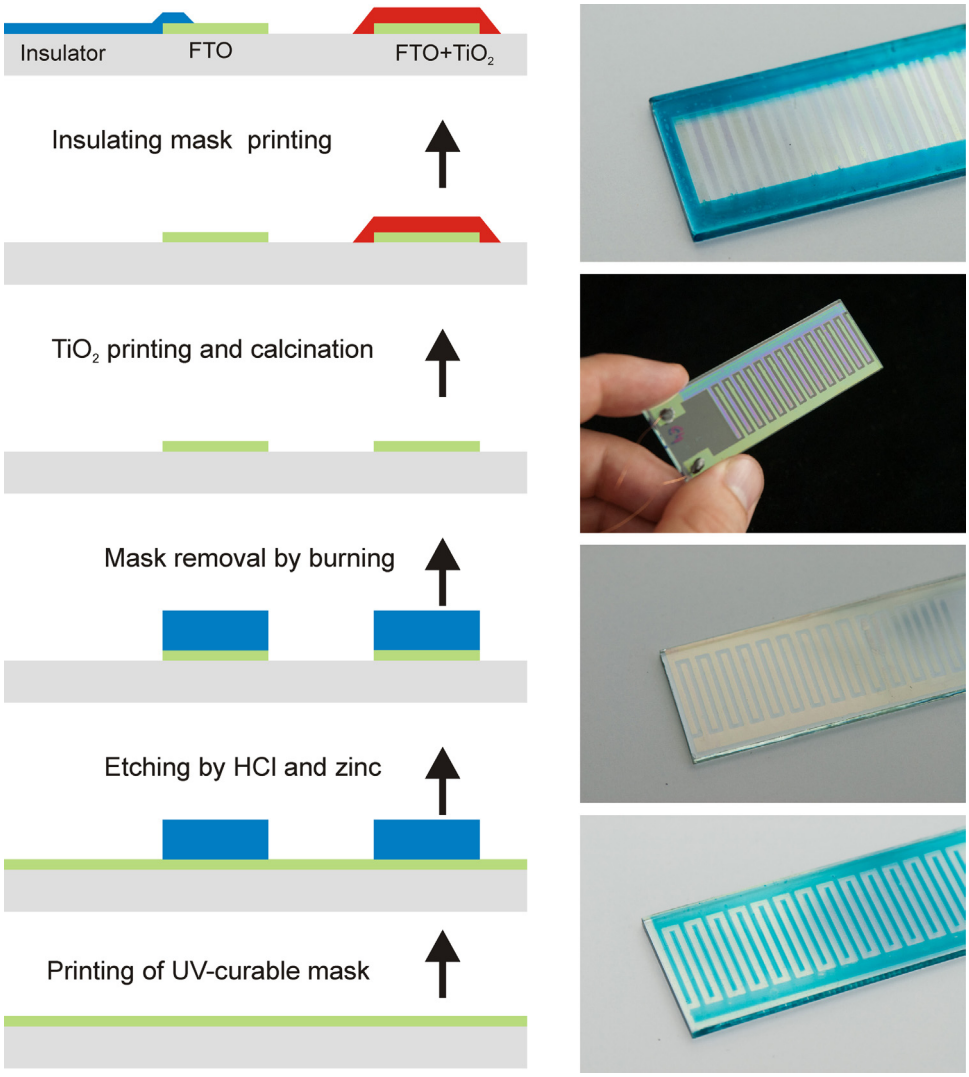


**Fig. 1.** IDE cell fabrication procedure.

band holes generated in the immobilized photocatalyst [22]. Upon oxidation, presumably resulting from the attack of a hydroxyl radical, terephtalic acid is oxidized into hydroxyterephtalic acid, which gives a strong fluorescence signal at 425 nm. This approach proved to be very convenient for our experimental setup, because a single radiation source could be used for both the activation of the photocatalyst as well as the excitation of the fluorescent probe generated during the course of the reaction. The emitted fluorescence was collected by a quartz collimating lens mounted in the lateral wall of the cell holder and projected into an optical fiber attached to an Ocean Optics Redtide spectrometer. The spectrometer driving software allowed for a convenient automated recording of the fluorescence intensity. Calibration was performed using hydroxyterepthalic acid standard (Sigma–Aldrich).

## 3. Results and discussion

### 3.1. Optimization of printing conditions

During inkjet printing on a nonporous, nonabsorbing surface, the surface tension of printed ink and the surface energy of the substrate must closely match in order to ensure optimal wetting behaviour and smooth, but well defined wet layer formation [23]. If the printed liquid is wetting the surface too much, excessive positive dot gain or even pattern bleeding [24] may occur. On the other hand, poor wetting of substrate by the printed ink results into spontaneous shrinking of the printed ink (negative dot gain), or the formation of a bumpy surface resembling the texture of an orange peel [25–27].

While the printer setup and conditions for flawless patterning of the reverse micelles titania ink had been established in our previous work [18], the UV curable ink workflow needed to be optimized in order to produce well resolved patters and good reproducibility. Fig. 2 depicts the key points of this process: the FTO surface after baking is excessively wetted by the printed ink and heavy ink spreading totally ruins the edges of the printed pattern (a). After treatment with the dewetting agent, ink spreading is avoided, but ink is actually dewetting the surface too much and the printed pattern size is reduced (b). Finally, the best results were obtained by treating the FTO glass with the dewetting agent followed by rinse in dodecylbenzene sulfonate, which resulted into just the right degree of wetting producing excellent rendition of even the finest lines down to 100 μm (c).

### 3.2. Physical properties of devices

For routine checking during sample fabrication, optical microscopy is the preferred tool. However, as all the layers are

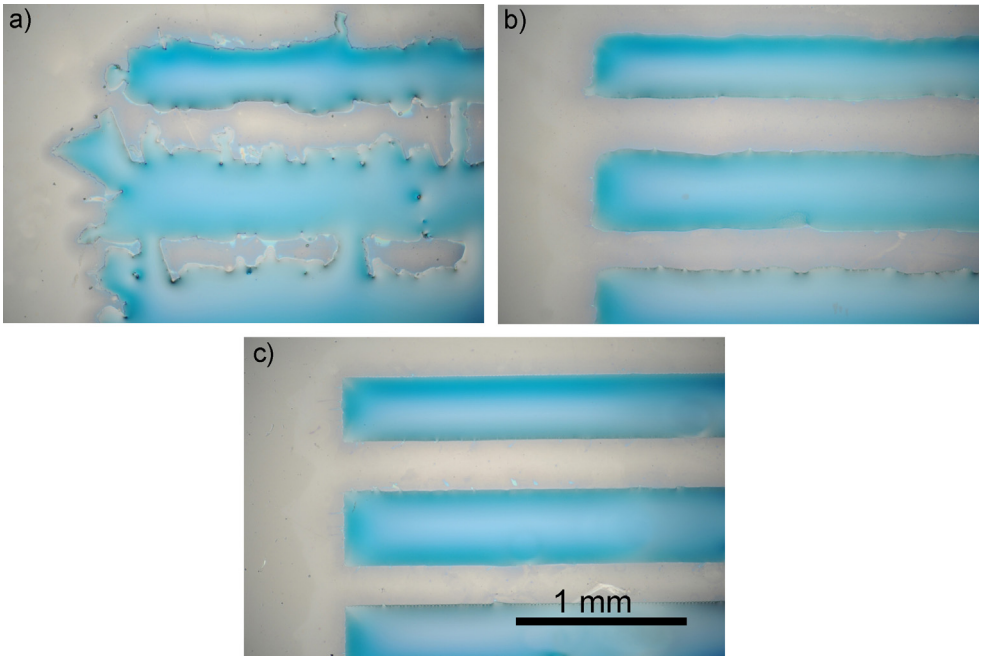


**Fig. 2.** Influence of substrate treatment on the print quality: (a) FTO surface after baking is excessively wetted by the printed ink with significant positive dotgain and irregular ink bleeding, (b) application of the dewetting agent suppresses ink spreading but ink is actually dewetting the surface too much, resulting into slight negative dotgain, (c) treatment by the dewetting agent plus dodecylbenzene sulfonate produces just the right degree of wetting with excellent definition of pattern edges.

transparent, images tend to be faint and have low contrast. Therefore SEM images are included to depict the device structure. Fig. 3 shows the edge of a finger covered by titania layer. Titania fingers have been designed intentionally 10% wider (1100 and 550 μm) in order to ensure complete coverage of the FTO fingers as well as their edges. This overlap is clearly visible in the middle darkest band of Fig. 3(a). In the same figure we can also observe that the FTO edge is not particularly smooth, which is probably the result of under-etching by the aggressive FTO etching bath. It seems that with the present etching process the minimum width of FTO patterns is limited to approximately 100 μm. The cross-sectional view of the finger confirms the smoothness and evenness of the titania coating resulting from previous optimization.

Profilometric scanning over the centre part of the device reveals repeating units of "titania finger - insulating space - counter electrode finger (FTO) - insulating space". Fig. 4 depicts the record of a stylus profilometric scan across 2 fingers of a 1000–1000–1000–1000 μm device fabricated with 4 cycles of titania deposition. The thickness of the FTO finger (left part of the trace, approximately 250 nm) and of the FTO + titania layer (right part of the trace, approximately 400 nm) can be exactly determined and the overlap of the wider titania strip is also clearly visible. Figs. 5 and 6 illustrate the optical properties and phase composition of the reverse micelles originated titania layers. Strong interference coloring observed visually expresses itself in the typical periodic peaks in the diffuse reflectance spectra. The phase composition was investigated by XRD and the presence of pure anatase phase was confirmed. Further details about the properties of this particular type of titania coating can be found in our previous communication [28].

### 3.3. Photoelectrochemical properties

The (conductivity) cell constants, $\kappa$, of the interdigitated finger device were close to the ones calculated using ref. [29]. A structure of 200 μm wide fingers and spaces was already fine enough to obtain a $\kappa$ value below 0.01 $cm^{-1}$. The cells reported in this study,

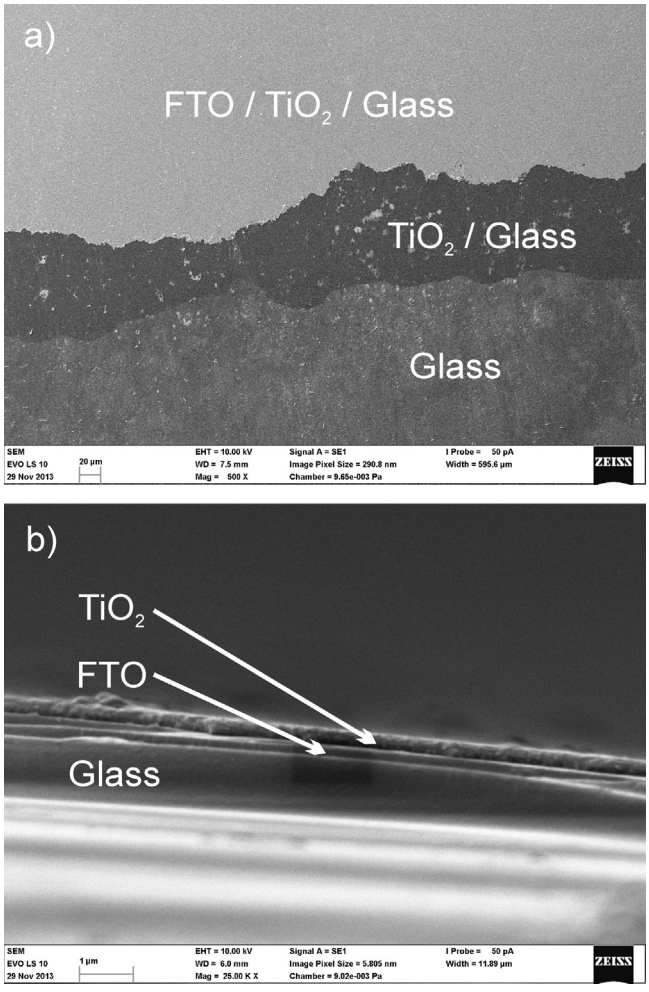


**Fig. 3.** SEM images of the IDE cells: (a) top view of the boundary of FTO finger overprinted by titania, (b) cross-section of a finger.

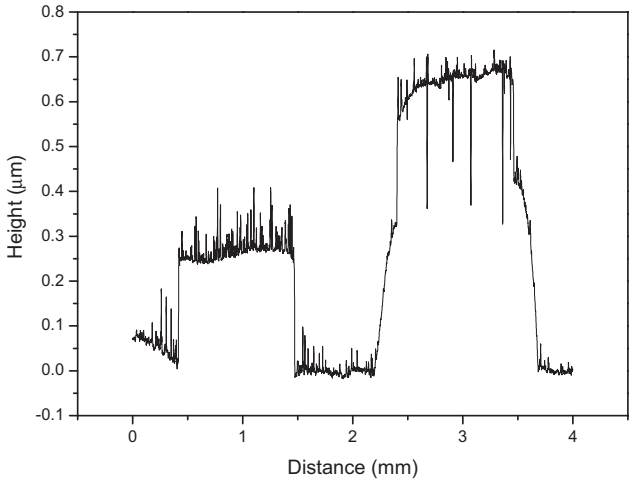


**Fig. 4.** Profilometric scan of a pair of fingers on a 1000–1000–1000–1000 μm device with 4 cycles of titania deposition yielding an approximately 400 nm thick titania coating.

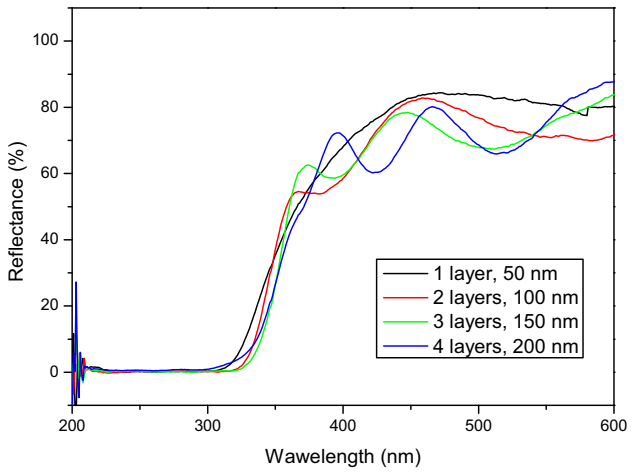


**Fig. 5.** Diffuse reflectance spectra of printed titania layers.

i.e. cells with 500 and 1000 μm wide fingers, featured cell constants of 0.0136 and 0.0271 $cm^{-1}$, respectively. A typical photoelectrochemical response of one of the finger devices in two different electrolytes of different conductivity is shown in Figs. 7 and 8. Finer fingers in the case of the 500 μm device result in lower cell

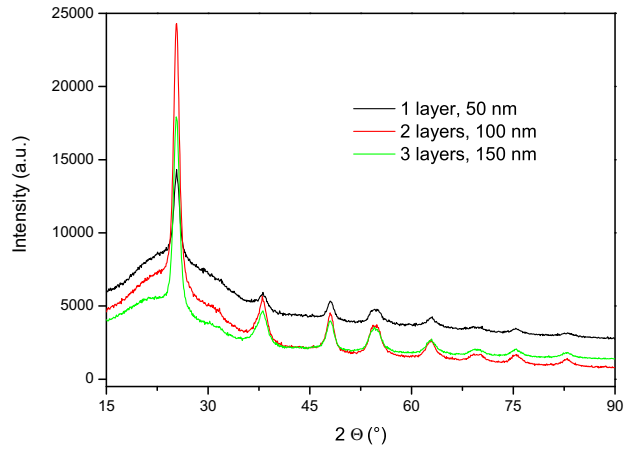


**Fig. 6.** XRD patterns of $TiO_2$ films, Cu-$K_\alpha$ irradiation.

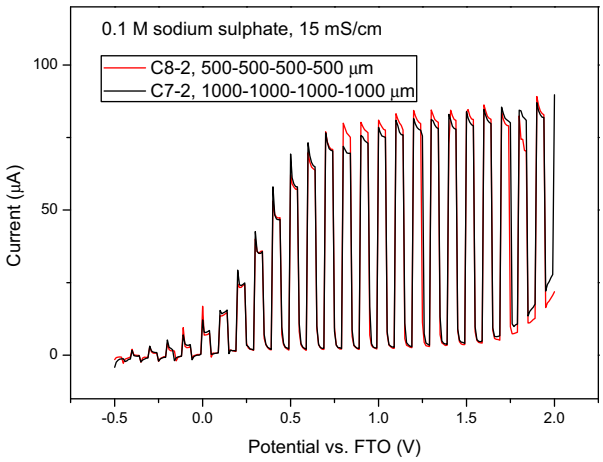


**Fig. 7.** Chopped photocurrent response curve in sodium sulfate electrolyte.

constants, which are beneficial for suppression of *iR* drop in electrolytes of low conductivities.

### 3.4. Electrophotocatalysis

Finally, an example of photodegradation of a solution of terephthalic acid under UVA irradiation and assisted by electrical bias, using a 1000–1000–1000–1000 device with 200 nm thick $TiO_2$ fingers is shown at Fig. 9. During the course of the experiment, the fluorescence due to an intermediary product (OH-substituted) increased and would eventually decrease down to zero as the fluorescent intermediate is further oxidised. The fluorescence at 425 nm plotted as a function of time reflects the initial reaction rate. While the blank checks show essentially no reaction, we can observe a doubling of the reaction rate (with respect to the unbiased case) when an external bias of 1 V was applied. From the initial slopes of the traces, the production rates, $v$, can be calculated taking into account the total volume of the solution. These production rates, considering Farday's law of electrolysis, are related to the electrical charge passed (photocurrent, $i_{photo}$). The Faradaic efficiency, $f$, of the process is calculated using $f = vF/i_{photo}$. The value of 0.009 obtained for the experiment shown in Fig. 9 is satisfactory given the fact that a very low concentration of electroactive species ($1.10^{-5}$ M) was used. Polychromatic light centered at 365 nm was used for this experiment. The IPCE (incident photon-to-current

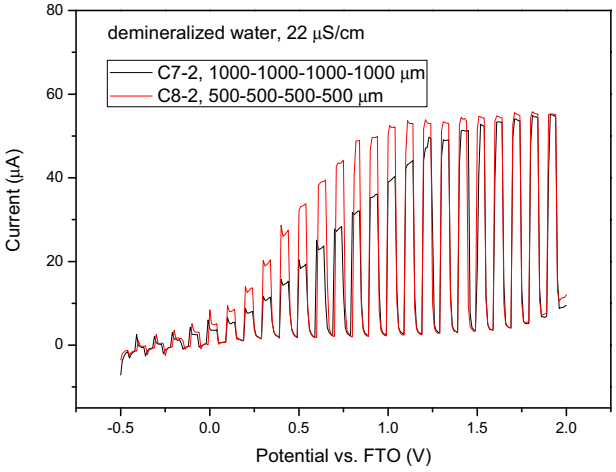


**Fig. 8.** Chopped photocurrent response curve in demineralized water.

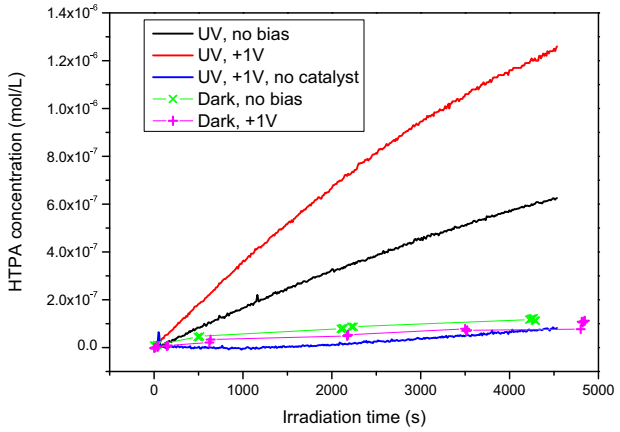


**Fig. 9.** Concentration profiles of HTPA under various experimental conditions.

efficiency) was 0.13 at 365 nm for 200 nm thick electrodes. Values of *f* were found close to values obtained for the degradation of phthalic acid in a parallel plate reactor [30]. While the datasets of the irradiated samples were measured continuously in 10 s intervals, the dark ones needed to be measured discontinuously only a few times during the reaction duration because a single radiation source was used for both catalyst activation and fluorescent probe excitation.

## 4. Conclusion

Inkjet material printing was successfully employed for the fabrication of planar interdigitated photoelectrochemical cells. A mixed subtractive and additive approach was adopted and all the functional and auxiliary layers were printed by an experimental inkjet printer Fujifilm Dimatix 2831. Inkjet printing proved to be an elegant method for sol delivery to the substrate. It provides a complete control over the deposition process parameters together with an excellent efficiency of precursor use. Wetting issues associated with the substrate-ink interfacial interactions were controlled by substrate treatment with suitable surfactants.

The process of FTO patterning by etching with the help of a protecting printed mask is very convenient and can be easily adopted for pattering of other materials as well. Although the resolution of printed masks can not compete with the well established resist technologies, it may be well suited for the fabrication of large footprint devices requiring a low degree of integration (solar cells, electroluminescent modules etc.). The absence of a resist development step makes the fabrication process much more environment friendly. Moreover, it does not require any special material or equipment as it can be performed with ordinary flatbed or roll printers and UV-curable inks.

Devices with regular finger arrangement and widths ranging from 200 to 2000 μm were conveniently fabricated and so were several other lay-outs including reduced gap ones or devices with different finger widths of working and counter electrodes. The benefits of finer fingers are clearly demonstrated, resulting in lower cell constants which are beneficial for the suppression of *iR* drop in electrolytes of low conductivities. With the present technology, 200 μm fingers seem to be fine enough for work with electrolytes with ionic strength typical for drinking water.

Comparative photocatalytic and electrophotocatalytic experiments with terephtalic acid as model contaminant compound proved the beneficial role of external electrical bias in suppressing photogenerated electron-hole recombination in the semiconducting photocatalyst. In this way, more efficient charge separation in the electric field of the IDE device has been demonstrated by the acceleration of terephtalic acid oxidation, which was conveniently monitored by the fluorescent signal of its dominant oxidation product, hydroxyterephtalic acid.

## Acknowledgements

The authors thank the Technology Agency of the Czech Republic for support through project TA03010548 and the Ministry of Education, Youth and Sports of the Czech Republic for support through project CZ.1.07/2.3.00/30.0005.

## References

[1] R. van Grieken, J. Marugan, C. Sordo, C. Pablos, Catal. Today 144 (2009) 48–54.
[2] M. Tasbihi, C.R. Ngah, N. Aziz, A. Mansor, A.Z. Abdullah, L.K. Teong, A.R. Mohamed, Ind. Eng. Chem. Res. 46 (2007) 9006–9014.
[3] M. Neumann-Spallart, Chimia 61 (2007) 806–809.
[4] G. Waldner, A. Bruger, N.S. Gaikwad, M. Neumann-Spallart, Chemosphere 67 (2007) 779–784.
[5] P. Fernandez-Ibanez, S. Malato, O. Enea, Catal. Today 54 (1999) 329–339.
[6] I.M. Butterfield, P.A. Christensen, A. Hamnett, K.E. Shaw, G.M. Walker, S.A. Walker, C.R. Howarth, J. Appl. Electrochem. 27 (1997) 385–395.
[7] P.S. Shinde, P.S. Patil, P.N. Bhosale, A. Bruger, G. Nauer, M. Neumann-Spallart, C.H. Bhosale, Appl. Catal. B-Environ. 89 (2009) 288–294.
[8] M. Neumann-Spallart, Electrochim. Acta 56 (2011) 8752–8757.
[9] F.C. Krebs, Sol. Energ. Mater. Sol. Cells 93 (2009) 394–412.
[10] G.D. Martin, S.D. Hoath, I.M. Hutchings, Iop, Inkjet printing - the physics of manipulating liquid jets and drops Conference on Engineering in Physics - Synergy for Success, London, ENGLAND, 2006.
[11] P. Calvert, Chem. Mater. 13 (2001) 3299–3305.
[12] H. Sirringhaus, T. Shimoda, MRS Bull. 28 (2003) 802–806.
[13] E. Tekin, P.J. Smith, U.S. Schubert, Soft Matter 4 (2012) 703–713.
[14] W. Tang, L.R. Feng, J.Q. Zhao, Q.Y. Cui, S.J. Chen, X.J. Guo, J. Mater. Chem. C 2 (2014) 1995–2000.
[15] M.W. Wang, D.C. Pang, Y.E. Tseng, C.C. Tseng, J. Taiwan Inst. Chem. Eng. 45 (2014) 1049–1055.
[16] G. Tarapata, M. Marzecki, in: R.S. Romaniuk (Ed.), Photonics Applications in Astronomy, Communications, Industry, and High-Energy Physics Experiments 2013, 2013.
[17] J.T. Kwon, S.H. Eom, B.S. Moon, J.K. Shin, K.S. Kim, S.H. Lee, Y.S. Lee, Bull. Korean Chem. Soc. 33 (2012) 464–468.
[18] P. Dzik, M. Morozova, P. Kluson, M. Vesely, J. Adv. Oxid. Technol. 15 (2012) 89–97.
[19] J.D. Swartz, L.F. Deravi, D.W. Wright, Adv. Func.l Mater. 20 (2010) 1488–1492.
[20] E. Sowade, J. Hammerschmidt, T. Blaudeck, R.R. Baumann, D. Polster, T. Baumgartel, H. Graaf, C. von Borczyskowski, R. Wagner, F. Cichos, SIST, Inkjet printing of polymer microspheres, in: NIP 25: Digital Fabrication 2009, Technical Program and Proceedings, 2009, pp. 788–790.
[21] L.F. Deravi, J.D. Swartz, D.W. Wright, Piezoelectric inkjet printing of biomimetic surfaces for enzyme encapsulation, in: D. Schulze Hagenest (Ed.), NIP24/Digital Fabrication 2008: 24th International Conference on Digital Printing Technologies, Technical Program and Proceedings, 2008, pp. 504–507.
[22] U. Cernigoj, M. Kete, U.L. Stangar, Catal. Today 151 (2010) 46–52.
[23] E. Chow, J. Herrmann, C.S. Barton, B. Raguse, L. Wieczorek, Anal. Chim. Acta 632 (2009) 135–142.
[24] S.C.L. Sousa, A.D. Mendes, P.T. Fiadeiro, A.M.M. Ramos, Ind. Eng. Chem. Res. 53 (2014) 4660–4668.
[25] J.A. Roper, R. Urscheler, P. Salminen, E. Moore, R. Tappi, Metered Size Press Forum Ii, Tappi Proceedings, 1998, pp. 37–55.
[26] G. KigleBoeckler, Tappi J. 79 (1996) 194–198.
[27] M. Matsuta, J. Coat. Technol. 59 (1987) 61–64.
[28] M. Morozova, P. Kluson, J. Krysa, P. Dzik, M. Vesely, O. Solcova, Sensor. Actuat. B-Chem. 160 (2011) 371–378.
[29] W. Olthuis, W. Streekstra, P. Bergveld, Sensor. Actuat. B-Chem. 24 (1995) 252–256.
[30] M. Neumann-Spallart, S.S. Shinde, M. Mahadik, C.H. Bhosale, Electrochim. Acta 111 (2013) 830–836.

*Molecules* **2015**, *20*, 16582-16603; doi:10.3390/molecules200916582

OPEN ACCESS

*molecules*

**ISSN 1420-3049**

www.mdpi.com/journal/molecules

*Article*

# Cold-Setting Inkjet Printed Titania Patterns Reinforced by Organosilicate Binder

**Marcela Králová [1], Petr Dzik [2,*], Vít Kašpárek [1], Michal Veselý [2] and Jaroslav Cihlář [1]**

[1] Central European Institute of Technology, Brno University of Technology, Technicka 3058/10, Brno 61600, Czech Republic; E-Mails: marcela.kralova@ceitec.vutbr.cz (M.K.); vit.kasparek@ceitec.vutbr.cz (V.K.); jaroslav.cihlar@ceitec.vutbr.cz (J.C.)

[2] Faculty of Chemistry, Brno University of Technology, Purkynova 118, Brno 61200, Czech Republic; E-Mail: vesely-m@fch.vutbr.cz

* Author to whom correspondence should be addressed; E-Mail: dzik@fch.vutbr.cz; Tel.: +420-541-149-411; Fax: +420-541-211-697.

Academic Editors: Wing-Kei Ho and Jimmy C. Yu

*Received: 8 June 2015 / Accepted: 24 August 2015 / Published: 11 September 2015*

**Abstract:** A hybrid organo-silica sol was used as a binder for reinforcing of commercial titanium dioxide nanoparticles (Evonic P25) deposited on glass substrates. The organo-silica binder was prepared by the sol-gel process and mixtures of titania nanoparticles with the binder in various ratios were deposited by materials printing technique. Patterns with both positive and negative features down to 100 µm size and variable thickness were reliably printed by Fujifilm Dimatix inkjet printer. All prepared films well adhered onto substrates, however further post-printing treatment proved to be necessary in order to improve their reactivity. The influence of UV radiation as well as of thermal sintering on the final electrochemical and photocatalytic properties was investigated. A mixture containing 63 wt % of titania delivered a balanced compromise of mechanical stability, generated photocurrent density and photocatalytic activity. Although the heat treated samples yielded generally higher photocurrent, higher photocatalytic activity towards model aqueous pollutant was observed in the case of UV cured samples because of their superhydrophilic properties. While heat sintering remains the superior processing method for inorganic substrates, UV-curing provides a sound treatment option for heat sensitive ones.

**Keywords:** titania; silica binder; material printing; direct patterning; UV-curing

## 1. Introduction

Environmental pollution is becoming very serious problem and the demand for safe drinking water is continuously increasing with increasing population growth. Disinfection and decontamination are considered as conventional methods for water treatment. Their main disadvantages are energetic and operational demands, requirement of intensive chemical treatments the residuals of which can even increase the problems with pollution and decontamination [1]. New techniques such as advanced oxidation processes could improve the effectivity of these traditional water treatment processes because of their lower energy demands and less chemicals used [2]. Photocatalysis is one such method applicable not only for water treatment, but also for air cleaning and self-cleaning solid surfaces. Its principle is based on electrons and holes separation caused by the absorption of UV light and their diffusion to the semiconductors surface where they can take part in various red-ox reactions. During the past years, this technique has been widely applied in environmental purification tasks [3,4] as well as in artificial photosynthesis [5]. Titanium dioxide has become the most investigated and the most prominently used photocatalyst [6,7] because of its relatively high photoactivity, biological and chemical inertness, competitive price and creation of stable solutions [8].

Generally, the employment of freely suspended powder photocatalysts brings some disadvantages such as strong tendency to aggregation, low adsorption capacity, sedimentation and deposit formation [9]. Moreover, the unavoidable need of catalyst separation from the solution after the treatment and can prohibitively complicate large scale processes. To overcome these drawbacks, the photocatalyst can be immobilized by the anchoring onto various substrates. Titania coatings have been successfully fabricated by both gas-phase methods [10–12] as well as wet-coating methods [13–15] and both approaches resulted into highly active immobilized photocatalysts [16].

Recently, the traditional wet-coating methods such as spin-coating, dip-coating, doctor blade coating *etc*., have been challenged by a new approach most often termed as material printing [17]. The process essentially involves the deposition of layers and patterns by means of traditional printing techniques where conventional color inks have been replaced by special functional inks. Strictly speaking, this technique has been around for the past 60 years but was actually limited to screen printing of pulverized metal pigment inks during the fabrication of conductive tracks in the electronic industry [18]. During the past decade, the concept of material printing has been intensively developed and the portfolio of applicable printing techniques has broadened significantly [19].

While essentially all traditional printing techniques can be adopted for printing of functional patterns, inkjet printing [20] occupies quite a prominent position. Despite quite narrow viscosity and particle size limits, it is most suitable for lab-scale prototype development or customized production as no hardware printing form is required, *i.e*., patterns designed as computer files can be printed directly. Moreover, up-scaling from the lab level is easily accomplished merely by switching to a bigger format printer. Inkjet printing has been successfully used for the deposition of a variety of functional liquids, such as conducting polymers [21–23], dispersions of catalyst nanoparticles [24], *etc*. Numerous biochemical applications have been reported, such as tissue scaffolds [25,26] or cellular patterns [27,28]. Moreover, many prototype multicomponent devices such as capacitors [29], transistors [30], electronic filters [31], and organic light-emitting diodes [32] have been successfully fabricated. Recently we reported on a fully printed semiconductor-based photoelectrochemical cell [33].

Titania-silica mixtures represent a perspective group of materials that have recently been used as catalysts and supporting materials [34,35]. Titania-silica mixtures were found to improve the photocatalytic properties of pure titanium dioxide [36], increase the specific surface area [37] and improve the adsorption properties [38]. However, in order to be able to deposit the titania-silica film by material printing, an ink with appropriate properties needs to be formulated. Two distinct approaches to this task can be easily identified:

The first one is based on the sol-gel process, *i.e.*, soluble titanium salts and/or titanium alkoxides are complexed by suitable chelates, pre-crosslinked by partial hydrolysis and the resulting metastable colloidal sols are then printed onto a substrate, gelled and converted into dense or porous oxide layer [39].

The second approach is based on the synthesis of stable colloidal suspension of nanocrystalline $TiO_2$ followed by the delivery of this suspension onto a substrate by some of the numerous material printing techniques. Bernacka-Wojcik and coworkers recently demonstrated [40] a disposable biosensor integrating an inkjet printed photodetector fabricated by printing a commercial dispersion of titania particles with a desk-top office printer equipped with a thermal inkjet head. A similar approach was adopted by Yang *et al*. [41] who used a dispersion of $TiO_2$ printed by a modified office inkjet printer to produce an oxygen demand sensing photoanode and by Arin *et al*. [42] who fabricated photocatalytically active $TiO_2$ films by inkjet printing of nanoparticle suspensions obtained from microwave-assisted hydrothermal synthesis. Inkjet printing has been successfully employed also for the deposition of doped titania nanoparticles [43] as well as for the fabrication of DSSCs [44] titania photoanodes. Various methods have been utilized for the dispersing and stabilization of ultrafine printable suspensions, including ultrasound [45], microemulsions [46] and co-solvent mixtures [47]. The authors of this paper have recently reported the fabrication of titania patterns by inkjet printing of rutile nanodispersions originating from hydrothermal processes [48] and also the fabrication of printed composite titania-silica photoanodes [49].

The key difference between these two discussed approaches is determined by the post-deposition treatment requirements. The sol-gel originated coatings generally require oxidative heat processing in order to remove the organic fraction of the sol and induce crystallization of the oxide being created, while the suspension originated layers do not require heat treatment *per se* since prefabricated crystalline particles had been deposited. Yet, some form of further treatment and/or the presence of a binder may be necessary even in the case of the suspension originated coatings in order to ensure sufficient mechanical stability, adhesion to substrate and/or processing of further components present in the coating. However, if the treatment does not involve excessive heating, the deposition onto organic polymeric substrates becomes possible.

In this paper, we report on the fabrication of titanium dioxide layers by direct inkjet pattering of nanocrystalline suspension. Recently reported organo-silica binder [50] was mixed with commercial titania nanoparticles in order to improve printed layer mechanical properties. Inkjet printable formulations with various ratios of titania to binder were formulated and patterns of different thickness were printed onto soda-lime, Pyrex and FTO glass substrates. Printed green body patterns were further processed by thermal treatment or UV curing. The physical, chemical, electrical and photocatalytic properties of printed, sintered and UV-cured patterns were in detail investigated and the influence of post-deposition processing on printed layer properties was elucidated.

## 2. Results and Discussion

### *2.1. Printed Layers Imaging*

For quick on-the-fly checking as well as the whole printed area inspection, optical microscopy and photomicrography are the preferred tools. First, one-layered samples of all tested formulations were compared in order to evaluate the printability of used formulations and substrate interactions. We observed that although all tested formulations were jettable, with increasing titania fraction the print quality worsened. Apparently, the silica binder helps to stabilize the titania particles, preventing aggregation and also improving the flow of the suspension during hydrodynamic stress accompanying transport through the print head. While the print quality of Ti_1 and Ti_2 formulations was essentially flawless, occasional nozzle blockage and/or diverted droplets occurred more often in the case of Ti_3 and Ti_4. Ti_5 required regular nozzle purging and cleaning to ensure acceptable print quality (Figure 1).

Multilayer printing was performed in the wet-to-dry manner, *i.e.*, the previous layer was completely dry before printing the following one started. No problems such as bleeding or mottling which are usually associated with this procedure were observed here and the inks proved to be well suited for fabrication of thick patterns by multiple overprinting. However, after comparing the full range of studied layer thicknesses, we found out that with increasing number of layers banding artifacts started to develop at the boundaries of individual bands following the scanning motion of the printhead. The phenomenon was further studied by profilometry and resolved by adjustment of the printing formulation composition (see below).

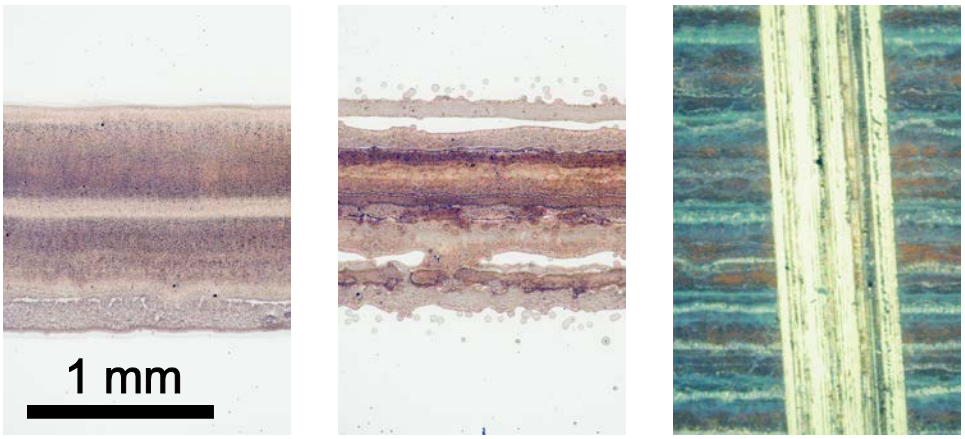


**Figure 1.** Optical micrographs of the printed layers showing the influence of ink composition on print quality. Formulation Ti_1 (**left**) featured good layer uniformity and excellent edge definition, but formulation Ti_5 (**middle**) suffered from occasional nozzle blockage and diverted droplets. The **right** image depicts a 3-layered patch of Ti_3 formulation featuring the banding artifacts and a scratch made with the pencil just harder than the layers itself.

### *2.2. Pencil-Hardness Test*

The hardness of thin layers was determined in the whole range of hardness according the standard. The hardness of pencil that was not able to scratch the film was considered as the hardness of the film. Figure 1 depicts the results of a 3-layered patch of Ti_3 formulation scratching with the pencil just harder

than the layers itself. Printed layers as well as heat treated layers were investigated by this method and significant differences were found. We observed that increasing of silica content in the printing formulation (from Ti_5 to Ti_1) led to the formation of harder films in the case of both printed as well as sintered samples. Moreover, the films showed a higher hardness after sintering process that is probably caused by the creation of silica network during the thermal treatment process. The results are summarized in Table 1.

**Table 1.** Hardness data for 3-layered samples.

| Sample Name | ISO 15184 Hardness | |
|---|---|---|
| | UV Cured | Sintered |
| Ti_1 | 6B | 10H |
| Ti_2 | 8B | 10H |
| Ti_3 | 8B | 10H |
| Ti_4 | 8B | F |
| Ti_5 | 8B | 5B |

*2.3. Thermogravimetric Analysis*

Thermogravimetric behaviour was studied for all prepared printed mixtures. The samples shared common trends and a typical record is depicted at Figure 2. In the first temperature region (up to 120 °C), there was the highest weight loss which was attributed to the evaporation of adsorbed solvents (ethanol and butanol). This evaporation is represented by endothermic peak. The weight loss in the second temperature region (up to 315 °C) is related to the oxidation of $CH_3$- groups from the MTEOS precursor. The oxidation is represented by exothermic peak at temperature around 255 °C. Any further weight loss cannot be observed beyond 315 °C. The other significant exothermic peak appeared at the temperature of 581 °C. This peak is associated with the phase transformation of amorphous $SiO_2$ to tridymite [51]. Okada *et al*., discovered that silica matrix shift the temperature transformation of $TiO_2$ from amorphous phase to anatase phase [52] so we supposed that in our case the phase transformation of anatase to rutile occurred also at higher temperature. Therefore, the exothermic peak at 691 °C is attributed to the mentioned transformation. The last peak at temperature 978 °C had endothermic character and it is connected with melting point of titania-silica system.

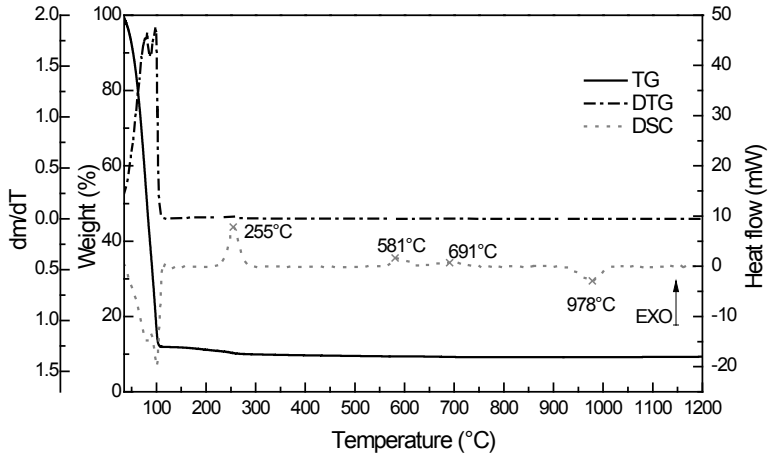


**Figure 2.** The record from thermogravimetric analysis for Ti_3.

*2.4. Profilometry*

During a preliminary testing, we discovered that there was virtually no influence of the processing mode on the thickness of printed patterns. All "green body" printed, sintered as well as UV-cured samples exhibited essentially identical values. This behavior was expected, since most of the printing formulation dry mass is constituted by titania nanoparticles forming a rigid structure permeated by the binder. Therefore, the profilometric thickness measurement was systematically conducted on the printed samples only (Figure 3).

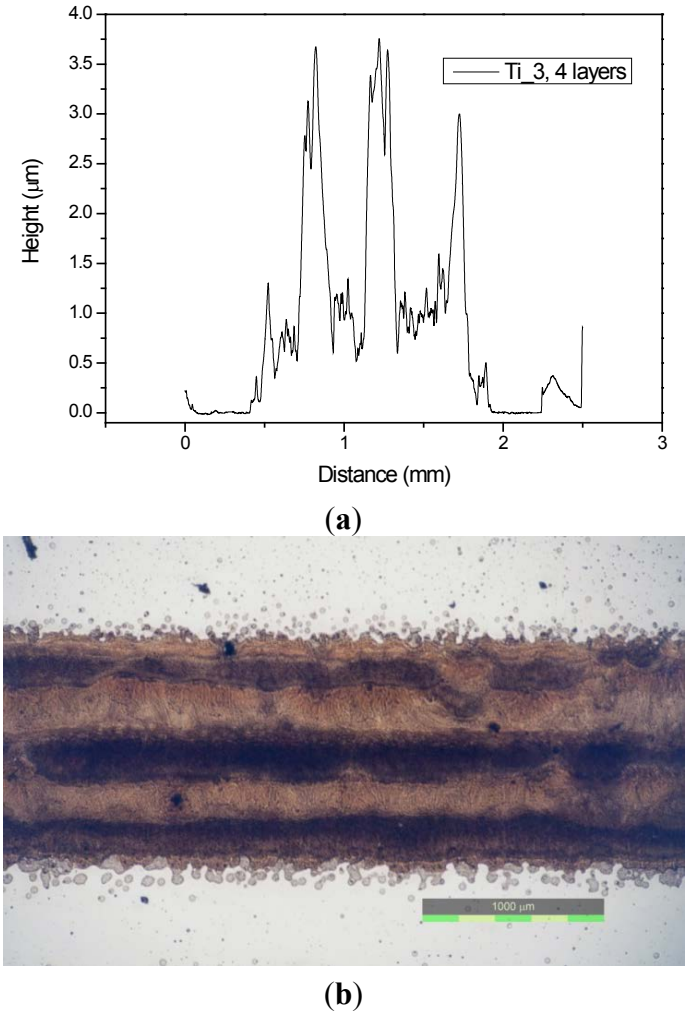


(**a**)

(**b**)

**Figure 3.** Banding patterns recorded in profilometric scan (**a**) and as seen in optical microscope (**b**).

Complete results of profilometric measurements for all samples are summarized in Table 2. The thickness is generally increasing with increasing titania content, with the exception of Ti_5 sample. We assume that the amount of printed ink in this case was actually lowered by occasional nozzle blockage. The RMS roughness calculated from a 3 mm scan length is relatively high with respect to the layer thickness. At such great scan length, it does not reflect the particle size but rather the banding artifacts observed in optical microscope and discussed above. Their geometrical distribution along the scan direction corresponds to the width of the printhead which confirms their cause and origin.

**Table 2.** Thickness and roughness of printed samples.

| | Ti_1 | | Ti_2 | | Ti_3 | | Ti_4 | | Ti_5 | |
|---|---|---|---|---|---|---|---|---|---|---|
| | **Thickness (μm)** | **Rms (μm)** | **Thickness (μm)** | **Rms (μm)** | **Thickness (μm)** | **Rms (μm)** | **Thickness (μm)** | **Rms (μm)** | **Thickness (μm)** | **Rms (μm)** |
| 1L | 0.512 | 0.252 | 0.555 | 0.239 | 0.573 | 0.263 | 0.766 | 0.480 | 0.748 | 0.282 |
| 2L | 0.708 | 0.493 | 0.776 | 0.468 | 0.916 | 0.333 | 1.173 | 0.579 | 0.995 | 0.489 |
| 3L | 1.024 | 0.771 | 1.214 | 0.700 | 1.330 | 0.741 | 1.708 | 1.017 | 1.273 | 0.727 |
| 4L | 1.301 | 1.201 | 1.353 | 0.723 | 1.489 | 1.106 | 1.837 | 1.073 | 1.524 | 0.867 |
| 5L | 1.746 | 1.588 | 1.763 | 1.092 | 1.906 | 1.113 | 2.224 | 1.275 | 2.008 | 1.089 |

### *2.5. Atomic Force Microscopy*

The topography and roughness on the nanometer scale were analyzed by atomic force microscopy (Figure 4). Selected results for the three layered samples are summarized and compared with profilometric roughness in Table 3. On contrary to the profilometric measurements, the data obtained from AFM indicate much lower roughness of *ca*. 40 nm. With respect to the scan size (500 × 500 nm), we conclude that this figure includes the contribution of primary particles size (primary crystallite size of 21 nm is declared by the supplier) and the sub-milimeter artifacts which influenced the profilomeric roughness determination remain neglected by AFM. Moreover, we discovered that the roughness of all sample sets was decreasing with increasing layers count. Such behavior can be explained by the interaction of freshly printed material with the previous dry porous layer, filling the cavities created during drying of the previous one so the surface is more compact and the roughness is lower.

**Table 3.** RMS roughness (nm) of printed samples obtained from AFM.

| **Sample** | **Number of Layers** | | | | |
|---|---|---|---|---|---|
| | **1L** | **2L** | **3L** | **4L** | **5L** |
| Ti_1 | 60 | 49 | 39 | 28 | 26 |
| Ti_2 | 74 | 45 | 39 | 40 | 34 |
| Ti_3 | 76 | 45 | 43 | 42 | 40 |
| Ti_4 | 78 | 55 | 53 | 40 | 37 |
| Ti_5 | 74 | 38 | 28 | 27 | 21 |

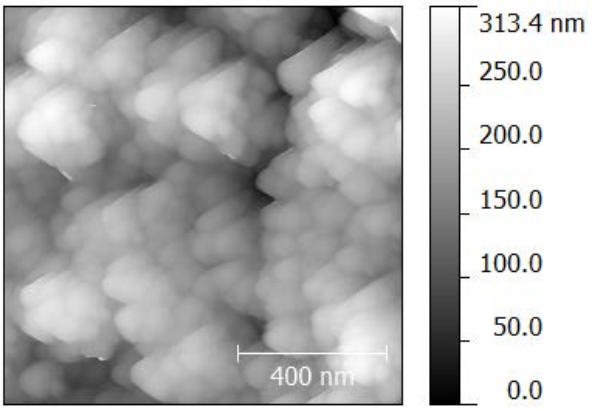


**Figure 4.** Topography of the sample Ti_4_P_4L.

*2.6. Scanning Electron Microscopy*

The structure of the samples was examined by scanning electron microscopy. We discovered that there is no significant visual difference between the UV cured and sintered layers (Figure 5). The particle size in both cases was estimated between 20 and 40 nm which corresponds to the particle size declared for titania P25. It indicates that during the temperature treatment process, the particles were not subject to further aggregation. Moreover, we found that in case of Ti_1, where the fraction of $TiO_2$ (Table 4) was the lowest, a discontinuous phase of titania particles forming isolated islands was formed (Figure 5, top). The other compositions with higher titania fraction seem to feature a rigid structure of communicating titania particles permeated by the binder (Figure 5, middle and bottom).

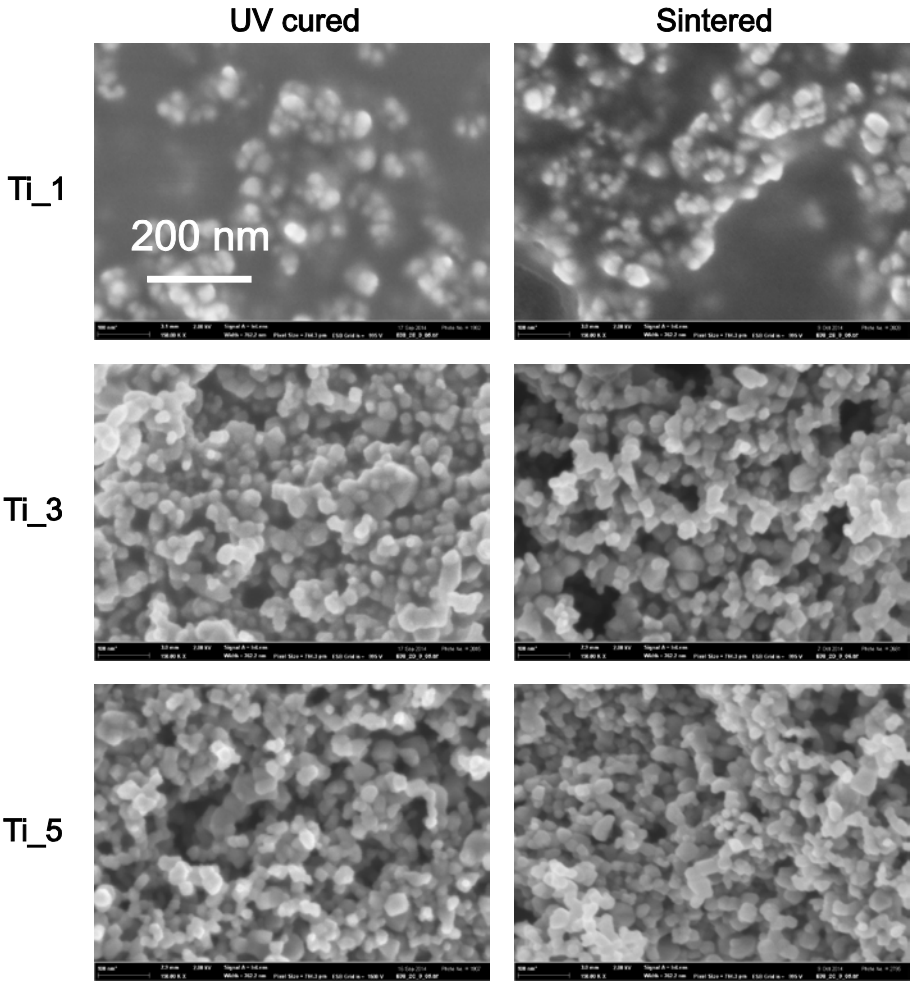


**Figure 5.** Images from SEM analysis; comparison of UV cured and sintered layers (3 layered samples).

SEM images also allowed the comparison of different number layers Figure 6. We could observe the presence of pores both in the UV cured and thermally sintered samples and their frequency of occurrence was decreasing with increasing number of layers. This result was expected on the basis of previous AFM roughness determination. The recorded SEM images fully confirmed the suggested explanation of this phenomenon—decreasing roughness with increasing number of printed layers is caused by filling the cavities created during drying of the previous layer with freshly printed material.

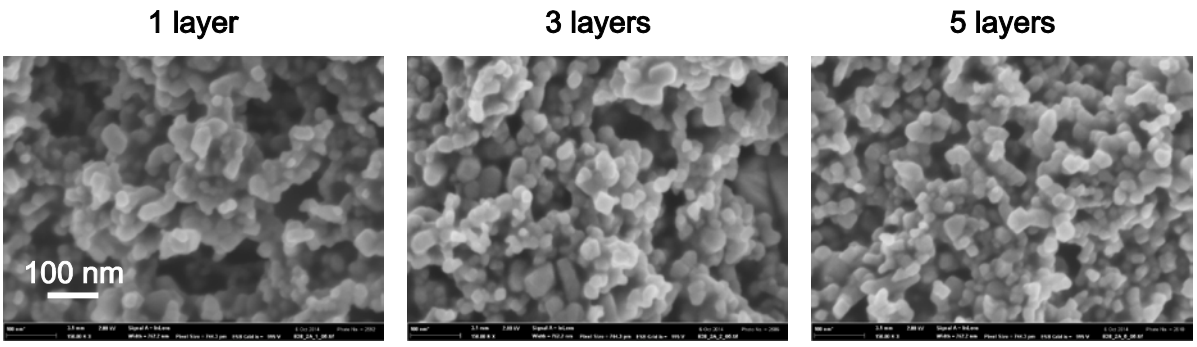


**Figure 6.** Flattening surface topology of sintered Ti_3 sample set with increasing number of printed layers as seen by SEM.

### *2.7. Contact Angle Measurement*

The photoinduced superhydrophility was examined by the sessile drop contact angle measurement on three layered samples. These samples were chosen according the results from optical and scanning electron microscopy. This study involved the comparison of printed and sintered sample sets. UV-cured sets were omitted as they exhibited superhydrophilic nature at the end of the curing process. We confirmed that printed layers had hydrophobic character which was caused by presence of methyl groups in silica binder [50]. Although these groups were inevitably oxidized during the sintering process, yet the character of these layers still remained hydrophobic. On the other hand, photocatalytic degradation of methyl groups which occurred during the post-printing UV curing caused changing the wetting properties to superhydrophilic. As superhydrophilic surface is considered that one where the water droplet applied on surface is immediately spread and its contact angle is lower than 5°. We discovered that the superhydrophilic wetting was reached after 90 min only for printed layers whereas this time was insufficient for sintered layers. When we compared all samples we found out that the contact angle decreased in an order depending on the amount of titania in the printing composition, with the greatest titania fraction sample being the fastest (Figure 7). This trend is observed for printed as well as for sintered layers.

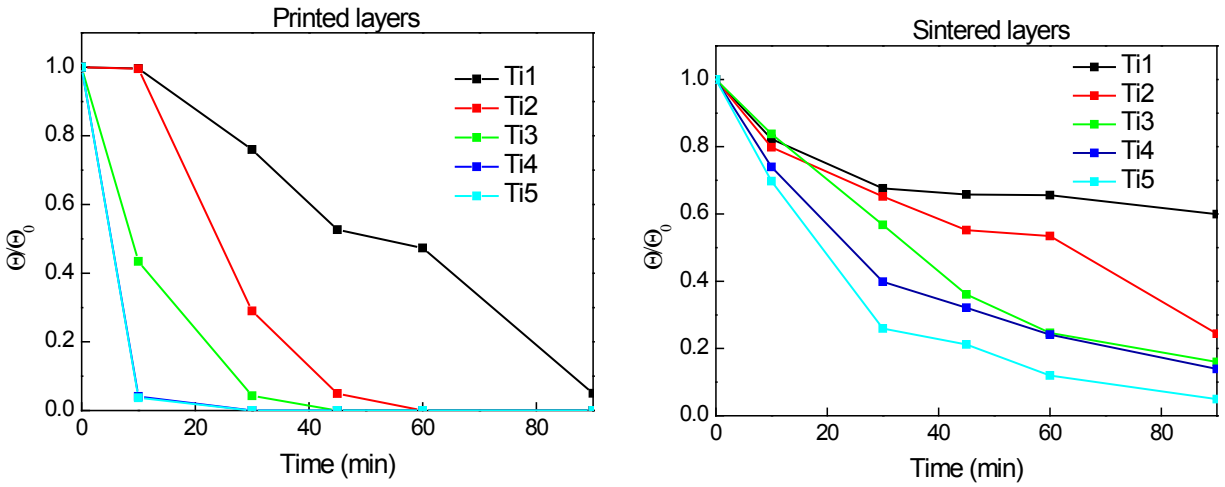


**Figure 7.** *Cont.*

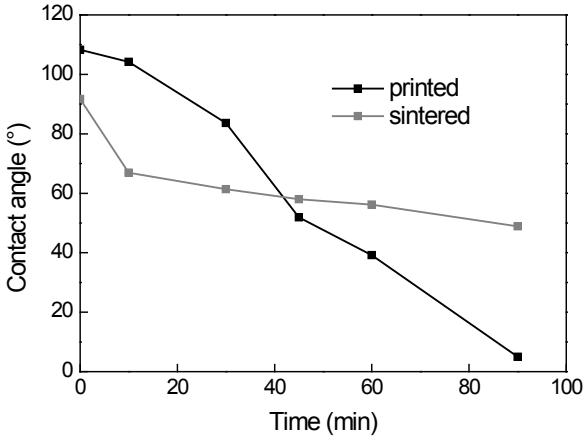


**Figure 7.** The dependence of relative contact angle on irradiation time for three layered samples. Printed "green body" layers (**top left**), thermally sintered layers (**top right**) and the comparison of absolute contact angle values for printed and sintered sample Ti_1 (**bottom**).

### *2.8. Electrochemical Characterization*

Linear sweep voltammetry has been used for the characterization of electrochemical properties. The photoelectrochemical response curve of the cell, *i.e.*, the photocurrent generated plotted as a function of applied voltage, provides valuable information about the irradiated semiconductor properties. The depicted voltammograms represent the polarization curves of the studied sample in dark and under UV irradiation. In the positive potential range, the contribution of photogenerated current is obvious indicating free charge carrier formation and collection resulting from the absorption of UV quanta.

A typical photoelectrochemical response of one of the printed electrodes under continuous UV irradiation and in the dark is depicted at Figure 8. The working electrode consisted of a 3-layered 1 $cm^2$ circular patch printed on FTO glass substrate. Three complete cyclic scans were recorded in this measurement in order to confirm the stability and repeatability of the setup. The "light" curve describes the profile of the total photocurrent delivered by the device, *i.e.*, the number of free charge carriers generated in the semiconductor and drawn into the external circuit by the applied voltage. The photocurrent steeply increases in the 0–0.5 V range, and then reaches a plateau where the current density is essentially independent on the voltage. If we compare samples of identical area and thickness, the photocurrent magnitude then becomes a comparative indicator of the semiconductor "quality", *i.e.*, its efficiency of charge carriers generation, separation and conduction. Since the samples were printed, their area and thickness is very well defined and reproducible and therefore we can use the measured photocurrent data to compare and evaluate various samples.

The figures depict that the photoresponse of printed green body cell is very poor, yielding approximately 8 $\mu A/cm^2$. Such a low photocurrent can be attributed to a very high resistivity of the layer resulting from the limited contact between titania nanoparticles observed at the SEM images (Figure 5), which are surrounded by the insulating organosilica binder containing residual methyl groups [50]. Therefore further processing is necessary in order to induce mineralization of the layer and improving the semiconducting properties. Sintering ensures not only complete mineralization, but also titania crystallite redistribution and improved contact with the substrate conductor. The positive effect of sintering is obvious as the response curve reaches 160 $\mu A/cm^2$ of photocurrent density. On the other hand, the UV-cured response curve

delivered current density of 60 μA/cm$^2$. While the UV-curing is capable of removing residual methyl groups by photocatalytic oxidation, no particle redistribution can be expected during this type of layer processing.

The overall performance of all samples is summarized and compared at Figure 8 where several trends can be easily identified: As one may expected, photocurrent density is increasing with titania content in all three studied processing options since the fraction of photosensitive component is increasing. Minor decrease of photocurrent density for Ti-5-sintered and Ti-5-UVcured samples can be attributed to reduced amount of ink ejected from the printing head due to blocked nozzle issues and/or layer wear during sample manipulation and washing caused by too low binder content and resulting compromised mechanical stability. For all titania-binder ratios, sintering resulted into approximately 2.5 times greater photocurrent values than in the case of UV-curing. So although sintering remains superior processing method if high photocurrents are desired, UV-curing provides a sound option for heat sensitive substrates.

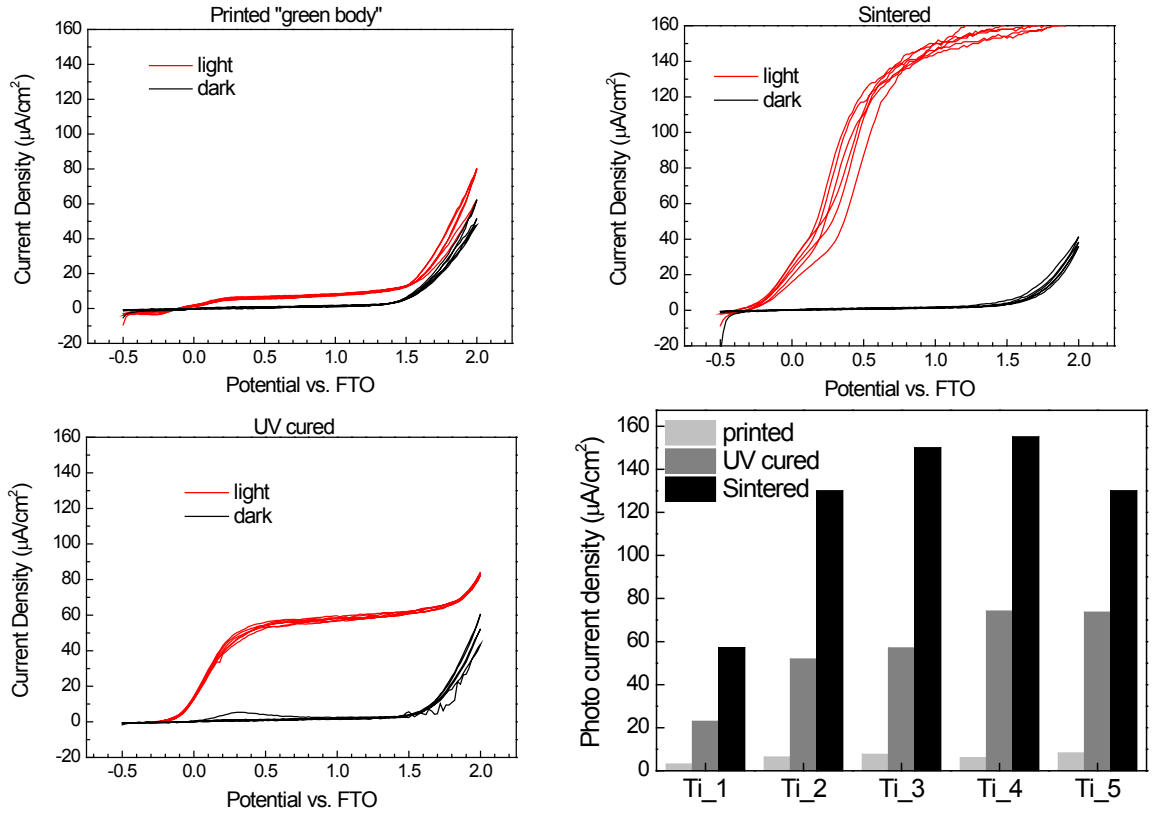


**Figure 8.** Comparison of generated photocurrents for Ti_3_3L sample. Printed "green body" electrode (**top left**), thermally sintered (**top right**), UV cured (**bottom left**) and the summary of photocurrent density (μA/cm$^2$) at 1 V potential for all the studied sample sets (**bottom right**).

### *2.9. Photocatalytic Activity*

Terephtalic acid was used as a model aqueous pollutant for evaluation of photocatalityc activity of the printed samples. Hydroxyterephtalic acid is its main oxidation product which can be conveniently detected by its fluorescence peaking and 425 nm. During the course of this experiment, the fluorescence due to the intermediary product (OH-substituted) would first increase, slow down and eventually decrease down to zero as the fluorescent intermediate is further oxidized, following the typical kinetic profile of

series reactions. The recorded fluorescence intensity is proportional to hydroxyterephtalic concentration and can be used directly as quantitative indicator if samples of the same size and thickness are compared.

Samples used for this experiment consisted of 3-layered, 20 × 20 mm titania patch printed onto pyrex glass plate. Fluorescence intensity records plotted at Figure 9 show the initial phase of the reaction, *i.e.*, the intermediate build-up. In the case of UV-cured sample set, the reaction proceeds faster and the slowing-down of the intermediate production rate becomes apparent during the experiment timeframe. UV-cured samples Ti_1 and Ti_2 exhibit lower initial rates than the others because of lower titania content in the layer. No difference in the reaction initial rate was observed for UV-cured samples Ti_3, Ti_4 and Ti_5, suggesting that the rate-controlling factor is other than titania content in the layer. On the other hand, the sintered samples exhibited much lower initial reaction rate. The influence of titania content on the initial reaction rate is more pronounced in this case as it consistently increases with increasing titania fraction.

The overall lower activity of sintered samples when compared to the UV-cured ones can be attributed to lower adsorption of aqueous reactant due to the hydrophobic nature of sintered samples demonstrated during the contact angle measurement. This suggestion is further supported by the shape of the fluorescence intensity curves recorded for the sintered samples: we actually see a gradual acceleration of the reaction, which is caused by *in-situ* UV-induced hydrophilization of the catalyst interface resulting into increasing adsorption of the aqueous substrate to be oxidized.

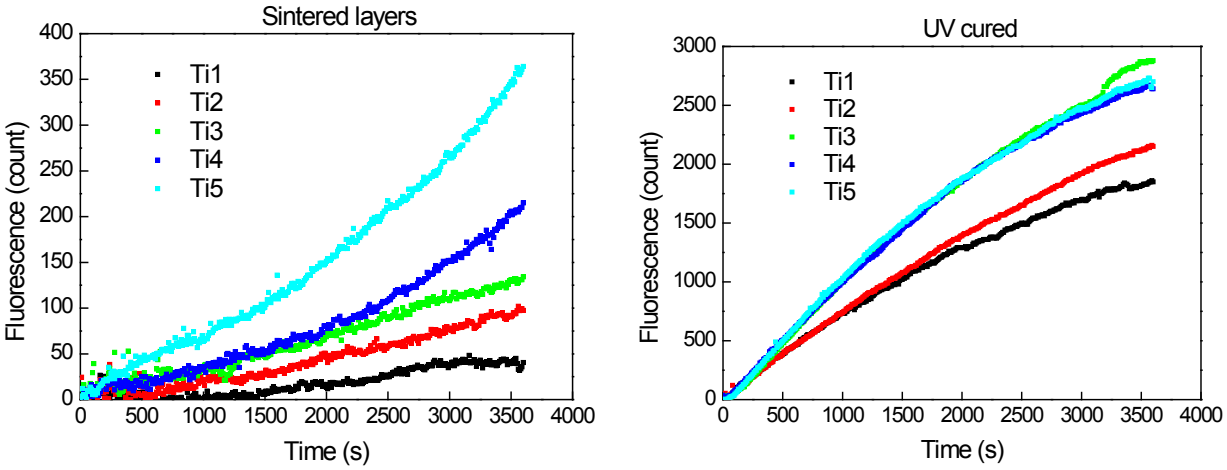


**Figure 9.** Records of hydroxyterephtalic acid fluorescence intensity *vs.* irradiation time for sintered (**left**) and UV-Cured (**right**) sample sets.

### *2.10. Print Quality Optimization*

The above presented results indicate a promising potential of the studied material for a number of applications. Plain photocatalytic remediation of water has been convincingly demonstrated by the binder inventors [50] and confirmed by our experiment. However, the reported titania-silica composite represents a highly interesting material for photonic and electrophotocatalytic applications too, as demonstrated by our linear voltammetry experiments. Moreover, the UV-curing post-printing treatment option enables the deposition on organic flexible substrates and inkjet printing allows for direct patterning of arbitrary patterns. Such capability may be highly useful for the fabrication of electrochemical sensors [53,54],

photochemical cells with special electrode geometry [55] or inverted structure polymer solar cells [56–58] because in all these devices patterned titania layers are needed.

In order to optimize the reported hybrid titania-silica coating for these advanced applications, further attempt to improve the quality of printed layers was made. The main goal was to improve the printed titania layer smoothness and remove banding artifacts. After analyzing the experimental results, we selected the formulation Ti_3, where the titania–silica volume ratio was 2.5:1.5, as the optimal printing mixture, since it delivered a balanced compromise of printing reliability, print quality, mechanical stability, electrical and photocatalytic properties.

A new batch of formulation Ti_3 was prepared in the same way as reported above, but milling with glass balls was prolonged to 3 days and the formulation was further diluted 1 + 1 by hexanol. The new ink was filled into the Dimatix cartridge and printed with the previously used settings. A line resolution test was printed onto FTO glass and the printouts were processed by UV-curing only, as this is the preferred processing option for flexible substrate based organic electronic structures. SEM imaging and profilometric analysis was performed in order to evaluate the resolution limit and surface quality of patterns printed in this way.

Figure 10 depicts the obtained results for several finest-line section of the resolution test. The prolonged milling and further ink dilution certainly contributed to the elimination larger aggregates which could get stuck in the nozzles and therefore no diverted droplets can be observed. The low volatility of hexanol enabled wet film leveling before drying, suppressed the banding issues and contributed to much smoother surface finish of the layers printed with the optimized composition. Although some protruding aggregates are still present and the individual droplet imprints are apparent, the print quality much improved both in terms of edge definition and smoother surface finish. With the optimized formulation, patterns with both positive and negative features down to 100 µm size are possible to print.

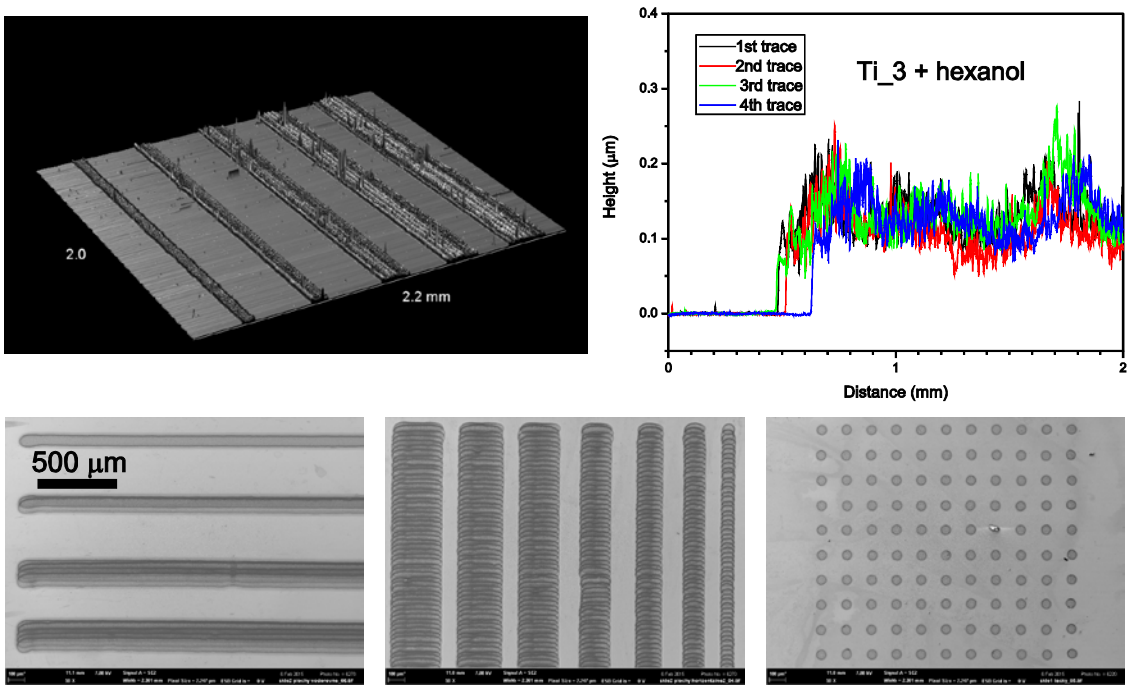


**Figure 10.** Profilometric mapping (**top**) and SEM images (**bottom**) of line resolution test printed with optimized Ti_3 formulation.

## 3. Experimental Section

### *3.1. Preparation of Silica Binder*

The silica matrix was prepared through the sol-gel process at low temperature according the procedure described in work of Gregori *et al*. [50] where methyltriethoxysilane (MTEOS, ABCR) was used as the silica precursor. In the first step, MTEOS (60 $cm^3$) was hydrolysed in acidic water (70 $cm^3$) and the created mixture was continuously stirred for 1 h at laboratory temperature. Subsequently, the distillation at 115 °C was carried out to remove the released alcohol. The distillation was stopped in the moment of white suspension formation and immediately, 37 $cm^3$ of cold water was added to increase the phase separation. After the cooling to laboratory temperature, diethyl ether (90 $cm^3$) was added to the solution to extract the remaining water and subsequently the whole water phase was removed. Diethyl ether was evaporated under reduce pressure and finally, the rest matter was diluted in ethanol (50 $cm^3$). The dry mass content was determined gravimetrically and adjusted to 0.28 $g/cm^3$.

### *3.2. Printing Deposition*

For the sake of convenient testing of various silica-titania ratios, stock dispersion of titanium dioxide in anhydrous ethanol was mixed first, having the same dry mass content as the silica binder solution. The printing formulation was then prepared by mixing varying volumes of silica binder solution, titania dispersion and viscosity-controlling solvent (butanol) in 20 mL glass vials. Approximately 3 g of 1 mm diameter glass balls were added to each vial and they were kept shaking for minimum 2 days on an oscillating plate shaker set to 900 rpm. Table 4 outlines the composition of all printing formulations.

**Table 4.** Composition of printing formulations.

| Sample | Stock Dispersion of $TiO_2$ in Ethanol (mL) c = 0.28 g/mL | Silica Sol in Ethanol (mL) c = 0.28 g/mL | Butanol (mL) | Titania Fraction in Dry Mass (wt %) |
|---|---|---|---|---|
| Ti_1 | 1.5 | 2.5 | 6 | 38 |
| Ti_2 | 2 | 2 | 6 | 50 |
| Ti_3 | 2.5 | 1.5 | 6 | 63 |
| Ti_4 | 3 | 1 | 6 | 75 |
| Ti_5 | 3.5 | 0.5 | 6 | 88 |

Printing of prepared inks was performed with an experimental inkjet printer Fujifilm Dimatix 2831 (Fujifilm Dimatix, Santa Clara, CA USA). The printer features a disposable 16-nozzle piezoelectric jetting printhead coupled with a 2 mL polyethylene ink tank. It is capable of printing on A4 size substrates with a resolution of up to 5080 dpi, *i.e*., 5 μm. Both substrate and printhead can be heated in order to speed up solvent evaporation and reduce ink viscosity, respectively. A stroboscopic camera provides still images or slow-down video for the observation of drop formation process, while another fiducial camera is used for precise substrate positioning and aligning of subsequently print layers. The printer has been successfully employed for the deposition of a wide variety of functional and auxiliary layers and during the past years has de facto become the industrial standard tool for ink development and testing.

Generally, the following procedure was repeated for each tested formulation: the prepared ink was loaded into a syringe and a blunt needle was attached to the syringe lure ports. The ink was filled into the Dimatix ink tank and the Dimatix 10 pL printing head was attached to the tank and the set was mounted into the Dimatix printer. The drop formation characteristics of all formulations were checked by means of the built-in stroboscopic camera and interaction of the printed material with the substrate was observed by an optical microscope. At the beginning of the preliminary testing period, the optimal printing conditions were found: Dimatix Model fluid 2 waveform, 18 V driving voltage, nozzle temperature 30 °C, substrate temperature 40 °C. Nozzle span was set to 30 μm (*i.e.*, 33.3 drops per mm, 1111 drops per $mm^2$). Printing was repeated up to 5 times to obtain different overall thicknesses of titania-silica layers. Complete drying took place after printing each layer, so that the following layer was printed in the "wet-to-dry" manner.

All tested ink formulations (see Table 4) were used for the fabrication of 5 parallel samples sets containing various test patches the size and shape of which were designed according to the experimental technique they were intended for. All the patterns in the set were printed in a range of thicknesses of 1 to 5 layers by repeated overprinting in a wet-to-dry manner, *i.e.* the previous layer was completely dry before printing the following one started. Actually, each sample set was printed in 3 copies to allow for various curing methods (see below). Simple rectangular patterns 20 × 20 mm were printed onto standard 26 × 76 mm Pyrex microscope slides for photocatalytic activity experiments. This pattern was also printed soda-lime microscope slides for hardness evaluation. A line resolution test pattern was printed onto the same substrate for profilometric and AFM investigation. A miniaturized version of the line resolution test was printed FTO coated glass slides for SEM imaging. 1 $cm^2$ circular patch was printed onto FTO glass slide for photoelectrochemical measurements.

The deposition process was finalized by curing. One copy of each sample set let dry at ambient temperature and is further referred to as "printed" (P) sample set. The second one was calcined at 450 °C in air and is further referred to as "sintered" (S) sample set. The third one was immersed into demineralized water and placed 30 cm under an industrial processing UV lamp (model 80 BQL7, 248 W, Ultralight AG, Schaanwald, Liechtenstein) for 10 h and was called "UV cured" sample set (UV).

### *3.3. Characterization of Thin Films*

The printed mixtures were examined using thermogravimetric analysis in order to understand the processes taking place during thermal processing. The analysis was performed in a thermoanalyser (TGA; 6300 TG-DTA, Seiko Instruments, Chiba, Japan) under the following parameters: a mixture of argon and air atmosphere (1:1 by volume), temperatures range of 35–1200 °C with temperature ramp of 5 °C/min up to 100 °C and afterwards 10 °C/min, and a flow rate of 400 $cm^3$/min.

The hardness of the three layered samples was analyzed though the standard pencil hardness test [59]. Pencils with different hardness were successively placed into the pencil tester, from the hardest to the softest, and the hardness of pencil that will not cut into or gouge the film was evaluated as the hardness of the layer. The pencils were held in the tester firmly against the film at 45° angle and the speed of the tester was approximately 1 mm/s.

The thickness and roughness of the printed layers was evaluated using a DektakXT profilometer (Bruker, Billerica, MA, USA). In this analysis, a diamond tip got to the contact of sample surface and moved across the sample for the distance of 3 mm with a contact force of 5 mN. The vertical position of

the diamond stylus generates an electric signal from which the final thickness is calculated. The roughness of the printed layers was calculated also from this measurement according the Formula (1) [60] where Rms means root mean square average, *z* are widths of peaks profile and *n* is number of peaks. The samples were scanned perpendicular to the direction of print head movement so that the printed bands merging could be evaluated:

$$R_{RMS} = \sqrt{\frac{1}{n}\sum_{i=1}^{n} z^2} \quad (1)$$

The quality of prepared layers was investigated by an optical microscope Nikon Eclipse E200 connected with a D5000 digital camera (Nikon, Tokyo, Japan). The influence of silica amount in printing composition was examined and the obtained results served for evaluation of the best printing composition and conditions. The morphology of the samples was investigated by scanning electron microscopy (SEM, Ultra Plus, Carl Zeiss, Oberkochen, Germany) where the structure of different layers number as well as printed *vs.* sintered samples were compared. The topography of prepared samples was performed by atomic force microscopy (AFM, Dimension Icon, Bruker) in tapping mode. Each analysis was carried out in the center of the sample from area 1 $\mu m^2$. Next the topology we investigated also roughness of the sample. In this case we found $R_a$ which is arithmetic average of the absolute values defined by Equation (2) [61]:

$$R_a = \frac{1}{l}\int_0^l \left|Z(x) \times dx\right| \quad (2)$$

The photoinduced hydrophilicity was studied through the contact angle measurement of water sessile droplet on the titania/silica surfaces by an OCA20 instrument (DataPhysics Instruments GmbH, Filderstadt, Germany). The total volume of deposited droplets was 5 μL and the records of droplets were taken in the 5 s after their formation. The wetting properties of printed, as well as sintered layers were examined. At first, the water droplet contact angle was measured on freshly prepared samples and afterwards each film was irradiated by UV light with intensity of 10 $mW/cm^2$ (Lynx-L, Osram Sylvania, Danvers, MA, USA). The time required for conversion of properties from hydrophobic to hydrophilic was investigated. The final contact angle in certain time was calculated as the average of five measurements.

Photoelectrochemical characterization was performed by linear sweep voltammetry at room temperature using a two-electrode setup with the 1 $cm^2$ titania patches. The printed FTO slide was scratched with a diamond knife and thus two isolated FTO strips were created. One strip with the printed titania patch served as the working electrode and the opposite naked FTO strip as the counter electrode. This setup was fitted into a custom build quartz cuvette. The cuvette was filled with 0.1 M phosphate buffer (pH = 7) and fitted onto an optical bench equipped with a fluorescent UV-A lamp emitting a broad peak centered at 365 (Sylvania Lynx-L 11 W). A magnetic stirrer was placed beneath the cuvette and a magnetic flea inside the cuvette provided efficient electrolyte mixing. The lamp emission was monitored by a X97 Irradiance Meter with a UV-3701 probe (Gigahertz Optic, Türkenfeld, Germany) and the irradiance was set to 3 $mW/cm^2$ by adjusting the lamp-to-cuvette distance. Measurements of generated photocurrents were performed with an electrometer build on the basis of National Instruments Labview platform and supplying a linear voltage gradient of 10 mV/s from −0.5 to 2 V.

Photocatalytic experiments were conducted with the same cell and light source as the electrochemical response curves were measured with. Recently, terephtalic acid was suggested as a model compound for monitoring the oxidative activity of valence band holes generated in the immobilized photocatalyst [62]. Upon oxidation, presumably resulting from the attack of a hydroxyl radical, terephtalic acid is oxidized into hydroxyterephtalic acid, which gives a strong fluorescence signal at 425 nm. This approach proved to be very convenient for our experimental setup, because a single radiation source could be used for both the activation of the photocatalyst as well as the excitation of the fluorescent probe generated during the course of the reaction. The emitted fluorescence was collected by a quartz collimating lens mounted in the lateral wall of the cell holder and projected into an optical fiber attached to a Redtide spectrometer (Ocean Optics, Dunedin, FL, USA). The spectrometer driving software allowed for a convenient automated recording of the fluorescence intensity. Calibration was performed using hydroxyterepthalic acid standard (Sigma Aldrich, St. Louis, MO, USA).

## 4. Conclusions

The primary aim of this work was to find the optimal inkjet printable formulation and processing conditions for the fabrication of (electro)photocatalytic thin films consolidated by hybrid organosilicate binder. Several different ratios of titania and binder were tested and we were able to prepare semi-transparent homogeneous layers of arbitrary shape and thickness by repeated overprinting using all the studied compositions. The employed binder proved to have positive effect on titania particles stabilization and also acts as a lubricant enabling printing formulations with high solids loading (0.112 g/mL). Such concentrated inks can be effectively used for the fabrication of relatively thick coatings by a single pass of printing head which reduces printing time and eliminated artifacts originating from the interaction of wet and dry ink.

The printed green-body patterns exhibited good mechanical properties, but required further processing for a number of reasons. First, the hybrid organosilicate binder needed to be mineralized in order to become insoluble. Secondly, further processing is also necessary in order to improve the charge transfer properties and thirdly, it renders the catalyst surface superhydrophilic which is beneficial for photocatalytic activity. The post-printing processing is possible to carry out either by sintering at elevated temperature in oxidizing environment, or by UV curing through photocatalytic effect of the nanocrystalline titania.

All freshly printed films were superhydrophobic due to the residual methyl groups present in the binder. UV curing was found to induce both methyl groups mineralization as well as hydrophilic conversion. However, thermal sintering resulted only in methyl group mineralization, but sintered layers remained hydrophobic. Sintered layers can be converted to hydrophilic state by further UV curing, but their conversion towards hydrophilic properties takes more time than the conversion of green body printed films.

From the electrochemical point of view, the surface hydrophilicity does not seem to have much influence. Photocurrent density is increasing with titania content in all three studied processing options since the fraction of photosensitive component is increasing. For all tested formulations, sintering resulted into approximately 2.5 times greater photocurrent values than in the case of UV-cured electrodes. So while sintering remains the superior processing method for inorganic substrates, UV-curing provides a sound option for heat sensitive substrates.

As far as the photocatalytic activity is concerned, we discovered significant differences between the two studied post-printing processing options. Sintered layers showed very low activity, presumably due to poor adsorption of aqueous pollutants on their hydrophobic surface. However, acceleration of their activity was observed during the reaction, apparently as the surface was being converted into hydrophilic by the incident UV radiation during the course of the reaction. UV-cured sample series showed much higher activity and the kinetic profile of the first intermediate showed shape typical for the kinetic model of serial reactions.

Finally, sample Ti_3 in which the titania-silica volume ratio was 63 wt %, was evaluated as the best since it delivered a balanced compromise of mechanical stability, electrical and photocatalytic properties. We proceeded to our secondary experimental goal with this formulation, *i.e*., the optimization of print resolution and surface finish. The milling time was prolonged, the formulation was further diluted with hexanol and printing mode changed to single nozzle mode in order to provide maximum print quality. Electronic imaging and stylus profilometry confirmed that patterns with both positive and negative features down to 100 μm size are possible to print with this formulation and printing setup. The described technology is well suited for fabrication of various devices where thin patterned titania layers are needed.

## Acknowledgments

Authors thank to the Ministry of Education, Youth and Sports of the Czech Republic for support by project CZ.1.07/2.3.00/30.0005 and to Central European Institute of Technology (CEITEC). Authors also appreciate the work of Jan Cupera who performed SEM analysis and Dalibor Sulc who provide the images from AFM analysis.

## Author Contributions

The ideas of the whole work arose as the result of a discussion between Marcela Kralova, Petr Dzik, Michal Vesely and Jaroslav Cihlar. Afterwards the text was written by Marcela Kralova and Petr Dzik. Thermogravimetric behavior was investigated and consequently written out by Vit Kasparek.

## Conflicts of Interest

The authors declare no conflict of interest.

## References

1. Malato, S.; Blanco, J.; Caceres, J.; Fernandez-Alba, A.R.; Aguera, A.; Rodriguez, A. Photocatalytic treatment of water-soluble pesticides by photo-Fenton and $TiO_2$ using solar energy. *Catal. Today* **2002**, *76*, 209–220.
2. Hinkova, A.; Henke, S.; Bubnik, Z.; Pour, V.; Salova, A.; Slukova, M.; Sarka, E. Degradation of food industrial pollutants by photocatalysis with immobilized titanium dioxide. *Innov. Food Sci. Emerg. Technol.* **2015**, *27*, 129–135.
3. Fujishima, A.; Zhang, X.; Tryk, D.A. $TiO_2$ photocatalysis and related surface phenomena. *Surf. Sci. Rep.* **2008**, *63*, 515–582.

4. Levchuk, I.; Rueda-Márquez, J.J.; Suihkonen, S.; Manzano, M.A.; Sillanpää, M. Application of UVA-LED based photocatalysis for plywood mill wastewater treatment. *Sep. Purif. Technol.* **2015**, *143*, 1–5.
5. Ismail, A.A.; Bahnemann, D.W. Photochemical splitting of water for hydrogen production by photocatalysis: A review. *Sol. Energy Mater. Sol. Cells* **2014**, *128*, 85–101.
6. Li, X.; Liu, P.; Mao, Y.; Xing, M.; Zhang, J. Preparation of homogeneous nitrogen-doped mesoporous $TiO_2$ spheres with enhanced visible-light photocatalysis. *Appl. Catal. B* **2015**, *164*, 352–359.
7. Mayer, B.K.; Daugherty, E.; Abbaszadegan, M. Disinfection byproduct formation resulting from settled, filtered, and finished water treated by titanium dioxide photocatalysis. *Chemosphere* **2014**, *117*, 72–78.
8. Lopez Fernandez, R.; McDonald, J.A.; Khan, S.J.; Le-Clech, P. Removal of pharmaceuticals and endocrine disrupting chemicals by a submerged membrane photocatalysis reactor (MPR). *Sep. Purif. Technol.* **2014**, *127*, 131–139.
9. Wang, B.; de Godoi, F.C.; Sun, Z.; Zeng, Q.; Zheng, S.; Frost, R.L. Synthesis, characterization and activity of an immobilized photocatalyst: Natural porous diatomite supported titania nanoparticles. *J. Colloid Interface Sci.* **2015**, *438*, 204–211.
10. Dunnill, C.W.; Kafizas, A.; Parkin, I.P. Cvd production of doped titanium dioxide thin films. *Chem. Vap. Depos.* **2012**, *18*, 89–101.
11. Kelly, P.J.; West, G.T.; Ratova, M.; Fisher, L.; Ostovarpour, S.; Verran, J. Structural formation and photocatalytic activity of magnetron sputtered titania and doped-titania coatings. *Molecules* **2014**, *19*, 16327–16348.
12. Tay, B.K.; Zhao, Z.W.; Chua, D.H.C. Review of metal oxide films deposited by filtered cathodic vacuum arc technique. *Mater. Sci. Eng. R-Rep.* **2006**, *52*, 1–48.
13. Macwan, D.P.; Dave, P.N.; Chaturvedi, S. A review on nano-$TiO_2$ sol-gel type syntheses and its applications. *J. Mater. Sci.* **2011**, *46*, 3669–3686.
14. Akpan, U.G.; Hameed, B.H. The advancements in sol-gel method of doped-$TiO_2$ photocatalysts. *Appl. Catal. A Gen.* **2010**, *375*, 1–11.
15. Putz, J.; Aegerter, M.A. Versatile wet deposition techniques for functional oxide coatings on glass. *Glass Sci. Technol.* **2004**, *77*, 229–238.
16. Sobczyk-Guzenda, A.; Pietrzyk, B.; Szymanowski, H.; Gazicki-Lipman, M.; Jakubowski, W. Photocatalytic activity of thin $TiO_2$ films deposited using sol–gel and plasma enhanced chemical vapor deposition methods. *Ceram. Int.* **2013**, *39*, 2787–2794.
17. Krebs, F.C. Fabrication and processing of polymer solar cells: A review of printing and coating techniques. *Sol. Energy Mater. Sol. Cells* **2009**, *93*, 394–412.
18. Riegel, S.; Mutter, F.; Lauermann, T.; Terheiden, B.; Hahn, G. Review on screen printed metallization on *p*-type silicon. *Energy Procedia* **2012**, *21*, 14–23.
19. Choi, H.W.; Zhou, T.; Singh, M.; Jabbour, G.E. Recent developments and directions in printed nanomaterials. *Nanoscale* **2015**, *7*, 3338–3355.
20. Martin, G.D.; Hoath, S.D.; Hutchings, I.M. Inkjet Printing—The Physics of Manipulating Liquid Jets and Drops. *J. Phys.: Conf. Ser.* **2008**, *105*, doi:10.1088/1742-6596/105/1/012001.

21. Ballarin, B.; Fraleoni-Morgera, A.; Frascaro, D.; Marazzita, S.; Piana, C.; Setti, L. Thermal inkjet microdeposition of pedot: PSS on ITO-coated glass and characterization of the obtained film. *Synth. Met.* **2004**, *146*, 201–205.
22. Morrin, A.; Ngamna, O.; O'Malley, E.; Kent, N.; Moulton, S.E.; Wallace, G.G.; Smyth, M.R.; Killard, A.J. The fabrication and characterization of inkjet-printed polyaniline nanoparticle films. *Electrochim. Acta* **2008**, *53*, 5092–5099.
23. Yoshioka, Y.; Jabbour, G.E. Desktop inkjet printer as a tool to print conducting polymers. *Synth. Metals* **2006**, *156*, 779–783.
24. Taylor, A.D.; Kim, E.Y.; Humes, V.P.; Kizuka, J.; Thompson, L.T. Inkjet printing of carbon supported platinum 3-D catalyst layers for use in fuel cells. *J. Power Sour.* **2007**, *171*, 101–106.
25. Radulescu, D.; Dhar, S.; Young, C.M.; Taylor, D.W.; Trost, H.J.; Hayes, D.J.; Evans, G.R. Tissue Engineering Scaffolds for Nerve Regeneration Manufactured by Ink-Jet Technology. In Proceedings of the Symposium on Next Generation Biomaterals, Pittsburgh, PA, USA, 25–28 September 2005; pp. 534–539.
26. Zhang, C.H.; Wen, X.J.; Vyavahare, N.R.; Boland, T. Synthesis and characterization of biodegradable elastomeric polyurethane scaffolds fabricated by the inkjet technique. *Biomaterials* **2008**, *29*, 3781–3791.
27. Xu, T.; Gregory, C.A.; Molnar, P.; Cui, X.; Jalota, S.; Bhaduri, S.B.; Boland, T. Viability and electrophysiology of neural cell structures generated by the inkjet printing method. *Biomaterials* **2006**, *27*, 3580–3588.
28. Xu, T.; Jin, J.; Gregory, C.; Hickman, J.J.; Boland, T. Inkjet printing of viable mammalian cells. *Biomaterials* **2005**, *26*, 93–99.
29. Liu, Y.; Cui, T.H.; Varahramyan, K. All-polymer capacitor fabricated with inkjet printing technique. *Solid-State Electron.* **2003**, *47*, 1543–1548.
30. Kawase, T.; Shimoda, T.; Newsome, C.; Sirringhaus, H.; Friend, R.H. Inkjet printing of polymer thin film transistors. In Proceedings of the 5th International Conference on Nano-Molecular Electronics (ICNME2002), Kobe, Japan, 10–12 December 2002; pp. 279–287.
31. Chen, B.; Cui, T.H.; Liu, Y.; Varahramyan, K. All-polymer rc filter circuits fabricated with inkjet printing technology. *Solid-State Electron.* **2003**, *47*, 841–847.
32. Bharathan, J.; Yang, Y. Polymer electroluminescent devices processed by inkjet printing: I. Polymer light-emitting logo. *Appl. Phys. Lett.* **1998**, *72*, 2660–2662.
33. Dzik, P.; Veselý, M.; Králová, M.; Neumann-Spallart, M. Ink-jet printed planar electrochemical cells. *Appl. Catal. B* **2015**, *178*, 186–191.
34. Byrne, H.E.; Mazyck, D.W. Removal of trace level aqueous mercury by adsorption and photocatalysis on silica-titania composites. *J. Hazard. Mater.* **2009**, *170*, 915–919.
35. Akly, C.; Chadik, P.A.; Mazyck, D.W. Photocatalysis of gas-phase toluene using silica-titania composites: Performance of a novel catalyst immobilization technique suitable for large-scale applications. *Appl. Catal. B* **2010**, *99*, 329–335.
36. Kibombo, H.S.; Koodali, R.T. Heterogeneous photocatalytic remediation of phenol by platinized titania-silica mixed oxides under solar-simulated conditions. *J. Phys. Chem. C* **2011**, *115*, 25568–25579.

37. Khalil, K.M.S.; Elsamahy, A.A.; Elanany, M.S. Formation and characterization of high surface area thermally stabilized titania/silica composite materials via hydrolysis of titanium(iv) tetraisopropoxide in sols of spherical silica particles. *J. Colloid Interface Sci.* **2002**, *249*, 359–365.
38. Li, Z.J.; Hou, B.; Xu, Y.; Wu, D.; Sun, Y.H.; Hu, W.; Deng, F. Comparative study of sol-gel-hydrothermal and sol-gel synthesis of titania-silica composite nanoparticles. *J. Solid State Chem.* **2005**, *178*, 1395–1405.
39. Attia, S.M.; Wang, J.; Wu, G.M.; Shen, J.; Ma, J.H. Review on sol-gel derived coatings: Process, techniques and optical applications. *J. Mater. Sci. Technol.* **2002**, *18*, 211–218.
40. Bernacka-Wojcik, I.; Senadeera, R.; Wojcik, P.J.; Silva, L.B.; Doria, G.; Baptista, P.; Aguas, H.; Fortunato, E.; Martins, R. Inkjet printed and "doctor blade" $TiO_2$ photodetectors for DNA biosensors. *Biosens. Bioelectron.* **2010**, *25*, 1229–1234.
41. Yang, M.; Li, L.H.; Zhang, S.Q.; Li, G.Y.; Zhao, H.J. Preparation, characterisation and sensing application of inkjet-printed nanostructured $TiO_2$ photoanode. *Sens. Actuat. B* **2010**, *147*, 622–628.
42. Arin, M.; Lommens, P.; Hopkins, S.C.; Pollefeyt, G.; van der Eycken, J.; Ricart, S.; Granados, X.; Glowacki, B.A.; van Driessche, I. Deposition of photocatalytically active tio2 films by inkjet printing of $TiO_2$ nanoparticle suspensions obtained from microwave-assisted hydrothermal synthesis. *Nanotechnology* **2012**, *23*, 165603–165613.
43. Loffredo, F.; Grimaldi, I.A.; Del Mauro, A.D.G.; Villani, F.; Bizzarro, V.; Nenna, G.; D'Amato, R.; Minarini, C. Polyethylenimine/n-doped titanium dioxide nanoparticle based inks for ink-jet printing applications. *J. Appl. Polym. Sci.* **2011**, *122*, 3630–3636.
44. Cherrington, R.; Hughes, D.J.; Senthilarasu, S.; Goodship, V. Inkjet-printed $TiO_2$ nanoparticles from aqueous solutions for dye-sensitized solar cells (DSSCs). *Energy Technol.* **2015**, *3*, 866–870.
45. Fasaki, I.; Siamos, K.; Arin, M.; Lommens, P.; van Driessche, I.; Hopkins, S.C.; Glowacki, B.A.; Arabatzis, I. Ultrasound assisted preparation of stable water-based nanocrystalline $TiO_2$ suspensions for photocatalytic applications of inkjet-printed films. *Appl. Catal. A* **2012**, *411*, 60–69.
46. Zori, M.H.; Soleimani-Gorgani, A. Ink-jet printing of micro-emulsion $TiO_2$ nano-particles ink on the surface of glass. *J. Eur. Ceram. Soc.* **2012**, *32*, 4271–4277.
47. Oh, Y.; Yoon, H.G.; Lee, S.N.; Kim, H.K.; Kim, J. Inkjet-printing of $TiO_2$ co-solvent ink: From uniform ink-droplet to $TiO_2$ photoelectrode for dye-sensitized solar cells. *J. Electrochem. Soc.* **2012**, *159*, B35–B39.
48. Černá, M.; Veselý, M.; Dzik, P.; Guillard, C.; Puzenat, E.; Lepičová, M. Fabrication, characterization and photocatalytic activity of $TiO_2$ layers prepared by inkjet printing of stabilized nanocrystalline suspensions. *Appl. Catal. B* **2013**, *138–139*, 84–94.
49. Dzik, P.; Veselý, M.; Kete, M.; Pavlica, E.; Štangar, U.L.; Neumann-Spallart, M. Properties and application perspective of hybrid titania-silica patterns fabricated by inkjet printing. *ACS Appl. Mater. Interfaces* **2015**, *7*, 16177–16190.
50. Gregori, D.; Benchenaa, I.; Chaput, F.; Therias, S.; Gardette, J.L.; Leonard, D.; Guillard, C.; Parola, S. Mechanically stable and photocatalytically active $TiO_2/SiO_2$ hybrid films on flexible organic substrates. *J. Mater. Chem. A* **2014**, *2*, 20096–20104.
51. Kaufman, L. Calculation of multicomponent ceramic phase diagrams. *Phys. B + C* **1988**, *150*, 99–114.
52. Okada, K.; Yamamoto, N.; Kameshima, Y.; Yasumori, A.; MacKenzie, K.J.D. Effect of silica additive on the anatase-to-rutile phase transition. *J. Am. Ceram. Soc.* **2001**, *84*, 1591–1596.

53. Tian, L.; Wang, B.; Chen, R.; Gao, Y.; Chen, Y.; Li, T. Determination of quercetin using a photo-electrochemical sensor modified with titanium dioxide and a platinum(II)-porphyrin complex. *Microchim. Acta* **2015**, *182*, 687–693.
54. Jain, R.; Pandey, P. Electrochemical sensor mediated by synthesis of CDO nanoparticles-titanium dioxide composite modified glassy carbon electrode for quantification of zolmitriptan. *J. Electrochem. Soc.* **2013**, *160*, H687–H692.
55. Neumann-Spallart, M. Photoelectrochemistry on a planar, interdigitated electrochemical cell. *Electrochim. Acta* **2011**, *56*, 8752–8757.
56. Li, F.; Chen, C.; Tan, F.; Li, C.; Yue, G.; Shen, L.; Zhang, W. Semitransparent inverted polymer solar cells employing a sol-gel-derived $TiO_2$ electron-selective layer on FTO and $MoO_3$/Ag/$MoO_3$ transparent electrode. *Nanoscale Res. Lett.* **2014**, *9*, 1–5.
57. Ranjitha, A.; Muthukumarasamy, N.; Thambidurai, M.; Velauthapillai, D.; Kumar, A.M.; Gasem, Z.M. Inverted organic solar cells based on CD-doped $TiO_2$ as an electron extraction layer. *Superlattices Microstruct.* **2014**, *74*, 114–122.
58. Thambidurai, M.; Kim, J.Y.; Ko, Y.; Song, H.-J.; Shin, H.; Song, J.; Lee, Y.; Lee, C. Muthukumarasamy, N.; Velauthapillai, D.; High-efficiency inverted organic solar cells with polyethylene oxide-modified Zn-doped $TiO_2$ as an interfacial electron transport layer. *Nanoscale* **2014**, *6*, 8585–8589.
59. *ISO 15184: Paints and Varnishes, Determination of Film Hardness by Pencil Test*; ISO: Geneva, Switzerland, 1998.
60. Christensen, M.; Rasmussen, J.T.; Simonsen, A.C. Roughness analysis of single nanoparticles applied to atomic force microscopy images of hydrated casein micelles. *Food Hydrocoll.* **2015**, *45*, 168–174.
61. Littringer, E.M.; Mescher, A.; Schroettner, H.; Achelis, L.; Walzel, P.; Urbanetz, N.A. Spray dried mannitol carrier particles with tailored surface properties—The influence of carrier surface roughness and shape. *Eur. J. Pharm. Biopharm.* **2012**, *82*, 194–204.
62. Cernigoj, U.; Kete, M.; Stangar, U.L. Development of a fluorescence-based method for evaluation of self-cleaning properties of photocatalytic layers. *Catal. Today* **2010**, *151*, 46–52.

*Sample Availability*: Samples of the hybrid organosilica binder and inkjet-printed titania patterns are available from the authors.

Article

Journal of
Nanoscience and Nanotechnology
Vol. 15, 6550–6558, 2015
www.aspbs.com/jnn



# Photocatalytic and Antimicrobial Activity of Printed Hybrid Titania/Silica Layers

Michal Veselý[1,*], Petr Dzik[1], Mária Veselá[1], Marko Kete[2], and Urška Lavrenčič Štangar[2]

[1] *Brno University of Technology, Faculty of Chemistry, Purkynova 118, 612 00 Brno, Czech Republic*
[2] *University of Nova Gorica, Laboratory for Environmental Research, Vipavska Cesta 13, 5000 Nova Gorica, Slovenia*

Stable mixed dispersion of $TiO_2$ and $SiO_2$ was developed and hybrid $TiO_2/SiO_2$ layers were fabricated by the direct inkjet patterning technique. The prepared layers were tested for photoinduced hydrophilicity and their photocatalytic activity was tested using stearic acid and dichloroindophenol as model compounds. The antimicrobial activity of prepared layers was tested and evaluated by the traditional plate counting method according to ISO 27447:2009, using *Escherichia coli* CCM 3988. Material printing proved to be well suited for the deposition of this complex nanoparticulate ink and samples with variable thickness were conveniently fabricated. Printed layers are able to change their surface properties from hydrophobic to superhydrophilic and also decompose the model contaminants rapidly.

**Keywords:** $TiO_2/SiO_2$, Printed Layers, Photocatalysis, Antimicrobial, Stearic Acid, UV LED.

## 1. INTRODUCTION

Sol-gel synthesized nanocrystalline titania dispersions are excellent raw materials for wet coating formulations, providing a good level of control over the crystallinity of the resulting layer. Although the nanocrystalline titania dispersions are capable to deliver excellent photocatalytic performance, it is very difficult to anchor $TiO_2$ nanoparticles to the substrate without thermal fixing. Therefore, in order to produce a cold setting formulation, it is necessary to add a binder which will cement the nanoparticles together and provide necessary adhesion to the substrate surface at the same time. Silica can act as such a binder.[1–9] Ideally, such binder should preferably not significantly decrease the photocatalytic activity of $TiO_2$.[10, 11]

Although titania coatings have been fabricated by countless different processes, wet coating techniques constitute a very popular and usually simpler alternative to vacuum processes requiring sophisticated instrumentation. Many different wet-coating techniques have been proposed, such as dip-, spin- or spray-coating, doctor blade or roller spreading, etc. However, recently these traditional methods have been to certain extent replaced by modified printing techniques.[12] Of these, inkjet material deposition seems to be especially promising. The technique shares the basic principles with conventional inkjet printing,[13] i.e., tiny droplets of a low-viscosity liquid are precisely deposited onto a substrate by means of a thermal or a piezoelectric printhead.[14] In the case of material printing, the ink is a specially formulated liquid used for transporting a functional component onto the substrate surface.[15–19]

Cold-setting processes yielding stable titania layers are very attractive for the fabrication of photoelectrochemical functional or auxiliary coatings on the surface of heat sensitive substrates. The key involved mechanisms of titania layer building and fixing include e.g., UV-curing of titanium alkoxide binder,[20] the incorporation of mineral binder such as amorphous silica,[1] atomic layer deposition over a mesoporous template,[21] low temperature CVD fed with custom molecular precursor,[22] titanium alkoxide decomposition in supercritical carbon dioxide,[23] or cold isostatic pressing of standard P-25 grade of titania.[24] The cold deposition process at ambient conditions is also advantageous for the fabrication of photocatalytic self-cleaning coatings for outdoor application on concrete, stainless steel or automobile components.[2, 3, 5, 6]

In order to evaluate the photocatalytic activity of any immobilized titania layer, various different tests were proposed. However, only a few of them have reached a general acceptance articulated in the form of ISO standard. Several ISO standards were introduced recently for

*Author to whom correspondence should be addressed.

 1533-4880/2015/15/6550/009 doi:10.1166/jnn.2015.10870

the purpose of testing of titania layers for industrial application.[25] Each of these ISO standards for photocatalytic activity evaluation gives information about suitability for different application domain.

Titanium dioxide layers performance can in some instances compete with the conventional disinfection methods. Novel disinfection methods are being sought to provide additional means of protection in a number of areas which need to be kept sterile or with only small and suppressed population of bacteria and fungi. Thin and transparent layers of titania seem to provide such a function efficiently.[26–28]

Microbiological studies often require the enumeration of total bacteria in experimental models or environmental samples. There are several existing assays for the determination of cell viability, including:
(1) classical (conventional) culture methods (i.e., plate counting),
(2) microscopic based enumeration methods, e.g., flow cytometry, direct epifluorescent filter technique (DEFT) and fluorescent *in situ* hybridization (FISH);
(3) molecular method (immunological method or indirect method based on enzymatic activity of cells).

Classical (conventional) culture methods are technically simple, sensitive and capable of reliable detection of defined microorganisms. Their principal drawback is that they are labour- and time-consuming. However, their ease of use, and the historical reliance of microbiologists on culture-based methods, have spawned a tradition in which they are still widely used in analytical laboratories and continue to provide a standard against which newer techniques are compared.[29, 30]

ISO standard 27447 defines the types of material tested for antibacterial activity-ceramic tiles or clothes and bacteria for testing (*Staphylococcus aureus, Escherichia coli, Klebsiella pneumoniae*) including nutrients broth and agar for plating. Being quite recent, the standard has been acquiring its acceptance gradually and so far only a limited number of studies have employed it for antimicrobial testing.[31–35] Although the ISO 27447 standard is primarily intended for the assessment of antibacterial activity of smooth surfaces, the procedure can be adopted for the evaluation of antifungal activity employing yeasts, too.

In this paper, we would like to inform about the fabrication and photocatalytic properties of novel hybrid titania-silica coatings which can be conveniently fabricated by material printing techniques and which can be deposited onto a wide variety of surfaces at normal atmospheric conditions without the need of high-temperature fixing. We employed a low-temperature modification of the so called brick-and-mortar strategy[36] based on mixing prefabricated nanocrystalline titania "bricks" with "mortar" consisting of amorphous silica binder. The "mortar" is capable of enhancing both the mechanical and physicochemical properties of the coatings. Apart from acting as the binding agent,[1] colloidal silica can further improve other material properties, such as the coating adhesion,[37] increase the natural hydrophilicity of the material,[38] promote the adsorption of reactants[39] and influence the thermal stability.[40]

Coatings used for this study have been fabricated by inkjet printing of a stable suspension of nanocrystalline titania and amorphous silica particles. Hybrid titania-silica coatings and patterns fabricated in this way feature significant photocatalytic activity. We investigated the self-cleaning properties of printed layers by photoinduced hydrophilic conversion, fatty acid degradation and dye photoreduction. Moreover, their antimicrobial activity was tested using *Escherichia coli* CCM 3988 according to ISO standard 27447.

## 2. EXPERIMENTAL DETAILS

### 2.1. Chemicals

The following chemicals in this study were used as purchased: titanium(IV) tetraisopropoxide (TTIP) from Fluka, tetraethoxysilane (TEOS) from Baker, Levasil 200/30% colloidal $SiO_2$ from Starck, propane-2-ol, ethylene glycol from Penta, 2-propoxyethanol, acridine orange, 2,6-dichloroindophenol, 2-methylpropan-1-ol, propan-2-ol, propane-1,2,3-triol, stearic acid, toluene from Sigma-Aldrich, polyvinylpyrolidon Luviskol K20 from BASF. All aqueous solutions were prepared by using highly pure water from the NANO pure system (Barnstead). Alkaline surfactant Neodisher LM3 from dr. Weigert was used for degreasing and cleaning of all substrates.

#### 2.1.1. Sol Synthesis

Preparation procedure of the titania/silica sol is described in detail in the patent application.[9] Herein, a short description is given: In round-bottom flask absolute ethanol (6.78 mL) was mixed with TTIP (41.67 mL). Separately, 2.778 mL of perchloric acid (70%) was added in 250 mL of double deionized water. This acidified water was then added dropwise during stirring to the mixture of absolute ethanol and TTIP. After that the reflux was started and after 48 h we obtained stable sol which was denoted as sol A. Separately, TEOS (1.11 mL) and Levasil 200/30% (1.7 mL) was mixed in the beaker, during stirring HCl (32%, 30 $\mu$L) was added and finally 1-propanol (5 mL) to obtain silica binder solution. Final sol used in this study was prepared by mixing sol A with $SiO_2$ binder. The molar ratio between $TiO_2$:$SiO_2$ was set to 1:1 according to the results of previous testing. This stock sol was further diluted with a solvent mixture containing propane-2-ol (25 mL), 2-propoxyethanol (25 mL) and ethylene glycol (2 mL).

#### 2.1.2. Sample Preparation

Patterning was performed with experimental inkjet printer Fujifilm Dimatix 2831. The prepared printing formulation was sonicated for 5 min and then loaded into a

syringe. A 0.45 $\mu$m membrane filter (Pall Corporation, USA) and a blunt needle were attached to the syringe luer port. The printing formulation was filtered and filled into the Dimatix ink tank. Dimatix 10 pL printing head was attached to the tank and mounted into the Dimatix printer. The previously determined optimal printing conditions were set: Dimatix Model fluid 2 waveform, 20 V driving voltage, nozzle temperature 30 °C, substrate temperature 40 °C. Nozzle span was set to 40 $\mu$m (i.e., 251001 drops on $20 \times 20$ mm in one layer). Standard size microscopic glass plates ($25 \times 75$ mm, Paul Marienfeld, Germany) and custom cut $50 \times 50$ mm (Merci, Czech Republic) glass plates were used as substrate. Simple rectangular patterns $20 \times 20$ mm and $40 \times 40$ mm were printed onto the microscopic and custom-cut glass substrates, respectively. Printing was repeated up to 4 times to obtain different thicknesses of resulting $TiO_2/SiO_2$ layers. The printed pattern of $20 \times 20$ mm was built of $1.06 \times 10^{-5}$ mol of titanium dioxide in one layer (0.85 mg). Complete drying took place after printing each layer, so the following layer was printed in the "wet-to-dry" manner. The deposition process was finalized by forced drying at hot air oven at 110 °C for 30 min.

#### 2.1.3. Thickness of Printed Layers

SEM imaging was performed on JEOL JSM-7600F scanning electronic microscope. The same machine was used for layer thickness estimation by observing sample cross-section.

#### 2.1.4. Redox Dye Ink Layers

A stock solution of 2,6-dichloroindophenol ink was prepared by mixing of 10 wt% solution of polyvinylpyrrolidone in propan-2-ol (3 mL), propan-2-ol (3 mL), 2-propoxyethanol (3 mL), glycerol (0,2 mL) and of 2,6-dichlorindophenol (30 mg). This ink was printed onto the samples of hybrid $TiO_2/SiO_2$ layers using Fujifilm Dimatix printer. Nozzle temperature was kept at 30 °C, substrate temperature 45 °C. Nozzle span was set to 30 $\mu$m (i.e., 445 779 drops on $20 \times 20$ mm in one layer). The total 2,6-dichloroindophenol loading was $5.011 \times 10^{-8}$ mol on the $20 \times 20$ mm patch, which corresponds to $3.634 \times 10^{-3}$ mg $\cdot$ cm$^{-2}$.

#### 2.1.5. Stearic Acid Layers

The printing solution was prepared by mixing 1 mL of stearic acid in toluene stock solution (30 g/L) and 9 mL of 2-methylpropan-1-ol. This ink was printed on samples with hybrid $TiO_2/SiO_2$ layers using Fujifilm Dimatix printer in two layers. Nozzle temperature was 24 °C, substrate temperature 50 °C. Nozzle span was set to 20 $\mu$m (i.e., 2 004 002 drops on $20 \times 20$ mm patch in two layers, which resulted into $2.348 \times 10^{-7}$ mol on $20 \times 20$ mm in two layers or $1.503 \times 10^{-2}$ mg $\cdot$ cm$^{-2}$).

#### 2.1.6. Microorganism and Nutrient Media

*Escherichia coli* CCM 3988 was used as model microorganisms in this study and was obtained from the Czech Collection of Microorganisms maintained at Masaryk University Brno, Faculty of Science. The bacterial strain was grown aerobically in Nutrient broth (HiMedia, India) at 37 °C. Solid medium of agar plates was prepared using respective media and 2% agar powder (HiMedia, India) and was used in the plate count method for the analysis of investigated samples.

### 2.2. Photocatalytic Activity Measuring

#### 2.2.1. Photoinduced Hydrophilicity

The contact angle of water droplets on hybrid $TiO_2/SiO_2$ samples was measured using the Contact Angle System OCA 20 and SCA 20 software. A 5 $\mu$L droplet of deionized water was placed on hybrid $TiO_2/SiO_2$ sample. The samples were discontinuously irradiated by a mercury vapour lamp (Fig. 1) with intensity of 2.5 mW $\cdot$ cm$^{-2}$ and then transferred into the contact angle measuring machine located nearby in the same room. The temperature has been maintained at $25 \pm 2$ °C.

#### 2.2.2. Redox Dye Ink Layers

Recently, the benefits of photocatalytic activity testing by means of redox indicator inks have been convincingly demonstrated.[41] We adopted this approach and the experiment was performed in a special dedicated photochemical reactor developed by the authors. It consists of a simple housing holding a sample of photocatalytic self-cleaning glass over a collimating lens terminated optical fibre. This "plate reactor" was further equipped with two LEDs positioned opposite the collimating lens (Fig. 2). One of them, emitting at 650 nm, served as the light source for measurement of absorbance with a RedTide USB650 UV-VIS spectrophotometer (Ocean Optics), while the second diode (UVLUX320-HL-3, Roithner LaserTechnik) emitting at

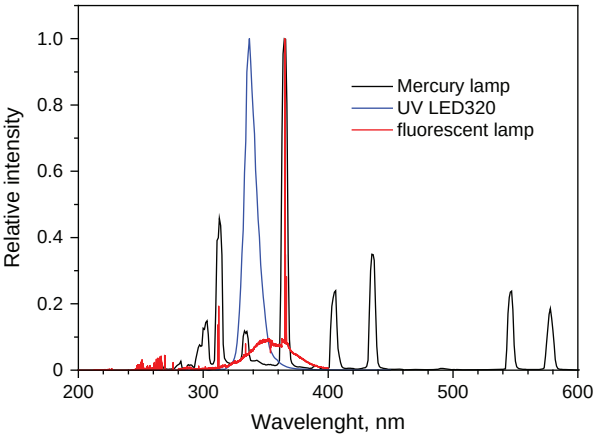


**Figure 1.** Emission spectra of medium pressure mercury lamp Osram HQL 125 W, fluorescent Sylvania Lynx-S 11 W lamp and UV LED UVLUX320-HL-3.

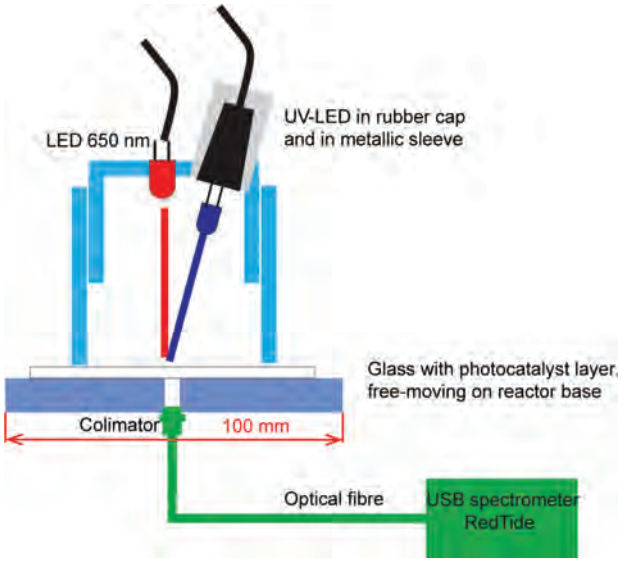


**Figure 2.** Photochemical reactor for photocatalytic degradation of redox dye ink.

337 nm, served as the actinic radiation source for $TiO_2$ excitation. Irradiance was set to 0.5 $mW \cdot cm^{-2}$. The investigated sample of self-cleaning glass coated with a layer indicator ink[42] containing 2,6-dichloroindophenol, placed in the reactor and the absorbance drop was measured in 5 s increments at 650 nm.

#### 2.2.3. Stearic Acid Layers

Photocatalytic degradation of stearic acid printed on hybrid $TiO_2/SiO_2$ samples was monitored using FTIR transmission spectra measured by FTIR spectrometer Nicolet Impact 400. The samples were off-line irradiated by medium pressure mercury lamp OSRAM HQL 125 W. Irradiance was set to 2.5 $mW \cdot cm^{-2}$ in UV-A region.

### 2.3. Antimicrobial Activity Measuring

The microbial culture for the photocatalytic test was prepared as follows: one gelatine disk of microbial culture of *Escherichia coli* CCM 3988 inoculated into an Erlenmeyer flask containing 50 mL of Nutrient broth and incubated for 48 h at 37 °C. After incubation, this bacteria suspension was suitably diluted with deionized water to obtain the count of $4.7 \times 10^5$ cfu/mL and further used in experiment. 75 $\mu$L of purified bacteria suspension was dropped onto 15 min pre-irradiated $TiO_2/SiO_2$ $20 \times 20$ mm film on glass plate and covered with $20 \times 20$ mm microscopic cover glass. No leakage was allowed. The active areas and bacteria suspension volume were slightly adopted, but the cell concentration according to ISO standard 27447:2009 (Glass adhesion method) was kept. The bacterial suspension was delivered and spread by the same way on all samples. Three samples of $TiO_2/SiO_2$ layer and two samples of pure glass were irradiated by four fluorescent lamps Sylvania Lynx-S 11 W with a maximum of energy at 365 nm. Irradiance of 0.5 $mW \cdot cm^{-2}$ was maintained by lamp distance adjustment (Fig. 3). At the same time two samples of $TiO_2/SiO_2$ layer and two samples of pure glass were kept in dark. After exposure, all samples were washed out with 10 mL of double deionized water and 1 mL of each washing suspension was placed in 3 Petri dishes. 15 mL of nutrient agar kept at 45 °C was added to each Petri dish, allow them to stand for 15 minutes at room temperature. When the agar medium solidifies, the Petri dishes are placed upside down and incubated for 48 hours at 37 °C. For washing efficiency test, immediately after delivery the bacterial suspension on two samples of pure glass, the bacterial suspension was washed out with 10 mL of deionized water and cultivated by the same way. Colony counting after 48 hours was performed. Each sample was tested 3 times.

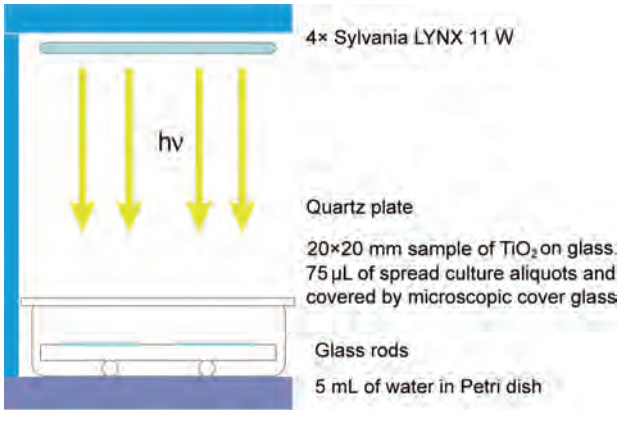


**Figure 3.** Wet chamber for antimicrobial activity testing.

## 3. RESULTS AND DISCUSSION

### 3.1. Thickness of $TiO_2/SiO_2$ Layers

Thickness is without any doubt one of the most important parameters influencing the physicochemical properties of thin layers. SEM cross-section images are depicted in Figure 4. The cut was directed perpendicular towards the direction of the printhead movement. In this way we were able to observe the whole length of the cut and check for printing artefacts and general thickness uniformity. Excellent evenness without any significant variations was observed, indicating flawless printability of the used formulation and well managed printed bands merging. Sample thickness was measured at 10 randomly selected spots along the cut and values are reported at Table I together with calculated amount of delivered $TiO_2$ in $TiO_2/SiO_2$ layers.

### 3.2. Photocatalytic Activity

#### 3.2.1. Redox Dye Ink Layers

Degradation of a dye 2,6-dichloroindophenol to its colourless form can be expressed by following reaction scheme.[43, 44]

$$\text{DCIP} + \text{glycerol} \xrightarrow{TiO_2/UVA\ light} \text{leuco-DCIP} + \text{glyceraldehyde} \quad (1)$$

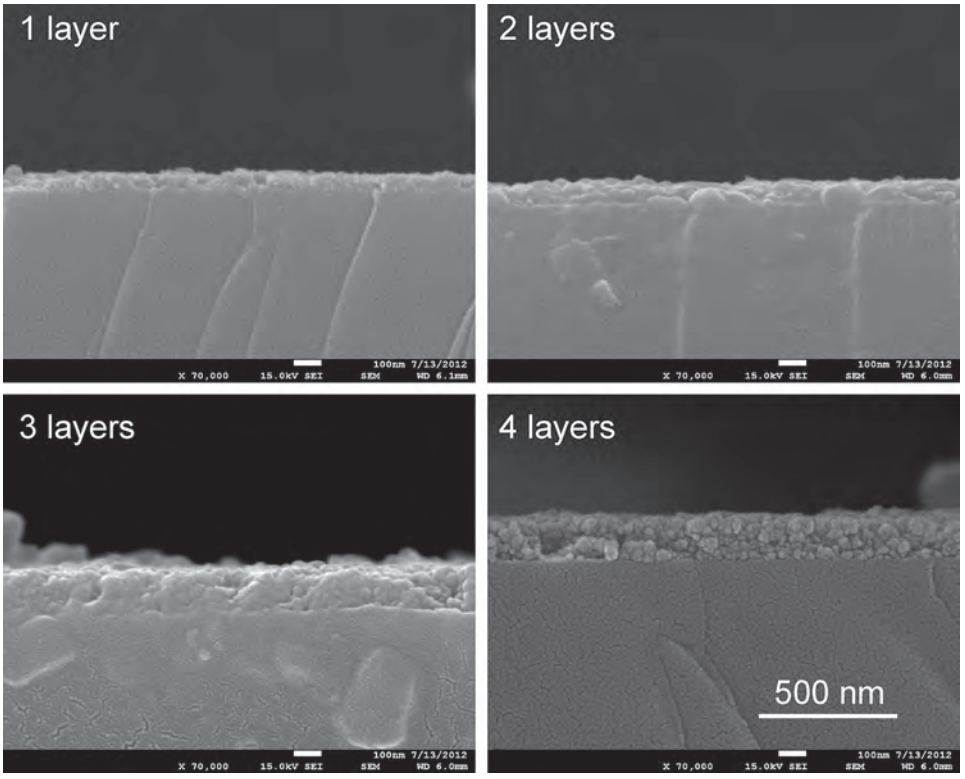


**Figure 4.** SEM cross-section images of $TiO_2/SiO_2$ layers on glass.

We discovered that the dependence of relative absorbance on time is linear so it means that photochemical degradation of DCIP ink runs according to the zero order kinetics. The oxidation reaction of the DCIP ink is a complicated process affected namely by glycerol concentration in the polymer layer. The degradation reaction rate can be characterized by its formal rate constant. An experiment with the blank sample (without the photocatalyst) was also carried out and the resulting final value of direct photolysis rate constant of the ink was subtracted from the final measurement rate constant values to obtain the net formal rate constant corresponding to photocatalytic efficiency of tested hybrid layers $TiO_2/SiO_2$. The formal rate constant was calculated according to the Eq. (3), where the slope of the straight line is a ratio of rate constant and initial concentration of 2,6-dichloroindophenol $k'$. The calculated values increased with number of printed $TiO_2/SiO_2$ layers: $(0{,}128 \pm 0{,}002) \times 10^{-4}$, $(1{,}265 \pm 0{,}007) \times 10^{-4}$, $(3{,}167 \pm 0{,}009) \times 10^{-4}$, $(4{,}483 \pm 0{,}016) \times 10^{-4}$, $(5{,}682 \pm 0{,}044) \times 10^{-4}$ $min^{-1}$ for 0 to 4 layers respectively (Fig. 5).

$$c_A = c_{A_0} - kt \tag{2}$$

$$\frac{c_A}{c_{A_0}} = 1 - \frac{k}{c_{A_0}}t = 1 - k't \tag{3}$$

### 3.2.2. Photoinduced Hydrophilicity

The hydrophilic properties of prepared layers were evaluated by measuring the water contact angle as a function of the exposure time. We discovered that after 150 min of irradiation the average water contact angle on the sample with four layers decreased to 12% of original angle. Absolute values were near to 10 degrees. All initial contact angles were higher than 80°. After the irradiation of these layers by UV light with intensity of irradiation 2,5 $mW \cdot cm^{-2}$ all samples became more hydrophilic (Fig. 6). This could be explained by two ways. One of them is that by

**Table I.** Thickness of $TiO_2/SiO_2$ layers measured by SEM.

| Number of layers | Average thickness [nm] | Standard deviation [nm] | Calculated amount of $TiO_2$ [$mg \cdot cm^{-2}$] |
|---|---|---|---|
| 1 | 41.1 | 7.9 | 0.213 |
| 2 | 73.2 | 21.9 | 0.425 |
| 3 | 115.9 | 34.3 | 0.638 |
| 4 | 153.2 | 10.2 | 0.850 |

**Table II.** Half-life of stearic acid degradation in very thin layer on $TiO_2/SiO_2$.

| No. of $TiO_2/SiO_2$ layers | Half-life [s] |
|---|---|
| 0 | 10762 |
| 1 | 1142 |
| 2 | 650 |
| 3 | 415 |
| 4 | 392 |

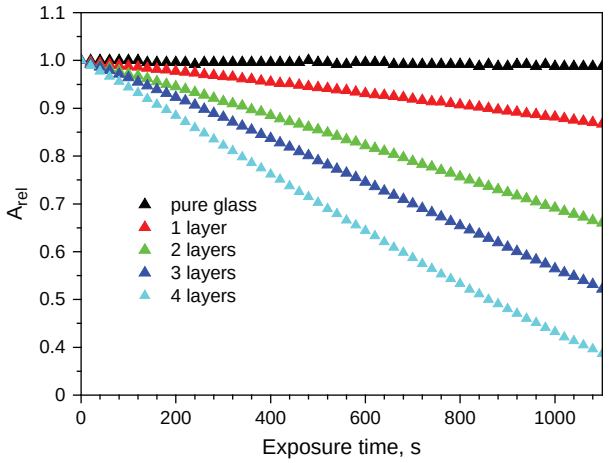


**Figure 5.** Photocatalytic degradation of 2,6-dichloroindophenol.

UV irradiation the holes are transferred to the surface, creating oxygen vacancies most likely at the two coordinated bridging sites, which are suitable for dissociative water adsorption. Photoexcited electrons are also transferred to the surface $Ti^{4+}$, forming $Ti^{3+}$ followed by the electron transfer to adsorbed oxygen molecules.[45, 46] When the surface defect is generated, water and oxygen compete to dissociatively adsorb on it. These results suggest that the oxygen vacancy (O-) is favourable for dissociating water, resulting in abundant basic Ti–OH groups on the surface of the UV-irradiated $TiO_2$ coating as follows:

$$(Ti^{3+} - O^{-}) + H_2O \rightarrow Ti - OH + H_2 \quad (4)$$

where Ti in the Ti–OH group is +4 charged.[45]

But on the other side, recent communication by Zubkov[47] and co-workers reports that gas phase $O_2$ is necessary to cause the photoinduced hydrophilicity effect. They explain also the hydrophilic properties of irradiated water droplet on photocatalytic surface due to the establishment of the critical surface condition at the perimeter of a water droplet, which covers a hydrocarbon molecules coated $TiO_2$ surface. They showed that the photooxidation of adsorbed hydrocarbon occurs preferentially beyond the perimeter of the water droplet and expansion of the droplet immediately leads to drop spreading into $TiO_2$ surface regions that are unshielded by liquid water during irradiation.[47]

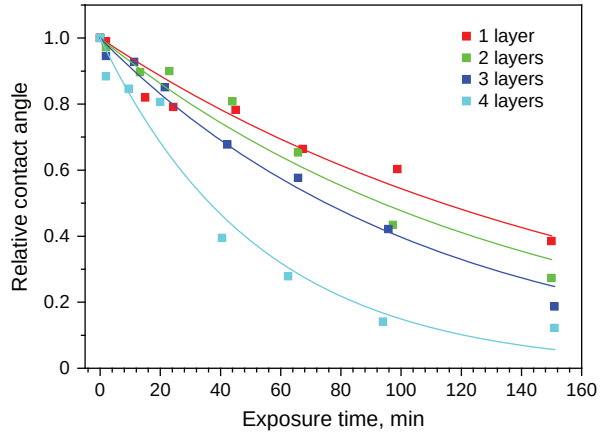


**Figure 6.** Photoinduced hydrophilisation of hybrid $TiO_2/SiO_2$ layers.

### 3.2.3. Stearic Acid Layers

Stearic acid is an attractive model compound because of its similarity to many of the waxy, hydrophobic solids that adhere to glass in the real world. The kinetics of its removal is zero-order, i.e., independent of how much is deposited, except for very thin films.[48]

$$CH_3(CH_2)_{16}COOH + 26O_2 \xrightarrow{h\nu \geq E_{bg}} 18CO_2 + 18H_2O \quad (5)$$

The destruction of stearic acid can be indirectly measured via monitoring the amount of generated $CO_2$ using gas chromatography[49] or FTIR,[50] through the change in thickness of the stearic acid film using ellipsometry,[51] but the generally preferred and simplest method is by monitoring the disappearance of the infrared absorption[52] of the stearic acid film as a function of time.

We employed the last mentioned approach and integral absorbance values of the printed stearic acid layer in the range of 3200–2600 $cm^{-1}$ were recorded by FTIR spectrometer. The fastest concentration decrease showed the samples with 3 and 4 layers of $TiO_2/SiO_2$. For the total removal of stearic acid ($1.503 \times 10^{-2}$ $mg \cdot cm^{-2}$) from the photocatalytic surface, the exposure dose of 8.5 $J \cdot cm^{-2}$, 6.8 $J \cdot cm^{-2}$, 3.2 $J \cdot cm^{-2}$ is sufficient for 1 to 3 and 4 layers, respectively (Fig. 7).

The small amount of $TiO_2/SiO_2$ found in 1 and 2 layered samples (approx. 40 and 80 nm) leads to a slow photocatalyst activation and therefore causes an induction period. After activation period, the reaction obeys to the formal first order kinetics, which is consistent with

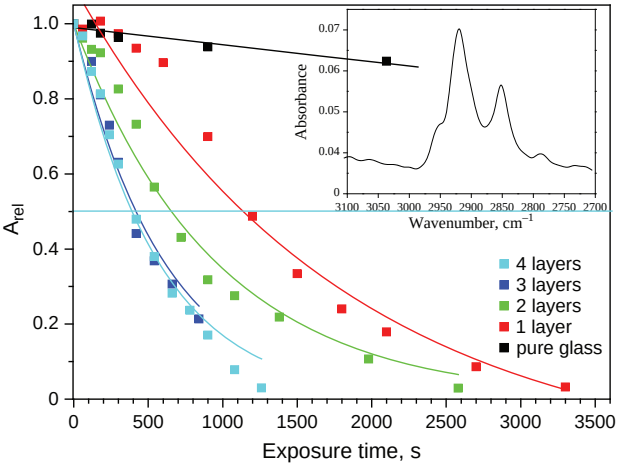


**Figure 7.** Photocatalytic degradation of stearic acid and FTIR spectrum of stearic acid (inside graph).

the results reported by other authors.[53–55] The half-lives (Table II) were 1142, 650, 415 and 392 s for 1 to 4 layers of $TiO_2/SiO_2$, respectively. The kinetic profile of stearic acid degradation is affected by several aspects. It depends on homogeneity, roughness, thickness of photocatalyst and thickness of stearic acid. In the case of a very thin stearic acid layer on a superhydrophilic photocatalyst, the clusters of stearic acid are likely to be formed. Only in this particular case, the degradation rate can be described by the first order kinetics. If the stearic acid is thick and uniform, the degradation rate would obey the zero order kinetics since we can expect a linear decrease of the fatty acid layer thickness. However, the stearic acid degradation kinetics observed on real samples is not unambiguous and usually is between zero and first order kinetics.[48]

### 3.3. Antimicrobial Activity

The death of a bacterial cell has long been defined as the inability of a cell to grow to a visible colony on bacteriological media. However, with traditional culture methods, one can observe bacterial death only in a retrospective way. Intermediate states like cell injury are difficult to detect with the plating method.[56] Obviously, a cell suffering from stresses may not be able to propagate itself for a certain period of time and would be therefore identified as dead by the plating method.[29, 30] Such a phenomenon was not investigated in this study.

When evaluating the cell viability on exposed photocatalytic surface, the following aspects should be considered: the plate count method relies on colony counting. However, a colony originated from several cells is indistinguishable from a colony originated from a single cell. It should be noted that plate count detects only a fraction of microorganisms which are able to grow and form colonies in a given medium in a selected incubation period.[27, 30] A cell culture irradiated on photocatalytic surface is subjected to stress.[57] Subsequently, smaller colonies and smaller cells are observed to grow in the cell counting cultivation stage.[27] A cell with partly damaged cell wall is not capable of reproduction or requires a certain time lag to recover from the stress. In this case the colony will not grow. Nevertheless, there are several viability indicators that can be assessed at the single-cell level without cell cultivation. These indicators are based mostly on fluorescent molecules, which can be detected with epifluorescence microscopy, solid state cytometry, or flow cytometry.[27, 30, 58–60] Each indicator is based on criteria that reflect different levels of cellular integrity or functionality.[61]

Similarly, if the damage is low, the fluorescent staining will not differentiate the cell correctly. The opposite situation can also take place, i.e., a damaged cell exhibits itself as a dead by the staining method, but it overcomes the stress during cultivation and establishes a colony. These phenomena cause differences of cell viability determination and thus errors in antimicrobial activity of titanium dioxide thin layers.

The important point is that the ISO standard 27447 defines the testing surface area, bacterial suspension volume and the number of bacterial cells within quite narrow limits. The incident radiation intensity is rather low and originates from the presumption that the self-cleaning surfaces will be irradiated predominantly by daylight or by artificial light sources with a low UV intensity. The struggle for precisely defined workflow resulted into laborious and time-consuming way of antibacterial activity testing.[62]

Photocatalyst antimicrobial activity was calculated according to following equations:

$$R_L = [\log(B_L/A) - \log(C_L/A)] = \log(B_L/C_L) \quad (6)$$

$$\Delta R_L = \log(B_L/C_L) - [\log(B_D/A) - \log(C_D/A)] = \log(B_L/C_L) - \log(B_D/C_D) \quad (7)$$

Where $R_L$ is the photocatalyst antimicrobial activity value after UV irradiation of intensity $L$, $\Delta R_L$ is the photocatalyst antimicrobial activity value with UV irradiation (variable introduced and defined by ISO 27447, which takes into account interactions of bacteria with photocatalyst surface after being kept in dark), $A$ is the average number of viable bacteria of non-treated specimens just after inoculation, $B_L$ is the average number of viable bacteria of non-treated specimens after UV irradiation of intensity $L$, $C_L$ is the average number of viable bacteria of photocatalyst treated specimens after UV irradiation of intensity $L$, $B_D$ is the average number of viable bacteria of non-treated specimens after being kept in dark, $C_D$ is the average number of viable bacteria of photocatalyst treated specimens after being kept in dark.

One of the problems with comparing studies on photocatalytic disinfection is that different workers have used different test methods. Many of them have used the survival ratio instead of the quantities defined by ISO 27447. Especially, when the fluorescent staining techniques are employed, the survival ratio is one of the most frequently used measures for antimicrobial activity expression. For the purpose of comparison, the survival ratio from our plate count results was calculated as follows:

$$SR = C_L/C_D \quad (8)$$

The survival ratio in Eq. (8) is not specified by the ISO standard, we used this calculation for comparison to other published results which use this quantity obtained by other live/dead method, e.g., fluorescence staining. The results of the plate count method indicate that *E. coli* is significantly sensitive to the reported hybrid $TiO_2/SiO_2$ layers (Fig. 8).

Similar conclusion can be drawn on the basis of the photocatalyst antimicrobial activity value with UV irradiation ($\Delta R_L$). This figure (Eq. (7)) expresses the net activity

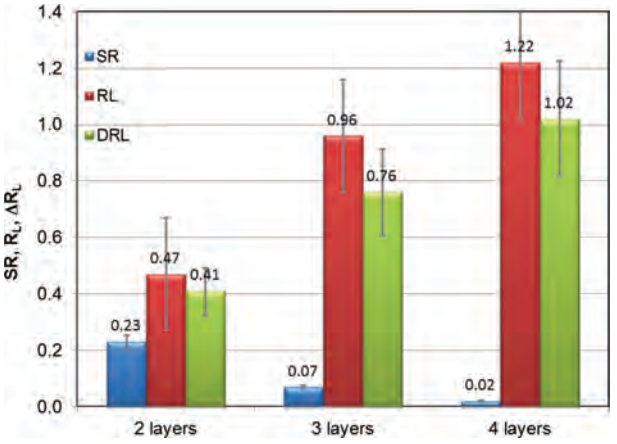


**Figure 8.** Antibacterial activity of irradiated $TiO_2/SiO_2$ layers. For $SR$, $R_L$, $\Delta R_L$ explanation see Eqs. (6) to (8).

corrected for the other stressors such as the action of non-irradiated catalyst, temperature, lack of nutrients etc.[27, 30] So far, just a few papers discussing this issue and following the ISO 27447 strictly have been published.[33, 35, 63]

The advantages of standardized method ISO 27447 can be summarized as follows: The method is simple and does not require special equipment. The important point is that the conditions of testing (incl. irradiation) are standardized.

Drawbacks of standardized method ISO 27447 are mainly:

(1) the method is very time consuming process–test of one sample takes about 11 hours if it is performed by one person;

(2) plate count method of live/dead cell distinguishing shows usually error about 20 %.

We suggest consider a modification of the standard allowing to evaluate the number of living bacteria after bacteria washout by other methods, which may improve the method accuracy.

## 4. CONCLUSION

Material printing proved to be well suited for the deposition of this complex nanoparticulate ink and hybrid $TiO_2/SiO_2$ films with thickness ranging from 41 to 153 nm were conveniently fabricated by repeated overprinting of 1 to 4 layers, respectively. Further advantages of this fabrication technique include the efficiency of liquid precursor use. While in the case of conventional wet coating techniques such as spin-coating or dip-coating most of the deposited liquid is wasted, with inkjet printing only a minor fraction of the ink is consumed for printhead purging and most of the ink is actually printed on the substrate. Moreover, inkjet printing allows for smooth upscaling, as industrial printers handling both rigid or roll media up to several meters width are readily available. However, the most prominent advantage is the possibility of direct patterning, which enables us to effectively fabricate planar patterns with fine details (down 10 micron with conventional printheads). Although the patterning advantage was not fully exploited in this study since only simple rectangular patterns were used, it may be of a key importance for the production of functional titania patterns on organic substrates.

The photocatalytic and biocidic properties were investigated and discussed by several generally recognized methods. Printed layers are able to change their surface properties from hydrophobic to hydrophilic during one hour of UV-A irradiation set at recommended intensity. The thickest layers exhibited a drop in the water droplet contact angle below 10% of original value on non-irradiated surface within 2 hours of UV-A irradiation.

The self-cleaning properties were tested on model contaminants: We followed the decolourization reaction of 2,6-DCIP by UV-VIS spectroscopy and the decomposition of stearic acid by FTIR. The rate constant of 2,6-DCIP decolourization was $5{,}682 \pm 0{,}044 \times 10^{-4}$ $min^{-1}$ in the case of the thickest layer. Stearic acid degradation profile was described by the formal first order rate kinetics and the thickest layers exhibited half-life of 392 s. These values account for significant photocatalytic activity of the studied samples and prove its suitability for self-cleaning coatings application. Although more active titania coatings may have been prepared by other methods, it is important to realize that the described samples were fabricated by completely cold process at ambient temperature and pressure. This enables the deposition on heat sensitive substrates such as polymer foils and roll to roll processing.

Apart from self-cleaning activity, the reported films feature significant biocide activity as well. The *E. coli* survival ratio was 0.02 and $\Delta R_L$ according to ISO 27447 was 1.02 for the 4-layered sample and it clearly justifies this conclusion. However, while the photocatalytic activity evaluation performed in the described reactors is rather straightforward and convenient due to automated experimental data recording, the assessment of biocide activity according to the present standard remains labour intensive time consuming.

**Acknowledgment:** Authors thank to Ministry of Education, Youth and Sports of Czech Republic for support by project MEB091141 and by project LD14131. Slovenian Research Agency is also acknowledged for co-financing bilateral research visits.

## References and Notes

1. H. Shibata, H. Sakai, P. Rangsunvigit, T. Hirano, and M. Abe, *Surface Coatings International Part B-Coatings Transactions* 86, 125 **(2003)**.
2. L. Pinho and M. J. Mosquera, *Applied Catalysis B: Environmental* 134–135, 205 **(2013)**.
3. R. Fateh, R. Dillert, and D. Bahnemann, *Langmuir* 29, 3730 **(2013)**.
4. L. Pinho, J. C. Hernandez-Garrido, J. J. Calvino, and M. J. Mosquera, *Physical Chemistry Chemical Physics* 15, 2800 **(2013)**.

5. Z. Liu, F. Chen, P. Fang, S. Wang, Y. Gao, F. Zheng, Y. Liu, and Y. Dai, *Applied Catalysis A: General* 451, 120 **(2013)**.
6. B. S. Boroujeny, A. Afshar, and A. Dolati, *Thin Solid Films* 520, 6355 **(2012)**.
7. L.-X. Guan, N. Zhao, and M.-M. Yao, *Adv. Mater. Res.* Durnten-Zurich, Switz, Materials Science and Information Technology II, 532–533, 153 **(2012)**.
8. G. N. Shao, A. Hilonga, Y. N. Kim, J.-K. Kim, G. Elineema, D. V. Quang, S. J. Jeon, and H. T. Kim, *Chem. Eng. J.* Amsterdam, Neth. 198–199, 122 **(2012)**.
9. U. Cernigoj and S. U. Lavrencic, WO2010053459A1 **(2010)**.
10. M. H. Lee, U. M. Patil, S. T. Kochuveedu, C. S. Lee, and D. H. Kim, *Bull. Korean Chem. Soc.* 33, 3767 **(2012)**.
11. U. Černigoj, U. L. Štangar, P. Trebše, and M. Sarakha, *Journal of Photochemistry and Photobiology A: Chemistry* 201, 142 **(2009)**.
12. F. C. Krebs, *Solar Energy Materials and Solar Cells* 93, 394 **(2009)**.
13. J. Heinzl and C. H. Hertz, *Advances in Imaging and Electron Physics* 65, 91 **(1985)**.
14. G. D. Martin, S. D. Hoath, I. M. Hutchings, and Iop, Inkjet Printing—the Physics of Manipulating Liquid Jets and Drops, *Conference on Engineering in Physics-Synergy for Success* London, England **(2006)**.
15. P. Calvert, *Chemistry of Materials* 13, 3299 **(2001)**.
16. H. Sirringhaus and T. Shimoda, *MRS Bulletin* 28, 802 **(2003)**.
17. J. Miettinen, V. Pekkanen, K. Kaija, P. Mansikkamäki, J. Mäntysalo, M. Mäntysalo, J. Niittynen, J. Pekkanen, T. Saviauk, and R. Rönkkä, *Microelectronics Journal* 39, 1740 **(2008)**.
18. M. Singh, H. M. Haverinen, P. Dhagat, and G. E. Jabbour, *Advanced Materrials* 22, 673 **(2010)**.
19. E. Tekin, P. J. Smith, and U. S. Schubert, *Soft Matter* 4, 703 **(2012)**.
20. Y. Oh, S. N. Lee, H. K. Kim, and J. Kim, *Journal of the Electrochemical Society* 159, H777 **(2012)**.
21. A. K. Chandiran, A. Yella, M. Stefik, L. P. Heiniger, P. Comte, M. K. Nazeeruddin, and M. Gratzel, *Acs Applied Materials and Interfaces* 5, 3487 **(2013)**.
22. D. C. Gilmer, W. L. Gladfelter, D. G. Colombo, C. J. Taylor, J. Roberts, S. A. Campbell, H. S. Kim, G. D. Wilk, and M. A. Gribelyuk, Low Temperature Chemical Vapor Deposition of Titanium Dioxide Thin Films Using Tetranitratotitanium(IV), *Chemical Aspects of Electronic Ceramics Processing*, edited by P. N. Kumta, A. F. Hepp, D. B. Beach, B. Arkles, and J. J. Sullivan, Mater. Res. Soc., Warrendale, Pa **(1998)**, p. 45.
23. H. Uchida, A. Otsubo, K. Itatani, and S. Koda, *Japanese Journal of Applied Physics Part 1-Regular Papers Brief Communications and Review Papers* 44, 1901 **(2005)**.
24. H. C. Weerasinghe, P. M. Sirimanne, G. P. Simon, and Y. B. Cheng, *Progress in Photovoltaics* 20, 321 **(2012)**.
25. A. Mills, C. Hill, and P. K. J. Robertson, *J. Photochem. Photobiol., A* 237, 7 **(2012)**.
26. S. Thabet, M. Weiss-Gayet, F. Dappozze, P. Cotton, and C. Guillard, *Applied Catalysis B: Environmental* 140–141, 169 **(2013)**.
27. S. Pigeot-Rémy, F. Simonet, D. Atlan, J. C. Lazzaroni, and C. Guillard, *Water Research* 46, 3208 **(2012)**.
28. V. Jasson, L. Jacxsens, P. Luning, A. Rajkovic, and M. Uyttendaele, *Food Microbiol* 27, 710 **(2010)**.
29. U. Žvab, M. Marušič, and U. Štangar, *Applied Microbiology and Biotechnology* 96, 1341 **(2012)**.
30. U. Žvab, U. Lavrenčič Štangar, and M. Bergant Marušič, *Applied Microbiology and Biotechnology* 98, 1925 **(2014)**.
31. V. Ducman, V. Petrovič, and S. D. Škapin, *Ceramics International* 39, 2981 **(2013)**.
32. P. S. M. Dunlop, C. P. Sheeran, J. A. Byrne, M. A. S. McMahon, M. A. Boyle, and K. G. McGuigan, *Journal of Photochemistry and Photobiology A: Chemistry* 216, 303 **(2010)**.
33. H. A. Foster, D. W. Sheel, P. Sheel, P. Evans, S. Varghese, N. Rutschke, and H. M. Yates, *Journal of Photochemistry and Photobiology A: Chemistry* 216, 283 **(2010)**.
34. V. M. Sousa, C. M. Manaia, A. Mendes, and O. C. Nunes, *Journal of Photochemistry and Photobiology A: Chemistry* 251, 148 **(2013)**.
35. Y. Yao, T. Ochiai, H. Ishiguro, R. Nakano, and Y. Kubota, *Applied Catalysis B: Environmental* 106, 592 **(2011)**.
36. J. M. Szeifert, D. Fattakhova-Rohlfing, J. Rathousky, and T. Bein, *Chemistry of Materials* 24, 659 **(2012)**.
37. D. H. Ryu, S. C. Kim, S. M. Koo, and D. P. Kim, *Journal of Sol–Gel Science and Technology* 26, 489 **(2003)**.
38. Y. S. Shen, *Rsc Advances* 2, 5957 **(2012)**.
39. H. J. Kim, Y. G. Shul, and H. S. Han, *Topics in Catalysis* 35, 287 **(2005)**.
40. N. Bao, Z. T. Wei, Z. H. Ma, F. Liu, and G. B. Yin, *Journal of Hazardous Materials* 174, 129 **(2010)**.
41. A. Mills, J. Hepburn, and M. McFarlane, *ACS Applied Materials and Interfaces* 1, 1163 **(2009)**.
42. A. Mills, M. McGrady, J. Wang, and J. Hepburn, *International Journal of Photoenergy* 2008, 6 **(2008)**.
43. A. Mills and M. McGrady, *Journal of Photochemistry and Photobiology A: Chemistry* 193, 228 **(2008)**.
44. A. Mills, M. McGrady, J. Wang, and J. Hepburn, *Int. J. Photoenergy* 1 **(2008)**.
45. Y. Han, D. Chen, J. Sun, Y. Zhang, and K. Xu, *Acta Biomaterialia* 4, 1518 **(2008)**.
46. T. Watanabe, A. Nakajima, R. Wang, M. Minabe, S. Koizumi, A. Fujishima, and K. Hashimoto, *Thin Solid Films* 351, 260 **(1999)**.
47. T. Zubkov, D. Stahl, T. L. Thompson, D. Panayotov, O. Diwald, and J. T. Yates, Jr., *J. Phys. Chem. B* 109, 15454 **(2005)**.
48. D. Ollis, *Applied Catalysis B: Environmental* 99, 478 **(2010)**.
49. H. Hidaka, S. Yamada, S. Suenaga, J. Zhao, N. Serpone, and E. Pelizzetti, *Journal of Molecular Catalysis* 59, 279 **(1990)**.
50. A. Mills and J. Wang, *Journal of Photochemistry and Photobiology A: Chemistry* 182, 181 **(2006)**.
51. J. T. Remillard, J. R. McBride, K. E. Nietering, A. R. Drews, and X. Zhang, *The Journal of Physical Chemistry B* 104, 4440 **(2000)**.
52. Y. Paz, Z. Luo, L. Rabenberg, and A. Heller, *Journal of Materials Research* 10, 2842 **(1995)**.
53. H. Limage, F. D. Tichelaar, R. Closset, S. Delvaux, R. Cloots, and S. Lucas, *Surface and Coatings Technology* 205, 3774 **(2011)**.
54. L. Peruchon, E. Puzenat, A. Girard-Egrot, L. Blum, J. M. Herrmann, and C. Guillard, *Journal of Photochemistry and Photobiology A: Chemistry* 197, 170 **(2008)**.
55. M. Piispanen and L. Hupa, *Applied Surface Science* 258, 1126 **(2011)**.
56. T. Verdier, M. Coutand, A. Bertron, and C. Roques, *Building and Environment* 80, 136 **(2014)**.
57. T. Verdier, M. Coutand, A. Bertron, and C. Roques, *Coatings* 4, 670 **(2014)**.
58. F. Joux and P. Lebaron, *Microbes Infect* 2, 1523 **(2000)**.
59. L. V. Zhukova, J. Kiwi, and V. V. Nikandrov, *Colloids and Surfaces B: Biointerfaces* 97, 240 **(2012)**.
60. P. Liu, W. Duan, Q. Wang, and X. Li, *Colloids Surf. B Biointerfaces* 78, 171 **(2010)**.
61. M. Berney, F. Hammes, F. Bosshard, H.-U. Weilenmann, and T. Egli, *Appl. Environ. Microbiol.* 73, 3283 **(2007)**.
62. ISO 27447:2009. Fine ceramics (advanced ceramics, advanced technical ceramics)–Test method for antibacterial activity of semiconducting photocatalytic materials. *International Organization for Standardization* **(2009)**.
63. J. Krysa, E. Musilova, and J. Zita, *Journal of Hazardous Materials* 195, 100 **(2011)**.


Received: 28 February 2014. Accepted: 15 October 2014.

*Molecules* **2015**, *20*, 14552-14564; doi:10.3390/molecules200814552

OPEN ACCESS

*molecules*

**ISSN 1420-3049**

www.mdpi.com/journal/molecules

*Article*

# Optical Properties of Titania Coatings Prepared by Inkjet Direct Patterning of a Reverse Micelles Sol-Gel Composition

**Veronika Schmiedova [1,*], Petr Dzik [1], Michal Vesely [1], Oldrich Zmeskal [1], Magdalena Morozova [2] and Petr Kluson [2]**

[1] Faculty of Chemistry, Brno University of Technology, Purkynova 118, Brno 61200, Czech Republic; E-Mails: dzik@fch.vutbr.cz (P.D.); vesely-m@fch.vutbr.cz (M.V.); zmeskal@fch.vutbr.cz (O.Z.)

[2] Institute of Chemical Process Fundamentals of the ASCR, Rozvojova 135, Prague 16502, Czech Republic; E-Mails: morozova@icpf.cas.cz (M.M.); Kluson@icpf.cas.cz (P.K.)

* Author to whom correspondence should be addressed; E-Mail: xcschmiedova@fch.vutbr.cz; Tel.: +420-541-149-396; Fax: +420-541-211-697.

Academic Editors: Jimmy C. Yu and Wing-Kei Ho

*Received: 17 June 2015 / Accepted: 21 July 2015 / Published: 12 August 2015*

**Abstract:** Thin layers of titanium dioxide were fabricated by direct inkjet patterning of a reverse micelles sol-gel composition onto soda-lime glass plates. Several series of variable thickness samples were produced by repeated overprinting and these were further calcined at different temperatures. The resulting layers were inspected by optical and scanning electronic microscopy and their optical properties were investigated by spectroscopic ellipsometry in the range of 200–1000 nm. Thus the influence of the calcination temperature on material as well as optical properties of the patterned micellar titania was studied. The additive nature of the deposition process was demonstrated by a linear dependence of total thickness on the number of printed layers without being significantly affected by the calcination temperature. The micellar imprints structure of the titania layer resulted into significant deviation of measured optical constants from the values reported for bulk titania. The introduction of a void layer into the ellipsometric model was found necessary for this particular type of titania and enabled correct ellipsometric determination of layer thickness, well matching the thickness values from mechanical profilometry.

**Keywords:** material printing; inkjet; ellipsometry; titanum dioxide; optical properties

## 1. Introduction

Titanium dioxide has been attracting the attention of researchers for the past several decades, it is probably the most extensively studied transition metal oxide [1] because of its unique photo-induced properties, high refractive index, transmittance in the visible spectral range and general chemical stability. It is an excellent semiconductor material, which crystallizes in three different structures: anatase (tetragonal), rutile (tetragonal) and brookite (orthorhombic) [2]. The rutile phase is studied mainly in terms of its optical properties. Recently, the optical and electrical properties of anatase and rutile showed that the major difference between the two phases is the greater optical band gap and a smaller electron effective mass of anatase compared with the rutile phase [3]. Rutile has one of the largest refractive indexes, and also has high dispersion. Anatase phase can develop during crystallization temperatures below 600 °C, while at higher temperatures it is converted to the more stable rutile form. The low-temperature anatase phase is interesting primarily for its efficient electron-hole generation upon irradiation by UV and corresponding photocatalytic effects [4]. Rutile is stable at high temperatures, shows weaker photoactivity and is primarily used for functional coatings in optics, photonics, microelectronics *etc.* $TiO_2$ thin films have particular application potential due to its specific properties such as chemical stability, high refractive index, high dielectric constant and transparency in the visible region of the spectrum [2].

Spectroscopic ellipsometry (SE) is a nondestructive optical method that allows the study of optical properties of materials forming thin layers. This technique is based on measuring the state of polarization of the incident and reflected light waves [5]. There is no need to modify the samples as for optical profilometry or interferometry, in the case of which the layer must be reflective and is therefore usually covered by evaporated aluminum. It is possible to determine the complex refractive index by this method and it is equally suited for nondestructive determination of layer thickness.

$TiO_2$ thin layers have been successfully prepared by a number of deposition processes including both gas phase methods (PVD and CVD) and liquid phase ones (dip-, spin- or spray-coating, doctor blade spreading, roller coating *etc.*). Generally, the wet coating techniques constitute a simpler alternative to the vacuum processes requiring sophisticated instrumentation and are therefore favored for large-scale manufacturing. Obviously, a suitable liquid precursor formulations need to be developed for these wet-coating techniques. The sol-gel approach proved to be well suited for this purpose and its advantages and benefits were demonstrated repeatedly [6–12]. The process usually starts with soluble titanium salts and/or titanium alkoxides which are complexed by suitable chelates, pre-crosslinked by partial hydrolysis and the resulting metastable colloidal sols are then coated onto substrate, gelled and converted into dense or porous oxide layer. Thermal calcination is the most common way to achieve this conversion but low temperature alternatives are available as well [13].

However, recently the traditional wet-coating methods have been replaced to a great extent by modified printing techniques [14]. Of these, inkjet material deposition seems to be especially promising [15]. The technique shares basic principles with conventional inkjet printing, *i.e.*, tiny droplets of a low-viscosity liquid are precisely deposited onto a substrate by means of thermal or piezoelectric printhead. In the case of material printing, the ink is a specially formulated low-viscosity liquid used for transporting a functional component onto the substrate surface. Material printing has been successfully used to deliver a wide variety of functional materials and to form thin films, fine 2D patterns and even 3D structures [16].

The authors of this paper have previously reported the deposition of sols based on reverse micelle templates [17] by inkjet printing. The resulting titania patterns showed interesting sensing properties [18] as well as photocatalytic activity [19] and the material inkjet printing approach was found extremely useful due to its precision, repeatability, inherent patterning capability and efficiency of material consumption. In this paper, we present the results of a further study of reverse-micelles-inkjeted titania focused on the optical properties of these layers.

## 2. Results and Discussion

Reverse micelles sol-gel formulation was successfully printed by a Dimatix 2831 printer (Fujifilm Dimatix Inc., Santa Clara, CA, USA) as a simple rectangular pattern 10 mm × 10 mm on glass. The printing process was repeated up to five times to get different thicknesses of the resulting $TiO_2$ layers, producing a 5-patch series for each studied calcination temperature. The resulting layers we can observe by optical microscope and by profilometry are smooth, shiny, clear and transparent, with a strong color tint that is the result of light interference. Inkjet printing proved to be an elegant method for sol delivery to a substrate. It provides a complete control of the deposition process parameters together with an excellent efficiency of precursor use. Moreover, the possibility of precise patterning and the ease of up-scaling make this type of deposition very appealing for the production of photonic devices such as sensors, solar electrochemical cells, patterned coatings, *etc.* [20–25].

Figure 1 shows the visual characteritics of prepared samples as seen in the optical microscope with a 4× magnifying lens. We can observe visually homogeneous surface of B–E series, free of cracks and only rarely spoiled by dust particles.

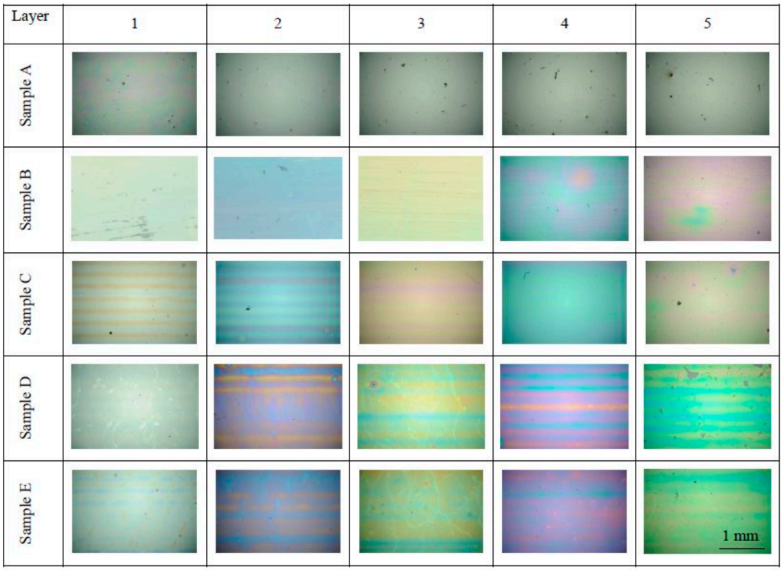


**Figure 1.** The layer surface as seen by optical microscopy. The matrix shows all the studied samples arranged according to the temperature of processing (rows, sample sets A–E) and according to the number of printed layers (columns, 1–5 layers). At this magnification, the field of view of each photo corresponds to the area 3137 μm × 2083 μm.

On some samples, slight banding artifact pattern has developed as the result imperfect band merging during the printing process. However, the A sample series visual appearance is much different, with only

traces of interference coloring present at the single layer sample and being apparently much thicker than the corresponding patches from other sample series.

We conclude the 200 °C calcination temperature is not sufficient for complete mineralization of the sol and $TiO_2$ crystallization therefore this series was omitted from further ellipsometric study (see further discussion of XRD patterns and Table 1 summarizing thickness data for confirmation). Figure 2 shows the SEM and AFM records of the surface layer clearly depicting the micellar template imprints manifested as the globular surface structure known from previous studies of this type of titania layers [26].

**Table 1.** Thickness of prepared samples as determined by ellipsometry.

| Samples | A (200 °C) | B (300 °C) | C (400 °C) | D (500 °C) | E (600 °C) |
|---|---|---|---|---|---|
| Layers | Thickness (nm) | | | | |
| 1 | 465.3 | 89.4 | 97.9 | 63.7 | 56.3 |
| 2 | 918.3 | 161.9 | 185.6 | 150.5 | 148.1 |
| 3 | 1607.1 | 251.2 | 261.2 | 230.2 | 229.9 |
| 4 | 2296.5 | 318.5 | 331.6 | 294.8 | 298.3 |
| 5 | 2670.7 | 408.7 | 384.1 | 353.2 | 357.4 |

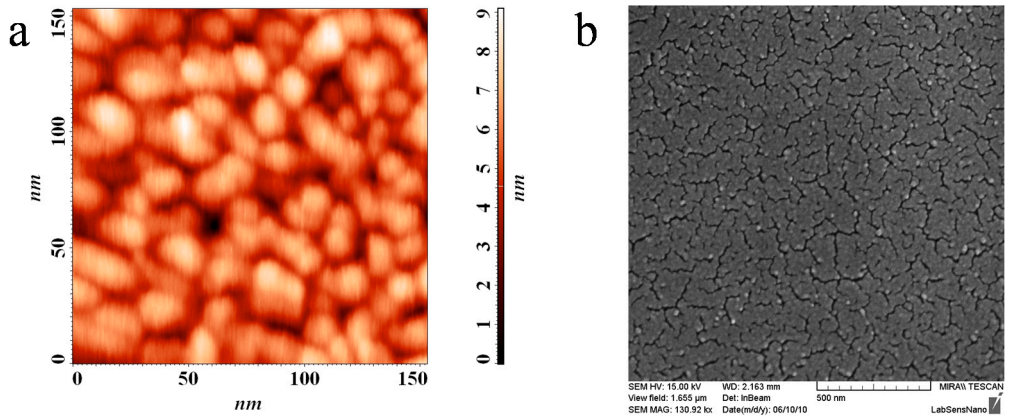


**Figure 2.** AFM (**a**) and SEM (**b**) scans of the printed layer surface.

Figure 3 depicts the recorded ellipsometric data expressed in terms of complex refractive index. We can observe the undulating patterns which represent interference and different thicknesses.

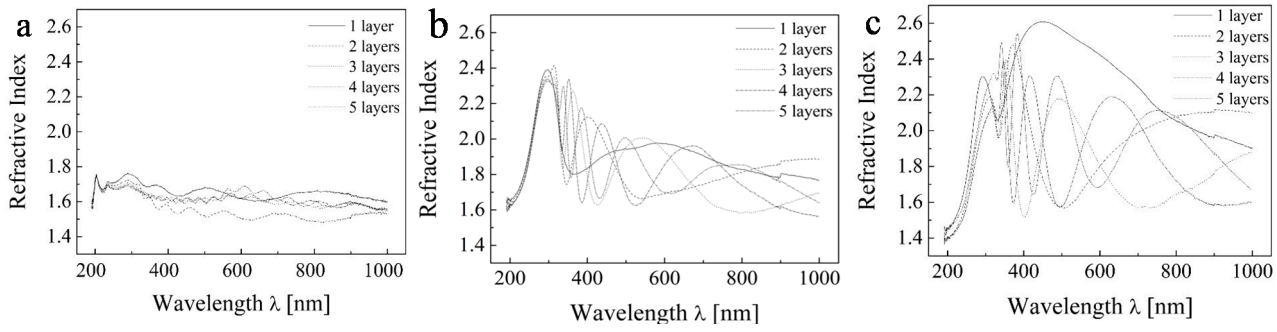


**Figure 3.** Ellipsometric experimental data of $TiO_2$ for the range 200–1000 nm for (**a**) sample A; (**b**) sample C; and (**c**) sample E.

We used Raman spectroscopy to detect the crystalline structure (Figure 4, Table 2) of prepared thin films. Our spectrum confirmed the presence of anatase phase. The anatase phase exhibits major peaks at about 635, 514, 396 and 144 $cm^{-1}$.

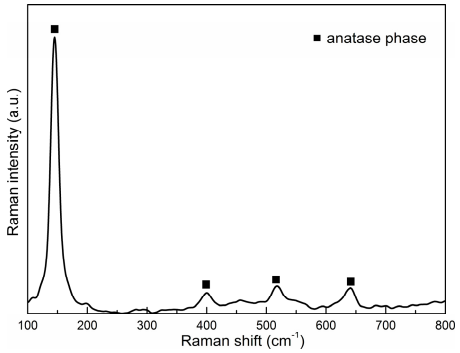


**Figure 4.** Raman spectra.

**Table 2.** Characteristic of the studied $TiO_2$ thin layers prepared by sol-gel method.

| Sample | Temperature (°C) | Supposed Crystal Phase by Raman Spectroscopy |
|---|---|---|
| A | 200 | incomplete mineralization and/or crystallization |
| B | 300 | amorphous |
| C | 400 | Anatase |
| D | 500 | Anatase |
| E | 600 | Anatase |

Figure 5 shows obtained X-ray diffraction (XRD) spectra for to study the crystallinity of the films that as the annealing temperature increases the intensity and linewidth of the (101) diffraction peak. All the diffraction peaks of $TiO_2$ can be indexes as anatas (Anatase XRD JCPDS card no. 78-2486). As expected, with increasing calcination temperature the crystatalinity improves which is manifested by more prominent diffraction peaks of samples calcined at higher temperatures.

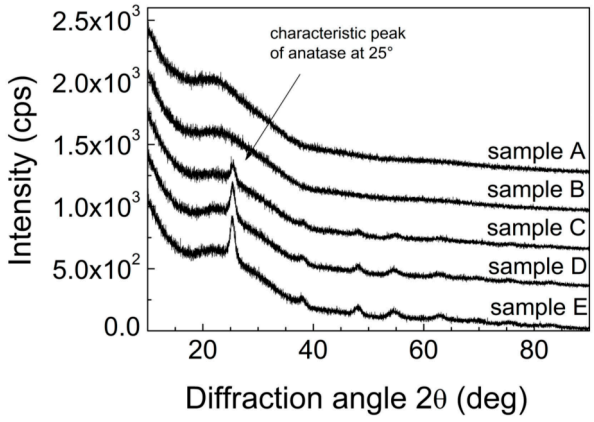


**Figure 5.** XRD patterns for samples A–E.

*2.1. Simplest Model of Studied Sample*

Initially, the ellipsometric spectra were analyzed on the basis of the simplest dispersion model consisting of glass/$TiO_2$ layers (Figure 6). As is evident from Figure 7, there are considerable variations

between the published results for $TiO_2$ optical constants and the results which were obtained using the simple model. For example, the previously reported values of *n* (633 nm) was observed to be in the range of 2.43–2.50 for single anatase crystals obtained by the deposition on the substrate heated to 250 °C [27].

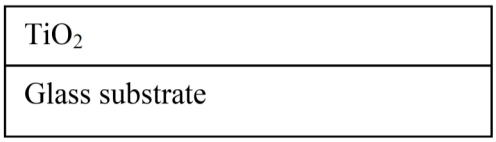


**Figure 6.** A schematic outline of the used ellipsometric model.

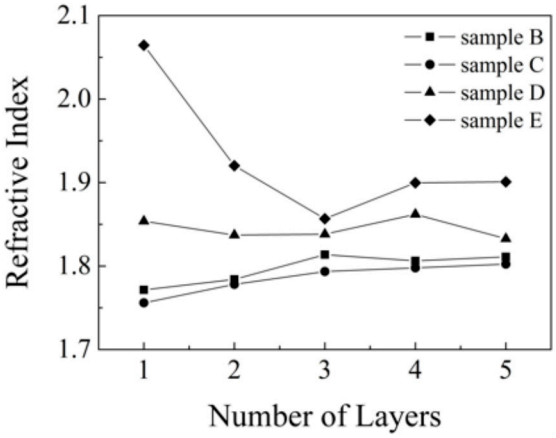


**Figure 7.** Refractive index on studied samples each of layers at 590 nm wavelength after fitting.

However, the computed thickness values of the layers obtained by fitting this simple model agree with the results obtained using a mechanical profilometer fairly well, with the exception of the thickest sample, where a deviation of 23% was observed. The results of both methods for all samples analyzed (layers 1–5) are given in Tables 1 and 3.

**Table 3.** Thickness of prepared samples as determined by mechanical profilometer.

| Sample | A (200 °C) | B (300 °C) | C (400 °C) | D (500 °C) | E (600 °C) |
|---|---|---|---|---|---|
| Layer | Thickness (nm) | | | | |
| 1 | 288.9 | 63.3 | 80.0 | 96.0 | 77.9 |
| 2 | 542.2 | 145.8 | 153.4 | 156.5 | 159.1 |
| 3 | 894.1 | 196.7 | 227.5 | 223.8 | 216.0 |
| 4 | 1025.6 | 305.8 | 307.1 | 273.1 | 295.3 |
| 5 | 1752.0 | 331.0 | 390.7 | 389.4 | 370.6 |

### *2.2. Complex Model of Studied Samples*

Since crystalline anatase phase was previously proved to be present in the layers calcined at 400–500 °C [18], but the value the calculated refractive index is not in agreement with optical parameters for $TiO_2$, we need to adopts a more complex model for experimental data fitting (Figure 8). This model was suggested on the basis of studying the images from electron and AFM microscopy, where the surface topology clearly manifesting the globular surface structure resulting from the micellar templating became

obvious. This new model consist of two layers: the bottom one consists of the compact $TiO_2$ inherited from the simple model and a top surface layer consisting of pure $TiO_2$ mixed with variable void fraction.

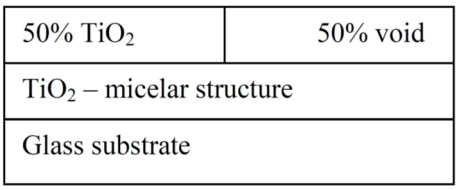


**Figure 8.** Used ellipsometric model which involves a layer with an additional void.

Within this model we investigated two variables: the ratio of thicknesses of the two layers and also the ratio of $TiO_2$ and void in the upper layer. First, we studied the fraction effect of the void in the upper layer. For these calculations we finally assumed that 90% of the total thickness is represented by nonporous $TiO_2$ and 10% builds up the surface voided layer (the explanation of selecting this particular thickness ratio follows in the paragraph below). We confirmed the expected fact that the void fraction value greatly influences the dispersion dependence of the refractive index on the wavelength. Obviously, with increasing void fraction the global index of refraction of the whole layer system is decreasing. However, if we attempt to substitute a solid layer by a composite one consisting of a solid material and a certain fraction of void, then with increasing void fraction the refractive index of the complementary solid fraction must increase as well in order to keep the global refractive index constant. This situation is modeled at Figure 9. Based on this modeling, we adopted the 50% void fraction as a reasonable starting point.

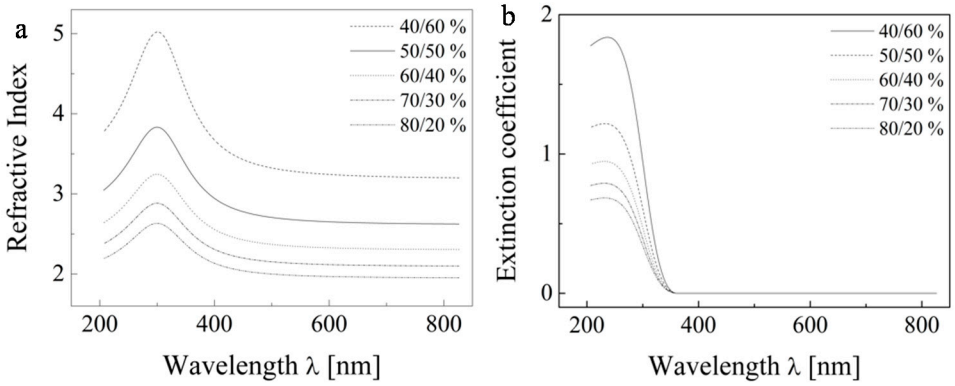


**Figure 9.** The dispersion dependence of the refractive index (**a**) and extinction coefficient (**b**) of the pure $TiO_2$ solid fraction only.

Subsequently, we attempted a further tuning of the ellipsometric model by optimizing the second variable, *i.e.* the thickness ratio of the two layers. The results are presented at Figure 10 for sample B (one layer) and the ratio of $TiO_2$/void in the upper layer is set to 50/50% by the previous analysis. The figure shows that the ratios of thicknesses of layers have much smaller role. Nevertheless, the ratio 90/10% was selected because it provided the best match to refractive index values reported for $TiO_2$ at 590 nm.

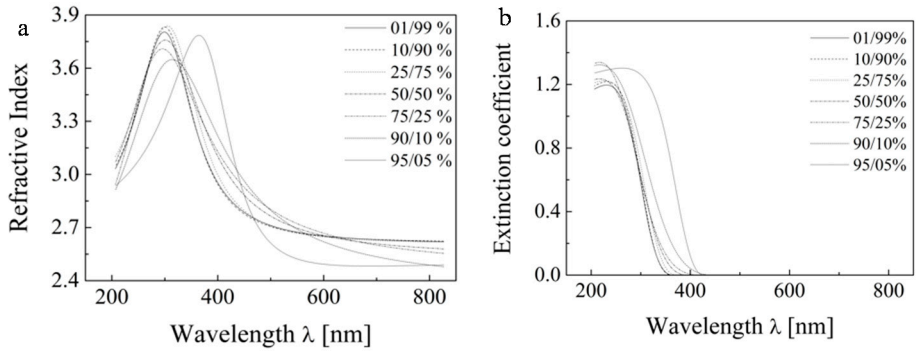


**Figure 10.** The dispersion dependence of the printed samples for various thickness ratios of the two sublayers of the refractive index (**a**) and extinction coefficient (**b**).

Once the thickness ratio 90/10 was selected, this ellipsometric model was applied to all studied samples. These results are depicted in Figure 11 and Table 4.

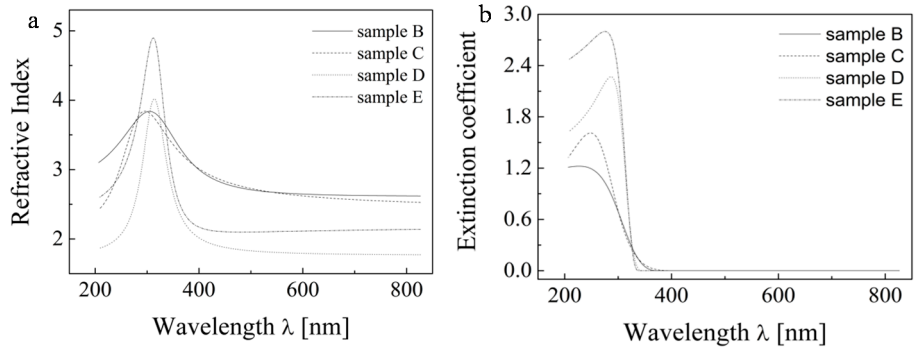


**Figure 11.** The final computed refractive index (**a**) and extinction coefficient (**b**) values for studied samples on their first layer.

**Table 4.** Properties refractive index of prepared materials $TiO_2$ by sol-gel method at 590 nm wavelength.

| Samples | B (300 °C) | C (400 °C) | D (500 °C) | E (600 °C) |
|---|---|---|---|---|
| Layers | Refractive Index | | | |
| 1 | 2.650 | 2.628 | 1.794 | 2.112 |
| 2 | 2.690 | 2.705 | 2.422 | 2.578 |
| 3 | 2.768 | 2.717 | 2.809 | 2.618 |
| 4 | 2.803 | 2.764 | 2.817 | 2.779 |
| 5 | 2.792 | 2.811 | 2.768 | 2.914 |

We can see that the refractive index value is in the range of 2.6 to 2.9 for most of our samples, which matches well the reported values. For the sample series calcined at lower temperatures (B, C) we can note slight increase of refractive index values with increasing layer thickness, probably due to better crystallite development in the thicker samples. However, an anomalous decrease of the refractive index value with decreasing layer thickness can be observed in the case of the more heated sample series D and E. We expect that during calcination at elevated temperatures in the proximity of glass softening temperature, a significant material diffusive mixing takes place, this phenomenon has been observed

earlier [28] and is known to have a detrimental effect on the photocatalytic performance of titania layers resulting from sodium ions diffusion into titania lattice. It seems that the thinner one- and two-layered samples suffer the most due to the contaminant diffusion path length being comparable to the total layer thickness, while the thicker samples are less sensitive because only a fraction of their thickness is contaminated. Moreover, the negative effect of diffusing contaminants can be eliminated by improved crystallization in the thicker samples.

Obviously, sodium diffusion can be eliminated by using another substrate such as quartz or silicon. Titania coating deposited onto these substrates can be processed at much higher temperatures which would open the pathway to ellipsometric investigation of phase change from anatase to rutile. However, working with different substrates would require the modification of our ellipsometric models and would go far beyond the scope of this paper.

## 3. Experimental Section

Nanostructured micellarly templated $TiO_2$ layers were prepared by inkjet printing of our previously optimized [18] sol onto soda-lime glass plates (25 mm × 75 mm) usually used for microscopy. Sol deposition and patterning was performed with a dedicated Fujifilm Dimatix 2831 material inkjet printer. The drop formation characteristics were monitored by means of the built-in stroboscopic camera and the interaction with substrate was inspected by an optical microscope. Optimal printing conditions were defined in the previous studies: Dimatix Model fluid 2 waveform, 20 V driving voltage, nozzle temperature 30 °C, substrate temperature 40 °C, and nozzle span was kept constant 20 μm.

The annealing temperatures after deposition are summarized in Table 2. Printing was repeated several times in a wet-to-wet manner. Step-wedge like samples were fabricated by repeated overprinting onto a single 26 mm × 76 mm glass slide. They consisted of five square patches 10 mm × 10 mm with gradually increasing number of layers. This study started with five parallel samples series denoted as A, B, C, D, and E, all printed in exactly the same way. However, they were calcined at different temperatures (see Table 2) and the duration of the thermal treatment was 4 h. Raman spectroscopy was employed for the determination of crystal phase of the studied samples.

Microphotographs were recorded using Nikon Eclipse E200 optical microscope equipped with a Nikon D5000 digital camera and Nikon Camera Control Pro 2 software (Nikon, Tokyo, Japan). Polarised light was used to enhance the interference-originating color of the printed layers. Captured raw images were conveniently cropped, color balanced and organized by Adobe Lightroom. Scanning electronic microscopy was performed on the MIRA II LMU (Tescan, Warrendale, PA, USA) and AFM analysis was done on the Ntegra Prima by NT-MDT (Santa Clara, CA, USA). Physical thickness of the layers was determined by a Dektak XT mechanical profilometer (Bruker, Tucson, AZ, USA).

A UVISEL 2 spectroscopic ellipsometer [27] by Jobin-Yvon (Palaiseau, France) was used for recording the wavelength dependency of the principal ellipsometric quantities $\psi$ and $\Delta$ at the angle of 70°. The setup of the phase modulated ellipsometer is as follows: xenon source (spectral range 1.5–5.5 eV) polarizer/modulator/sample/analyzer/monochromator and detector (photomultiplier). The experimental ellipsometric angles $\psi$ and $\Delta$ are a measure of the polarization change of the incident light wave as it is reflected at the different interfaces in the film profile. In order to determine the optical constants, the film thickness and the surface roughness, a model film structure has to be established. In this simple

single layer case, the model consists of a glass substrate and a dense $TiO_2$ layer. Optional 50% $TiO_2$:50% void surface layer, which simulates the surface roughness, may be added to improve the accuracy of modelling and the New Amorphous model was used for this purpose. It's based on Forouhi-Bloomer formulation. The absorption coefficient is given by Equation (1) and refractive index given by Equation (2):

$$k(\omega) = \begin{cases} \dfrac{f_j(\omega-\omega_g)^2}{(\omega-\omega_j)^2+\Gamma_j^2} & ;\text{for } \omega > \omega_g \\ 0 & ;\text{for } \omega \le \omega_g \end{cases} \quad (1)$$

where is $\omega_j = (E_{\sigma*} - E_\sigma)/\hbar$ difference the basic frequency and the excited state, $\Gamma_j = \gamma/2$ is the broadening term of the peak absorption and coefficient $f_j = A$ is proportional to the strength of the oscillator:

$$n(\omega) = n_\infty + \frac{B_j(\omega-\omega_j)+C_j}{(\omega-\omega_j)^2+\Gamma_j^2} \quad (2)$$

where $B_j = \dfrac{f_j}{\Gamma_j}\left[\Gamma_j^2 - (\omega_j-\omega_g)^2\right]$ and $C_j = 2 f_j \Gamma_j (\omega_j - \omega_g)$ are coefficients. Where $n_\infty$ is refractive index for $\omega \to \infty$, $\omega_j$ is the energy at which the extinction coefficient is maximum (peak of absorption), $f_j$ is related to the strength of the extinction coefficient peak, $\omega_g$ is the energy band gap and $\Gamma_j$ is the broadening term of the peak of absorption. Recorded spectra in combination with different ellipsometric models were processed in the DeltaPsi software package (HORIBA Scientific Systems, Longjumeau Cedex, France) and a complete optical characterization was attempted.

Since both the printed $TiO_2$ layers and the glass substrates are transparent, it is important to suppress the backside reflections [29] from transparent glass substrates. These unwanted backside reflections must be accounted for in the fit model or suppressed by experimental arrangement. A common technique used to eliminate backside reflections is to focus the probing beam onto an area small enough to permit the separation of the front and the back reflection. Alternatively, the reflections can be suppressed by modifying the reverse side of substrate opposite the measurement spot. This can be accomplished by mechanical grinding using a fine sandpaper or, as in our case, painting the reverse side by black marker.

## 4. Conclusions

The paper presents the results of a comprehensive study on the optical properties of $TiO_2$ layers consisting of micellarly templated $TiO_2$ fabricated by material printing. We studied the influence of the ratio of thicknesses of the both layers and void fraction effects on the optical properties of the layer forming material. We demonstrate that the influence of voids on the properties of the layer is substantial—at 50% void fraction the refractive index of the complementary fraction increased 1.8 times (from 1.7 to 2.4 for a wavelength of 590 nm). On the other hand, the influence of the ratio of thicknesses of the upper and lower layers was not so critical. Nevertheless, the ratio 90%/10% was selected because it provided the best match to refractive index values reported for $TiO_2$ at 590 nm. After the incorporation of these two variables into the ellipsometric model, a reasonably good agreement between calculated and tabulated values of the refractive index was obtained.

**Acknowledgments**

This work was supported by the projects from the Ministry of Industry and Trade of the Czech Republic (Grant FR-TI1/144), project from the Technology Agency of the CR (Grant TA03010548) and from "Centre for Materials Research at FCH BUT" No. CZ.1.05/2.1.00/01.0012 supported by ERDF.

**Author Contributions**

V.S. performed the ellipsometric measurements, participated on the fitting of measured data to ellipsometric models suggested by O.Z., wrote the manuscript and prepared the figures. P.D. fabricated and processed the studied sample set and co-authored on the manuscript writing while M.V. managed the reverse-micelles ink development and printing optimization. M.M. was responsible for the early development of the original spin-coated formulations and later participated with P.D. on their modification for inkjet printing. P.K. is the author of the reverse micelles sol-gel concept and in later stages contributed to the discussion section of the manuscript.

**Conflicts of Interest**

The authors declare no conflict of interest.

**References**

1. Sharma, S.K.; Vishwas, M.; Rao, K.N.; Mohan, S.; Reddy, D.S.; Gowda, K.V.A. Structural and optical investigations of $TiO_2$ films deposited on transparent substrates by sol-gel technique. *J. Alloys Compd.* **2009**, *471*, 244–247.
2. Ben Naceur, J.; Mechiakh, R.; Bousbih, F.; Chtourou, R. Influences of the iron ion ($Fe^{3+}$)-doping on structural and optical properties of nanocrystalline $TiO_2$ thin films prepared by sol-gel spin coating. *Appl. Surf. Sci.* **2011**, *257*, 10699–10703.
3. Viseu, T.M.R.; Almeida, B.; Stchakovsky, M.; Drevillon, B.; Ferreira, M.I.C.; Sousa, J.B. Optical characterisation of anatase: A comparative study of the bulk crystal and the polycrystalline thin film. *Thin Solid Films* **2001**, *401*, 216–224.
4. Li, S.; Qiu, J.; Ling, M.; Peng, F.; Wood, B.; Zhang, S. Photoelectrochemical characterization of hydrogenated $TiO_2$ nanotubes as photoanodes for sensing applications: From uniform ink-droplet to $TiO_2$ photoelectrode for dye-sensitized solar cells. *ACS Appl. Mater.* **2013**, *5*, 11129–11135.
5. Alvarez-Herrero, A.; Fort, A.J.; Guerrero, H.; Bernabeu, E. Ellipsometric characterization and influence of relative humidity on $TiO_2$ layers optical properties. *Thin Solid Films* **1999**, *349*, 212–219.
6. Attia, S.M.; Wang, J.; Wu, G.M.; Shen, J. ; Ma, J.H. Review on sol-gel derived coatings: Process, techniques and optical applications. *J. Mater. Sci. Technol.* **2002**, *18*, 211–218.
7. Akpan, U.G.; Hameed, B.H. The advancements in sol-gel method of doped-$TiO_2$ photocatalysts. *Appl. Catal. A Gen.* **2010**, *375*, 1–11.
8. Arconada, N.; Duran, A.; Suarez, S.; Portela, R.; Coronado, J.M.; Sanchez, B.; Castro, Y. Synthesis and photocatalytic properties of dense and porous $TiO_2$-anatase thin films prepared by sol-gel. *Appl. Catal. B Environ.* **2009**, *86*, 1–7.

9. Kluson, P.; Kacer, P. Preliminary specification of the structure of photoactive $TiO_2$ by the surfactant-mediated sol-gel method. *Chem. Listy* **2000**, *94*, 432–436.
10. Macwan, D.P.; Dave, P.N.; Chaturvedi, S. A review on nano-$TiO_2$ sol-gel type syntheses and its applications. *J. Mater. Sci.* **2011**, *46*, 3669–3686.
11. Mechiakh, R.; Ben Sedrine, N.; Chtourou, R.; Bensaha, R. Correlation between microstructure and optical properties of nano-crystalline $TiO_2$ thin films prepared by sol-gel dip coating. *Appl. Surf. Sci.* **2010**, *257*, 670–676.
12. Yokosuka, Y.; Oki, K.; Nishikiori, H.; Tatsumi, Y.; Tanaka, N.; Fujii, T. Photocatalytic degradation of trichloroethylene using N-doped $TiO_2$ prepared by a simple sol-gel process. *Res. Chem. Intermed.* **2009**, *35*, 43–53.
13. Bartkova, H.; Kluson, P.; Bartek, L.; Drobek, M.; Cajthaml, T.; Krysa, J. Photoelectrochemical and photocatalytic properties of titanium (IV) oxide nanoparticulate layers. *Thin Solid Films* **2007**, *515*, 8455–8460.
14. Krebs, F.C. Fabrication and processing of polymer solar cells: A review of printing and coating techniques. *Sol. Energy Mater. Sol. Cells* **2009**, *93*, 394–412.
15. Heinzl, J.; Hertz, C.H. Ink-jet printing. *Adv. Imaging Electron Phys.* **1985**, *65*, 91–171.
16. Calvert, P. Inkjet printing for materials and devices. *Chem. Mater.* **2001**, *13*, 3299–3305.
17. Morozova, M.; Kluson, P.; Dzik, P.; Vesely, M.; Baudys, M.; Krysa, J.; Solcova, O.; The influence of various deposition techniques on the photoelectrochemical properties of the titanium dioxide thin film. *J. Sol-Gel Sci. Technol.* **2013**, *65*, 452–458.
18. Morozova, M.; Kluson, P.; Krysa, J.; Dzik, P.; Vesely, M.; Solcova, O. Thin $TiO_2$ films prepared by inkjet printing of the reverse micelles sol-gel composition. *Sens. Actuators B* **2011**, *160*, 371–378.
19. Dzik, P.; Morozova, M.; Kluson, P.; Vesely, M. Photocatalytic and self-cleaning properties of titania coatings prepared by inkjet direct patterning of a reverse micelles sol-gel composition. *J. Adv. Oxid. Technol.* **2012**, *15*, 89–97.
20. Dzik, P.; Vesely, M.; Kralova, M.; Neumann-Spallart, M. Ink-jet printed planar electrochemical cells. *Appl. Catal. B Environ.* **2015**, *178*, 186–191.
21. Vidmar, T.; Topic, M.; Dzik, P.; Opara Krasovec, U. Inkjet printing of sol-gel derived tungsten oxide inks. *Sol. Energy Mater. Sol. Cells* **2014**, *125*, 87–95.
22. Cerna, M.; Vesely, M.; Dzik, P.; Guillard, Ch.; Puzenat, E.; Lepicova, M. Fabrication, characterization and photocatalytic activity of $TiO_2$ layers prepared by inkjet printing of stabilized nanocrystalline suspensions. *Appl. Catal. B Environ.* **2013**, *138*, 84–94.
23. Oh, Y.; Yoon, H.G.; Lee, S.N.; Kim, H.K.; Kim, J. Inkjet-printing of $TiO_2$ co-solvent ink: From uniform ink-droplet to $TiO_2$ photoelectrode for dye-sensitized solar cells. *J. Electrochem. Soc.* **2012**, *159*, B34–B38.
24. Bao, B.; Li, M.; Li, Y.; Jiang, J.; Gu, Z.; Zhang, X.; Jiang, L.; Song, Y. Patterning fluorescent quantum dot nanocomposites by reactive inkjet printing. *Small* **2015**, *11*, 1649–1654.
25. Kuang, M.; Wang, J.; Bao, B.; Li, F.; Wang, L.; Jiang, L.; Song, Y. Inkjet printing patterned photonic crystal domes for wide viewing-angle displays by controlling the sliding three phase contact line. *Adv. Opt. Mater.* **2014**, *2*, 34–38.

26. Morozova, M.; Kluson, P.; Krysa, J.; Zlamal, M.; Solcova, O.; Kment, S.; Steck, T. Role of the template molecular structure on the photo-electrochemical functionality of the sol-gel titania thin films. *J. Sol-Gel Sci. Technol.* **2009**, *52*, 398–407.
27. Mardare, D.; Hones, P. Optical dispersion analysis of $TiO_2$ thin films based on variable-angle spectroscopic ellipsometry measurements. *Mater. Sci. Eng. B* **1999**, *68*, 42–47.
28. Cerna, M.; Vesely, M.; Dzik, P. Physical and chemical properties of titanium dioxide printed layers. *Catal. Today* **2011**, *161*, 97–104.
29. Synowicki, R.A. Suppression of backside reflections from transparent substrates. *Phys. Status Solidi C* **2008**, *5*, 1085–1088.

*Sample Availability*: Samples of the compounds are available from the authors.

ACS APPLIED MATERIALS & INTERFACES

Research Article

www.acsami.org

# Properties and Application Perspective of Hybrid Titania-Silica Patterns Fabricated by Inkjet Printing

Petr Dzik,*[,†] Michal Veselý,[†] Marko Kete,[‡] Egon Pavlica,[‡] Urška Lavrenčič Štangar,[‡] and Michael Neumann-Spallart[§]

[†]Faculty of Chemistry, Brno University of Technology, Purkynova 118, 612 00 Brno, Czech Republic

[‡]School of Environmental Sciences, University of Nova Gorica, Vipavska 13, SI-5000 Rožna dolina, Nova Gorica Slovenia

[§]Groupe d'Étude de la Matière Condensée (GEMaC), CNRS/Université de Versailles, 45, avenue des États-Unis, 78035 Versailles CEDEX, France

**ABSTRACT:** A hybrid titania-silica cold-setting sol has been developed that can be deposited onto a wide variety of surfaces without the need for high-temperature fixing and that is suitable for material printing deposition. Thin hybrid titania-silica coatings were patterned onto glass and PET substrates by inkjet printing. Well-defined hybrid titania-silica patterns, with thicknesses ranging from 40 to 400 nm, were fabricated by overprinting 1 to 10 layers. Excellent mechanical, optical, and photocatalytic properties were observed, making the reported material well suited for the fabrication of transparent self-cleaning coatings both on mineral and organic substrates. The printed patterns exhibit photoelectrochemical activity that can be further improved by thermal or photonic curing. A concept of fully printed interdigitated photoelectrochemical cells on flexible PET substrates utilizing the reported hybrid photocatalyst is disclosed as well.

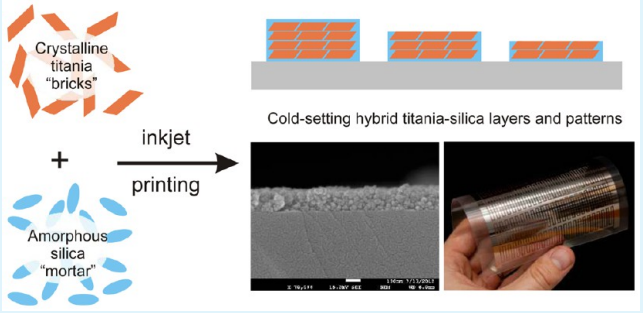


**KEYWORDS:** *photocatalysis, material printing, inkjet printing, direct patterning, titanium dioxide, silica, binder*

## 1. INTRODUCTION

Metal oxide semiconductors, especially titanium dioxide, and their related photocatalytic processes have been the subjects of intensive research for the past four decades. The primary discovery of the photoelectrochemical splitting of water on titanium dioxide electrodes[1] has gradually evolved into a broad technological field of applied photocatalysis. This technology may have the potential to address some of the most urgent technological challenges,[2] especially if solar light is employed as the irradiation source.[3]

Basically, any photocatalytic process is initiated by the photogeneration of electron−hole pairs in a semiconductor crystal lattice, which results from the absorption of UV (or even visible light in the case of a narrow band gap semiconductor) quanta of energy equal to or higher than the corresponding band gap. The electrons and holes can either recombine, dissipating the absorbed energy as heat, or remain separated and available for redox reactions with electron-donor or acceptor species adsorbed at the semiconductor surface or localized in the electrical double layer surrounding the particle.[4]

While photocatalytic processes utilizing the slurried form of a catalyst deliver excellent performances because of their inherently high surface area, a photocatalyst immobilized onto a suitable support is usually the preferred form for practical applications. Upon immobilization, the free surface of the catalyst inevitably decreases, resulting into a loss of catalytic performance because of limited mass transport. Conversely, immobilized systems are not burdened by the need for catalyst recovery, which could otherwise prohibitively increase the operational costs. Both the gas phase deposition and the wet coating method have been successfully adopted for the preparation of immobilized photocatalyst layers.[5]

Titanium dioxide is definitely the most popular and promising material among transition metal semiconductors for photocatalytic applications. $TiO_2$ is both widely commercially available and also easy to prepare by various methods that yield different titania grades. It has been successfully used for the design of many commercial devices that decompose hazardous substances in our living environment based on the strong oxidizing power of its photogenerated holes and its high photostability. So far, we have witnessed the proposal and successful application of photocatalytic phenomena for water purification[6] and disinfection,[7] toxic waste treatment,[8] air purification and deodorizing,[9] and self-cleaning,[10] self-disinfecting,[11] and superhydrophilic antifogging[12] surfaces.

Self-cleaning surfaces generally belong to one of two types of surfaces: hydrophobic or hydrophilic. The main characteristic of hydrophobic surfaces containing specific polymers or waxes is a

Received: October 16, 2014
Accepted: July 7, 2015
Published: July 7, 2015





DOI: 10.1021/acsami.5b03494
ACS Appl. Mater. Interfaces 2015, 7, 16177−16190

very high contact angle between the water droplet and the support (>150°). Consequently, the adhesion of the dirty spherical water droplet to the support is prevented. Another possible approach to prevent the adhesion of water droplets is the use of hydrophilic coatings composed of transition metal oxides, most typically $TiO_2$, as explained above. Such coatings contribute to self-cleaning for two reasons. First, the presence of UV radiation and water molecules induce chemical changes on the surfaces (oxygen vacancies are created and subsequently filled by hydroxyl ions), causing them to become highly hydrophilic with a very low water contact angle (<5°). Such high hydrophilicity enhances the adhesion of water, and the slightly adsorbed inorganic dirt particles are easily washed away by e.g., rainwater. Second, organic debris deposits are photocatalytically destroyed by the photogenerated hole−electron pairs.

Although titania coatings have been fabricated by countless different processes, wet coating techniques constitute a very popular and usually simpler alternative to vacuum processes requiring sophisticated instrumentation. Many different wet coating techniques have been proposed, such as dip-, spin-, or spray-coating, doctor blade, or roller spreading.[13] However, these traditional methods have been recently replaced by modified printing techniques,[14] among which inkjet material deposition seems to be especially promising. The technique shares the basic principles of conventional inkjet printing,[15] i.e., tiny droplets of a low-viscosity liquid are precisely deposited onto a substrate by means of a thermal or a piezoelectric printhead.[16] In the case of material printing, the ink is a specially formulated liquid used for transporting a functional component onto the substrate surface.[17]

However, to perform any of the above-mentioned traditional wet coating processes or novel modified printing techniques, a suitable liquid formulation carrying the functional component (titanium dioxide photocatalyst in this case) needs to be developed. Two distinct approaches to this task can be easily identified:

The first approach is based on the sol−gel process, i.e., soluble titanium salts and/or titanium alkoxides are complexed by suitable chelates, precross-linked by partial hydrolysis, and the resulting metastable colloidal sols are then coated onto a substrate, gelled, and converted into dense or porous oxide layers.[18] Thermal calcination is the most common way to achieve this conversion, but low temperature alternatives are available.[19] Inkjettable titania formulations based on this approach were reported by Arin[20] and Manga.[21] The authors of the present paper have reported the deposition of conventional sol−gel formulations based on tetraisopropoxy titanate and acetyl acetone by a modified office inkjet printer.[22] Thick multilayer coatings were printed with the help of poly(ethylene glycol) acting as a viscosity-modifying, templating, and anticracking agent.[23] Sols based on reverse micelle templates[24] were also successfully adapted for inkjet printing, and the printed patterns showed interesting sensing properties as well as photocatalytic activity.[25]

Much experimental attention has also been paid to explore the second possible approach leading to printed $TiO_2$ films. This alternative route is based on the synthesis of stable colloidal suspensions of nanocrystalline $TiO_2$ followed by the delivery of this suspension onto a substrate by means of inkjet printing. Bernacka-Wojcik and co-workers recently demonstrated[26] a disposable biosensor integrating an inkjet printed photodetector fabricated by printing a commercial dispersion of titania particles with a desktop office printer equipped with a thermal inkjet head. A similar approach was adopted by Yang et al.[27] who used a dispersion of $TiO_2$ printed by a modified office inkjet printer to produce an oxygen demand sensing photoanode and by Arin et al.[28] who fabricated photocatalytically active $TiO_2$ films by inkjet printing of nanoparticle suspensions obtained from microwave-assisted hydrothermal synthesis. The authors of the present paper have recently reported the fabrication of titania patterns by inkjet printing of rutile nanodispersions originating from hydrothermal processes.[29]

The obvious issue inherently associated with this second approach is the adhesion of the deposited material to the substrate. The aggregated nanoparticles left after solvent evaporation only have very limited adhesion to the substrate and need to be fixed in some way. The above-referenced examples employed the most common solution to this problem, i.e., heat treatment at 300−500 °C. However, more sophisticated solutions have been reported. Cold-setting processes yielding stable titania layers are very attractive for the fabrication of photoelectrochemical functional or auxiliary coatings on the surface of heat-sensitive substrates. This is especially true in the case of dye-sensitized solar cells, where the adoption of cheap flexible polymer supports is considered a necessary condition for commercial success. A great deal of attention has therefore been paid to this problem, and several interesting processes have been reported so far. The key lies in the mechanisms of titania layer building, and the processes to address the above-mentioned necessary condition included e.g., UV-curing of a titanium alkoxide binder,[30] incorporation of a mineral binder such as amorphous silica,[31] atomic layer deposition over a mesoporous template,[32] low temperature CVD fed a with custom molecular precursor,[33] titanium alkoxide decomposition in supercritical carbon dioxide,[34] or cold isostatic pressing of standard P-25 grade titania.[35]

In this paper, we communicate our development of a hybrid titania-silica cold-setting sol that can be deposited onto a wide variety of surfaces without the need for high-temperature fixing and that is suitable for material printing. We employed a low-temperature modification of the so-called brick-and-mortar strategy[36] based on mixing prefabricated nanocrystalline titania "bricks" with "mortar" consisting of an amorphous silica binder.

The synthetic route of the "bricks", i.e., the photocatalytically active component, was inspired by Yun et al.[37] who prepared a sol starting from titanium tetraisopropoxide in acidic aqueous solution and kept it for several hours under reflux to induce the crystallization of the amorphous $TiO_2$ already present in the primary reaction mixture. The "mortar" consisting of amorphous $SiO_2$ is capable of enhancing both the mechanical and physicochemical properties of the coatings. Apart from acting as the binding agent,[31] colloidal silica can improve adhesion,[38] increase the natural hydrophilicity of the material,[39] promote the adsorption of reactants,[40] and influence the thermal stability.[41]

The original titania-silica stock dispersion[42] was further modified by the addition of a suitable solvent system, and thus, a stable inkjettable formulation was developed. Thin hybrid titania-silica coatings were patterned onto glass and PET substrates by inkjet printing, and their material characteristics were closely investigated. A detailed report of the material properties of the resulting coatings, a brief evidence of their photocatalytic activity, and an envisaged proof of concept application are disclosed in this paper.

## 2. EXPERIMENTAL SECTION

**2.1. Chemicals and Substrates.** The chemicals in this study were used as purchased: terephthalic acid (TPA) from Alfa Aesar, NaOH


DOI: 10.1021/acsami.5b03494
ACS Appl. Mater. Interfaces 2015, 7, 16177−16190

from Sigma-Aldrich, titanium(IV) tetraisopropoxide (TTIP) and hydroxyethyl-cellulose (HEC) from Fluka (Product Nr.: 54290), tetraethoxysilane from J.T. Baker, acetonitrile from Fischer Scientific, 96% ethanol from Itrij, Levasil 200/30% colloidal $SiO_2$ from H.C. Starck, propane-2-ol and ethylene glycol from Penta, and propoxyethanol from Sigma-Aldrich. All aqueous solutions were prepared by using highly pure water from the NANOpure system (Barnstead).

Soda-lime glass plates were used as substrates (microscope slides 26 mm × 76 mm, Paul Marienfeld, Germany and custom cut 50 × 50 mm, Merci, Czech Republic). Commercial 2 mm-thick FTO-coated glass (Sigma-Aldrich) cut in 25 × 45 mm slides was used for the fabrication of samples for photoelectrochemical analysis. These slides were scratched parallel to the longer edge with a diamond knife, and two isolated FTO strips were thus created on a single substrate. Substrates of both types were sonicated in Neodisher LM alkaline detergent, rinsed with isopropyl alcohol, and dried in a flow of nitrogen.

**2.2. Sol Synthesis.** The preparation procedure of the titania/silica sol is described in detail in the patent application.[42] Herein, a short description is given: in a round-bottom flask, absolute ethanol (6.78 mL) was mixed with TTIP (41.67 mL). Separately, 2.778 mL of perchloric acid (70%) was added to 250 mL of double deionized water. This acidified water was then added dropwise to the mixture of absolute ethanol and TTIP under stirring. Then, the reflux was started, and after 48 h, a stable sol, denoted sol A, was obtained. Separately, TEOS (1.11 mL) and Levasil 200/30% (1.7 mL) were mixed in a beaker, HCl (32%, 30 $\mu$L) was added under stirring, and finally, 1-propanol (5 mL) was added to produce the silica binder solution. The final sol used in this study was prepared by mixing sol A with the $SiO_2$ binder. The molar ratio of $TiO_2$ and $SiO_2$ was set to 1:1 according to the results of previous testing. This particular ratio was denoted 1A, and the corresponding solution was stored as a stock material for the subsequent study described in this paper.

The stock sol 1A was further used for the formulation of a stable "ink" suitable for deposition by piezoelectric inkjet printing. A mixed diluent (MD) was prepared by mixing 25 mL of isopropyl alcohol, 25 mL of propoxyethanol, and 2 mL of ethylene glycol. The stock sol 1A was diluted with variable amounts of the mixed diluent, and a series of printing formulation candidates was prepared and denoted 1B, 1C, 1D, and 1E (see the Results and Discussion section for dilution details). The viscosities, densities, and surface tensions of the resulting formulations were measured by an automatic viscosimeter AVMn (Anton Paar), a density meter DMA4500 (Anton Paar), and a rheometer AR-G2 (TA Instruments), respectively. Preliminary printing tests were performed with all these candidates.

**2.3. Optimization of the Ink and Printing Conditions.** Jettability and patterning tests were performed with an experimental Fujifilm Dimatix 2831 inkjet printer. The prepared printing formulation candidates were sonicated for 5 min and then loaded into a syringe. A 0.45-$\mu$m membrane filter (Pall Corporation, USA) and a blunt needle were attached to the syringe luer port. The printing formulation was filtered and filled into the Dimatix ink tank. A Dimatix 10-pL printing head was attached to the tank and mounted onto the Dimatix printer. At the beginning of the preliminary testing period, the optimal printing conditions were determined: Dimatix Model fluid 2 waveform, 20 V driving voltage, a nozzle temperature of 30 °C, and a substrate temperature of 40 °C. The nozzle span was set to 40 $\mu$m (i.e., 25 drops per mm, 625 drops per $mm^2$). The drop formation characteristics of all the candidates were studied by means of a built-in stroboscopic camera, and the interaction of the printed material with the substrate was observed with an optical microscope. The printing settings were kept constant during the evaluation of the printing performance of all the candidate formulations. The printing performance of all the candidates was evaluated at this stage, and the best performing formulation was selected for the subsequent studies (formulation 1C, see below the Results section).

**2.4. Sample Fabrication.** The best performing ink formulation was subsequently used for the fabrication of a series of thin hybrid titania-silica film samples of variable thicknesses. Simple square 20 × 20 mm and 40 mm × 40 mm patterns were printed onto the microscopic and custom-cut glass substrates, respectively. Printing was repeated up to four times to obtain different overall thicknesses of titania-silica layers. Each layer was completely dried after printing so that the following layer was printed in the "wet-to-dry" manner. The deposition process was finalized by drying at 110 °C for 30 min to remove the high-boiling point components of the printing composition.

A 1 × 1 cm square patch was printed on one of the FTO strips created by scratching the FTO slides, thus forming the working photoanode, while the second strip remained naked for use as the counter electrode. Photoelectrodes of various thicknesses, with the thickest consisting of ten overprinted layers, were fabricated.

**2.5. Sample Analysis.** Microphotographs of the printed layers were recorded using a Nikon Eclipse E200 optical microscope equipped with a Nikon D5000 digital camera used with the Nikon Camera Control Pro 2 software. SEM imaging and elemental analysis were performed on a JEOL JSM-7600F scanning electron microscope. The same machine was used for layer thickness estimation by observation of the sample cross sections. The phase composition and crystallinity of the films and powder samples were studied with Panalytical Empyrean and Siemens D5000 X-ray diffractometers. Powder samples were prepared by drying 20 mL of the stock sol 1A and crushing the resulting flakes to fine powder in a quartz mortar.

The film topography was investigated by AFM with a Veeco CP-II instrument operating in the noncontact mode. The probe tip radius was estimated from the minimum feature size to be of approximately 50 nm. The micrographs of different samples were acquired at approximately the same position at the center of the layer, thereby avoiding any possible border effects. At approximately the same position, we scratched the $TiO_2$ layer with a sharp inox needle. The scratch did not damage the surface of the bottom substrate but enabled the determination of the thickness of the $TiO_2$ layer. The film topography was characterized by the mean square root of the deviation of the heights from the average height ($\sigma$), which is known as the RMS roughness.

The layer thickness was further confirmed by spectroscopic ellipsometric measurements using a Horiba UVISEL spectroscopic ellipsometer in the 200−800 nm range. The optical properties of the printed layers were further characterized by measuring the total transmittance spectra using an Agilent Cary 100 UV−vis spectrophotometer equipped with an integrating sphere. Diffused reflectance spectra were recorded using an Ocean Optics Redtide UV−vis spectrometer, a PX-2 xenon light source and related to a Labsphere Spectralon (r) diffuse reflectance standard. The band gap energy was estimated from Tauc plots[43] based on the Kubelka−Munk function of the reflectance data of bulk powder samples for the XRD analysis.

The hardness of the prepared titania films was studied by the "pencil hardness test" according to the ISO 15184 standard.[44] The pencils used as a measure of the relative hardness exhibit 17 distinct degrees of hardness, ranging from the hardest 9H grade to the softest 9B grade. The hardness of the layer is the same as the hardness of the pencil that does not cause any defect on its surface. Despite being only a relative measure, this method enjoys a general acceptance in the coating industry,[45] and many commercial devices performing this test in manual or semi-automatic ways are available. On the other hand, only smooth surfaces can be measured, and this method is destructive. The scratched coatings were imaged with a Nikon Eclipse E200 optical microscope equipped with a Nikon D5000 digital camera.

Photoelectrochemical characterization was performed at room temperature using a two-electrode setup with the 1 $cm^2$ titania-silica patch on FTO as the working electrode and the opposite naked FTO strip as the counter electrode. This setup was fitted into a 3 cm light path fluorescence cell, and the measurement was performed with a single source measurement unit. The cell was filled with 0.1 M phosphate buffer (pH = 7) and fitted onto an optical bench equipped with a mercury vapor medium pressure lamp and a narrow bandwidth interference filter centered at 365 nm. The lamp emission was monitored with a Gigahertz Optic X97 Irradiance Meter with a UV-3701 probe, and the irradiance was set to 3 mW/$cm^2$ by adjusting the aperture of the lamp. Photocurrent measurements were performed with an electrometer driven by the National Instruments LabVIEW platform and by supplying a linear voltage gradient of 10 mV $s^{-1}$ from −0.5 to 2 V. For chronoamperometric measurements under illumination, the applied


DOI: 10.1021/acsami.5b03494
ACS Appl. Mater. Interfaces 2015, 7, 16177−16190

**Table 1. Composition and Properties of the Printing Formulations**

| | | surface tension (mN/m) | | density (g/cm$^3$) | | viscosity (mPa·s) | | |
|---|---|---|---|---|---|---|---|---|
| | mixing volumetric ratio of 1A + MD | mean | SD | mean | SD | mean | SD | Z-number |
| 1E | 0 + 10 | 26.23 | 0.18 | 0.8556 | 0.0012 | 2.1830 | 0.0059 | 9.705 |
| 1D | 1 + 9 | 27.17 | 0.18 | 0.8837 | 0.0015 | 3.2444 | 0.0069 | 6.754 |
| 1C | 2 + 8 | 27.84 | 0.19 | 0.9004 | 0.0016 | 3.8768 | 0.0113 | 5.775 |
| 1B | 4 + 6 | 28.60 | 0.16 | 0.9372 | 0.0012 | 4.7276 | 0.0097 | 4.898 |
| 1A | 10 + 0 | 32.84 | 0.13 | 1.0222 | 0.0020 | 5.4214 | 0.0134 | 4.779 |

voltage was set to 1 V, and the lamp radiation was manually chopped at 30 s intervals.

The self-cleaning photocatalytic activity of the different films was demonstrated by a fluorescence test with a solid organic contaminant containing terephthalic acid. The detailed procedure is published elsewhere[46] and describes in full detail all the steps of this sensitive, reliable, and quantitative photocatalytic test consisting of the following steps: (1) preparation of a transparent organic coating (sodium salt of terephthalic acid in cellulose host) over the photocatalyst layer, (2) irradiation of the coating for different times in a photochamber and washing the coating with ethanol/water solution, and (3) analysis of the extracted solution containing oxidized products by high performance liquid chromatography with fluorescence detection (HPLC-FLD).

## 3. RESULTS AND DISCUSSION

**3.1. Optimization of the Ink Formulation and Printing Conditions.** The ink surface tension, substrate surface energy, and ink viscosity are the most prominent factors influencing droplet formation and layer merging during the inkjet printing of a functional liquid onto a nonporous nonabsorbing substrate. Apart from these ink properties, the substrate temperature also plays a very important role because it is the main factor influencing the solvent evaporation rate. Lower temperatures result in slow drying, mottling, and dust accumulation, while higher temperatures lead to premature evaporation and banding pattern formation. These general rules also prove to be valid in the case of our hybrid titania-silica sol. The 3-component mixed diluent used for stock sol dilution deliver optimal jetting and drying characteristics. The major components, isopropyl alcohol and propoxyethanol, work as fluid vehicle by carrying suspended titania and silica particles. They differ significantly in their volatility, which contributes to the gradual drying and seamless merging of the printed bands. The minor component, ethylene glycol, acts as humectant that prevents the ink from drying in the printhead nozzles. Table 1 summarizes the dilution ratios and corresponding densities of the printing formulations. Figure 1 depicts the viscosity and surface tension of the tested formulations. Formulation 1C, containing 20 vol % of the stock sol 1A, was identified as optimal for providing a balanced compromise between printing reliability and sufficient dry mass content.

The final surface topologies of the printouts depend on complex interactions between the drop-shaping forces and the surface properties of the substrate used. Several distinctive phases have been identified during drop-spreading on solid nonabsorbing substrates: a kinematic phase, a spreading phase, a relaxation phase, and a wetting phase.[47] The drop dynamics and film formation can be predicted to a certain degree by theoretical descriptors such as the Weber number ($We = \delta \cdot v^2 \cdot d/\sigma$), Ohnesorge number ($Oh = \eta/\sqrt{(d \cdot \sigma \cdot \delta)}$), $Z$ number ($Z = \sqrt{(d \cdot \sigma \cdot \delta)}/\eta$), and Reynolds number ($Re = \delta \cdot v^2 \cdot d/\eta$), where $\delta$ is the density, $v$ is the drop velocity, $d$ is the diameter of the nozzle, $\sigma$ is the surface tension, and $\eta$ is the viscosity of the liquid. Table 1 also gives the values of the $Z$ number that were used as the

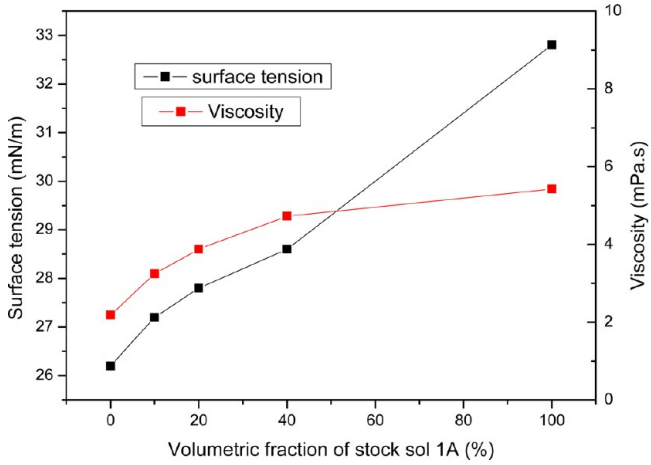


**Figure 1.** Dependence of the viscosity and surface tension of the tested formulations on the dilution.

indicator of drop formation and printability (e.g., capillary breakoff length and time, droplet volume, and satellite formation). While some theories predict a stable drop formation in drop-on-demand systems when $Z > 2$,[48] others determined that a printable fluid should have a $Z$ value between 1 and 10.[49] It is also known that the lower limit is governed by the viscosity of the fluid and its printing ability, while the upper limit is determined by the point at which multiple drops are formed instead of a single droplet.[50] In our study, the $Z$ values were in the range of 4−9.

The recommended optimal viscosity range for jetting with a Dimatix printer is 10−12 mPa·s, and the recommended optimal surface tension is 28−33 mN/m. Despite the relatively low viscosity of all the studied mixing ratios, their jetting performance was excellent, and a nozzle blockage was only rarely observed. Moreover, printing of the low-viscous formulation did not require viscosity reduction by print head heating, therefore enabling printing at ambient temperature, which was beneficial for the suppression of nozzle drying.

**3.2. Layer Surface Morphology.** The AFM scans of the $TiO_2$ layers are presented in Figure 2. The surface morphology in the micrometer range is characterized by the formation of agglomerated grains. The diameter of the observed grains was less than or equal to the radius of the AFM probe tip, which is approximately 50 nm. Comparing the observed diameter of the grains, we note that the diameter did not exhibit a significant dependence on the number of layers, confirming that the average grain diameter did not depend on the number of deposited layers but on the size of the deposited nanoparticles. Because the same nanoparticle composition was used for successive layers, the average diameter did not change. Similar results were obtained from the surface roughness ($\sigma$) measurements: $\sigma$ was calculated from 10 $\mu$m × 10 $\mu$m area topography scans and ranged between 10 and 16 nm. Generally, $\sigma$ gradually increased with the number


DOI: 10.1021/acsami.5b03494
ACS Appl. Mater. Interfaces 2015, 7, 16177−16190

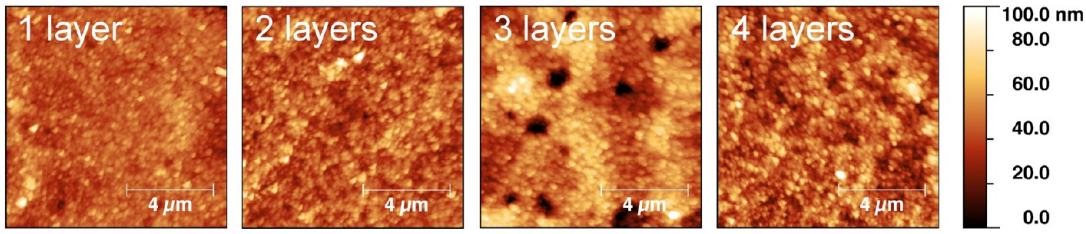


**Figure 2.** AFM images of the printed samples.

of layers. However, the third layer (Figure 2(c)) presents marginally higher roughness than the fourth layer (Figure 2(d)). This is because the AFM topography imaging was performed after the photoactivity tests. Particularly in the case of the 3-layer films (Figure 2(c)), large voids were observed probably because of film damage. Although these voids were excluded from the $\sigma$ calculation, the roughness of the surface around these voids was slightly increased, resulting in increased $\sigma$. In addition to $\sigma$, we also measured the film thickness (see Table 2).

**Table 2. Summary of Thickness Data**

| | AFM | | SEM | | ellipsometry | |
|---|---|---|---|---|---|---|
| layer | thickness (nm) | RMS (nm) | average thickness (nm) | SD | thickness (nm) | model error (nm) |
| 1 | 37 | 10 | 41 | 7.9 | 42 | 0.4 |
| 2 | 71 | 11 | 73 | 21 | 72 | 0.2 |
| 3 | 149 | 16 | 115 | 34 | 119 | 0.5 |
| 4 | 161 | 13 | 163 | 10 | 172 | 0.3 |

A more detailed view of the surface texture is provided by SEM (Figure 3). We can resolve the individual grains making up larger flakes. The layer was compact without any obvious regular porosity. A few random grooves or pores seemed to develop in the thicker samples, but the layer was generally even without any major defects or deposition artifacts. The SEM technique was also used to observe layer cross sections (see below).

**3.3. Thickness.** Thickness is the most important parameter influencing the physicochemical properties of thin layers. Multiple techniques were used to measure and verify the thickness of the printed samples. Because inkjet printing may not necessarily produce even-thickness layers because of the banding phenomenon or clogged nozzles, measuring the samples several times with different methods also provided a means to verify the thickness uniformity.

The SEM cross-section images are depicted in Figure 4. The cut was directed perpendicular to the direction of the printhead movement. In this way, we were able to observe the entire length of the cut and check for printing artifacts and general thickness uniformity. Excellent evenness without any significant variations was observed, indicating the flawless printability of the used formulation and well managed merging of the printed bands. The sample thickness was measured at 10 randomly selected spots along the cut, and the values are reported in Table 2. During the AFM study, the samples of all thicknesses were mechanically scratched, and the resulting edge was analyzed. The accuracy and repeatability of this technique depends on the quality of the scratch. Deformations of soft layers and contamination by peeled material are difficult to avoid and are clearly visible as bright specs in Figure 5. The AFM scans and extracted edge profiles for a single measurement are also reported in Table 2. In addition, the ellipsometric data recorded for the optical characterization were used for the thickness calculation (see the ellipsometric characterization below for details).

The results of all three employed methods are summarized in Table 2 and Figure 6. Because the measurements by the three techniques were performed on different samples, the reasonably good match between the obtained results indicates the good repeatability of both the sample fabrication process and the measurements. The mean thickness of a single layer was approximately 40 nm.

**3.4. Mechanical Hardness.** The pencil hardness test was performed according to the relevant ISO standard. Figure 7 depicts the optical micrograph for pencils 2B and 3B. We can easily identify the long straight scratches corresponding to entirely removed layers caused by the 2B pencil, while the softer 3B pencil only produced trails of shiny silver graphite flakes on the surface of the analyzed sample. Thus, we can conclude that the thickness of the printed layers is equivalent to that of a 3B pencil.

**3.5. Phase Composition.** The presence of the anatase phase in the powder sample is manifested by an intense peak at the XRD diffraction angle of $2\theta = 25.4°$, followed by less intense peaks at 38°, 48°, 54°, 62°, etc. (see Figure 8).[51] The peak broadening associated with submicrometer particles is also observed. Quite surprisingly, the peaks at $2\theta = 30.8°$ and 42.4° indicate the presence of brookite. The determination of the brookite content could have been conducted by comparing the peak areas, which, in this particular case, would be difficult to perform unambiguously because of the extensive peak broadening and diffraction maxima overlap. While the formation of brookite at elevated temperatures during the hydrothermal treatment of amorphous titania slurries and organic templates is well documented,[52] its formation at ambient pressure and temperature is less common. Nonetheless, several recent papers confirm our observation and also report brookite formation under similar synthetic conditions.[53,54] The photocatalytic activity of pure brookite is generally inferior to that of anatase but is strongly influenced by its morphology,[55] and mixtures of these two phases can benefit from synergistic effects.[56,57]

**3.6. Optical Properties.** The total transmission spectra depicted in Figure 9 were referenced to the substrate and therefore reflect the transmission characteristics of the coating only. It is worth noting the perfect transmission in the entire visible region and the absence of interference coloring that is otherwise typical for titania coatings. Figure 10 shows a comparison of the visual appearance of typical samples obtained by sol–gel-calcination (left) and the samples used in this study. Apparently, while the sol–gel-calcination originated samples show strong interference coloring originating in their high refractive index, the reported samples exhibit no visual manifestation of the deposited layer, which makes them well suited for the fabrication of self-cleaning coatings on transparent glass surfaces.


DOI: 10.1021/acsami.5b03494
ACS Appl. Mater. Interfaces 2015, 7, 16177–16190

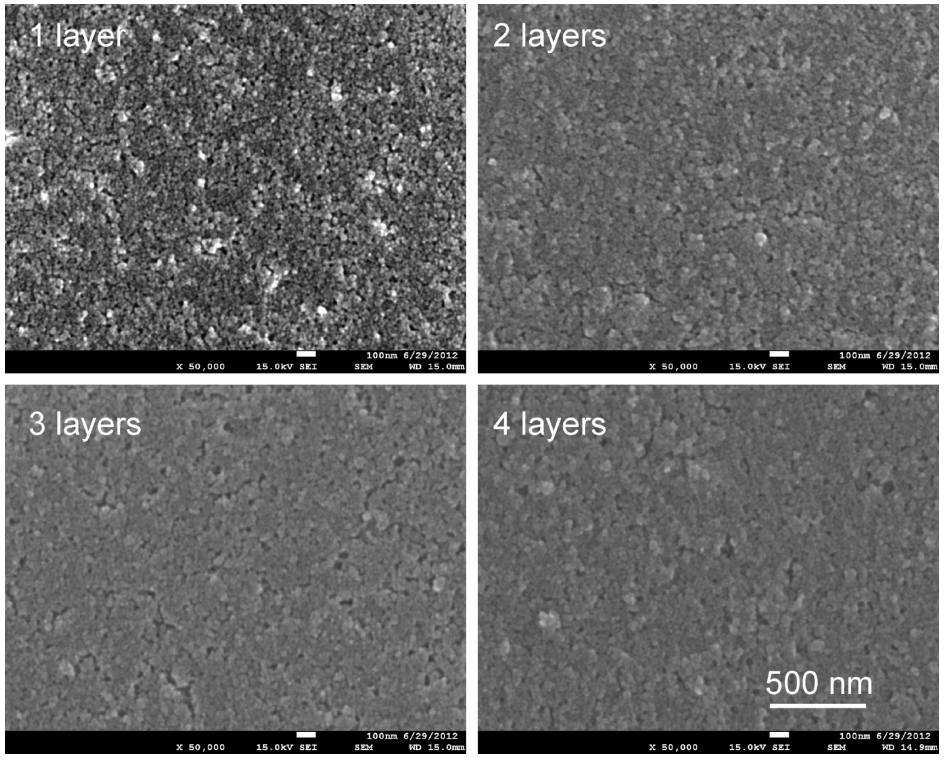


**Figure 3.** SEM images of the printed samples.

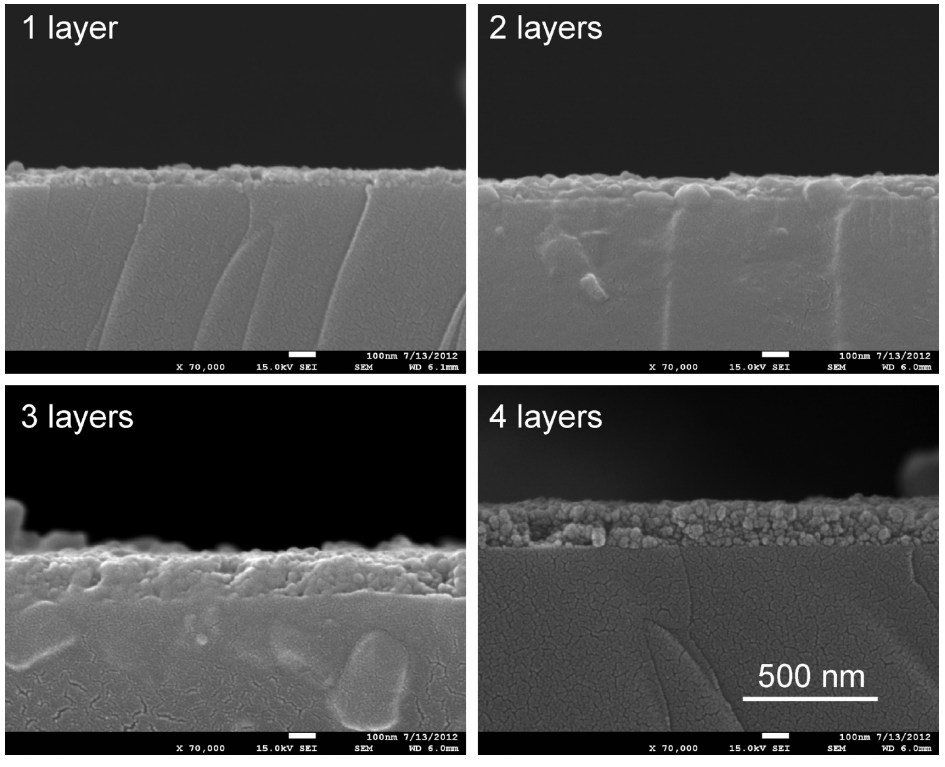


**Figure 4.** SEM cross section images of the studied samples.

The transmittance plot also indicates that significant absorption occurs below 390 nm. The bandgap was estimated from the Tauc plot depicted in Figure 11. The indirect transition was observed at approximately 3.2 eV, corresponding to 387 nm. The ellipsometric analysis was used for thickness determination and for the determination of the optical constants. The new amorphous ellipsometric model[58] was adopted for both the titania and silica components. The adopted ellipsometric model consists of a mixed titania-silica layer topped by a thin surface roughness layer (see Figure 12). The layer thickness, titania/silica ratio, and model parameters were varied in the fitting procedure. The resulting fitted ellipsometric spectra show


DOI: 10.1021/acsami.5b03494
ACS Appl. Mater. Interfaces 2015, 7, 16177−16190

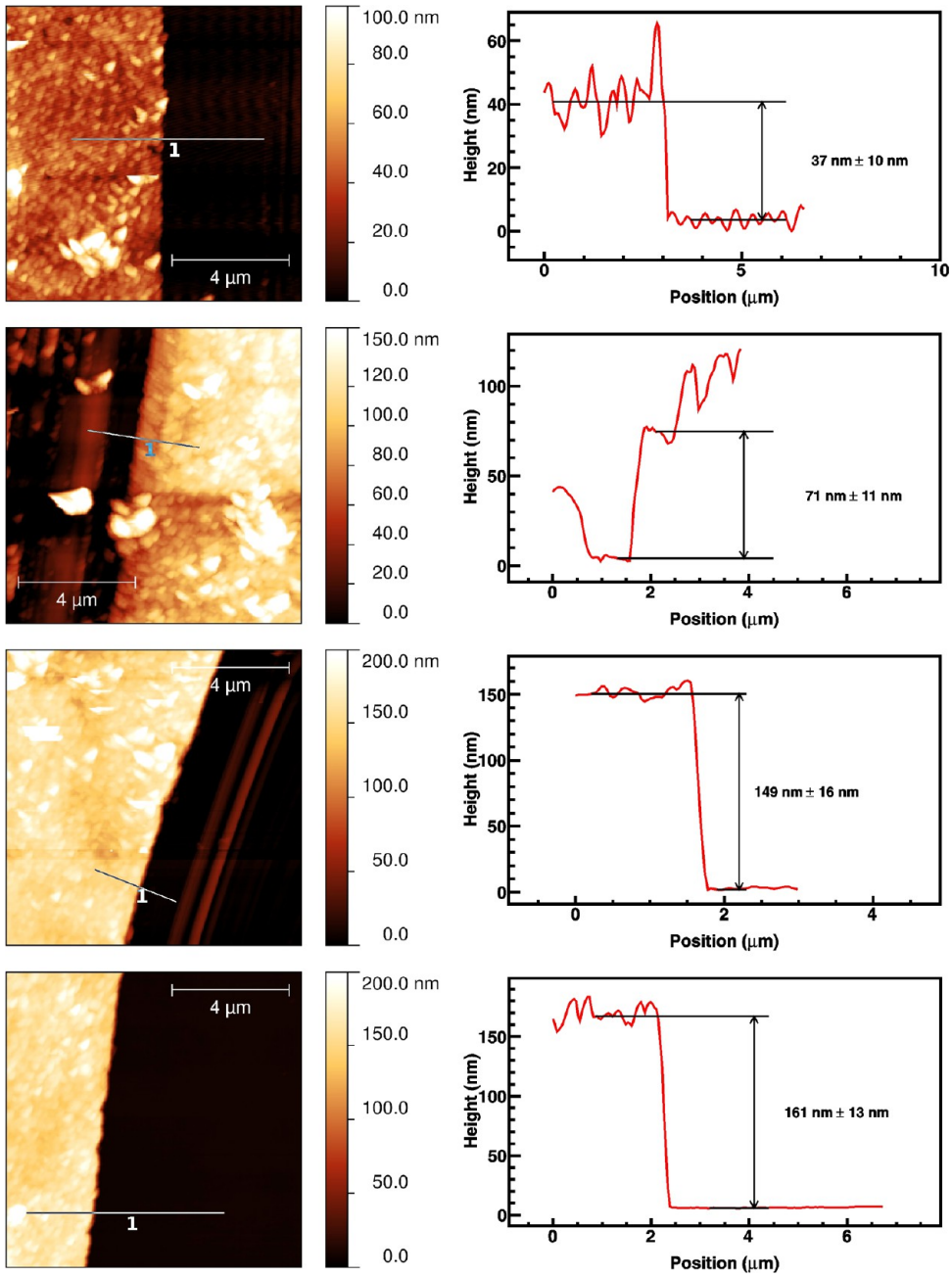


**Figure 5.** AFM determination of layer thickness.

excellent match with the measured data ($\chi^2$ well below 0.1). While both the thickness and the titania-silica volume ratio values resulting from the fitting procedure were in good agreement with the measured and real values, respectively, the resulting fitted model parameters had to be significantly altered from the default values for bulk materials. The difference can be attributed to the small size and imperfect crystallinity of the titania particles constituting the studied layer.

**3.7. Photoelectrochemical Properties.** The dependence of the current density on the linearly increasing voltage ramp for the thickest 10-layered sample is illustrated in Figure 13. Because the absorbance of the regular set of 40−160 nm samples was rather low, their photocurrents were also poor. Therefore, thicker photoelectrodes consisting of more overprinted layers were fabricated, and the thickest 10-layered one (ca. 400 nm) finally exhibited an appreciable photocurrent response. The depicted linear voltammogram represents the polarization curves of the studied sample in the dark and under UV irradiation. In the positive potential range, the contribution of the photogenerated current indicates free charge carrier formation and collection, which result from the absorption of UV quanta. The response curve of a typical 100 nm sol−gel originated titania photoelectrode is given for comparison: it features much larger photocurrents and a current plateau[59] in the region of ca. 0.2−1.2 V. Unfortunately, in the case of hybrid titania-silica photoelectrodes, the photocurrent is much lower, and the typical plateau is hardly recognizable.

The chronoamperometric record (Figure 14) illustrates the efficiency, stability, and repeatability of photocurrent generation at a constant potential of 1 V vs the FTO counter electrode. Again, a typical 100 nm sol−gel originated titania photoelectrode response is plotted for comparison. Both depicted samples


DOI: 10.1021/acsami.5b03494
ACS Appl. Mater. Interfaces 2015, 7, 16177−16190

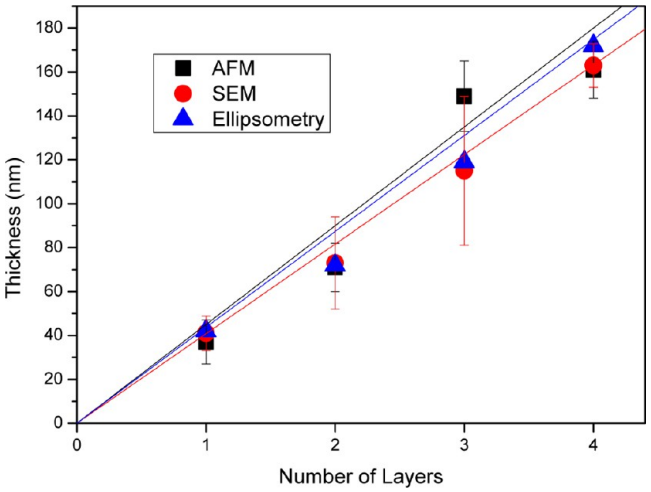


**Figure 6.** Comparative thickness analysis by different methods.

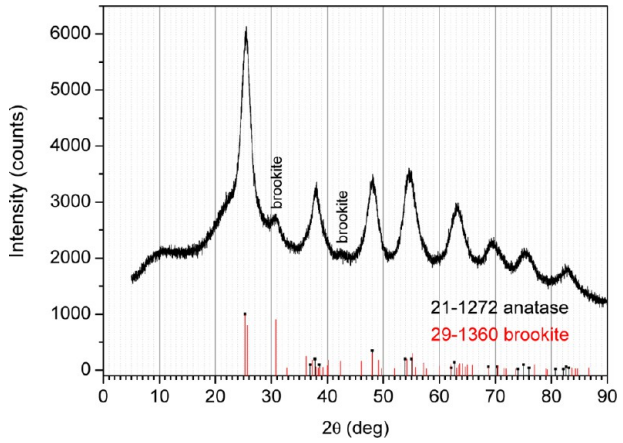


**Figure 8.** XRD diffraction pattern of the printed titania-silica mixture.

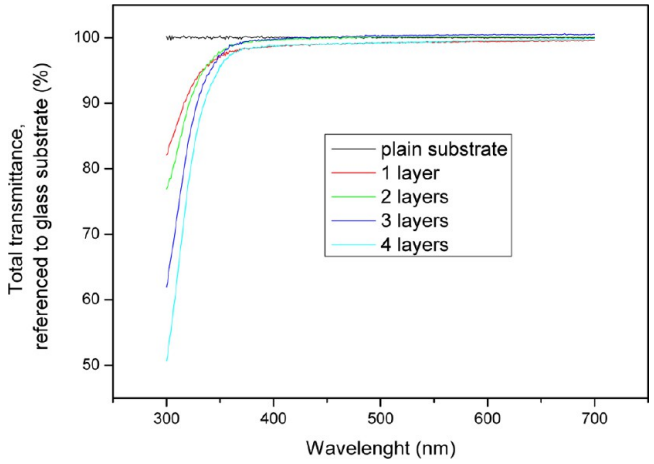


**Figure 9.** Total transmission UV−vis spectra of the printed layers referenced to the glass substrate.

feature a sharp increase upon irradiation, fast photocurrent equilibrium establishment, and a sharp current decay upon irradiation blocking. However, the photocurrent density of the hybrid 400 nm-thick layer is approximately 10 times smaller than the photocurrent generated in the 100 nm-thick sol−gel-calcination originated titania. Such low photocurrent can be attributed to the limited contact between the titania nanoparticles that are surrounded by the insulating binder and the possibly residual solvent molecules adsorbed on the surface of both the titania and silica nanoparticles. Yet, as shown in Figure 14, the electrodes exhibit essentially no wear or corrosion even after prolonged illumination (10 voltammetric cycles, 40 min).

**3.8. Confirmation of Photocatalytic Activity.** All four printed layers were tested by a novel, highly sensitive, fluorescence-based method which is based on the deposition of a thin transparent solid layer of terephthalic acid (TPA) over a titania layer. After irradiation of such a system of layers with UV-A light, highly fluorescent hydroxyterephthalic acid (HTPA) − among other degradation products − is formed due to a reaction between the photoexcited $TiO_2$ and terephthalic acid and can be finally detected by different analytical methods (HPLC-FLD, spectrofluorometer). Figure 15 depicts the kinetic profiles of the HTPA formed during the photocatalytic test conducted with the studied samples. The only difference with respect to the photocatalytic tests described in a published paper[46] was the use of a special plastic holder with 12 or 14 holes (Φ = 9 mm), which was attached to the sample surface using silicon grease. The purpose of such a holder was to separate the parts of the tested photocatalytic layers from one another, creating "wells with a photocatalytic bottom", which allowed us to take a sample from a photocatalytic surface at different times of irradiation for analysis. The samples were obtained by washing

**Figure 7.** Optical micrographs of the pencil hardness test showing the scratched surface by a 2B pencil (right), while the softer 3B pencil leaves graphite flakes on the surface of the analyzed sample (left).



DOI: 10.1021/acsami.5b03494
ACS Appl. Mater. Interfaces 2015, 7, 16177−16190

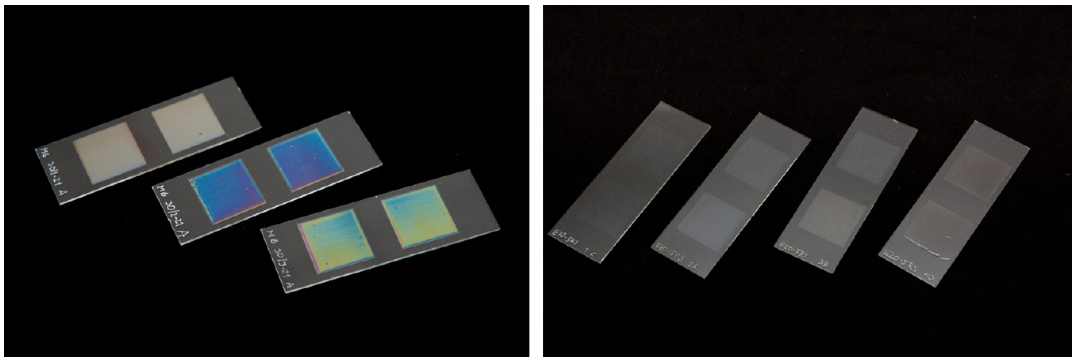

**Figure 10.** Visual appearance of the titania test patches originating from sol−gel-calcination (left; 1, 2, and 3 layers equivalent to 50, 100, and 150 nm, respectively) and hybrid titania-silica patches (right), both fabricated by inkjet printing.

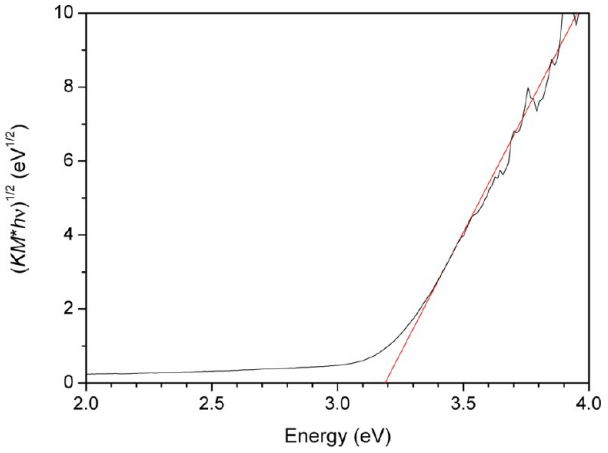


**Figure 11.** Tauc plot used for bandgap determination. The Kubelka−Munk function (KM) was calculated from the diffuse reflectance spectra of the powders.

the "wells" with an automatic pipet using an ethanol/water mixture. The UV source for the photocatalytic degradation was chosen as suggested in the above-mentioned publication, and the HPLC analyses and fitting of the data according to a simplified kinetic analysis were carried out according to the same publication.[46]

According to our published work, we can conclude that despite the different HTPA and HBA formation rates, the thickness of the photocatalytic layer is in good correlation with the photocatalytic activity of the sample, which is clearly reflected in the increased photocatalytic activity. Table 3 summarizes the HTPA formation rate constants and also provides a comparison with an established commercial self-cleaning glass.

## 4. APPLICATION PERSPECTIVE

While the benefits and application niches of titania direct pattering have been listed in the introduction, at this point we would like to mention one more specific example illustrating the advantage of the direct patterning approach and the application potential of the reported material: because the charge carrier generation and transport capability of the reported titania-silica hybrid coating are conserved to a certain extent in the hybrid titania-silica layer, we were able to employ it for the fabrication of interdigitated photoelectrochemical cell prototypes intended for water purification.

Recently, the obvious advantage of using an electrical bias in photocatalytic reactions on immobilized semiconductor layers has been demonstrated.[60] The strategy is based on enhancing the electron−hole separation and consequently increasing the quantum yield of the pollutant degradation by the application of an electrical bias, which is possible when the photocatalyst is deposited on an electrically conducting substrate.[61−63] However, in the resulting electrochemical cell, the *iR* drop is one of the factors limiting high-current throughput at moderate bias. If the

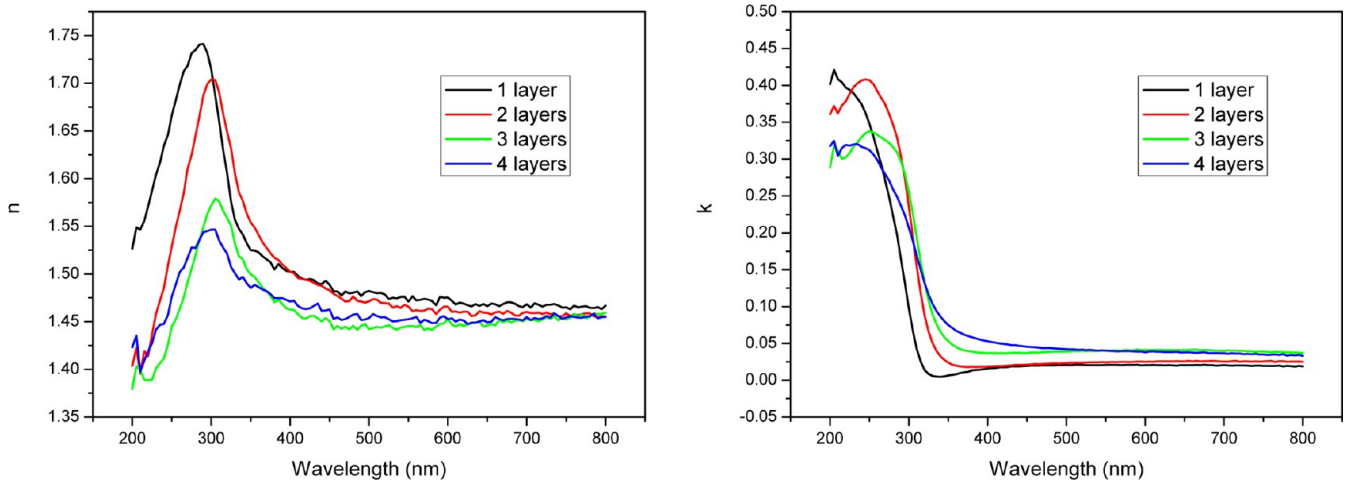


**Figure 12.** Ellipsometric analysis results−spectral dependencies of the refractive index (left) and extinction coefficient (right). For thickness results, see Table 2 and Figure 6.



DOI: 10.1021/acsami.5b03494
*ACS Appl. Mater. Interfaces* 2015, 7, 16177−16190

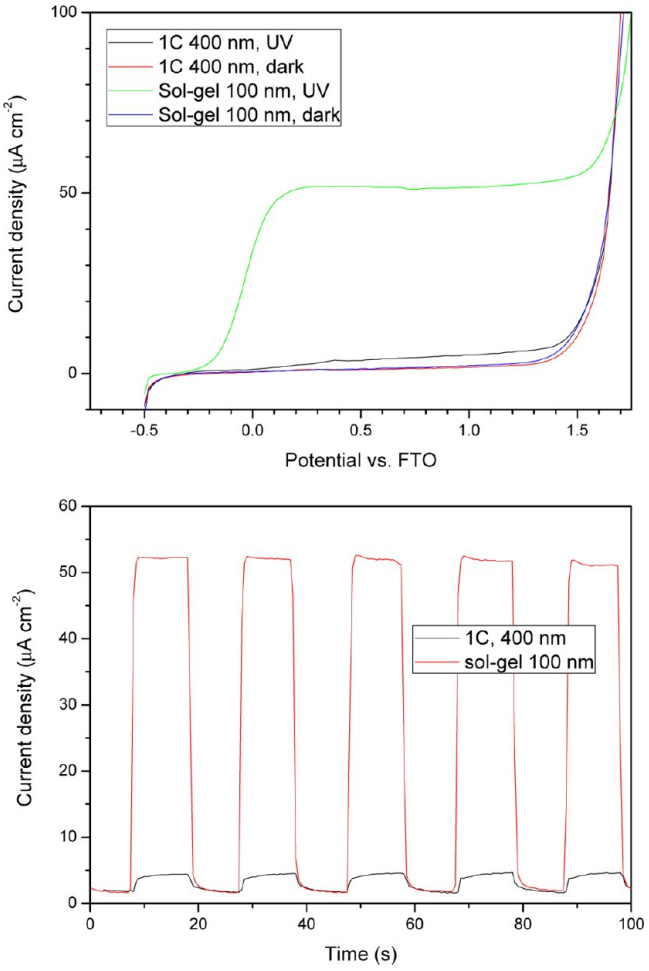


**Figure 13.** *i*-V curves of titania electrodes fabricated by different methods (top) and chronoamperometric records comparing the currents generated at 1 V bias (bottom).

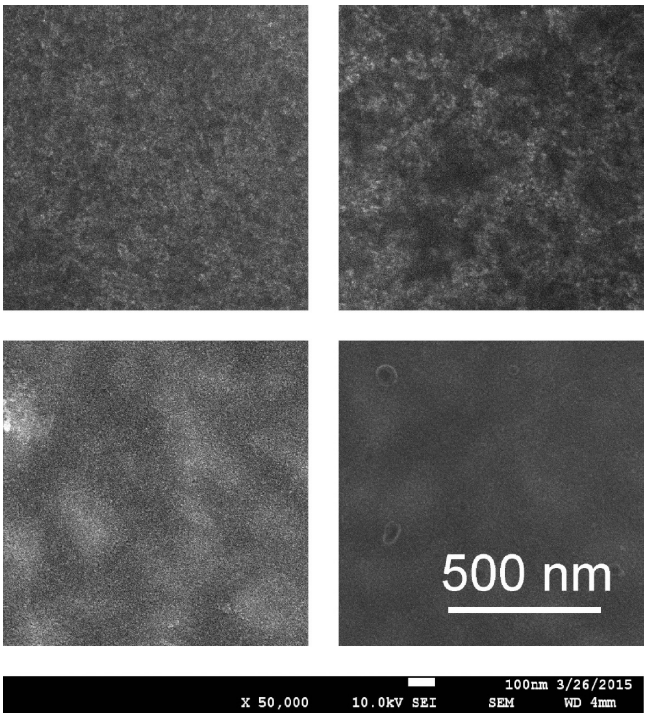


**Figure 14.** SEM images of the electrode surface. Hybrid titania-silica (top row) and sol−gel (bottom) images before (left column) and after (right) voltammetric experiments. Grains of the substrate FTO layer are apparent in the sol−gel samples.

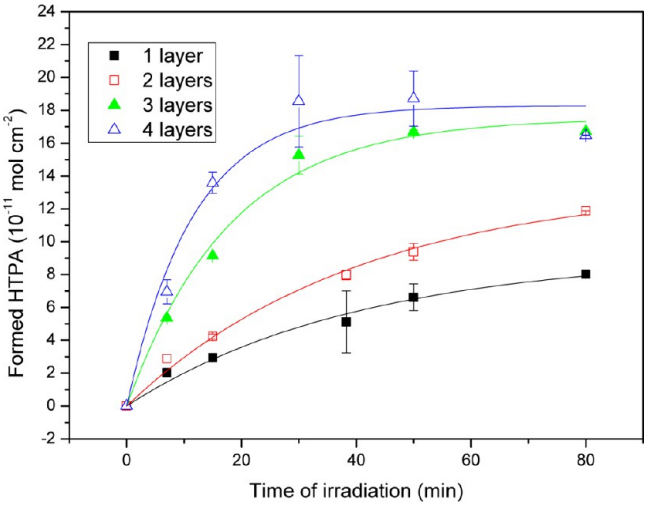


**Figure 15.** HTPA evolution during UV-A irradiation (moles of HTPA per $cm^2$).

**Table 3. HTPA Formation Rate Constants Depending on the Number of Printed Layers**

| no. of layers−typical thickness (nm) | HTPA formation rate constant [$10^{-9}$ M/min] |
|---|---|
| 1−40 | 9.1 ± 1.0 |
| 2−80 | 13.4 ± 1.1 |
| 3−120 | 38.9 ± 3.5 |
| 4−160 | 63.3 ± 10 |
| Pilkington Activ | 2.54 ± 0.27 |

treatment of low ionic strength media (drinking water) is envisaged, means for minimizing the *iR* drop must be secured.

One such means is achieved by using a parallel plate reactor with two opposite electrodes with a small space between them through which the electrolyte is passed.[64] However, the pressure build-up is considerable in a module consisting of many such cells. This drawback can be avoided by using a planar electrochemical cell with two interdigitated electrodes (IDE). The working electrode consists of an electrical conductor covered by semiconducting titanium dioxide. The counter electrode material is not critical as long as sufficient electrical conductivity and corrosion resistance is provided and interdigitated geometry is respected. Such a design ensures two key functions: (1) it suppresses the main obstacle to the efficient use of the absorbed photons, i.e., the recombination of the photogenerated charge carriers, by applying an external electrical bias to the semiconducting photocatalyst and (2) it avoids the reduction of the generated photocurrent due to the *iR* drop, even in electrolytes of low ionic strength. These features make the device an interesting candidate for the photoelectrocatalytic purification of drinking water. The decomposition of model pollutants has been observed on centimeter-scale prototype devices fabricated by standard lithographic techniques using optical copying through contact masks for resist patterning.[65]

The reported hybrid titania-silica formulation may be a potentially useful material for the fabrication of larger devices, which is carried out solely by material printing. Recently, such devices have been fabricated in our lab by a hot process involving


DOI: 10.1021/acsami.5b03494
ACS Appl. Mater. Interfaces 2015, 7, 16177−16190

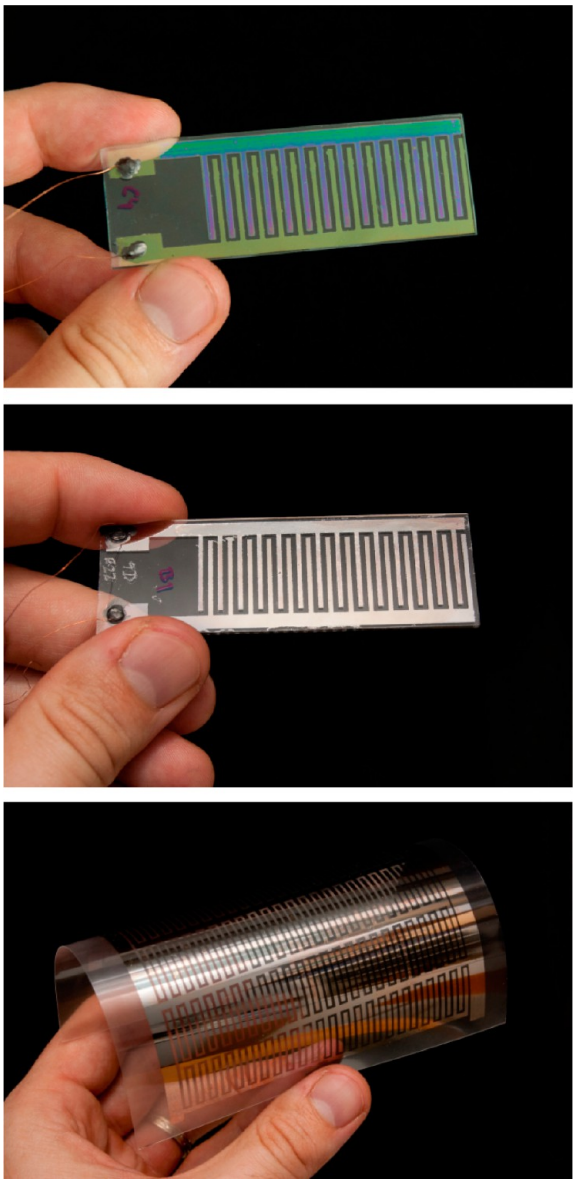

**Figure 16.** IDE devices fabricated on various substrates: sol−gel-calcination originated titania electrode printed over interdigitated ITO collectors (top), hybrid titania-silica sol printed on top of platinum electrodes (middle), and a prototype 10 × 10 cm IDE device fabricated on a PET substrate (bottom).

the printing of a reverse micelle-based sol−gel[25,66] formulation onto a prepatterned ITO layer and calcining at 450 °C (Figure 16, top). They have been employed for the degradation of model aqueous pollutants, and significant acceleration of the process has been observed.[67] With the reported formulation readily available, we have investigated the option of switching to a cold process, where the active semiconducting layer would be patterned by direct inkjet printing of the reported formulation (Figure 16, middle). Possible further upscaling has been demonstrated by the fabrication of 10 × 10 cm prototypes on PET substrates, which feature interdigitated electrodes fabricated by inkjet printing of nanosilver ink (Figure 16, bottom).

However, as presented in the previous section, the electrochemical properties of the original 1C formulation are rather poor, and the low photocurrent densities do not allow for efficient photoelectrochemical oxidation of pollutants in water. Therefore, two modifications of the deposition process were made to improve its performance:

1) The titania-silica ratio was altered in favor of higher titania content. A new stock sol (2A) containing 75 mol % of titania and 25 mol % of silica was mixed, and a new printing ink (2C) was prepared using the same solvent doses as in the original 1A and 1C formulations. The printability of the 2C ink was equally good, but the reduced binder content resulted into somewhat poorer layer hardness equivalent to 4B on the pencil scale.

2) Various postprinting curing processes were introduced. Thermal sintering of the printed pattern may be one option, inducing not only the complete mineralization of organic compounds but also titania crystallite redistribution and improved contact with the conducting substrate. However, such a process is not compatible with plastic substrates. Photonic annealing may be able to deliver comparable results[68] and ensure compatibility with plastic substrates as the time scale of the process is in the millisecond range, meaning that the required conversion occurs much faster than the thermal damage of the substrate. High-intensity UV-curing was recently reported[69] for photocatalytic coatings of similar composition loaded onto polymeric fibers.

To investigate the possible improvement of the electrochemical properties by these processes, another set of 1 $cm^2$ electrodes on FTO substrates was printed with the new 2C formulation (10 layers, 400 nm thickness), and various postprinting processing options were selected: one sample was left to dry naturally (marked as the "green body" layer), one was sintered in air at 450 °C for 30 min, one was UV-cured by immersion in a water bath placed 20 cm below an industrial UV−C lamp (model 80 BQL7, 250 W, Ultralight AG, Liechtenstein), and one sample was photonically sintered by exposure to xenon lamp radiation (BP 307, Eurosep Instruments, France). As only a continuously operating lamp was available, photonic annealing was improvised by manually moving the sample into the lamp beam and out in 10 s cycles with 20% duty (2 s irradiation + 8 s dark, 100 cycles total). In this way, the substrate overheating was eliminated, and the sample temperature did not exceed 100 °C. A sol−gel originated electrode acting as a reference was also included in this experiment. Linear sweep voltammetry and amperometry measurements were performed in the same way as with the previous samples.

The photocurrent response curves depicted in Figure 17 indicate that significant but not equal improvement with respect to the performance of the original 1C formulation has been reached for all the tested postprinting processing methods. The sol−gel process originated layers still remained superior in terms of photocurrent generation efficiency, closely followed by the thermally sintered titania-silica layers originating from the 2C formulation. The photonically annealed and UV-cured layers delivered lower photocurrent densities, but a nonetheless acceptable value approaching 20 $\mu A/cm^2$ was achieved with the photonically annealed electrode. The shape of the response curve was similar in all cases, with a well-developed constant current plateau between 0.2 and 1.2 V. As for the amperometry records, all depicted samples featured a sharp current increase upon irradiation, quick photocurrent equilibrium establishment, and a sharp current decay upon irradiation blocking.

Prototype IDE devices of various sizes and finger densities were fabricated on both glass and PET substrates with photonically annealed electrodes, and their oxidizing activity on various model and real pollutants was investigated. Figure 18 depicts the comparison of the short-circuited (electric bias = 0 V between the finger families) and 1 V bias modes of operation of a


DOI: 10.1021/acsami.5b03494
ACS Appl. Mater. Interfaces 2015, 7, 16177−16190

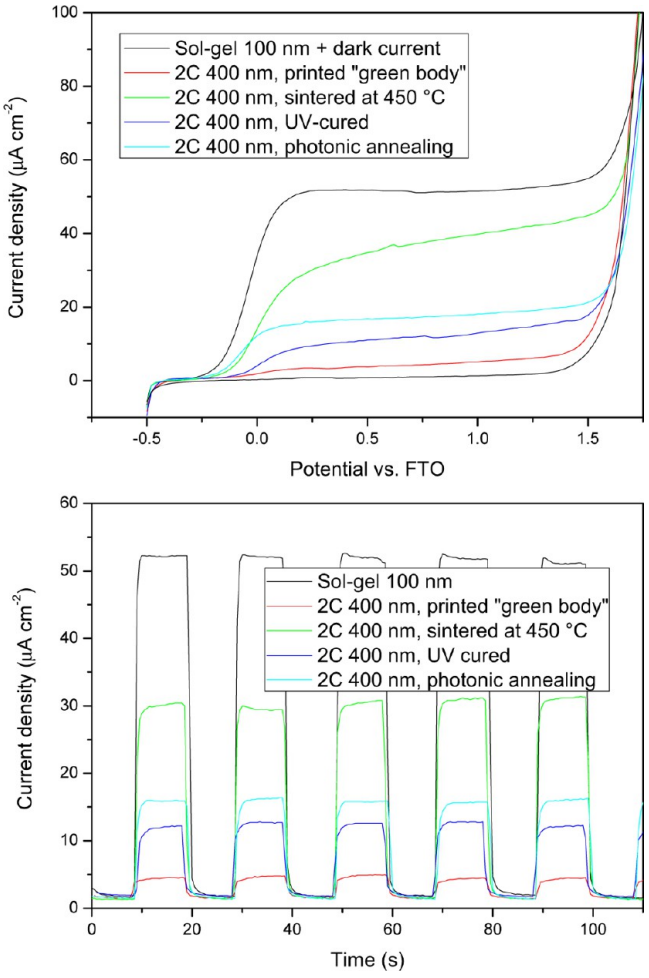


**Figure 17.** Linear voltammetry (top) and amperometry (bottom) records for various postprinting processing options.

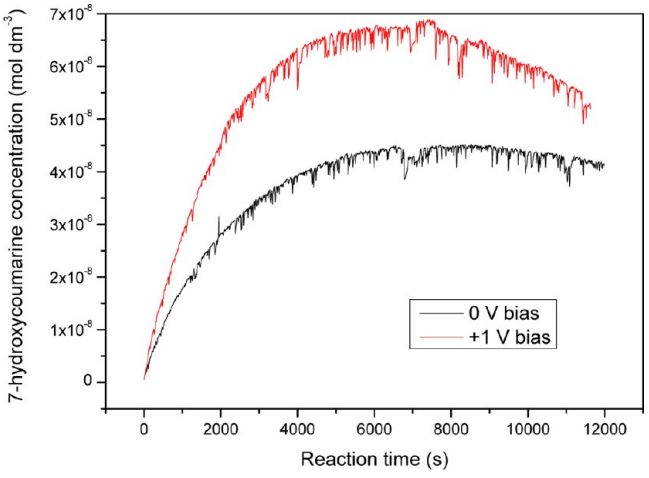


**Figure 18.** 7-Hydroxycoumarine concentration during the illumination of an IDE device (pairs of 1000 $\mu$m wide titania-silica and FTO fingers) immersed in an aqueous solution of coumarin ($c_0$ = 0.1 mM). The finger families were biased against each other at 0 V or at 1 V.

1000 $\mu$m fingered cell (outline as in Figure 16, middle) when a $1 \times 10^{-4}$ molar solution of coumarin is used as the electrolyte. Coumarin is another very useful fluorescent probe for monitoring the oxidative activity of photocatalysts because one of its oxidation products, 7-hydroxycoumarin, is formed at a constant and repeatable quantum yield and is easily monitored by its strong fluorescence at 460 nm.[70] Figure 18 depicts the changes in 7-hydroxycoumarine concentration (obtained from its fluorescence at 460 nm) during the experiment, forming the typical profile of a reaction intermediate: first, we witness a sharp increase followed by a gradual decrease as 7-hydroxycoumarine is further oxidized. A significant acceleration of the initial rate of 7-hydroxycoumarin formation in the photoelectrocatalytic mode is evident and accounts for suppressed electron−hole recombination in the photoelectrocatalytic experiment at 1 V bias.

## 5. CONCLUSION

In this paper, we report our contribution to the technology of cold-setting of liquid phase-originated titania coatings. We developed a hybrid titania-silica sol, based on the brick-and-mortar approach, which can be deposited onto a wide variety of surfaces without the need for high-temperature fixing and are suitable for inkjet material printing. The previously patented stock sol containing nanocrystalline titania and amorphous silica particles and with excellent shelf life was used for the formulation of an inkjettable solution. Its printability was theoretically evaluated based on the *Z*-number descriptor and was subsequently confirmed with the research and development level *de facto* standard Fujifilm Dimatix printhead. In this way, well-defined thin hybrid titania-silica patterns of thicknesses ranging from 40 to 160 nm were fabricated by overprinting 1 to 4 layers. Photoelectrodes of up to 400 nm thickness were fabricated by overprinting 10 layers.

Inkjet printing proved to be an elegant method for sol delivery to a substrate. It provides complete control of the deposition process parameters together with an excellent efficiency of precursor use. Moreover, the possibility of precise patterning and the ease of up-scaling make this type of deposition very appealing for the production of sensors, solar cells, etc.

Detailed characterization of the physicochemical properties of the studied samples indicates excellent mechanical and optical properties, making the reported material well suited for the fabrication of transparent self-cleaning coatings on both mineral and organic substrates. The obvious issue of a polymeric substrate resisting to photocatalytic degradation could be easily addressed by the introduction of a pure silica barrier layer. The observed photocatalytic activity is superior to that of commercial CVD-originating products even with the thinnest layer used in this study.

As expected, the photoelectrochemical properties of printed titania nanoparticles were inevitably altered by the introduction of silica in the layer composition. The generated photocurrent density in the hybrid titania-silica samples fabricated with the 1C formulation (1:1 titania to silica molar ratio) was far inferior to the photocurrent response of pure, well-condensed, and crystallized titania electrodes prepared by the sol−gel-calcination process and used as reference.

However, after increasing the titania fraction to 75 mol % and using a postprinting treatment that induced the mineralization of the adsorbed residual solvents and contaminants, the redistribution of titania crystallites, and an improved contact with the conducting substrate, much improvement in the electrochemical properties of printed titania has been achieved. Although thermal sintering remains superior to other postprinting processing methods, photonic annealing and UV−C curing are capable of delivering appreciable photocurrent values and enable deposition on organic substrates. Such processes may be generally useful for


DOI: 10.1021/acsami.5b03494
ACS Appl. Mater. Interfaces 2015, 7, 16177−16190

the preparation of large-area electrodes or interlayers in photonic devices.

Further development of the printed interdigitated electrochemical cells concept was achieved using the reported material. Prototype IDE devices of various sizes and finger densities were fabricated on both glass and PET substrates with the photonically annealed electrodes. Comparative photocatalytic and photoelectrocatalytic experiments with coumarin as the model aqueous contaminant confirmed the functionality of the photoannealed working electrodes based on the beneficial role of an external electrical bias in suppressing photogenerated electron−hole recombination in the semiconducting photocatalyst. The PET-based 10 × 10 cm prototype cell marks the direction for further development: flexible, large-footprint IDE devices will allow the construction of easily replaceable and lightweight IDE cell modules.

## AUTHOR INFORMATION


### Corresponding Author

*E-mail: petr@dzik.cz.


### Notes

The authors declare no competing financial interest.

## ACKNOWLEDGMENTS

The authors wish to thank the Ministry of Education, Youth and Sports of the Czech Republic for support by projects *LD14131 Printed Functionalities* and *LO1211 Materials Research Centre at FCH BUT - Sustainability and Development*, with financial support from the *National Program for Sustainability I*.

## REFERENCES


(1) Fujishima, A.; Honda, K. Electrochemical Photolysis of Water at a Semiconductor Electrode. *Nature* **1972**, *238*, 37−38.

(2) Chen, X.; Shaohua, S.; Guo, L.; Mao, S. S. Semiconductor-Based Photocatalytic Hydrogen Generation. *Chem. Rev.* **2010**, *110*, 6503−6570.

(3) Pelaez, M.; Nolan, N. T.; Pillai, S. C.; Seery, M. K.; Falaras, P.; Kontos, A. G.; Dunlop, P. S. M.; Hamilton, J. W. J.; Byrne, J. A.; O'Shea, K.; Entezari, M. H.; Dionysiou, D. D. A Review on the Visible Light Active Titanium Dioxide Photocatalysts for Environmental Applications. *Appl. Catal., B* **2012**, *125*, 331−349.

(4) Fujishima, A.; Hashimoto, K.; Watanabe, T. *Tio2 Photocatalysis: Fundamentals and Applications*; Bkc: Tokyo, 1999.

(5) Sobczyk-Guzenda, A.; Pietrzyk, B.; Szymanowski, H.; Gazicki-Lipman, M.; Jakubowski, W. Photocatalytic Activity of Thin Tio2 Films Deposited Using Sol−Gel and Plasma Enhanced Chemical Vapor Deposition Methods. *Ceram. Int.* **2013**, *39*, 2787−2794.

(6) Silva, C. P.; Otero, M.; Esteves, V. Processes for the Elimination of Estrogenic Steroid Hormones from Water: A Review. In *Environmental Pollution*; Elsevier Ltd.: England, 2012; pp 38−58.

(7) Mahmood, M.; Baruah, S.; Anal, A.; Dutta, J. Heterogeneous Photocatalysis for Removal of Microbes from Water. *Environ. Chem. Lett.* **2012**, *10*, 145−151.

(8) Vinu, R.; Madras, G. Environmental Remediation by Photocatalysis. *J. Indian Inst. Sci.* **2010**, *90*, 189−230.

(9) Park, S.; Kim, H. R.; Bang, H.; Fujimori, K.; Kim, B. S.; Kim, S. H.; Kim, I. S. Fabrication and Deodorizing Efficiency of Nanostructured Core-Sheath Tio2 Nanofibers. *J. Appl. Polym. Sci.* **2012**, *125*, 2929−2935.

(10) Wang, C. Y.; Tang, H. J.; Pang, S. H.; Qiu, J. X.; Tao, Y. Enhancing Sunlight Photocatalytic Efficiency of Self-Cleaning Glass by Coating $ZnFeO_4$-$TiO_2$ Film. *Rare Met. Mater. Eng.* **2008**, *37*, 548−551.

(11) Dunlop, P. S. M.; Sheeran, C. P.; Byrne, J. A.; McMahon, M. A. S.; Boyle, M. A.; McGuigan, K. G. Inactivation of Clinically Relevant Pathogens by Photocatalytic Coatings. *J. Photochem. Photobiol., A* **2010**, *216*, 303−310.

(12) Gan, W. Y.; Lam, S. W.; Chiang, K.; Amal, R.; Zhao, H. J.; Brungs, M. P. Novel Tio2 Thin Film with Non-Uv Activated Superwetting and Antifogging Behaviours. *J. Mater. Chem.* **2007**, *17*, 952−954.

(13) Putz, J.; Aegerter, M. A. Versatile Wet Deposition Techniques for Functional Oxide Coatings on Glass. *Glass Sci. Technol.* **2004**, *77*, 229−238.

(14) Krebs, F. C. Fabrication and Processing of Polymer Solar Cells: A Review of Printing and Coating Techniques. *Sol. Energy Mater. Sol. Cells* **2009**, *93*, 394−412.

(15) Heinzl, J.; Hertz, C. H. Ink-Jet Printing. *Adv. Imaging Electron Phys.* **1985**, *65*, 91−171.

(16) Martin, G. D.; Hoath, S. D.; Hutchings, I. M. *Iop In Inkjet Printing - the Physics of Manipulating Liquid Jets and Drops*; Conference on Engineering in Physics - Synergy for Success, London, England, Oct 05; London, England, 2006.

(17) Tekin, E.; Smith, P. J.; Schubert, U. S. Inkjet Printing as a Deposition and Patterning Tool for Polymers and Inorganic Particles. *Soft Matter* **2008**, *4*, 703−713.

(18) Attia, S. M.; Wang, J.; Wu, G. M.; Shen, J.; Ma, J. H. Review on Sol-Gel Derived Coatings: Process, Techniques and Optical Applications. *J. Mater. Sci. Technol.* **2002**, *18*, 211−218.

(19) Bartkova, H.; Kluson, P.; Bartek, L.; Drobek, M.; Cajthaml, T.; Krysa, J. Photoelectrochemical and Photocatalytic Properties of Titanium (Iv) Oxide Nanoparticulate Layers. *Thin Solid Films* **2007**, *515*, 8455−8460.

(20) Arin, M.; Lommens, P.; Avci, N.; Hopkins, S. C.; De Buysser, K.; Arabatzis, I. M.; Fasaki, I.; Poelman, D.; Van Driessche, I. Inkjet Printing of Photocatalytically Active Tio2 Thin Films from Water Based Precursor Solutions. *J. Eur. Ceram. Soc.* **2011**, *31*, 1067−1074.

(21) Manga, K. K.; Wang, S.; Jaiswal, M.; Bao, Q. L.; Loh, K. P. High-Gain Graphene-Titanium Oxide Photoconductor Made from Inkjet Printable Ionic Solution. *Adv. Mater.* **2010**, *22*, 5265−5270.

(22) Dzik, P.; Vesely, M.; Chomoucka, J. Thin Layers of Photocatalytic Tio2 Prepared by Inkjet Printing of a Solgel Precursor. *J. Adv. Oxid. Technol.* **2010**, *13*, 172−183.

(23) Černá, M.; Veselý, M.; Dzik, P. Physical and Chemical Properties of Titanium Dioxide Printed Layers. *Catal. Today* **2011**, *161*, 97−104.

(24) Morozova, M.; Kluson, P.; Krysa, J.; Zlamal, M.; Solcova, O.; Kment, S.; Steck, T. Role of the Template Molecular Structure on the Photo-Electrochemical Functionality of the Sol-Gel Titania Thin Films. *J. Sol-Gel Sci. Technol.* **2009**, *52*, 398−407.

(25) Morozova, M.; Kluson, P.; Krysa, J.; Dzik, P.; Vesely, M.; Solcova, O. Thin Tio2 Films Prepared by Inkjet Printing of the Reverse Micelles Sol-Gel Composition. *Sens. Actuators, B* **2011**, *160*, 371−378.

(26) Bernacka-Wojcik, I.; Senadeera, R.; Wojcik, P. J.; Silva, L. B.; Doria, G.; Baptista, P.; Aguas, H.; Fortunato, E.; Martins, R. Inkjet Printed and "Doctor Blade" Tio2 Photodetectors for DNA Biosensors. *Biosens. Bioelectron.* **2010**, *25*, 1229−1234.

(27) Yang, M.; Li, L. H.; Zhang, S. Q.; Li, G. Y.; Zhao, H. J. Preparation, Characterisation and Sensing Application of Inkjet-Printed Nanostructured Tio2 Photoanode. *Sens. Actuators, B* **2010**, *147*, 622−628.

(28) Arin, M.; Lommens, P.; Hopkins, S. C.; Pollefeyt, G.; Van der Eycken, J.; Ricart, S.; Granados, X.; Glowacki, B. A.; Van Driessche, I. Deposition of Photocatalytically Active Tio2 Films by Inkjet Printing of Tio2 Nanoparticle Suspensions Obtained from Microwave-Assisted Hydrothermal Synthesis. *Nanotechnology* **2012**, *23*, 165603−165613.

(29) Černá, M.; Veselý, M.; Dzik, P.; Guillard, C.; Puzenat, E.; Lepičová, M. Fabrication, Characterization and Photocatalytic Activity of Tio2 Layers Prepared by Inkjet Printing of Stabilized Nanocrystalline Suspensions. *Appl. Catal., B* **2013**, *138−139*, 84−94.

(30) Oh, Y.; Lee, S. N.; Kim, H. K.; Kim, J. Uv-Assisted Chemical Sintering of Inkjet-Printed Tio2 Photoelectrodes for Low-Temperature Flexible Dye-Sensitized Solar Cells. *J. Electrochem. Soc.* **2012**, *159*, H777−H781.

(31) Shibata, H.; Sakai, H.; Rangsunvigit, P.; Hirano, T.; Abe, M. Preparation and Photocatalytic Activity of Titania Particulate Film with Silica as Binder. *Surf. Coat. Int., Part B* **2003**, *86*, 125−130.




DOI: 10.1021/acsami.5b03494
*ACS Appl. Mater. Interfaces* 2015, 7, 16177−16190

(32) Chandiran, A. K.; Yella, A.; Stefik, M.; Heiniger, L. P.; Comte, P.; Nazeeruddin, M. K.; Gratzel, M. Low-Temperature Crystalline Titanium Dioxide by Atomic Layer Deposition for Dye-Sensitized Solar Cells. *ACS Appl. Mater. Interfaces* **2013**, *5*, 3487−3493.
(33) Gilmer, D. C.; Gladfelter, W. L.; Colombo, D. G.; Taylor, C. J.; Roberts, J.; Campbell, S. A.; Kim, H. S.; Wilk, G. D.; Gribelyuk, M. A. Low Temperature Chemical Vapor Deposition of Titanium Dioxide Thin Films Using Tetranitratotitanium(Iv). In *Chemical Aspects of Electronic Ceramics Processing*; Kumta, P. N., Hepp, A. F., Beach, D. B., Arkles, B., Sullivan, J. J., Eds.; 1998; pp 45−50.
(34) Uchida, H.; Otsubo, A.; Itatani, K.; Koda, S. Low-Temperature Deposition of Polycrystalline Titanium Oxide Thin Film on Si Substrate Using Supercritical Carbon Dioxide Fluid. *Jpn. J. Appl. Phys., Part 1* **2005**, *44*, 1901−1906.
(35) Weerasinghe, H. C.; Sirimanne, P. M.; Simon, G. P.; Cheng, Y. B. Cold Isostatic Pressing Technique for Producing Highly Efficient Flexible Dye-Sensitised Solar Cells on Plastic Substrates. *Prog. Photovoltaics* **2012**, *20*, 321−332.
(36) Szeifert, J. M.; Fattakhova-Rohlfing, D.; Rathousky, J.; Bein, T. Multilayered High Surface Area "Brick and Mortar" Mesoporous Titania Films as Efficient Anodes in Dye-Sensitized Solar Cells. *Chem. Mater.* **2012**, *24*, 659−663.
(37) Yun, Y. J.; Chung, J. S.; Kim, S.; Hahn, S. H.; Kim, E. J. Low-Temperature Coating of Sol-Gel Anatase Thin Films. *Mater. Lett.* **2004**, *58*, 3703−3706.
(38) Ryu, D. H.; Kim, S. C.; Koo, S. M.; Kim, D. P. Deposition of Titania Nanoparticles on Spherical Silica. *J. Sol-Gel Sci. Technol.* **2003**, *26*, 489−493.
(39) Shen, Y. S. A New Hypothesis of Micro-Region Acid Sites Regarding the Surface Acidity of Binary Oxides. *RSC Adv.* **2012**, *2*, 5957−5960.
(40) Kim, H. J.; Shul, Y. G.; Han, H. S. Photocatalytic Properties of Silica-Supported Tio2. *Top. Catal.* **2005**, *35*, 287−293.
(41) Bao, N.; Wei, Z. T.; Ma, Z. H.; Liu, F.; Yin, G. B. Si-Doped Mesoporous Tio2 Continuous Fibers: Preparation by Centrifugal Spinning and Photocatalytic Properties. *J. Hazard. Mater.* **2010**, *174*, 129−136.
(42) Černigoj, U.; Lavrenčič Štangar, U. Priprava $Tio_2/Sio_2$ Solov in Njihova Uporaba Za Nanos Samočistilnih in Protizarositvenih Prevlek. 2009.
(43) Tauc, J.; Grigorov, R.; Vancu, A. Optical Properties and Electronic Structure of Amorphous Germanium. *Phys. Status Solidi B* **1966**, *15*, 627−637.
(44) Standardization, I. O. f., Iso 15184: Paints and Varnishes, Determination of Film Hardness by Pencil Test. Geneva, Switzerland, 1998.
(45) Huang, C.; Wu, S. Y.; Tsai, C. Y.; Liu, W. T. The Growth of Organosilicon Film Using a Hexamethyldisilazane/Oxygen Atmospheric Pressure Plasma Jet. *Thin Solid Films* **2013**, *529*, 292−295.
(46) Cernigoj, U.; Kete, M.; Stangar, U. L. Development of a Fluorescence-Based Method for Evaluation of Self-Cleaning Properties of Photocatalytic Layers. *Catal. Today* **2010**, *151*, 46−52.
(47) Rioboo, R.; Marengo, M.; Tropea, C. Time Evolution of Liquid Drop Impact onto Solid, Dry Surfaces. *Exp. Fluids* **2002**, *33*, 112−124.
(48) Fromm, J. E. Numerical-Calculation of the Fluid-Dynamics of Drop-on-Demand Jets. *IBM J. Res. Dev.* **1984**, *28*, 322−333.
(49) Reis, N.; Derby, B. In *Ink Jet Deposition of Ceramic Suspensions: Modelling and Experiments of Droplet Formation*; Symposium on Materials Development for Direct Write Technologies: San Francisco, CA, 2000; pp 65−70.
(50) Jang, D.; Kim, D.; Moon, J. Influence of Fluid Physical Properties on Ink-Jet Printability. *Langmuir* **2009**, *25*, 2629−2635.
(51) Howard, C. J.; Sabine, T. M.; Dickson, F. Structural and Thermal Parameters for Rutile and Anatase. *Acta Crystallogr., Sect. B: Struct. Sci.* **1991**, *47*, 462−468.
(52) Shen, X. J.; Zhang, J. L.; Tian, B. Z.; Anpo, M. Tartaric Acid-Assisted Preparation and Photocatalytic Performance of Titania Nanoparticles with Controllable Phases of Anatase and Brookite. *J. Mater. Sci.* **2012**, *47*, 5743−5751.
(53) Vargeese, A. A.; Muralidharan, K. Effect of Anatase-Brookite Mixed Phase Titanium Dioxide Nanoparticles on the High Temperature Decomposition Kinetics of Ammonium Perchlorate. *Mater. Chem. Phys.* **2013**, *139*, 537−542.
(54) Nikkanen, J. P.; Huttunen-Saarivirta, E.; Zhang, X. X.; Heinonen, S.; Kanerva, T.; Levanen, E.; Mantyla, T. Effect of 2-Propanol and Water Contents on the Crystallization and Particle Size of Titanium Dioxide Synthesized at Low-Temperature. *Ceram. Int.* **2014**, *40*, 4429−4435.
(55) Lopez-Munoz, M. J.; Revilla, A.; Alcalde, G. Brookite Tio2-Based Materials: Synthesis and Photocatalytic Performance in Oxidation of Methyl Orange and as(Iii) in Aqueous Suspensions. *Catal. Today* **2015**, *240*, 138−145.
(56) Gai, L.; Duan, X.; Jiang, H.; Mei, Q.; Zhou, G.; Tian, Y.; Liu, H. One-Pot Synthesis of Nitrogen-Doped Tio2 Nanorods with Anatase/Brookite Structures and Enhanced Photocatalytic Activity. *CrystEngComm* **2012**, *14*, 7662−7671.
(57) Tay, Q.; Liu, X.; Tang, Y.; Jiang, Z.; Sum, T. C.; Chen, Z. Enhanced Photocatalytic Hydrogen Production with Synergistic Two-Phase Anatase/Brookite Tio2 Nanostructures. *J. Phys. Chem. C* **2013**, *117*, 14973−14982.
(58) Forouhi, A. R.; Bloomer, I. Optical Dispersion-Relations for Amorphous-Semiconductors and Amorphous Dielectrics. *Phys. Rev. B: Condens. Matter Mater. Phys.* **1986**, *34*, 7018−7026.
(59) Morozova, M.; Kluson, P.; Krysa, J.; Dzik, P.; Vesely, M.; Solcova, O. Thin Tio 2 Films Prepared by Inkjet Printing of the Reverse Micelles Sol-Gel Composition. *Sens. Actuators, B* **2011**, *160*, 371−378.
(60) Butterfield, I. M.; Christensen, P. A.; Hamnett, A.; Shaw, K. E.; Walker, G. M.; Walker, S. A.; Howarth, C. R. Applied Studies on Immobilized Titanium Dioxide Films as Catalysts for the Photoelectrochemical Detoxification of Water. *J. Appl. Electrochem.* **1997**, *27*, 385−395.
(61) Neumann-Spallart, M. Aspects of Photocatalysis on Semiconductors: Photoelectrocatalysis. *Chimia* **2007**, *61*, 806−809.
(62) Waldner, G.; Bruger, A.; Gaikwad, N. S.; Neumann-Spallart, M. Wo3 Thin Films for Photoelectrochemical Purification of Water. *Chemosphere* **2007**, *67*, 779−784.
(63) Fernandez-Ibanez, P.; Malato, S.; Enea, O. Photoelectrochemical Reactors for the Solar Decontamination of Water. *Catal. Today* **1999**, *54*, 329−339.
(64) Shinde, P. S.; Patil, P. S.; Bhosale, P. N.; Bruger, A.; Nauer, G.; Neumann-Spallart, M.; Bhosale, C. H. Uva and Solar Light Assisted Photoelectrocatalytic Degradation of Ao7 Dye in Water Using Spray Deposited Tio2 Thin Films. *Appl. Catal., B* **2009**, *89*, 288−294.
(65) Neumann-Spallart, M. Photoelectrochemistry on a Planar, Interdigitated Electrochemical Cell. *Electrochim. Acta* **2011**, *56*, 8752−8757.
(66) Dzik, P.; Morozová, M.; Klusoň, P.; Veselý, M. Photocatalytic and Self-Cleaning Properties of Titania Coatings Prepared by Inkjet Direct Patterning of a Reverse Micelles Sol-Gel Composition. *J. Adv. Oxid. Technol.* **2012**, *15*, 89−97.
(67) Dzik, P.; Veselý, M.; Králová, M.; Neumann-Spallart, M. Ink-Jet Printed Planar Electrochemical Cells. *Appl. Catal., B* **2015***17818610.1016/j.apcatb.2014.09.030.
(68) Drahi, E.; Blayac, S.; Borbely, A.; Benaben, P. Impact of Ink Synthesis on Processing of Inkjet-Printed Silicon Nanoparticle Thin Films: A Comparison of Rapid Thermal Annealing and Photonic Sintering. *Thin Solid Films* **2015**, *574*, 169−176.
(69) Gregori, D.; Benchenaa, I.; Chaput, F.; Therias, S.; Gardette, J. L.; Leonard, D.; Guillard, C.; Parola, S. Mechanically Stable and Photocatalytically Active Tio2/Sio2 Hybrid Films on Flexible Organic Substrates. *J. Mater. Chem. A* **2014**, *2*, 20096−20104.
(70) Cernigoj, U.; Stangar, U. L.; Trebse, P.; Sarakha, M. Determination of Catalytic Properties of Tio2 Coatings Using Aqueous Solution of Coumarin: Standardization Efforts. *J. Photochem. Photobiol., A* **2009**, *201*, 142−150.


DOI: 10.1021/acsami.5b03494
*ACS Appl. Mater. Interfaces* 2015, 7, 16177−16190

Catalysis Today 230 (2014) 188–196

Contents lists available at ScienceDirect

Catalysis Today

journal homepage: www.elsevier.com/locate/cattod

# Preparation and characterization of doped titanium dioxide printed layers

Marcela Kralova[a,*], Petr Dzik[a,b,**], Michal Vesely[a,b], Jaroslav Cihlar[a]

[a] Central European Institute of Technology, Brno University of Technology, Technicka 3058/10, 616 00 Brno, Czech Republic
[b] Faculty of Chemistry, Brno University of Technology, Purkynova 118, 612 00 Brno, Czech Republic

ARTICLE INFO

*Article history:*
Received 23 June 2013
Received in revised form 2 September 2013
Accepted 15 September 2013
Available online 12 October 2013

*Keywords:*
Doped titanium dioxide
Material printing
Stearic acid
2,6-Dichloroindophenol

ABSTRACT

Thin layers of doped titanium dioxide on Pyrex glass were prepared by the material printing technique. Titanium dioxide was synthesized by the sol–gel method employing titanium(IV)isopropoxide as the precursor. A dedicated experimental inkjet printer Fujifilm Dimatix 2831 was used for the coating process. The influence of various solvents onto sol jettability was investigated. The mixture of absolute ethanol and 2-butanol was finally adopted because of its optimum viscosity and rate of evaporation. A series of experiments with different printing conditions was carried out, the optimum printing settings were determined. Consequently, iron and silver dopants were incorporated into the sol. The influence of doping on the photocatalytic activity of $TiO_2$ as well as the shift of absorption edge towards high wavelengths was investigated. The quality of all layers was studied by optical microscopy. The surface topology was evaluated by atomic force microscopy. The study of surface structure was performed using scanning electron microscopy. Crystallite phases of prepared $TiO_2$ were investigated by X-ray diffraction analysis. Band gap energy was determined by UV–vis reflection spectroscopy. The photocatalytic activity of printed thin films was examined as a degradation rate of stearic acid and 2,6-dichloroindophenol under UV radiation.



## 1. Introduction

In recent papers, photocatalytics decomposition of dye compounds [1–4] as well as simple organic compounds [5–8] has been thoroughly discussed. The most usual photocatalyst is titanium dioxide due to its specific properties, mostly the optical and electronics ones, chemical stability, non-toxicity and relatively low cost. When the $TiO_2$ is illuminated by an appropriate light source, the photocatalyst generates pairs of electrons and holes inside its crystalline lattice. Free electrons are produced in the conduction band and the holes in the valence one. Because $TiO_2$ has a large band gap (anatase form of titania about 3.2 eV) only a small fraction of solar light (about 5%) from the UV region can be utilized. Therefore, a lot of studies have tried to develop a photocatalytic system which can be activated under visible light irradiation [9–11]. Many reports have been dedicated to the modification of $TiO_2$ by doping of different elements, using metals as well as non-metals. The aim of this work was to shift the absorption edge into the visible light region which can consequently lead to higher activity [12–15]. The most usual non-metals dopants for modification of the physical properties of $TiO_2$ such as optical and photoelectrochemical properties are N [16], Cl [17], S [18], F [19]. On the other hand doping by metal ions is performed to extend the spectral response of $TiO_2$ to the visible light region. Transition metal ions such as Fe, V, Mo, W, Cr have been reported as possible dopants of titanium dioxide [20–23].

The photocatalytic activity of $TiO_2$ strongly depends on the preparation methods and on the post-treatment conditions. It has decisive influence on the chemical and physical properties [24,25]. Sol–gel is one of the most successful techniques how to prepare nanosized metallic oxides with high photocatalytic activity [26]. In the sol–gel process, titanium dioxide is usually prepared by the reaction of hydrolysis and polycondensation of titanium alkoxides ($Ti(OR)_n$) to form oxopolymers, which are consequently transformed into an oxide network [27]. Controlled hydrolysis has to be ensured during whole process to obtain homogeneous titania network. Therefore, some of the chelating agents have to be added to the precursor [28]. Condensation reaction is usually followed by a gelation process and subsequently by calcination.

Titanium dioxide photocatalyst can be used in different forms: as a powder or as an immobilized layer on various substrates. A lot of various wet coating techniques have been proposed, such as dip-coating, spin-coating, spray-coating and many others. One of the

* Corresponding author. Tel.: +420 541143340.
** Corresponding author at: Faculty of Chemistry, Brno University of Technology, Purkynova 118, 612 00 Brno, Czech Republic.
*E-mail addresses:* marcela.cerna@ceitec.vutbr.cz (M. Kralova), petr@dzik.cz (P. Dzik).

0920-5861/$ – see front matter © 2013 Elsevier B.V. All rights reserved.
http://dx.doi.org/10.1016/j.cattod.2013.09.018

novel deposition methods is material printing. The term "material printing" refers to the material deposition by (e.g. inkjet) printing where traditional colour ink is replaced by a liquid media. Comparison of material printing with other deposition techniques generally favours this method due to a lot of advantages. The most important of them is the possibility of direct pattering. Printhead can be used to focus the liquid media droplets on a specified place of the substrate and thus create various patterns directly, without any mask or lithographic processing.

The final surface topology of printouts depends on both the drop formation mechanism and surface properties of the substrate used. Various dynamic phenomena have been observed on the three-phase boundary after droplet landing such as splashing, spreading, receding, bouncing and crown formation. Rioboo et al. [29] have identified the phases of drop spreading: kinematic phase, spreading phase, relaxation phase and wetting phase. Drop dynamics and film formation can be to a certain degree predicted by theoretical descriptors such as Weber number ($We = \delta v^2 d/\sigma$), Ohnesorge number ($Oh = \eta/\sqrt{(d\sigma\delta)}$), $Z$ number ($Z = \sqrt{(d\sigma\delta)}/\eta$) and Reynolds number ($Re = \delta v^2 d/\eta$), where $\delta$ is the density, $v$ is the drop velocity, $d$ is the diameter of nozzle, $\sigma$ is the surface tension and $\eta$ is the viscosity of printable liquid. While these models were developed for Newtonian fluids, most commercially available inks are non-Newtonian fluids since they contain different additives. Nevertheless, it seems reasonable to apply these models also for non-Newtonian fluids in order to assess the printability of the inks [30–33].

## 2. Materials and methods

### 2.1. Sol synthesis

Titanium tetraisopropoxide (TTIP) (p.a.) was used as a precursor for the preparation of titanium dioxide by the sol–gel synthesis. Firstly, 20 mL of 2-butanol was mixed with 1.9 mL of acetyl-acetone (p.a.). Acetyl-acetone (AcAc) was used as a chelating agent to prevent uncontrolled hydrolysis. This mixture was added dropwise under a continuous stirring to 5.15 mL of TTIP. Consequently, absolute ethanol (22.5 mL) with small amount of water (0.343 mL) was added drop by drop to the prepared mixture to start the hydrolysis and condensation reaction. Finally, polyethylene glycol (p.s.) with the average molecular weight 1500 was added. PEG was used as an anticracking agent. The concentration of PEG was set to 4 g/L as the most suitable for printing deposition [34]. Final printing mixture consisted of 3 mL of titania solution and 2 mL of α-terpineol (96%, Sigma–Aldrich).

The goal of this work was to investigate the doping influence by iron as well as silver on the photocatalytic properties of final $TiO_2$. The influence on band gap energy as well as on the shifting of the absorption edge towards higher wavelength was examined. Different amount of iron (III) acetylacetonate was added to prepared titania sol (mole concentration 3%, 5%, 7%). The samples were noted Ti; 3Fe; 5Fe; 7Fe. Silver nitrate was dissolved in the sol with mole concentration 2% and the samples were noted Ag; Ag_3Fe; Ag_5Fe; Ag_7Fe.

The viscosities, densities and surface tension of the resulting formulations were measured by automatic viscosimeter AVMn (Anton Paar), density meter DMA4500 (Anton Paar), and by rheometer AR-G2 (TA Instruments), respectively. Printability of all formulations was evaluated on the basis of theoretical models and confirmed by printing tests.

### 2.2. Printing deposition

Pyrex glass substrates of size 30 mm × 30 mm × 3 mm were used for titania immobilization. Firstly, it was necessary to pre-treat the glass plates in aqueous solution of detergent Neodisher (BMT, Czech Republic) in an ultrasound for 10 min to remove all dust and fat and other residues which could contaminate the surface. Consequently, these substrates were immersed to solution of Abesone (commercial dodecylbenzene sulphonic acid based surfactant) to enhance their wetting by the printed sol.

Titanium sols were deposited onto the Pyrex plates using an experimental printer FUJIFILM Dimatix (Dimatix Materials Printer DMP-2831). During filling the cartridge ink tank by the printing formulation, it was necessary to filter it through a 0.45 μm mesh size syringe filter in order to eliminate any aggregates and solid contaminants which might clog the printhead nozzles. The Dimatix 10 pL printhead containing 16 nozzles was attached to the filled ink tank and mounted into the Dimatix printer. The nozzle temperature was set up to 30 °C and the piezo driving voltage was set to 22 V. The "model liquid 2" waveform proved to be well useful for our sols. We studied the influence of different coating conditions on final structure of thin layers. We compared three droplet pitches (20 μm, 30 μm, 40 μm), three substrate temperatures (30 °C, 40 °C, 50 °C) and four levels of film thickness (from 1 to 4 layers printed in the "wet-to-wet" manner, i.e., the following layer was printed immediately after the previous one without any delay for drying). Finally, the printed substrates were placed onto a hot plate (temperature 110 °C) for 30 min to quickly evaporate the solvents and fix the layer. Subsequently, they were calcinated at 450 °C for 4 h with the ramp of 3 °C/min. After that, the samples were carefully investigated and the best deposition conditions were determined.

### 2.3. Characterization

The structure and quality of prepared layers were examined by optical microscope Nikon Eclipse E200. All prepared titania thin films were optically transparent, smooth and shiny. In the case of iron-doped samples we observed yellowish colouring. The $TiO_2$ layers adhered well to the Pyrex glass substrates after the calcination process. Optical micrographs were recorded by a digital camera Nikon D5000 mounted on the optical microscope.

Afterwards, the sample structure as well as homogeneity of titania thin layers were investigated by scanning electron microscopy (SEM Carl Zeiss Ultra Plus). Simultaneously, analysis of chemical composition was carried out by EDS (Oxford X-max with silicon drift detector). The influence of iron and silver doping was evaluated. The surface topology was further studied by atomic force microscopy (AFM NT-MDT Prima).

Crystal phase composition of $TiO_2$ was investigated by X-ray diffraction pattern measurement by using Cu Kβ as the radiation source. The samples were analyzed as prepared by printing, i.e., thin layers on the Pyrex substrate, and the scan range was from 20° to 90°. We used X-ray diffractometer SmartLab, Rigaku. Consequently, the crystallite size was calculated according to the Scherrer equation, where $B$ is constant equal 0.94, λ is the wavelength which is equal to 1.54 Å and $\beta$ is the width of peak at a half of the maximum height.

$$d = \frac{B\lambda}{\beta \cos\theta} \quad (1)$$

The analysis of band gap energy was performed by a reflectance measurement of powdered samples. The remaining volume of sols with different amount of iron and silver which had remained after printing was transformed to powdery oxide phase by calcination at the temperature of 450 °C for 4 h. Resulting powders were finely ground and used reflectance measurement carried out using a UV–vis spectrometer equipped with a reflectance fibre probe. The optical path consists of several optical fibres where six of them are connected with the lamp providing illumination of the sample (xenon strobe lamp) and one reading fibre connected to the

spectrometer. The reflectance was measured in the range of wavelength from 200 nm to 850 nm and a barium sulphate pressed pellet was used as a reflectance standard. Molar absorption coefficient was calculated according the formula ($\alpha = (1-R)^2/2R$), which is derived from the Kubelka–Munk theory.

The band gap energy was calculated for direct as well as for indirect transition. For the direct transition, the dependence of $(\alpha h\nu)^2$ on $(h\nu)$ is plotted where $(h\nu)$ is the photon energy. For the indirect one, we have to plot $(\alpha h\nu)^{1/2}$ as a function of photon energy. Consequently, band gap energy was found out from extrapolation of molar absorption coefficient to zero [35].

### 2.4. Photocatalysis

Photocatalytic activity of thin $TiO_2$ layers was evaluated as a degradation rate of stearic acid and 2,6-dichloroindophenol (DCIP) under UV radiation. Stearic acid was chosen as a model compound due to its very high stability under UV illumination in the absence of photocatalysts, and because of the kinetics of SA decomposition is usually simple and zero order [36]. Material printing was used once again for precise and repeatable deposition of stearic acid onto the titania layers. The printing composition mixture consisted of 1 mL of solution of stearic acid in toluene (30 g/L) and 9 mL of isobutyl alcohol. Deposition conditions were the following: temperature of substrate was 50 °C, droplet pitch was 20 μm. We printed two layers in order to create a sufficient thickness of stearic acid (0.01 mg/cm$^2$). The mineralization process was studied by FT-IR spectrometer (Nicolet Impact 400) and was manifested as the change of an integrated area under the absorption peaks in the 2700–3100 cm$^{-1}$ region. Osram HQL 125 W lamp with intensity of 2 mW/cm$^2$ was used as the irradiation source. The FT-IR absorption spectrum was measured offline (i.e., the irradiation was interrupted) in regular time intervals. Values of the peak area were calculated as an average of eight measurements from different areas of the irradiated layers.

Apart from the stearic acid experiment, photocatalytic activity was investigated also as the degradation rate of DCIP. This common dye offers the possibility of rapid visual qualitative and quantitative assessment of photocatalytic activity [37]. Similarly to the previous case, also DCIP was printed onto the titania surface. The conditions of this coating were the following: temperature of substrate was 45 °C, droplet pitch was 3 μm, and amount of layers was 3. In this case, the printed formulation consisted of 3 mL of 10% solution of polyvinylpyrrolidone in isopropyl alcohol, 3 mL of isopropyl alcohol, 3 mL of 2-propoxyethanol, 0.2 mL of glycerol, 30 mg of DCIP. The radiation source used in this case was UV diodes with wavelengths 320 nm (UVLUX 320-HL-3) and 374 nm (XSL-370-TB-5), both supplied by Roithner Laser. The intensity of irradiation was 1 mW/cm$^2$. Performing two experiments with different irradiation source should reveal the effect of doping.

The experiment was performed in a special in-house constructed reactor. It consists of a visible LED working as the light source for absorbance measurement and a slightly off-axis mounted UV LED working as the acting radiation source for photocatalyst activation. Both LEDs are mounted on the top of a light-tight measuring chamber covering the catalyst coated by a layer of indicator ink. Its photocatalytic decolourization was monitored by UV–vis spectroscopy – a collimator is mounted below the analyzed sample and aligned with the visible LED. Optical fibre then connects the collimator with an Ocean Optics Red-Tide UV–vis spectrometer and its software provides automated on-line data collecting every 1 min. The maximum absorption peak of DCIP is at the wavelength 600 nm so visible LED was selected accordingly. The same spectrometer can be also used for the determination of incident radiation intensity.

**Table 1**
Reological properties of prepared printing mixtures.

| | Surface tension (mN/m) | Density (g/cm$^3$) | Viscosity (mPa s) | $Z$ |
|---|---|---|---|---|
| Ti | 24.7173 | 0.8582 | 4.2238 | 4.8764 |
| 3Fe | 24.9028 | 0.8737 | 4.2628 | 4.8935 |
| 5Fe | 23.5392 | 0.8743 | 4.3140 | 4.7029 |
| 7Fe | 24.6895 | 0.8736 | 4.3189 | 4.8091 |
| Ag | 24.6358 | 0.8745 | 4.2191 | 4.9199 |
| Ag_3Fe | 24.7803 | 0.8735 | 4.2319 | 4.9165 |
| Ag_5Fe | 24.8115 | 0.8728 | 4.4085 | 4.7208 |
| Ag_7Fe | 24.9012 | 0.8771 | 4.4276 | 4.7205 |

## 3. Results and discussion

### 3.1. Printing conditions

Table 1 shows the values of $Z$ number which is one of the indicators used for the evaluation of drop formation behaviour (e.g. capillary break-off length and time, droplet volume and satellite formation). Some theories predict a stable drop formation in drop-on-demand systems when $Z > 2$ [38] while others determined that a printable fluid should have a $Z$ value between 1 and 10 [39]. It is also known that its lower limit is governed by the viscosity of fluid and its printing ability, while the upper limit is determined by the point at which multiple drops are formed instead of single droplet [32]. In our study the $Z$ values were around 5 for all optimized formulations reported in Table 1. Therefore, regardless of the differences in the theories we presume good printability of all the sols. This theoretical estimation was confirmed by empirical observations during printing. The drop formation characteristics of all compositions were studied by means of stroboscopic camera and interaction with substrate was observed by an optical microscope. Their jetting performance was excellent and so was the sol shelf-life in both filled cartridges and storage bottles. Nozzle blockage was only rarely observed and if occurred, it was easily recovered by the first following head cleaning cycle. No precipitation, aggregation, separation or gelling was observed over the period of 4 months.

The non-doped sol without iron or silver was used for the study of different deposition conditions and its influence on the final character of prepared films. Namely, the amount of cracks and the compactness of the layers were evaluated. The substrate temperature was the first factor the influence of which we investigated. We worked at temperature 30 °C, 40 °C and 50 °C. 30 °C was evaluated as the most favourable. We observed that in cases of 40 °C and 50 °C the solvent evaporated too fast which resulted to the creation of banding patterns (Fig. 1). After the comparison of different droplet pitch values we discovered that 40 μm is too high drop distance which means that the droplets were placed too far and the layers were not compact. On the other hand, droplet pitch 20 μm means formation of thicker layers which leads to higher stress during the calcination process. Subsequently, it caused creation of higher amount of cracks (Fig. 1). Droplets pitch 30 μm was evaluated as the best. Finally, we compared the samples consisting of different number layers. We observed a natural trend that higher amount of layers caused thicker coating and more cracks in the structure. Two-layered sample was discovered as the most suitable. The coverage of Pyrex substrate was not sufficient in case of one layer. On the other side, three or four layers leaded to formation of too high amount of cracks and the creation of non-homogeneous films (Fig. 1).

### 3.2. Analysis of the structure

Structure and homogeneity of titania thin layers was investigated by scanning electron microscopy. The layer of pure $TiO_2$ and

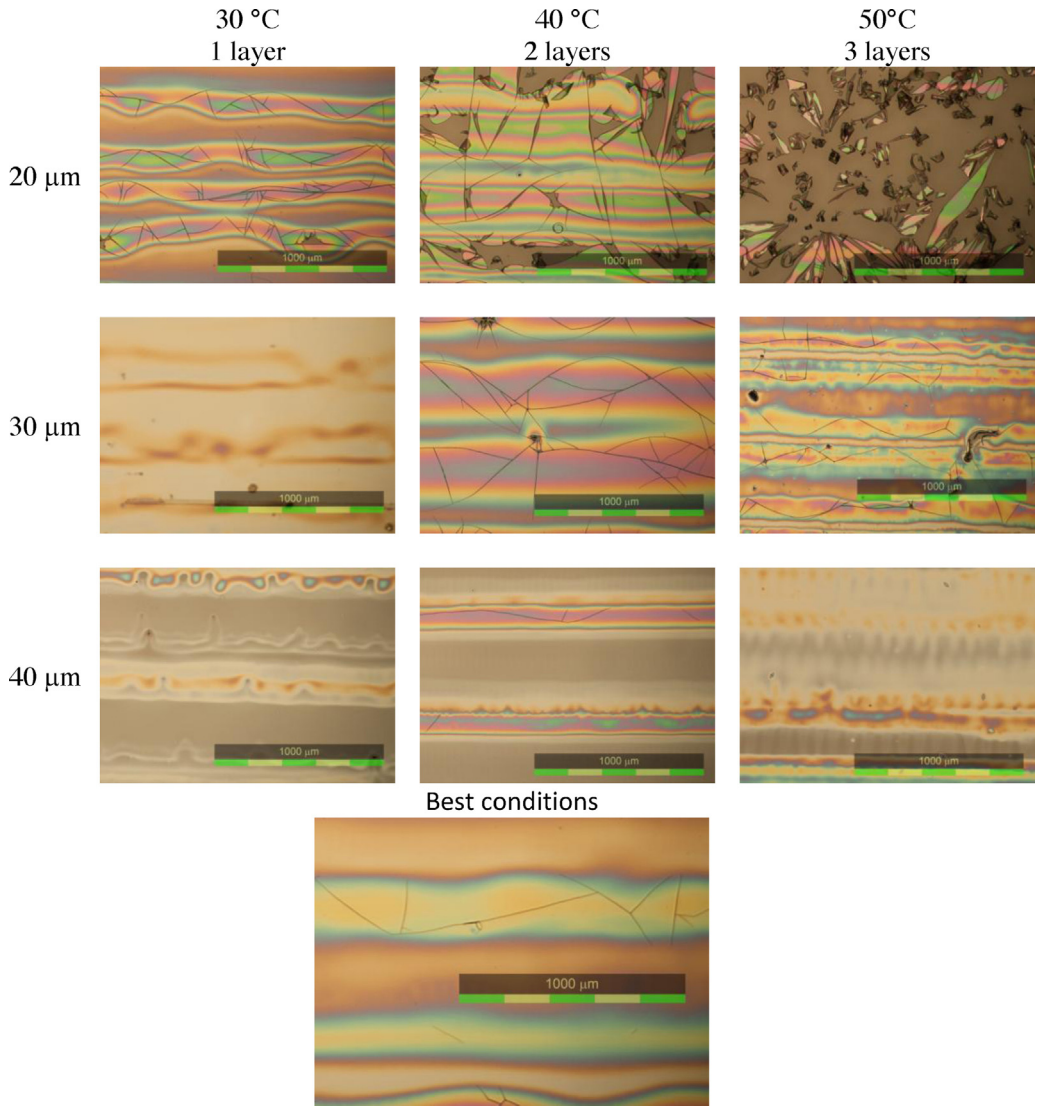


**Fig. 1.** Images from optical microscope; lines represents three different used droplets pitches; columns represent different substrates temperatures and amounts of layers; last image shows the best conditions (30 °C, 30 μm, 2 layers).

doped layers were compared. We discovered that all prepared samples were homogenous without any cracks. The grain size of $TiO_2$ doped by silver was a little higher than in case of pure anatase or $TiO_2$ doped by iron. Nevertheless, the grain size did not exceeded value of 10 nm (Fig. 2).

Chemical composition of layer was evaluated by EDS analysis performed simultaneously with SEM analysis. The results are shown in Fig. 3. Because the layers were quite thin we observe peak for Si which belongs to the substrate as the most intensive signal. In the case of doped titania we, can observed also peaks for Fe as well as for Ag. Peaks for Au and Pd occur in the spectra due to using AuPd as the metallization paste.

The topology of printed layers was evaluated by atomic force microscopy. The measurement was performed on the area of 0.25 $\mu m^2$. The record from this analysis is shown in Fig. 2. Grains of size approximately 10 nm are clearly apparent and account probably for titania grains. However we can find also bigger grains up to 25 nm which are attributed to the presence of silver nanoparticles.

### 3.3. XRD analysis

The crystal phase of prepared layers was investigated using X-ray diffraction. Pure anatase phase was determined in all samples.

**Table 2**
Crystallize sizes.

| | Crystallite size (nm) |
|---|---|
| Ti | 12.3 |
| 3Fe | 19.8 |
| 5Fe | 21.0 |
| 7Fe | 22.4 |
| Ag | 23.8 |
| Ag_3Fe | – |
| Ag_5Fe | – |
| Ag_7Fe | 22.4 |

In the case of doped $TiO_2$ we were not be able observed any specific peaks of iron or silver. We supposed that these peaks are hidden in the peak for anatase (Fig. 4).

It is well known that with increasing width of peaks the crystallite size decreases. This behaviour is described by the Scherrer equation (1). Most of our obtained peaks were wide which indicated that crystallite size was very low. The exact value of crystallite sizes is summarized in Table 2. We can observe values generally comparable to the estimated ones based on SEM imaging. We discovered that crystallite size in case of doped $TiO_2$ is higher than for pure

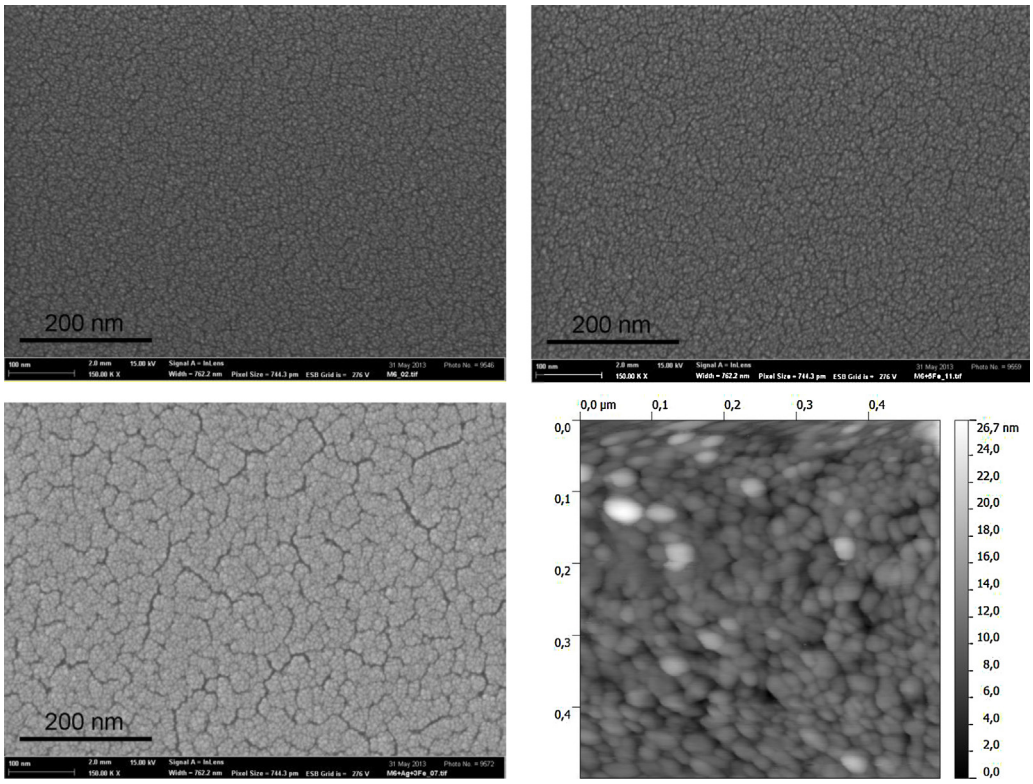


**Fig. 2.** Images form SEM analysis, pure $TiO_2$ (top, left); Fe-$TiO_2$ (top, right); Ag-$TiO_2$ (bottom, left) and AFM analysis Ti_Ag_3Fe (bottom, right).

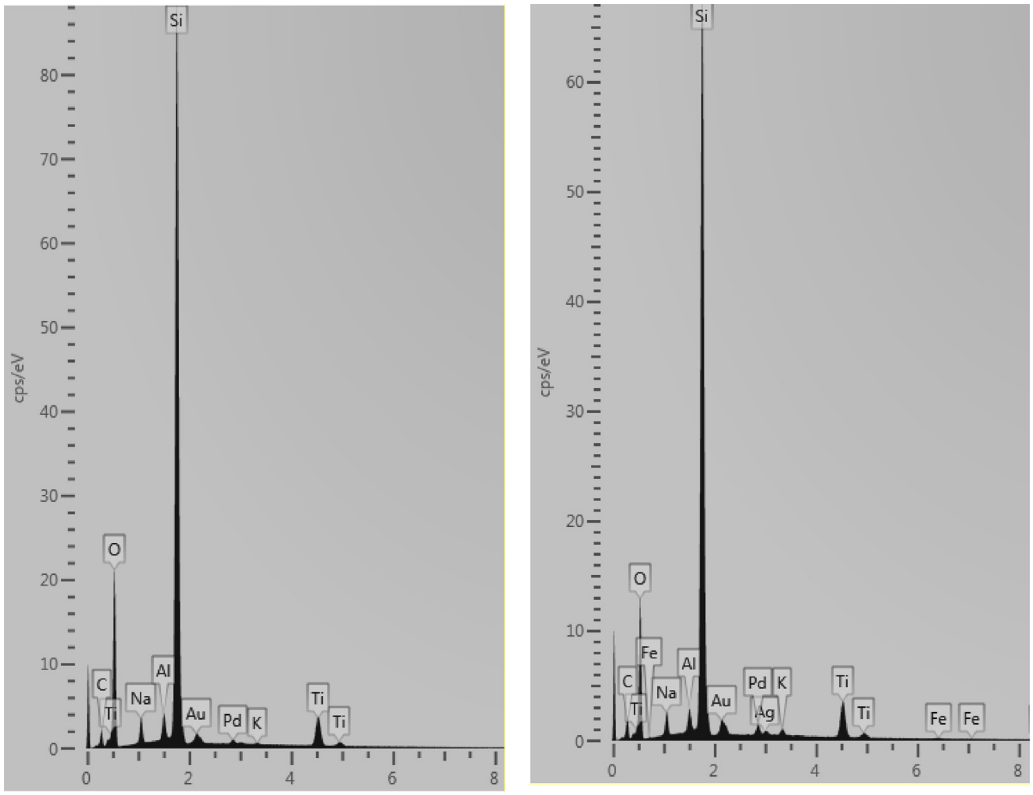


**Fig. 3.** Chemical composition of two layers; pure $TiO_2$ (left); $TiO_2$ doped by Ag and Fe (7%) (right).

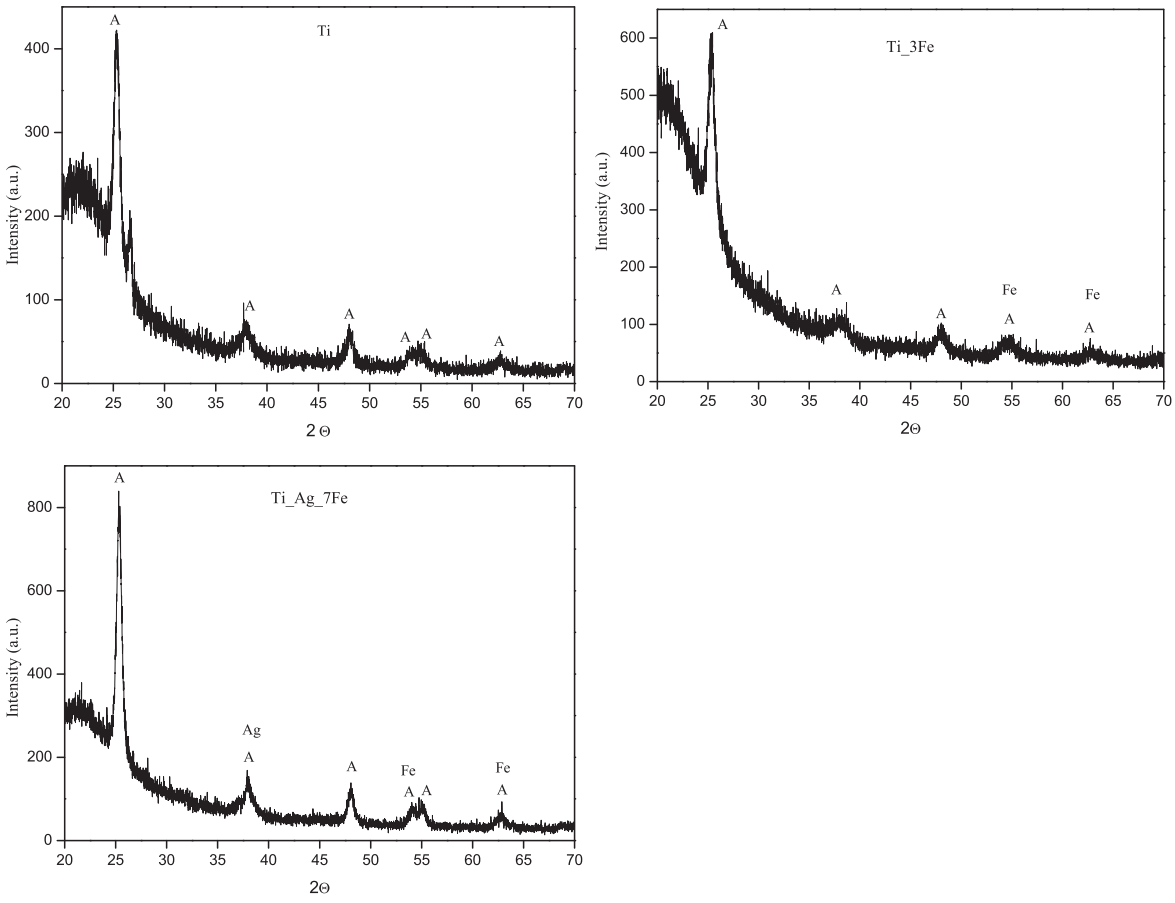


**Fig. 4.** XRD spectra; pure titania (top, left), Ti_3Fe (top, right) and Ti_Ag_7Fe (bottom, left).

titania. Crystallite sizes for samples Ag_3Fe as well as for Ag_5Fe were not measured because of too low peaks intensity.

### 3.4. Band gap energy

The absorption coefficient was calculated according to equation mentioned in Section 2.3 from reflectance measurement. Obtained coefficient was plotted as a function of photon energy for both type of transition, direct as well as indirect. Consequently, the band gap energy was determined by the extrapolation of the linear part of this dependence to zero. Because the powdered samples with silver were dark, the band gap energy could not be found out for these doped $TiO_2$. It means that in these cases, most of the falling light was absorbed so only small portion was reflected.

We discovered that all prepared $TiO_2$ samples were direct photocatalysts. Obtained band gap energies were followed: Ti (3.20 eV), 3Fe (2.77 eV), 5Fe (2.60 eV) and 7Fe (2.52 eV). We found out that with increasing iron content the band gap energy was decreasing. It means that iron caused red shift of absorption edge.

### 3.5. Photocatalysis

#### 3.5.1. Stearic acid

FT-IR absorption spectra of stearic acid during the degradation process are shown in Fig. 5. Three main peak of stearic acid are situated in range from 2600 to 3200 $cm^{-1}$. This decomposition reaction took place under the UV radiation with intensity 2 $mW/cm^2$. Three peaks are observed in the spectrum: 2958 $cm^{-1}$, 2923 $cm^{-1}$ and 2853 $cm^{-1}$, corresponding to the methyl and methylene groups of stearic acid, respectively.

Naturally, the maxima of the peaks are decreasing during the degradation of stearic acid. Simultaneously, a blank experiment (without photocatalyst) was performed. In this case, no change in the stearic acid FT-IR absorption spectrum over the irradiation period occurred (Fig. 5).

The overall comparison of photocatalytic activity of prepared samples is shown in Fig. 5. As we can observe, pure $TiO_2$ without iron or silver is the most active sample. We observed that with increasing amount of iron the rate of degradation was lower. It indicates that iron was probably adsorbed in the specific sites which lead to decreasing final photocatalytic activity. Total time of 60 min was sufficient for total decomposition of stearic acid of all samples. In case of pure $TiO_2$ required time was only 20 min.

We realized that 20 min duration of the experiment was sufficient for a complete removal of stearic acid only for pure $TiO_2$. Reaction time 60 min was necessary for most of the samples.

#### 3.5.2. 2,6-Dichloroindophenol

Apart from stearic acid, photocatalytic activity was evaluated also as the degradation rate of DCIP. Dechloration accompanied by discoloration is the first step of the degradation process. Subsequently, further oxidation of the carbon molecular skeleton takes place. It leads to the formation of short carboxylic acids. Finally, these acids undergo decarboxylation and they are totally cleaved to $CO_2$ and water [40–42]. UV–vis spectroscopy is easy and suitable technique for analysis the discolouration. DCIP was chosen as a model compound of dye-polluted waste water which is one of the target application fields for photocatalytic process. DCIP was suitable dye because of an easy spectroscopic detection and more over due to its reasonably low absorption at wavelengths 360–400 nm. The absorption maximum of DCIP is at wavelength 600 nm (Fig. 6).

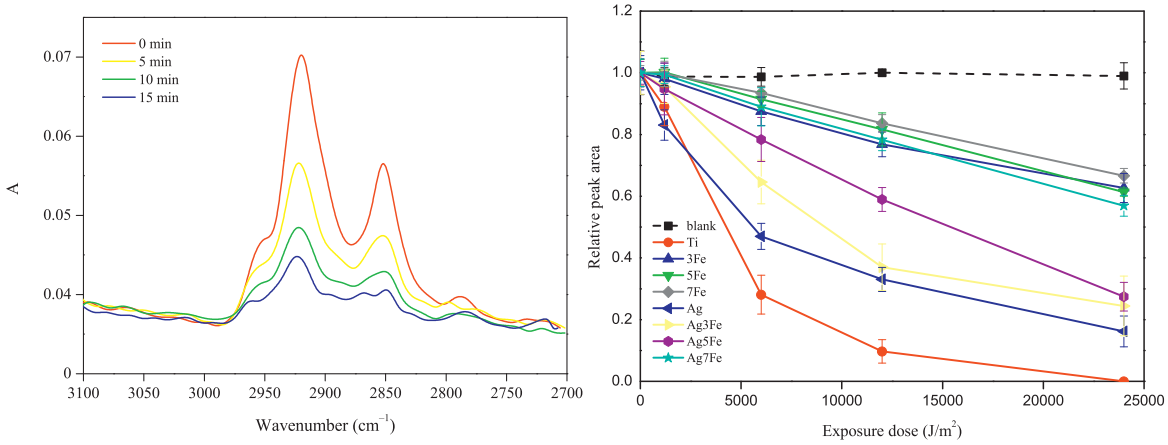


**Fig. 5.** FT-IR absorption spectra of stearic acid during the degradation process (left) and decreasing of relative peaks areas.

DCIP as well as stearic acid was printed onto the titania dioxide layers and a thin coating of indicator ink resulted. In order to investigate the influence of dopant type and amount, two LED diodes with absorption maximum at wavelengths 320 nm and 374 nm (Fig. 6) were applied for this purpose. The intensity of used lights was carefully set to 1 mW/cm$^2$ in both cases. However, it is important to realize that this irradiation intensity was delivered by different molar photonic flux: one photon of 320 nm carries approximately 6.21E-18 J while one photon of 374 nm carries 5.31E-18 J. Therefore, to achieve identical energy flux, the 374 nm source needs to emit cca 1.17 times more photons than the 320 nm source.

Decreasing of DCIP absorption was observed during the experiments and the fibre spectrophotometer was conveniently used for automated online recording of absorbance. It was measured continuously and data were saved each one minutes. Total time of one experiment was 25 min because this time was sufficient for complete decolouration for some samples. Finally, the rate constant was calculated as an average from three independent measurements. Simultaneously, a blank experiment (no catalyst) was performed and its rate constant was subtracted from obtained rate constant of samples with catalyst in order to the rates for direct photocatalysis of DCIP.

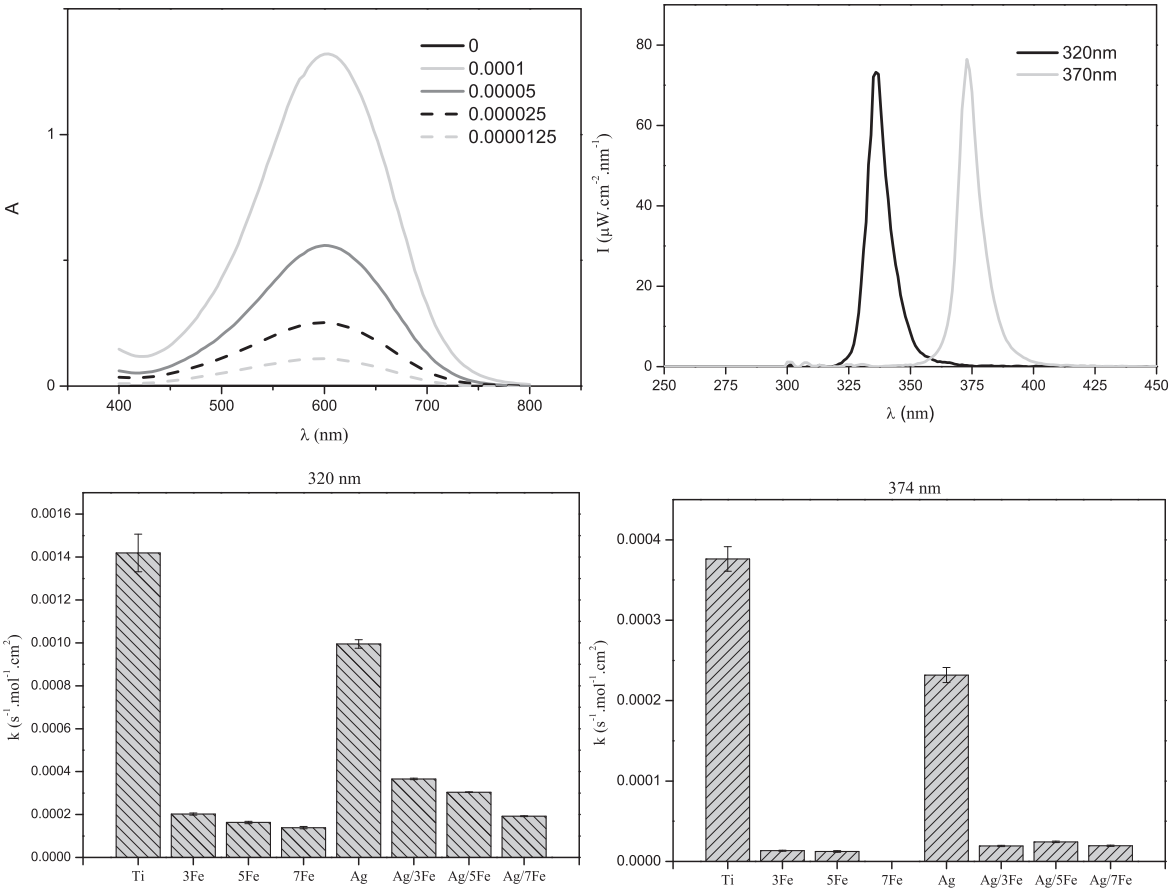


**Fig. 6.** DCIP decomposition, absorption spectra of DCIP for different initial concentrations (top, left); emission spectra of LED diodes (top, right); comparison of rate constant of the samples for diode 320 nm (bottom, left) and comparison of rate constant of the samples for diode 370 nm (bottom, right).

The results from this measurement are summarized in Fig. 6. We discovered that increasing amount of iron in the sample leads to decreasing of photocatalytic activity. This dependence was observed for both used wavelengths. This result indicates that iron ions were adsorbed to the active site which caused a reduction of $TiO_2$ activity. Silver had a positive effect on the photocatalytic activity in the presence of iron. On the other side, this co-catalyst alone caused the decreasing of titania activity but not so high as in case of iron. We explained this decreasing by using a too high amount of silver. Generally, small concentration of silver causes creation of more active $TiO_2$ [43,44]. We supposed that in our cases, the concentration was too high and some particles were adsorbed on the active site which leaded to certain decreasing of photocatalytic activity.

After the comparison of rate constants for diodes with absorption maximum of 320 nm and 370 nm we found out that increasing of wavelength resulted into decreasing of photocatalytic activity.

## 4. Conclusion

Iron and silver doped titanium dioxide was synthesized by the sol–gel process employing PEG as the anticracking agent and conveniently deposited by inkjet material printing. The solvent type and concentration in the printing formulation was optimized and the concentration of PEG was set to 4 g/L providing a good compromise between the intensity of its effect and the viscosity increase inevitably accompanying its introduction into the printing formulation. Full rheological characterization was performed and the jetting performance was theoretically evaluated by means of *Z*-number rheologic model. Empirical jetting behaviour confirmed the positive expectations and all formulation showed flawless printability. The *Z*-number was practically identical for all studied formulations therefore printed catalyst samples of equal quality were possible to prepare and the influence of added amount of iron and silver on the final physical properties as well as photocatalytic activity were investigated. These samples were compared with pure $TiO_2$ fabricated in the same way.

Once well performing jettable compositions were ready, different printing conditions were tested and the quality of created thin films was studied. Temperature of 30 °C, droplet pitch 30 μm and two overprinted layers were eventually evaluated as the best conditions. These were eventually used for the fabrication of the doped samples set investigated in this study. After firing the printed layers at 450 °C, homogeneous compact layers with grain size around 10 nm were obtained.

We observed that structure of the film was only slightly changed with the silver addition. In this case we could observe higher grains. In the case of iron we did not see any differences. From XRD analysis we found out that pure anatase phase was present in all samples. Band gap energy of non-doped titania was determined at 3.20 eV which is a typical value for pure anatase. Subsequently, we observed that with increasing amount of Fe band the gap energy decreased. This decrease of band gap indicates that shift of absorption edge to higher wavelength occurred however it did not lead to increasing of photocatalytic activity. We were not able to measure $E_g$ for silver doped titania because of a uniform dark grey colour of prepared powders resulting into a high absorption of light and very small reflection with no pronounced peaks nor edges.

Photocatalytic activity of prepared layers was quite high [45] however we did not observed any increase of their activity in the case of doped $TiO_2$ samples [46,47]. Decomposition of SA was performed at 20 min and DCIP was completely decomposed in 25 min for the best samples. From the strictly photocatalytic activity point of view, our simple experiments involving silver nitrate and iron (III) acetylacetonate did not result into any breakthrough in the field of titania doping and red-shift sensitization. However, we managed to formulate sol–gel based inkjettable formulation capable to contain a wide varied of dopants and delivering consistent printing performance. The original un-doped formulation remains interesting on its own because of its jetting reliability and certainly deserves further study employing another doping agents.

## Acknowledgements

Authors thank to Ministry of Education, Youth and Sport of Czech Republic for support by project CZ.1.07/2.3.00/30.0005, also by project LD12004 and also to Central European Institute of Technology (CEITEC). Authors also appreciate the work of Zdenek Spotz who performed XRD analysis, Jan Cupera who provides SEM imaging, David Skoda who carried out AFM analysis and Jitka Krouska for rheological characterization.

## References

[1] M.P. Seabra, I.M.M. Salvado, J.A. Labrincha, Ceramics International 37 (2011) 3317.
[2] A.V. Agafonov, A.V. Vinogradov, Journal of Sol–Gel Science and Technology 49 (2009) 180.
[3] Y. Wu, J. Zhanga, L. Xiao, F. Chen, Applied Surface Science 256 (2010) 4260.
[4] G.C. Collazzo, E.L. Foletto, S.L. Jahn, M.A. Villett, Journal of Environmental Management 98 (2012) 107.
[5] G. Kenanakis, N. Katsarakis, Applied Catalysis A: General 378 (2010) 227.
[6] G. Kenanakisa, Z. Giannakoudakis, D. Vernardou, C. Savvakis, N. Katsarakis, Catalysis Today 151 (2010) 34.
[7] M. Mrowetz, E. Selli, Journal of Photochemistry and Photobiology A: Chemistry 180 (2006) 15.
[8] M. Karkmaz, E. Puzenat, C. Guillard, J.M. Herrmann, Applied Catalysis B: Environmental 51 (2004) 183.
[9] T.H. Kim, V.R. Gonzalez, G. Gyawali, S.H. Cho, T. Sekino, Catalysis Today 212 (2013) 75.
[10] X.Z. Shen, Z.C. Liu, S.M. Xie, J. Guo, Journal of Hazardous Materials 162 (2009) 1193.
[11] Y.H. Tseng, D.S. Sun, W.S. Wu, H. Chan, M.S. Syue, H.C. Ho, H.H. Chang, Biochimica et Biophysica Acta 1830 (2013) 3787.
[12] N.R. Khalida, E. Ahmeda, Z. Hong, Y. Zhang, M. Ahmadag, Current Applied Physics 12 (2012) 1485.
[13] L. Cui, Y. Wang, M. Niu, G. Chen, Y. Cheng, Journal of Solid State Chemistry 182 (2009) 2785.
[14] C.S. Chi, J. Choi, Y. Jeong, O.Y. Lee, H.J. Ohhfdash, Thin Solid Films 519 (2011) 4676.
[15] W. Pingxiao, T. Jianwen, D. Zhi, Materials Chemistry and Physics 103 (2007) 264.
[16] Z. Zhang, X. Wang, J. Long, Q. Gu, Z. Ding, X. Fu, Journal of Catalysis 276 (2010) 201.
[17] X.K. Wanga, C. Wanga, W.Q. Jianga, W.L. Guoc, J.G. Wang, Chemical Engineering Journal 189/190 (2012) 288.
[18] Y. Liu, J. Liu, Y. Lin, Y. Zhang, Y. Wei, Ceramics International 35 (2009) 3061.
[19] S. Yang, S. Guo, D. Xu, H. Xue, H. Kou, J. Wang, G. Zhu, Journal of Fluorine Chemistry 150 (2013) 78.
[20] K. Bhattacharyya, A.K. Patra, P.U. Sastry, A.K. Tyagi, Journal of Alloys and Compounds 482 (2009) 256.
[21] S. Yuan, R.Q. Sheng, J.L. Zhang, F. Chen, Surface Science and Catalysis 165 (2007) 261.
[22] F.J. Ren, Y.H. Ling, J.Y. Feng, Applied Surface Science 256 (2010) 3735.
[23] J.G. Yu, Q.J. Xiang, M.H. Zhou, Applied Catalysis B 17 (2009) 595.
[24] J.G. Yu, H.G. Yu, B. Cheng, X.J. Zhao, J.C. Yu, W.K. Ho, Journal of Physical Chemistry B 107 (2003) 13871.
[25] A. Panniello, M.L. Curri, D. Diso, A. Licciulli, V. Locaputo, A. Agostiano, R. Comparelli, G. Mascolo, Applied Catalysis B 121 (2012) 190.
[26] R.S. Sonawane, S.G. Hegde, M.K. Dongare, Materials Chemistry and Physics 77 (2002) 744.
[27] C. Su, B.Y. Hong, C.M. Tseng, Catalysis Today 96 (2004) 119–126.
[28] M. Wu, G. Lin, D. Chen, G. Wang, D. He, S. Feng, R. Xu, Chemistry of Materials 14 (2002) 1974.
[29] R. Rioboo, M. Marengo, C. Tropea, Experiments in Fluids 3 (2002) 112.
[30] R. Crooks, J. Cooper-White, D.V. Boger, Chemical Engineering Science 56 (2001) 5575.
[31] S. Yangsoo, K. Chongyoup, Journal of Non-Newtonian Fluid 1–3 (2009) 78.
[32] V. Bergeron, D. Bonn, J.Y. Martin, L. Vovelle, Nature 405 (2000) 772.
[33] D. Jang, D. Kim, J. Moon, Langmuir 5 (2009) 2629.
[34] M. Cerna, M. Vesely, P. Dzik, Catalysis Today 161 (2011) 97.
[35] K.M. Reddy, S.V. Manorama, A.R. Reddy, Materials Chemistry and Physics 78 (2002) 239.

[36] A. Mills, Y.J. Wang, Journal of Photochemistry and Photobiology A: Chemistry 182 (2006) 181.
[37] A. Mills, Y.M. McGrady, Journal of Photochemistry and Photobiology A: Chemistry 193 (2008) 228.
[38] J.E. Fromm, IBM Journal of Research and Development 3 (1984) 322.
[39] N. Reis, B. Derby, Materials Research Society Symposium Proceedings (2000) 117.
[40] V. Brezova, M. Ceppan, M. Vesely, L. Lapcik, Chemical Papers 45 (1991) 233.
[41] D.F. Ollis, Environmental Science and Technology 19 (1985) 480.
[42] R.W. Matthews, Journal of the Chemical Society, Faraday Transactions 1 85 (1989) 1291.
[43] R.P. Suri, H.M. Thornton, M. Muruganandham, Environmental Technology 33 (2012) 1651.
[44] Y. Zhang, Y. Huang, Y. Wang, X. Ji, S.J. Shih, B. Jia, Journal of Nanoscience and Nanotechnology 6 (2009) 3904.
[45] C.W. Dunnill, K. Page, Z.A. Aiken, S. Noimark, G. Hyett, A. Kafizas, J. Pratten, M. Wilson, I.P. Parkin, Journal of Photochemistry and Photobiology A: Chemistry 220 (2011) 113.
[46] P. Bouras, E. Stathanos, P. Lianos, Applied Catalysis B: Environmental 73 (2007) 51.
[47] J.O. Carneiro, V. Teixeira, A. Portintha, L. Dupak, A. Magalhaes, P. Coutinho, Vacuum 78 (2005) 37.

Catalysis Today 230 (2014) 152–157

Contents lists available at ScienceDirect

Catalysis Today

journal homepage: www.elsevier.com/locate/cattod

# Photo-electrochemical properties of ZnO and $TiO_2$ layers in ionic liquid environment

P. Dytrych [a], P. Kluson [a,*], P. Dzik [b], M. Vesely [b], M. Morozova [a], Z. Sedlakova [a], O. Solcova [a]

[a] Institute of Chemical Process Fundamentals, Academy of Sciences of the Czech Republic, Rozvojova 135, Prague 6, Czech Republic
[b] Faculty of Chemistry, Brno University of Technology, Purkynova 118, Brno, Czech Republic

ARTICLE INFO

*Article history:*
Received 20 July 2013
Received in revised form 10 October 2013
Accepted 11 October 2013
Available online 8 November 2013

*Keywords:*
Room temperature ionic liquids
Reverse micelles
Piezoelectric jet printing
Semiconducting metal oxides

ABSTRACT

Photoinduced electrochemical functionality of uniform $TiO_2$ and ZnO films prepared by sol–gel method, in the former case in the reverse micelle environment, was studied using a specific type of ionic liquids as electrolytes. The coating part was arranged as piezoelectric ink-jet printing. Ionic liquids could be regarded as nanostructured fluids with two distinctive kinds of spatial domain: one ionic, the other non-polar. The driving force for the segregation of the nonpolar chains is energetic. They are excluded from the cohesive network of positive and negative charges that is formed by the charged groups of the ions in close contact. If side-chains are too short they do not disturb the ionic network significantly and, they do not possess enough conformational freedom to adopt low energy configuration. By increasing the chain-length the role of its spatial arrangement becomes important. Such features must be reflected in their specific behaviour as electrolytes in the contact with photoactive semiconducting thin films. Attention was also paid to the correlation of the values of generated photocurrent densities in layers with the fluidity and conductivity of the used ionic liquids.



## 1. Introduction

In the past years endless number of ZnO, $CeO_2$, $TiO_2$, etc. based functional materials have been described. In terms of their photo-induced functionality two types of mutually dependent sub-functionalities must be always considered. The primary function is associated with the photo-induced generation of the hole–electron pair. If the particular material is identified as sufficiently effective in this manner it can be considered for the next step, for example as heterogeneous photocatalyst. Uniform functional films of nanoscopic metal oxides could be produced in many possible routines. One of such methods is the bottom-up generation of ordered structure nanoparticles in cores of reverse micelles [1,2]. The overall process is organized as the sol–gel method, the coating technique then as piezoelectric jet printing [3–6].

Undoubtedly titanium and zinc oxides are the most extensively studied transition-metal oxides. There are many possible applications that might be taken into account depending on their structural and functional features. Here we report on the possible utilization of various types of room temperature ionic liquids (RTILs) as electrolytes in the step of functional characterization of the produced nanoscopic ZnO and $TiO_2$ films. Hundreds of structurally different ionic liquids are currently available. However, the most commonly used are those with the imidazolium type of cation combined either with hexafluorophosphate or tetrafluoroborate counter ions. Another attractive group of ILs might be ranked among quaternary ammonium salts (QAS) [7]. Ionic liquids could be regarded as nanostructured fluids with two distinctive kinds of spatial domain: one ionic, the other non-polar. The driving force for the segregation of the nonpolar chains is believed to be energetic. They are excluded from the cohesive network of positive and negative charges that is formed by the charged groups of the ions in close contact [8,9]. If the side-chains are too short, they do not disturb the ionic network significantly and, also, they do not possess enough conformational freedom to adopt a low energy configuration. However, increasing the chain-length the role of its spatial arrangement becomes much more important. Obviously such features must be also reflected in their specific behaviour as electrolytes in the contact with photoactive semiconducting thin films [10–13].

To the best of our knowledge electrochemical interactions of these types of RTILs with the reverse micelles templated semiconducting nanoparticles have not been reported yet. Special attention was also paid to the correlation of the values of generated photocurrent densities in layers with the fluidity and conductivity of the used RTIL's.

* Corresponding author. Tel.: +420 220 390 340; fax: +420 220 920 661.
*E-mail addresses:* kluson@icpf.cas.cz, p.kluson@seznam.cz, kluson@seznam.cz (P. Kluson).
*URL:* http://www.icpf.cas.cz/hana (P. Kluson).

0920-5861/$ – see front matter © 2013 Elsevier B.V. All rights reserved.
http://dx.doi.org/10.1016/j.cattod.2013.10.048

## 2. Experimental part

### 2.1. Layer's preparation

All $TiO_2$ and ZnO layers were prepared by means of the sol–gel method. The $TiO_2$ films were produced from titanium isopropoxide in the reverse micelles used as molecular templates at very low water to surfactant ratio. This modification allows generation of very uniform particles as specified in details elsewhere [1,2,14–16]. The method was previously optimized for piezoelectric ink-jet printing [3–6]. The ZnO films were prepared by standard sol–gel technique involving diethanolamine (DEA) (p.a., Penta, Czech Republic), zinc acetate dihydrate (ZA) (Sigma Aldrich) and propan-2-ol as solvent. The molar ratio between ZA and DEA was held at 1:1, and the concentration of ZA was 0.45 mol $L^{-1}$. First propan-2-ol was mixed with ZA for 10 min to form a clear and transparent solution. Subsequently DEA was added to the solution and the arising sol was stirred for 5 min.

In both cases inkjet printer Fujifilm Dimatix 2830 was used for deposition of the liquid sols on substrates. The sol was loaded into the Dimatix ink tank and the Dimatix 10 pL printing head with the piezoelectric nozzles attached to the tank. This equipment was mounted into the Dimatix printer. As substrate the conductive ITO glass (5–15 Ω $cm^{-1}$, Delta-Technologies Ltd., USA) and the soda-lime microscopic glass plates were used. In the case of $TiO_2$ layers drying (110 °C for 30 min) and calcination steps (450 °C for 4 h) were performed after each coating cycle. ZnO layers were treated by drying (110 °C for 30 min) and then calcined at 500 °C for 4 h. These conditions were already previously optimized [1,3–6,14–18].

### 2.2. Layers' structural and functional characterizations

The crystallographic form and the particle size of the $TiO_2$ and ZnO layers were determined by XRD analysis (Panalytical-MRD diffractometer with the Cu anode) and by Raman spectroscopy (Raman Dispersive Spectrometer Nicolet Almega XR). Surface properties of the layers were studied by SEM (Hitachi S4700) and AFM (Thericroscopes) microscopy techniques. Layers' thicknesses were evaluated from SEM images. Values of absorption edges were elucidated from UV–Vis spectra (Perkin-Elmer Lambda 35 equipped with a Labsphere RSA-PE-20 integration sphere).

The photo-induced properties of the $TiO_2$/ITO and ZnO/ITO electrodes in 0.1 M $Na_2SO_4$ solution as electrolyte were investigated by means of photo-electrochemical measurements under UV irradiation in the three-electrode Pyrex cell. Prepared films were used as working electrodes and they were irradiated with the light beam of the wavelength of 365 nm. A saturated Ag/AgCl electrode and a platinum plate were used as the reference and the auxiliary electrodes, respectively. The incident light intensity was measured by UV-meter (UV Light Meter UVA-365). The irradiation intensity was 0.4 mW $cm^{-2}$ at 365 nm. Detailed description of the electrochemical set-up and the used electrochemical methodology were reported previously [19–21].

Initially a cyclic voltammetry (CV) was carried out. The CV was carried out from −200 mV to 1200 mV. The linear change of potential was 50 mV $s^{-1}$. The next measurement was a linear voltammetry (LV) with the linear speed of potential change 10 mV $s^{-1}$ and starting again at −200 mV. The light was switched on after 5 s and kept on for 5 s. Afterwards the light was switched off for the next 5 s. These periods were repeated until the potential hit the final value of 1200 mV against the saturated Ag/AgCl electrode. The next method was the amperometry at constant voltage of 0.6 V. In the first 30 s and the last 30 s the irradiation was switched off. Finally the OCP (open circuit potential) was performed. The OCP started with 30 s in the dark then the layers were irradiated for 60 s followed by 60 s of dark.

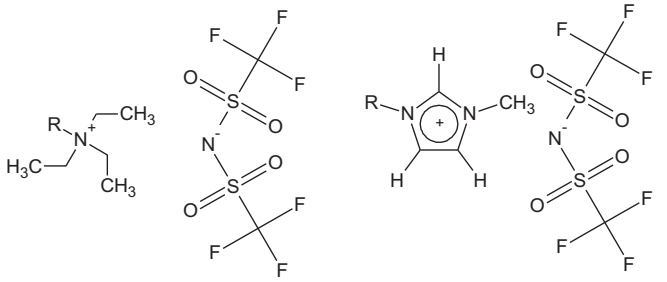


**Fig. 1.** (a) *N*-alkyl-triethylammonium bis(trifluoromethanesulfonyl) imides ($N_{[R,222]}Tf_2N$, $R$ = 4, 8 and 12). (b) *N*-alkyl, *N*′-methylimidazolium bis(trifluoromethanesulfonyl) imides (RMIM $Tf_2N$, $R$ = 2, 3 and 4).

Besides 0.1 M $Na_2SO_4$ specific types of ionic liquids were used as electrolytes [7]. Photo-electrochemical behaviour of the $TiO_2$/ITO and ZnO/ITO electrodes in the ionic liquid (RTIL) environment was monitored using the same sequence of electrochemical methods as for the $Na_2SO_4$ electrolyte. Molecular structures of the used ionic liquids are shown in Fig. 1. The ionic liquids differed in the number of carbons on the quaternary bonded nitrogen atom (QAS), and on nitrogen in imidazolium (RMIM). In Table 1 properties of ionic liquids employed to construct the Walden plot [22,23] are summarized. Tabled values were used to specify the current density by means of the dynamic viscosity and conductivity.

## 3. Results and discussion

### 3.1. Characterization of $TiO_2$ and ZnO thin layers

All prepared $TiO_2$ layers produced by piezoelectric inkjet printing possessed the crystallographic form of anatase (0 0 0 1 dominating orientation). The particle size was 6 ± 2 nm evaluated by the Scherrer equation, and 8 ± 2 nm and by the deconvolution method [24,25]. The only crystallographic form determined in the thin layers of ZnO was wurtzite with predominant 0 0 0 2 orientation. The particle size was 12 ± 2 (15 ± 2) (Table 2). For the surface morphology AFM analysis was employed. It provided information on the relative surface roughness expressed here as the rms factor (Table 2, Fig. 2.). All tested samples consisted of three layers (produced in 1–3 consecutive coating cycles as optimized previously [3–6,17]). The thicknesses of films were estimated from the SEM images (Fig. 2). It was found that the $TiO_2$ sample with same number of inkjet printed cycles revealed the thickness approximately of 340 nm, the ZnO layers were about 250 nm. Locations of absorption edges of nanoparticulate $TiO_2$/ITO and ZnO/ITO electrodes were evaluated from absorption spectra for $TiO_2$ and ZnO layers deposited on microscopic glass (Table 2). For $TiO_2$ the absorption edge was located around 365 nm with very sharp discontinuity, for ZnO it was determined at around 385 nm with less sharp increase of absorption.

### 3.2. Electrochemical properties in standard electrolyte environment

All prepared layers possessed very good photo-induced charge separation characteristics. Dependence of the generated current density on the linearly increased potential is illustrated in Fig. 3. The linear voltammetry plot represents the polarization curves of the ink-jet printed $TiO_2$ and ZnO film electrodes in 0.1 mol $L^{-1}$ $Na_2SO_4$ solutions. These measurements proved their distinctive behaviour in the UV region, in which all layers reacted immediately and reproducibly to the illumination. Values of the generated

**Table 1**
Physical and chemical properties of the studied RTILs.

| $T = 25\,^{\circ}C$ (298.15 K) | Dynamic viscosity $\eta$ [Pa s] | Conductivity $\sigma$ [S m$^{-1}$] | Molar volume [cm$^3$ mol$^{-1}$] |
|---|---|---|---|
| EMIM $Tf_2N$ | 0.032 | 0.91 | 257.9 |
| PMIM $Tf_2N$ | 0.0416 | 0.62 | 274.8 |
| BMIM $Tf_2N$ | 0.0626 | 0.41 | 291.2 |
| $N_{[4,222]}Tf_2N$ | 0.179 | 0.92 | 327.9 |
| $N_{[8,222]}$ $Tf_2N$ | 0.239 | 0.60 | 395.8 |
| $N_{[12,222]}$ $Tf_2N$ | 0.322 | 0.26 | 464.3 |

**Table 2**
Structural characteristics of the $TiO_2$ and ZnO layers.

| Thin layer | XRD | Particle size/ deconvolution [nm] | Particle size/ Scherrer [nm] | Raman spectroscopy | Absorption edge [nm] | Thickness [nm] | AFM rms factor (nm) |
|---|---|---|---|---|---|---|---|
| $TiO_2$ | Anatase | $8 \pm 2$ | $6 \pm 2$ | Anatase | 365 | $340 \pm 30$ | 1.4 |
| ZnO | Wurtzite | $15 \pm 2$ | $12 \pm 2$ | Wurtzite | 385 | $250 \pm 30$ | 1.5 |

photocurrents in the positive potential area for $TiO_2$ were constant and it reached the characteristic plateau at both irradiated intervals. At negative potential (−200 mV) the photocurrents were also generated, however, their values were significantly lower with the gradual growth to the constant level. ZnO thin layers also revealed a very good photo-response in the UV region. Nevertheless their photo-response stability was not as good as for the $TiO_2$ films (see also Fig. 3.).

Values of generated photocurrents were measured at constant potential (0.6 V) by amperometry. The obtained curves indicate the photocurrent–time behaviour of the layers. This experiment shows the efficiency of the prepared $TiO_2$ and ZnO electrodes to reach in the 5 min and 20 min irradiation interval almost a constant photocurrent. The photo-generated current decreased slowly and the steady state was reached after 5 min for $TiO_2$, (see Fig. 3. right), but the absolute value of the photo-generated current was low in comparison with previously reported $TiO_2$ layers prepared with assistance of various types of plasma [14,16,17,19]. The very small but highly uniform $TiO_2$ particles having their origin the reverse-micelle templating environment increased enormously the surface to volume ratio. The inter-particle contacts then may serve as efficient recombination centres decreasing the measured current densities. For ZnO the current density reached higher values, but the stability in time was not as good as for $TiO_2$. The measured samples embodied the very sharp maximum of the reached photocurrent densities. This so-called current peak appears immediately at the first moment of the irradiation. Further, the curves decrease slowly to get the steady state values. The instantaneous increase of generated photocurrent densities means a rapid electrons–holes generation and separation at the space charge region. The decrease is assigned to their recombination.

The open circuit potential (OCP) was measured to focus on the evaluation of the efficiency of separation of electrons and holes. The photo-potential ($E_{oc}$) decay was also measured. Upon the UV irradiation the open circuit potential shifts immediately to more negative values, which reflects rising of the major charge carriers (electrons)

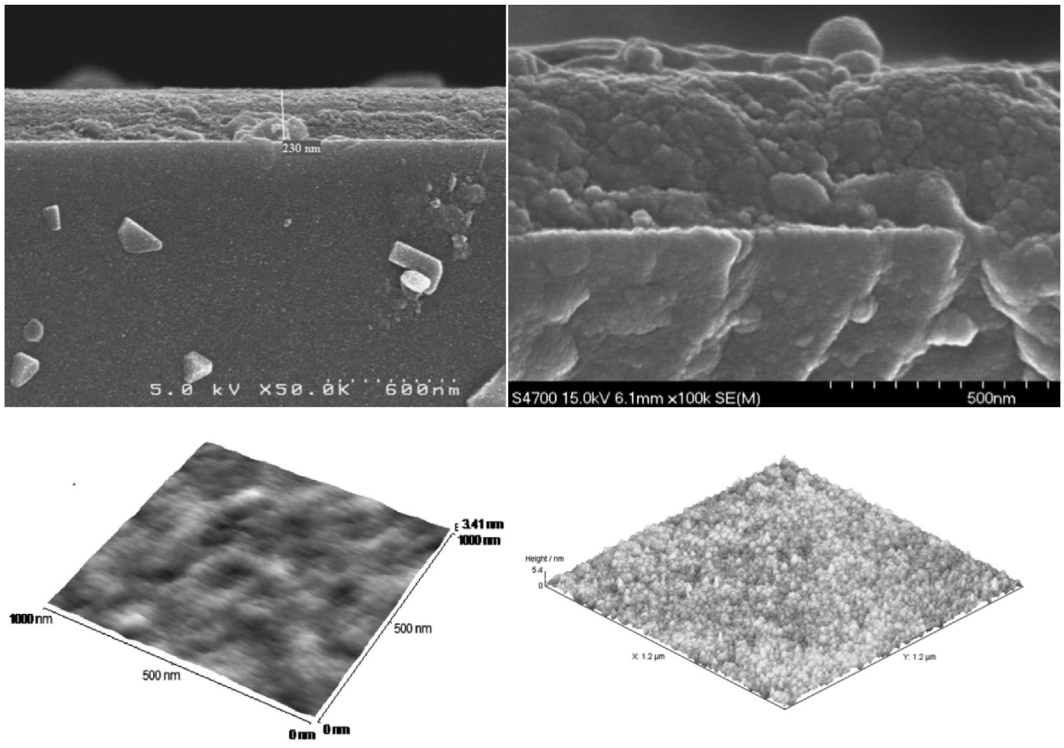


**Fig. 2.** SEM and AFM images of ZnO (left) and $TiO_2$ (right) layers.

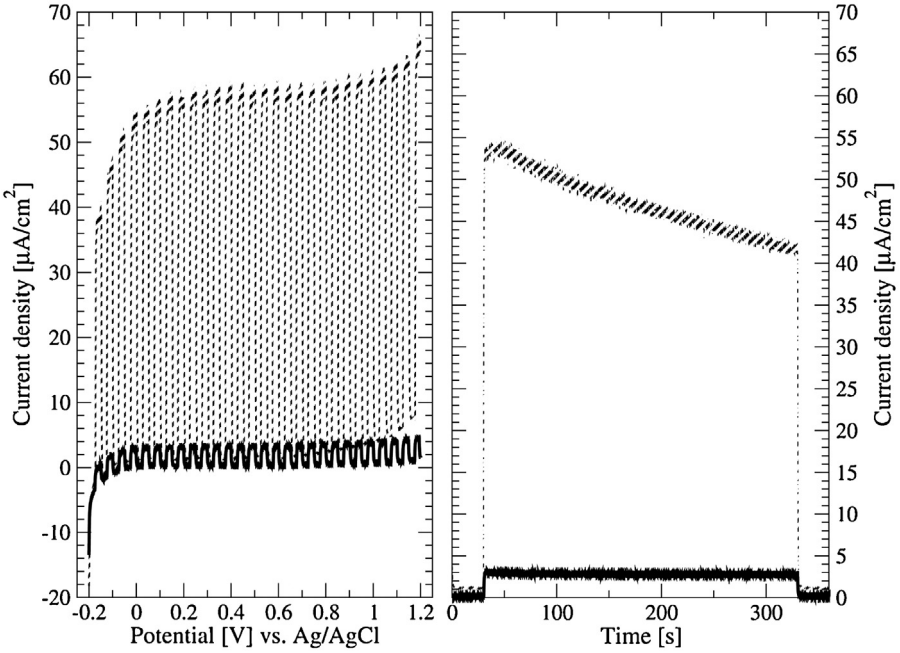


**Fig. 3.** Linear voltammogram (left) and amperogram (right) of ZnO (thin lines) and $TiO_2$ (thick lines) with 0.1 M $Na_2SO_4$ as electrolyte.

concentration for both types of ink-jet printed layers. The potential regresses to the original values after the light is switched off slowly and reaches the starting potential after approximately 150 s. The constant $E_{oc}$ values in the UV-light period correspond to the steady state concentration of not recombined electrons. The amount of photo-excited electrons reacts either with an electron scavenger (e.g. oxidizable species) or with the photo-generated holes or migrates through layers to the conductive substrate.

### 3.3. RTILs as electrolytes

For determination of the photo-electrochemical features of RTILs as electrolytes in the contact with the prepared semiconducting films the same testing algorithm as previously was applied with special focus on amperometry and open circuit potential measurements.

The photo-generated current of the electrochemical system involving RTILs showed an interesting behaviour. It is noteworthy the values of generated photocurrent densities (Fig. 4) in both types of layers almost perfectly correlate with the fluidity and conductivity of RTILs (Table 1). The highest currents were obtained for EMIM $Tf_2N$, the lowest for $N_{[12,222]}$ $Tf_2N$. The absolute values of photocurrents were higher for systems involving RTIL's than for $Na_2SO_4$ solutions. We think that ionic liquids create a continuous interlayer within $TiO_2$ and ZnO layers (a capacitive layer), and thus they may enhance the transfer of generated charge transport to the electrolyte.

Values of OCP for both types of layers showed similar trends. The high concentrated and high viscous electrolyte ($N_{[8,222]}$ $Tf_2N$) was able to create a thin layer of RTIL on the semiconductor. Formation of holes and electrons after irradiation by UV light was almost immediate and this event was not the limiting step of the whole charge generation (Fig. 4, bottom). After switching off the light the restoration of new equilibrium tends to depend on the viscosity of RTIL, due to the limiting diffusion current. The creation of new equilibrium for the low viscous, high conductive (mobile) solution of $Na_2SO_4$ was not limited by the low mobility of charge carriers in contrast to RTILs.

The inter-ratio of current densities for every RTIL showed similar trends for both types of layers. Probably the generated photocurrent densities for individual RTILs are affected by their polarity and viscosity. Therefore, the modified empirical law found by Walden [22,23] was applied to specify the effect of growing alkyl chain in the series of chosen RTIL. In the original paper of Walden [23] it was postulated that the product of equivalent conductivity and the dynamic viscosity remains the same for electrolytes behaving similar to solutions of KCl in water. The Walden rule distinguishes parts with different ionic and fluidic properties.

$$\Lambda^0 \times \eta^\alpha = \text{constant} \quad (1)$$

Eq. (1) represents the Walden rule in which $\Lambda^0$ is the limiting molar conductivity [$\Omega^{-1}$ cm$^2$ mol$^{-1}$], $\eta$ is the dynamic viscosity in [Pa s], and $\alpha$ is the adjustable parameter for fitting the experimental data. As was shown [26–28] ionic liquids of our series confirm well the Walden rule with $\alpha \approx 1$ with almost the same behaviour comparable with standard KCl solutions. This leads to an idea to normalize the photo-generated current to the dynamic viscosity and the equivalent conductivity. When the photocurrent densities are taken relative by means of viscosities and conductivities (Table 1) new trends arise (Fig. 5).

The over-laying curves of the specific current density correspond to the analogous system of RTILs, similarly as observed for the Walden plot. The same property was found for both types of thin layer electrodes in the RTILs electrolyte. For the system of ZnO and RMIM $Tf_2N$, a small deviation in the behaviour according to the Walden rule was found. Therefore the RMIM $Tf_2N$ were purified by solid liquid extraction [29] and measured again as previously. With this particular case (example) it was demonstrated that the used opto-electrochemical system could be potentially also utilized for effective and rapid determination of purity of BMIM $Tf_2N$ and PMIM $Tf_2N$ ionic liquids (Fig. 6). It can be seen that the pure ionic liquid reveals a higher photo-generated current density in comparison to

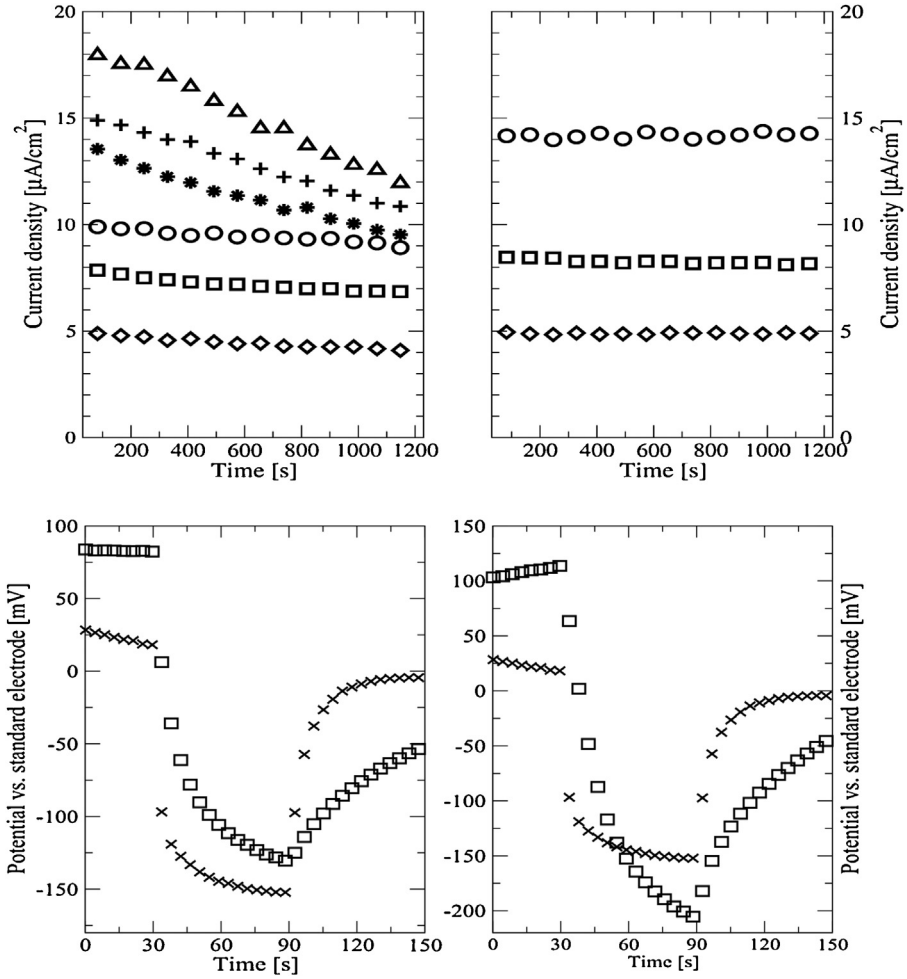


**Fig. 4.** Amperograms (top) and open circuit potentials (bottom) for experiments with RTILs as electrolytes with ZnO (left) and $TiO_2$ (right). The corresponding curves for RTILs are shown with different symbols: triangles (EMIM $Tf_2N$), crosses (PMIM $Tf_2N$), stars (BMIM $Tf_2N$), circles ($N_{[4,222]}$ $Tf_2N$), squares ($N_{[8,222]}$ $Tf_2N$) and diamonds ($N_{[12,222]}$ $Tf_2N$).

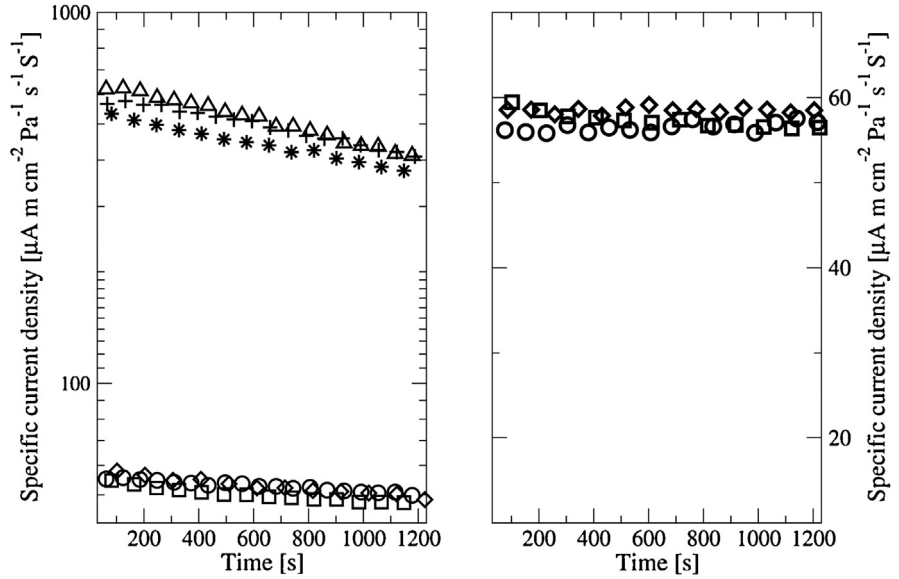


**Fig. 5.** Specific current densities calculated from original data for ZnO and for both types of RTIL's (left) and $TiO_2$ with $N_{[x,222]}$ $Tf_2N$ (right).

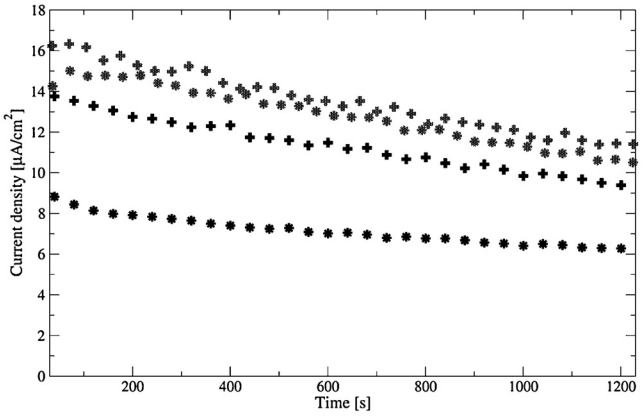


**Fig. 6.** Comparison of current densities for contaminated and purified BMIM $Tf_2N$ (black stars, resp. grey stars) and PMIM $Tf_2N$ (black crosses, resp. grey crosses).

the contaminated one. This can be due to the loss of ionicity and to the increase of viscosity. The difference in the current density is small, but clearly evident.

## 4. Conclusion

The $TiO_2$/ITO and ZnO/ITO electrodes prepared by piezoelectric ink-jet printing were stable and possessed very good photo-induced functional properties. The obtained electrochemical characteristics reflected the ability to react immediately on the UV light signal by generation the charge carriers. The measurements also confirmed a high potential of the photo-electrochemistry tests for evaluation the role of the used RTILs as electrolytes in a series of individual $N_{[R,222]}$ $Tf_2N$ and RMIM $Tf_2N$. The electrochemical system with RTILs behaved almost perfectly according to the experimental Walden rule. We believe that the change of polarity decreasing with growing alkyl chain results in a rapid change in the photo-electrochemical behaviour for both types of semiconductor layers. The alkyl chain obviously decreased the molar conductivity of the molecule due to decreasing the polarity/mass ratio and increasing the value of the dynamic viscosity.

## Acknowledgment

Authors gratefully acknowledge the financial contribution of the Technology Agency of the Czech Republic, Project no. TA03010548.

## References

[1] P. Kluson, P. Kacer, T. Cajthaml, M. Kalaji, J. Mater. Chem. 11 (2001) 644–655.
[2] C. Sanchez, B. Julian, P. Belleville, M. Popall, Mater. Chem. 15 (2005) 3559–3592.
[3] P. Dzik, M. Vesely, J. Chomoucka, J. Adv. Oxid. Technol. 13 (2010) 172–183.
[4] M. Morozova, P. Kluson, J. Krysa, P. Dzik, M. Vesely, O. Solcova, Sens. Actuators, B 160 (2011) 371–378.
[5] M. Morozova, P. Kluson, O. Solcova, P. Dzik, M. Vesely, M. Baudys, J. Krysa, J. Sol-Gel Sci. Technol. 65 (2013) 452–458.
[6] P. Dzik, M. Morozova, P. Kluson, M. Vesely, J. Adv. Oxid. Technol. 15 (2012) 89–97.
[7] T. Floris, P. Kluson, L. Bartek, H. Pelantova, Appl. Catal., A 366 (2009) 160–165.
[8] M.F. Costa Gomes, J.N. Canongia Lopes, A.A.H. Padua, in: B. Kirchner (Ed.), Ionic Liquids—Topics in Current Chemistry, vol. 290, Springer Verlag, Berlin–Heidelberg, 2009 (Chapter 5).
[9] B. Kirchner, in: B. Kirchner (Ed.), Ionic Liquids—Topics in Current Chemistry, vol. 290, Springer Verlag, Berlin–Heidelberg, 2009 (Chapter 7).
[10] M. Armand, F. Endres, D. MacFarlane, H. Ohno, B. Scronati, Nat. Mater. 8 (2009) 621–629.
[11] E. Binneti, A. Panniello, R. Tommasi, J. Phys. Chem. 25 (2013) 12923–12929.
[12] T. Fujimoto, K. Awaga, Phys. Chem. Chem. Phys. 15 (2013) 8983–9006.
[13] H.Y. Huang, D.J. Chien, G.G. Huang, P.Y. Chen, Electrochim. Acta 56 (2012) 204–209.
[14] M. Morozova, P. Kluson, J. Krysa, M. Zlamal, O. Solcova, S. Kment, T. Steck, J. Sol-Gel Sci. Technol. 52 (2009) 398–407.
[15] S. Mason, P. Holliman, M. Kalaji, P. Kluson, J. Mater. Chem. 19 (2009) 3517–3523.
[16] S. Kment, P. Kluson, H. Bartkova, J. Krysa, O. Churpita, M. Cada, P. Virostko, M. Kohout, Z. Hubicka, Surf. Coat. Technol. 202 (2008) 2379–2385.
[17] P. Kluson, S. Kment, M. Morozova, S. Hejda, P. Dytrych, M. Slater, J. Krysa, Chem. Pap. 66 (2012) 446–460.
[18] M. Morozova, P. Kluson, J. Krysa, Ch. Gwenin, O. Solcova, J. Sol-Gel Sci. Technol. 58 (2011) 175–201.
[19] S. Kment, P. Kluson, V. Stranak, P. Virostko, J. Krysa, Z. Hubicka, Electrochim. Acta 54 (2009) 3352–3360.
[20] G. Waldner, J. Krysa, Electrochim. Acta 50 (2005) 4498–4504.
[21] G. Waldner, R. Gomez, M. Neumann-Spallart, Electrochim. Acta 52 (2007) 2634–2639.
[22] C. Schreiner, S. Zugmann, R. Hartl, H.J. Gores, J. Chem. Eng. Data 55 (2009) 1784–1788.
[23] P. Walden, Z. Phys. Chem. 55 (1906) 207–246.
[24] P. Scardi, M. Leoni, R. Delhez, J. Appl. Crystallogr. 37 (2004) 381–388.
[25] P. Scardi, M. Leoni, Acta Crystallogr. 58 (2002) 190–196.
[26] D. Rooney, J. Jacquemin, R. Gardas, Top. Curr. Chem. 290 (2009) 185–212.
[27] N. Fontanals, F. Borrull, R.M. Marcé, Trends Anal. Chem. 41 (2012) 15–26.
[28] K. Machanova, J. Jacquemin, Z. Wagner, M. Bendova, Proc. Eng. 42 (2012) 1229–1241.
[29] I. Cerna, P. Kluson, M. Bendova, T. Pekarek, T. Floris, H. Pelantova, Chem. Eng. Proc. 50 (2011) 264–271.

Solar Energy Materials & Solar Cells 125 (2014) 87–95

Contents lists available at ScienceDirect

Solar Energy Materials & Solar Cells

journal homepage: www.elsevier.com/locate/solmat

# Inkjet printing of sol–gel derived tungsten oxide inks

Tjaša Vidmar [a,*], Marko Topič [a], Petr Dzik [b], Urša Opara Krašovec [a]

[a] University of Ljubljana, Faculty of Electrical Engineering, Tržaška cesta 25, 1000 Ljubljana, Slovenia
[b] Faculty of Chemistry, Institute of Physical and Applied Chemistry, Purkyňova 118, Královo Pole, 61200 Brno, Czech Republic

ARTICLE INFO

*Article history:*
Received 13 June 2013
Received in revised form
15 January 2014
Accepted 7 February 2014
Available online 15 March 2014

*Keywords:*
$WO_3$ layer
Peroxopolytungstic sol
Inkjet printing
Printed electronics
Chromism

ABSTRACT

Tungsten (VI) oxide – $WO_3$ is a widely studied functional inorganic semiconductor material with exceptional chromogenic properties. It is used in energy efficient systems such as smart windows, sensors, displays, storage units, photocatalysts and solar cells. Layers of $WO_3$ are generally produced using expensive vacuum deposition techniques. In this paper, the inkjet printing of sol–gel derived tungsten inks on glass and transparent conductive oxide is reported. Peroxo sol–gel synthesis was used to prepare peroxopolytungstic acid sols which were then modified using different solvents to obtain a suitable jetting ink. Described are the rheological and structural properties of $WO_3$ inks, the dynamics of $WO_3$ droplets and the morphology and quality of $WO_3$ printouts. The functionality of these transparent $WO_3$ layers is successfully demonstrated in an electrochromic device.



## 1. Introduction

Tungsten (VI) oxide–$WO_3$ is arguably the most efficient inorganic electrochromic material with excellent electrochromic properties both in the visible and infrared part of the spectrum. It allows high coloration efficiencies (21 – 167 $cm^2/C$) and is relatively inexpensive with typical electrochromic systems costing between 10 and 1000 $\$/m^2$ [1–4]. It can be used as either a buffer layer or as a p-/n-type semiconductor, in sensors, displays, storage units, photocatalysts and solar cells [5]. More recently attention has focussed on integrating inorganic metal oxide layers (e.g. $WO_3$, $V_2O_5$, and $MoO_3$) into organic optoelectronic systems such as organic photovoltaics (OPV) and organic light emitting diodes (OLED) as a means of improving efficiency, stability and system longevity [6,7].

Tungsten (VI) oxide has a defect perovskite structure based on corner sharing $WO_6$ octahedra. Crystallization occurs in a variety of modifications including monoclinic, tetragonal and cubic phase depending on how the $WO_6$ octahedra are interconnect. This in turn depends on synthesis, deposition and process parameters: such as annealing temperature and surface treatment ($O_2$ or $H_2$ plasma) of the $WO_3$ layers [3–8]. Its structure is also affected by ion intercalation where the electrochemical insertion of Li ions leads to the ordering of the crystalline structure from monoclinic through tetragonal and finally to the cubic phase [9]. The structure of the $WO_3$ layer influences semiconductor properties, coloration efficiency, stability and coloring–bleaching kinetics [3–8].

The layers of $WO_3$ are typically created by RF vacuum sputtering, chemical vapor deposition (CVD), electrodeposition or from either dip-coating or spin-coating coating suspensions or solutions made by sol–gel processing [1]. Unfortunately, these methods do not meet the requirements of today's electronic production systems, which demand cheaper and variable mass production methods. For example coating techniques are limited in their control of deposition, multi-layered structures and patterning. The increasing demands of consumable electronics search for low-cost deposition techniques, therefore digital printing techniques are gaining importance. Amongst them inkjet printing is one of the most promising methods. It allows precise and contact-less transfer, the use of diverse materials, sampling and multi-layer construction at low price [10]. This will require the development of new functional inks that will avoid inhomogeneous film formation, formation of cracks, irregular and deformed printed lines and defects like coffee ring and fishbone effects [11,12]. To obtain homogeneous layers optimum properties of the ink (viscosity, surface tension and evaporation rate) and printing settings (voltage, the shape of pulse, substrate and ink temperature, size and speed of ink drops) must be adopted [13]. The properties of printable functional ink can be controlled by combining solvents to control viscosity, surface tension and evaporation rate, as recently reported by Chouki and Schoeftner [14]. An ideal ink for a Drop on Demand – DOD inkjet system should have a viscosity of 0.002 – 0.03 Pa s and a surface tension of 30 mN/m [15]. Additionally, ink viscosity needs to allow the smooth delivery of the ink between the printer head and the cartridge. The other important property is the surface tension of the ink which plays an important role on the interaction between the printer nozzle and ink, as well

* Corresponding author.

http://dx.doi.org/10.1016/j.solmat.2014.02.023
0927-0248 

as on the spreading of the drops over the substrate surface. Ideally the surface tension must be such that the printing ink is held in the nozzle without dripping while allowing a droplet to spread over the substrate to form a continuous film [16].

The rheological and structural properties of $WO_3$ inks vary according to temperature, pH, water content and the concentration of $H_2O_2$ [17]. The sols referred to inks are Newtonian fluids, which mean that their viscosity is independent of flow rate, whereas the gels show non-Newtonian behavior and become dilatants, whose viscosity increases with the rate of shear strain [18]. Importantly, the homogeneity of printouts depends on the mechanism of drop formation and this varies with a fluid's and surface properties. Various dynamic phenomena are also observed during drop formation such as splashing, spreading, receding, bouncing and crown formation. Rioboo et al. [19] have analyzed the phases of drop spreading: kinematic phase, spreading phase, relaxation phase and wetting phase. Drop dynamics and film formation can be predicted with various computational simulations and studied using the Weber number ($We=\delta v^2 d/\sigma$), Ohnesorge number (Oh=η/sqrt(δσd)=1/Z) or $Z$ number ($Z=\delta\sigma d/\eta$) and Reynolds number ($Re=\delta v^2 d/\eta$), where $\delta$ is the density, $v$ is the drop velocity, $d$ is the diameter of nozzle, $\sigma$ is the surface tension and $\eta$ is the viscosity of the printable liquid. Drop dynamics and the impact of droplets on the substrate surface are of great interest in deposition techniques such as spraying or inkjet printing. These models were developed for Newtonian fluids and despite that most commercially available inks are non-Newtonian and contain various additives these models can still be used to assess the printability of the inks [20–23].

Printing of functional sol–gel materials is a new and under-explored area of research. There exist a few reports describing inkjet printing of for example $SiO_2$, ZnO, $TiO_2$, and $V_2O_5$ inorganic layers by applying sol–gel made inks. These were used as transparent electrically conductive (TCO) and dielectric substrates, components for photoactive layers, layers for chromogenic systems and sensors [9]. To our knowledge no publication exists with regards to printing of $WO_3$ sols. The only relevant publication [24] describes the inkjet printing of suspensions based on $TiO_2$ and $WO_3$ nano-powders using different solvents and additives. Inkjet printing of sol–gel functional materials is complex and besides the necessary fine tuning of their rheological properties, there is a need to control gelation of inks and how materials interact.

In this paper, the focus is on inkjet printing of inorganic sol–gel derived tungsten inks. The aim was to obtain homogenous transparent $WO_3$ printouts applicable for use in electrochromic devices. The tungsten inks were synthesized following the peroxo sol–gel route [25] but modified for inkjet printing on glass and transparent conductive oxide (TCO) substrates. Different $WO_3$ inks were synthesized based on different solvent compositions having different rheological and physicochemical properties. Their effects on inkjet printing on glass and TCO–glass substrates are discussed.

## 2. Experimental

### 2.1. Preparation of a $WO_3$ ink

Step one involved the synthesis of a $WO_3$ sol. First, peroxo-tungsten acid (PTA) was synthesized by reacting 5 g of tungsten monocrystalline powder (99.9%, Aldrich) with 20 ml of hydrogen peroxide (30%, Belinka). The reaction is strongly exothermic. Sols where then prepared by adding solvent to the PTA solution at 120 °C. Two $WO_3$ sols used in this study as inks where prepared with two different solvents: 2-propanol (puriss, Sigma-Aldrich) and a mixture of 2-propanol and 2-propoxy ethanol (puriss, Sigma-Aldrich). The inks are referred to as $WO_3$-1 for a $WO_3$ sol based on 2-propanol and as $WO_3$-2 for a $WO_3$ sol based on a mixture of 2-propanol and 2-propoxy ethanol.

The addition of alcohol resulted in the formation of the W-ether (esterification) that polymerizes to peroxopolytungstic acid (P-PTA) [25]. The ink appeared slightly orange and contained 27.7 mmol of tungsten per 30 ml of sol. To improve the ink stability and inkjet jetting properties the primary inks were further diluted to 60 ml with solvent. The diluted inks are marked as d-$WO_3$-1 and d-$WO_3$-2.

### 2.2. Deposition of $WO_3$ layers

A layer of $WO_3$ was printed on glass and glass coated with a fluorine doped $SnO_2$–K-glass (sheet resistance 13 Ω/□) substrates. Substrates were initially cleaned with 2 vol% mucasol (Sigma Aldrich) aqueous solution, distilled water and 2-propanol or 2-propanol/2-propoxy ethanol. Inkjet printing was performed using a piezoelectric Dimatix Materials Printer Series 2800 (Fujifilm Dimatix Inc.) equipped with a silicon print head cartridges having 16 nozzles, each with a nominal drop volume of 10 pL. We varied different printing settings, such as substrate, ink temperature, jetting voltage, printing frequency, drop spacing and cartridge angle.

### 2.3. Characterization

The viscosity of the $WO_3$ inks was measured at 20 °C using Vibro Viscometer model SV-1A. Contact angles, surface tension and surface energy measurements of the substrates were made using a Krüss DSA 100 goniometer using the static sessile drop method. The contact angle was evaluated by the circle fitting method, based on the outline of a droplet as shown in Fig. 1. The surface tension was then calculated from the measured contact angles of distilled water, diiodomethane and formamide using the Owens–Wendt model. Surface tension of the $WO_3$ inks was determined using the stalagmometric method.

The chemical structure of the $WO_3$ inks was determined using a Perkin Elmer FT-IR System Spectrum GX in the geometry of the attenuated total internal reflection – ATR ($500-4000\ cm^{-1}$). Quality and morphology were monitored with a digital optical camera (Digi 2.0 Micro Scale) and a scanning electron microscope (JSM 6060-LV, JEOL). Image analysis (ImageJ tools) was used to show the shape and size of droplets printed at voltages from 10 to 40 V using different formulations of $WO_3$ inks. The thickness of the $WO_3$ layers was measured with a surface profilometer (Taylor-Hobson Ltd.). Estimated thickness of $WO_3$ layers was between 0.2 and 1.0 μm and dependent on the concentration of $WO_3$ inks, printer settings and the annealing process. The quality of adhesion

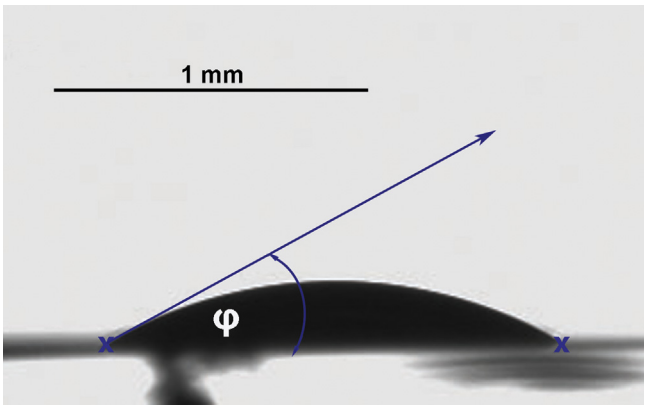


**Fig. 1.** Contact angle of distilled water on glass substrate.

**Table 2**
Contact angles of test liquids and calculated surface energy of glass substrate.

| Substrate | Contact angle of test liquids (deg) | | | Calculated surface tension (mN/m) |
|---|---|---|---|---|
| | Distilled water | Diiodomethane | Formamide | |
| Glass | 32.4 | 48.5 | 11.7 | 63.1 |

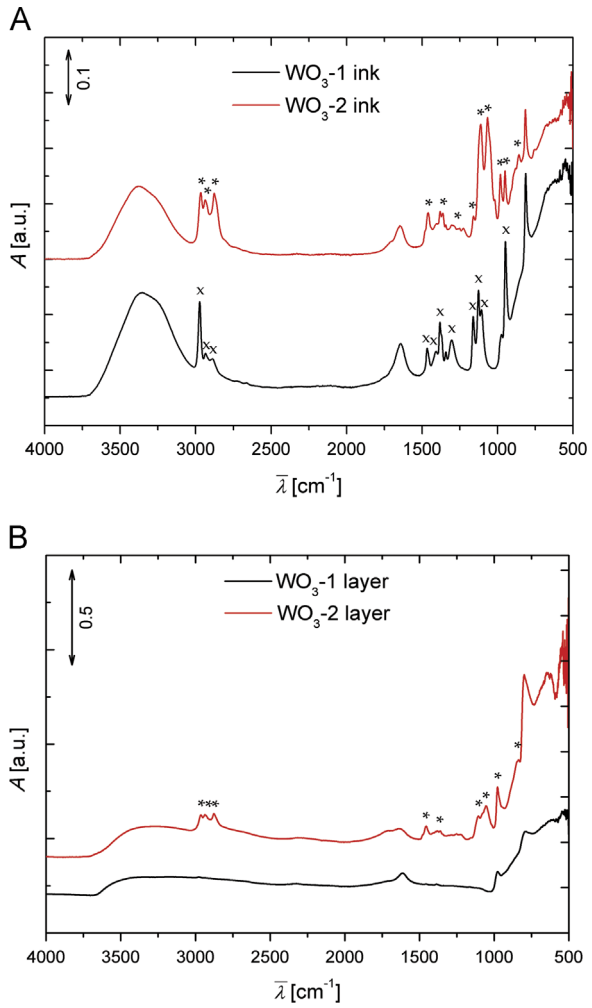


**Fig. 2.** FT-IR spectrum of $WO_3$-1 and $WO_3$-2 inks (A) and corresponding layers dried at room temperature (B). (*denotes typical peaks of 2-propoxy ethanol and x denotes peaks of 2-propanol).

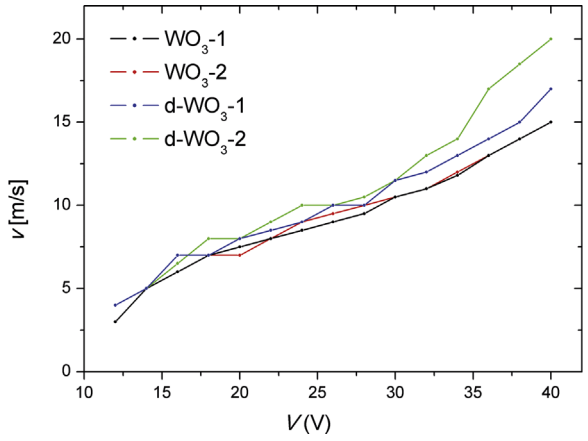


**Fig. 3.** The velocity of concentrated and diluted $WO_3$ inks vs applied voltage.

**Table 1**
Density, viscosity, surface tension and Z number of $WO_3$ inks at $20 \pm 0.5$ °C.

| $WO_3$ inks | Density ($g/cm^3$) | Viscosity (mPa s) | Surface tension (mN/m) | *Z* number (/) |
|---|---|---|---|---|
| $WO_3$-1 | 1.05 | $8.4 \pm 0.01$ | $22.1 \pm 0.003$ | 3 |
| $WO_3$-2 | 1.12 | $11.1 \pm 0.03$ | $25.5 \pm 0.01$ | 2 |
| d-$WO_3$-1 | 0.92 | $4.7 \pm 0.02$ | $21.8 \pm 0.03$ | 4 |
| d-$WO_3$-2 | 0.96 | $5.2 \pm 0.02$ | $25.0 \pm 0.02$ | 4 |

of the $WO_3$ layers was ascertained using the 1 mm cross-cut tester (Byko-cut Universal, Byk Gardner).

## 3. Results and discussion

The rheological and physicochemical properties (viscosity and surface tension) of four $WO_3$ inks have been analyzed. The printability of the inks using inkjet printing was determined by calculating the Weber and *Z* number and an analysis of the printed $WO_3$ droplets was made.

### *3.1. Rheological, physicochemical and structural properties of $WO_3$ inks*

The viscosity and surface tension are the most important properties of printing ink. Solvents for piezoelectric inkjet printing should have a viscosity around 0.01 Pa s and surface tension of 30 mN/m, in addition they must have low vapor pressure. Standard $WO_3$ sols prepared via the peroxo route are based on highly volatile ethanol [26] which has a viscosity of 6.1 mPa s and surface tension of 27.2 mN/m at 20 °C. The high evaporation rate of ethanol can clog nozzles resulting in layering defects like an inhomogeneity, a coffee ring, or the fishbone effect [11]. To avoid these problems the $WO_3$ ink was prepared by replacing ethanol with 2-propanol (ink $WO_3$-1) and 2-propanol/2-propoxy ethanol mixture (ink $WO_3$-2). The result was a higher ink viscosity and a lower surface tension. While the addition of 2-propoxy ethanol, as a higher boiling point solvent (b.p. 150 °C, [27]) slowed evaporation. The stability of $WO_3$-1 and $WO_3$-2 inks, prior to gelation, is limited to 1 month if refrigerated. The stability of the ink can be prolonged by diluting the $WO_3$ inks with the corresponding solvent, to obtain ink d-$WO_3$-1 and d-$WO_3$-2 (see Section 2). This enabled the preparation of a thinner layer preventing cracking of the layers after the evaporation of the solvents.

To achieve good wetting, the surface tension of the substrate must be ideally for (10 mN/m) than the surface tension of the printable liquid. Diodomethane, distilled water and formamide were used as test liquids to determine the surface tension of the glass substrate. The resultant contact angle measurements and calculated surface tension are presented in Table 2. The calculated surface tension of the glass substrate is 63.1 mN/m, which is more than 30 mN/m higher than the surface tension of the inks.

Unfortunately, it was not possible to determine the surface tension of TCO substrate precisely due to its complex surface roughness and sensitivity to the storage conditions after cleaning.

Results reveal that the surface tension between glass substrate and the ink is not perfectly matched, and to further optimize the printing process improvements based on surface cleaning and substrate treatment or ink modification should be investigated.

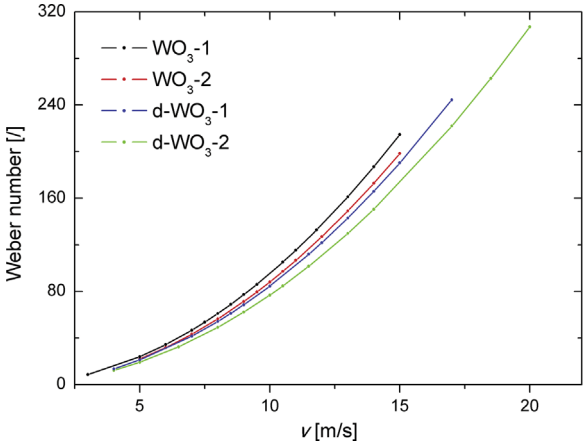


**Fig. 4.** Weber number at different velocities of $WO_3$ inks.

### 3.2. IR spectroscopy of $WO_3$ inks

The $WO_3$ inks prepared via the sol–gel peroxo route are based on peroxopolytungstic acid (P-PTA). The structure of P-PTA has been determined by Nanba et al. [28] and consists of a polyanion in which a 6-membered ring of corner-shared polyhedra such as $WO_5(O_2)$ or $WO_6$ are sandwiched between $W_3O_{10}$ units consisting of edge shared $WO_6$ octahedra. The complex structure of the P-PTA suggests the existence of specific vibrational modes in the IR spectrum. The IR spectrum of the P-PTA contains the following: stretching modes of terminal ($\nu$W=O at 980 $cm^{-1}$), corner sharing ($\nu$W–O–W at 600 – 650 $cm^{-1}$) and edge sharing ($\nu$W–O–W at 700–750 $cm^{-1}$) stretching W–O modes, while bending modes appear below 450 $cm^{-1}$. In addition, the presence of the peroxo groups in the P-PTA structure is shown by the presence of W–O–O–W and W–O–O modes at 800 – 830 $cm^{-1}$ and 560 $cm^{-1}$, respectively. Stretching modes incorporating the vibration of hydrogen bonded $H_2O$ appear between 3500 and 3000 $cm^{-1}$, while the bending mode appears at approx. 1600 $cm^{-1}$. For a detailed vibrational band assignment of P-PTA see Ref. [29].

The IR spectra of fresh $WO_3$-1 and $WO_3$-2 inks (Fig. 2) also show, besides the modes assigned to the solvents, a band at 980 $cm^{-1}$ ($\nu$W=O), an intense band at 810 $cm^{-1}$ (W–O–O–W), a broad band peaking around 630 $cm^{-1}$ ($\nu$W–O–W corner sharing octahedra) and a band at 550 $cm^{-1}$ (W–O–O). Bending W–O modes were not observed since they appear outside the range of the spectrometer. Comparisons of the spectra of fresh inks ($WO_3$-1 and $WO_3$-2) show no differences regarding the vibrational modes

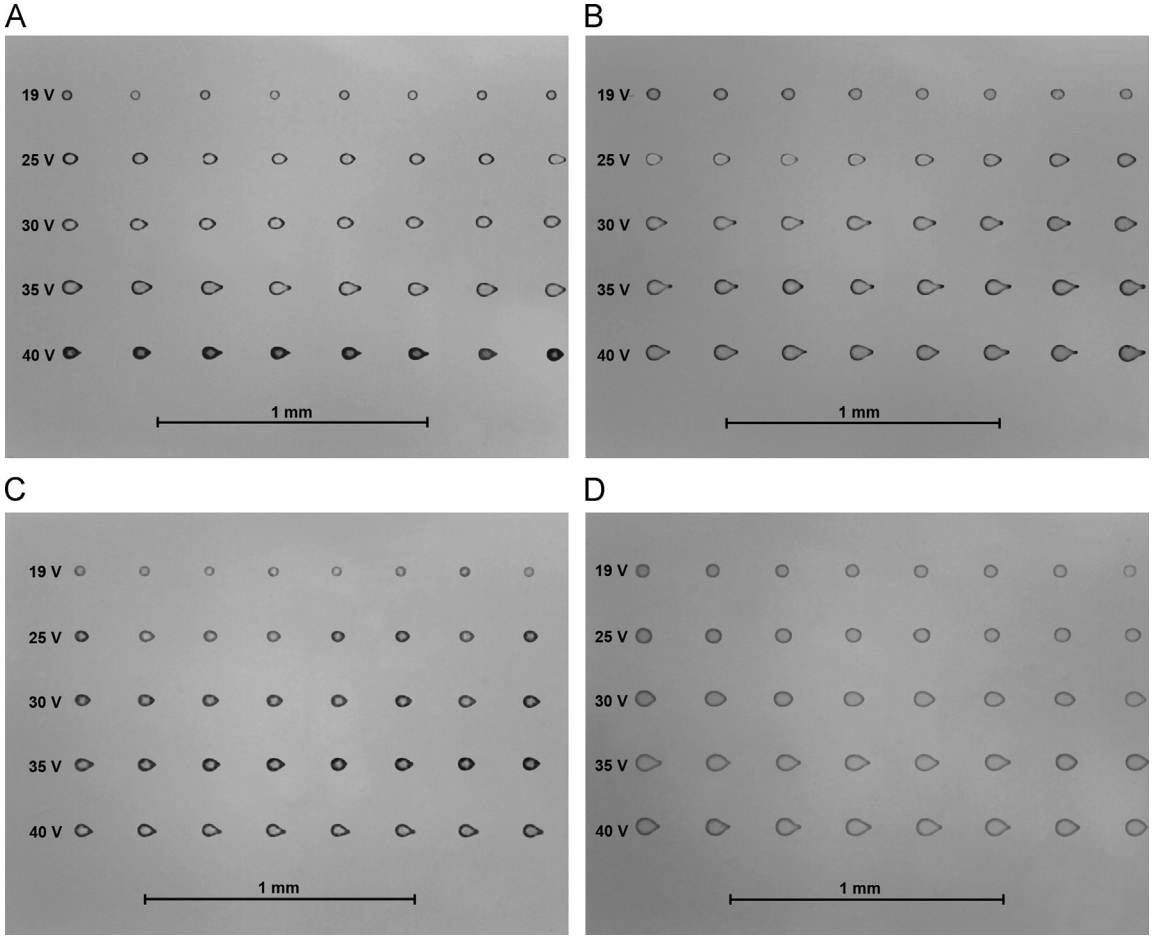


**Fig. 5.** Optical microscopic images of dried droplets of concentrated $WO_3$ sol–gel ink printed on glass (top) and TCO substrate (bottom) at voltages of 19 – 40 V. Pictures A and C correspond to $WO_3$-1 ink and pictures B and D to $WO_3$-2 ink.

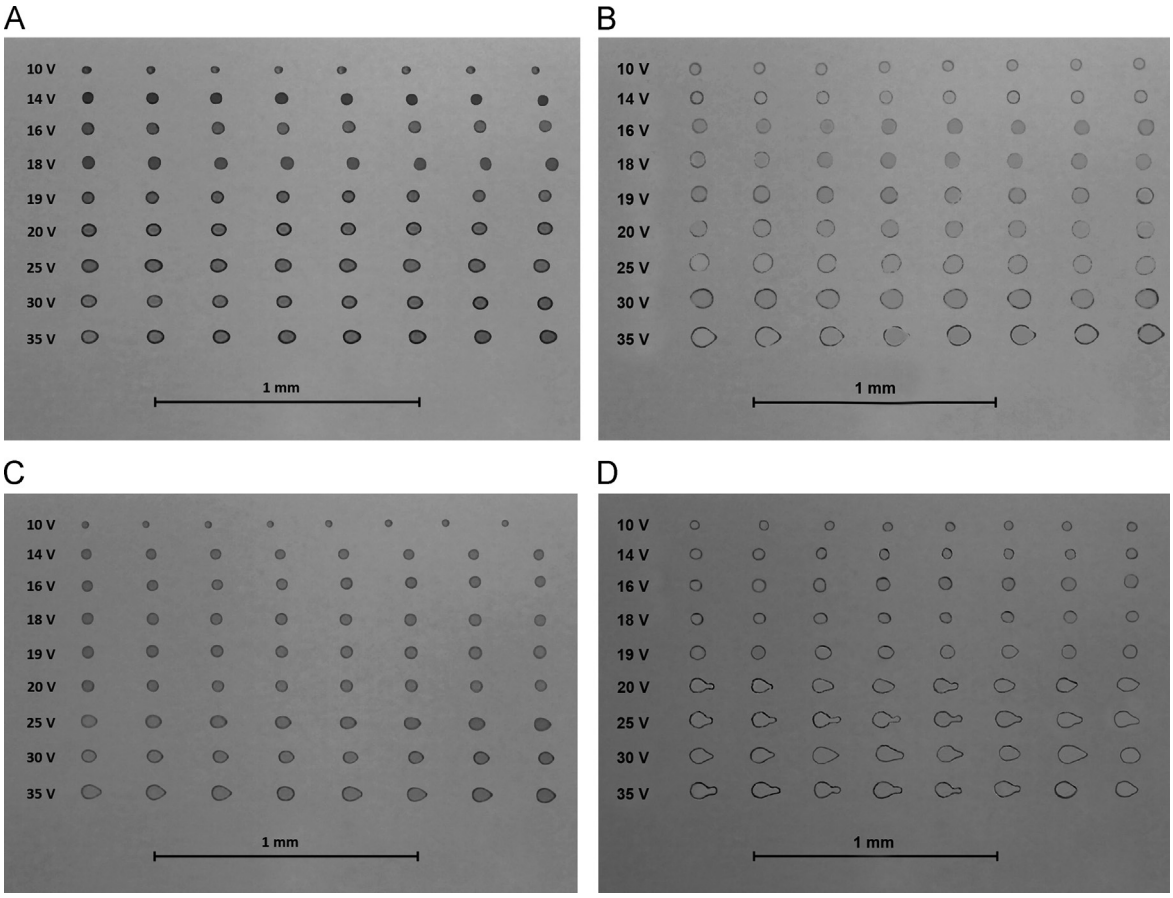


**Fig. 6.** Optical microscopic images of dried droplets of diluted $WO_3$ sol–gel ink printed on glass (top) and TCO substrate (bottom) at voltages of 10 – 35 V. Pictures A and C correspond to $WO_3$-1 ink and pictures B and D to $WO_3$-2 ink.

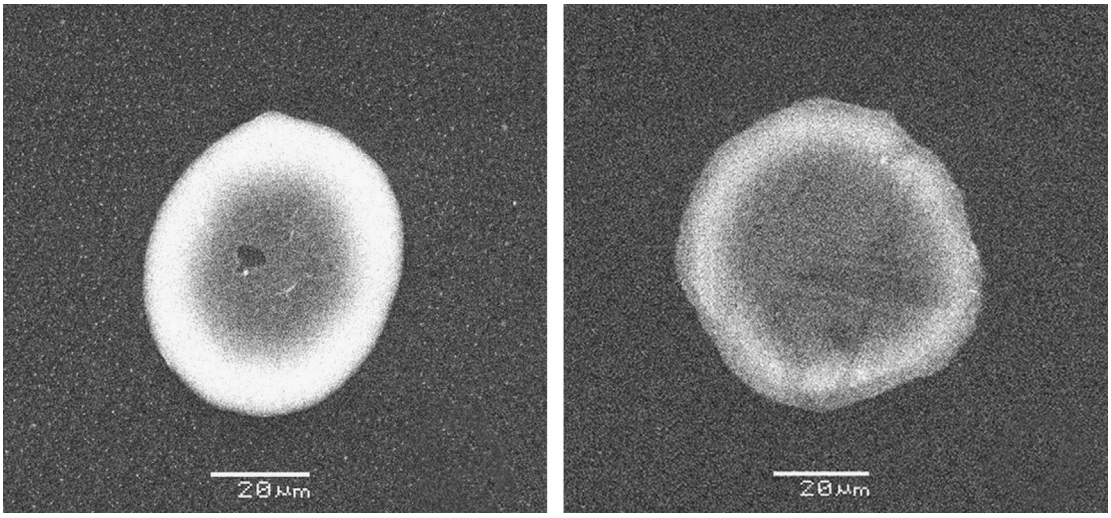


**Fig. 7.** SEM images of printed $WO_3$ droplets using sol $WO_3$-2 (left) and diluted sol d-$WO_3$-2 (right) on glass at 19 V.

characteristic of P-PTA. Alternatively, the spectra of the inks dried at RT for 1 h show that 2-propanol (ink $WO_3$-1) completely evaporates while 2-propoxyethanol is still present in the $WO_3$-2 ink. In addition, the intensity of the W–O–O–W mode at 810 $cm^{-1}$ shows the content of the peroxo groups is much higher in the $WO_3$-2 ink dried at RT. Decomposition of the peroxo groups is therefore faster in ink $WO_3$-1. This is due to the slower decomposition of the peroxo groups $(O_2)^{2-}$ with chelating properties in ink $WO_3$-2. Its stability is also prolonged. The stability of the P-PTA inks based on different solvents is under investigation.

The XRD spectra of dip-coated P-PTA xerogel films and films treated at 150 °C revealed amorphous structure [29]. Transmission

electron spectroscopy of the xerogel layers confirmed the presence of up to 2 nm large clusters of monoclinic $WO_3$ modification that are embedded in amorphous tungsten oxide matrix [30].

### 3.3. Dynamics of $WO_3$ droplets

Droplet dynamics and the formation of a printed film can be predicted by theoretical models. To determine the printability of concentrated and diluted $WO_3$ inks calculating the Weber ($We=\delta v^2 d/\sigma$) and $Z$ number ($Z=\delta\sigma d/\eta$) was done. First, the velocity of inks ($v$) droplets at different voltages was determined using the Dimatix Drop Watcher set-up. The results for different inks are shown in Fig. 3. As expected, printing velocity increases with increasing voltage. The datasets do show overlap in the lower voltage range; above 25 V we can clearly see that higher $v$ values are characteristic for diluted inks (d-$WO_3$-1 and d-$WO_3$-2) due to their lower viscosity while the more concentrated viscous samples have lower velocities (Table 1).

Drop formation (single droplet, satellite droplets and droplet break up) and spreading on solid substrates are dominated by material properties (internal, surface tension and viscous forces of fluids) and drop parameters (drop velocity and drop diameter) [21]. Dynamics of droplet spreading can be characterized by the Weber and $Z$ number. The best formulation of droplet behavior is the use of both parameters; moreover the $Z$ number includes viscosity which is an important and variable property for printing of sol–gel materials. A liquid drop with a high Weber number spreads out under the influence of the impact-induced inertia, whereas at low Weber number the capillary force tends to resist the droplet from spreading at the contact line. The relative importance between the capillary and viscous forces is scaled by the $Z$ number. At low $Z$ number fluid viscosity plays a major role in inhibiting drop spreading and at high $Z$ number the dominant role is played by surface tension. In inkjet printing drop spreading is dominated by inertial forces and resisted primarily by viscous forces. The $Z$ number for the $WO_3$ inks varies from 2 to 4, and increases with viscosity and surface tension [31]. Fig. 4 shows the Weber number at different velocities of concentrated and diluted $WO_3$ inks. Results reveal the same trend in the Weber number vs velocity of droplets for all the $WO_3$ inks. A critical Weber number ($We_{critical}=12(1+1.077-Z^{-1.6})$) for concentrated $WO_3$ inks is around 15, while for diluted $WO_3$ inks it is around 13. If the $We_{critical}$ is surpassed, that is at higher velocities, it causes the appearance of satellite droplets or droplet break up and distortions in drop formation. The effect is a distorted, missing or inhomogeneous printed layer.

Table 1 shows the obtained $Z$ numbers which characterizes drop formation e.g., capillary break-off length and time, droplet volume and satellite formation. Some theories predict a stable drop formation in drop-on-demand systems when $Z>2$ [32],

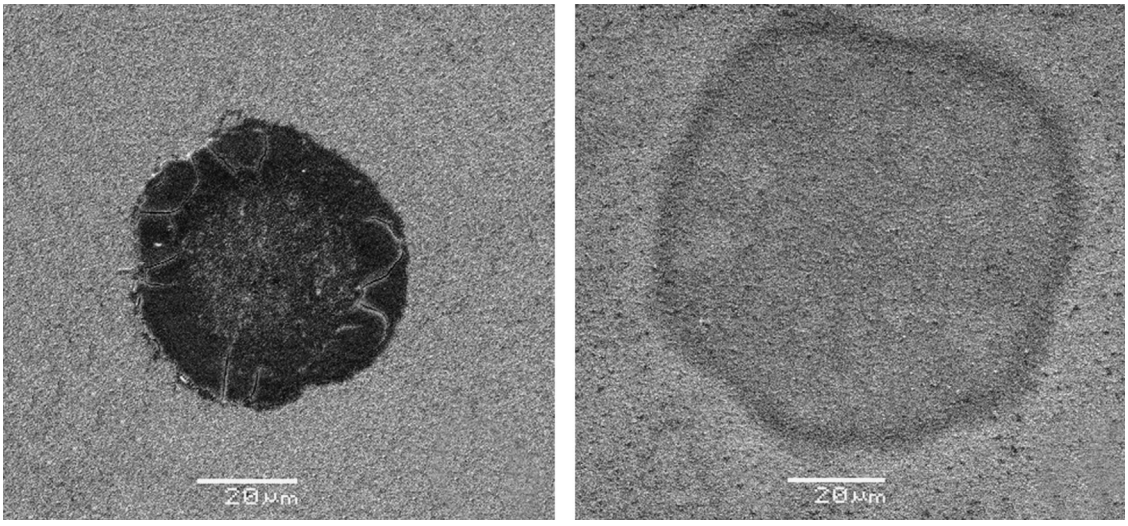


**Fig. 8.** SEM images of printed $WO_3$ droplets using sol $WO_3$-2 (left) and diluted sol d-$WO_3$-2 (right) on a TCO substrate at 19 V.

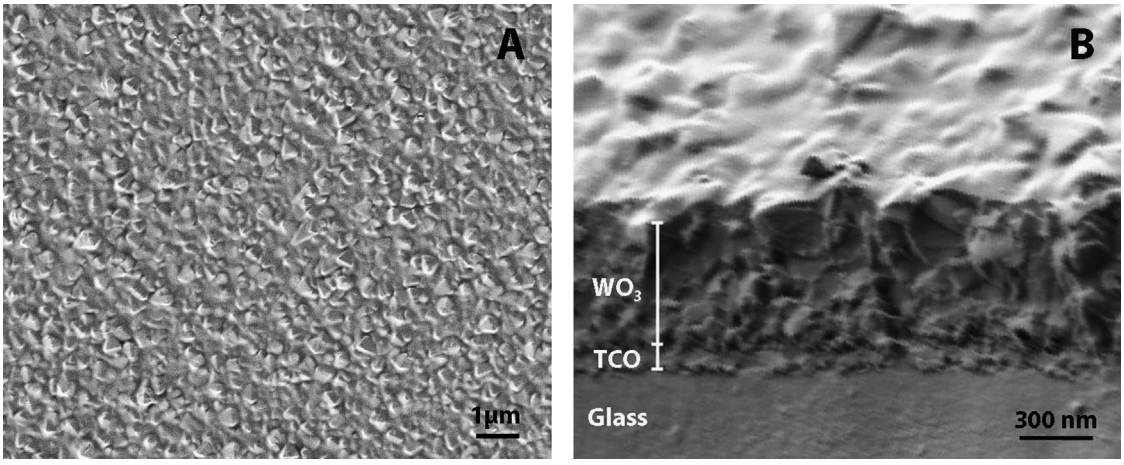


**Fig. 9.** SEM images of a $WO_3$-2 layer printed on a TCO substrate, surface (A) and cross section (B).

while others suggest a $Z$ value of between 1 and 10 [33]. The lower limit is governed by the viscosity of the fluid and its printing ability, while the upper limit is determined by the point at which multiple drops are formed in place of a single droplet [23].

The dilution of the inks slightly reduces the $We_{critical}$ value, making the diluted formulation theoretically more prone to drop formation defects at higher velocities and suggests that the studied ink formulations should be suitable for printing only at relatively low velocities. Yet, the reduction of $We_{critical}$ with dilution is only marginal. With increasing dilution, the $Z$ number increases as the viscosity term dominates, and $Z$ values shift with dilution from just an acceptable value of 2 to a much more optimistic value of approximately 4 (Table 1). This implies a trade-off between these two parameters and either an optimal formulation or, if necessary, another solvent is required. The drop formation process modeled by means of the Weber and $Z$ number is only one part of the story. Drop–substrate interactions governed mainly by ink and substrate surface tensions and discussed in the following chapter are no less important. An ink with inferior jetting performance is often justified by its special wetting behavior.

### 3.4. Inkjet printing of $WO_3$ inks

Studying the printability of four different $WO_3$ inks shows poor reproducibility of the printing process when using concentrated $WO_3$ inks (i.e. $WO_3$-1 and $WO_3$-2 inks). The main constraints were clogged nozzles, because the polymerization/gelation of the ink occurred during the printing process. Diluted $WO_3$ inks were much more favorable for inkjet printing due to their better stability.

Scanning electron microscopy and image analysis results are presented in Figs. 3 and 4 and show that lower voltages can be applied for the diluted $WO_3$ inks, which agrees with the determined $We_{critical}$ (see Section 3.3). Figs. 5 and 6 show different droplet shapes on both glass and TCO substrates which are related to the mismatch between the surface tension of the substrate and inks, and depends on material interaction. Results also show the effect of increasing printing voltages to the shape and deformation of the droplets. Printing settings vary depending on the form of the printed layers i.e., a homogenous plane or a complex forms, and dictates precision of the printing. The areas of the droplets are approximately 0.11 $mm^2$ at 10 V and up to 0.23 $mm^2$ for printing at 40 V.

Figs. 7 and 8 are SEM images of printed $WO_3$ droplets formed using ink $WO_3$-2 and diluted ink d-$WO_3$-2 on glass and TCO substrate at 19 V. The difference in contrast is due to the different conductivity of the substrates. The images show the difference in droplet printout that depends on the concentration of the printed ink and on the substrate. Droplets printed with concentrated inks are slightly deformed in shape and size, but especially on the TCO substrate where cracks appear at the edges due to the greater thickness. The estimated diameters of droplets printed using $WO_3$-2 ink are around 0.08 mm on both substrates, while printing the droplets using d-$WO_3$-2 ink leads to thinner and bigger printouts with a diameter of 0.12 mm on glass and 0.15 mm on the TCO substrate.

The SEM image shown in Fig. 9A indicates a rough surface structure of the printed $WO_3$-2 layer while the cross section image (Fig. 9B) indicates a good adhesion of the layer to the TCO substrate. The thickness of the printed $WO_3$-2 layer estimated from Fig. 9B is around 700 nm.

A cross-cut test performed on a $WO_3$-2 layer printed on a TCO substrate is shown in Fig. 10. The results show very good adhesion of the $WO_3$-2 layer to the TCO substrate because the edges of the cuts are smooth and none of the squares of the lattice is detached. Adhesion of the $WO_3$ layer tested with adhesion tape (Scotch Magic Tape, 3M) was also good. The layer did not peel off during testing.

### 3.5. Electrochromic devices containing an inkjet printed $WO_3$ layer

While printing $WO_3$ inks various problems occur including misdirected nozzles, non-jetting nozzles, non-matched and velocities, which are related to improper rheological and physicochemical properties of the $WO_3$ inks. The majority of issues were successfully solved by adding solvent or solvent mixture with low evaporation rates. To achieve simple and complex layers different variations of printing parameters including voltage, waveform, temperature and

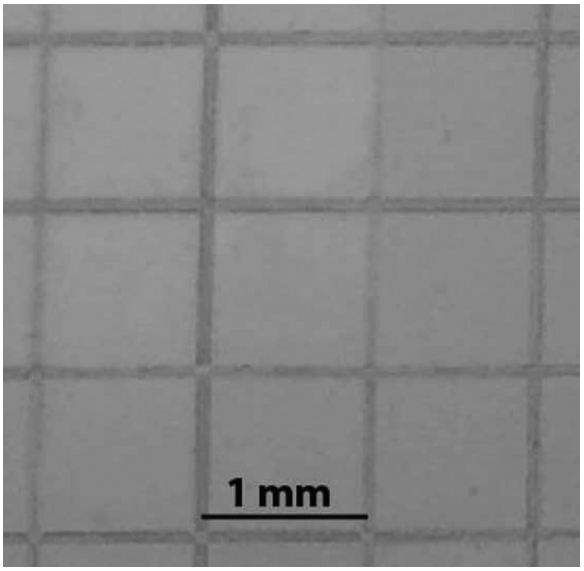


**Fig. 10.** Cross-cut of $WO_3$-2 layer deposited on TCO substrate.

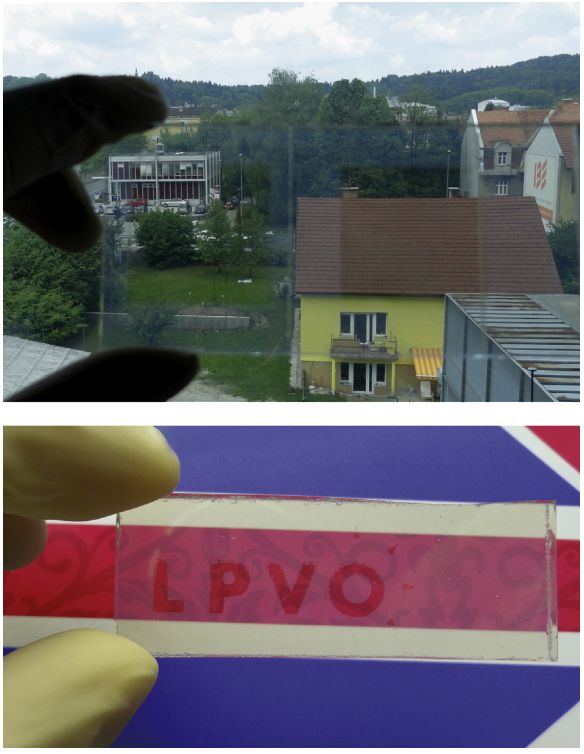


**Fig. 11.** Inkjet transparent $WO_3$-2 printouts.

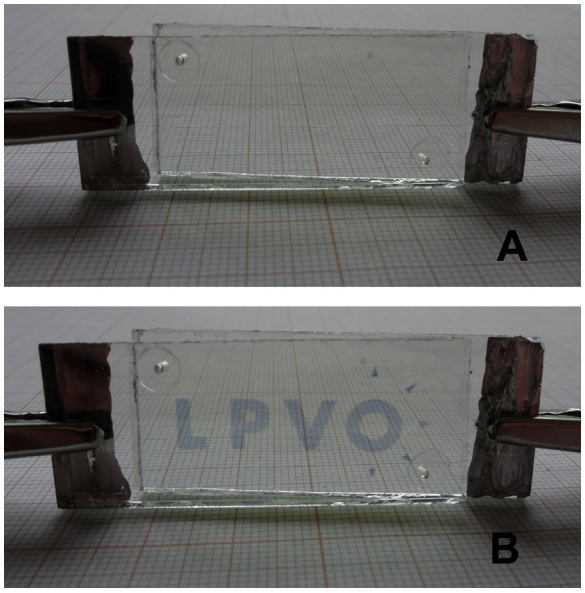


**Fig. 12.** Electrochromic display device with a printed $WO_3$-2 logotype in bleached (A) and colored state (B).

frequency were used. Two examples of transparent $WO_3$ printouts that do not show optical defects are shown in Fig. 11 and have been used to assemble an EC device. Our aim was to demonstrate the EC response of the layers rather than to optimize the EC device performance.

The functionality of the printed $WO_3$ layers is shown in an electrochromic (EC) display device with glass–TCO/$WO_3$-2/electrolyte/TCO–glass configuration (Fig. 12). For this a 0.5 M LiI and 0.005 M $I_2$ in propylene carbonate as an electrolyte was used. The EC device was colored and bleached at $+/-1.0$ V.

An additional EC device with the same configuration (glass–TCO/$WO_3$-2/electrolyte/TCO–glass), but with a square shaped $WO_3$-2 layer ($1.5 \times 1.5$ cm$^2$) was assembled. The important characteristics of the EC device such as optical modulation between the bleached and colored states and coloring/bleaching kinetics have been examined. Fig. 13 presents the transmittance spectra of the EC device in colored (at $-1$ V and $-1.5$ V) and bleached states (at 0 V and 1 V). Monochromatic transmittance at 550 nm of the EC device in the short circuit state (0 V) is 59%, while a fully bleached state is achieved at a positive potential (1 V) with a transmittance of 64%. The transmittance (at 550 nm) of the EC device in the colored state varies from 12% to 15% depending on the applied voltage.

The coloring/bleaching kinetics of the EC device under positive (1 V) and negative ($-1$ V) potential is presented in Fig. 14. The results show that coloring and bleaching is achieved within a few seconds (3–7 s), which shows the responsive nature of the EC device to the applied voltage.

Fig. 15 presents the 5th and 200th cyclic voltammogram of the printed EC device. The EC device reached a maximum current density of 2.15 mA/cm$^2$ at $-1$ V after 200 cycles. Comparison of the 5th and 200th CV response shows only a slight deterioration with cycling which demonstrates the good stability of the EC device. The EC device has a slightly bluish coloration under short circuit (without applied potential), so a positive potential is required for complete bleaching.

There are several established vacuum and non-vacuum techniques e.g., chemical vapor deposition (CVD), radio frequency (RF) sputtering deposition and electrodeposition exist for depositing chromogenic $WO_3$ films. The chromogenic performance of an EC device depends mostly on deposition and annealing process [34–36].

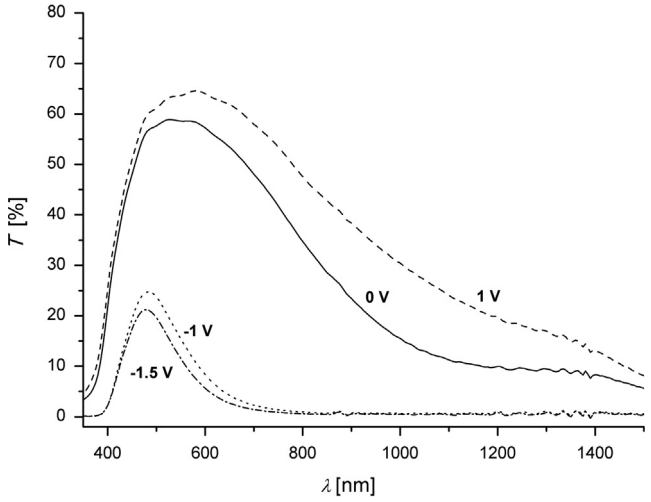


**Fig. 13.** Transmittance spectra of the EC device in colored ($-1$ V and $-1.5$ V) and bleached states (0 V and 1 V).

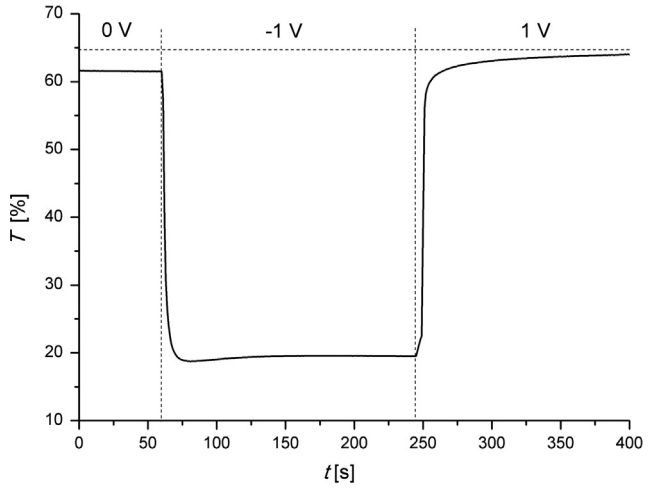


**Fig. 14.** Coloring/bleaching kinetics of the EC device under positive (1 V) and negative ($-1$ V) potential followed at wavelength of 550 nm.

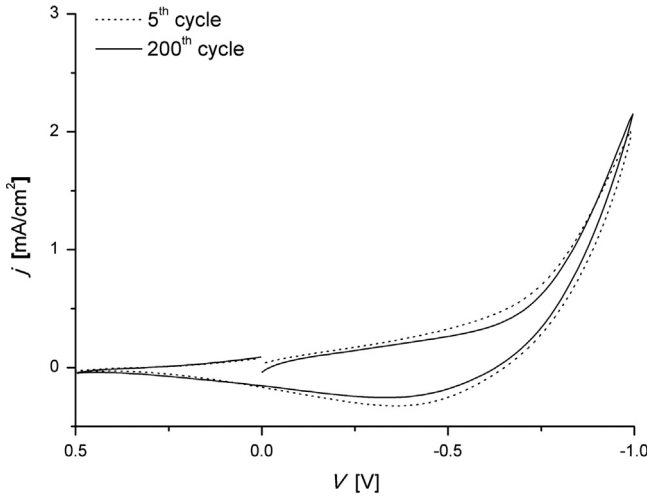


**Fig. 15.** Cyclic voltammograms (5th and 200th cycle) of the printed EC device.

Chemical vapor deposition and RF sputtering use dry deposition, whereas electrodeposition is a wet method. Also important is the flexibility of RF sputtering deposition conditions, which enables large area deposition of thin films under various conditions. All of these

methods give uniform and homogenous layers exhibiting good chromogenic performance with regards to stability, coloration and bleaching kinetics, transmission modulation and coloration efficiency. However, electrodeposition is the only low cost conventional procedure with the ability to produce amorphous or nanocrystalline coating over a large area at room temperature.

In comparison inkjet printing is relatively cost efficient, enables selective deposition over a large area, flexibility, and allows the use of different functional materials. Despite this, further optimization of the $WO_3$ ink is neccesary to improve the reproducibility of the method with respect to the homogeneity and uniformity of the printed $WO_3$ films.

## 4. Conclusions

This is the first report of inkjet printed transparent $WO_3$ layers using a sol–gel derived tungsten ink. A suitable $WO_3$ ink via the peroxo sol–gel route modified for piezoelectric inkjet printing on glass and TCO substrates was developed. To obtain optimal jetting properties of the ink four formulations of $WO_3$ inks with different ratios and combination of solvents were made and tested. The rheological and physicochemical properties of $WO_3$ inks can be adjusted for inkjet printing by correctly adjusting the printing settings so that transparent $WO_3$ printouts can be produced free of optical defects. The applicability of the printed $WO_3$ layer was successfully demonstrated in a functioning electrochromic device. This study opens up a new way for $WO_3$ layer manufacturing and could further the future development of chromogenic as well as other optoelectronic devices.

## Acknowledgments

Tjaša Vidmar would personally like to acknowledge the Slovenian Research Agency for providing her Ph.D. funding. Slovenian Research Agency is also acknowledged for funding the Research Program P2-0197. We would also like to thank the Faculty of Pharmacy (within University of Ljubljana) for the accessibility to the Krüss DSA 100 goniometer and the Jožef Stefan Institute for profilometric measurements.

## References

[1] P.M.S. Monk, R.J. Mortimer, D.R. Rosseinsky, Electrochromism and Electrochromic Devices, Cambridge, New York (2007) 139–151.
[2] R.D. Rauh, Electrochromic windows: an overview, Electrochim. Acta 44 (1999) 3165–3176.
[3] C. Gou, S. Yin, T. Sato, Tungsten oxide-based nanomaterials: morphological-control, properties, and novel applications, Rev. Adv. Sci. Eng. 1 (2012) 235–263.
[4] K.J. Patel, C.J. Panchal, V.A. Kheraj, M.S. Desai, Growth, structural, electrical and optical properties of the thermally evaporated tungsten trioxide ($WO_3$) thin films, Mater. Chem. Phys. 114 (2009) 475–478.
[5] S.K. Deb, Opportunities and challenges in science and technology of $WO_3$ for electrochromic and related applications, Sol. Energy Mater. Sol. cells 92 (2008) 245–258.
[6] H. Choi, B. Kim, M. J. Ko, D. K. Lee, H. Kim, S. H. Kim and K. Kim, Solution processed WO3 layer for the replacement of PEDOT:PSS layer for organic photovoltaic cells, Org. Electron. 6, 2012, 959–968.
[7] M. Vasilopoulou, G. Papadimitropoulosa, L.C. Palilisb, D.G. Georgiadoua, P. Argitisa, S. Kennouc, I. Kostisa, N. Vourdasa, N.A. Stathopoulosd, D. Davazogloua, High performance organic light emitting diodes using sub-stoichiometric tungsten oxide as an efficient hole injection layer, Org. Electron. 13 (2012) 796–806.
[8] C.G. Granqvist, Handbook of Inorganic Electrochromic Materials, Amsterdam: Elsevier, 1995, 17–389.
[9] U. Opara Krašovec, A.Š. Vuk, B. Orel, IR Spectroscopic studies of charged–discharged crystalline $WO_3$ films, Electrochim. Acta. 46 (2001) 1921–1929.
[10] M. Mosiadz, R.I. Tomov, S.C. Hopkins, G. Martin, D. Hardeman, B. Holzapfel, B. A. Glowacki, Inkjet printing of Ce0,8Gd0,2$O_2$ thin films on Ni–5% W flexible substrates, J. Sol–Gel Sci. Technol. 54 (2010) 154–164.
[11] Z. Cheng, R. Xing, Z. Hou, S. Huang, J. Lin, Patterning of light-emitting $YVO_4$:$Eu^{3+}$ thin films via inkjet printing, J. Phys. Chem. 21 (2010) 9883–9888.
[12] S. Jung, S. Hoath, M. Graham, I. Hutchings, A new method to assess the jetting behavior of drop-on-demand ink jet fluids, J. Imaging Sci. Technol. (2011) 10501-1–10501-6.
[13] D. Kim, Y. Jeong, C.Y. Koo, K. Song, J. Moo, Thin film transistors with ink-jet printed amorphous oxide semiconductors, Jpn. J. Appl. Phys. 49 (2010) (O5EBO6-1-O5EBO6-4).
[14] M. Chouiki, R. Schoeftner, Inkjet printing of inorganic sol–gel in and control of the geometrical characteristics, J. Sol–Gel Sci. Technol 1 (2011) 91–95.
[15] Dimatix Materials Printer DMP-2800 FAQs, Fujifilm DIMATIX Inc. (2008), 5 p.
[16] M. Yang, L. Li, S. Zhang, G. Li, H. Zhao, Preparation, characterisation and sensing application of inkjet-printed nanostructures TiO2 photoanode, Sensor Actuators B-Chem. 147 (2010) 622–628.
[17] K. Chang-Yeoul, L. Min, H. Seung-Hun, K. Eun-Kyung, $WO_3$ thin film coating from $H_2O$-controlled peroxotungstic acid and its electrochromic properties, J. Sol–Gel Sci. Technol. 53 (2010) 176–183.
[18] A.H. Barnes, An introduction to Rheology: Rheology Series 3, Oxford, United Kingdom (1989) 5–17 pp.
[19] R. Rioboo, M. Marengo, C. Tropea, Time evolution of liquid drop impact onto solid, dry surfaces, Exp. Fluids 33 (2002) 112–124.
[20] R. Crooks, J. Cooper-White, D.V. Boger, The role of dynamics surface tension and elasticity on the dynamics of drop impact, Chem. Eng. Sci. 56 (2001) 5575–5592.
[21] S. Yangsoo, K. Chongyoup, Spreading of inkjet droplet of non-Newtonian fluid on solid surface with controlled contact angle at low Weber and Reynolds numbers, J. Non-Newton. Fluid Mech. 1 – 3 (2009) 78–87.
[22] V. Bergeron, D. Bonn, J.Y. Martin, L. Vovelle, Controlling droplet deposition with polymer additives, Nature 405 (2000) 772–775.
[23] D. Jang, D. Kim, J. Moon, Influence of fluid physical properties on ink-jet printability, Langmuir 5 (2009) 2629–2635.
[24] A.S. Rações da Cruz, Dual phase inkjet printed electrochromic layers based on PTA and WOx/TiO2 nanoparticles for electrochromic applications (Ph.D. thesis), Monte de Caparica, Portugal (2010) 23–103.
[25] U. Opara Krašovec, Vibrational, electrochemical and gasochromic properties of tungsten (VI) oxide, molybdenum doped tin (IV) oxide and double oxides of cerium with transition metals films (Ph.D. thesis), 29–56.
[26] K. Yamanaka, H. Oakamoto, H. Kidou, T. Kudo, Peroxotungstic acid coated films for electrochromic display devices, Jpn. J. Appl. Phys. 25 (1986) 1420–1426.
[27] Chemical Book: 2-Propoxyethanol. ⟨http://www.chemicalbook.com/ChemicalProductProperty_EN_CB7203174.htm⟩, CAS number (2807-30-9), (2010).
[28] T. Nanba, S. Takano, I. Yasui, T. Kudo, Structural study of peroxopolytungstic acid prepared from metallic tungsten and hydrogen peroxide, J. Solid State Chem. 1 (1991) 47–53.
[29] B. Orel, U. Opara Krašovec, Gasochromic behavior of sol–gel Pd doped peroxopolytungstic acid (W-PTA) nano-composite films, J. Sol–Gel Sci. Technol. 14 (1999) 291–308.
[30] B. Orel, U. Opara Krašovec, N. Grošelj, M. Kosec, G. Dražič, R. Reisfeld, Gasochromic behavior of sol–gel derived Pd doped peroxopolytungstic Acid (W-PTA) nano-composite films, J. Sol–Gel. Sci. Technol. 14 (1999) 291–308.
[31] S. Jung, Fluid characterisation and drop impact in inkjet printing for organic semiconductor devices (Ph.D. thesis), 25–37.
[32] J.E. Fromm, Numerical calculations of the fluid dynamics of drop-on-demand jets, IBM J. Res. Dev. 3 (1984) 322–333.
[33] N. Reis, B. Derby, Ink jet deposition of ceramic suspensions: modelling and experiments of droplet formation, Mater. Res. Soc. Symp. Proc. (2000) 117–122.
[34] R.U. Kirss, L. Meda, Chemical vapor deposition of tungsten oxide, Appl. Organomet. Chem. (1998) 155–160.
[35] M. Deepa, M. Kar, S.A. Agnihotry, Electrodeposited tungsten oxide films: annealing effects on structure and electrochromic performance, Thin Solid Films (2004) 32–42.
[36] Y. Yamada, K. Tabata, T. Yashime, The character of $WO_3$ film prepared with RF sputtering, Sol. Energy Mater. Sol. Cells (2007) 29–37.

Langmuir

Article

pubs.acs.org/Langmuir

# High Photocatalytic Activity of Transparent Films Composed of ZnO Nanosheets

Jan Hynek,[†] Vít Kalousek,[‡] Radek Žouželka,[‡] Petr Bezdička,[†] Petr Dzik,[§] Jiří Rathouský,[‡] Jan Demel,*[,†] and Kamil Lang[†]

[†]Institute of Inorganic Chemistry of the AS CR, v. v. i., Husinec-Řež 1001, 250 68 Řež, Czech Republic

[‡]J. Heyrovský Institute of Physical Chemistry of the AS CR, v. v. i., Dolejškova 3, 182 23 Praha 8, Czech Republic

[§]Faculty of Chemistry, Brno University of Technology, Purkyňova 118, 612 00 Brno, Czech Republic

Supporting Information

**ABSTRACT:** Nanometric thin films were prepared by dip-coating and inkjet printing ZnO nanosheets on glass plates. The side-by-side alignment of the ZnO nanosheets on the substrate resulted in thin, transparent, oriented ZnO surfaces with the high-energy {001} facets exposed. The method of nanosheet deposition affected the film morphology; the dip-coated films were very smooth and nonporous, while the inkjet-printed films were rough and porous with the estimated void volume approximately 60−70% of the total film volume. The first-order rate constants for the photocatalytic degradation of 4-chlorophenol on the nanosheet-based films were approximately 2 times larger than those on nanocolumnar ZnO films or ZnO films prepared by the sol−gel technique. We attribute the high photocatalytic activity of the ZnO nanosheets to the fact that their {001} facets were predominantly exposed to the oxidized substrate. This surface arrangement and the simplicity of fabricating the ZnO nanosheet-based films make them promising for the construction of optical devices and dye-sensitized solar cells.

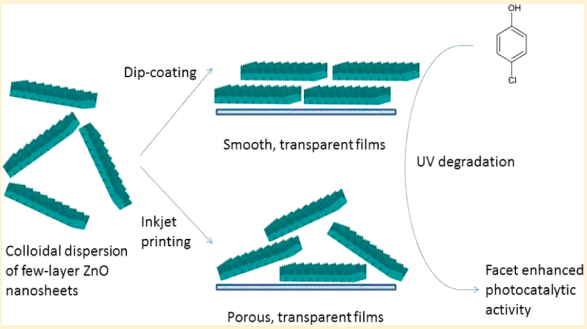


## INTRODUCTION

In recent years, nanocrystalline zinc oxide (ZnO) has attracted considerable attention because its chemical and physical properties can be tuned for many potential applications in optoelectronics and transparent electronics. ZnO is a wide band gap semiconductor with similar optical properties to $TiO_2$; however, ZnO has a higher light absorption coefficient.[1] ZnO has been recognized as a promising alternative to $TiO_2$ for the photocatalytic degradation of dyes.[2−9] The efficiencies of $TiO_2$ and ZnO photocatalysts in the degradation of organic pollutants in aqueous solutions can be compared under identical experimental conditions.[10−15] Thus, Sakthivel et al. reported the activities of $TiO_2$, ZnO, $SnO_2$, $ZrO_2$, $\alpha$-$Fe_2O_3$, $WO_3$, and CdS for the degradation of acid brown 14 using sunlight as an energy source and found that ZnO was the most active semiconductor of the series.[1]

The hexagonal wurtzite structure of ZnO consists of alternating planes of tetrahedrally coordinated oxygen and zinc atoms arranged along the *c*-axis. This anisotropy results in the spontaneous polarization of certain planes, e.g., {001} or {101}, whereas other planes are nonpolar, e.g., {100}.[16] ZnO nanostructures with predominantly high-energy facets exposed surface exhibit higher catalytic[17,18] and photocatalytic activities than those with exposed nonpolar facets.[19,20] The proportion of exposed high-energy facets can diminish rapidly during crystal growth due to the minimization of the surface energy; therefore, the synthesis of micro/nanoparticles terminated with high-energy facets is a challenge.[21] Research has also focused on preparing thin films of transition metal oxides, especially porous ones. These materials possess promising properties suitable for applications in a number of advanced technologies, such as solar cells, sensors, displays, catalysis, and photocatalysis.[22,23] Porous films have been prepared using a wide range of physical and chemical technologies; the most common methods are sol−gel and electrochemical techniques.[8,9,24]

To optimize the performance of mesoporous films, the material properties must be well-defined and controlled. One of the most successful methods for fabricating well-defined films, the so-called "brick and mortar" technique, was originally developed for $TiO_2$ and is based on the fusion of preformed nanocrystalline "bricks" using a surfactant-templated sol−gel "mortar", which acts as a structure-directing matrix and a chemical glue.[25−28] This method was also generalized for other oxides and mixed oxides.[29−34]

In this work, we fabricated thin, highly transparent films using ZnO nanosheets. The 0.6−0.7 nm thick nanosheets were built from 2 or 3 stacked ZnO tetrahedral layers.[35,36] The large

**Received:** October 16, 2013
**Revised:** December 11, 2013
**Published:** December 16, 2013

surface area of the nanosheet {001} planes makes the films suitable for catalytic, photocatalytic, and sensing applications. To explore different nanosheet arrangements, dip-coating and inkjet printing were used to prepare the films. The latter method has emerged as a promising wet-coating technique for large-scale deposition and direct patterning. As in conventional inkjet printing,[37] tiny droplets of a low-viscosity liquid are precisely deposited onto a substrate by a thermal or piezoelectric printhead.[38] Inkjet printing has been successfully employed to deposit a variety of functional materials, e.g., carbon nanotubes,[39] graphene,[40] metallic nanoparticles, proteins,[41] living cells,[42] semiconductive polymers,[43] and $TiO_2$ nanoparticles as photocatalytic coatings[44,45] or photoelectrochemical sensors,[46,47] in thin layers, two-dimensional patterns (arrays, gaps, sandwich structures), and three-dimensional structures.

To examine the effects of the crystallographic plane orientation on the photocatalytic properties of the ZnO surfaces, the photocatalytic degradation of 4-chlorophenol was performed. The photocatalytic activities of films prepared by the sol−gel technique and nanocolumnar ZnO films were also studied for comparison.

## EXPERIMENTAL SECTION

**Materials.** $Zn(NO_3)_2{\cdot}6H_2O$ and NaOH (both Lachner, Czech Republic); $Zn(CH_3COO)_2{\cdot}2H_2O$, monoethanolamine, and hexamethylenetetramine (all Lachema, Czech Republic); $C_{12}H_{25}OSO_3Na$ and 2-ethoxyethanol (both Sigma); and $CHCl_3$ (Penta, Czech Republic) were used as received. *n*-Butanol (BuOH) (Penta, Czech Republic) was dried with 3 Å molecular sieves (Sigma) for at least 2 days.

**Synthesis of Layered Zinc Hydroxide Intercalated with Dodecyl Sulfate (LZH-DS).**[35] $Zn(NO_3)_2{\cdot}6H_2O$ (20.1 g, 67.6 mmol) and $C_{12}H_{25}OSO_3Na$ (3.03 g, 10.5 mmol) were dissolved in 200 mL of water. A total of 50 mL of 0.75 M NaOH (37.5 mmol) was added dropwise to the vigorously stirred solution over 1 h at room temperature. Immediately after the addition of NaOH, the suspension was centrifuged (Hettich Rotina 35, 7000 rpm, 4 min) and washed three times with water. The white precipitate was air-dried at room temperature.

**Preparation of ZnO Nanosheets.**[36] 2.50 g of LZH-DS was suspended in 125 mL of BuOH. The mixture was stirred in a sealed flask at 80 °C for 24 h. The suspension was cooled and then centrifuged (10 000 rpm, 20 min), and the solid was washed with BuOH and redispersed in BuOH or $CHCl_3$. The dispersion was kept in the dark and was stable for over a month.

**Preparation of ZnO Films.** *Dip-Coating Method.* The films were prepared by dip-coating (velocity 0.5 mm $s^{-1}$) a ZnO nanosheet dispersion in $CHCl_3$ (~6.5 mg $mL^{-1}$) onto standard glass microscopic plates (25 × 75 mm). The plates were washed with peroxosulfuric acid and water and dried with a heat gun before the deposition. After each ZnO layer was deposited, the plate was washed with water and dried. After the deposition of the last layer, one side of the glass plate was washed with diluted hydrochloric acid and water. We prepared the films with 1−9 layers of the ZnO nanosheets.

*Inkjet Printing Method.* The films were printed onto microscopic glass plates using a DMP-2831 FUJIFILM Dimatix Materials printer equipped with a 16-nozzle piezoelectric printhead. The plates were sonicated for 10 min in a hot (60−70 °C) 20 wt % solution of Neodisher LM3 (alkaline cleaning agent) to ensure good wetting and adhesion of the ZnO nanosheets. A ZnO nanosheet dispersion in BuOH (12.7 mg $mL^{-1}$) was used as the printing ink. Immediately before printing, the dispersion was sonicated for 5 min to degas it and break apart particle agglomerates and then filtered through a 0.2 μm membrane filter (Pall Corporation). A Dimatix 10 pL printing head was attached to an empty ink tank and mounted in the printer. The following settings were used for printing: Dimatix Model fluid 2 waveform, driving voltage 16 V, nozzle temperature 30 °C, substrate temperature 40 °C, and nozzle span 25 μm. A 25 × 50 mm rectangular pattern was printed onto the plates and air-dried in the printer.

*Sol−Gel Method.* A solution of 0.5 M $Zn(CH_3COO)_2$ and 1 M monoethanolamine in 2-ethoxyethanol was prepared by suspending the zinc salt in 2-ethoxyethanol and then adding monoethanolamine. The suspension was heated to 40 °C to quickly dissolve the salt. The films were prepared by dip-coating on a freshly cleaned (by peroxosulfuric acid) microscopic plate. After air-drying, the plate was calcined in a furnace at 300 °C for 2 h.[48]

*Seed/Growth Method.* The nanocolumnar ZnO films were prepared by chemical bath deposition on a ZnO seeded layer similar to the procedure described earlier.[49] Dry microscopic plates were washed with chromic−sulfuric acid and water and then dip-coated using a ZnO nanosheet dispersion in $CHCl_3$. Then, the seeded plates were placed in aqueous mixture of 0.02 M hexamethylenetetramine and 0.02 M $Zn(CH_3COO)_2$ and heated to 80 °C upside down for 1 h. Every 10 min, the solution was shaken to remove bubbles from under the plate. After removing the plate from the bath, the upper side of the plate was washed with hydrochloric acid and water.

**Photocatalytic Experiments.** 4-Chlorophenol (initial concentration $1 \times 10^{-4}$ mol $L^{-1}$) was photocatalytically degraded in a 25 mL vessel at 25 °C. In the photoreactor, the solution was open to air and magnetically stirred; i.e., the concentration of dissolved oxygen was constant during the experiment because the solution was equilibrated with ambient air. A Sylvania Lynx-S 11 W BLB lamp was used as a 365 nm source, and its intensity was 1 mW $cm^{-2}$ at the film surface. The irradiated area of the ZnO film was 12.5 $cm^2$. In each experiment, eight 0.5 mL aliquots were removed at regular time intervals and analyzed by HPLC (Agilent Technologies 1200 series). The measured 4-chlorophenol concentrations were used to construct the kinetic curves. The first-order rate constants for the 4-chlorophenol degradation were calculated using a nonlinear regression fitting of the kinetic curves.

**Instrumental Methods.** Powder X-ray diffraction (XRD) patterns were recorded with a PANalytical X'Pert PRO diffractometer in the Bragg−Brentano geometry equipped with a conventional X-ray tube (Co Kα, 40 kV, 30 mA) and multichannel X'Celerator detector with an antiscatter shield. The beam passed through a 1/2° divergence slit, 1° antiscatter slit, and 0.04 rad Soller slit. The diffraction patterns were recorded in the range of 35°−45° with a step size of 0.033° and acquisition time of 2000 s per step, corresponding to a scan time of 95 min. The analysis was performed using the HighScore Plus software package (PANalytical, Almelo, The Netherlands, version 3.0) and JCPDS PDF-2 database.[50]

Scanning electron microscopy (SEM) images were collected using a JEOL JSM-6510lv microscope. Surface imaging was performed using an atomic force microscope (AFM) (Dimension Icon, Bruker) in the ScanAsyst mode with standard Si probes (SNL-10, Bruker). The absorption spectra of the films deposited on glass or quartz plates (SPI Supplies) were recorded using a PerkinElmer Lambda 35 spectrometer. The film thicknesses were measured using a KLA Tencor Alpha-step IQ surface profiler. The porosity and adsorption properties of the films were probed by measuring the krypton adsorption isotherms at the boiling point of liquid nitrogen (ca. 77 K) with a Micromeritics ASAP 2010 apparatus. Prior to the adsorption experiment, the films were evacuated at 150 °C overnight. The percentage of void volume was estimated using the absorbance of the film $A_{350}$ and the film thickness; the average absorbance at 350 nm of the nonporous layers prepared by dip-coating was 0.004 per 1 nm of the film thickness.

## RESULTS AND DISCUSSION

**Film Preparation.** The ZnO nanosheet dispersions were prepared according to the procedure recently developed in our laboratory.[35,36] The starting LZH-DS material was delaminated in BuOH to zinc hydroxide nanosheets, which were solvothermally transformed into the ZnO nanosheets flattened along the [001] direction. The procedure is an easily scalable one-pot reaction and produces ZnO nanosheet dispersions that are stable for over a month. The thicknesses of the prepared


dx.doi.org/10.1021/la404017q | Langmuir 2014, 30, 380−386

nanosheets were 0.6−0.7 nm and corresponded to 2 or 3 stacked ZnO tetrahedral layers. The lateral size varied between 15 and 25 nm. The nanosheets were arranged to form transparent films with a large {001} surface area by dip-coating and inkjet printing.

The ZnO nanosheets dispersed in chloroform were dip-coated on a glass substrate. The thickness of the film after one deposition procedure was approximately 10 nm. Therefore, multiple dip-coating cycles were performed to prepare films with thicknesses of up to 85 nm (Table 1). After each dip-coating cycle, the deposited layer was washed with water; otherwise, the ZnO film would be washed off during the next dip-coating cycle.

**Table 1. Morphological, Absorption, and Photocatalytic Properties of the Films Prepared by Dip-Coating and Inkjet Printing ZnO Nanosheets, Sol−Gel Processing, and the Seed/Growth (ZnO Nanocolumns) Method**

| method | no. of layers | thickness (nm) | SBET[a] ($cm^2$ $cm^{-2}$) | $A_{350}$[b] | $k$[c] ($min^{-1}$) |
|---|---|---|---|---|---|
| dip-coating | 1 | ∼10 | nd | 0.061 | 0.0005 |
| | 3 | ∼30 | nd | 0.124 | 0.0012 |
| | 5 | ∼50 | nd | 0.184 | 0.0020 |
| | 7 | 70 | nd | 0.276 | 0.0026 |
| | 9 | 85 | nd | 0.377 | 0.0037 |
| inkjet printing | 1 | 120 | nd | 0.141 | 0.0017 |
| | 2 | 230 | 11 | 0.314 | 0.0027 |
| | 3 | 275 | 14 | 0.454 | 0.0034 |
| | 4 | 350 | 16 | 0.577 | 0.0040 |
| | 5 | 425 | 32 | 0.725 | 0.0055 |
| sol−gel | 1 | 110 | 4 | 0.165 | 0.0012 |
| nanocolumns | − | 120 | nd | 0.435 | 0.0019 |

[a]SBET is the BET surface area related to the geometrical area of the film. [b]$A_{350}$ is the absorption at 350 nm calculated by subtracting the measured absorbance at 400 nm from the absorbance at 350 nm to minimize scattering effects. [c]$k$ is the first-order rate constant for 4-chlorophenol degradation. Based on two independent tests, the error in the rate constant was estimated to be less than 8%.

The ZnO nanosheet dispersions in BuOH were suitable for piezoelectric printing without modifying the solvent because of the optimal jetting characteristics of BuOH and stabilization of the formed nanosheets by adsorbed dodecyl sulfate molecules, which prevent particle aggregation even during the hydrodynamic stress that inevitably accompanies the piezoelectric printing process. The combination of these characteristics led to excellent printability as shown in Figure S1 of the Supporting Information.

Generally, the ink surface tension, substrate surface energy, and ink viscosity are the most important factors influencing droplet formation and layer merging during the inkjet printing of a functional liquid onto a nonporous, nonabsorbing substrate. The surface tension of BuOH matches well the surface energy of the glass surface, which allows for even wetting by the printed liquid. Despite the relatively low viscosity of BuOH (3.95 mPa s at 20 °C; the recommended optimal viscosity range for jetting with the Dimatix printer is 10−12 mPa s), the jetting process was reliable, and no satellite droplets were observed. Moreover, BuOH had an optimal evaporation rate, which contributed to uniform drying and smooth merging of printed bands, and because of the low viscosity formulation, the viscosity did not have to be reduced by printhead heating. These properties enabled printing at ambient temperature, which suppressed nozzle drying. Although the "ink" was a colloidal solution of ZnO nanosheets, nozzle blockage rarely occurred. A nozzle span of 25 $\mu$m (1600 drops/$mm^2$) resulted in quite dense droplet packing compared to that of a single droplet whose impact spot had a diameter of approximately 40 $\mu$m. This narrow nozzle span led to significant droplet overlap, which was undesirable because it prolonged the fabrication time; however, it allowed a large amount of the ZnO nanosheets to be delivered to the substrate and to create a 90−120 nm thick layer in a single pass of the printhead. We prepared ZnO films with 1−5 layers, resulting in thicknesses between 120 and 425 nm (Table 1).

**Film Morphology.** The preferential arrangement of the ZnO nanosheets in the films was confirmed by the XRD patterns (Figure 1). The intensity ratios of the (100) and (002) diffraction lines were approximately 0.1 and 0.4 for the dip-coated and inkjet-printed films, respectively. Because the corresponding ratio for crystalline ZnO (JCPDS 36-1451) is 1.3, the film ratios indicate that the nanosheets were preferentially oriented with the {001} planes parallel to the support. The very low value of 0.1 suggests that the dip-coating method led to better nanosheet orientation than inkjet printing. This result was expected because dip-coating allowed the nanosheets to be oriented at a slow rate at the substrate surface as the substrate was pulled off the dispersion, whereas during inkjet printing, the approximately 10 pL droplets fell rapidly onto the support, and the solvent then quickly evaporated.

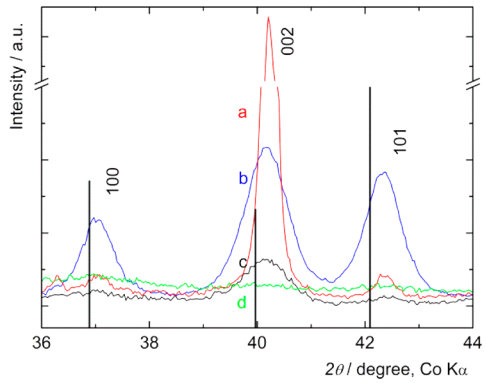


**Figure 1.** Powder XRD patterns of the (a) seed/growth film (nanocolumns), (b) inkjet-printed, five-layer film, (c) dip-coated, nine-layer film, and (d) sol−gel film compared to standard ZnO data in bars (JCPDS 36-1451).

The high degree of regularity of the dip-coated films was confirmed by AFM measurements (Figure 2). The flatness of the film surface was characterized by a roughness factor ($Ra$) of approximately 3.6 nm, which was comparable to that of a clean microscopic plate (2.4 nm). The AFM measurements of the inkjet-printed films confirmed that the printed ZnO nanosheets were less oriented, as demonstrated by an $Ra$ of 20 nm (Figure S2). The SEM images of the films were consistent with the AFM results (Figure S3a).

The nanocolumnar ZnO films were prepared using a standard chemical bath deposition procedure on a seeded ZnO layer prepared by dip-coating the ZnO nanosheets.[49] The vertical alignment of the nanocolumns was confirmed by SEM (Figure S3b) and XRD (Figure 1). The preferential orientation of the ZnO nanocolumns resulted in the disappearance of the (100) diffraction line. The hexagonal rods of the nanostructure


dx.doi.org/10.1021/la404017q | Langmuir 2014, 30, 380−386

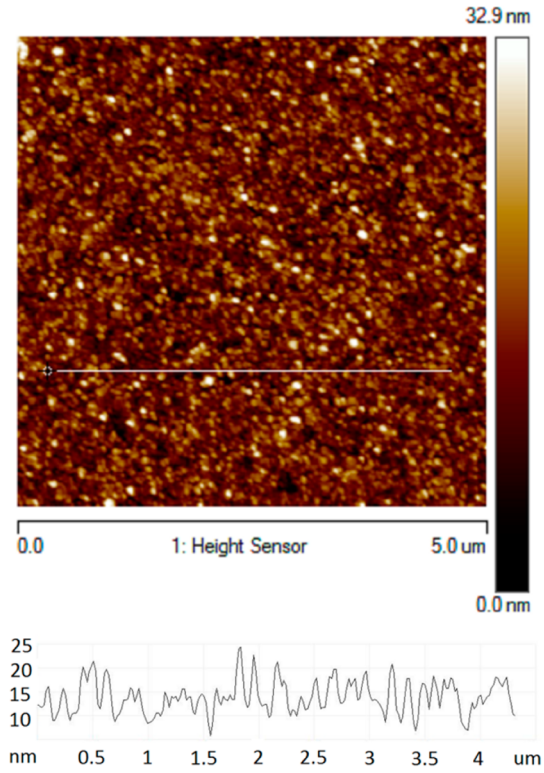


**Figure 2.** AFM image of the dip-coated ZnO film (nine layers) with a profile analysis along the white line (lower panel).

were covered predominantly with nonpolar facets, mainly {100} and {110}. The sol–gel method was used to prepare ZnO films with ridges and fiber-like structures (Figure S3c). The absence of diffractions in the XRD pattern indicated the presence of very small ZnO nanocrystals (Figure 1).

The UV/vis spectra of the dip-coated and inkjet-printed films exhibited a sharp absorption edge typical for a wide band gap semiconductor (Figure 3 and Figure S4). The films were transparent, and the absorption in the UV region linearly increased with an increase in the number of deposited layers. This observation indicates that the ZnO mass increased regularly as each layer was deposited. The UV/vis spectra of

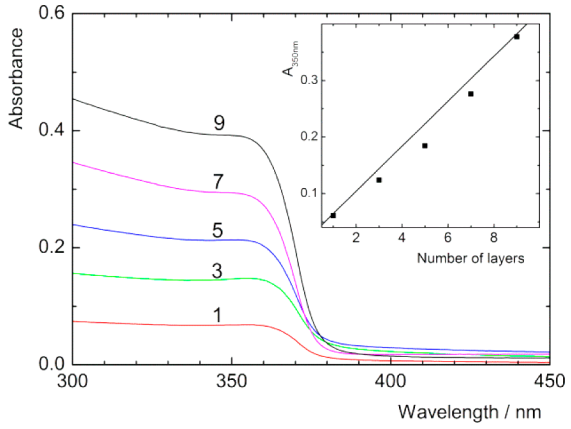


**Figure 3.** UV/vis absorption spectra of the dip-coated films with 1–9 layers of the ZnO nanosheets (denoted by the number above the curves). Inset: absorbance at 350 nm with an increasing number of the ZnO layers.

the ZnO nanocolumns and sol–gel film also showed the typical spectra of ZnO (Figure S5).

The textural properties of the films were determined by gas adsorption. Nitrogen and argon are the most commonly used adsorbates, but they cannot be used with materials such as thin films that have small surface areas in the range of tens of square centimeters. As an alternative, we used an adsorbate with a substantially lower saturation vapor pressure, krypton, at the boiling point of liquid nitrogen. The volume of adsorbed krypton on the dip-coated films was below the detection limit of the adsorption apparatus (several tens of $cm^2$), denoting that the surface areas of the films were comparable with the geometrical surface area (Figure 2). These results confirmed that the dip-coated films were compact and had no apparent porosity.

Because the inkjet-printed films adsorbed a larger volume of krypton than the dip-coated films, their surface area was measurable and was found to increase with an increase in the film thickness (Table 1). The five-layered films had the largest surface area of 32 $cm^2$ $cm^{-2}$. The adsorption isotherms for all the inkjet-printed films exhibited narrow hysteresis loops (Figure S6), indicating that the films had some porosity in the range of approximately 2–10 nm. Because the adsorption isotherms did not reach a limiting plateau at a relative pressure of 1, all of the films also contained pores larger than ca. 10 nm. The estimated void volume, based on the film thickness and its absorbance, was approximately 60–70% of the total film volume.

**Photocatalytic Activity of the ZnO Films.** The photocatalytic activities of films with different morphologies, i.e., smooth, nonporous, highly transparent dip-coated films, were compared to rather rough, porous inkjet-printed films. Additionally, we studied the photocatalytic activities of the sol–gel and nanocolumnar ZnO films to compare the performance of the nanosheet-based films to those with more common ZnO morphologies.

The photocatalytic degradation of 4-chlorophenol was used as a test reaction because 4-chlorophenol has good chemical stability, undergoes negligible photolysis, exhibits very low adsorption on the photocatalyst surface, and suitable analytic methods are available for the kinetic analysis. In addition, 4-chlorophenol is an important model pollutant in water remediation. The reaction mechanism of 4-chlorophenol degradation is complex and involves at least three separate pathways, namely hydroxylation, substitution, and direct charge-transfer oxidation, which form 4-chlorocatechol, hydroquinone, and nonaromatic compounds, respectively, as the primary intermediates.[51] Our previous studies and those of other groups have shown that the concentration of aromatic intermediates was close to the detection limit and often could not be reasonably evaluated.[52] Therefore, for comparative purposes, we calculated the first-order rate constants based on the disappearance of 4-chlorophenol and correlated them with the film characteristics, namely the thickness, UV absorbance, and, if possible, surface area (Table 1).

The kinetic curves of the 4-chlorophenol degradation, photocatalyzed by the inkjet-printed and dip-coated films, are presented in Figure 4 and Figure S7, respectively. The good reproducibility of the catalytic experiments was demonstrated by the small differences between two independent tests (less than 8% in the rate constant). Figure 5 illustrates the superior photocatalytic activities of the nanosheet-based films compared to nanocolumnar and sol–gel films. The rate constants for the


dx.doi.org/10.1021/la404017q | *Langmuir* 2014, 30, 380–386

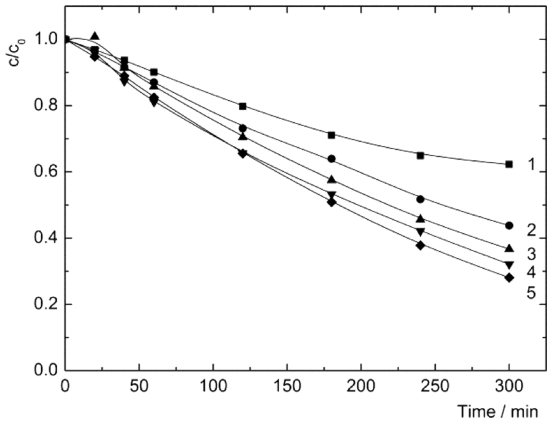


**Figure 4.** Photodegradation of 4-chlorophenol on the inkjet-printed ZnO films (the number of layers is specified at each curve). Each kinetic curve is an average of two independent experiments.

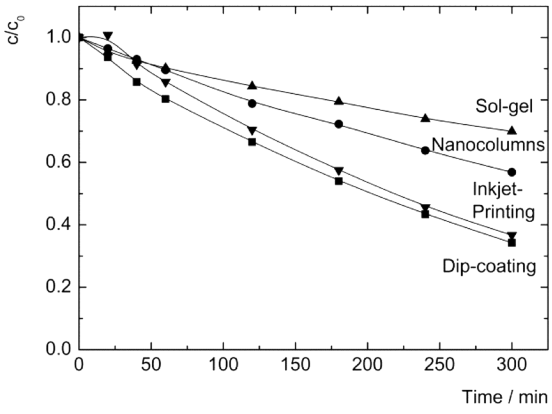


**Figure 5.** Effect of the ZnO morphologies on the photodegradation of 4-chlorophenol. The films were prepared by sol–gel processing (▲), seed/growth (nanocolumns) technique (●), dip-coating (nine layers) (■), and inkjet printing (three layers) (▼). The films were irradiated with 365 nm light. Each kinetic curve is an average of two independent experiments.

dip-coated and inkjet-printed films exhibited a nearly linear dependence on the UV absorbance (Figure 6). The curves coincide in the lower absorption region. It indicates a good mobility of electrons and holes in the films to the external

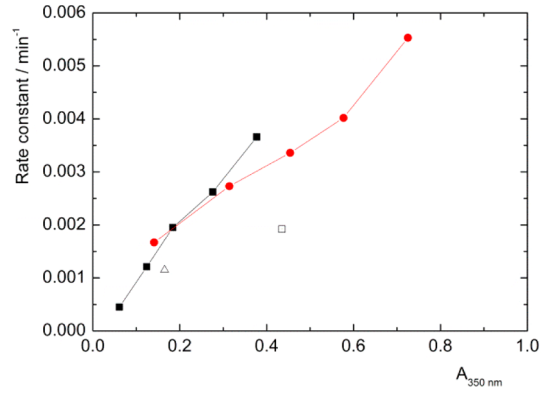


**Figure 6.** Dependence of the rate constant on the absorbance at 350 nm for the films prepared by dip-coating (■), inkjet printing (●), seed/growth (nanocolumns) technique (□), and sol–gel processing (△).

surface and explains the similar photocatalytic activities observed for the porous inkjet-printed and nonporous dip-coated films. The observed linearity is comparable to the behavior of multilayered mesoporous $TiO_2$ films tested under identical experimental conditions.[52] A long-term experiment to completely degrade 4-chlorophenol (Figure S8) using the inkjet-printed film indicated that complete degradation was achieved after 11–12 h of irradiation.

To test the stability of the ZnO films, two consecutive photocatalytic experiments were performed with each film. The inkjet-printed films were found to be the most stable, exhibiting slightly higher photocatalytic activity during the second run (Figure S8). On the other hand, the activities of the reused sol–gel and dip-coated films were substantially lower. The decrease in the amount of ZnO in the films, monitored during the photocatalytic experiments with UV/vis spectroscopy (Figure S9), clearly shows that the dip-coated and sol–gel films lost most of their ZnO mass during the first photocatalytic run. Generally, ZnO photocatalysts suffer from corrosion due to the hydrochloric acid produced during the mineralization of 4-chlorophenol and from photocorrosion that leads to ZnO dissolution.[53] In these experiments, the pH was constant, even after substantial degradation of 4-chlorophenol, which indicates that the produced hydrochloric acid could have only a minor effect. With respect to the stability, the inkjet-printed films were clearly superior to the dip-coated films.

The results show that inkjet printing allowed for the quick and reproducible fabrication of very active, photostable films with various amounts of ZnO. Importantly, the ZnO nanosheet-based films exhibited the best photoactivity; dip-coated (five layers) and inkjet-printed (three layers) films had approximately 1.5–1.7 times greater 4-chlorophenol degradation rate constants than those of the sol–gel and ZnO nanocolumns films with similar absorbances. These observations indicate that the morphology significantly enhanced the photocatalytic activity, and the porosity of the film played a minor role. The high photocatalytic activities of the inkjet-printed films can also be compared to those of $TiO_2$ films measured under identical experimental conditions. The rate constants of the inkjet-printed films (two layers) were approximately 1.8 times greater than those of mesoporous $TiO_2$ films (dip-coating, four layers) with a comparable UV absorbance.[52]

## ■ CONCLUSIONS

We fabricated transparent thin films composed of arranged ZnO nanosheets terminated by the high-energy {001} facets and tested them for the photocatalytic degradation of 4-chlorophenol. The films were prepared by dip-coating and inkjet printing, and their photocatalytic activities were compared to those of ZnO films with common morphologies:nanocolumns and sol–gel films. The nanosheet-based films had rate constants that were 1.5–1.7 times higher than those of the films prepared by sol–gel or composed of oriented nanocolumns. We ascribe the enhanced photocatalytic activity to higher surface area of polar {001} facets. The method of nanosheet deposition affected the porosity and photostability of the films, but the photocatalytic activities were comparable regardless of the deposition method. Printing ZnO nanosheet dispersions ("ZnO ink") on suitable supports can provide a facile means for fabricating large area well-defined transparent films or high-resolution patterns, which are needed for printed electronics. The physical properties (e.g., porosity) of the film


dx.doi.org/10.1021/la404017q | Langmuir 2014, 30, 380–386

can be tuned by using a various techniques to deposit the nanosheets. This tunability, combined with the predominantly high-energy {001} facets at the surface, makes the ZnO nanosheet-based films attractive for a wide range of applications in the construction of sensors, optical devices, and dye-sensitized solar cells.

## ■ ASSOCIATED CONTENT

### Supporting Information

Full experimental details (XRD, AFM, SEM, UV/vis, adsorption isotherms, and catalytic tests). This material is available free of charge via the Internet at http://pubs.acs.org.

## ■ AUTHOR INFORMATION


### Corresponding Author

*E-mail: demel@iic.cas.cz (J.D.).


### Notes

The authors declare no competing financial interest.

## ■ ACKNOWLEDGMENTS

This work was supported by the Czech Science Foundation (P207/10/1447, 13-09462P).

## ■ REFERENCES


(1) Sakthivel, S.; Neppolian, B.; Shankar, M. V.; Arabindoo, B.; Palanichamy, M.; Murugesan, V. Solar photocatalytic degradation of azo dye: comparison of photocatalytic efficiency of ZnO and $TiO_2$. *Sol. Energy Mater. Sol. Cells* **2003**, *77*, 65−82.

(2) Wang, H.; Xie, C.; Zhang, W.; Cai, S.; Yang, Z.; Gui, Y. Comparison of dye degradation efficiency using ZnO powders with various size scales. *J. Hazard. Mater.* **2007**, *141*, 645−652.

(3) Kamat, P. V.; Huehn, R.; Nicolaescu, R. A "sense and shoot" approach for photocatalytic degradation of organic contaminants in water. *J. Phys. Chem. B* **2002**, *106*, 788−794.

(4) Akyol, A.; Yatmaz, H. C.; Bayramoglu, M. Photocatalytic decolorization of Remazol Red RR in aqueous ZnO suspensions. *Appl. Catal., B* **2004**, *54*, 19−24.

(5) Lin, H.; Liao, S.; Hung, S. The dc thermal plasma synthesis of ZnO nanoparticles for visible-light photocatalyst. *J. Photochem. Photobiol., A* **2005**, *174*, 82−87.

(6) Chakrabarti, S.; Dutta, B. K. Photocatalytic degradation of model textile dyes in wastewater using ZnO as semiconductor catalyst. *J. Hazard. Mater.* **2004**, *B112*, 269−278.

(7) Daneshvar, N.; Salari, D.; Khataee, A. R. Photocatalytic degradation of azo dye acid red 14 in water on ZnO as an alternative catalyst to $TiO_2$. *J. Photochem. Photobiol., A* **2004**, *162*, 317−322.

(8) Pauporté, T.; Rathouský, J. Growth mechanism and photocatalytic properties for dye degradation of hydrophobic mesoporous ZnO/SDS films prepared by electrodeposition. *J. Microporous Mesoporous Mater.* **2009**, *117*, 380−385.

(9) Pauporté, T.; Rathouský, J. Electrodeposited mesoporous ZnO thin films as efficient photocatalysts for the degradation of dye pollutants. *J. Phys. Chem. C* **2007**, *111*, 7639−7644.

(10) Lizama, C.; Freer, J.; Baeza, J.; Mansilla, H. D. Optimized photodegradation of reactive blue 19 on $TiO_2$ and ZnO suspensions. *Catal. Today* **2002**, *76*, 235−246.

(11) Yeber, M. C.; Rodriguez, J.; Freer, J.; Baeza, J.; Duran, N.; Mansilla, H. D. Advanced oxidation of a pulp mill bleaching wastewater. *Chemosphere* **1999**, *39*, 1679−1688.

(12) Poulios, I.; Aetopoulou, I. Photocatalytic degradation of the textile dye reactive orange 16 in the presence of $TiO_2$ suspensions. *Environ. Technol.* **1999**, *20*, 479−487.

(13) Evgenidou, E.; Fytianos, K.; Poulios, I. Semiconductor-sensitized photodegradation of dichlorvos in water using $TiO_2$ and ZnO as catalysts. *Appl. Catal., B* **2005**, *59*, 81−89.

(14) Rabindranathan, S.; Devipriya, S.; Yesodharan, S. Photocatalytic degradation of phosphamidon on semiconductor oxides. *J. Hazard. Mater.* **2003**, *B102*, 217−229.

(15) Khodja, A. A.; Sehili, T.; Pilichowski, J. F.; Boule, P. Photocatalytic degradation of 2-phenylphenol on $TiO_2$ and ZnO in aqueous suspensions. *J. Photochem. Photobiol., A* **2001**, *141*, 231−239.

(16) Jiang, Z.-Y.; Kuang, Q.; Xie, Z.-X.; Zheng, L.-S. Syntheses and properties of micro/nanostructured crystallites with high-energy surfaces. *Adv. Funct. Mater.* **2010**, *20*, 3634−3645.

(17) Meunier, F. C. Mixing copper nanoparticles and ZnO nanocrystals: A route towards understanding the hydrogenation of $CO_2$ to methanol? *Angew. Chem., Int. Ed.* **2011**, *50*, 4053−4054.

(18) Liao, F.; Huang, Y.; Ge, J.; Zheng, W.; Tedsree, K.; Collier, P.; Hong, X.; Tsang, S. C. Morphology-dependent interactions of ZnO with Cu nanoparticles at the materials' interface in selective hydrogenation of $CO_2$ to $CH_3OH$. *Angew. Chem., Int. Ed.* **2011**, *50*, 2162−2165.

(19) Koch, U.; Fojtik, A.; Weller, H.; Henglein, A. Photochemistry of semiconductor colloids. Preparation of extremely small ZnO particles, fluorescence phenomena and size quantization effects. *Chem. Phys. Lett.* **1985**, *122*, 507−510.

(20) Mclaren, A.; Valdes-Solis, T.; Li, G.; Tsang, S. C. Shape and size effects of ZnO nanocrystals on photocatalytic activity. *J. Am. Chem. Soc.* **2009**, *131*, 12540−12541.

(21) Tang, D.; Allard, L. F.; Boley, A.; Smith, D. J.; Liu, J. Structure and morphology of polar and semi-polar pyramidal surfaces coating wurtzite ZnO micro-wires. *J. Mater. Sci.* **2013**, *48*, 3857−3862.

(22) Sanchez, C.; Boissiere, C.; Grosso, D.; Laberty, C.; Nicole, L. Design, synthesis, and properties of inorganic and hybrid thin films having periodically organized nanoporosity. *Chem. Mater.* **2008**, *20*, 682−737.

(23) Zhou, W.; Fu, H. Mesoporous $TiO_2$: Preparation, doping, and as a composite for photocatalysis. *ChemCatChem* **2013**, *5*, 885−894.

(24) Brinker, C. J.; Lu, Y. F.; Sellinger, A.; Fan, H. Y. Evaporation-induced self-assembly: Nanostructures made easy. *Adv. Mater.* **1999**, *11*, 579−585.

(25) Szeifert, J. M.; Fattakhova-Rohlfing, D.; Georgiadou, D.; Kalousek, V.; Rathouský, J.; Kuang, D.; Wenger, S.; Zakeeruddin, S. M.; Grätzel, M.; Bein, T. Brick and mortar strategy for the formation of highly crystalline mesoporous titania films from nanocrystalline building blocks. *Chem. Mater.* **2009**, *21*, 1260−1265.

(26) Němec, H.; Kužel, P.; Kadlec, F.; Fattakhova-Rohlfing, D.; Szeifert, J.; Bein, T.; Kalousek, V.; Rathouský. Ultrafast terahertz photoconductivity in nanocrystalline mesoporous $TiO_2$ films. *J. Appl. Phys. Lett.* **2010**, *96*, 062103.

(27) Szeifert, J.; Feckl, J.; Fattakhova-Rohlfing, D.; Liu, Y.; Kalousek, V.; Rathouský, J.; Bein, T. Ultrasmall titania nanocrystals and their direct assembly into mesoporous structures showing fast lithium insertion. *J. Am. Chem. Soc.* **2010**, *132*, 12605−12611.

(28) Szeifert, J. M.; Fattakhova-Rohlfing, D.; Rathouský, J.; Bein, T. Multilayered high surface area "brick and mortar" mesoporous titania films as efficient anodes in dye-sensitized solar cells. *Chem. Mater.* **2012**, *24*, 659−663.

(29) Fattakhova-Rohlfing, D.; Szeifert, J. M.; Yu, Q.; Kalousek, V.; Rathouský, J.; Bein, T. Low-temperature synthesis of mesoporous titania-silica films with pre-formed anatase nanocrystals. *Chem. Mater.* **2009**, *21*, 2410−2417.

(30) Müller, V.; Rasp, M.; Štefanić, G.; Ba, J.; Günther, S.; Rathouský, J.; Niederberger, M.; Fattakhova-Rohlfing, D. Highly conducting nanosized monodispersed antimony-doped tin oxide particles synthesized via nonaqueous sol-gel procedure. *Chem. Mater.* **2009**, *21*, 5229−5236.

(31) Müller, V.; Rasp, M.; Rathouský, J.; Niederberger, M.; Fattakhova-Rohlfing, D. Transparent conducting films of antimony-doped tin oxide with uniform mesostructure assembled from preformed nanocrystals. *Small* **2010**, *6*, 633−637.

(32) Liu, Y.; Szeifert, J. M.; Feckl, J. M.; Mandlmeier, B.; Rathouský, J.; Hayden, O.; Fattakhova-Rohlfing, D.; Bein, T. Niobium-doped

titania nanoparticles: Synthesis and assembly into mesoporous films and electrical conductivity. *ACS Nano* **2010**, *4*, 5373−5381.
(33) Fried, D. I.; Mueller, V.; Rathouský, J.; Fattakhova-Rohlfing, D. A facile synthesis of mesoporous crystalline tin oxide films involving a base-triggered formation of sol-gel building blocks. *Nanoscale* **2011**, *3*, 1234−1239.
(34) Liu, Y.; Rathouský, J.; Stefanić, G.; Hayden, O.; Bein, T.; Fattakhova-Rohlfing, D. Assembly of mesoporous indium tin oxide electrodes from nano-hydroxide building blocks. *Chem. Sci.* **2012**, *3*, 2367−2374.
(35) Demel, J.; Pleštil, J.; Bezdička, P.; Janda, P.; Klementová, M.; Lang, K. Layered zinc hydroxide salts: Delamination, preferred orientation of hydroxide lamellae, and formation of ZnO nanodiscs. *J. Colloid Interface Sci.* **2011**, *360*, 532−539.
(36) Demel, J.; Pleštil, J.; Bezdička, P.; Janda, P.; Klementová, M.; Lang, K. Few-layer ZnO nanosheets: Preparation, properties, and films with exposed {001} facets. *J. Phys. Chem. C* **2011**, *115*, 24702−24706.
(37) Heinzl, J.; Hertz, C. H. Ink-jet printing. *Adv. Imaging Electron Phys.* **1985**, *65*, 91−171.
(38) Tincher, W. C. Overview of digital printing and print head technologies. *AATCC Rev.* **2003**, *3*, 4−7.
(39) Wang, T. M.; Roberts, M. A.; Kinloch, I. A.; Derby, B. Inkjet printed carbon nanotube networks: The influence of drop spacing and drying on electrical properties. *J. Phys. D: Appl. Phys.* **2012**, *45*, 315304.
(40) Torrisi, F.; Hasan, T.; Wu, W. P.; Sun, Z. P.; Lombardo, A.; Kulmala, T. S.; Hsieh, G. W.; Jung, S. J.; Bonaccorso, F.; Paul, P. J.; Chu, D. P.; Ferrari, A. C. Inkjet-printed graphene electronics. *ACS Nano* **2012**, *6*, 2992−3006.
(41) Delaney, J. T.; Smith, P. J.; Schubert, U. S. Inkjet printing of proteins. *Soft Mater.* **2009**, *5*, 4866−4877.
(42) Guillotin, B.; Guillemot, F. Cell patterning technologies for organotypic tissue fabrication. *Trends Biotechnol.* **2011**, *29*, 183−190.
(43) Ballarin, B.; Fraleoni-Morgera, A.; Frascaro, D.; Marazzita, S.; Piana, C.; Setti, L. Thermal inkjet microdeposition of PEDOT:PSS on ITO-coated glass and characterization of the obtained film. *Synth. Met.* **2004**, *146*, 201−205.
(44) Černá, M.; Veselý, M.; Dzik, P. Physical and chemical properties of titanium dioxide printed layers. *Catal. Today* **2011**, *161*, 97−104.
(45) Dzik, P.; Morozová, M.; Klusoň, P.; Veselý, M. Photocatalytic and self-cleaning properties of titania coatings prepared by inkjet direct patterning of a reverse micelles sol-gel composition. *J. Adv. Oxid. Technol.* **2012**, *15*, 89−97.
(46) Morozová, M.; Klusoň, P.; Krýsa, J.; Dzik, P.; Veselý, M.; Šolcová, O. Thin $TiO_2$ films prepared by inkjet printing of the reverse micelles sol-gel composition. *Sens. Actuators, B* **2011**, *160*, 371−378.
(47) Morozová, M.; Klusoň, P.; Krýsa, J.; Veselý, M.; Dzik, P.; Šolcová, O. Thin $TiO_2$ films prepared by inkjet printing of the reverse micelles sol-gel composition. *Procedia Eng.* **2012**, *42*, 573−580.
(48) Thakur, V.; Verma, U. P.; Rajaram, P. Solvent dependent growth of fibrous and non-fibrous nanocrystalline thin films of ZnO. *J. Sol-Gel. Sci. Technol.* **2013**, *66*, 280−287.
(49) Saarenpää, H.; Sariola-Leikas, E.; Perros, A. P.; Kontio, J. M.; Efimov, A.; Hayashi, H.; Lipsanen, H.; Imahori, H.; Lemmetyinen, H.; Tkachenko, N. V. Self-assembled porphyrins on modified zinc oxide nanorods: Development of model systems for inorganic-organic semiconductor interface studies. *J. Phys. Chem. C* **2012**, *116*, 2336−2343.
(50) JCPDS PDF-2 database, International Centre for Diffraction Data, Newtown Square, PA, release 54, 2004.
(51) Li, X.; Cubbage, J. W.; Tetzlaff, T. A.; Jenks, W. S. Photocatalytic degradation of 4-chlorophenol. 1. The hydroquinone pathway. *J. Org. Chem.* **1999**, *64*, 8509−8524.
(52) Rathouský, J.; Kalousek, V.; Kolář, M.; Jirkovský, J. Mesoporous films of $TiO_2$ as efficient photocatalysts for the purification of water. *Photochem. Photobiol. Sci.* **2011**, *10*, 419−424.
(53) Neppolian, B.; Choi, H. C.; Sakthivel, S.; Banumathi, A.; Murugesan, V. Solar light induced and $TiO_2$ assisted degradation of textile dye reactive blue 4. *J. Hazard. Mater.* **2002**, *B89*, 303−317.

Applied Catalysis B: Environmental 138–139 (2013) 84–94

Contents lists available at SciVerse ScienceDirect

Applied Catalysis B: Environmental

journal homepage: www.elsevier.com/locate/apcatb

# Fabrication, characterization and photocatalytic activity of $TiO_2$ layers prepared by inkjet printing of stabilized nanocrystalline suspensions

Marcela Černá[a], Michal Veselý[a], Petr Dzik[a,*], Chantal Guillard[b], Eric Puzenat[b], Martina Lepičová[a]

[a] BrnoUniversity of Technology, Faculty of Chemistry, Purkynova 118, 612 00 Brno, Czech Republic
[b] Institut of Recherches sur la Catalyse et l'Environnement de Lyon, CNRS UMR 5256, Universite de Lyon, 2 Avenue Albert Einstein, Villeurbanne F-69622 cedex, France

ARTICLE INFO

*Article history:*
Received 22 October 2012
Received in revised form 11 February 2013
Accepted 18 February 2013
Available online 27 February 2013

*Keywords:*
Photocatalytic activity
Hydrothermal synthesis
Inkjet printing
Colloidal dispersion

ABSTRACT

Titanium dioxide ($TiO_2$) colloidal dispersions were synthesized by hydrothermal synthesis in acidic pH under various process conditions. Phase structure of prepared $TiO_2$ was identified as pure rutile by X-ray diffraction analysis and crystallite sizes determined by the Scherrer equation were in the range of 10–25 nm. These values correlated with particle sizes observed by transmission electron microscopy (TEM). Afterwards, the prepared $TiO_2$ dispersions were used for the formulation of stable inkjet printable "inks". Thin layers of nanocrystalline $TiO_2$ were deposited by inkjet printing onto soda-lime glass substrates. After sintering at 500 °C, thin patterned films were obtained. Their basic physicochemical properties were characterized by standard methods. Optical microscopy and SEM imaging revealed highly structured topography of samples surface. Layer hardness was equivalent to the B pencil as determined by the "Pencil Hardness Test". The topology and roughness were examined by atomic force microscopy and RMS roughness was in the range of 40–100 nm. Band gap energy of $TiO_2$ determined by UV–vis reflection spectroscopy was consistent with known rutile values. The photocatalytic activity of printed layers was evaluated on the basis of 2,6-dichloroindophenoldiscoloration rate monitored by UV–vis spectroscopy and did not exceed the performanceof Aeroxide P-25. Despite average photocatalytic performace of this particular $TiO_2$ type, inkjet printing proved to be an efficient method for the fabrication of patterned titania films originating from nanocrystalline precursor.



## 1. Introduction

Heterogeneous photocatalysis being a promising water and air purification technique, has attracted a great deal of attention in the last years [1–6]. The main advantage of this method compared to the traditional wastewater treatment, such as chlorination or ozonolysis is that a lot of persistent contaminants, (e.g. phenol, 4-chlorophenol, trichloroethylene and chlorobenzene) can be completely mineralized including their potentionally problematic degradation byproducts [7–9]. Among various oxide semiconductorsefficient for photocatalysis, titanium dioxide is the bestphotocatalyst because of its strong oxidizing power, nontoxicity and relatively long-term photostability [10].

Absorption of UV light causes the generation pair of an electron and a hole. The excited electrons are trapped by $O_2$ to form superoxide radical ion ($O_2$). The holes can react with adsorbed water to form reactive hydroxyl radicals (•OH). These radicals are considered to be the major active species responsible for the photocatalytic oxidation reaction. These hydroxyl radicals can by quantitatively detected by photoluminescence [11].

Three main different crystalline phases of titanium dioxide exists: anatase (tetragonal), rutile (tetragonal) and brookite (orthorhombic). However, only anatase and rutile have been used in most photocatalytic studies and the photocatalytic activity of amorphous titania is negligible [12]. Anatase phase shows a higher photocatalytic activity than rutile due to its lower recombination rate of photo-generated electrons and holes [13,14].

It is well known that the photocatalytic activity of $TiO_2$ strongly depends on the preparation methods and post-treatment conditions, since they both have a decisive influence on the chemical and physical properties of $TiO_2$ [15–16]. Many approaches to improve the photocatalytic activity of $TiO_2$have been proposed. Generally, modification of its morphology, crystal composition, crystallinity, and surface area are the most common [17–24]. Of these approaches, hydrothermal treatment is one of the most widely used methods for increasing the crystallinity of $TiO_2$ [25,26].

The hydrothermal method of $TiO_2$ particles preparation has many advantages. A major advantage of using the hydrothermal

* Corresponding author. Tel.: +420 541 149 411; fax: +420 541 211 697.
*E-mail address:* petr@dzik.cz (P. Dzik).

0926-3373/$ – see front matter © 2013 Elsevier B.V. All rights reserved.
http://dx.doi.org/10.1016/j.apcatb.2013.02.035

process is the ability to produce different crystalline phases without the need of subsequent thermal treatment as it provides the capacity to grow good-quality crystals and to control the crystalline composition simultaneously [27]. By changing the hydrothermal reaction conditions, such as the reaction temperature, pH values, reactant concentrations and molar ratio, crystalline products with different compositions, structures and morphologies have been obtained.

Nanocrystalline dispersions of titanium dioxide, either of the hydrothermal or any other origin, are very efficient for the photocatalytic degradation of various pollutants. However, photocatalytic reactions utilizing the slurried form of catalyst are burdened by the need for catalyst recovery. Therefore, photocatalyst immobilised onto suitable support is usually the preferred form for practical application. Although titania coatings have been fabricated by countless different processes, wet coating techniques constitute a very popular approach. At the same time, hydrothermally synthesized nanocrystalline titania dispersions are excellent raw materials for wet coating formulations, providing a good level of control over the crystallinity of the resulting layer.

Many different wet-coating techniques have been proposed, such as dip-, spin- or spray-coating, doctor blade spreading, roller etc [28]. However, recently a new promising wet coating technique has become available. This novel approach is usually termed inkjet material deposition or shortly material printing. The technique shares the basic principles with conventional inkjet printing, i.e. tiny droplets of a low-viscosity liquid are precisely deposited onto a substrate by means of thermal or piezoelectric printhead. In the case of material printing, the ink is a specially formulated liquid used for transporting a functional component onto the substrate surface [29–33].

Material printing has been successfully employed for the deposition of a great variety of functional materials, titanium dioxide including. Generally, two different approaches can be identified when discussing titania printed layers: The printing “ink” can be based on the sol–gel chemistry utilizing an organometallic precursor in the form of stable sol. Printed ink dries to form a xerogel layer which is further processed into oxide layer usually by calcination at 300–500 °C [34–40]. The second route relies on the formulation of stable colloidal suspension of nanocrystalline $TiO_2$ followed by a delivery of this suspension onto substrate by means of the inkjet printing [41–47]. Naturally, the free-standing nanoparticles have only very limited adhesion to substrate and need to be fixed e.g. by heat sintering or the addition of suitable binder [48].

In this paper, we report the influence of different hydrothermal conditions on the physical properties and photocatalytic activity of prepared $TiO_2$. Hydrothermally prepared titania slurries were deposited onto soda-lime glass substrates by material printing and effect of layers thickness was investigated.

## 2. Experimental

### 2.1. Hydrothermal synthesis of $TiO_2$

Colloidal dispersion of titanium dioxide was prepared by hydrothermal synthesis using titanium oxochloride($TiOCl_2$) as a precursor. $TiOCl_2$ was added dropwise to 480 mL of potassium hydroxideaqueous solution with concentration 5 mol $L^{-1}$ to neutral reaction. KOH was used as the precipitation agent. Mixture was washed several times to remove excess of chloride ions which can have a negative influence on final $TiO_2$ photocatalytic activity [49]. According to our previous finding, acidic environment is much better for photocatalytic activity of colloidal $TiO_2$ than basic medium [50]. So HCl (p.s.)(0.9 mL) was added to $TiO_2$ mixture for decreasing final pH value to 1. The mixtures were hydrothermally treated under different conditions. The influence of temperatures and duration of hydrothermal synthesis on the final properties of prepared samples was investigated. We used temperature 110 °C and 160 °C. These particular temperatures were selected arbitrarily to include samples processed at a temperature close to the boiling point of water (which is favourable from the practical engineering and energy consumption point of view) and a sample set processed at a significantly higher temperature. According to our previous experience the difference of 50 °C was expected to be sufficient to induce significant differences in the properties of prepared samples. Treatment duration was 6 h, 24 h and 48 h yielding 6 samples of nanocrystalline titania dispersions.

### 2.2. Thin layer printing

Soda-lime glass platesof size 50 mm × 50 mm × 1.1 mm were used for $TiO_2$ immobilization. Firstly, it was necessary to pre-treat the soda-lime glass plates in sulphuric acid in order to prevent sodium ions diffusion which would have caused a reduction of photocatalytic activity [51,52]. Just after and before the layer coating, the plates were washed in an aqueous surfactant solution to remove of dust, grease and other residues which might have contaminated the surface during plate storage.

Titania application was performed in an innovative way utilizing an experimental printer FUJIFILM Dimatix (Dimatix Materials Printer DMP-2831). In order to fully exploit the full potential of this device, printing inks needed to be formulated and optimized proving stable and reliable jetting:1 mL of hydrothermally synthesized $TiO_2$dispersion was mixed with 1 mL HCl (p. s.) and 1 mL surfactant (see Section 3.4. for surfactant choice discussion) and 1 ml $H_2O$, respectively.

The prepared formulation was stable and was used directly as the printing ink. Before filling the cartridge ink tank, it was necessary to sonicate the ink for 5 min and filter it through a 0.45 μm size syringe filter in order to eliminate any aggregates and solid contaminants which may clog the printhead nozzles.

The Dimatix 10 pL printhead containing 16 nozzles was attached to the filled ink tank and mounted into the Dimatix printer. The nozzle temperature was set to 40 °C which was beneficial for further viscosity reduction without increasing the evaporation rate from printing nozzles too much. Nozzle span was set to 20 μm, i.e. 2500 drops per $mm^2$. Dimatix model liquid 2 waveform was used and the piezo driving voltage was set to 22 V.

One-layer and two-layer samples were coated by this method for all six samples. The printing of two layers was performed in the so called “wet-to-dry” manner, meaning that the first layer was completely dry before printing the second one. Simultaneously with the synthesized $TiO_2$, we printed also one- and two-layer samples with an ink prepared from commercial $TiO_2$ (Evonik Aeroxide P-25) which was used as a comparative standard. A simple 4 cm square pattern was printed in the middle of the 5 cm square glass plate. Finally, the printed substrates were placed into a calcination furnace and printed titania layers were fixed by heating with a ramp of 3 °C/min and keeping at 500 °C for 30 min.

### 2.3. Characterization

Crystallinity of $TiO_2$ was examined from X-ray powder diffraction pattern measurement by using Cu Kα as the radiation source. We used X-ray diffractometer Empyrean, Panalytical for this analysis. The titania powder was prepared by drying the hydrothermally synthesized colloidal dispersion at the temperature of 50 °C to constant weight.

Subsequently, the crystallite size was calculated using Scherrer Eq. (1), where $B$ is constant equal 0.94, λ is the wave length which is equal to 1.54 Å and $\beta$ is the width of peak at a half of maximal height.

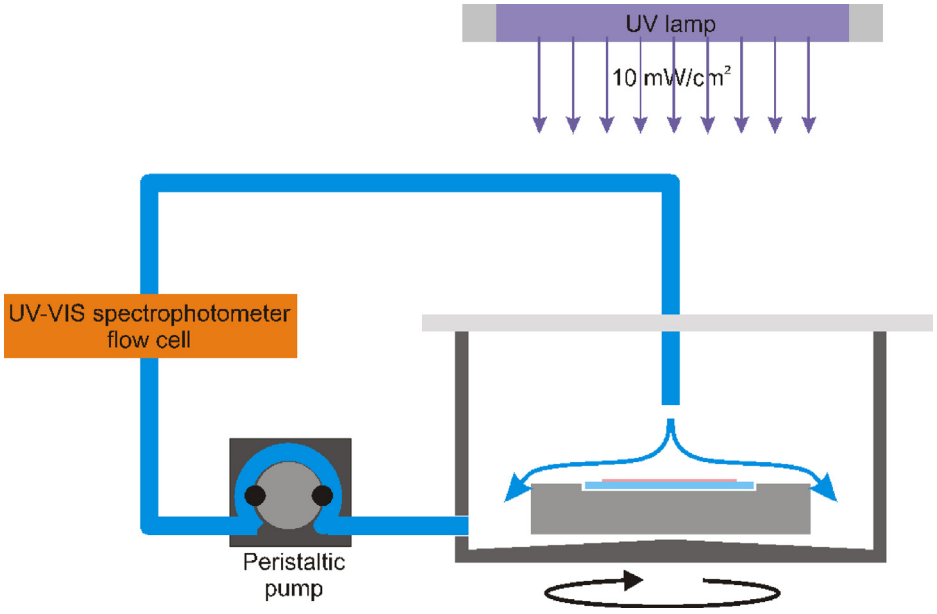


**Fig. 1.** Arrangement of photocatalytic reactor.

The influence of different time, temperature and pH of process was studied.

$$d = \frac{B \cdot \lambda}{\beta \cdot \cos\theta} \quad (1)$$

Transmission electron microscopy (TEM) was used for the analysis of prepared $TiO_2$ crystallite size as well as their shape. We used a JEOL JEM 2010 microscope operated at 200 kV, equipped with a $LaB_6$ tip. The samples were prepared by simply putting a drop of the solution containing the particles on a holey-carbon thin film supported on a microscopy copper grid.

The band gap of the prepared $TiO_2$ was evaluated from diffused reflectance measurement. We used fiber UV–vis spectrometer equipped with two lamps, deuterium lamp for UV region and halogen lamp for VIS area. The optical path consists of several optical fibers where six of them are connected with the lamps providing illumination of the sample and one reading fiber connected to the spectrometer. Reflectance was measured in the range of wavelength from 290 nm to 500 nm and barium sulfate was chosen as a reference. Molar absorption coefficient was calculated using the following formula (1), which is derived from Kubelka-Munk theory where $\alpha$ is molar absorption coefficient and $R$ is reflectance.

$$\alpha = \frac{(1-R)^2}{2R} \quad (2)$$

Direct as well as indirect transitions were examined. For direct transition, the dependence of $(\alpha{\cdot}h{\cdot}\nu)^2$ on $(h{\cdot}\nu)$ is plotted where $(h{\cdot}\nu)$ is the photon energy. On the other hand, $(\alpha{\cdot}h{\cdot}\nu)^{1/2}$ as a function of photon energy was plottted for the indirect transition, and we calculated the band gap energy from extrapolation of molar absorption coefficient to zero [53].

The amount of deposited $TiO_2$ particles was determined by gravimetric method. We measured the weight of glass substrate before printing and then after thermal fixing of the printed titania layer. Consequently, all prepared samples were imaged by optical microscopy where we evaluated their homogeneity. Nikon Eclipse E200 microscope was used for this purpose. Images were recorded by a digital camera Nikon D5000 mounted on the optical microscope. The quality of one-layers as well as double-layers was compared.

Hardness of prepared titania films was studied by "Pencil hardness test" according to standard ISO 15184 [54]. The pencils differed in their hardness. Today there are 17 degrees of the hardness, from 9H what is the hardest to 9B what means the softest. The hardness of the layer is the same as the hardness of the pencil which does not cause any defect on its surface. This method was chosen because it is very rapid and inexpensive. On the other hand only smooth surfaces are useful and this method is destructive technique.

The surface topology of prepared layers was studied by atomic force microscopy AFM. Veeco Di CP-II (Dymek, Japan) machine in a tapping mode was used for this purpose. Images from scanning electron microscopy were received from MIRA II LMU machine by Tescan and by this analysis we examined the surface morphology of prepared thin layer of $TiO_2$.

### 2.4. Photocatalyticactivity

Photocatalytic experiments were performed in aqueous solution of 2,6-dichloroindophenol (DCIP) with an initial concentration of $2 \times 10^{-5}$ mol $L^{-1}$. The sample was placed into a circulated batch reactor featuring a rotary sample holder (Fig. 1). Each sample was irradiated before the photocatalytic reaction by UV radiation with intensity 7.5 mW $cm^{-2}$ for 10 min in order to activate the titania photocatalysts. UV radiation was provided by Philips Metal-halide lamp HPA 400/30 SD. The intensity was measured by Gigahertz Optic X97 Irradiance meter with X9-7 probe. Consequently, 70 mL of reaction solution was poured into the reactor and the reactor chamber was immediately covered by a UV-transparent PE foil to prevent solution evaporation. Continuous flow of the model substance was maintained by a peristaltic pump. Due to the circular movement of the sample holder the model solution was evenly spread over the whole active surface and a constant thickness of the liquid film was maintained during the whole reaction. SpectraSuite Ocean Optics software of fibre spectrometer provided on-line data collecting every 1 min. Change of DCIP concentration was determined at 600 nm. All experiments ran for 40 min.

## 3. Results and discussion

### 3.1. XRD analysis

The X-ray diffraction patterns of the systems allowed us to identify the crystal phase in $TiO_2$ systems. All studied powders were

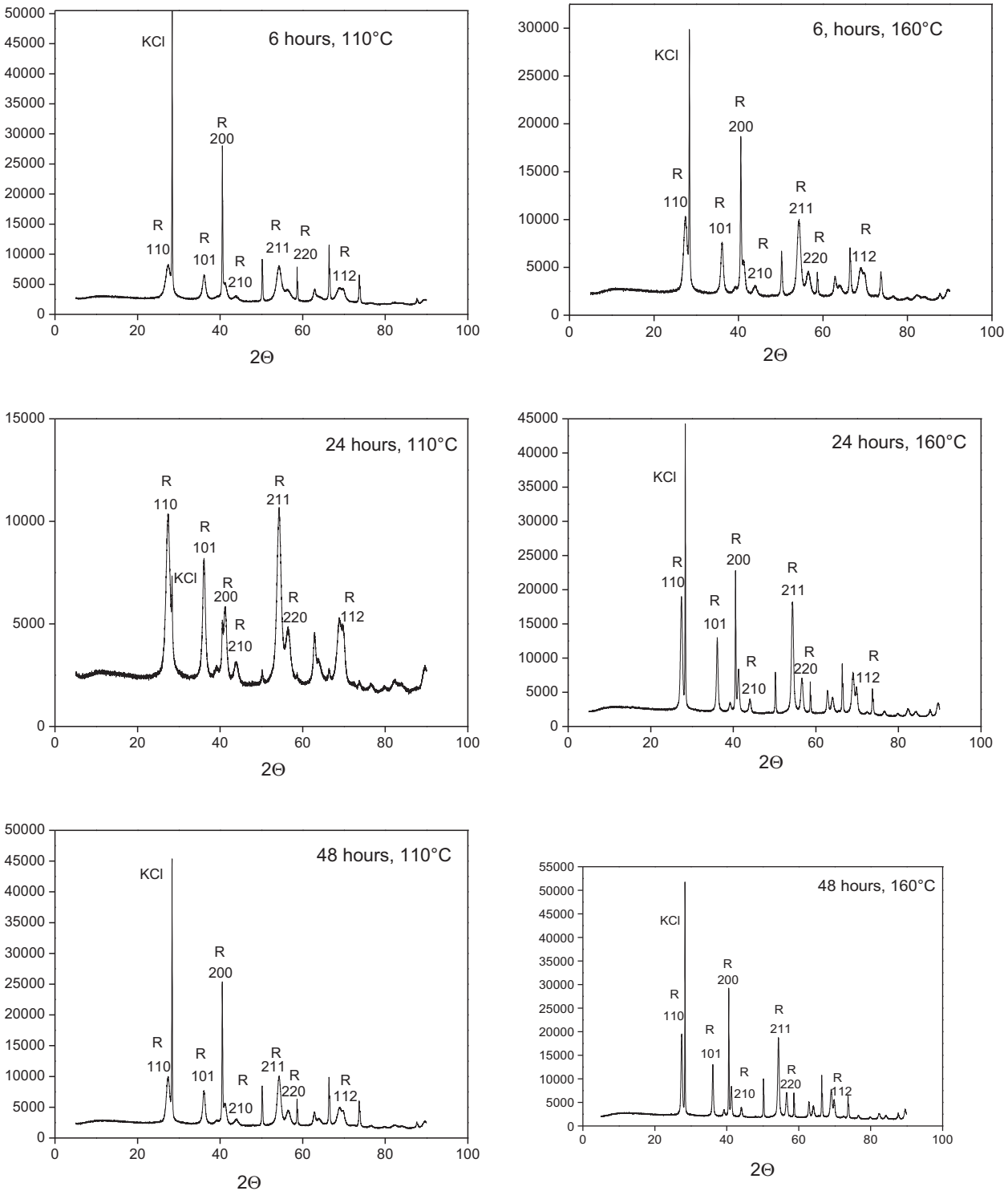


**Fig. 2.** XRD spectra of raw $TiO_2$ powders obtained from slurries synthesized at 110 °C (left) and 160 °C (right).

pure rutile (Fig. 2). This result indicates that the final crystallite phase is mostly dependent on pH, in less extent on the treatment temperature and time of hydrothermal synthesis. All investigated samples were prepared at pH 1 in contrast to the previous work [50] where $TiO_2$ was prepared at pH 2. This pH decreasing brought about change of $TiO_2$ crystallite phase from mixture of anatase and rutile to pure rutile. This result is in good agreement with published data of Yin et al. [55] where they observed that pure rutile is obtained at lower temperature of hydrothermal synthesis using pH around 1.

We can also observe quite intensive peak for KCl which could remain in the samples due to the insufficient washing of titania slurries.

Crystallite sizes were calculated using Scherrer Eq. (1). Obtained results are summarized in Table 1. We can observe that crystallite size decreases with increasing time of hydrothermal

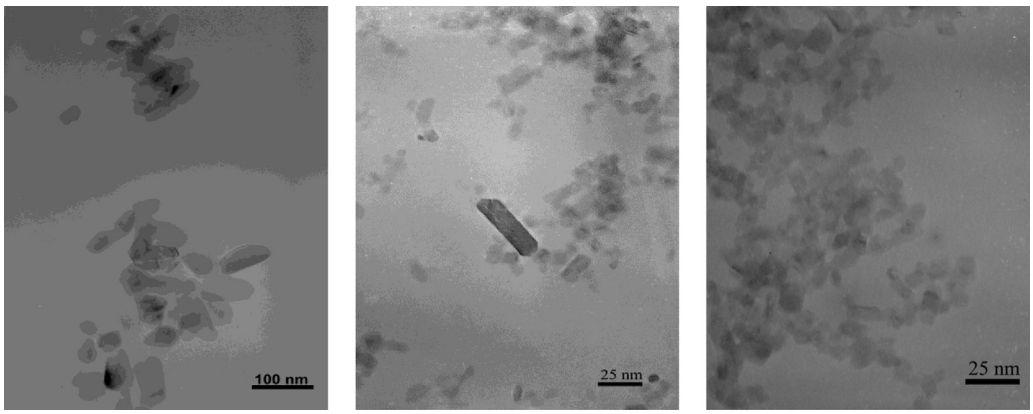


**Fig. 3.** TEM images of $TiO_2$ synthesized at 160 °C; 6 h (left), 24 h (middle), 48 h (right).

**Table 1**
Crystallite size (nm).

| 110 °C | | | 160 °C | | |
|---|---|---|---|---|---|
| 6 h | 24 h | 48 h | 6 h | 24 h | 48 h |
| 12 nm | 10 nm | 9 nm | 26 | 20 | 12 |

synthesis. This dependence was observed for both temperatures.

### 3.2. Transmission electron microscopy

Transmission electron microscopy shows that particle size decreases with increasing time of hydrothermal synthesis. We also studied the shape of prepared titania particles. We can observe rods (Fig. 3) which is typical shape for rutile phase of $TiO_2$.

### 3.3. Evaluation of band gap

Absorption coefficient was calculated according Eq. (2)from reflectance measurement (Fig. 4) and consequently used to establish the type of band-to-band transition in these $TiO_2$ nanoparticles. The dependence of molar absorption coefficient was recorded as a function of the photon energy for direct as well as for indirect transition (Fig. 5). Subsequently, the extrapolation for value $\alpha = 0$ was performed from which the band gap energy was found. Generally, it is known that band gap energy of $TiO_2$ in anatase phase is 3.23 eV and rutile phase 3.03 eV. Results summarized in Table 2 show that all prepared $TiO_2$ were direct semiconductors.

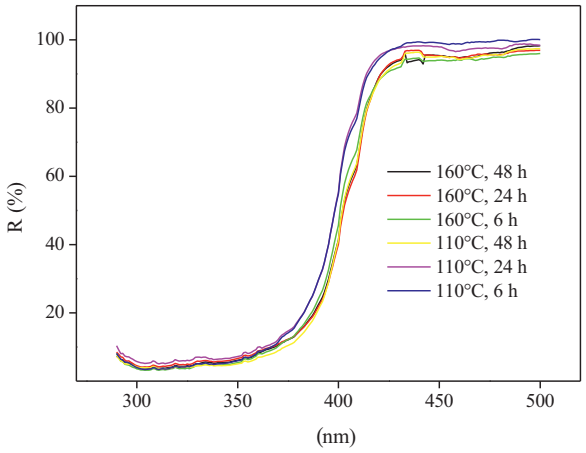


**Fig. 4.** Result from reflectance measurement of powder $TiO_2$.

### 3.4. Preparation of thin layers by inkjet printing

Hydrothermally synthesized $TiO_2$ was deposited onto soda-lime glass plates by material printing. Titania dispersions were used for the formulation of water based printing inks. Organic solvents are generally more preferred for industrial inkjet formulations because of greater possibilities to control wetting, evaporation rate and nozzle drying issues, but their use is accompanied by greater environmental impact (VOC emissions, waste disposal etc.). Water was therefore chosen as a greener alternative in this case.

Because $TiO_2$ particles can aggregate which would cause the problem with clogging of printed head nozzle and consequently their damage we have to avoid the aggregation by adding a surfactant. Three different surfactant Fig. 6 were tried; non-ionic surfactant (Tween 20), cation active surfactant (CTAB) and anion active surfactant (Dodecylbenzene Sulfonic Acid, Abeson). We found that only anion active surfactant has the required effect and the aggregation of colloidal particles was completely suppressed. Non-ionic (Tween 20) leaded to decreasing of aggregation but in insufficient extend. CTAB caused the precipitation of titania particles from the solution. Therefore all samples were printed using an anion active surfactant. HCl was added in order to maintain the required pH providing the surface charge of titania particles. Abeson, being a surfactant with anion-active character, is thus capable of effective stabilization of positively charged colloidal particles of $TiO_2$. Water was added to reach the optimum viscosity of the printing formulation (10 mPa s). Viscosity is one of the key properties that determine the printability. Wetting ability, i.e. the printing ink surface tension, plays also an important role in both the jetting process as well as the wet layer formation. Reasonably good wetting even on glass surface was provided by the relatively high surfactant concentration.

The stability of prepared $TiO_2$ colloidal dispersions was an issue of a previous study [50]. The stability of used printed mixtures was

**Table 2**
Summarised of band gap energy.

| Temperature | Time | Direct transition | Indirect transition |
|---|---|---|---|
| 110 °C | 6 h | 3.019 eV | 3.348 eV |
| | 24 h | 2.984 eV | 3.272 eV |
| | 48 h | 2.983 eV | 3.282 eV |
| 160 °C | 6 h | 2.990 eV | 3.319 eV |
| | 24 h | 2.972 eV | 3.303 eV |
| | 48 h | 2.977 eV | 3.274 eV |

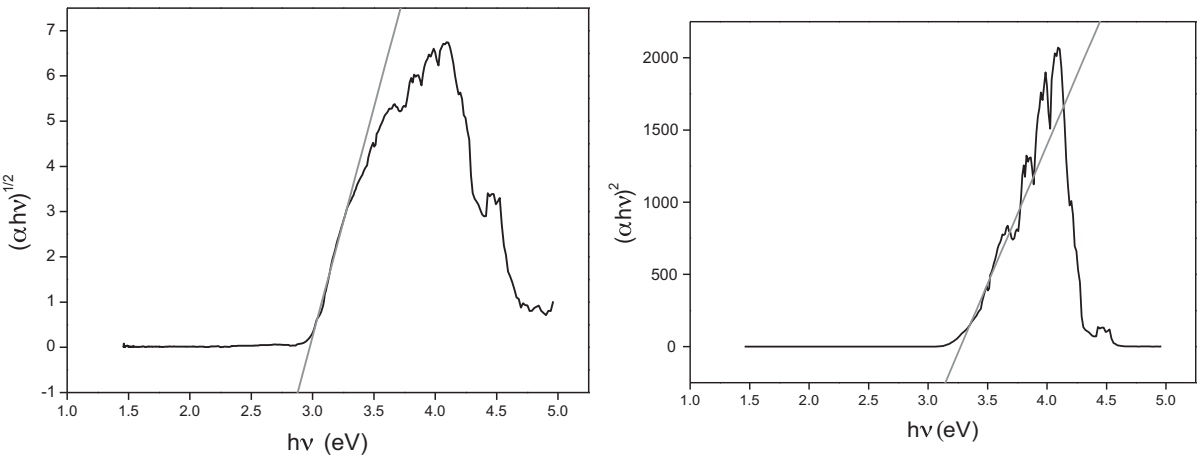


**Fig. 5.** Evaluation of band gap energy from direct transition (left) and indirect transition (right) for sample 160 °C, 48 h.

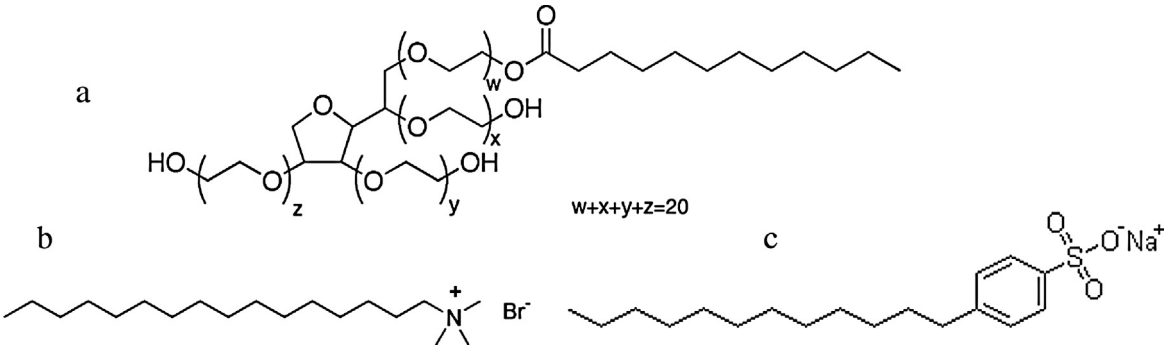


**Fig. 6.** Used surfactant, (a) non-ionic Tween 20, (b) cation active CTAB, (c) anion active Abeson.

sufficient because any sedimentation was not observed during 1 month of storage. All prepared samples were consumed within this time so no further data on stability is available.

Since one-layered as well as double-layered films of $TiO_2$ were prepared, the influence of layers thickness on the final photocatalytic activity was investigated apart from the time and temperature variables of the hydrothermal process. All prepared films were fixed on the substrate drying at temperature 500 °C for 30 min. This final heat treatment is necessary in order to remove the non-volatile organic fraction of the printing formulation (i.e. the surfactant), to sinter the titania particles together and to provide sufficient adhesion to the glass substrate.

### 3.5. Gravimetric analysis

The amount of $TiO_2$ particles deposited onto soda-lime glass was examined by gravimetric measurement of the substrate before and after the printing process. The obtained results are summarized in Table 3. We confirmed that in the case of double-layers the amount of deposited titania increased twice. This result indicates that deposition process was stable and reliable during the whole printing process and no nozzle clogging took place.

**Table 3**
Total amount of deposited $TiO_2$ per 16 $cm^2$ sample area.

| Temperature | Time (h) | 1 layer (g) | 2 layer (g) |
|---|---|---|---|
| 110 °C | 6 | 0.0015 | 0.0028 |
| | 24 | 0.0012 | 0.0023 |
| | 48 | 0.0015 | 0.0030 |
| 160 °C | 6 | 0.0011 | 0.0021 |
| | 24 | 0.0011 | 0.0026 |
| | 48 | 0.0008 | 0.0020 |
| P-25 | | 0.0006 | 0.0014 |

### 3.6. Optical microscopy

The quality of prepared layers was investigated using Nikon Eclipse E200 optical microscope connected with a digital camera Nikon D70. 20× magnifying lens were used. This was sufficient because the main purpose of this imaging was to monitor the homogeneity of prepared layers. The $TiO_2$ films deposited on soda-lime glass plates by material printing method show milky colour and they adhered well to the glass substrate after the fixing process. All prepared layers were quite compact and homogeneous without any noticeable cracks. All double-layers were darker which was caused by higher amount of $TiO_2$ in the layers (Fig. 7). No significant difference was observed using different hydrothermal conditions.

### 3.7. Investigation of layers hardness

The hardness of titania layers was examined by "Pencil Hardness test" according to standard ISO 15184. This study was carried out only for two-layer samples where we supposed lower adhesion than in case of one-layers. The test was performed using a mechanical device.The pencils with different hardness were used and we studied the extend of caused damage. We can observe defect in titania layer caused by pencil with hardness HB in Fig. 8. However no defect is obvious using pencil with hardness B (Fig. 8). These results indicate that the hardness of our layers corresponded to "B" pencil hardness.

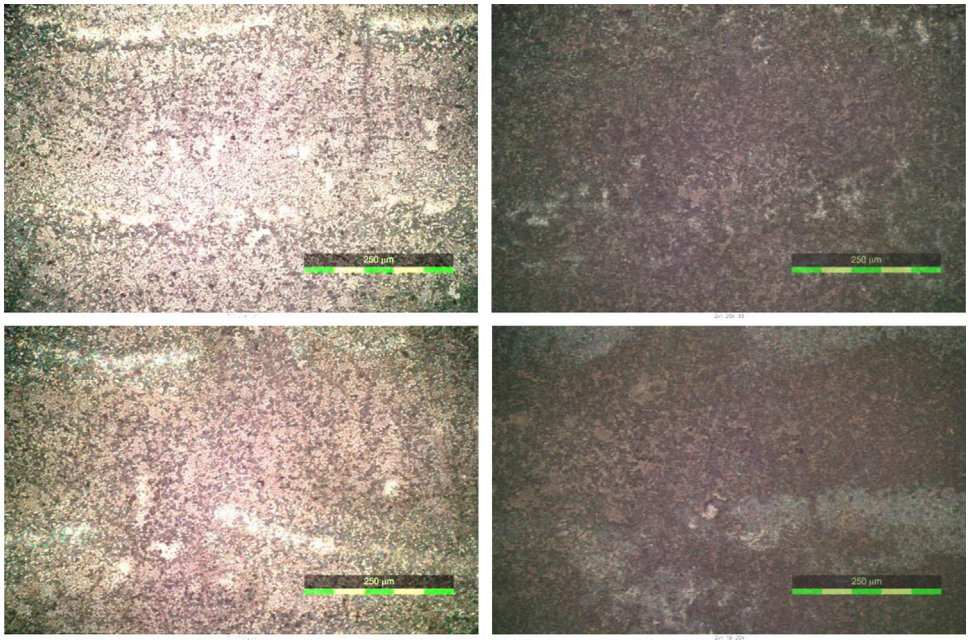

**Fig. 7.** Images from optical analysis, top–synthesizes at 160 °C for 6 h, 1 layer (left) and 2 layers (right); bottom. synthesized at 110 °C for 48 h, 1 layer (left) two layer (right).

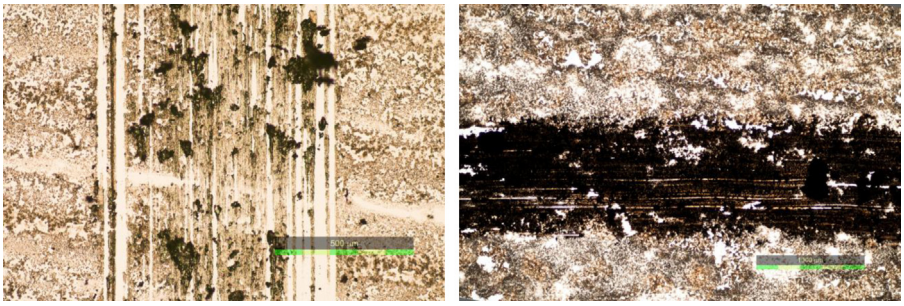

**Fig. 8.** Titania layers after pencil hardness test for HB pencil hardness (left) and B pencil hardness (right).

### 3.8. Scanning electron microscopy

The morphology of titania printed layers was studied by SEM analysis. The grain size of $TiO_2$ and the homogeneity of prepared layers were compared for samples synthesized under different conditions. This analysis confirmed that with increasing time of hydrothermal treatment the homogeneity of printed layers increased (Fig. 9). It is in a good agreement with the results from TEM analysis (Fig. 3). The grain size of each sample was evaluated and we found that the grain size decreases with increasing time of treatment. These results were observed for both temperatures.

### 3.9. Atomic force microscopy

We confirmed the result from SEM measurements by AFM analysis where we observed that with increasing time of hydrothermal treatment the grain size decreases (Fig. 10). The comparison of grain sizes was carried out from scans across 1 $\mu m^2$ area. We also examined the roughness of prepared layers from 25 $\mu m^2$ area. Roughness ($R_q$) increases with increasing time of hydrothermal treatment (Table 4).

### 3.10. Photocatalysis

The photocatalytic activity was evaluated as the rate of DCIP degradation reaction carried out in a circulated batch reactor. The degradation of DCIP takes place in several steps. The first one is dechloration which is accompanied by discoloration. Consequently, the oxidation of the carbon skeleton occurs which leads to the formation of short-chain carboxylic acids. Finally, these acids undergo decarboxylation and are totally cleaved to $CO_2$ and water [56–59]. Decolourization can be conveniently measured as absorbance decreasing by UV–vis spectroscopy. This method is very attractive for the purpose of studying photocatalytic activity due to its low demands for instruments and labour. Nevertheless, the authors are well conscious of the problems inherently associated by using any dye molecule: dye molecules are complex systems and during their degradation many intermediates compete for oxidation by reactive oxygen species [60,61]. From the scientific point of view, the use of simple molecules such as formic acid or dichloroacetic acid would be preferable [62]. On the other hand

**Table 4**
Roughness of titania printed layers.

| Temperature | Time (h) | Roughness (nm) |
|---|---|---|
| 110 °C | 6 | 40 |
| | 24 | 84 |
| | 48 | 91 |
| 160 °C | 6 | 60 |
| | 24 | 53 |
| | 48 | 105 |

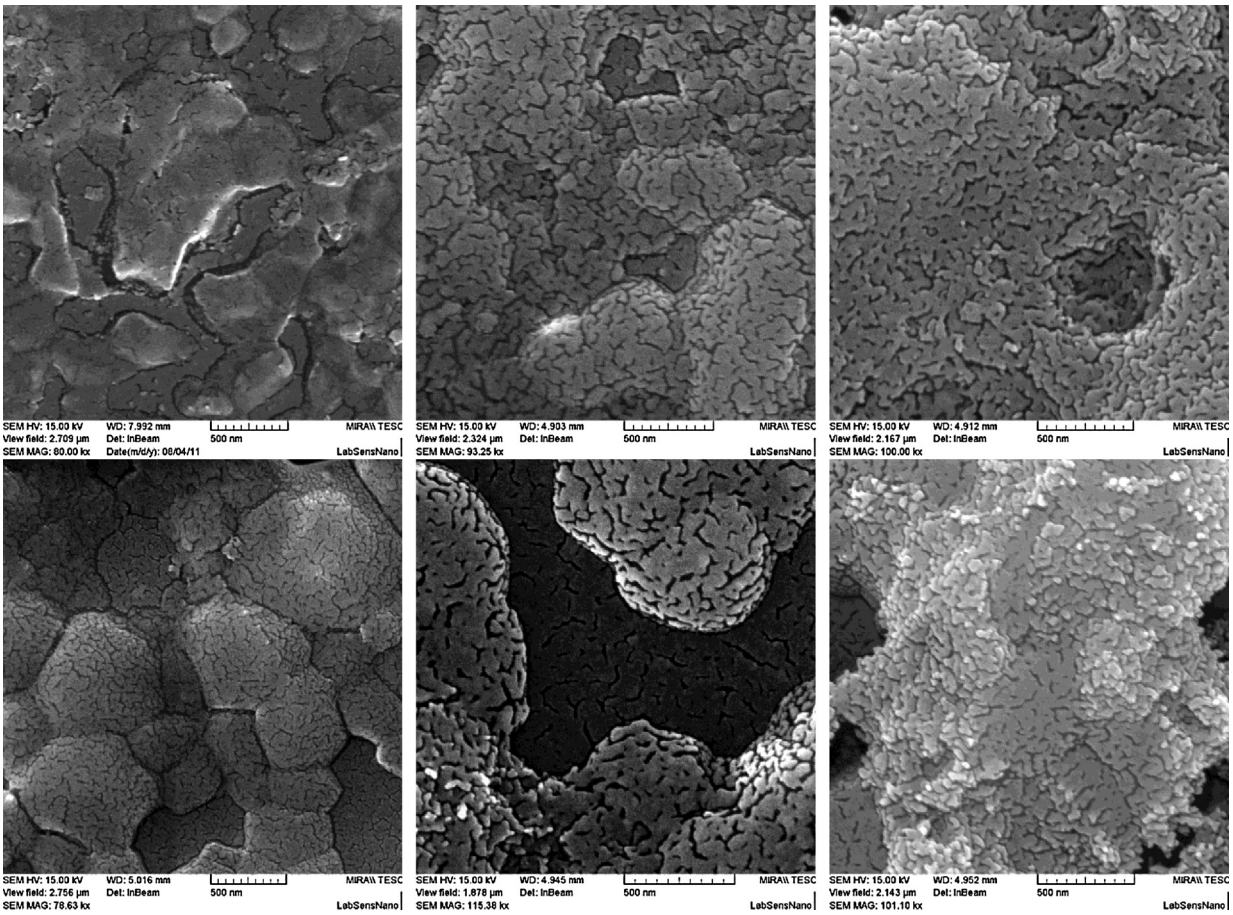


**Fig. 9.** SEM images for one- layers samples of titania synthesized at 110 °C (top) and 160 °C (bottom) for different time; 6 h (left); 24 h (middle); 48 h (right).

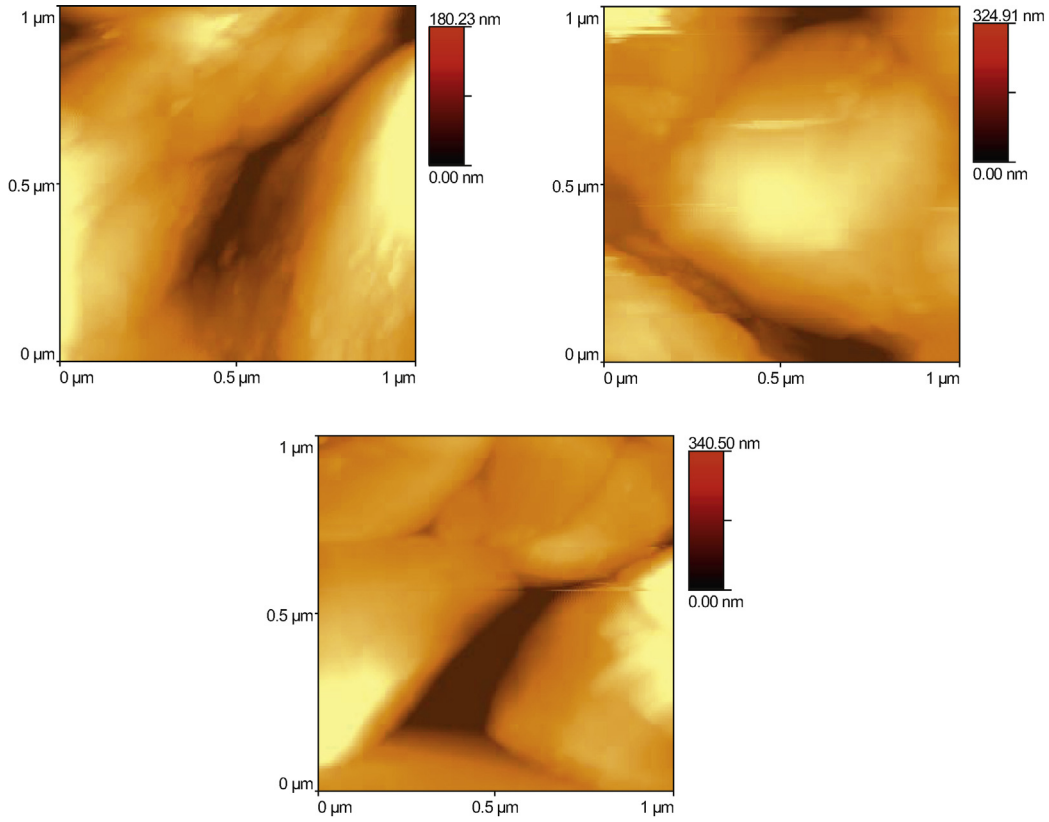


**Fig. 10.** Images form AFM analysis, comparison of titania grain size treated for different time; 6 h (left, top); 24 h (right, top), 48 h (left, bottom).

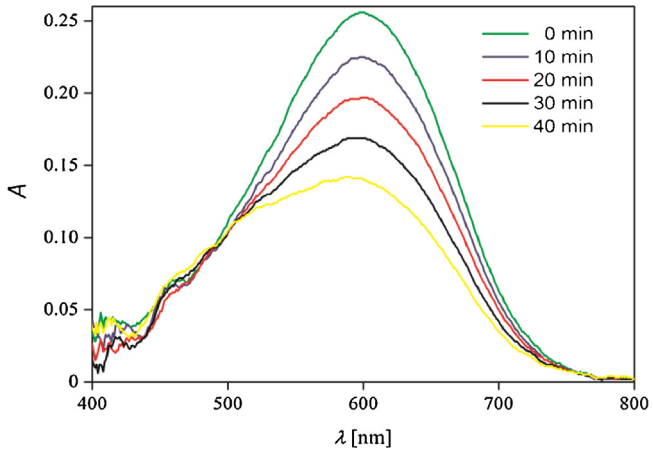


**Fig. 11.** Absorption spectrum of DCIP during 40 min of degradation.

**Table 5**
Formal 1st order rate constant, their standard errors and conversion degree for experiment took place using intensity 7.5 mW cm$^{-2}$.

| Sample | | | $k$ (min$^{-1}$) | SE (min$^{-1}$) | Conversion degree (%) |
|---|---|---|---|---|---|
| 110 °C | 6 h | 1 layer | 0.0002 | 0.0001 | 51.0 |
| | | 2 layers | 0.0090 | 0.0005 | 66.4 |
| | 24 h | 1 layer | 0.0049 | 0.0003 | 61.6 |
| | | 2 layers | 0.0163 | 0.0009 | 74.9 |
| | 48 h | 1 layer | 0.0130 | 0.0007 | 69.6 |
| | | 2 layers | 0.0212 | 0.0012 | 79.2 |
| 160 °C | 6 h | 1 layer | 0.0084 | 0.0005 | 68.6 |
| | | 2 layers | 0.0083 | 0.0005 | 67.4 |
| | 24 h | 1 layer | 0.0122 | 0.0008 | 72.8 |
| | | 2 layers | 0.0153 | 0.0009 | 76.3 |
| | 48 h | 1 layer | 0.0271 | 0.0015 | 83.1 |
| | | 2 layers | 0.0313 | 0.0017 | 86.0 |
| P-25 | | 1 layer | 0.0284 | 0.0017 | 84.5 |
| | | 2 layers | 0.0344 | 0.0019 | 87.7 |

the choice of DCIP is relevant because the treatment of dye-polluted waste water is one of the target application fields for photocatalytic process. Moreover, DCIP is a good model dye molecule because of an easy spectrophotometric detection and also a reasonably low absorption at wavelengths 360–400 nm.

The absorption maximum of DCIP is at wavelength of 600 nm (Fig. 11). 70 mL of DCIP with initial concentration of $2.5 \times 10^{-5}$ g L$^{-1}$ was used for photocatalytic experiments. Absorbance was recorded each minute and total reaction time was forty minutes which was sufficient for a total discoloration of DCIP. The influence of amount of $TiO_2$ (comparison one- and two-layers) as well as time and temperature of hydrothermal treatment was investigated. The photocatalytic activity was compared with common commercial $TiO_2$ (Evonik Aeroxide P-25). A blank experiment (no catalyst) was performed and its rate constant was subtracted from the obtained rate constants of prepared titania printed layers in order to correct the rates for direct photolysis of DCIP.

The dependence of natural logarithm of relative concentration versus reaction time was linear for all prepared titania layers (Fig. 12). So we assumed that reaction runs according the first order kinetics within the studied range. The reaction rate constants ($k$), their standard errors (SE) and conversion degree were calculated (Table 5).

The analysis was performed with intensity 7.5 mW cm$^{-2}$. We found out that the double-layered samples were more active. This result was supposed because of higher presence of $TiO_2$ in the double-layers, i.e. more photocatalyst and so higher amount of photoactive sites.

Although the amount of deposited $TiO_2$ in case of double-layered samples increased twice (Table 3) we did not observe

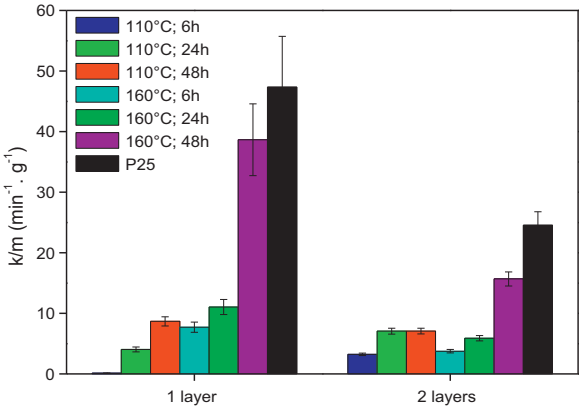


**Fig. 13.** Photocatalytic activity per gramof photocatalysts.

increasing of photocatalytic activity two times. It means that not all titania particles participated in the photocatalytic degradation process. This can be caused either by insufficient intensity of incident radiation and resulting self-shadowing of the thicker photocatalyst layers or by limited access of DCIP to deep buried catalyst particles resulting into mass-transfer limiting the reaction rate.

When we compared $TiO_2$ hydrothermally treated for different time we discovered that samples synthesized for longest time were the most active (Fig. 13, Table 5). It could be caused by the decreasing of particle size with increasing of treated time which was found by TEM and SEM analysis and also by increase of

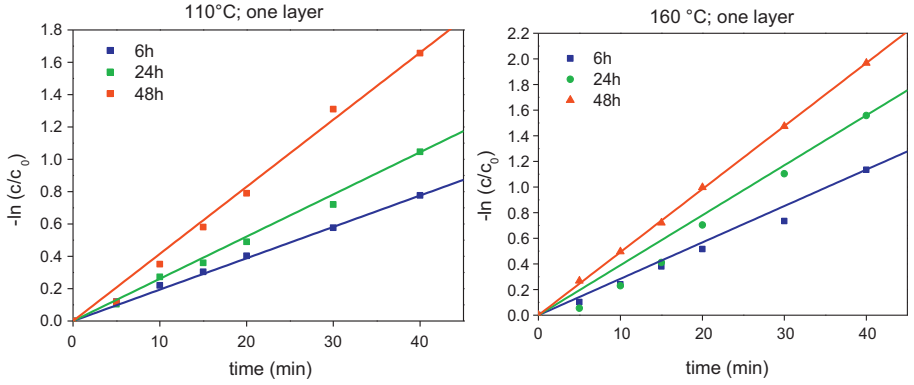


**Fig. 12.** Dependence of ln ($c/c_0$) on time for one layer samples (110 °C and 160 °C).

roughness (Table 4). Smaller crystallite size leads to higher specific surface area and to increasing of photocatalytic activity [63].

In order to compare the relative efficiency of all prepared samples, the observed photocatalytic activities were related per 1 g of photocatalyst (Fig. 13). The final standard error of these related values is influenced by the SE of both partial measurement (calculation of constant rate and SE of weighting). Final standard error was calculated according the equation (3) [64] where $SE_k$ is standard error of calculated rate constant, $SE_m$ is standard error of the mass and $SE_{k/m}$ is final standard error of the rate constant per 1 g of photocatalyst. When the considered values are independent $r$ is equal to 0. When there is a total dependence $r$ is equal 1. Because the rate constant is dependent on the amount of photocatalysts only in a small range and consequently it is independent we considered $r$ equal to 0

$$\left(\frac{SE_{k/m}}{k/m}\right)^2 = \left(\frac{SE_k}{k}\right)^2 + \left(\frac{SE_m}{m}\right)^2 - 2r\left(\frac{SE_k}{k}\right)\left(\frac{SE_m}{m}\right) \quad (3)$$

P25 was the better photocatalyst than our samples. Most of prepared samples had activity much lower than P25, only $TiO_2$ synthesized for 48 h at 160 °C showed a comparable activity.

This difference between our $TiO_2$ and P25 was probably caused by the different phase of $TiO_2$. In case of P25 there was mixture of anatase and rutile however all our titania were pure rutile. So this result was expected because it is well known that mixture of anatase and rutile is much more active than only pure anatase or pure rutile.

## 4. Conclusion

Six $TiO_2$ colloidal dispersions were synthesized by the hydrothermal process. We investigated the influence of process conditions on their material properties. TEM analysis shows that particle size decreased with increasing time of synthesis. In all cases, pure rutile was prepared that implies that neither time nor temperature of hydrothermally treatment have significant influence on the final crystalline phase. Phase depends mainly on the pH used and it was the same in all samples in this study. Using a less acidic pH level (2–3) would probably result into the formation of a mixture of anatase and rutile or pure anatase. Another process parameter which could lead to the creation of rutile phase is possibly insufficient washing of the primary slurry. From the band gap energy analysis we found out that all prepared $TiO_2$ samples were direct semiconductors.

Consequently, synthesized $TiO_2$ dispersions were used for the formulation of stable "inks" and deposited onto soda-lime glass plates by inkjet printing. Only anion-active surfactants could be used for preparation of stable printing formulations. One-layered and two-layered samples were prepared and fixed by heating to 500 °C.

The quality of prepared layers was investigated by optical microscopy. The layers of $TiO_2$ were homogeneous, compact without any cracks. The adhesion of these layers corresponds to B pencil hardness. The morphology and particle size were evaluated by SEM and AFM analysis. We observed decreasing particle size with increasing duration of hydrothermally synthesis. This result confirmed the result from TEM analysis.

In all cases, the photocatalytic activity of double-layer samples was greater than the activity of single-layer ones. As far as the influence of the hydrothermal treatment conditions is concerned, the greatest photocatalytic activity was observed from the longest treated sample. However, the commercial de-facto standard catalyst Evonik Aeroxide P-25 still provided better activity than our best sample. This result was supposed because the activity of pure rutile is generally lower than the activity of pure anatase or anatase and rutile mixtures [65]. The use of less acidic environment during the synthesis of $TiO_2$ might be a viable option for reaching higher photocatalytic activity in future experiment. Despite average photocatalytic performace of this particular $TiO_2$ type, inkjet printing proved to be an efficient method for the fabrication of patterned titania films originating from nanocrystalline precursor.

## Acknowledgements

Authors thank to Ministry of Education, Youth and Sports of Czech Republic for support by project OC10050 and the Czech Science Foundation for support through project 104/09/P165. Authors also appreciate the work of Jana Chomoucká who provided SEM imaging at the LabSensNano laboratory of Faculty of Electrical Engineering and Communication, Brno University of Technology. We also thank the three anonymous reviewers for valuable comments helping us to crown our work by this publication.

## References

[1] M.R. Hoffman, S.T. Martin, W. Choi, D.W. Bahnemann, Chemical Reviews 95 (1995) 69.
[2] M.A. Fox, M.T. Dulay, Chemical Reviews 93 (1993) 341.
[3] J. Zhao, T. Wu, K. Wu, K. Oikawa, H. Hidaka, N. Serpone, Environmental Science and Technology 32 (1998) 2394.
[4] F.B. Li, X.Z. Li, Applied Catalysis A 228 (2002) 15.
[5] J.G. Yu, X.J. Zhao, Q.N. Zhao, Thin Solid Films 379 (2000) 7.
[6] H.G. Yu, S.C. Lee, C.H. Ao, J.G. Yu, Journal of Crystal Growth 280 (2005) 612.
[7] Y. Ding, G.O. Lu, P.F. Greenfield, Journal of Physical Chemistry B 104 (2000) 4815.
[8] S.J. Kim, H.G. Lee, S.J. Kim, J.K. Lee, E.G. Lee, Applied Catalysis A 242 (2003) 89.
[9] A.L. Linsebigler, G. Lu, J.T. Yates Jr., Chemical Reviews 95 (1995) 735.
[10] J. Yu, H. Yu, B. Cheng, M. Zhou, X. Zhao, Journal of Molecular Catalysis A 253 (2006) 112.
[11] Q. Xiang, J. Yu, P.K. Wong, Journal of Colloid and Interface Science 357 (2011) 163.
[12] Y.V. Kolen'ko, B.R. Churagulov, M. Kunts, L. Mazerolles, C. Colbeau-Justin, Applied Catalysis B 54 (2004) 51.
[13] A.L. Linsebigler, G. Lu, J.T. Yates, Chemical Reviews 95 (1995) 735.
[14] J. Yu, J.C. Yu, W. Ho, Z. Jiang, New Journal of Chemistry 26 (2002) 607.
[15] J.G. Yu, H.G. Yu, B. Cheng, X.J. Zhao, J.C. Yu, W.K. Ho, Journal of Physical Chemistry B 107 (2003) 13871.
[16] A. Panniello, M.L. Curri, D. Diso, A. Licciulli, V. Locaputo, A. Agostiano, R. Comparelli, G. Mascolo, Applied Catalysis B 121 (2012) 190.
[17] M. Andersson, L. Osterlund, S. Ljugstrom, A. Palmqvist, Journal of Physical Chemistry B 106 (2002) 10674.
[18] J.C. Yu, L. Zhang, Z. Zheng, J. Zhao, Chemistry of Materials 15 (2003) 2280.
[19] S.H. Elder, Y. Gao, X. Li, J. Liu, D.E. McCready, C.F. Windisch, Chemistry of Materials 10 (1998) 3140.
[20] J. Overstone, K. Yanagisawa, Chemistry of Materials 11 (1999) 2770.
[21] M.N. Ghayyal, H. Kebaili, M. Joseph, D.P. Deberker, P. Eloz, J. De Coninck, E.M. Gaigneaux, Applied Catalysis B 115 (2012) 276.
[22] Q. Xiang, K. Lv, J. Yu, Applied Catalysis B 96 (2010) 557.
[23] J. Yu, J. Xiong, B. Cheng, S. Liu, Applied Catalysis B 60 (2005) 211.
[24] J. Yu, B. Wang, Applied Catalysis B 94 (2010) 295.
[25] V.F. Stone Jr., R.J. Davis, Chemistry of Materials 10 (1998) 1468.
[26] X.Y. Chuan, M. Hirano, M. Inagaki, Applied Catalysis B 51 (2004) 255.
[27] J.A. Stride, N.T. Tuong, Solid State Phenomena 162 (2010) 261.
[28] H. Schmidt, M. Menning, http://www.solgel.com/articles/Nov00/coating.htm
[29] A.V. Lemmo, D.J. Rose, T.C. Tisone, Current Opinion in Biotechnology 9 (1998) 615.
[30] P. Calvert, Chemistry of Materials 13 (2001) 3299.
[31] P. Cooley, D. Wallace, B. Antone, Journal of Laboratory Automation 7 (2002) 33.
[32] J. Miettinen, V. Pekkanen, K. Kaija, P. Mansikkamäki, J. Mäntysalo, M. Mäntysalo, J. Niittynen, J. Pekkanen, T. Saviauk, R. Rönkkä, Microelectronics Journal 39 (2008) 1740.
[33] M. Singh, H.M. Haverinen, P. Dhagat, G.E. Jabbour, Advanced Materials 22 (2010) 673.
[34] A. Matsuo, R. Gallage, T. Fujiwara, T. Watanabe, M. Zoshimura, Journal of Electroceramics 16 (2006) 533.
[35] K.K. Manga, S. Wang, M. Jaiswal, Q. Bao, K.P. Loh, Advanced Materials 22 (2010) 5265.
[36] M. Arin, P. Lommens, N. Avci, S.C. Hopkins, K. De Buysser, I.M. Arabatzis, I. Fasaki, D. Poelman, I. Van Driessche, Journal of the European Ceramic Society 6 (2011) 1067.
[37] P. Dzik, M. Vesely, J. Chomoucka, Journal of Advanced Oxidation Technologies 13 (2010) 172.
[38] M. Cerna, M. Vesely, P. Dzik, Catalysis Today 1 (2011) 97.
[39] M. Morozova, P. Kluson, J. Krysa, P. Dzik, M. Vesely, O. Solcova, Sensors and Actuators B 160 (2011) 371.

[40] P. Dzik, M. Morozova, P. Kluson, M. Vesely, Journal of Advanced Oxidation Technologies 15 (2012) 89.
[41] S.J. Kim, D.E. Mckean, Journal of Materials Science Letters 17 (1998) 141.
[42] I. Bernacka-Wojcik, R. Senadeera, P.J. Wojcik, L.B. Silva, G. Doria, P. Baptista, H. Aguas, E. Fortunato, R. Martins, Biosensors and Bioelectronics 5 (2010) 1229.
[43] M. Yang, L. Li, S. Zhang, G. Li, H. Zhao, Sensors and Actuators B 2–3 (2010) 622.
[44] M. Arin, P. lommens, S.C. Hopkins, G. Pollefeyt, J. Van der Eycken, S. Ricard, X. Granados, B.A. Glowacki, I. Van Driessche, Nanotechnology 16 (2012) 165603.
[45] I. Fasaki, K. Siamos, M. Arin, P. Lommens, I. Van Driessche, S.C. Hopkins, B.A. Glowacki, I. Arabatzis, Applied Catalysis A 411–412 (2012) 60.
[46] Y. Oh, H.G. Yoon, S.N. Lee, H.K. Kim, J. Kim, Journal of the Electrochemical Society 159 (2012) B35.
[47] M. Hosseini Zori, A. Soleimani-Gorgani, Journal of the European Ceramic Society (2012) http://dx.doi.org/10.1016/j.jeurceramsoc.2012.06.005
[48] H. Shibata, H. Sakai, P. Rangsunvigit, T. Hirano, M. Abe, Surface Coatings International Part B: Coatings Transactions 86 (2003) 125.
[49] A. Piscopo, D. Robert, J.V. Weber, Applied Catalysis B 35 (2001) 117.
[50] M. Cerna, C. Guillard, E. Puzenat, M. Veselz, P. Dzik, International Journal of Chemical and Environmental Engineering 2 (2011) 255.
[51] J-M. Herrmann, H. Tahiri, C. Guillard, P. Pichat, Catalysis Today 54 (1999) 131.
[52] Y. Paz, A. Heller, Journal of Materials Research 12 (1997) 2759.
[53] K.M. Reddy, S.V. Manorama, A.R. Reddy, Materials Chemistry and Physics 78 (2002) 239.
[54] ISO 15184: Paints and varnishes, Determination of film hardness by pencil test, 1998.
[55] H. Yin, Y. Wada, T. Kitamura, S. Kambe, S. Murasawa, H. Mori, T. Sakata, S. Yanagida, Journal of Materials Chemistry 11 (2001) 1694.
[56] V. Brezova, M. Ceppan, M. Vesely, L. Lapcik, Chemical Papers 45 (1991) 233.
[57] D.F. Ollis, Environmental Science and Technology 19 (1985) 480.
[58] R.W. Matthews, Journal of the Chemical Society, Faraday Transactions 1 85 (1989) 1291.
[59] M. Cerna, M. Veselz, P. Dzik, Catalysis Today 161 (2001) 97.
[60] B. Ohtani, Chemistry Letters 37 (2008) 217.
[61] H. Kisch, W. Macyk, ChemPhysChem 3 (2002) 399.
[62] J. Ryu, W. Choi, Environmental Science and Technology 42 (2008) 294.
[63] D.S. Kim, S.Y. Kwak, Applied Catalysis A 323 (2007) 110.
[64] K. Doerffe, K. Eckschlager, Optimální Postup Chemické Analýzy, SNTL, Leipzing, 1998, p. 22.
[65] J. Yu, G. Wang, B. Cheng, M. Zhou, Applied Catalysis B 69 (2007) 171.

J Sol-Gel Sci Technol (2013) 65:452–458
DOI 10.1007/s10971-012-2957-6

ORIGINAL PAPER

# The influence of various deposition techniques on the photoelectrochemical properties of the titanium dioxide thin film

**M. Morozova · P. Kluson · P. Dzik · M. Vesely · M. Baudys · J. Krysa · O. Solcova**

Received: 26 October 2012 / Accepted: 28 December 2012 / Published online: 12 January 2013


**Abstract** Thin sol–gel $TiO_2$ layers deposited on the conductive ITO glass by means of three various deposition techniques (dip-coating, inkjet printing and spray-coating) were used as photoanode in the three-compartment electrochemical cell. The thin $TiO_2$ films were treated at 450 °C and after calcination all samples possessed the crystallographic form of anatase. The relationship between surface structure and photo-induced conductivity of the nanostructured layers was investigated. It was found that the used deposition method significantly influenced the structural properties of prepared layers; mainly, the formation of defects and their quantity in the prepared films. The surface properties of the calcined layers were determined by XRD, Raman spectroscopy, SEM, AFM, UV–Vis analyses and by the optical microscopy. The photo-induced properties of nanoparticulate $TiO_2$/ITO photoanode were studied by electrochemical measurements combined with UV irradiation.

**Keywords** Titanium dioxide · Dip-coating · Inkjet printing · Spray-coating · Photo-electrochemical properties

M. Morozova (✉) · P. Kluson · O. Solcova
Institute of Chemical Process Fundamentals of the ASCR, v. v. i., Rozvojova 2/135, Prague 6 165 02, Czech Republic
e-mail: morozova@icpf.cas.cz

P. Dzik · M. Vesely
Faculty of Chemistry, Brno Univesity of Technology, Purkynova 464/118, 612 00 Brno, Czech Republic

M. Baudys · J. Krysa
ICT Prague, Department of Inorganic Technology, Technicka 5, 166 28 Prague 6, Czech Republic

## 1 Introduction

The photovoltaic effect was discovered in 1839 by French physicist A. E. Becquerel and since this time the idea of converting the sunlight into the electric power has evoked a great interest [1]. In the generation of electric current the photovoltaic effect consists of material which is actually a semiconductor exposed to the light. The absorbed photons with corresponding energy create the electron–hole pairs and at the junction between two different materials an electric potential difference can be set up [2]. The electrons then take a part of the current in an external electrical circuit.

Thanks to these photo-excited properties titanium dioxide ($TiO_2$) has been the very favoured semiconductor for such studies. $TiO_2$ has become very attractive material since 1972, when Fujishima and Honda [3] described its photocatalytic activity. Unfortunately, $TiO_2$ absorbs only the UV light part of the solar spectrum owing to its large band gap. Low efficiency of the solar energy conversion by this semiconductor oxide similarly as the limited activity (only in the UV area) are crucial and do not enable to develop the application for the effective conversion of sunlight to electrical power. Nevertheless, the light response is sufficient for application of $TiO_2$ in the field of photocatalysis, photo-electrochemistry and sensing. The most prominent applications are photocatalytic water and air purification [4, 5]. Its specific physical and chemical properties predetermine the other applications of $TiO_2$; the use as a gas sensor, thin layer photoanode and as a part of "sandwich" electrode or fuel cells [6–8]. The major interest is focused on the sensor field [9, 10]. The semiconductor-liquid interface possesses the very specific photoelectrochemical properties and it represents the interesting and promising area in electrochemistry. The

present and the future practical applications of the semiconductor electrode can include the liquid junction solar cells, photoelectrolysis cells for photolytic water splitting and sensing technology [11].

The nanostructured electrode materials with uniform nanoparticles could be prepared by physical (PVD), physically-chemical (PECVD) or purely chemical methods [12]. The sol–gel technique is the most common and successful method for the uniform nanoparticle preparation. This wet chemical method offers approaches to the synthesis of metal oxides with the controlled structure, morphology, particles sizes and even the chemical composition of the final material. The sol–gel chemistry is based on inorganic polymerization reactions [13]. In the case of $TiO_2$, the nanoparticle synthesis includes hydrolysis and polycondensation of titanium alkoxides in an organic solvent. Due to rheological properties of the prepared liquid it is possible to create fibres by spinning or thin films by various deposition techniques [14].

A number of articles concerning various deposition techniques of the thin layer preparation from liquid precursors have been reported [15]. Each of them refers to advantages and disadvantages of the applied method. The dip-coating belongs to the traditional and the widely used method of the thin layer preparation. It is based on dipping the substrate into the sol and pulling it out at constant and the well-defined speed [16]. The layer thickness could be controlled by the pull-out speed, by the time interval which the substrate spends in a liquid and/or by the viscosity of the liquid sol.

The spray-coating is the other elementary technique which applies liquid precursor on the substrate by the spray head with one three-axe system nozzle. The system is able to cover homogenously the large substrate areas by droplets of liquid solution [17]. Usually, this technique is widely used in industry, e.g. for organic lacquer deposition.

Inkjet printing has appeared recently as a new way of the sol application. The inkjet print head contains an array of piezoelectric nozzles ejecting very small droplets of a low viscosity ink or other functional liquid. The possibility of a complete control over the deposition process parameters and precise patterning without the need of any mechanical or optical masking make this deposition method very appealing for the production of sensors, solar cells etc. [18–20].

This study is a follow-up to our recently published articles [21–23] and it is focused on comparison of the photo-induced conductivity of the thin $TiO_2$/ITO electrode deposited by three various deposition techniques. The thin $TiO_2$ layers were prepared by the sol–gel method using molecular tamplating, which allows a production of uniform particles in layers. This article presents a summary of the photoelectrochemical and structural properties of the thin layers prepared by the sol–gel method and created on conductive substrate by dip-coating, spray-coating and inkjet printing.

## 2 Experimental

### 2.1 Preparation of the thin $TiO_2$ layers

The thin $TiO_2$ layers were prepared by means of the templated sol–gel process. A homogenous sol was synthesized by addition of titanium isopropoxide (TTIP, 99.999 %, Sigma–Aldrich) to the inverse micellar solution. The reverse micelles were created by the molecular template TX 102 (non-ionic surfactant, Sigma–Aldrich) in the nonpolar environment of cyclohexane (Aldrich, 99.9 %, HPLC grade) or xylene (Sigma–Aldrich, xylenes). The detailed information about the sol–gel preparation had already been reported [21–23]. The sol with cyclohexane was used for the dip-coating in original molar ratio of compounds (1:1:1) and for the spray-coating the volume was diluted (1:2 / sol:solvent). In the case of the inkjet printing the nonpolar environment had to be changed to xylene since cyclohexane sol not only had poor jetting performance but also disturbed the plastic ink storage tank. $TiO_2$ films were deposited on one side of the indium tin oxide conductive glass (ITO, 5–15 Ω, Delta-Technologies Ltd.) or on the soda-lime microscopic glass plates (25 × 75 mm, Marienfeld, Germany), respectively, and then calcined at 450 °C for 4 h. The samples on ITO were prepared for electrochemical characterization and thin layers on microscopic glass were used for optical characterization.

The sol application was performed by dip-coating, spray-coating and inkjet printing. For dipping a laboratory dip-coater (ID-Lab coater 4) was used. The substrate was dipped into the sol where was kept for 30 s and then it was pulled with velocity 6 cm $min^{-1}$. Among the single dip-coating cycles the samples were heated. The semi-industrial equipment developed at ICT Prague was used for the sol deposition by the method of spray-coating. This set up is composed of a sliding beam with the spraying head and a sliding samples holder. The shift rate of spraying head was 7 cm $min^{-1}$ and the substrate distance from the nozzle was 15 cm. In this case the samples were treated by the one final calcination step after finalization of the spray cycles. An experimental inkjet printer Fujifilm Dimatix 2,831 was used for the printed layer preparation. The xylene-based sol was loaded into the Dimatix ink storage tank through a 0.45 μm syringe filter and Dimatix 10 pL print head was attached. The tank and print head were installed into the printer and the following settings were used for printing: Dimatix Model fluid 2 waveform, 20 V driving voltage, nozzle temperature 30 °C, substrate temperature 40 °C,

nozzle span 20 μm. Printing each single layer was followed by a gelling and drying phase (30 min at 110 °C). The finished samples were then calcined.

### 2.2 Layer's characterization

Surface properties of the calcined layers were determined by XRD, Raman, SEM, AFM, UV–Vis analyses and by the optical microscopy. The photo-induced properties of nanoparticulate $TiO_2$/ITO layers were investigated by means of electrochemical measurements combined by UV irradiation. Photo-induced electrochemical behaviour of $TiO_2$ electrode was measured by potentio-dynamic methods in the three-electrode Pyrex cell. This cell contained the basic electrolyte (0.1 M $Na_2SO_4$) and was equipped by the window. Through the window the light beam with the wavelength 365 nm irradiated the sample which was used as a working electrode. A saturated Ag/AgCl electrode and a platinum plate were used as the reference and the auxiliary electrodes, respectively. The exposed surface area of the working $TiO_2$/ITO electrode was 1 $cm^2$ and the photoelectrochemical reaction was monitored by the potentiostatic set-up. The incident light intensity was measured by UV-meter (UV Light Meter UVA-365) and recalculated to Incident-Photon-Current-conversion-Efficiency (IPCE) [24]. The light intensity was 10 mW $cm^{-2}$ at 365 nm for experiments. The detailed description of the electrochemical set-up and the used electrochemical methods had been reported previously [21–23].

## 3 Results and discussion

### 3.1 Structural properties

Material prepared by the templated sol–gel method revealed the size and structural uniformity. The prepared layers usually possess high transparency, surface homogeneity, size and structure uniformity and very high adhesion to substrate. Figure 1 shows the XRD patterns of the thin $TiO_2$ films deposited on the microscopic glass plates. It is obvious that anatase was the only crystallization phase of the thin $TiO_2$ films prepared on ITO glass by all applied deposition techniques. Moreover, the crystallographic structure was independently confirmed by Raman spectroscopy. By means of XRD measurement the size of anatase crystals was also determined (see Table 1). The size depends on the deposition technique and it is slightly rising between 7 and 10 nm in the order: dip-coating, inkjet printing, spray-coating.

For the surface morphology studies AFM and SEM analyses were employed. Corresponding images of the layer surfaces are shown in Fig. 2. Furthermore, AFM

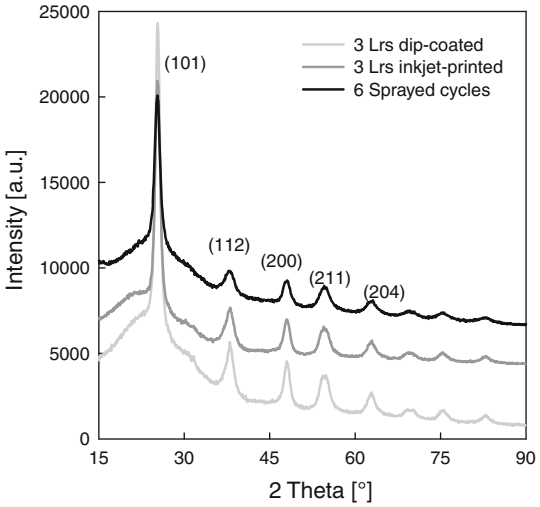


**Fig. 1** XRD patterns of the thin sol–gel $TiO_2$ films prepared by various deposition techniques

measurement provides information about the relative surface roughness expressed as rms values (results in Table 1). The smoothest surface (rms factor <1) without remarkable defects was detected for the dip-coated samples. The relatively uniform surface was also observed for thin films generated by inkjet printing. The sprayed layers possess the lower surface homogeneity. The AFM results are corroborated by the surface images obtained by SEM analysis. The characteristic porous structure can be easily identified for the sprayed films likewise for the printed samples, however, being a little rough. All prepared layers evince the very good mechanical stability.

The layer thicknesses were determined from SEM images, where the layer edge was depicted. It was found that the layer thickness for the three dip-coated, three inkjet-printed and six sprayed cycles reached relatively comparable values about 330 nm. Results are summarized in Table 1.

In the photoelectrochemical measurements the absorption edge position of the semiconductor used as photoanode is one of the most important parameters. The absorption spectra were also studied for $TiO_2$ layers

**Table 1** Characteristics of the produced layers

| Layers | Rms factor (nm) | Particles size[a] (nm) ± 1 nm | Thickness SEM (nm) ± 10 nm | $E_{OC}$ (mV) |
|---|---|---|---|---|
| Dip-coating | 0.4 | 7 | 330 | −460 |
| Inkjet printing | 1.4 | 8 | 340 | −420 |
| Spray-coating | 2.2 | 10 | 310 | −400 |

[a] From XRD measurement

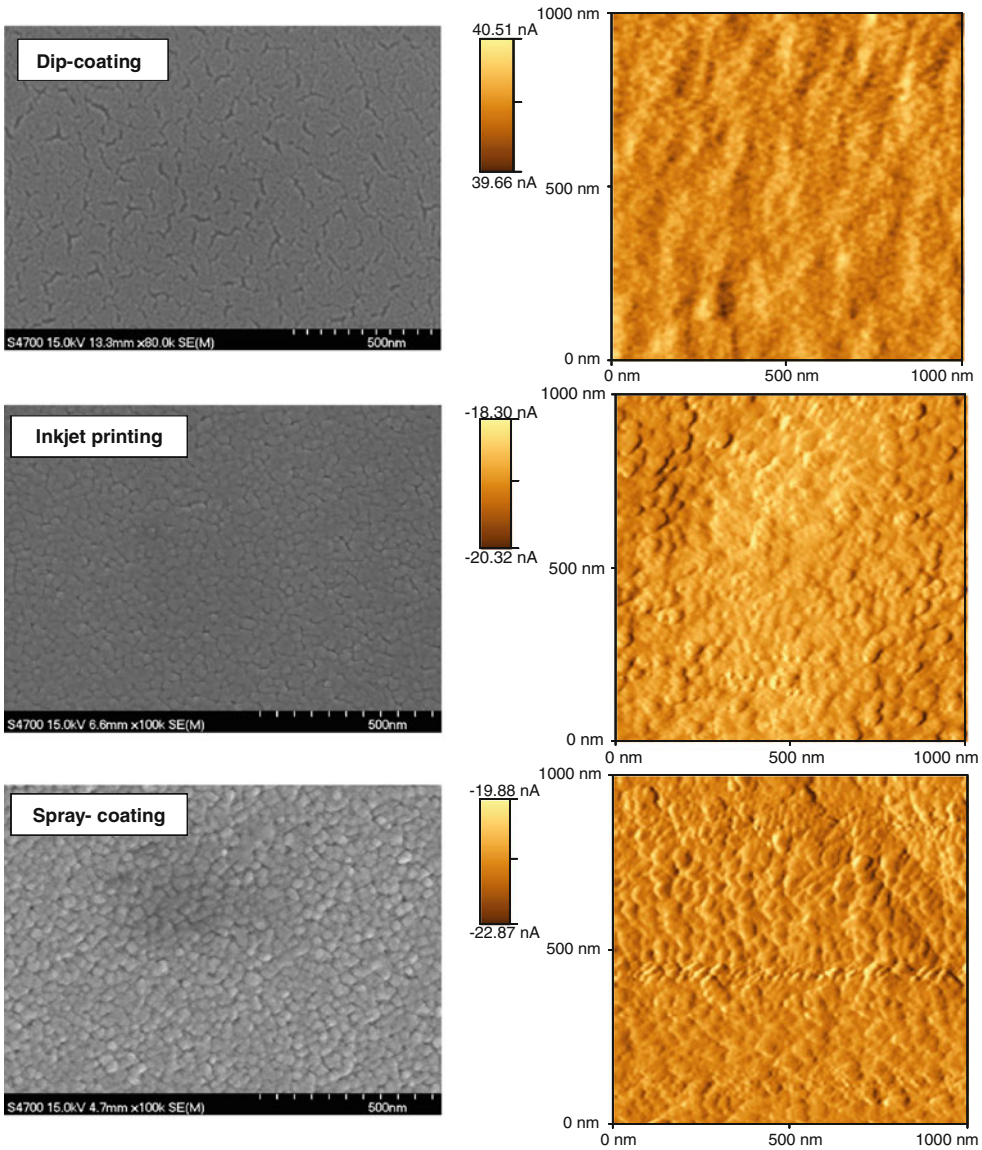


**Fig. 2** SEM and AFM images of layers surface

deposited on microscopic glass (see Fig. 3). The UV–Vis measurement took place in the device equipped with integration sphere where transmittance and reflectance spectra were measured. The blue-shift caused by the effect of the small size particles was observed. The absorption edge was determined approximately at 350 ± 5 nm for all tested layers.

Figure 4a–c made with the help optical microscope illustrate the surface morphology of thin films produced by dip-coating, spray-coating and inkjet printing. As can be seen a visual appearance provided by the optical microscopy show a homogeneous layers with the smooth surface for samples prepared by dip-coating and inkjet printing without the larger extent of the obvious surface defects. Nevertheless, some heterogeneity in the printed layer thickness reflected in the light interference was macroscopically visible. On the other hand, the sprayed layers possess a great amount of the surface heterogeneity, which is visible by the naked eyes. This fact is obviously caused by the relatively big and unequal droplets ejected by the nozzle and these droplets cannot create a homogenous surface. However, the sprayed layers owing to the highest roughness and heterogeneity could possess higher surface, which then could be useful for the better adsorption of oxidizable species from solution.

### 3.2 Photoelectrochemical properties

The photo-induced properties of semiconductors use to be interpreted as the band gap excitation of the oxide film in the aqueous electrolyte which leads to the photogeneration valence band holes. The electrons shift to the conducting band, where they can move through the solid. This process can be quantified by measuring the number of the

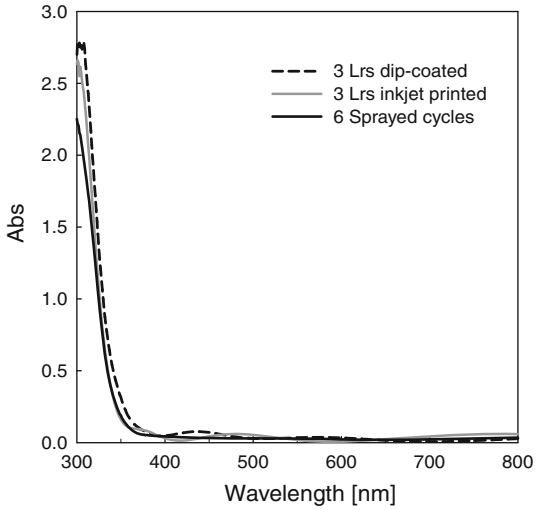


**Fig. 3** UV–Vis absorption spectra

photogenerated conduction band electrons (IPCE) [24, 25]. In this study the photoelectrochemical measurements of the $TiO_2$/ITO photoanode prepared by the three various deposition techniques were carried out in the described electrochemical cell. Dependence of the generated current density (recalculated to IPCE values) on the linear increasing potential and the photocurrent-time behaviour of the thin films was investigated similarly as dependence of the potential change on time of the UV light irradiation.

Figure 5 represents the linear voltammogram of the three dip-coated layers, three inkjet printed layers and six cycles of the sprayed layers in the light–dark 5 s irradiation period. These photocurrent-potential curves prove the ability of the layers to react on the UV light signal immediately and repeatedly. All tested samples have shown the constant values of the generated photocurrents (plateau) at positive potentials. In the case of the negative potential the photocurrents values were lower and have grown gradually to the constant level.

As can be seen in Fig. 5, values of the generated photocurrent differ for layers prepared by deposition techniques. These differences in IPCE values are probably caused by the various surface/bulk defects concentration in the prepared thin films. In principle, surface and bulk defects play a very important role in the photoactivation processes owing to the divergence of the diffusion mechanism for the various types of defects [26, 27]. The influence of defects on $TiO_2$ electric properties has been reported; the higher photocurrent (the higher electron–hole pair separation efficiency) the lower ratio of bulk/surface defects (the lower among of places where the generated charge carriers can recombine) [26–29]. From the photoelectrochemical experiments it follows that the layers with the lowest value of photogenerated current and thus the highest ratio of bulk to surface defects were prepared by

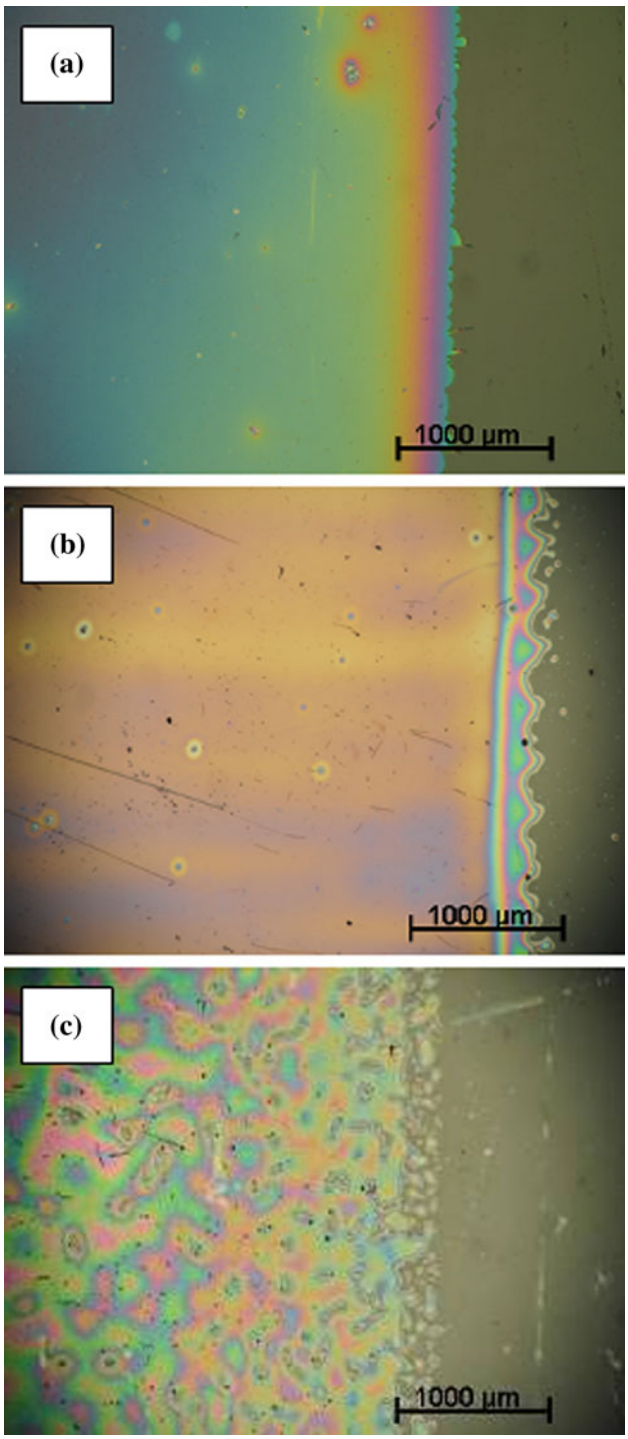


**Fig. 4** Optical surface image of (**a**) 1 dip-coated layer, (**b**) 1 inkjet-printed layer, (**c**) 6 sprayed cycles layer

the spray coating method, whereas the dip-coated layers form the homogeneous thin film immediately, and thus the bulk defects are minimized. Therefore, this method possesses the lowest ratio of the bulk to surface defects. The spray coating and the inkjet printing techniques are based on the same principle of the drops spreading on substrate.

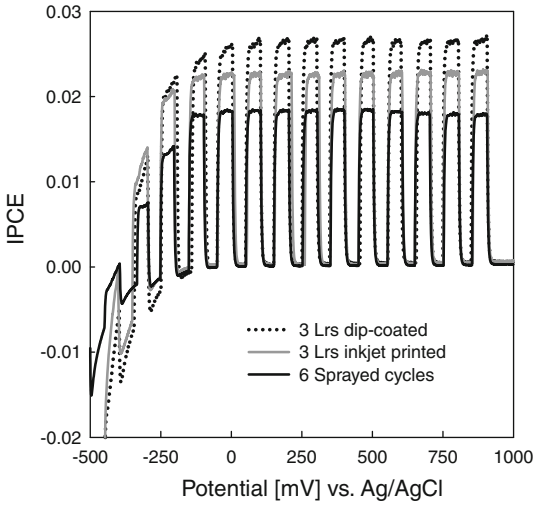


**Fig. 5** The polarization curves of the coated, printed and sprayed $TiO_2$ layers, scan rate 0.01 V $s^{-1}$, the incident light intensity 10 mW $cm^{-2}$

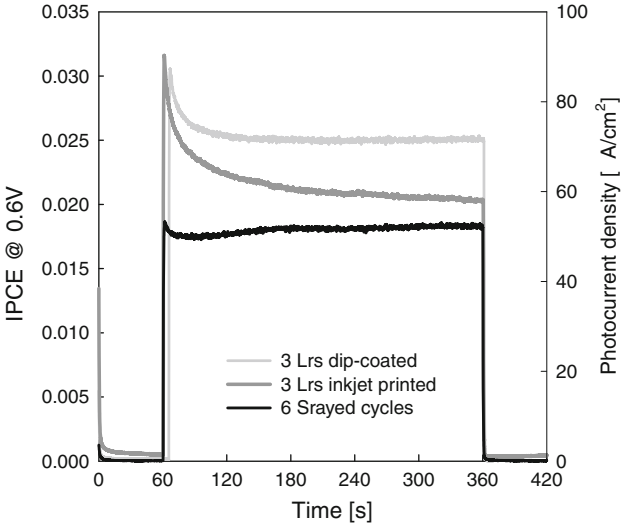


**Fig. 6** The photocurrent-time behaviour of the $TiO_2$/ITO anodes prepared by dip-coating, inkjet printing and spray-coating techniques, the incident light intensity was 10 mW $cm^{-2}$, constant potential 0.6 V

Evidently, it can lead to creation a higher amount of bulk defects. It is necessary to note that even though the differences of the generated photocurrent are rather low, this trend was observed for all experimental measurements.

The IPCE values obtained from the linear voltammetry are confirmed by the amperometry in Fig. 6. By this method the long-term stability of the photo-excited species in the films and the generated photocurrent as a function of time at the constant inserted potential (600 mV) can be determined. The $TiO_2$/ITO electrode was 5 min irradiated and during this interval the constant values of photocurrent were reached. There is evident (in Fig. 5) that the sharp maximum of the IPCE values was more obvious for the inkjet printed layers. This so called current peak appears immediately at the first moment of irradiation. Further, the curves very slowly decrease to get the steady state values. The instantaneous increase of IPCE values means a rapid electron–hole generation/separation and the decrease is assigned to their recombination.

The open circuit potential (OCP), also called the equilibrium potential, which provides information on the thermodynamically tendency of a material to electrochemical oxidation and about the kinetics of separation and recombination of the electron–hole pairs, was also studied. The OCP measurements record dependence of the changing potential on time. The photopotential decay ($E_{oc}$) was monitored upon the UV irradiation of the $TiO_2$/ITO electrode. Generally, photopotential is the difference between the potential values at the beginning of the irradiation period and at the end. Potential values at the beginning of irradiation shift immediately to more negative values, which indicate the increase of the electron concentration. In the UV light period, the $E_{oc}$ has reached constant values, which correspond to the steady state concentration of the not recombined electrons. The maximum photopotential is normally obtained for zero photocurrent. The potential regresses back to the original values after the light is switched off. The obtained $E_{oc}$ values for individual applied techniques are summarized in Table 1. The measured results from OCP experiment correspond with the detected trend of IPCE values in amperometry: the sample with the highest photocurrent possess also the highest photopotential decay.

## 4 Conclusion

Three deposition techniques of the templated sol–gel method were applied for formation of $TiO_2$ thin layers consisting of the small uniform particles. It was found that the used deposition techniques influenced the type of created defects similarly as their amount and ratio of the surface/bulk defects in the prepared thin films. These defects probably arise from the means of the sol deposition on substrates similarly as from the sol volume presented on substrate at calcination. Evidently, the surface and bulk defects in $TiO_2$ thin layer play very important roles in photoinduced processes. By choice of the liquid sol deposition method the surface/bulk defect concentration in layers can be controlled.

It was proved that decreasing ratio of the bulk to surface defects improved the charge carriers (electron–hole pairs) separation efficiency. Thus, the photocurrent generation could be significantly enhanced. In general, it is obvious that structural properties, especially the surface morphology can significantly influence the local surface chemistry.

To compare their photoelectrochemical properties $TiO_2$ layers supported on ITO glass were tested as $TiO_2$/ITO photoanode. All tested photoanodes possessed very good photo-induced properties; moreover, a very fast response to the light signal was proved even for the low light intensity. On the other hand, the observed differences in the reached IPCE values for the photoanodes prepared by dip-coating, inkjet printing and spray-coating were relatively low.

It can be summarized that each of the deposition techniques offers some advantages as well as disadvantages. The dip-coating method forms the best homogeneous thin film with minimum of the bulk defects and thus the highest IPCE values and the photogenerated current. The inkjet printing method also forms the homogeneous thin film with a low amount of the bulk defects and the high IPCE values. Moreover, this technique enables printing of the regular as well as the irregular patterns. The spray coating method reveals the rather lower IPCE values and the photogenerated current, but this method enables to cover any surface by the nanosized $TiO_2$ layers even if the area would be larger.

**Acknowledgments** This work was supported by the Grant Agency of the Czech Republic, project no. GP 104/09/P165, as well as Technology Grant Agency TA01020804. Authors also appreciate the work of J. Hnat, ICT Prague, for providing SEM images and Z. Matej, Charles University in Prague, for XRD measurements.

## References

1. M. Gratzel (2000) Book rev 403:363
2. M. Gratzel (2001) Nature 414:338
3. Fujishima A, Honda K (1972) Nature 238:32
4. Butterfield IM, Christensen PA, Curtis TP, Gunlazuardi J (1997) Water Res 31:675
5. Zou L, Luo Y, Hooperc M, Hu E (2006) Environ Technol 27:359
6. Kozlowska K, Lukowiak A, Szczurek A, Dudek K, Maruszewski K (2004) Opt Appl 35:783
7. Kavan L, Gratzel M, Rathousky J, Zukal A (1996) J Electrochem Soc 143:394
8. Bach U, Lupo D, Moser JE, Weissortel F, Salbeck J, Spreitzer H, Gratzel M (1998) Nature 395:583
9. Bott AW (1998) Electrochemistry of semiconductors. Curr Sep 17:3
10. Carp O, Huisman C (2004) A Reller. Prog Solid State Chem 32:33
11. Nozik A, Memming R (1996) J Phys Chem 100:13061
12. Kment S, Kluson P, Stranak V et al (2009) Electrochim Acta 54:3352
13. Li M, Schnablegger H, Mann S (1999) Nature 402:393
14. Livage J, Sanchez C, Henry M, Doeuff S (1989) Solid State Ion 32(33):633
15. H. Schmidt, M. Mennig (2000) Wet Coating technologies for glass, The sol-gel gateway http://www.solgel.com/articles/Nov00/coating.htm
16. Fretwell R, Douglas P (2001) J Photochem Photobiol A Chem 143:229
17. Shide P, Sadale S, Patil P, Bhodale P, Brüger A, Neumann-Spallart M, Bhosale C (2008) Sol Energy Mater Sol Cells 92:283
18. Dzik P, Vesely M, Chomoucka J (2010) J Adv Oxid Technol 13:2
19. Dzik P, Morozova M, Kluson P, Vesely M (2012) J Adv Oxid Technol 15:1
20. Le HP (1998) Imaging Sci Technol 42:49
21. Morozova M, Kluson P, Krysa J, Zlamal M, Solcova O, Kment S, Steck T (2009) J Sol-Gel Sci Technol 52:398
22. Morozova M, Kluson P, Krysa J, Gwenin Ch, Solcova O (2011) J Sol-Gel Sci Technol 58:175
23. Morozova M, Kluson P, Krysa J, Dzik P, Vesely M, Solcova O (2011) Sens Actuator B Chem 160:371
24. Krysa J, Zlamal M, Waldner G (2007) J Appl Electrochem 37:1313
25. Kavan L, Stoto T, Gratzel M, Fitzmaurice D, Shklover V (1993) J Phys Chem 97:9493
26. Diebold U (2003) Surf Sci Rep 48:53
27. Kong M, Li Y, Chen X, Tian T (2011) J Am Chem Soc 133:16414
28. Nakato Y, Akanuma H, Magari Y, Yae S, Shimizu J, Mori H (1997) J Phys Chem B 101:4934
29. Weibel A, Bouchet R, Knauth P (2006) Solid State Ion 177:229

Available online at www.sciencedirect.com

SciVerse ScienceDirect

Procedia Engineering 42 (2012) 573 – 580

Procedia Engineering

www.elsevier.com/locate/procedia

20th International Congress of Chemical and Process Engineering CHISA 2012
25 – 29 August 2012, Prague, Czech Republic

# Electrochemical properties of $TiO_2$ electrode prepared by various methods

M. Morozova[a], P. Kluson[a], J. Krysa[a], M. Vesely[b], P. Dzik[b], O. Solcova[a] a*

[a] *Institute of Chemical Process Fundamentals of the ASCR, v. v. i., Rozvojová 135, Prague 165 02, Czech Republic*
[b] *Brno univesity of Technology, Faculty of Chemistry, Purkynova 464/118, Brno 612 00, Czech Republic*

**Abstract**

Thin transparent $TiO_2$ layers were created on the conductive ITO glass by means of the templated sol-gel technique and by the subsequent calcination at 450˚ C. The sol-gel method using molecular templating is based on a chemical process utilizing hydrolysis and polycondesation of metal alkoxides in the core of reverse micelles which allows a production of uniform particles in layers. The sol-gel method was chosen by reason of the sol-gel layers electrodes are transparent and possess very stabile surface. For the preparation of the thin sol-gel $TiO_2$ films, numerous deposition techniques were applied. This contribution is focused on the study of structural and photo-electrochemical properties of the sol-gel nanostructured layers deposited by two various techniques (a dip-coating and an inkjet printing). The sol's viscosity, concentration, solvent volatility, speed of pulling etc. may influence the final structural properties of layers, such as film thickness, nanoparticles size and surface morphology. The surface properties were determined by XRD, Raman, SEM, AFM and UV-Vis analyses. Photo-induced electrochemical properties were measured by potentiodynamic methods in the three-compartment electrochemical cell. This Pyrex cell contained supporting electrolyte (0.1M $Na_2SO_4$) and the $TiO_2$/ITO electrode was used as a working electrode. As an UV source the polychromatic mercury lamp was employed and the wavelength of the incident light was focused by an interference filter on 365 nm.



*Keywords*: Titanium dioxide, sol-gel, photoelectrochemistry, dip-coating, inkjet printing

* Corresponding author. Tel.: +420 220 390 279; fax: +420 220 920 661.
*E-mail address*: solcova@icpf.cas.cz.

1877-7058 © 2012 Published by Elsevier Ltd.
doi:10.1016/j.proeng.2012.07.450

## 1. Introduction

Nanoscaled titanium dioxide ($TiO_2$) in thin layer or powder forms appertains to the most extensively studied semiconductors. This metal oxide is a promising semiconductor frequently used as a photocatalyst in the advanced oxidation processes (water or air purification) due to its non-toxicity, chemical stability, photocatalytic activity and low cost [1-4]. Especially, thin films as the nanostructured electrode materials have become very important in fields of photovoltaics, energy storage, sensing, photoelectrocatalysis etc. [5,6]. As generally known, the photoactivity arises from the semiconductor nature, especially from the ability of the light quantum absorption followed by the charge carrier generation. $TiO_2$ in crystallographic form of anatase has become an interesting candidate as an n-type photoanode due to its excellent efficiency to generate the electron-hole pairs [7,8].

Preparation of the nanostructured electrode materials with highly uniform nanoparticles has been investigated by many groups [9-11]. The most commonly used method is the sol–gel technique utilizing the molecular templates. The main advantage of this purely chemical method lies in a possibility of layer preparation under laboratory conditions as well as the possibility to tailor $TiO_2$ layer properties by varying preparation conditions. Nanoparticles with controlled chemical composition, size distribution, uniformity and dispersion can be readily synthesized using reverse micelles [12-14]. Layers prepared in this way possess usually highly transparency, surface homogeneity, size, structure uniformity and very high adhesion to substrate in comparison with the particulate layers.

Nowadays, a variety of deposition techniques for the liquids deposition, such as dip-, spin- or spray-coating, doctor blade, roller etc., has been appeared and each of them offers some advantages and disadvantages [15]. There are three traditional method of thin layer preparation from liquid precursors: spin-coating, spray-coating and dip-coating. Dip-coating belongs to the traditional and widely used methods of the thin layer preparation. It is based on dipping the substrate into the sol and pulling it out at constant speed. Spray-coating is the other elementary technique which applies liquid sol on the substrate by the spray head with one three-axe system nozzle. And the last method spin-coating uses centrifugal force to form a film of liquid precursor [15-17]. As a new process of the sol application the ink-jet printing has been appeared. This technique proved to be very elegant and clean method for liquids deposition and direct patterning [18].

The sol viscosity, concentration, solvent volatility and the speed of pulling influence the resulting film thickness and structural properties. This contribution is focused on the study and the comparison of structural and photo-electrochemical properties of the sol-gel nanostructured $TiO_2$/ITO electrode deposited by dip-coating and inkjet printing.

## 2. Experimental

### *2.1. Layers preparation*

Thin transparent $TiO_2$ layers were created on the one side of the conductive ITO glass (5–15 Ω, Delta-Technologies Ltd., USA) and on the soda-lime microscopic glass plates by means of the templated sol-gel technique and by the subsequent calcination at 450˚ C for 4 h. The sol-gel method using molecular tamplating is based on a chemical process utilizing hydrolysis and polycondesation of metal alkoxides in the core of reverse micelles which allows a production of uniform particles in layers. The reverse micelles were created by molecular templates TX 102 (Sigma–Aldrich) in the nonpolar environment of cyclohexane (Aldrich, 99.9%, HPLC grade) or xylene (p.a., Penta, Czech Republic). In the core of the created micelles a small amount of demineralised water was added. As titan precursor the titanium

isopropoxide (TTIP, 99.999%, Sigma–Aldrich) was used drop-wise. The sol-gel with cyclohexane was used for the dip- and spray- coating techniques. In the case of ink-jet printing the nonpolar environment has been changed to xylene by reason that cyklohexane disturbed the plastic print head [19].

The sol application was performed by laboratory dip-coater (ID-Lab coater 4). The substrate was dipped into the sol where it was kept for 30 s and then substrate was pulled with velocity 6 cm/min. After the each dip-coating cycle the samples were heat-treated. An adapted experimental inkjet printer Fujifilm Dimatix 2830 was used for preparation of the printed layers. Xylene sol was loaded into the Dimatix ink tank and the Dimatix 10 pL printing head with the piezoelectric nozzles was attached to the tank. Then this equipment was mounted into the Dimatix printer. Then small droplets (10 pL) were ejected from the print nozzles and they fall onto ITO glass. After the every new printed layer a gelling and drying step was performed [18].

### *2.2. Characterization*

The deposited thin films were treated by calcination and the surface properties were determined by XRD (Panalytical-MRD laboratory diffractometer with the Cu anode), Raman spectroscopy (Raman Dispersive Spectrometer Nicolet Almega XR), SEM (Hitachi S4700), AFM microscope (Thericroscopes) and optical microscope equipped with Nikon D5000 digital camera. The layer thickness was evaluated by Ocean Optics USB4000 diode array photometer with fibre optic reflectance probe (NanoCalc). Values of absorption edges of layers were obtained from UV–Vis spectra (Perkin-Elmer Lambda 35 equipped with a Labsphere RSA-PE-20 integration sphere).

### *2.3. Photoelectrochemical measurement*

Photoelectrochemical measurements were performed at room temperature in the three-electrode Pyrex cell by means of electrochemical methods. All potentials were referred to Ag/AgCl/KCl(sat) electrode, whereas a Pt sheet was used as a counter electrode. The exposed area of the working $TiO_2$/ITO electrode for UV illumination and photoelectrochemical reaction was 1 $cm^2$. Measurements were performed with a computer-controlled Voltalab 10 PGZ-100 potentiostat. For all electrochemical experiments 0.1 M solution of $Na_2SO_4$ in ultrapure water (0.06 μS $cm^{-1}$) was used as working electrolyte. A 500 W polychromatic lamp (Hg, LOT-Oriel) with a water filter was used for UV–Vis irradiation and the incident light beam was modified with an interference filter (Melles Griot) producing spectrally narrow flux of photons (365 ± 10 nm). The applied irradiance was measured with an UV sensor (UVA Light Meter) with intensity 10 mW $cm^{-2}$ in the most experiments. Obtained incident light intensity was recalculated to Incident-Photon-Current-conversion-Efficiency (IPCE). The layer photoexcitation properties were characterized by linear voltammetry, amperometry and open circuit potential (OCP) [20].

## 3. Results and discussion

### *3.1. Structural properties*

Figure 1 (a and b) made by optical microscope illustrates the surface morphology of sample produced by dip-coating and ink-jet printing. As can be seen a visual appearance provided by the optical microscopy shown a homogenous layers with smooth surface without the higher extent of surface defects.

Nevertheless, some heterogeneity in the printed layer thickness reflected in the light interference was macroscopically visible.

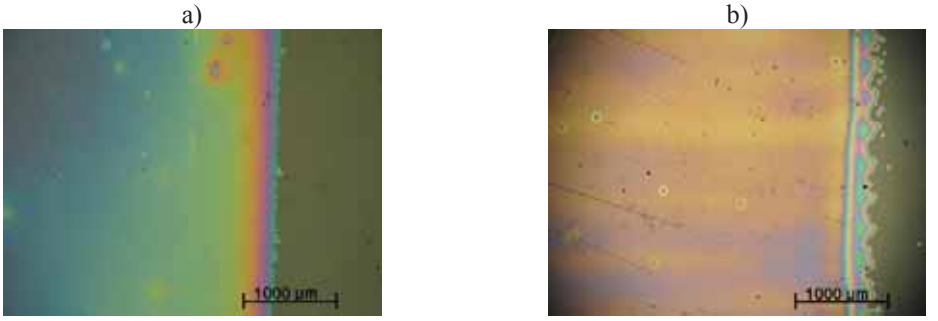


Fig. 1. The layer's surfaces as seen by optical microscopy (a) 1 dip-coated layer; (b) 1 inkjet printed layer

Figure 2(a, b) depicts the surface morphology of sample produced by the three ink-jet printed cycles and three dip-coated cycles recorded by SEM and AFM. The more detailed view at the surface morphology made by SEM shows a smooth porous surface without the higher extent of surface defects which corroborate the results form the optical microscopy. The relative surface roughness expressed as the roots mean square values (RMS) was studied by AFM. Very smooth surface (RMS factor < 1) was detected for the dip-coated layers.

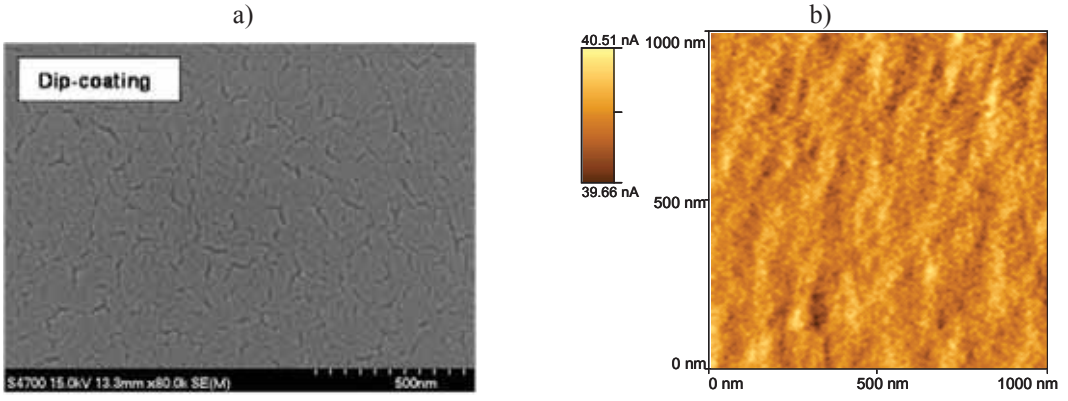

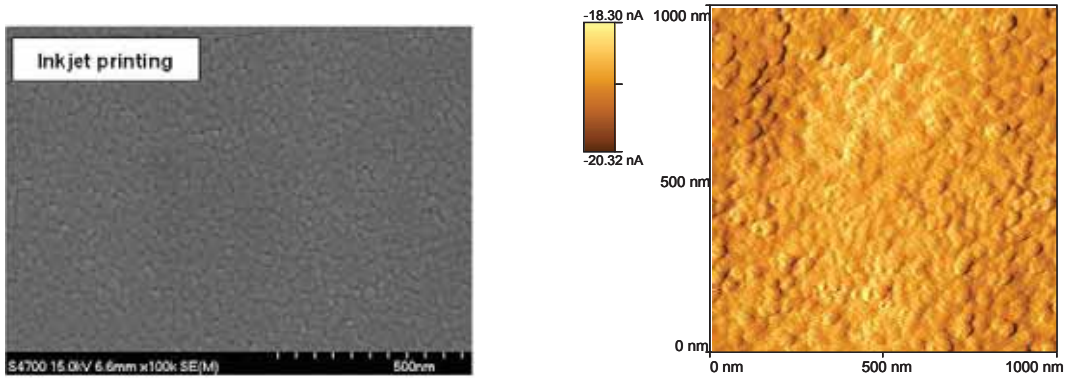


Fig. 2. The images of the 3 dip-coated and 3 inkjet printed layers surface as seen by (a) SEM and (b) AFM

The thin $TiO_2$ layers produced by various deposition methods possess the crystallographic form of anatase, which was determined by XRD analysis and confirmed Raman spectroscopy. The particles size in layer was obtained from the XRD diffraction lines and calculated by special method (Table 1). The layers thicknesses were investigated from images made by SEM and the absorption edge for both samples was determined from absorption spectra approximately at 355 nm.

Table 1. Characteristics of the produced layers

| Layers | RMS factor [nm] | Particles size [nm] | Thickness of 3 layers [nm] | Eoc [mV] |
|---|---|---|---|---|
| Dip-coating | 0,5 | 7 | 330 | -460 |
| Inkjet printing | 3,6 | 8 | 340 | -400 |

### *3.2. Photoelectrochemical properties*

All prepared layers possess very good photoinduced properties. The dependence of the generated current density (recalculated to IPCE values) on the linear increasing potential is illustrated in Fig. 4. This linear voltammogram represents polarization curves of the three dip-coated and the ink-jet printed cycles $TiO_2$ film electrodes. The plot proves the ability of the layers to react on the UV light signal immediately and repeatedly. A very fast photo-response was a general property of all tested layers and represents an important feature that might be appreciated practically (fast response of a sensor). The generated photocurrents in the positive potential area were constant with time and reached characteristic plateau at every irradiated intervals. At negative potential (−400 mV) the photocurrents were also generated, however the values were lower and it can be seen the gradual growth to the constant level.

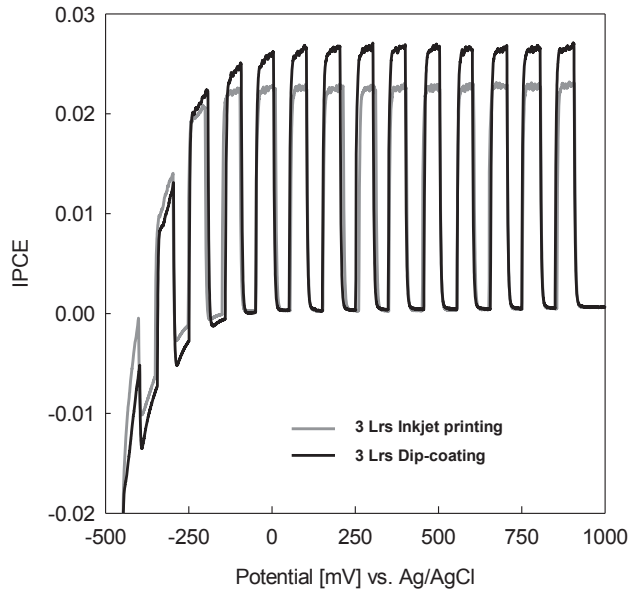


Fig. 4. The polarization curves of the coated and printed $TiO_2$ layers, scan rate 0.01 V $s^{-1}$, the incident light intensity 10 mW/$cm^2$

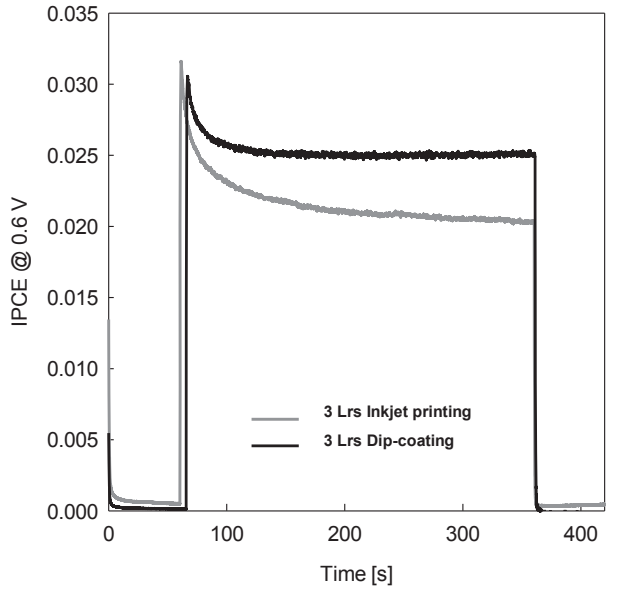


Fig. 5. Photocurrent-time behavior of the prepared $TiO_2$/ITO anodes. The incident light intensity was 10 mW/$cm^2$, constant potential 0.6 V

The values of generated photocurrent were measured at constant potential (0.6 V) by amperometry measurement. This experiment shows the efficiency of the prepared $TiO_2$/ITO electrode to reach in the 5 min irradiation interval constant photocurrent. The obtained curves indicate the photocurrent-time behavior of the layers. The measured samples embodied the very sharp maximum of the reached IPCE values which was much obvious for the inkjet printed layers. This so called current peak appears immediately at the first moment of the irradiation. Further, the curves decrease very slowly to get a steady state values. The instantaneous increase of IPCE values means a rapid electrons-holes generation and separation at the space charge region. The decrease is assigned to their recombination.

The open circuit potential (OCP) represents the experiment focused on evaluation the kinetics of efficient separation of electrons and holes. The photopotential (Eoc) decay was measured and the obtained Eoc values are summarized in Table 1. Upon UV irradiation, the open circuit potential shifts immediately to more negative values which reflects rising of the major charge carriers (electrons) concentration. The potential regresses to the original values after the light is switched off. The constant Eoc values in the UV light period correspond to the steady state concentration of the not recombined electrons. The amount of photoexcited electrons reacts either with an electron scavenger (e.g. oxidisable species) or with the photogenerated holes or migrates through layers to the conductive substrate.

## 4. Conclusions

It was proved that the prepared $TiO_2$/ITO electrodes ($TiO_2$ thin layers deposited on ITO glass by dip-coating and inkjet printing technique and used as photoanode) are stable and possess good photoinduced properties. The structural properties, especially the surface morphology, and also the photoelectrochemical behavior, mainly the generated photocurrent values, are slightly different. The structural distinction was caused by the used deposition technique. In the photoelectrochemical measurement the differences are very negligible. The obtained electrochemical curves of layers reflect the ability to react on UV light signal by generation of the charge carriers. The electrochemical measurements confirmed the high potential of photoelectrochemistry for detection of the semiconductor oxides photoactivity.

## 5. Acknowledgements

This work was supported by the Grant Agency of the Czech Republic, project no. GP 104/09/P165, as well as Technology Grant Agency TA01020804.

## 6. References

[1] Malato S, Fernandez-Ibanez P, Maldonado MI, Blanco J, Gernjak W. Decontamination and disinfection of water by solar photocatalysis: Recent overview and trends. *Catal Today* 2009;**147**:1-2.

[2] Butterfield IM, Christensen PA, , Hamnett A, Shaw KE, , Walker G.M. Applied studies on immobilized titanium dioxide films ascatalysts for the photoelectrochemical detoxification of water. *J Appl Electrochem* 1997,**27**:4-385.

[3] Calvo M, Candal R, Bilmes S. Photooxidation of Organic Mixtures on Biased TiO2 Films, *Environ Sci Technol* 2001;**35**:20-4132.

[4] Attar AS, Ghamsari MS, Hajiesmaeilbaigi F. Synthesis and characterization of anatase and rutile $TiO_2$ nanorods by template-assisted method. *J Mat Sci* 2008;**43**:17-5924.
[5] Huang XJ, Choi YK. Chemical sensors based on nanostructured materials. *Sensors Actuators B* 2007;**122**:659.
[6] Fabregat-Santiago F, Mora-Sero I, Garcial-Belmonte G, Bisquert J. Cyclic voltammetry studies of nanoporous semiconductors. Capacitive and reactive properties of nanocrystalline $TiO_2$ electrodes in aqueous electrolyte, *J Phys Chem B* 2003;**107**:3-758.
[7] Hashimoto K, Irie H, Hujishima A. TiO2 photocatalysis: a historical overview and future prospects, *Jpn J Appl Phys* 2005; **44**:12-8269.
[8] Gracia F, Holgado J, González-Elipe A. Photoefficiency and optical, microstructural, and structural properties of $TiO_2$ thin films used as photoanodes, *Langmuir* 2004;**20**:5-1688.
[9] Ying L, Hon LS, White T, Withers R, Hai LB. Controlled nanophase development in photocatalytic titania, *Mater Trans* 2003;**44**:7-1328.
[10] Zhang YX, Li GH, Wu YC, Luo YY, Zhang LD. The formation of mesoporous $TiO_2$ spheres via a facile chemical process, *J Phys Chem B* 2005;**109**:12-5478.
[11] Sanchez C, Arribart H, Guille MMG. Biomimetism and bioinspiration as tools for the design of innovative materials and systems. *Nat Mater* 2005;**4**:4-277.
[12] Li M, Schnablegger H, Mann S, Coupled synthesis and self-assembly of nanoparticles to give structures with controlled organization, *Nature* 1999;**402**:6760-393.
[13] Crans DC, Baruah B, Ross A, Levinger NE. Impact of confinement and interfaces on coordination chemistry: using oxovanadate reactions and proton transfer reactions as probes in reverse micelles, *Coord Chem Rev* 2009;**253**:17-2178.
[14] Addamo M, Augugliaro V, Di Paola A, Garcia-Lopez E, Loddo V, Marci G, Palmisano L. Photocatalytic thin films of TiO2 formed by a sol–gel process using titanium tetraisopropoxide as the precursor. *Thin Solid Films* 2008;**516**:12-3802.
[15] Schmidt H, Mennig M, Wet Coating Technologies for Glass, The Sol-Gel Gateway, http://www.solgel.com/articles/Nov00/coating.htm, 2000
[16] Schubert D, Dunkel W. Spin coating from a molecular point of view: its concentration regimes, influence of molar mass and distribution. *Mat Res Innovat* 2003;**7**:5-314.
[17] Fretwell R; Douglas P. An active, robust and transparent nanocrystalline anatase $TiO_2$ thin film - Preparation, characterisation and the kinetics of photodegradation of model pollutants. *J Photochem Photobiol A: Chemistry* 2001;**143**:2-229.
[18] Dzik P, Vesely M, Chomoucka J. Thin layers of photocatalytic TiO2 prepared by inkjet printing of a sol gel precursor, *J Adv Oxid Technol* 2010;**13**:2-172.
[19] Morozova M, Kluson P, Krysa J, Dzik P, Vesely M, Solcova O. Thin $TiO_2$ films prepared by inkjet printing of the reverse micelles sol–gel composition, *Sensors and Actuators B* 2011;**160** -371.
[20] Morozova M, Kluson P, Krysa J, Zlamal M, Solcova O, Kment S, Steck T. Role of the template molecular structure on the photoelectrochemical functionality of the sol–gel titania thin films. *J Sol-Gel Sci Technol* 2009;**52**:3-398.

# Photocatalytic and Self-cleaning Properties of Titania Coatings Prepared by Inkjet Direct Patterning of a Reverse Micelles Sol-gel Composition

**Petr Dzik*,[1], Magdalena Morozová[2], Petr Klusoň[2], and Michal Veselý[1]**

[1]Brno University of Technology, Faculty of Chemistry, Purkyňova 118, 61200 Brno, Czech Republic
[2]Institute of Chemical Process Fundamentals ASCR, Rozvojová 2, 165 02 Prague 6, Czech Republic

## Abstract:

An optimized reverse micelles sol-gel composition was deposited by inkjet direct patterning onto glass supports. Experimental "material printer" Fujifilm Dimatix 2831 was used for sol patterning. Printing was repeated up to 4 times in wet-to-dry manner and photocatalytic coatings of various thickness were obtained after final thermal calcination. Basic material properties of prepared coating were studied by optical microscopy, electron and atomic force imaging, Raman, XRD and UV-VIS spectrometry. Photocatalytic activity was evaluated by dye and fatty acid degradation rate as well as photoinduced hydrophilic conversion rate. Reverse micelles proved to be viable synthetic route for the preparation of titania coatings with even structure and their compatibility with inkjet direct patterning deposition was demonstrated.



## Introduction

For the past 4 decades, titanium dioxide has been the subject on an intensive research. What was started by Fujishima and Honda's seminal report (1) on photo-electrochemical splitting of water on titanium dioxide electrodes, has gradually developed into a broad technological field of applied photocatalysis. So far we have witnessed the proposals and successful application of photocatalytic phenomena for water purification (2), toxic waste treatment (3), air purification (4), self-cleaning and self-disinfecting surfaces (5) as well as superhydrophilic antifogging ones (6).

Water-in-oil emulsions consisting of reverse micelles continue to receive a great deal of attention. This approach proved to be especially useful for controlled synthesis of various nanosized ceramic materials with a narrow size distribution. Reverse micelles are nanometer-scale surfactant association colloids formed in a nonpolar organic solvent useful as potential microreactors (7). Titanium dioxide particles synthesized by controlled hydrolysis of titanium precursor in such micelles suffer from amorphous structure. Therefore the reverse micelles synthetic route is often coupled with a hydrothermal treatment (8) or the sol-gel process performed inside micelles is followed by thermal calcination or super-critical extraction (9) in order to produce crystalline titania nanoparticles.

Undoubtedly, the sol-gel process definitely proved its benefits and potential so far. However, the sol-gel chemistry is only one part of the story – in order to produce titania layers, the liquid sol formulation must be coated onto a substrate. Many different coating techniques have been proposed, such as dip-, spin- or spray-coating, doctor blade spreading, roller etc. (10). While all these techniques proved to be useful, they are buried by some inherent limitations. These include, but are not limited to: sensitivity to surface defects, limited coating area, ambient humidity interference, efficiency of precursor use. Fortunately, a new promising deposition technique has become available recently. The novel approach is usually termed inkjet material deposition or shortly material printing. The technique shares the basic principles with conventional inkjet printing, i.e. tiny droplets of a low-viscosity liquid are precisely deposited onto a substrate by means of thermal or piezoelectric printhead. In the case of material printing, the ink is a specially formulated liquid used for transporting a functional component onto the substrate surface.

This technique is very robust and outperforms the traditional ones in most aspects:

- Sensitivity to **surface defects** is strongly suppressed, because a defect is simply overprinted. In the worst cases it may eventually disrupt the layer homogeneity, but it certainly won't influence its surroundings.
- **Coating area** is limited solely by the printer design. Inkjet printers handling roll media of a meter width or rigid media of several square meters area are common nowadays in the printing industry. Such printers can be easily converted for printing functional liquids instead of original colored inks.

*Corresponding author; E-mail address: petr@dzik.cz

- **Environmental sealing**: The ink is kept in airtight tanks and tubing until printing so evaporation and humidity absorption is eliminated.
- **Efficiency of sol consumption**: A tiny fraction of the ink is consumed for print head cleaning and purging, but most of the ink is actually delivered to the substrate.
- The most important advantage this technique brings is the possibility of **direct patterning**, i.e. the fabrication of 2D patterns on the substrate without the need of any mechanical or optical masking.

Material printing has been successfully employed for the deposition of a great variety of functional materials forming thin layers, various patterns 2D (arrays, gaps, sandwich) and even 3D structures. As far as printed titania is concerned, several important papers are worth mentioning.

Yoshimura and Gallage summarized the general ideas of direct patterning in a neat review (11). They proposed several possible pathways leading to ceramic films, distinguishing between "inkjet reaction", "inkjet deposition" and "inkjet printing" methods. However, in their illustrative example, the preparation of $TiO_2$ films by inkjet printing was limited to patterning small letters and simple shapes onto a substrate heated to 548 K.

A lot of experimental attention has been paid to explore the most direct way leading to $TiO_2$ printed films: synthesis of stable colloidal suspension of nanocrystalline $TiO_2$ followed by a delivery of this suspension onto substrate by means of inkjet printing. Kim and Mckean (12) have studied the stability aqueous dispersion of commercial $TiO_2$ powder stabilized by proprietary polymeric dispersants. With their best and most stable samples, they were able to print the suspension by thermal inkjet printhead and obtained $TiO_2$ patterns on transparent polymeric foil. However, while they focus solely on the dispersion stability issues, problems of layer fixing and adhesion were not addressed.

Bernacka-Wojcik and coworkers recently demonstrated (13) a disposable biosensor integrating an inkjet printed, dye sensitized $TiO_2$ photodetector to be used in conjunction with DNA detection method based on non-cross-linking hybridization of DNA-functionalized gold nanoparticles. For the photodetector preparation, a commercial dispersion of titania particles was printed by a desk-top office printer equipped with a thermal inkjet head. A similar approach was adopted by Yang (14), who used an in-house synthesized dispersion of $TiO_2$ printed by a modified office inkjet printer to produce an oxygen demand sensing photoanode.

Matsuo and coworkers chose a totally different approach (15). Rather than printing heterogenenous dispersion of titania particles, they employed a colloidal organometallic sol for the preparation of titania layers. Their somewhat complex approach included a two-step preparation of the printing "ink" (sol based on titanium tetraisopropoxide, ethanol and nitric acid was evaporated and then re-dissolved in a mixture of ethanol and water to give 0.02 M Ti concentration). Printing was performed by a single jet piezo device onto substrate heated to 275 °C.

Manga and co-workers (16) utilized a similar approach to prepare an inkjet printed photosensor based on graphene oxide/titanium dioxide composite layer. However, the use of traditional sol-gel method did not prove to be favorable because of limited compatibility of aqueous graphene oxide solutions with titanium alkoxide sols. Instead, an aqueous solution of ionic organotitanate salt was employed.

Recently, Arin et al. (17) demonstrated a significant modification of the traditional sol-gel composition. With the help of complexing agents such as citric acid, they were able to formulate a sol-gel composition with water as the main solvent. Further, they prepared photocatalytic coatings by printing this sol with a large-orifice (90 um) single-nozzle experimental printer.

The authors of this paper have previously reported (18) the deposition of conventional sol-gel formulations based on tetraisopropoxy titanate and acetyl acetone by a modified office inkjet printer equipped with piezoelectric print head (Epson R220). In this way they were able to prepare thin layers of $TiO_2$ with excellent optical properties and photocatalytic performance comparable to dip- or spin-coated layers. Thick multilayer coatings were printed with the help of poly(ethylene glycol) acting as viscosity modifying, templating and anti-cracking agent (19).

In this letter, the authors inform about their further achievements concerning titania coatings deposited by inkjet printing. The presented study deals with the modification of previously reported (20) dip-coated reverse micelles sol-gel composition for inkjet direct patterning of titania coatings. The reverse-micelles route has been the preferred one due to favorable material properties of resulting layers. However, a more convenient deposition method than the originally used dip-coating was sought mainly with respect to further applications of resulting titania coatings (sensors, photovoltaics). Inkjet printing was the obvious choice because of the reason listed above. This paper discusses the basic material properties as well as photocatalytic and self-cleaning performance of prepared titania layers. A separate paper (21) describing the sol development,

optimization, the photoexcitation properties of the $TiO_2$ printed layers and the ability of photocurrent generation is published simultaneously with this one.

## Experimental

### *Sol Deposition by Inkjet Direct Patterning*

The optimised sol formulation (see (21) for details) was prepared by mixing 15.3 ml xylene (p.a., Penta, Czech Republic) with non-ionic surfactant Triton X 102 (Sigma-Aldrich) in a glass beaker placed on a magnetic stirrer. 0.06 ml of demineralized water was added causing the solution to turn first milky opaque and clarify within 10 minutes of intensive stirring. Titanium isopropoxide (TTIP, 99.999% trace metals basis, Sigma-Aldrich) was added drop-wise making the solution color change to deep yellow. Prepared sol was stored ant room temperature in airtight bottles and was stable for 6 months at least.

Experimental inkjet printer Fujifilm Dimatix 2831 was used for sol deposition and patterning. Prepared sol was sonicated for 5 minutes and then loaded into a syringe. A 0.2 um membrane filter (Pall Corporation, USA) and a blunt needle were attached to the syringe luer port and the sol was filtered and filled into the Dimatix ink tank in once. A Dimatix 10 pL printing head was attached to the tank and mounted into the Dimatix printer. The following settings were used for printing: Dimatix Model fluid 2 waweform, 20 V driving voltage, nozzle temperature 30 °C, substrate temperature 40 °C, nozzle span 20 um. Since the sol is a true analytical solution and does not contain any solid components, the jetting performace was excellent and nozzle blockage was rarely observed. Anyway, if nozzle blockage occurred, it was usually easily recovered by the first following head cleaning cycle.

Two sizes of soda-lime glass substrates were used for printing the sol: Standard microscopic plates (25×75 mm, Paul Marienfeld, Germany) and custom cut plates (50×50 mm, Merci, Czech Republic). Plates of both sizes were pre-treated by boiling in 9 M sulfuric acid for 1 hour in order to remove the surface sodium ions. Without such treatment, sodium ions would migrate (22) during the calcination process into the forming $TiO_2$ layer and could reduce the photocatalytic activity (23, 24).

A simple rectangular pattern 20×20 mm and 40×40 mm were printed onto the microscopic and custom-cut plates, respectively. The printing process was repeated up to 4 times to obtain various thicknesses of the resulting $TiO_2$ layers: each printing phase was followed by a gelling and drying phase (30 min at 110 °C) The finished samples were then calcined in air for 4 hours at 450 °C.

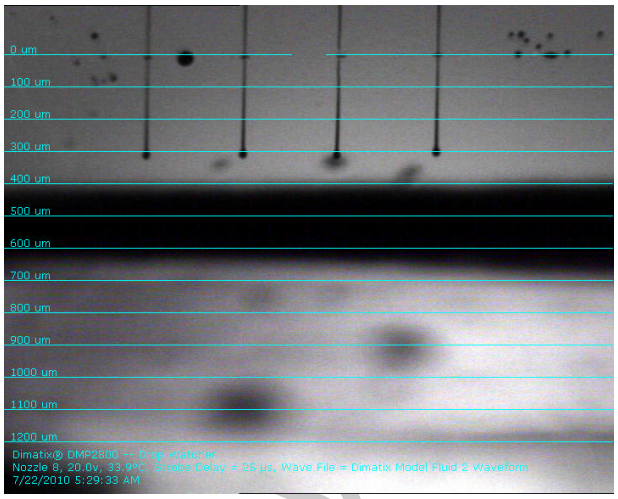


**Figure 1.** Even droplet formation of the optimised sol composition as viewed by the Dimatix stroboscopic camera.

### *Layer Characterization*

Microphotograps of printed layers were recorded using Nikon Eclipse E200 optical microscope equipped with a Nikon D5000 digital camera and Nikon Camera Control Pro 2 software. Polarised light was used to enhance the interference-originating color of the printed layers. Captured raw images were conveniently processed and organized by Adobe Lightroom.

Structural analysis of the prepared thin films was performed by Raman spectroscopy (Raman Dispersive Spectrometer Nicolet Almega XR), scanning electron microscope ( Hitachi S4700, Tescan MIRA II LMU) and AFM microscope (Ntegra Prima by NT-MDT). Diffuse reflectance UV-Vis spectra were recorded by Ocean Optics Redtide spectrophotometer with reflectance fiber probe.

### *Photocatalytic Experiments*

Photocatalytic activity in aqueous environment was evaluated on the basis 2,6-dichloroindophenol (DCIP) degradation rate. A simple two-chamber batch reactor circulated by a peristaltic pump was used. DCIP solution of $2\times10^{-5}$ mol/L starting concentration was circulated between the reaction chamber containing the glass plate with printed photocatalyst and the storage chamber. Ocean Optics transmittance dip-probe was inserted into the storage chamber and attached to the Ocean Optics Redtide spectrophotometer. This set-up enabled fully automated on-line absorbance measurements. The UV irradiation was provided by a medium pressure mercury lamp (OSRAM HQL 125W, without the fluorescent bulb). The intensity of UV radiation was 10 W $m^{-2}$ and it was measured by Gigahertz Optic X97 Irradiance Meter with X9-7 probe. A water cell was used to remove IR radiation.

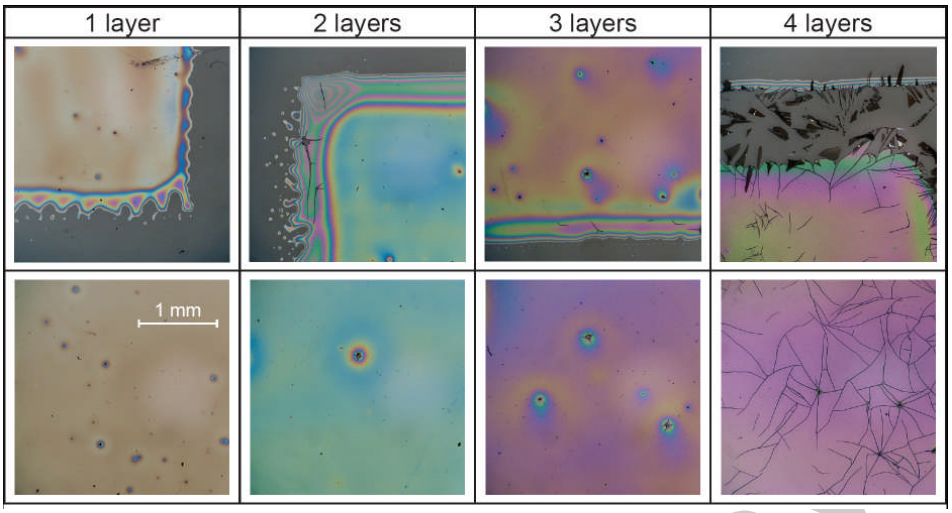


**Figure 2.** Optical micrographs of printed titania layers showing the edge (top row) and central area (bottom row).

Photocatalytic activity of prepared titania coatings towards solid organic matter was evaluated on the basis of fatty acid thin film degradation monitored by FTIR spectrometry. Stearic acid (SA) was used in this experiment. SA film was again deposited by inkjet printing: printing ink was prepared by mixing 1 ml of 0.1 molar solution of SA in toluene with 9 ml of isobutanol. This ink was filtered through 0.2 um membrane filter and loaded into a Dimatix ink tank. The tank was attached to a 10 pL print head and mounted into the Dimatix 2831 printer set to 20 um nozzle span. A single layer was printed onto previously prepared samples of $TiO_2$. Only a half of the sample was covered by SA in order to keep a naked $TiO_2$ surface for reference background measurement. Samples were irradiated by medium pressure mercury vapor lamp (OSRAM HQL 125W, without the fluorescent bulb). The integral irradiation intensity in the range 300-400 nm was 0.2 W $m^{-2}$ (determined by Gigahertz Optic X97 Irradiance Meter with X9-7 probe). IR spectra were recorded on a Nicolet Impact 400 FTIR spectrophotometer in regular time intervals and the integral absorbance in the 3000-2700 $cm^{-1}$ region (corresponding to various modes of C-H vibration) was noted down.

Water droplet contact angle values before and during irradiation were used for monitoring of surface wetting and its photoinduced change. We used an OCA-20 device (DataPhysics, Germany) and utilized the sessile drop method. Drop volume was 5 µl and the drop shape was recorded appr. 15 s after deposition at 5 different places onto an aged sample (3 months in darkness). Then the samples were irradiated by an UV lamp and the contact angle was monitored in the same manner in regular time interval, until it dropped below 5°. We used medium pressure mercury vapor lamp (OSRAM HQL 125W, without the fluorescent bulb). The integral irradiation intensity in the range 300–400 nm was 0.21 W $m^{-2}$ (determined by Gigahertz Optic X97 Irradiance Meter with X9-7 probe).

A combined experiment simulating the re-hydrophilization of a soiled photocatalytic surface was performed as well. The printed photocatalyst samples were overprinted by a SA film and irradiated in the same way as for the FTIR study. However, this time the water droplet contact angle change upon irradiation was monitored on these smeary glass plates, giving indirect information about the fatty acid removal and a measure of the rate of surface re-hydrophilization.

## Results and Discussion

### *Material Properties of Patterned Titania*

Figure 2 illustrates the visual appearance of prepared samples as seen in the optical microscope. The catalyst layers are smooth, glossy, clear and transparent, with a slight color tint originating from light interference. Cracking takes place in the thickest 4-layered sample and on the edges of other samples where the thickness is increased by edge effects. The adhesion of 1-3 layered samples is very good and no abrasion has been observed even after repeated use. Some abrasion has been observed on the cracked 4-layered samples upon mechanical rubbing.

SEM images at Figure 4 show the characteristic even porous structure free of defects. SEM cross-sectional images were also used to determine the layer thickness which is appr. 110 nm per single layer. AFM imaging revealed the globular structure originating from the micellar nature of sol. It is evident that the printed and calcined layer maintained the imprints of individual micelles very well. On the other hand, the globular surface topology is extremely regular with

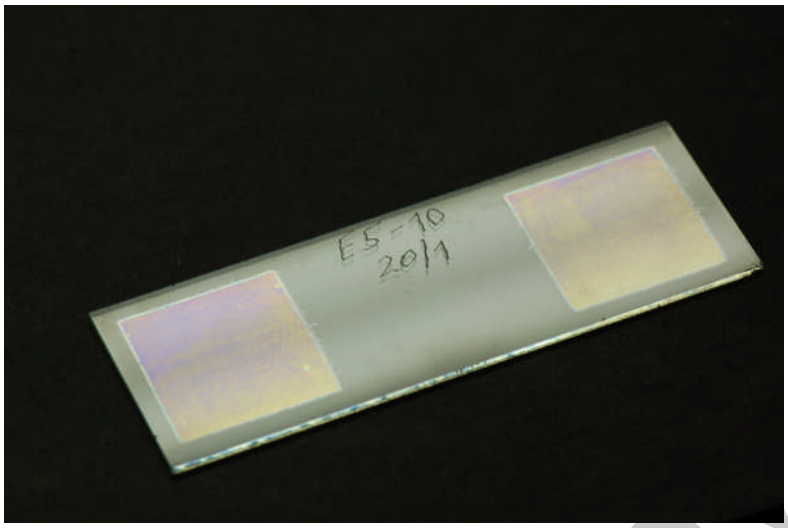


**Figure 3.** Macroscopic appearance of printed samples. Catalyst has been printed as two square patterns 20x20 mm on to this microscopic glass.

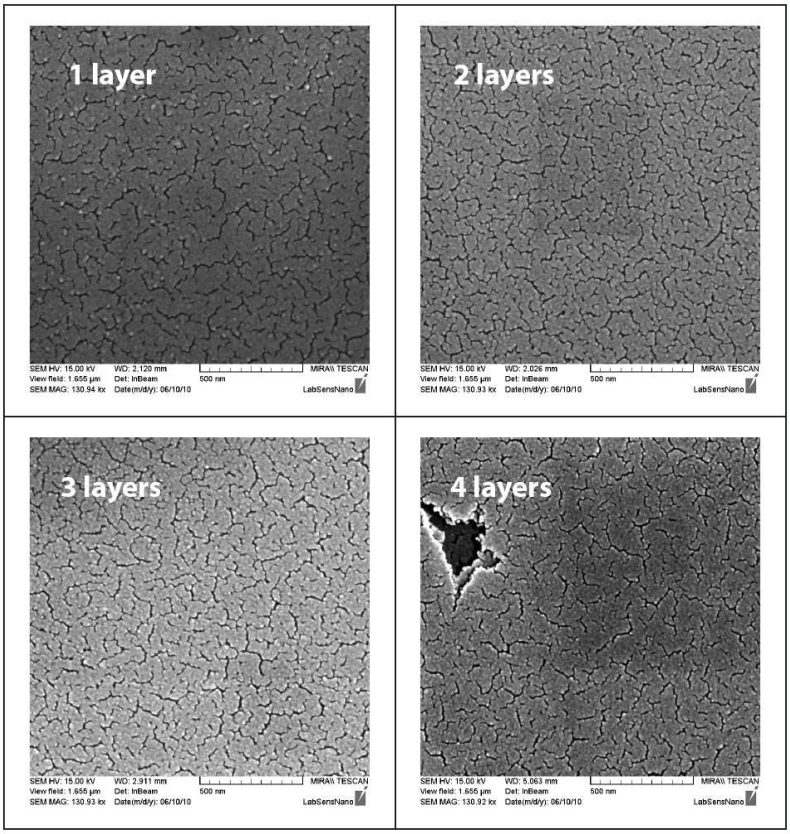


**Figure 4.** SEM images of printed photocatalyst.

minimal vertical deviations and therefore contributes to the very high smoothness of the printed layer. RMS roughness of 3-layered sample was 3.7 nm. Raman spectroscopy and XRD was used to study the phase structure. Both confirmed pure anatase phase in all printed samples, details are discussed at (21). Diffuse reflectance spectra of prepared samples are presented at Figure 6.

### *Photocatalytical Performance*

DCIP is one of the many dye molecules feasible as a model pollutant compound to study photocatalytic activity. Dechloration is the first step of its degradation and is accompanied by discoloration (25). Then further oxidation of the aromatic skeleton goes on, producing carboxylic acids as the main intermediates. The discoloration is naturally very easily detected by UV-VIS

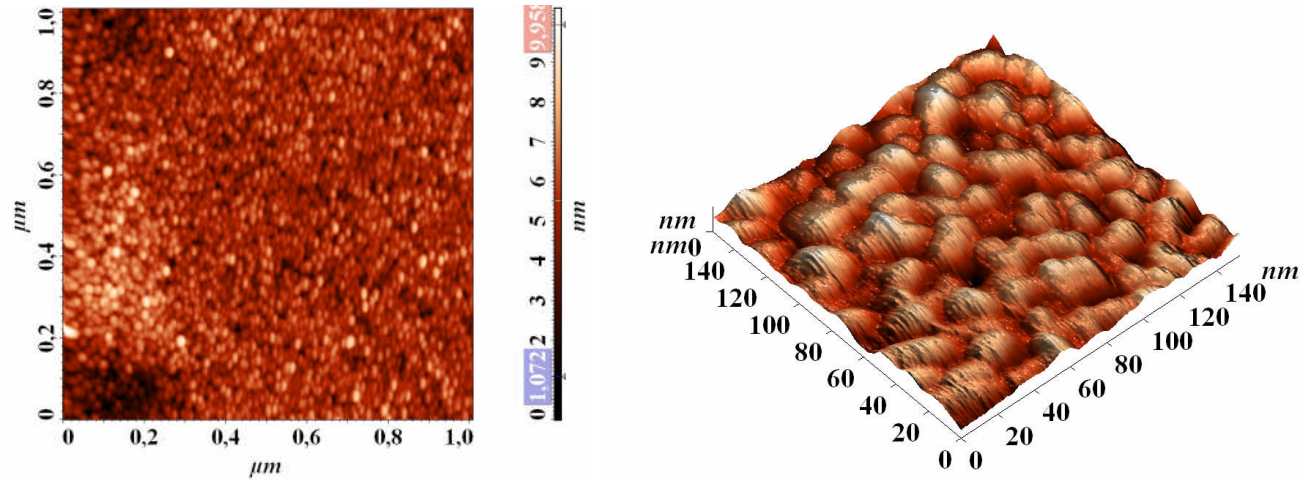


**Figure 5.** AFM scans of printed photocatalyst single layer.

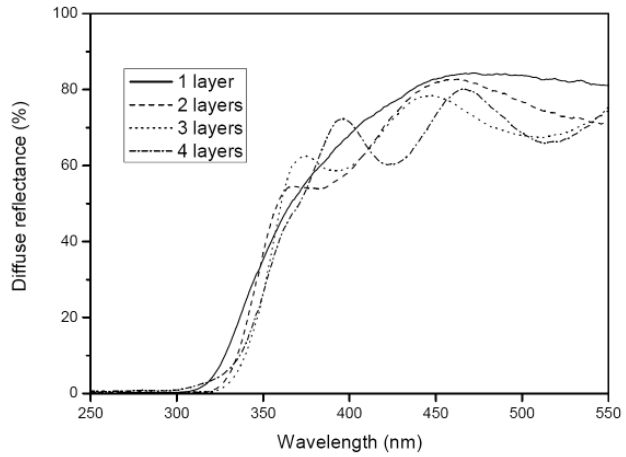


**Figure 6.** Diffuse reflectance UV-VIS spectra of printed photocatalyst.

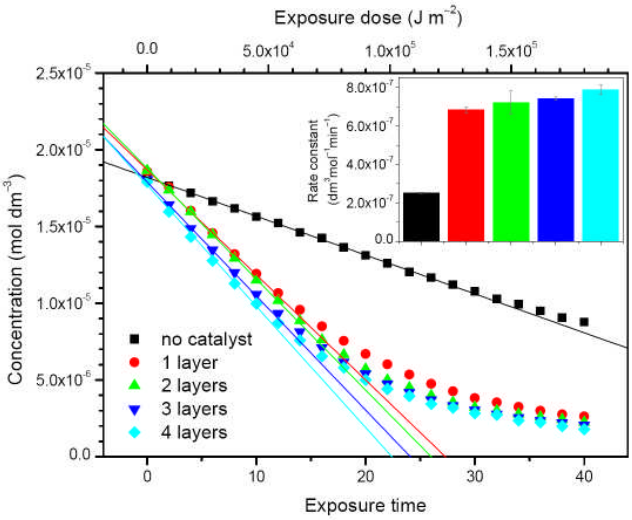


**Figure 7.** DCIP decolorization.

spectrometry. DCIP has an absorbance maximum at 600 nm, the reduction rate of which reflects the photocatalytic reactivity of $TiO_2$ upon UV irradiation. Unfortunately, a photocatalytic system degrading dye molecules becomes very complex and eventually enables many competitive reaction pathways, including the injection of the dye photoexcited electrons into the conduction band of $TiO_2$ (26, 27). Analyzing and understanding such a complicated system can be extremely difficult. On the other hand, photocatalytic processes are thought to be a good candidates for the remediation of industrial wastewaters, including those containing dyes, so using a simple dye molecule for activity testing certainly makes sense.

Figure 7 shows the graphical plot of recorded kinetic data averaged from 5 repeated experiments. The decrease of DCIP concentration calculated from absorbance measurements at 600 nm has been plotted as the function of irradiation time and corresponding exposure dose. Data trend analysis suggests a linear decrease of DCIP concentration as long as a sufficient amount of reactant is present (appr. till 50% conversion). Thus the zero-order rate constant are plotted in the figure inset. Error bars of the concentration data are not plotted for the sake of readability, however they were used for the calculation of rate constant error bars which are plotted in the inset indeed. Worth noting is the poor stability of DCIP in the absence of photocatalyst, i.e. the blank check for direct photolysis. Apparently, with this particular light source the DCIP is prone to quick photolysis. The catalyzed samples degrade 3-4 times faster and the influence of catalyst thickness is marginal. It seems that with this particular reactor design, the reaction rate is limited by mass-transfer processes rather than photon absorption and/or charge generation phenomena which could be expected to be strongly depending on the layer thickness.

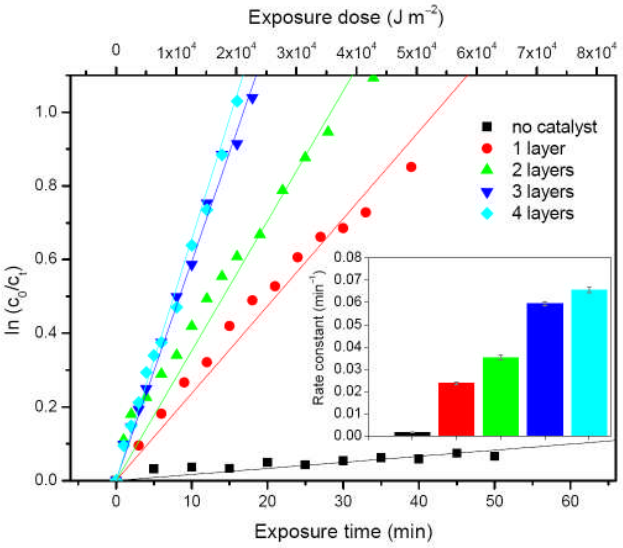


**Figure 8.** Degradation of stearic acid.

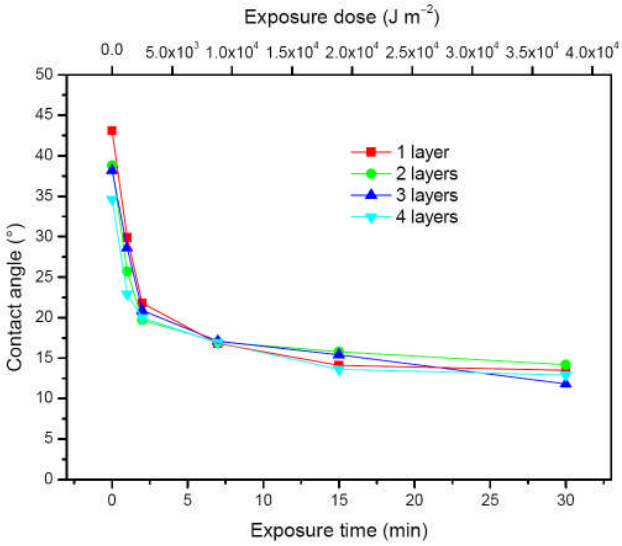


**Figure 9.** Photoinduced hydrophilization.

On contrary, the photocatalytic activity towards solid fatty acid is strongly influenced by the layers thickness. Figure 8 illustrates the kinetic data obtained from the stearic acid degradation experiment. Relative decrease in the integral peak area of FTIR absorption bands over the range 2700-3000 cm$^{-1}$ has been plotted as the function of irradiation time and corresponding exposure dose. Data were obtained from the averaging of 5 parallel batches whose deviations were well below 1% making the error bars invisible. The pseudo-first order rate constants and their errors linear fitting are plotted in the figure inset.

The observed trends are in a good agreement with previous findings (28). The degradation process follows pseudo first-order kinetics and the rate is strongly dependent on the layers thickness. Although the oxidative cleavage of stearic acid takes place only on the interface, the reactive species are generated deep in the catalyst layer. Apparently, a single layer of catalyst is too thin to absorb all the incident photons and therefore the efficiency of absorption is increasing with increasing layer thickness, resulting into a significant dependence of the degradation rate on the number of layers. Stearic acid proved to be highly stable in the absence of photocatalyst layer which is manifested by the almost constant absorbance value of reference blank sample bearing no catalyst layer.

Photoinduced hydrophilic conversion of aged photocatalyst surface is another popular method to characterize the activity of immobilized photocatalyst. Preliminary results have been disclosed at (21). This time we report data of a repeated experiment on the complete sample set including all 4 samples. Figure 9 shows its dependence on exposure time and corresponding exposure dose expressed in J m$^{-2}$. The initial water droplet contact angle of cca 40° is reduced to 15° within 15 minutes. Increasing of the exposure dose beyond this point will not cause further lowering of the contact angle. Therefore a superhydrophilic wetting (contact angle < 10°) has not been reached on this type of titania. This behavior corresponds well with the very high smoothness and low porosity detected by AFM: a superhydrophilic surface needs to be rougher and more porous to enhance wetting by water adsorbed in surface pores and 2D microcapillary action (29, 30). No significant influence of the layer thickness on the hydrophilic conversion rate has been observed, reflecting the strictly interfacial nature of the process.

The results of the re-hydrophilization experiment are given at Figure 10. Recorded contact angle values averaged from 5 parallel experiments were again plotted as a function of exposure time and corresponding exposure dose. Standard deviation was below 5% and therefore the errors bars weren't plotted either.

Although this method gives only indirect information about the fatty acid concentration, it is quite popular alternative to the FTIR based detection, because it can be used on virtually any surface (31). Quite surprisingly, the initial contact angle varies for 3 and 4 layered samples. With respect to the high activity of these thicker coatings, it is possible that samples were "contaminated" by exposure to actinic radiation before the experiment. At the final stage of experiment, contact angle just below 10° was observed on all samples, indicating better wetting than in the case of pristine catalyst wetting (Figure 9). This behavior might have been facilitated by the degradation product of fatty acid acting as surfactants.

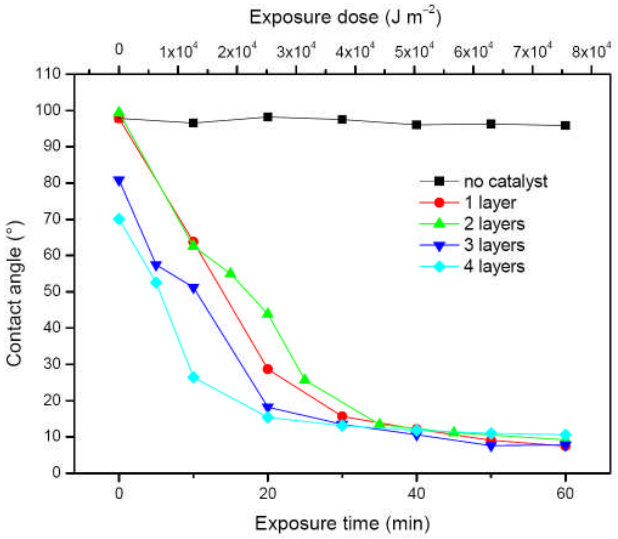


**Figure 10.** Photoinduced re-hydrophilization of greasy photocatalyst surface.

## Conclusions

A reverse-micelle organotitanate sol composition was printed by experimental inkjed printer onto glass support. After thermal calcination, titania coating of various thickness were obtained. The coatings were smooth and transparent (with the exception of 4-layered samples which cracked significantly), consisting of pure anatase phase structure. SEM and AFM analysis revealed a well preserved globular surface topology with low surface roughness.

Photocatalytic and self-cleaning activity was described by some of the well established techniques. A linear decrease of DCIP concentration was observed up to cca. 50% conversion and the corresponding zero-order rate constants were calculated, showing 3-4 times faster degradation of the catalyzed samples and the influence of catalyst thickness being marginal. On the other hand, the degradation process of SA follows the pseudo first-order kinetics the rate of which is strongly dependent on the layers thickness. The initial water droplet contact angle of cca. 40° is reduced to 15° within 15 minutes and prolonged exposure will not cause further lowering of the contact angle. At the final stage of the re-hydrophilization experiment, contact angle just below 10° was observed on all samples.

Direct patterning performed by piezoelectric inkjet printing proved to be an attractive method for depositing liquid formulations onto solid supports. It provides clean, efficient and highly repeatable way of coating. Moreover, it is easy to up-scale to coat large substrates by means of industrial large-format printers and at the same time it brings the possibility to produce 2D patterns with micrometer accuracy. These features make direct inkjet patterning one of the prominent deposition techniques for the quickly expanding field of printed electronics.

## Acknowledgement

This work has been supported by projects 104/09/P165 and 203/08/H032 of the Czech Science Foundation. Authors also appreciate the work of Jana Chomoucká who provided SEM imaging at the LabSensNano laboratory of Faculty of Electrical Engineering and Communication, Brno University of Technology.

## References

(1) Fujishima, A.; Honda, K. *Nature* **1972**, *238*, 37-38.

(2) Bui, T.H. et al. *Res. Chem. Intermed*. **2007**, *33*, 421-431.

(3) Le-Clech, P.; Lee, E.K.; Chen, V. *Water Res*. **2006**, *40*, 323-330.

(4) Kim, S.B.; Hwang, H.T.; Hong, S.C. *Chemosphere* **2002**, *48*, 437-444.

(5) Chin, P.; Ollis, D.F. *Catal. Today* **2007**, *123*, 177-188.

(6) Sakai, N.; Fujishima, A.; Watanabe, T.; Hashimoto, K. *J. Phys. Chem. B* **2001**, *105*, 3023-3026.

(7) Chhabra, V et al. *Langmuir* **1995**, *11*, 3307.

(8) Inaba, R. et al. *J. Mol. Catal. A: Chem*. **2006**, *1-2*, 247-254.

(9) Kluson, P. et al. *Mater. Lett*. **2007**, *61*, 2931-2934.

(10) Schmidt, H.; Mennig M. http://www.solgel.com/articles/Nov00/coating.htm

(11) Yoshimura, M.; Gallage, R. *J. Solid State Electrochem*. **2008**, 775-782.

(12) Kim, S.-J.; Mckean, D.E. *J. Mater. Sci. Lett*. **1998**, *17*, 141-144.

(13) Bernacka-Wojcik, I. et al. *Biosens. Bioelectron*. **2010**, *5*, 1229-1234.

(14) Yang, M. et al. *Sens. Actuators, B* **2010**, *2-3*, 622-628.

(15) Matsuo, A. et al. *J. Electroceram*. **2006**, *16*, 533-536.

(16) Manga, K.K. et al. *Adv. Mater*. (Weinheim, Ger.) **2010**, *22*, 5265-5270.

(17) Arin, M. et al. *J. Eur. Ceram. Soc*. **2011**, *6*, 1067-1074.

(18) Dzik, P. et al. *J. Adv. Oxid. Technol*. **2010**, *13*, 172-183.

(19) Černá, M. et al. *Catal. Today* **2011**, *1*, 97-104.

(20) Morozova, M. et al. *J. Sol-Gel Sci. Technol*. **2009**, *52*, 398-407.

(21) Morozova, M. et al. *Sens. Actuators, B*, **2011**, *160*, 371-378.

(22) Zita, J. et al. *J. Photochem. Photobiol. A* **2010**, *216*, 194-200.

(23) Yu, J.C. et al. *Appl. Catal. B*, **2002**, *36*, 31-43.
(24) Guillard, C. et al. *Appl. Catal. B* **2002**, *39*, 331-342.
(25) Brezová, V. et al. *Chem. Pap*. **1991**, *45*, 233-246.
(26) Ohtani, B. *Chem. Lett*. **2008**, *37*, 217.
(27) Kisch, H.; Macyk, W. *Chem.Phys.Chem*. **2002**, *3*, 399.
(28) Mills, A.; McFarlane, M. *Catal. Today* **2007**, *1-2*, 22-28.
(29) Yu, J.C. et al. *J. Mater. Chem*. **2002**, *12*, 81-85.
(30) J. Bico et al. *Colloids Surf. A* **2002**, *206*, 41-46.
(31) Lavrenčič Štangar U. et al. *Advances in Science and Technology* **2010**, *68*, 126.

*Received for review September 4, 2011. Revised manuscript received December 27, 2011. Accepted December 28, 2011.*

Sensors and Actuators B 160 (2011) 371–378

Contents lists available at ScienceDirect

Sensors and Actuators B: Chemical

journal homepage: www.elsevier.com/locate/snb

# Thin $TiO_2$ films prepared by inkjet printing of the reverse micelles sol–gel composition

M. Morozova [a,*], P. Kluson [a], J. Krysa [a], P. Dzik [b], M. Vesely [b], O. Solcova [a]

[a] Institute of Chemical Process Fundamentals ASCR, Rozvojova 2, 165 02 Prague 6, Czech Republic
[b] Brno University of Technology, Faculty of Chemistry, Purkynova 118, 612 00 Brno, Czech Republic

ARTICLE INFO

*Article history:*
Received 9 June 2011
Received in revised form 14 July 2011
Accepted 28 July 2011
Available online 19 August 2011

*Keywords:*
Titanium oxide
Sol–gel
Inkjet printing
Photocatalysis
Photo-electrochemistry

ABSTRACT

The presented study deals with the adaptation and optimization of the reverse micelles sol–gel composition to make it feasible for inkjet printing. The solvent choice and viscosity adjustment issues essential for reliable jetting performance are discussed. The layer morphology and material properties were in detail investigated by optical, scanning electron and atomic force microscopy as well as Raman spectroscopy and XRD analysis. Photocatalytic activity of the printed layers was evaluated on the basis of stearic acid thin film degradation monitored by FTIR spectrometry. The photoexcitation properties of the $TiO_2$ layers and the ability of their photocurrent generation were investigated by electrochemical methods.



## 1. Introduction

Nanoscale semiconductor oxides in the thin layer form for sensors, optical electrodes, and solar cells have recently evoked great interest [1–4]. As generally known, their photo-induced properties arise from the semiconductor nature, especially from the ability of the light quantum absorption followed by the charge carrier generation [5,6]. Titanium dioxide in crystallographic form of anatase is a promising semiconductor widely used in the field of advanced oxidation processes and photoelectrochemical sensing due to its excellent efficiency to generate the electron-hole pairs [7,8]. In recent years, gas sensing properties of $TiO_2$ for various applications have been studied by many groups [9–11]. Pure or doped $TiO_2$ can find application as sensor for alcohols, reducing/oxidizing gases ($NO_2$, CO, $H_2$, $O_2$), chemical oxygen demand (COD) determination or a range of organic compounds (glucose, oxalic acid) detecting.

Preparation of the nanostructured electrode materials with highly uniform nanoparticles has been investigated by many groups [12,13]. The most commonly used method is the sol–gel technique utilizing the molecular templates. Nanoparticles with controlled chemical composition, size distribution, uniformity and dispersion are readily synthesized using reverse micelles [14,15]. For the first time reverse micelles were used as nano-templates for material synthesis in 1982 [16]. Afterwards these self-organised multimolecular structures have been utilized for a wide range of applications [17]. Micro-emulsions are generally formed from mixtures of non-polar solvent, surfactant and polar solvent, usually water. Layers prepared in this way possess usually highly transparency, homogeneity, size and structure uniformity.

So far the sol–gel process, no doubts, proved its benefits. However, in order to produce titania layers, the liquid sol must be coated onto a substrate. Various coating techniques have been used for this purpose, such as dip-, spin- or spray-coating, doctor blade, roller etc. [18]. Recently, a new promising deposition technique has appeared. The novel approach is usually termed inkjet material deposition or shortly material printing. The technique shares the basic principles with conventional inkjet printing, i.e. tiny droplets of a low-viscosity liquid are precisely deposited onto a substrate by means of thermal or piezoelectric print head. In the case of material printing, the ink is the specially formulated liquid purposed for transporting functional components onto the substrate surface.

With this method sensitivity to surface defects is strongly suppressed because a defect is simply overprinted. It may eventually disrupt the layer's homogeneity, but it certainly does not influence its surroundings. Coated area is limited by the printer design – printers handling roll media of a meter width or rigid media of several square meters area are common nowadays. The ink is kept in airtight tanks and tubing until printing, and thus evaporation and humidity absorption is eliminated. A tiny fraction of the ink is consumed for print head cleaning and purging, but most of the ink is delivered to the substrate. This technique also brings the possibility of direct patterning, i.e. the fabrication of 2D patterns

* Corresponding author. Tel.: +420 220390282; fax: +420 220920661.
*E-mail address:* morozova@icpf.cas.cz (M. Morozova).

0925-4005/$ – see front matter © 2011 Elsevier B.V. All rights reserved.
doi:10.1016/j.snb.2011.07.063

**Table 1**
Composition and properties of prepared sols.

| Sol designation | *X* | 2*X* | 3*X* | 4*X* |
|---|---|---|---|---|
| Xylene [ml] | 5.1 | 10.2 | 15.3 | 20.4 |
| Triton X 102 [ml] | 2.5 | | | |
| Water [ml] | 0.06 | | | |
| TTIP [ml] | 1 | | | |
| Density [g/cm$^3$] | 0.94 | 0.91 | 0.90 | 0.89 |
| Viscosity [mPa s] | 4.86 | 2.03 | 1.44 | 1.18 |
| Viscosity standard deviation [%] | 0.5 | 0.3 | 0.3 | 0.2 |

on the substrate without the need of any mechanical or optical masking. Material printing has been successfully employed for the deposition of a great variety of functional materials forming thin layers, various patterns (arrays, gaps, sandwiches) and even 3D structures. Yoshimura and Gallage summarized the ideas of "direct patterning" in a neat review [19]. They proposed several possible pathways leading to ceramic films, distinguishing between "inkjet reaction", "inkjet deposition" and "inkjet printing" methods. Many other approaches have been reported in the recent past documenting the steeply increasing interest in this method [20–25].

Authors of this communication already reported [26] on the deposition of conventional sol–gel formulations based on tetraisopropoxy titanate and acetylacetone when using an inkjet printer equipped with piezoelectric print head (Epson R220). Thin layers of $TiO_2$ with excellent optical properties and photocatalytic performance comparable to dip- or spin-coated layers were prepared. Thick multilayer coatings were printed with help of poly(ethylene glycol) acting as viscosity modifying and anticracking agent [27].

In this study we report on the adaptation and optimization of the reverse micelles sol–gel composition to make it suitable for inkjet printing. The solvent choice and viscosity adjustment issues crucial for the reliable jetting performance are discussed. The layer morphology and material properties were in detail investigated by optical, scanning electron and atomic force microscopy, and by Raman and XRD analysis. Photocatalytic activity of the prepared inkjet layers was evaluated on the basis of the stearic acid thin film degradation monitored by FTIR spectrometry. The photoexcitation properties of the $TiO_2$ layers and the ability of photocurrent generation were investigated by photo-induced electrochemical methods.

## 2. Experimental

### 2.1. Sol optimization

The original reverse micelle sol formulation was using cyklohexane as non-polar solvent [28]. However, cyclohexane – excellent for the dip-coated layers, is not well suited for the inkjet printing. Its high volatility causes quick evaporation from the print head nozzle orifices and results into nozzle blockage. Moreover, its low surface tension and low viscosity impart "bad droplets" and excessive satellite droplets generation.

As an alternative for jetting, xylene was chosen. A set of samples with various concentrations was prepared (see Table 1): xylene (p.a., Penta, Czech Republic) was mixed with non-ionic surfactant Triton X 102 (Sigma–Aldrich) in a glass beaker placed on a magnetic stirrer and then demineralised water was added. Solution immediately turned milky opaque, but became clear within 10 min of stirring. Then titanium isopropoxide (TTIP, 99.999% trace metals basis, Sigma–Aldrich) was added drop-wise turning the solution colour to deep yellow. The viscosities and densities of the prepared sol compositions were measured by automatic viscosimeter AVMn (Anton Paar) and by densitometer DMA4500 (Anton Paar). Results are summarized in Table 1.

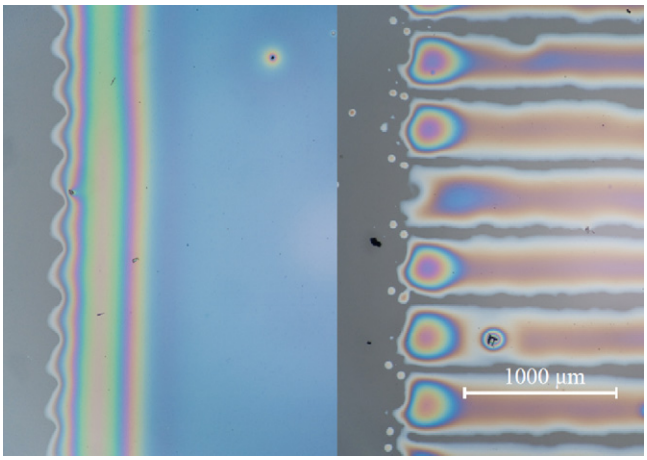


**Fig. 1.** Optical micrographs illustrating the wetting behaviour of the printed sols. Printing with 20 μm nozzle span (left) and 60 μm (right).

### 2.2. Thin layer preparation

Nanostructured $TiO_2$ layers were prepared by the inkjet printing of optimized sol (composition 3*X*) on soda-lime microscopic glass plates (25 mm × 75 mm, Paul Marienfeld, Germany and 50 mm × 50 mm, Merci, Czech Republic) and indium tin oxide (ITO) transparent conducting glass plate (5–15 Ω, 50 mm × 12.2 mm × 1.1 mm, Delta-Technologies Ltd., USA). The microscopic glass plates of both sizes were pre-treated by boiling in 9 M sulphuric acid for 1 h to guarantee removing the surface sodium ions to suppress the sodium ions migration into the forming $TiO_2$ layer. The ions migration could affect crystallization of $TiO_2$ [29] and thereby influence the photoinduced properties [30,31]. Then the microscopic glasses (both sizes) were immersed into the solution of Triton X 102 in propan-2-ol (1 vol.%) and quickly dried in $N_2$ flow immediately prior to printing. The conductive ITO glass was slightly pre-treated in detergent solution in ultrasonic bath for 40 min, subsequently treated by deionised water and dried at 50 °C.

Sol deposition and patterning was performed with experimental inkjet printer Fujifilm Dimatix 2831. The prepared sol compositions were sonicated for 5 min and then loaded into a syringe. A 0.2 μm membrane filter (Pall Corporation, USA) and a blunt needle were attached to the syringe luer port. The sol was filtered and filled into the Dimatix ink tank. Dimatix 10 pL printing head was attached to the tank and mounted into the Dimatix printer. The drop formation characteristics of all compositions were studied by means of built-in stroboscopic camera and interaction with substrate was observed by an optical microscope. During the preliminary testing period the optimal printing conditions were defined: Dimatix Model fluid 2 waveform, 20 V driving voltage, nozzle temperature 30 °C, substrate temperature 40 °C. Nozzle span was varied in the range 20–80 μm. Substrate temperature is the most prominent factor influencing layer formation. Lower temperatures result into slow drying and mottling while higher lead to premature evaporation and banding pattern formation.

The recommended optimal viscosity range for jetting with Dimatix printed is 10–12 mPa s. Therefore the most concentrated composition (*X*) was selected as the best choice; nevertheless the sol generally does not wet glass substrates well. Fig. 1 illustrates the wetting behaviour of the printed sol at different nozzle spans. In the case of 60 μm nozzle span the printed sol withdrew together and a banding structure results; while 20 μm nozzle span ensured a higher sol loading per unit area and completely covered the substrate surface. Naturally, such narrow nozzle span led to thicker layers. Application of the more concentrated sols (*X* and 2*X*) for printing results in thick layers with severe cracking. Owing to the

aims that produced layers should be approximately 100 nm per single printer pass, the more diluted composition (3*X*) was chosen. Despite its relatively low viscosity, the jetting performance was excellent and a nozzle blockage was observed only rarely. Moreover, printing of the low-viscous formulation did not require viscosity reduction by print head heating. It enabled printing at ambient temperature which was beneficial for nozzle drying suppression.

Simple rectangular patterns 5 mm × 12 mm, 20 mm × 20 mm, and 40 mm × 40 mm were printed onto the ITO plates, microscopic and custom-cut soda-lime glass substrates, respectively. Printing was repeated up to 4 times to obtain different thicknesses of resulting $TiO_2$ layers. After printing each layer, gelling and drying steps were repeatedly performed (30 min at 110 °C). The terminal gelling step was followed by calcination for 4 h at 450 °C in air.

### 2.3. Layer's characterizations

Structural analyses of the prepared films were performed by X-ray diffraction (Panalytical-MRD laboratory diffractometer with the Cu anode), Raman spectroscopy (Raman Dispersive Spectrometer Nicolet Almega XR), scanning electron microscope (Hitachi S4700, Tescan MIRA II LMU) and AFM microscope (Thericroscopes). The layer thickness was evaluated by Ocean Optics USB4000 diode array photometer with fibre optic reflectance probe (NanoCalc). Values of absorption edges of layers were obtained from UV–Vis spectra (Perkin-Elmer Lambda 35 equipped with a Labsphere RSA-PE-20 integration sphere).

Microphotographs of the printed layers were recorded using Nikon Eclipse E200 optical microscope equipped with Nikon D5000 digital camera and Nikon Camera Control Pro 2 software. Polarised light was used to enhance the interference-originating colour of the printed layers.

### 2.4. Photocatalytical and photoelectrochemical experiments

Surface wetting and its photoinduced change were studied by monitoring the water droplet contact angle before and during irradiation on an OCA-20 device (DataPhysics, Germany). Drop volume was 5 μl and the drop shape was recorded for 15 s after its deposition at 5 different positions. Then the samples were irradiated by an UV lamp and the contact angle was recorded in the same manner in regular time interval.

Photocatalytic activities of the films were evaluated on the basis of stearic acid (SA) thin film degradation monitored by FTIR spectrometry. SA film was also deposited by inkjet printing. Printing ink was prepared by mixing 1 ml of 0.1 M solution of SA in toluene with 9 ml of butan-2-ol, then filtered through 0.2 μm membrane filter and loaded into a Dimatix ink tank. A single layer was printed onto previously prepared samples of $TiO_2$. Only half of the sample was covered by SA in order to keep a naked $TiO_2$ surface as reference. In all experiments samples were irradiated by medium pressure mercury vapour lamp (Philips HPLN 125 W, without the fluorescent bulb) with the integral irradiation intensity 2 mW $cm^{-2}$ in the range 300–400 nm. IR spectra were recorded in regular time intervals and the integral absorbance in the 3000–2900 $cm^{-1}$ region (corresponding to various modes of C–H vibrations) was noted down.

Photoelectrochemical measurements were performed at room temperature in the three-electrodes Pyrex cell by means of electrochemical methods. All potentials were referred to Ag/AgCl/KCl(sat) electrode, whereas a Pt sheet was used as a counter electrode. The exposed area of the working $TiO_2$ electrode for UV illumination and photoelectrochemical reaction was 1 $cm^2$. Measurements were performed with a computer-controlled Voltalab 10 PGZ-100 potentiostat. For all electrochemical experiments 0.1 M solution of $Na_2SO_4$ in ultrapure water (0.06 μS $cm^{-1}$) was used as working electrolyte. A 500 W polychromatic lamp (Hg, LOT-Oriel) with a water filter was used for UV–Vis irradiation and the incident light beam was modified with an interference filter (Melles Griot) producing spectrally narrow flux of photons (365 ± 10 nm). The applied irradiance was measured with an UV sensor (UVA Light Meter) with intensity 10 mW $cm^{-2}$ in the most experiments. Obtained incident light intensity was recalculated to Incident-Photon-Current-conversion-Efficiency (IPCE) [32]. The layer photoexcitation properties were characterized by linear voltammetry, amperometry and open circuit potential (OCP). Linear voltammograms (LV) were recorded from −0.5 V to 1 V at a scan rate of 10 mV $s^{-1}$. The working electrode ($TiO_2$/ITO) was irradiated at the 5 s intervals of the UV light/dark periods. The generated photocurrent as a function of time at constant inserting potential (600 mV) was measured by amperometry. During this method the layers were irradiated for 5 min. The information about the electron-hole pairs recombination kinetics are provided by the open circuit potential (OCP) measurement. This experiment is again based on the light/dark interval combination. The detailed description of these methods has been reported previously [33].

## 3. Results and discussion

### 3.1. Structural properties

Fig. 2 depicts appearance of the printed layers as seen in the optical microscope. Smooth, shiny, transparent layers with strong interference colouring were produced. Samples consisting of 1–3 layers were completely crack-free, but 4 layered samples exhibited intensive cracking and reduced adhesion. Apparently, such thick layer could not withstand the stresses caused by organic fraction removal during calcination. 4-layered samples were therefore excluded from experiments.

Fig. 3(a) and (b) illustrates the surface morphology of sample produced by the three ink-jet printed cycles recorded by SEM and AFM. As we can see a visual appearance provided by the optical microscope shown a smooth surface without the higher extent of surface defects which was corroborated by the more detailed view at the surface morphology made by SEM (see Fig. 3(a)). The characteristic porous structure without discrepancies can be easily identified. The relative surface roughness expressed as the roots mean square values (RMS) obtained by AFM microscopy (see Fig. 3(b)) was low – 3.7 nm which confirmed the very smooth surface appearance of the printed layers. The layers also possess very good transparency and mechanical stability. Nevertheless some heterogeneity in the layer thickness reflected in the light interference was macroscopically visible.

The crystallographic form of the pure anatase present at the thin layers was detected by XRD analysis and confirmed by Raman spectroscopy on microscopic as well as ITO supporting glasses. Figs. 4 and 5 reveal characteristic diffraction lines as well Raman vibrations of the anatase crystallites with particle size of 8 ± 1 nm.

The layer thickness was determined from optical properties (reflection and interference) by spectroscopic method NanoCalc [34]. The thickness values of 3 deposited layers varied around 230 nm. The layer thickness estimated from SEM image (see Fig. 6) was approximately 340 nm. The differences in thickness values obtained by these two methods might have been caused by the porosity of prepared layers. Values from SEM provide the real geometrical thickness of the layer, including internal voids, while the results from optical measurements give the net optical thickness of $TiO_2$ interacting with the probing beam, which is of course smaller than the total geometrical thickness. Also, other phenomena such as surface roughness may influence the results obtained from the

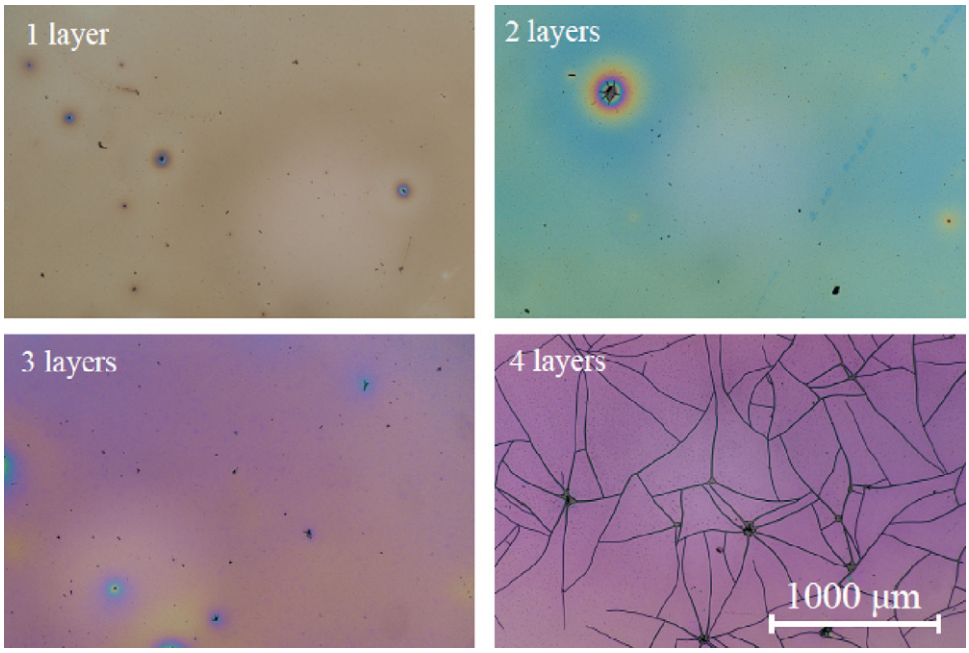


**Fig. 2.** The layer's surfaces as seen by optical microscopy.

optical method. Anyway, the optical measurement gives a very easy way of comparing the relative thicknesses of the studied layers.

The UV–Vis absorption spectra of the ink-jet printed $TiO_2$/ITO electrodes with variable number of deposited layers and pure ITO substrate are shown in Fig. 7. Only negligible shift of the absorption edge to higher wavelengths with the layer thickness increase was detected. The position of absorption edge was located at 350 nm.

### 3.2. Photocatalytic activity

Figs. 8 and 9 summarize results of the photocatalytic activity reaction tests. The experimental error of obtained results was lower than 5% for all tested samples. Photoinduced hydrophilic conversion was expressed as the rate of water droplet contact angle change. No influence of layer thickness has been observed in this case (see Fig. 8), indicating a strictly interfacial process. The initial contact angle of cca 40° is quickly reduced to 15° and even prolonged exposures do not cause further lowering, so a superhydrophilic wetting (contact angle < 10°) has not been reached on this type of titania. Such behaviour may be caused by the high smoothness and low porosity of the surface (as confirmed by AFM measurements). The superhydrophilic wetting is usually observed on rougher surfaces which tend to enhance wetting by water adsorbed in surface pores and 2D microcapillary action [35,36]. On the other hand, photocatalytic activity is strongly influenced by the layers thickness. Fig. 9 illustrates the kinetic data obtained from stearic acid degradation experiment. Relative decrease in the integral peak area of absorption bands over the range 2700–3000 $cm^{-1}$ has been plotted as the function of irradiation time and corresponding exposure dose. The degradation process follows pseudo-first order kinetics (see Fig. 9) where experimental points are in a good agreement with lines calculated according the quadratic equation. Stearic acid proved to be highly stable in the absence of photocatalyst layer which was manifested by the almost constant absorbance value of the reference blank sample bearing no catalyst layer. Although the oxidative cleavage of stearic acid takes place only on the surface, the reactive species are generated deep in the catalyst layer and migrate to the interface. Apparently, a single layer of catalyst is too thin to absorb all the incident photons and therefore the efficiency of absorption is increasing with increasing layer thickness, resulting into a significant dependence of the degradation rate on the number of layers.

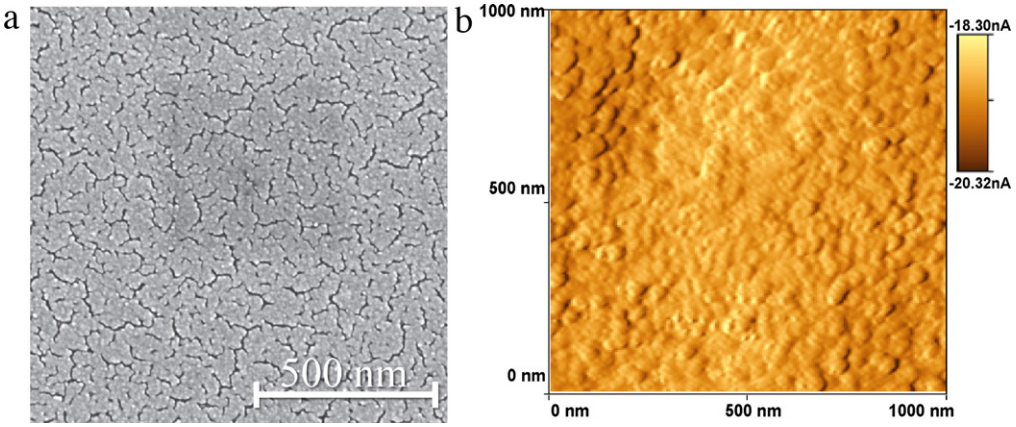


**Fig. 3.** The images of the 3 layers surface as seen by (a) SEM and (b) AFM.

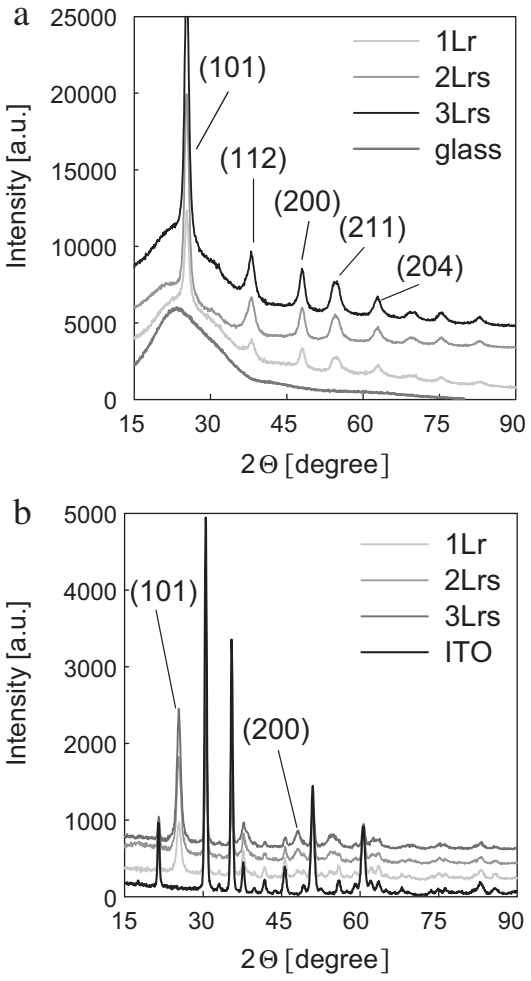


**Fig. 4.** XRD patterns of the printed layers (a) on microscopic glass, (b) on ITO glass.

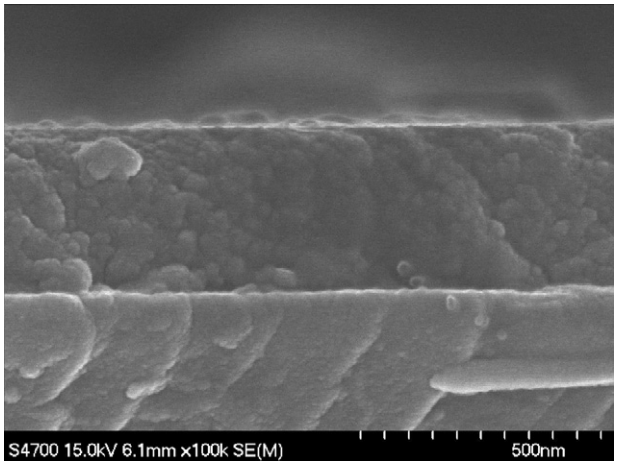


**Fig. 6.** SEM image of the $TiO_2$ film edge produced in 3 printed cycles.

### 3.3. Photoelectrochemical properties

The dependence of the generated current density (recalcutated to IPCE values) on the linear increasing potential is illustrated in Fig. 10. This linear voltammogram represents polarization curves of the ink-jet printed $TiO_2$ film electrode with different number of printed layers. The plot provides information of the layers efficiency to generate current upon irradiation and the efficiency to respond fast and repeatedly to the light signal. A very fast feedback to illumination with a light of the corresponding energy is a general feature of all tested layers. The generated photocurrents in the positive potential area were constant with time and reached characteristic plateau at every irradiated intervals. At negative potential (−400 mV) the photocurrents were also generated, however the values were lower and it can be seen the gradual growth to the constant level. The influence of the film thickness which depends on the number of printing cycles is also evident. The obtained IPCE values increase with the number of printed layers.

The amperometry measurements (Fig. 11) express the ability of the ink-jet printed $TiO_2$/ITO electrode to produce the measurable photocurrent values in the 5 min irradiation interval at constant potential 0.6 V. The obtained curves indicate the photocurrent-time

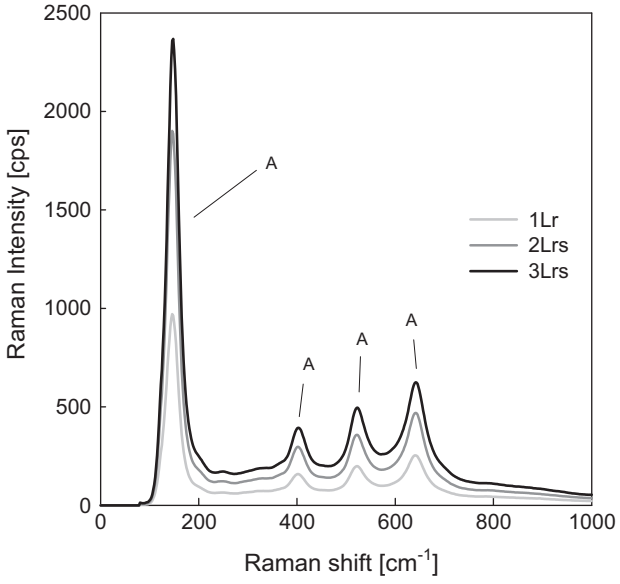


**Fig. 5.** Raman spectra with anatase (A) characteristic vibrations.

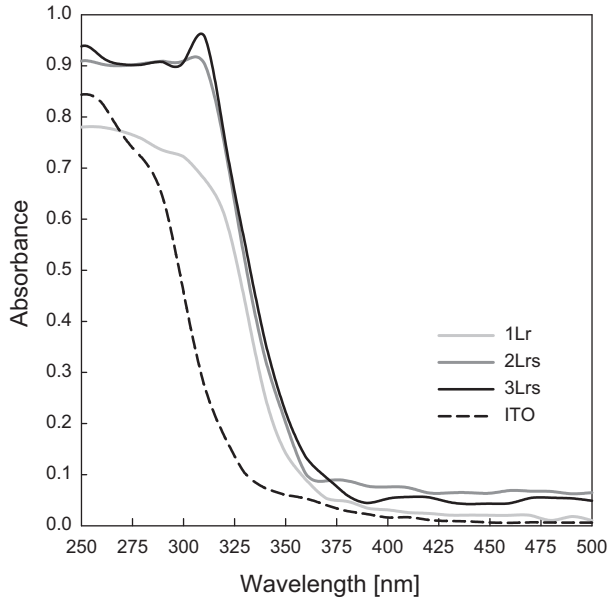


**Fig. 7.** UV–Vis absorption spectra of ITO substrate and the ink-jet printed layers.

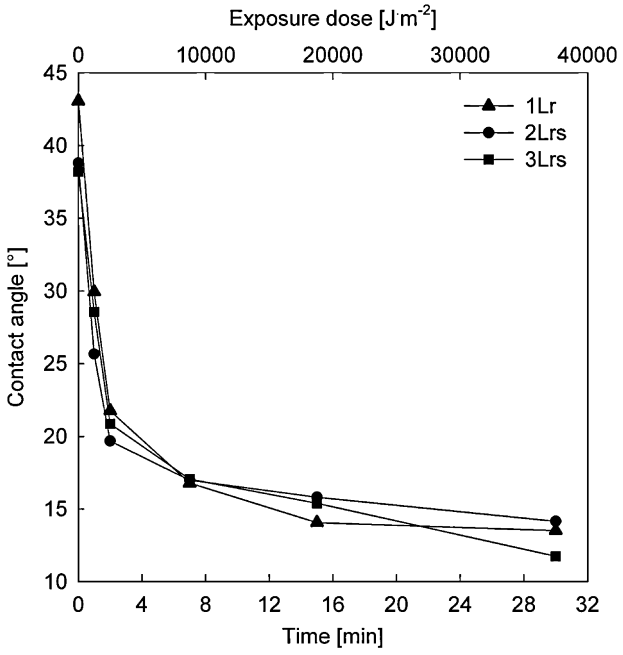


**Fig. 8.** Photoinduced hydrophilicity.

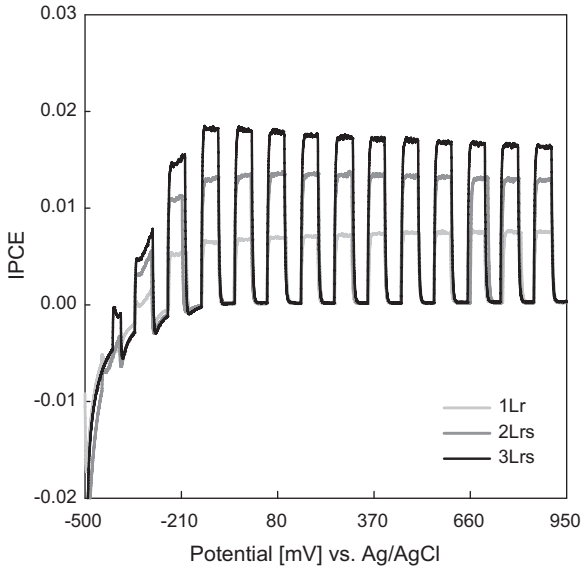


**Fig. 10.** The polarization curves of the printed $TiO_2$ layers, scan rate 0.01 V $s^{-1}$, the incident light intensity 10 mV $s^{-1}$.

behaviour of the layers. All measured samples embodied the very sharp maximum of the reached IPCE values. This so called current peak appears immediately at the first moment under the light. Further, the curves decrease very slowly to get a steady state values. The instantaneous increase of IPCE values means a rapid electrons-holes generation and separation at the space charge region. The decrease is assigned to their recombination. A fraction of the holes which reached the semiconductor surface at the first irradiation time captures electrons from the conduction band and/or accumulates at the surface [37,38]. The influence of the printed cycle number is evident; the IPCE values increase again with increasing thickness of the prepared layers.

The photopotential ($E_{oc}$) decay was also measured. Fig. 12 represents the dependence of the changing potential values on time. Upon UV irradiation, the open circuit potential shifts immediately to more negative values which reflects rising of the major charge carriers (electrons) concentration. The potential regresses to the original values after the light is switched off. The constant $E_{oc}$ values in the UV light period correspond to the steady state concentration of the not recombined electrons. The amount of photoexcited electrons reacts either with an electron scavenger (e.g. oxidisable species) or with the photogenerated holes or migrates through layers to the conductive substrate. The influence of the printed layers number can be seen, which is in agreement with results obtained from voltammetry and amperometry. The amount of accumulated electrons in the $TiO_2$ nanostructure electrode depends on the layer thickness. Generally, the higher photopotential values, the higher thickness of the $TiO_2$/ITO layers electrode.

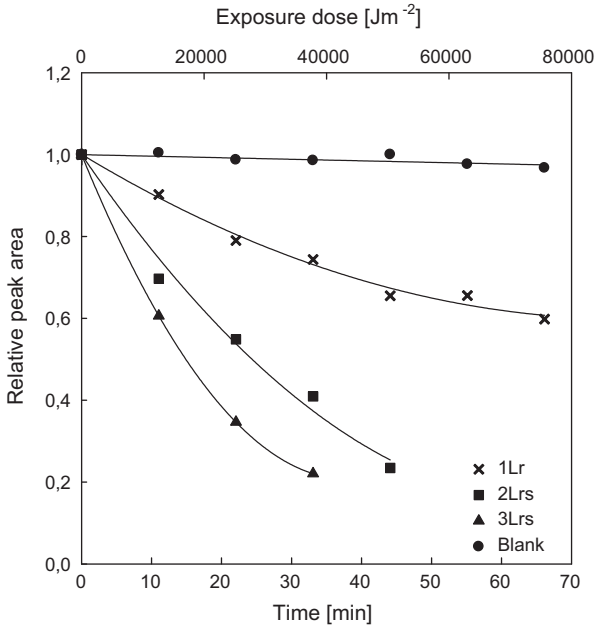


**Fig. 9.** Photocatalytic degradation of stearic acid.

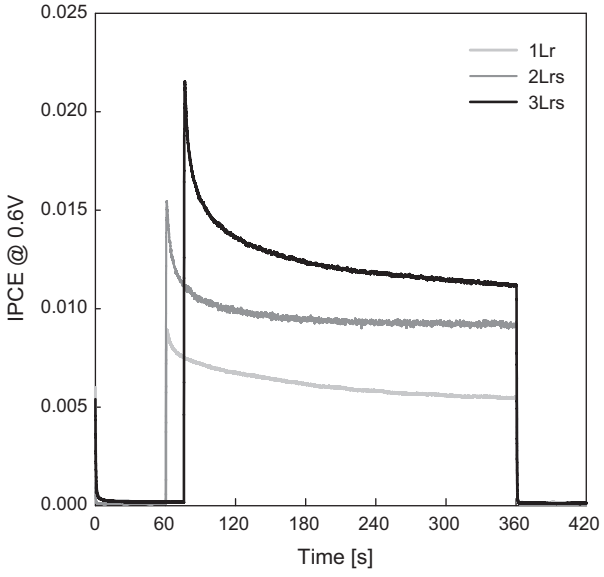


**Fig. 11.** Photocurrent-time behaviour of the prepared $TiO_2$/ITO anodes. Calculated IPCE values as a function of the layers thicknesses. The incident light intensity was 10 mV $s^{-1}$.

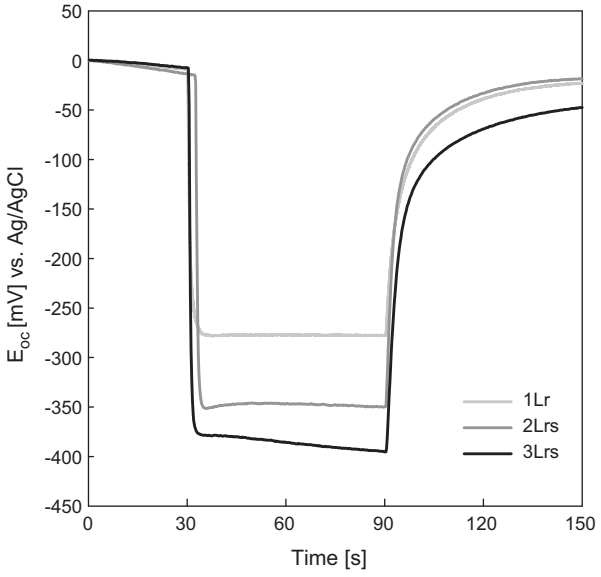


**Fig. 12.** Open circuit potential measurements.

## 4. Conclusions

The inkjet printing technique that enables printing of regular as well as irregular patterns was successfully applied to prepare thin $TiO_2$ layers deposited on substrates via the template sol–gel method. The substantial sol properties as viscosity and density were successfully optimized. Xylene was found as the suitable optimal non-polar solvent for the reverse micelle sol preparation owing to its low volatility and good surface tension. The printed layers possess smooth, homogeneous and transparent surface with low amount of defects.

The photoelectrochemical functionality and photocatalytic efficiency of the inkjet printed $TiO_2$ layers have also been discussed. The photocatalytic degradation of stearic acid revealed strong dependence of photocatalytic activity on the layers thickness. On the contrary, no influence of the layer thickness to photoinduced hydrophilicity has been noticed. It was proved that prepared $TiO_2$/ITO electrodes ($TiO_2$ thin layers on ITO glass used as photoanode) are stable and possess good photoinduced properties. The obtained electrochemical curves of layers reflect the ability to react on UV light signal by generation of the charge carriers. The electrochemical measurements confirmed the high potential of photoelectrochemistry for detection of the semiconductor oxides photoactivity. This study clearly proved the possibility of production of transparent functional thin layers deposited on various substrates by inkjet printing from the liquid sol utilized the reverse micelles system.

## Acknowledgements

Authors gratefully acknowledge the Grant Agency of the Czech Republic, project no. GD 203/08/H032, GA 104/09/0694 and GP 104/09/P165 as well as Academy of Sciences of the Czech Republic, program Nanotechnology for society – project no. KAN400720701. Authors also appreciate the work of J. Chomoucká, University of Technology Brno, and Z. Cílová, ICT Prague, for providing SEM images and Z. Matěj, Charles University in Prague, for XRD measurements.

## References

[1] M. Gratzel, Photoelectrochemical cells, Nature 414 (2001) 338–344.
[2] L. Kavan, M. Gratzel, J. Rathousky, A. Zukal, Electrochemical and photoelectrochemical investigation of single-crystal anatase, J. Am. Chem. Soc. 118 (1996) 6716–6723.
[3] J.L. Ferry, W.H. Glaze, Photocatalytic reduction of nitro organics over illuminated titanium dioxide: role of the $TiO_2$ surface, Langmuir 14 (1998) 3551–3555.
[4] U. Bach, D. Lupo, J.E. Moser, F. Weissortel, J. Salbeck, H. Spreitzer, M. Gratzel, Solid-state dye-sensitized mesoporous $TiO_2$ solar cells with high photon-to-electron conversion efficiencies, Nature 395 (1998) 583–585.
[5] K. Hashimoto, H. Irie, A. Hujishima, $TiO_2$ photocatalysis: a historical overview and future prospects, Jpn. J. Appl. Phys. 44 (2005) 8269–8285.
[6] F. Gracia, J. Holgado, A. González-Elipe, Photoefficiency and optical, microstructural, and structural properties of $TiO_2$ thin films used as photoanodes, Langmuir 20 (2004) 1688–1697.
[7] T. Berger, T. Lana-Villarreal, D. Monllor-Satoca, R. Gomez, Charge transfer reductive doping of nanostructured $TiO_2$ thin film's as a way to improve their photoelectrocatalytic performance, Electrochem. Commun. 8 (2006) 1713–1718.
[8] F. Fabregat-Santiago, I. Mora-Sero, G. Garcial-Belmonte, J. Bisquert, Cyclic voltammetry studies of nanoporous semiconductors. Capacitive and reactive properties of nanocrystalline $TiO_2$ electrodes in aqueous electrolyte, J. Phys. Chem. B 107 (2003) 758–768.
[9] K. Kozlowska, A. Lukowiak, A. Szczurek, K. Dudek, K. Maruszewski, Sol-gel coatings for electrical gas sensors, Opt. Appl. 35 (2004) 783–790.
[10] J.S. Chen, J.D. Zhang, Y.Z. Xian, X.Y. Ying, M.C. Liu, L.T. Jin, Preparation and application of $TiO_2$ photocatalytic sensor for chemical oxygen demand determination in water research, Water Res. 39 (2005) 1340–1346.
[11] M.G. Manera, P.D. Cozzoli, G. Leo, M.L. Curri, A. Agostiano, L. Vasanelli, R. Rella, Thin films of $TiO_2$ nanocrystals with controlled shape and surface coating for surface plasmon resonance alcohol vapour sensing, Sens. and Actuators B 126 (2007) 562–572.
[12] L. Ying, L.S. Hon, T. White, R. Withers, L.B. Hai, Controlled nanophase development in photocatalytic titania, Mater. Trans. 44 (2003) 1328–1332.
[13] Y.X. Zhang, G.H. Li, Y.C. Wu, Y.Y. Luo, L.D. Zhang, The formation of mesoporous $TiO_2$ spheres via a facile chemical process, J. Phys. Chem. B 109 (2005) 5478–5481.
[14] M. Li, H. Schnablegger, S. Mann, Coupled synthesis and self-assembly of nanoparticles to give structures with controlled organization, Nature 402 (1999) 393–395.
[15] D.C. Crans, B. Baruah, A. Ross, N.E. Levinger, Impact of confinement and interfaces on coordination chemistry: using oxovanadate reactions and proton transfer reactions as probes in reverse micelles, Coord. Chem. Rev. 253 (2009) 2178–2185.
[16] V. Uskokovic, M. Drofenik, Reverse micelles: inert nano-reactors or physicochemically active guides of the capped reactions, Adv. Colloid Interface Sci. 133 (2007) 23–34.
[17] V. Uskokovic, M. Drofenik, Synthesis of materials within reverse micelles, Surf. Rev. Lett. 12 (2005) 239–277.
[18] H. Schmidt, M. Mennig, Wet Coating Technologies for Glass, The Sol-Gel Gateway, http://www.solgel.com/articles/Nov00/coating.htm, 2000.
[19] M. Yoshimura, R. Gallage, Direct patterning of nanostructured ceramics from solution-differences from conventional printing and lithographic methods, J. Solid State Electrochem. 12 (2008) 775–782.
[20] S.J. Kim, D.E. McKean, Aqueous $TiO_2$ suspension preparation and novel application of ink-jet printing technique for ceramics patterning, J. Mater. Sci. Lett. 17 (1998) 141–144.
[21] I. Bernacka-Wojcik, R. Senadeera, P.J. Wojcik, L.B. Silva, G. Doria, P. Baptista, H. Aguas, E. Fortunato, R. Martins, Inkjet printed and doctor blade $TiO_2$ photodetectors for DNA biosensors, Biosens. Bioelectron. 25 (2010) 1229–1234.
[22] M. Yang, L.H. Li, S.Q. Zhang, G.Y. Li, H.J. Zhao, Preparation, characterisation and sensing application of inkjet-printed nanostructured $TiO_2$ photoanode, Sens. Actuators B-Chem. 147 (2010) 622–628.
[23] A. Matsuo, R. Gallage, T. Fujiwara, T. Watanabe, M. Yoshimura, On-site fabrication of ceramics films from solution precursors by ink-jet and spray assisted processes, J. Electroceram. 16 (2006) 533–536.
[24] K.K. Manga, S. Wang, M. Jaiswal, Q.L. Bao, K.P. Loh, High-gain graphene-titanium oxide photoconductor made from inkjet printable ionic solution, Adv. Mater. 22 (2010) 5265–5270.
[25] M. Arin, P. Lommens, N. Avci, S.C. Hopkins, K. De Buysser, I.M. Arabatzis, I. Fasaki, D. Poelman, I. Van Driessche, Inkjet printing of photocatalytically active $TiO_2$ thin films from water based precursor solutions, J. Eur. Ceram. Soc. 31 (2011) 1067–1074.
[26] P. Dzik, M. Vesely, J. Chomoucka, Thin layers of photocatalytic $TiO_2$ prepared by inkjet printing of a sol gel precursor, J. Adv. Oxid. Technol. 13 (2010) 172–183.
[27] M. Cerna, M. Vesely, P. Dzik, Physical and chemical properties of titanium dioxide printed layers, Catal. Today 161 (2011) 97–104, DOI:10.1016/j.cattod.2010.11.019.
[28] M. Morozova, P. Kluson, J. Krysa, M. Zlamal, O. Solcova, S. Kment, T. Steck, Role of the template molecular structure on the photo-electrochemical functionality of the sol-gel titania thin films, J. Sol-Gel Sci. Technol. 52 (2009) 398–407.
[29] J. Zita, J. Maixner, J. Krysa, Multilayer $TiO_2/SiO_2$ thin sol-gel films: effect of calcination temperature and Na+ diffusion, J. Photochem. Photobiol. A-Chem. 216 (2010) 194–200.
[30] J.C. Yu, J.G. Yu, J.C. Zhao, Enhanced photocatalytic activity of mesoporous and ordinary $TiO_2$ thin films by sulfuric acid treatment, Appl. Catal. B-Environ. 36 (2002) 31–43.

[31] C. Guillard, B. Beaugiraud, C. Dutriez, J.M. Herrmann, H. Jaffrezic, N. Jaffrezic-Renault, M. Lacroix, Physicochemical properties and photocatalytic activities of $TiO_2$-films prepared by sol-gel methods, Appl. Catal. B-Environ. 39 (2002) 331–342.
[32] J. Krysa, M. Zlamal, G. Waldner, Effect of oxidisable substrates on the photoelectrocatalytic properties of thermally grown and particulate $TiO_2$ layers, J. Appl. Electrochem. 37 (2007) 1313–1319.
[33] M. Morozova, P. Kluson, J. Krysa, Ch. Gwenin, O. Solcova, Oxalic acid sensors based on sol-gel nanostructured $TiO_2$ films, J. Sol-Gel Sci. Technol. 58 (2011) 175, doi:10.1007/s10971-010-2374-7.
[34] J. Zita, J. Krysa, A. Mills, Correlation of oxidative and reductive dye bleaching on $TiO_2$ photocatalyst films, J. Photochem. Photobiol. A-Chem. 203 (2009) 119–124.
[35] J.C. Yu, J.G. Yu, H.Y. Tang, L.Z. Zhang, Effect of surface microstructure on the photoinduced of porous $TiO_2$ thin films, J. Mater. Chem. 12 (2002) 81–85.
[36] J. Bico, U. Thiele, D. Quere, Wetting of textured surfaces, Colloids Surf. A-Physicochem. Eng. Asp. 206 (2002) 41–46.
[37] J.A. Byrne, B.R. Eggins, Photoelectrochemistry of oxalate on particulate $TiO_2$ electrode, J. Electroanal. Chem. 457 (1998) 61–72.
[38] S. Kment, H. Kmentova, P. Kluson, J. Krysa, et al., Notes on the photo-induced characteristics of transition metal-doped and undoped titanium dioxide thin films, J. Colloid Interface Sci. 348 (2010) 198–205.

## Biographies

**M. Morozova** graduated in MSc from Institute of Chemical Technology Prague in 2008. In the same year, she began her PhD study program at the Institute of Chemical Technology Prague; research has been provided at the laboratories of the Institute of Chemical Process Fundamentals, Academy of Sciences of the Czech Republic (ICPF ASCR) Prague. Her research is focused on the preparation of thin sol–gel layers utilizing the molecular templates, deposition techniques and layers characterization (physical properties, photo-electrochemical properties and photocatalytical activity).

**P. Kluson** obtained his PhD in 1995 at the Institute of Chemical Technology Prague (ICT Prague) and at State University of New York in Buffalo, USA. In 2000 he completed his post-doctoral research at University of Wales in Bangor, UK and at Imperial College of Science, Technology and Medicine in London, UK. Since 2003, he worked as the Associate Professor at ICT Prague. Now he is the Vice-Head of the Department of Catalysis and Reaction Engineering, Academy of Sciences of the Czech Republic and Head of the NCFC Group ICPF AS CR (Nanotechnology, Catalysis, Fine Chemicals). His research areas also include synthesis, characterization and application of functional nano-materials and special catalytic processes towards fine chemicals.

**J. Krysa** completed his PhD in 1995 at Institute of Chemical Technology Prague. Since 2003, he has been working as the Associate Professor at Department of Anorganic Chemistry. In 2008 he was subsequently promoted to Professor. He is specialised in photocatalysis with semiconducting metal oxides, waste-water treatment, advanced electrochemistry and materials research.

**P. Dzik** received his PhD at Brno University of Technology in 2006. Then he joined the University Academic Staff and has been working as Assistant Professor at the Institute of Physical and Applied Chemistry. His professional interests include applied photochemistry and photocatalysis, colour science, printing arts and functional material deposition by printing techniques.

**M. Vesely** received his PhD at Slovak Technical University in Bratislava in 1989. Then he worked as Assistant at Faculty of Chemical Technology of Slovak Technical University. From 1992 he has been working at Brno University of Technology, Faculty of Chemistry, from 1994 to 2006 as Vice-Dean and from 1995 as Professor associated at the same faculty. He is specialized in photochemistry, printing art and photocatalysis.

**O. Solcova** completed her PhD in 1990 at Institute of Chemical Process Fundamentals of the Czech Academy of Sciences. Since 2000, she has been working as the Head of the Centre for Textural Studies and since 2005 she has been the Head of the Department of Catalysis and Reaction Engineering and Deputy of the Institute of Chemical Process Fundamentals Scientific Board. Since 2008, she has been Deputy of the Institute of Chemical Process Fundamentals. Her research is focused on area of surface science, texture properties, membranes and transport phenomena, nanomaterial and special catalysis processes.

August 2011, Volume 2, No.4
International Journal of Chemical and Environmental Engineering

# Hydrothermal synthesis of $TiO_2$: influence of process conditions on photocatalytic activity

**M. Cerna[a], [b] C. Guillard[c], E. Puzenat[c], M. Vesely[a] and P. Dzik[a]**
[a] *Brno University of Technology, Faculty of Chemistry, Purkynova 118, 612 00 Brno, Czech Republic*
[c] *Institut de Recherches sur la Catalyse et l'Environnement de Lyon, CNRS UMR 5256, Universite de Lyon, Avenue Albert Einstein, Villeurbanne F-69622 cedex, France*
[b] *Corresponding author*
*E-mail:* xccernam@fch.vutbr.cz

**Abstract**

Colloidal solutions of titanium dioxide ($TiO_2$) were prepared from titanium oxo-chloride ($TiOCl_2$) which was used as precursor by hydrothermal treatment. The preparation of these suspensions was performed at different pH. Times and temperatures of hydrothermal treatment were varied. We studied the influence of these conditions on photocatalytic activity. Optical characterization of prepared colloidal suspensions of $TiO_2$ was accomplished using UV-VIS spectrometer with an integration sphere. The crystallinity and crystallite size was determined by X-ray diffraction (XRD). Consequently the particle size was evaluated by photon correlation spectroscopy and studied also by transmission electron microscopy (TEM). The photocatalytic activity of $TiO_2$ colloidal suspension was evaluated on the basis of formic acid degradation.

**Keywords:** $TiO_2$ colloidal solution, hydrothermal synthesis, organic pollution, water treatment, photocatalytic activity

## 1. Introduction

Heterogeneous photocatalysis as a water and air purification technique has attracted a great deal of attention in recent years [1-6]. The main advantage of this technique over other wastewater treatment methods (such as chlorination, ozonolysis) is that a broad variety of persistent compounds such as phenol, trichloroethylene and chlorobenzene, can be mineralized completely [7-9]. Among various oxide semiconductors, titania is very important photocatalyst owing to its strong oxidizing power, non-toxicity and long-term photostability.

Titanium dioxide ($TiO_2$) nanomaterials are used in a wide range of applications such as photocatalysis, separations, sensor devices, pigments and paints and dye-sensitised solar cells [10-11]. Many papers [12-16] have reported that the surface properties of $TiO_2$ including grain size, crystallinity, morphology, specific surface area, surface state, porosity and surface hydroxyl content obviously influence the photocatalytic activity of titania. It is well known that the photocatalytic activity of $TiO_2$ strongly depends on the preparation method as well as the post-treatment conditions, since they both have a decisive influence on the chemical and physical properties of $TiO_2$ [17].

Hydrothermal treatment is one of the most widely used methods for increasing the crystallinity of $TiO_2$. The application of elevated temperatures and pressures in an aqueous solution facilitates the conversion of amorphous $TiO_2$ into crystalline $TiO_2$ and causes an increase in its crystallinity. Hydrothermal treatment can also be used to change the morphology, microstructure and phase composition of materials by varying the reaction parameters [18].

The advantages of this method are:

Crystallization temperature for phase is bellow 200 °C.

By changing the process conditions (such as temperature, time, pH, reactant concentration, additives, ect.), various crystalline products with different composition, structure and morphology can be obtained.

Low energy consumption and environmentally friendly process.

Control of reaction conditions is easy and straightforward.

So the hydrothermal synthesis should be a good method for the preparation of semiconductor photocatalyst and other oxide powders.

## 2. Materials and methods

### *2.1 Preparation of colloidal $TiO_2$ solutions*

Titanium dioxide colloidal suspensions were prepared using $TiOCl_2$ as the precursor. KOH was used as the precipitating agent. Precursor was added dropwise to aqueous solution of KOH (with concentration 5 $mol \cdot dm^{-3}$) until neutral reaction of the resulting mixture. Then this

mixture was washed by water for several times to remove chloride ions. In this work, apart from the hydrothermal treatment conditions, we also studied the influence of different pH on final physical properties and photocatalytic activity of $TiO_2$. For this purpose, we added 0.25 $cm^3$ KOH (concentration 1 $mol \cdot dm^{-3}$) to the washed mixture to rise the final pH value to 10. Or 0.9 $cm^3$ HCl (p.s.) to lower the final pH value to 2. All prepared mixtures were the hydrothermally treated. We investigated the influence of different temperatures of the hydrothermal treatment (110 °C and 160 °C) and different time of treatment (6 hours, 24 hours and 48 hours) on physical and chemical properties of prepared colloidal suspensions.

*2.2 Optical characterization and evaluation of stability*

Optical characterization of $TiO_2$ solutions was performed using UV–VIS spectrometer equipped with an integration sphere (RSA-PE-20, Labsphere). The system consists of two lamps, one deuterium lamp for UV region and another tungsen lamp as a source of visible light. The measurement was performed in the range of 200–800 nm. We studied the change of transmission during 1 hour. By this method we compared the stability of samples prepared in different pH.

The influence of different time of hydrothermal treatment on the colloidal stability was evaluated by gravimetric measurement. We investigated the concentration of $TiO_2$ particles in the solutions immediately after the preparation and then after 1 day of sedimentation.

*2.3 Crystal structure*

Crystalline phase in the samples were identified from X-ray powder diffraction pattern measured by using CuKα as radiation source. Subsequently the crystallite size was calculated using Scherrer equation (1), where B is a constant equal to 0.94, λ is the wave length which is equal to 1.54 Å and β is the width of peak at a half of maximal height.

$$d = (B \cdot \lambda) / (\beta \cdot \cos(\theta)) \quad (1)$$

*2.4 Particle size measurement*

The particle size was examined by photon correlation spectroscopy. For this purpose we used dynamic light scattering analyzer Coulter N4 Plus. We measured the rate of particles diffusion through the solution and from this measurement the particle size could be determined.

*2.5 Transmission electron microscopy*

Analysis of size and shape of $TiO_2$ colloidal particles were studied by transmission electron microscopy. We used a JEOL JEM 2010 microscope operated at 200 kV, equipped with a $LaB_6$ tip. The samples were prepared by simply putting a drop of the solution containing the particles on a holey-carbon thin film supported on a microscopy copper grid

*2.6 Photocatalytic activity*

Photocatalytic activities of $TiO_2$ colloidal suspensions were evaluated by means of the degradation rate of formic acid (FA). FA was chosen because it undergoes direct mineralization to $H_2O$ and $CO_2$ without the creation of any stable intermediate species [19-22]. Moreover, it also represents a possible final step in the photodegradation of more complex organic compounds [23].

This experiment took place under ambient temperature in a Pyrex reactor with 50 $cm^3$ of reaction slurry under constant stirring. The final concentration of FA in solutions was 100 ppm and the concentration of $TiO_2$ in reaction solutions was 1 $g \cdot dm^{-3}$. First we placed the examined slurry into darkness for 30 minutes under continuous stirring in order to reach adsorption equilibrium of FA on $TiO_2$. During the FA photodegradation, 1 $cm^3$ of reaction solution was sampled for HPLC analysis. The total reaction time was 60 minutes. We compared the activity of our samples with commercial $TiO_2$ (P25, Degussa). The intensity of radiation used during the photocatalytic test was 7.209 $mW \cdot cm^{-2}$ in the UVA region, 2.044 $mW \cdot cm^{-2}$ in the UVB region and no radiation of the UVC region was presented.

## 3. Results and discussion

*3.1 Stability of $TiO_2$ suspension*

We examined the influence of pH on the final stability of $TiO_2$ colloidal solutions by UV–VIS spectroscopy. We measured all prepared samples during 1 hour each 10 minutes. The results show us the kinetic stability of $TiO_2$ suspensions. When we compared all samples we discovered that the samples prepared in acidic environment are more stable than samples prepared in basic one Fig. 1.

From the gravimetric measurement we discovered that the best time for hydrothermal treatment is 48 hours Fig. 2 (for these samples the concentration decrease is the lowest). No sedimentation was observed in the case of suspension prepared at the temperature 110 °C for 48 hours.

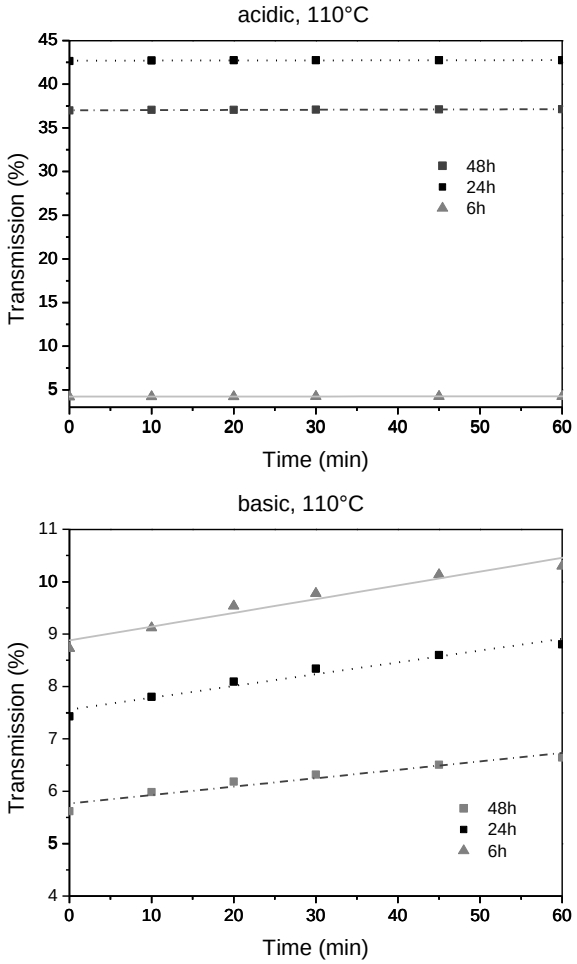


**Figure 1. Kinetic stability of prepared colloidal solutions**

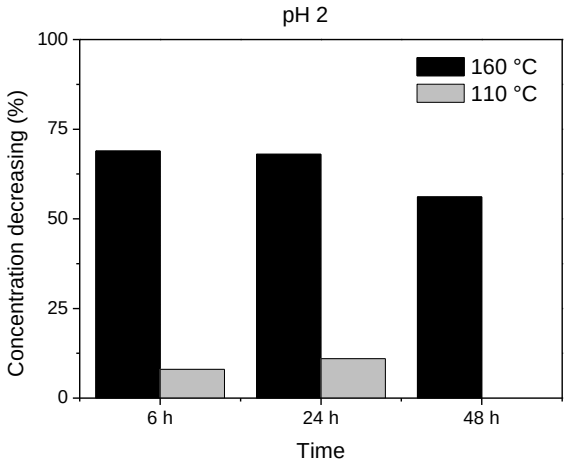


**Figure 2. Concentration decreasing after 1 day**

### *3.2 Crystal structure*

XRD was used to investigate the dependence of the final phase structure of $TiO_2$ powder on the pH values. From this analysis we found out that we obtained pure anatase in basic environment, while we received a mixture of rutile and anatase in the acidic environment Fig. 3. These results were generally obtained for all prepared samples.

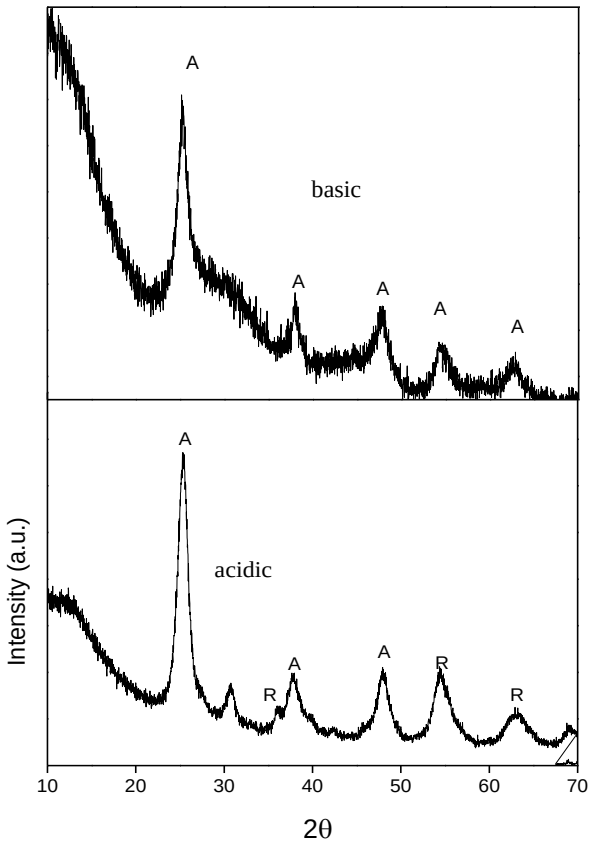


**Figure 3. Spectra from XRD**

Using Scherrer equation (1) we could calculate the mean crystallite size. The results from this calculation are summarized in Tab. 1.

**Table 1: Crystallite size (nm)**

| pH | Time | 110 °C | 160 °C |
|---|---|---|---|
| Basic | 6 h | 13.5 | 19.9 |
| | 24 h | 9.1 | 42.0 |
| | 48 h | 13.5 | 37.3 |
| Acidic | 6 h | 22.6 | 30.7 |
| | 24 h | 13.5 | 30.5 |
| | 48 h | 8.3 | 25.9 |

We discovered that the crystallite size decreases in the acidic environment with increasing time. However, we could observe no such dependence between the time of hydrothermal treatment and the crystallite size in the basic environment. After the evaluation the crystallite sizes for different temperatures we found out that with increasing temperature the crystallite size increases as well. This result is in a good agreement with previously published data [24, 25].

*3.3 Particle size measurement*

We investigated the particle size by photon correlation spectroscopy and we studied the influence of pH and varying hydrothermal conditions on the particle size. Based on this analysis, we conclude that at the temperature of 110 °C the particle size decreases with increasing time of hydrothermal treatment (Tab. 2). These results are in a good agreement with the results from XRD analysis. On the other hand, for the treatment temperature of 160 °C we obtained an opposite dependence. It means that with increasing treatment time the particle size increases. We could record such high values due to the aggregation so subsequently we examined the aggregation behavior of our particles by transmission electron microscopy.

We discovered that the particle sizes are higher for samples prepared in basic environment when we compared particle size for samples prepared in different pH (Tab.2).

**Table 2: Particle size (nm)**

| pH | Time | 110 °C | 160 °C |
|---|---|---|---|
| Basic | 6 h | 157.9 | 18.5 |
| | 24 h | 77.5 | 24.1 |
| | 48 h | 15.8 | 40.8 |
| Acidic | 6 h | 146.9 | 2.9 |
| | 24 h | 62.3 | 15.1 |
| | 48 h | 12.1 | 29.3 |

*3.4 Transmission electron microscopy*

Firstly, we studied the crystallite size for the samples prepared in the basic environment and the influence of treatment time. From XRD analysis we found out that there is no dependence between crystallite size and time of hydrothermal treatment. However, we received quite different results by TEM analysis. We found out that with increasing treatment time the crystallite size decreases (Fig. 5). It is the same dependence which we could observe in the acidic environment by XRD analysis. In Fig. 5 we can also see that in the case of sample which was treated for the longest time there is a quite high aggregation taking place. This aggregation could be the reason why we recorded such a high value of particle size by the photon correlation spectroscopy. Indeed, the particles are smaller than 15 nm actually.

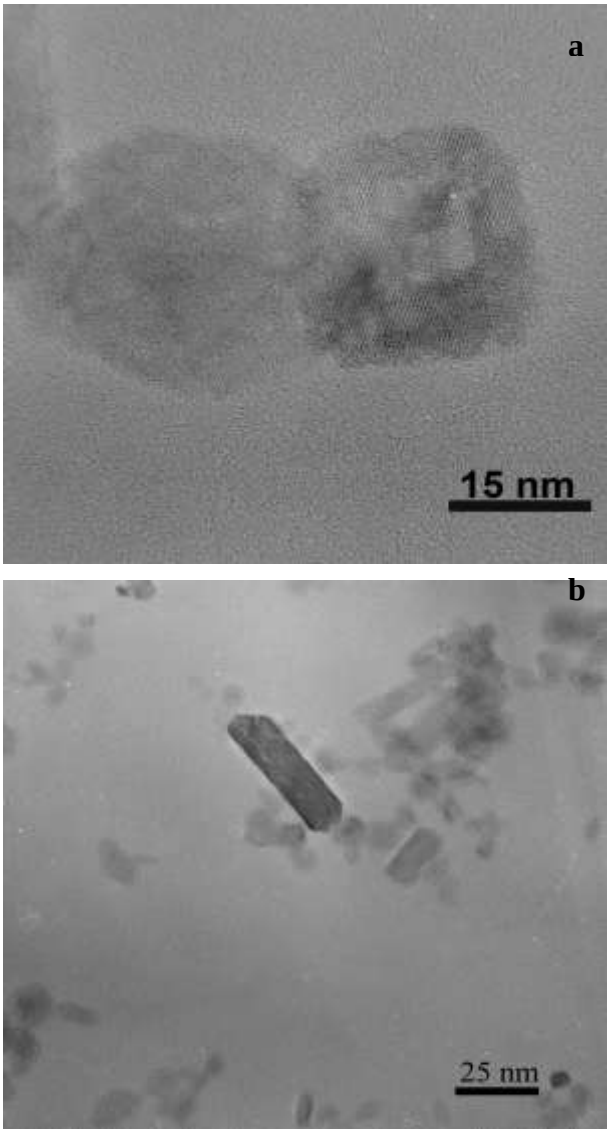


**Figure 4. TEM images, crystallite shape, a- basic environment, b- acidic environments**

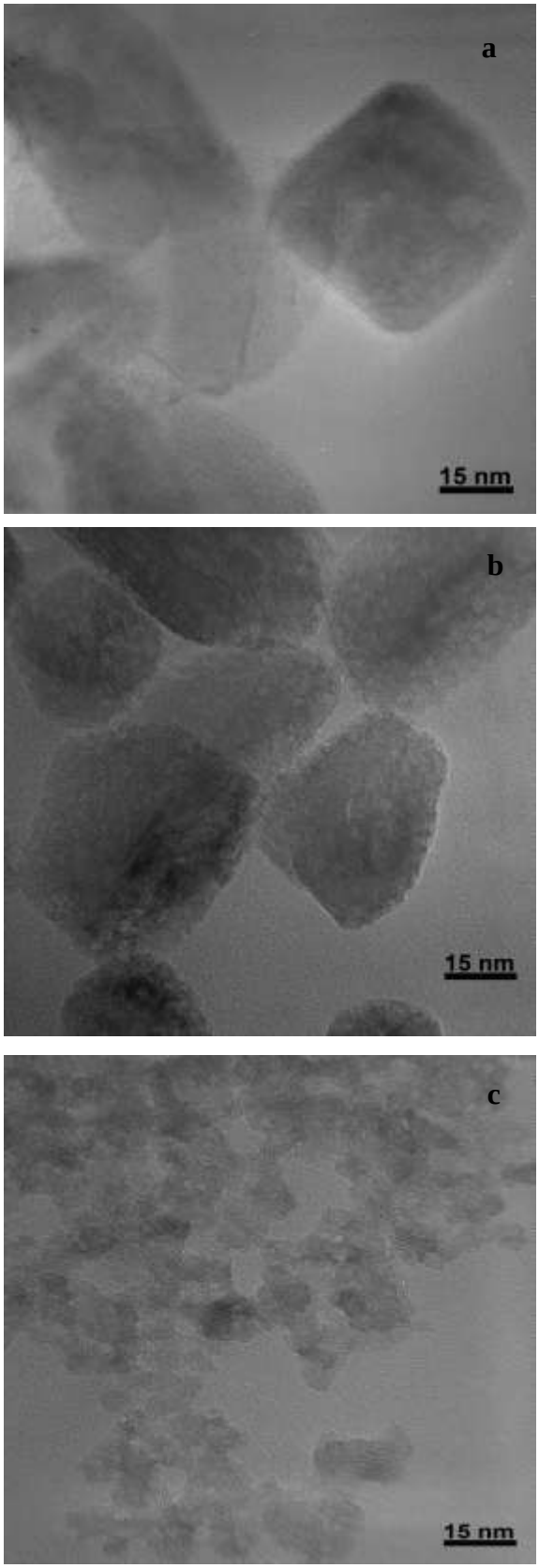


**Figure 5. TEM images for samples prepared at 160 °C in basic environments, a. 6 hours, b. 24 hours, c. 48 hours**

Subsequently, we investigated the crystallinity of prepared samples by TEM. We compared the particles shape of samples prepared at different pH values. We discovered that in the case of samples prepared in the basic environment there are only cubic particle present Fig. 4. This shape is typical for anatase. So we confirmed that the samples prepared in pH of 10 are pure anatase phase. In case of acidic environment we could observe apart from the cubic shape also rods (Fig. 5). This shape is typical for rutile [26]. So we affirmed that the samples prepared in pH of 2 consist of mixture of rutile and anatase. These results are consistent with the results of XRD analysis.

*3.5 Photocatalytic activity*

The photocatalytic activity was evaluated by the degradation rate of formic acid. For this purpose we used HPLC. We examined the decreasing of FA concentration caused by UV radiation. In Fig. 6 we can observe the profiles of time-dependent photocatalytic reactivity of our prepared samples. Since the dependence of relative concentration on time is linear within the studied range, we assumed the zero order kinetics model for this part of the reaction coordinate. Subsequently we calculated the reaction rate constants (k) and their standard errors (SE) for all prepared samples (Tab. 3).

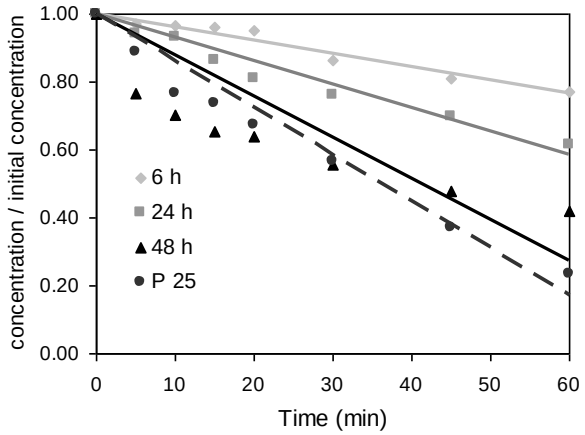


**Figure 6. Photocatalytic activity of samples prepared in basic environment at temperature 160 °C**

From this analysis we discovered that the most active $TiO_2$ colloidal suspensions originating from samples treated for the longest time (these samples have the highest reaction rate, Tab. 3). It could be caused very small particle size. Since with increasing treatment time the particle size decreases, therefore in the case of 48 hours the particle size is the smallest. It means that also the specific surface area plays a dominant role and it can significantly influence the photocatalytic activity. After comparing samples prepared in the acidic and basic environments, we found out that the samples prepared in acidic environment are more photocatalytically active. We supposed this is due to the generally known fact that the mixture of anatase and rutile has higher photocatalytic

activity than pure anatase. When we compare the different temperature we found out that the samples prepared in basic pH have higher activity at the temperature 160 °C but samples prepared in acid environment show the higher photocatalytic activity at the 110 °. Samples prepared at temperature 110 °C in pH of 2 perform the best from the photocatalytic activity point of view. Even the photocatalytic activities of reaction slurries prepared from samples treated for 24 and 48 hours are comparable to the activity of P 25.

**Table 3: Rate constants and their statistical errors**

| pH | Time | 110 °C | | 160 °C | |
|---|---|---|---|---|---|
| | | k $\cdot 10^{-2}$ ($min^{-1}$) | SE ($min^{-1}$) | k $\cdot 10^{-2}$ ($min^{-1}$) | SE ($min^{-1}$) |
| Basic | 6 h | 0.18 | 0.01 | 0.43 | 0.02 |
| | 24 h | 0.10 | 0.02 | 1.14 | 0.20 |
| | 48 h | 0.21 | 0.01 | 1.70 | 0.16 |
| Acidic | 6 h | 0.61 | 0.01 | 1.87 | 0.05 |
| | 24 h | 2.57 | 0.13 | 2.08 | 0.04 |
| | 48 h | 2.68 | 0.20 | 2.17 | 0.09 |
| P 25 | | 2.26 | 0,07 | | |

## 4. Conclusion

This paper has shown that time, temperature as well as pH value significantly affect the physical properties and photocatalytic activity of $TiO_2$ slurries. The varying time of hydrothermal treatment had a strong influence on the crystallite and particle size. With increasing time the particle size decreases which causes an increase of photocatalytic reactivity of these suspensions. The pH value of the starting solution effects the crystallinity, stability and photocatalytic activity. Basic conditions supported the creation of pure anatase whereas acidic conditions brought about the formation of rutile and anatase mixture. When we compared the different time of hydrothermal treatment we concluded the time of 48 hours as the best. The samples treated for this time were more stable and had the highest activity.

## ACKNOWLEDGMENT

Authors thank to Ministry of Education, Youth and Sports of Czech Republic for support by project FRVS2157/2011, by project OC10050 and by project

## REFERENCES


[1] M.R. Hoffmann, S.T. Martin, W. Choi, D.W. Bahnemann, "Enviromental applications of semiconductors photocatalysis," *Chem. Rev.*, vol. 95, pp. 69–96, 1995.

[2] M.A. Fox, M.T. Dulay, "Heterogenous photocatalysis," *Chem. Rev.*, vol. 93, pp. 341–357, 1993.

[3] J. Zhao et al, "Photoassisted Degradation of dye pollutants. 3. degradation of the cationic dye Rhodamine B in aqueous anionic surfactant/TiO2 dispersion under visible light irradiation: Evidence for the need of substrate adsorption on TiO2 particles", *Environ. Sci. Technol..*, vol. 32, pp. 2394–2400, 1998.

[4] F.B. Li, X.Z. Li, "Photocatalytic properties of gold/gild ion-modified titanium dioxide for wastewater treatment", *Appl. Catal.*, vol. 228, pp. 15–27, 2002.

[5] J.G. Yu, X.J. Zhao, Q.N. Zhao, "Effect of surface structure on photocatalytic activity of TiO2 thin films prepared by sol-gel method", *Thin solid films*, vol. 379, pp. 7–14, 2000.

[6] H.G. Yu, S.C. Lee, C.H. Ao, J.G. Yu, "Low-temperature fabrication and photocatalytic activity of clustered TiO2 particles formed on glass fibers", *J. Cryst. Growth*, vol. 280, pp. 612–619, 2005.

[7] Z. Ding, G.Q. Lu, P.F. Greenfield, "Role of the crystallite phase of TiO2 in heterogenous photocatalysis for phenol oxidation in water", *J. Phys. Chem. B*, vol. 104, pp. 4815–4820, 2000.

[8] S.J. Kim, H.G. Lee, S.J. Kim, J.K. Lee, E.G. Lee, "Photoredox properties of ultrafine rutile TiO2 acicular powder in aqueous 4-chlorophenol, Cu-EDTA and Pb-EDTA solutions", *Appl. Catal. A*, vol. 242, pp. 89–99, 2003.

[9] A.L. Linsebigler, G. Lu, J.T. Yates Jr., "Photocatalysis on TiO2 surfaces: Principles, mechanisms and selected results", *Chem. Rev.*, vol. 95, pp. 735–758, 1995.

[10] A. Hagfeldt, M. Gratzel, "Light-induced redox reactions in nanocrystalline systems", *Chem. Rew.*, vol. 95, pp. 49–68, 1995.

[11] X. Chen, S.S. Mao, "Titanium dioxide nanomaterials: synthesis, properties, modifications and applications", *Chem. Rev.*, vol. 107, pp. 2891–2959, 2007.

[[12] J.C. Yu, J.G. Yu, J.C. Zhao, "Enhanced photocatalytic activity of mesoporous and ordinary TiO2 thin filmy by sulphuric acid treatment", *Appl. Catal. B*, vol. 36, pp. 31–43, 2002.

[13] V. Subramanian, E.E. Wolf, P.V. Kamat, "Catalysis with TiO2/gold nanocomposites, Effect of metal particle size on the Fermi level equilibration", *J. Am. Chem. Soc.*, vol. 126, pp. 4943–4950, 2004.

[14] J.C. Yu, J.G. Yu, W.K. Ho, Z.T. Jiang, L.Z. Zhang, "Effect of F-doping on the photocatalytic activity and microstructures of nanocrystalline TiO2 powders", *Chem. Mater.*, vol. 14, pp. 3808–3816, 2002.

[15] B. Ohtani, Y. Ogawa, S. Nishimoto, "Photocatalytic activity of amorphous-anatase mixture of titanium (IV) oxide particles suspended in aqueous solutions", *J. Phys. Chem. B*, vol. 101, pp. 3746–3752, 1997.

[16] C.P. Sibu, S. Rajesch Kumar, P. Makundan, K.G.K. Warrier, "Structural modifications and associated properties of lanthanum oxide doped sol-gel nanosized titanium oxide", *Chem. Mater.*, vol. 14, pp. 2876–2881, 2002.

[17] J.G. Yu et al, "The effect of calcinations temperature on surface microstructure and photocatalytic activity of TiO2 thin films prepared by liquid phase deposition", *J. Phys. Chem. B*, vol. 107, pp. 13871–13879, 2003.

[18] K. Byrappa, M. Yoshimura, *Handbook of Hydrothermal Technology*, William Andrew Publishing, Inc., New York, 2001.

[19] R.W. Matthews, "Purification of water with near UV-illuminated suspensions of titanium dioxide", *Water research*, vol. 24, pp. 653–660, 1990.

[20] L. Davydov, P.G. Smirniotis, "Quantification of the primary processes in aqueous heterogenous photocatalysis using single-stage oxidation reactions", *J. Catal.*, vol. 191, pp. 105–115, 2000.

[21] R.J. Candal, W.A. Zeltner, M.A. Anderson, "Effect of pH and applied potential on photocurrent and oxidation rate of saline solutions of formic acid in a photoelectrocytalytic reactor", *Environ. Sci. Technol.*, vol. 34, pp. 3443–3451, 2000.

[22] D.S. Muggli, M.J. Backers, "Two active sites for photocatalytic oxidation of formic acid on TiO2: Effects of H2O and temperature", *J. Catal*, vol. 209, pp. 105–113, 2002.

[23] M. Mrowetz and E. Selli, "Photocatalytic degradation of formic and benzoic acids and hydrogen peroxide evolution in $TiO_2$ and ZnO water suspensions," *Journal of photochemistry and photobiology A: Chemistry*, vol. 180, pp. 15–22, 2006.

[24] H. Cheng, J. Ma, Z. Zhao and L. Qi, "Hydrothermal preparation of Uniform nanosize rutile and anatase particles," *Chem. Mater*, vol. 7, pp. 663–671, 1995.

[25] J. Yu, G. Wang, B. Cheng and M. Zhou, "Effect of hydrothermal temperature and time on the photocatalytic activity and microstructures of bimodal mesoporous $TiO_2$ powders," *Applied Catalysis B: Environmental*, vol. 69, pp. 171–180, 2007.

[26] D. Reyes-Coronado et al., "Phase-pure $TiO_2$ nanoparticles : anatase, brookite and rutile, " *Nanotechnology*, vol 19, pp. 1–10, 2008.

Nanoscale Research Letters
a SpringerOpen Journal

NANO EXPRESS Open Access

# Atomic force microscopy analysis of nanoparticles in non-ideal conditions

Petr Klapetek[1*], Miroslav Valtr[1], David Nečas[2], Ota Salyk[3] and Petr Dzik[3]

**Abstract**

Nanoparticles are often measured using atomic force microscopy or other scanning probe microscopy methods. For isolated nanoparticles on flat substrates, this is a relatively easy task. However, in real situations, we often need to analyze nanoparticles on rough substrates or nanoparticles that are not isolated. In this article, we present a simple model for realistic simulations of nanoparticle deposition and we employ this model for modeling nanoparticles on rough substrates. Different modeling conditions (coverage, relaxation after deposition) and convolution with different tip shapes are used to obtain a wide spectrum of virtual AFM nanoparticle images similar to those known from practice. Statistical parameters of nanoparticles are then analyzed using different data processing algorithms in order to show their systematic errors and to estimate uncertainties for atomic force microscopy analysis of nanoparticles under non-ideal conditions. It is shown that the elimination of user influence on the data processing algorithm is a key step for obtaining accurate results while analyzing nanoparticles measured in non-ideal conditions.

## Introduction

Nanoparticle analysis is an important challenge in the present nanoscale metrology. Nanoparticles are used in many fields of research and technology [1-5], and their proper characterization is, therefore, very important. Even if there are several general and well established experimental methods to nanoparticle analysis (optical methods [6-8], electrochemistry-based methods [9], electron microscopy [10,11], X-ray methods [10,12] and scanning probe microscopy [10,13]), their results differ mutually very often due to different effects of non-ideal measurement conditions [6,7,10,14].

In this article, we focus on nanoparticle analysis performed using atomic force microscopy (AFM) [15], which is one of the most popular scanning probe microscopy methods. The interaction of nanoparticles with the AFM probe was studied in the past quite extensively from the experimental point of view–from the point of nanoparticle measurement, AFM tip modification, or nanoparticle manipulation [10,13,16-18]. If the isolated nanoparticles of spherical shape are deposited on an ideally flat substrate, their size can be determined easily from the AFM image by measuring the nanoparticle image height [13]. This quantity is not influenced by tip-sample convolution effects and can provide accurate nanoparticle size results.

However, if the particles are deposited on rough substrates (or curved substrates generally), particle size analysis is not so straightforward and therefore many questions arise from the point of particle analysis implementation in AFM image processing software. Another effect strongly influencing the AFM analysis of nanoparticles is particle agglomeration and self-ordering on the substrate. In real measurements, we can often observe both effects. The statistical results of nanoparticle properties therefore rely on a good choice and correct use of AFM data evaluation algorithms, which adds a human error to the whole measurement process. From a metrology point of view, this approach is not satisfactory, as we cannot easily determine the measurement uncertainty.

The aim of this article is to investigate the influence of the substrate roughness and particle agglomeration on the statistical analysis of nanoparticle properties. We study the measurement uncertainty of nanoparticle parameters with respect to different nanoparticle data processing methods and scanning parameters (e.g., tip related effects). To do this, we employ a simple model that simulates the real particle deposition and ordering

* Correspondence: pklapetek@cmi.cz
[1]Czech Metrology Institute, Okružní 31, 638 00, Brno, Czech Republic
Full list of author information is available at the end of the article

on the substrate and the basic physical phenomena connected with this processes. Afterward, we simulate AFM scans obtained on modeled samples and we evaluate nanoparticle statistical properties using different data analysis methods. Finally, we compare the results with the nominal values of the nanoparticle statistical properties used for modeling on the first stage. This approach enables us to determine the level of confidence in AFM measurements of nanoparticles and to determine the limits of measurement uncertainty in these cases.

## Experimental arrangement

Atomic force microscopy measurements shown in Figure 1a-d to illustrate the numerical models connection to real data in this article were performed using AFM Explorer (Thermomicroscopes) in contact and non-contact mode, using standard contact (type MSCT-EXMT-A1) probes supplied by Veeco company and non-contact probes (type PPP-NCLR) supplied by NanoAndMore company. Measurements were performed in ambient conditions. Image resolution was between 500 × 500 pixels and 1, 000 × 1, 000 pixels, scan speed between 1 and 5 $\mu$m/s. Raw data obtained from the microscope were processed in Gwyddion open source software using the plane leveling algorithm [19].

Nanoparticle samples were prepared by spin-off coating, using a simple home-built apparatus; nanoparticles were dispersed in ethylene glycol [20] (palladium) resp. in water (polymer) and dried after deposition.

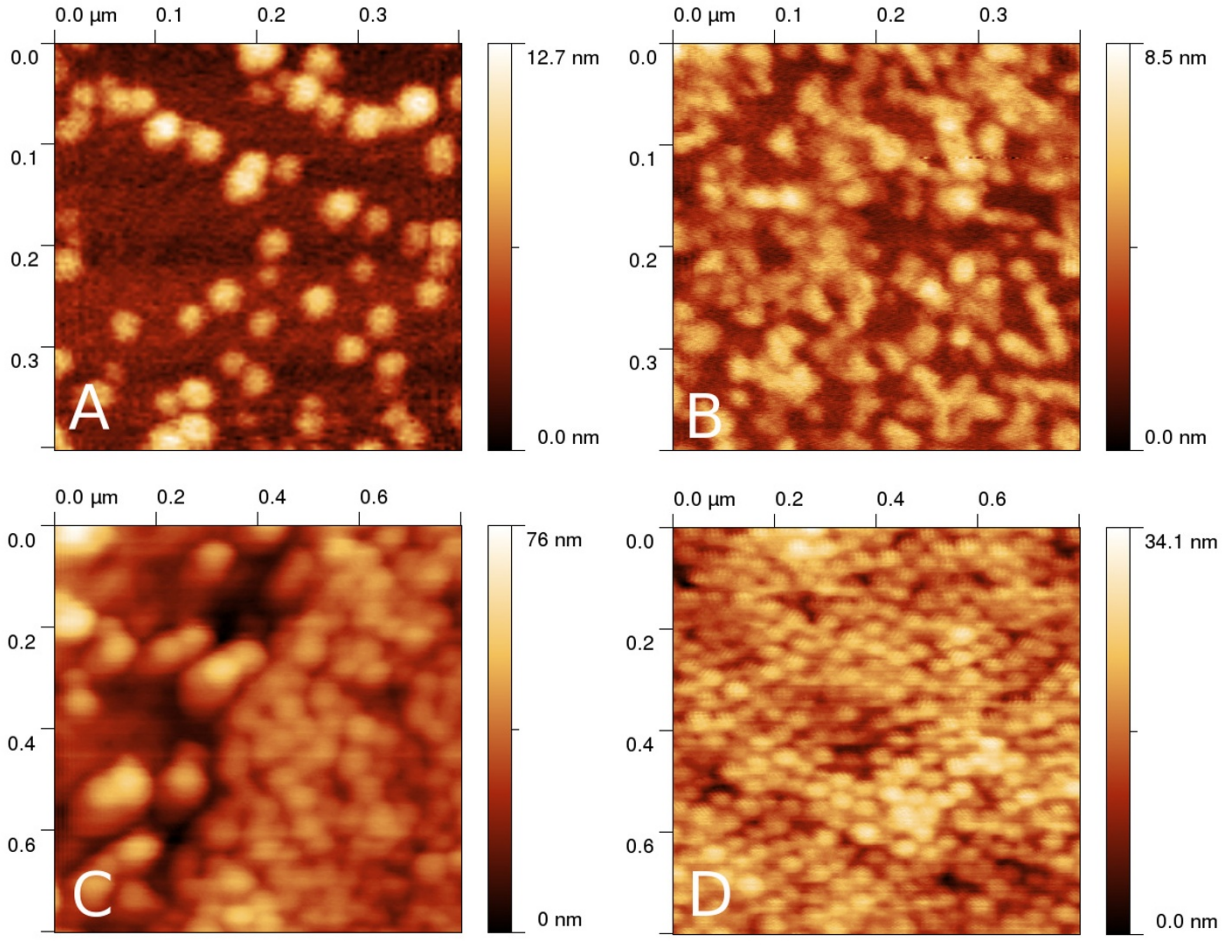


**Figure 1** Typical AFM nanoparticle measurement of palladium on flat (a) and rough silicon (b), polymer on rough (c) and flat silicon (d).

## Data modeling and analysis

In order to simulate the full process of nanoparticle deposition, measurement and analysis, data modeling was performed in several successive steps:

1. modeling of a **rough surface**.
2. simulation of **particle deposition** on the surface.
3. creation of virtual AFM images by **tip-sample convolution**.
4. nanoparticle **statistical analysis** using virtual AFM images and data processing software.

In order to simulate the effects of both surface roughness and nanoparticle clustering, we need to vary the following parameters in steps 1 -3:

- surface roughness (parametrized using the root mean square roughness and autocorrelation length),
- number of particles and their size (parametrized using the surface coverage and the particle radius),
- AFM tip shape (parametrized using the tip radius and the apex ratio).

The resulting nanoparticle statistical properties are then compared to values used in step 2 (particle deposition). The algorithms used for data modeling are described in more detail in the next two sections. All the data modeling and processing algorithms were implemented in Gwyddion open source software http://gwyddion.net and are available for public in the present version of software.

### Surface generation and particle deposition modeling

**Rough substrates** were modeled to have a Gaussian autocorrelation function [21], which is a simple model often used in many fields of surface physics [22].

First, a sufficiently large field filled by independent random numbers needs to be created, having these properties:

$$\langle \eta(\mathbf{r}) \rangle = 0 \tag{1}$$

$$\langle \eta(\mathbf{r}) \eta(\mathbf{r}') \rangle = \pi^{d/2} \delta(\mathbf{r} - \mathbf{r}'). \tag{2}$$

where $\eta$ ($\mathbf{r}$) is the random number at the position given by $\mathbf{r}$, $\eta$ ($\mathbf{r}'$) is the random number at the position given by $\mathbf{r}'$ and $d$ is the surface dimensionality (here $d$ = 2).

The surface $z(\mathbf{r})$ is created by performing a convolution according to the formula

$$z(\mathbf{r}) = 2^{d/2} \frac{\sigma T^{-d/2}}{\pi^{d/2}} \int_{-\infty}^{\infty} \exp\left[ -2 \frac{(\mathbf{r} - \mathbf{r}')^2}{T^2} \right] \eta(\mathbf{r}) \mathrm{d}\mathbf{r}', \tag{3}$$

where $\sigma$ and/or $T$ are the root mean square roughness and/or autocorrelation length corresponding to the surface to be constructed. As this integral is evaluated numerically, it is necessary to limit the computation to a sufficient area, depending on the decay of the Gaussian function inside the integral. The resulting values $z(\mathbf{r})$ form a surface with the required root mean square roughness $\sigma$ and autocorrelation length $T$.

Surface properties are therefore controlled by two parameters–the root mean square roughness ($\sigma$) and the autocorrelation length ($T$). Note that for our simulation, the autocorrelation length was kept constant and only the root mean square roughness was varied.

For **particle deposition**, a simple model similar to molecular dynamics calculations was constructed as described below. The aim of the model is to include basic interaction between nanoparticles and between a nanoparticle and the substrate and to model the effects of thermal and mechanical vibrations in nanoparticle dispersion (e.g., Brownian motion). In contrast to more rigorous models shown in literature [10,23], this model does not include the effects of nanoparticle atomistic structure or effects of the presence of the vapor phase [24]; however, as seen from the results, it is still able to generate images of nanoparticles very similar to real images observed using atomic force microscopy (see Figure 1a-d). In contrast to even simpler models (e.g., random placement of nanoparticles on substrate), it can include the nanoparticle self-organization effects, which are important phenomena affecting nanoparticle analysis in scanning probe microscopy as seen in Figure 1c-d.

In order to model the nanoparticle deposition, we used the following algorithms and physical models:

- Nanoparticles were modeled as Lennard-Jones spheres, the surface by an integrated Lennard-Jones potential [25,26].
- Verlet algorithm was used for the integration of the Newton equations.
- The Anderson thermostat was used to simulate Brownian motion of nanoparticles in a liquid (which is the nanoparticle deposition in practice).
- Nanoparticle velocities were damped during computation to simulate the decreasing mobility.

Typical images of nanoparticles obtained using this approach are given in Figure 2a, c. The developed algorithm enables us to create even more complex structures by varying the particle number, mobility and force constants between particles and between particle and substrate. A structure similar to a real measurement can be therefore obtained relatively easily even for other samples than those shown in Figure 1a-d.

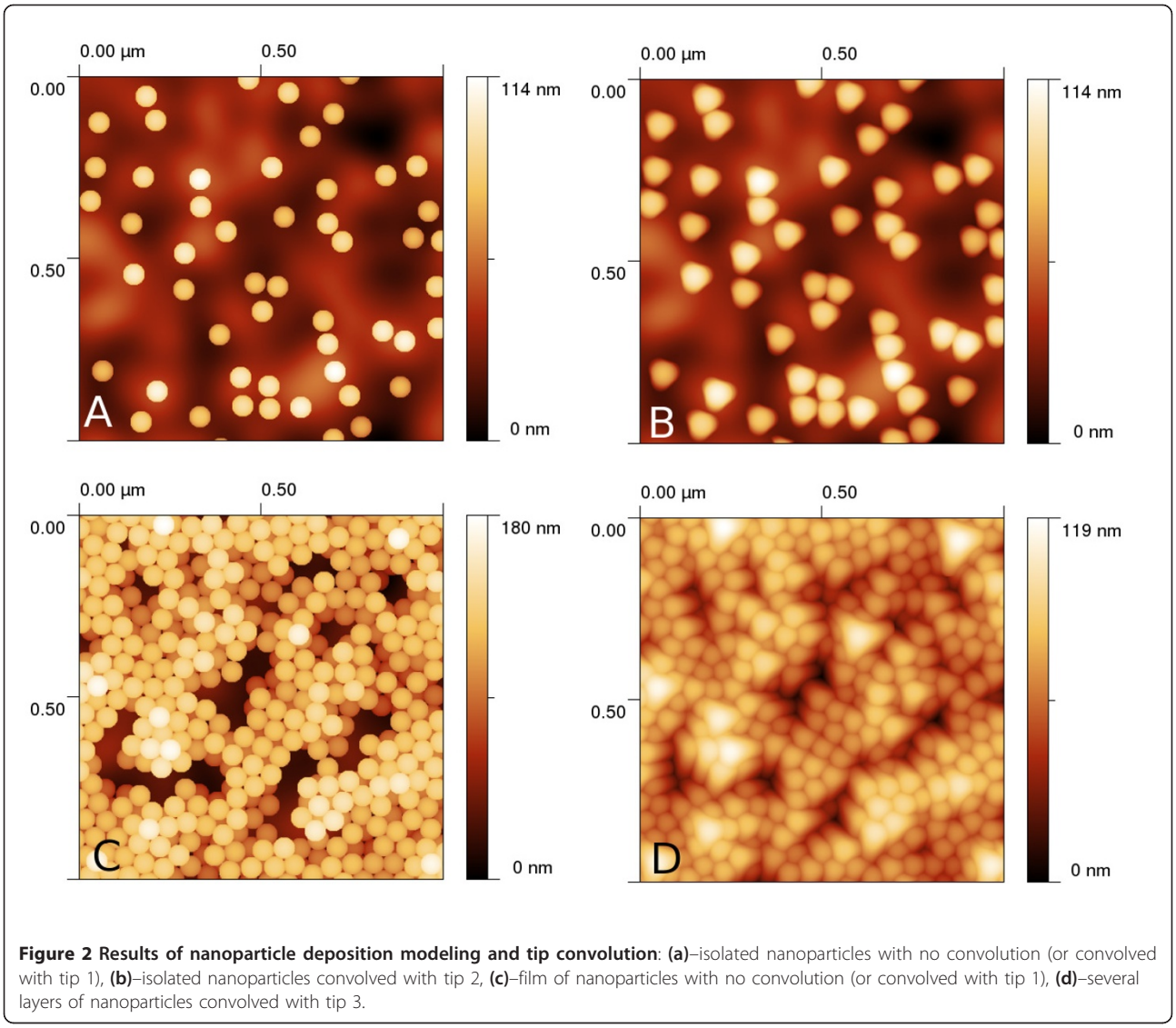


**Figure 2 Results of nanoparticle deposition modeling and tip convolution**: **(a)**–isolated nanoparticles with no convolution (or convolved with tip 1), **(b)**–isolated nanoparticles convolved with tip 2, **(c)**–film of nanoparticles with no convolution (or convolved with tip 1), **(d)**–several layers of nanoparticles convolved with tip 3.

### Virtual microscopy measurement and data evaluation

Virtual AFM measurement were performed using the dilation algorithm presented in Ref. [27]. As we focused on the analysis of statistical data processing methods in this article, we limited the selection of used AFM tips to a few commercially available probes (described by their nominal radius and aspect ratio parameters). The dilation algorithm returns simulated AFM images, determined morphologically as a convolution of rigid bodies. This approach is therefore valid under the assumption that there are no tip or sample changes due to tip-sample interaction. This could be in principle problematic for very soft materials or for extremely small nanoparticles whose geometry could change significantly due to tip-sample forces [28,29]. Examples of results of the dilation on simulated surfaces are given in Figure 2b, d. We can see that the resulting images are very similar to the real measurements (shown in Figure 1a-d). The effect of dilation on a single nanoparticle on a curved substrate is shown in Figure 3a. We can see that the tip convolution prevents the AFM from seeing the morphology below the nanoparticle. As there is no complete information about both nanoparticle and substrate geometry at these parts of AFM image, all the data processing algorithms need to make some assumptions regarding nanoparticle and substrate properties.

For the characterization of nanoparticles from AFM data, several algorithms can be used. The first stage is always the segmentation of data into separate particles. In principle, a simple thresholding can be used to do this for the case of isolated particles on a flat substrate. For rough or curved substrates and for agglomerated particles, this approach usually fails as we cannot determine an appropriate threshold value; therefore, we use a

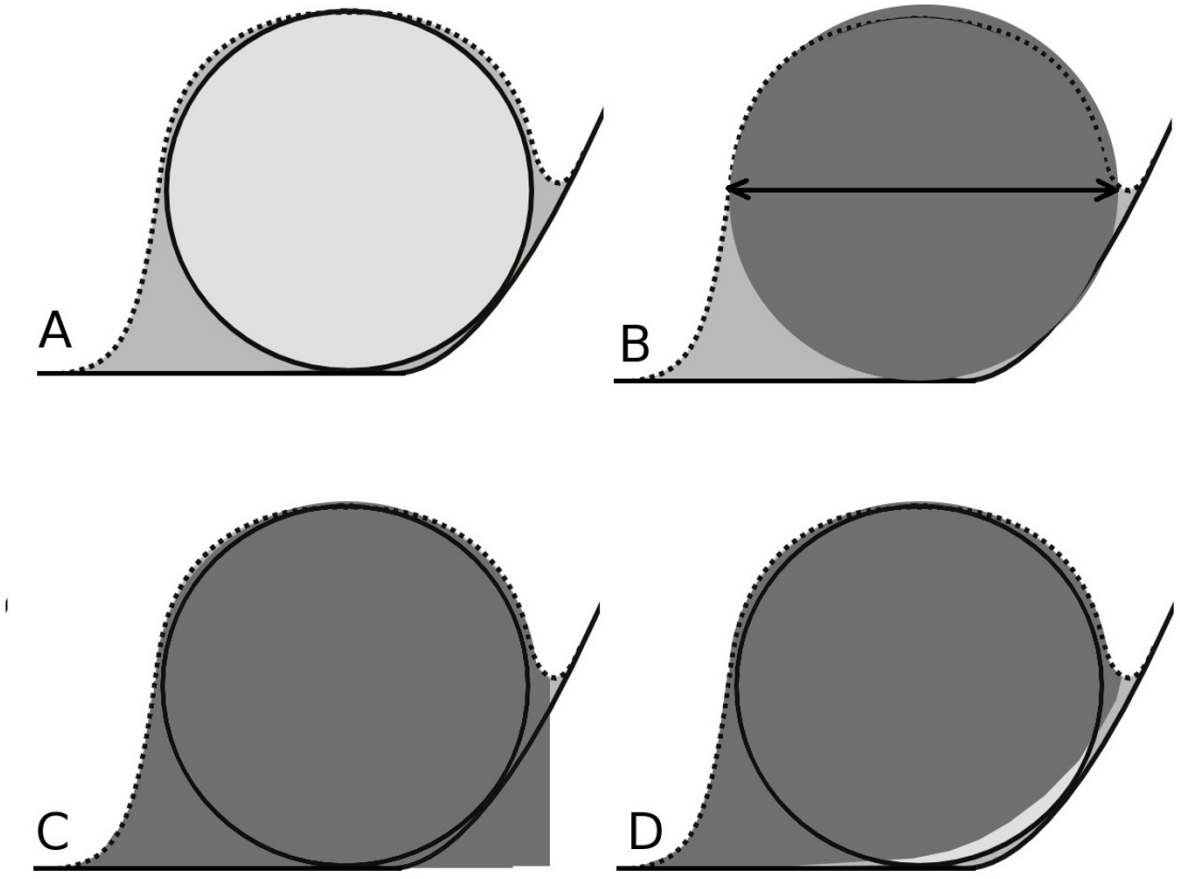


**Figure 3 Schematics of data processing methods**. Nanoparticle on curved substrate **(a)**. Solid lines denote the substrate and the nanoparticle, respectively, and the dotted line denotes the path of the AFM tip. The convolution effect on used data processing algorithms: **(b)**–nanoparticle projection, **(c)**– nanoparticle volume at minimum basis, **(d)**–nanoparticle volume at Laplacian basis. Light gray represents the nanoparticle. Medium gray shows the nanoparticle as seen by AFM (after tip convolution), dark gray represents volume determined by the data processing algorithm. Note that even Laplacian basis cannot properly determine the whole nanoparticle volume as the surface geometry below nanoparticle is unknown. As the power spectrum-based algorithm is a global one, it cannot be illustrated within this schematic figure.

watershed approach for image segmentation in this article.

The watershed algorithm is a relatively simple alternative to thresholding, providing much better segmentation on complex structures [30,31]. In this case, AFM data are first inverted in the $z$-direction. Virtual drops are then placed on the surface, leaving them to relax to minimum height, forming small "lakes." This is the first place (so-called location phase) after which the individual "lakes" are associated with a particle. After that, in the second phase (segmentation phase) the drops continue to be placed on the surface and relaxed, but unlike during the first phase, they are no longer allowed to merge. This leads to image segmentation. As a result, we obtain an image with marked individual grains.

The second stage is to convert marked grains into grain size distribution information of the nanoparticle characterization. We can divide the nanoparticle processing algorithms into three categories:

1. algorithms based on nanoparticle projection on the $xy$ plane. Even if this quantity can be highly affected by tip convolution, the effect of substrate curvature or particle agglomeration can be much smaller here than for height-based algorithms.

In this paper, this class of algorithms is represented by equivalent disk projection.

2. algorithms based on nanoparticle height or volume determination. For flat substrates and non-agglomerated particles, this class of algorithms leads to results that are not affected by tip-sample convolution effects. For curved substrates, they can differ in the treatment of the surface beneath the particle, which cannot be observed using the AFM. In this paper, this class of algorithms is represented by two methods–volume analysis using minimum boundary and Laplacian boundary method.

3. algorithms based on the statistical analysis of the whole measurement, e.g., autocorrelation function or power spectral density. These algorithms benefit from the self-organization of nanoparticles on substrate; in an ideal case, a honeycomb thin film is observed. In this work, power spectral density method is used.

There can be many varieties of details of the mentioned algorithms, providing slightly better or worse results in particular cases. In this article, we cannot discuss all of them. We aim to show the main trends in errors of different classes of algorithms under non-ideal conditions in order to estimate how much we can trust their results.

For nanoparticle radii evaluation, the following algorithms were used (all based on their Gwyddion implementation, see http://gwyddion.net):

- particle radius determined on the basis of equivalent disks (having the same area as the *xy* projection of particle). Here, the selected particle area (obtained from image segmentation, see above) is directly used as the particle cross-section. Particle volume is then calculated as volume of sphere having the same cross-section (see Figure 3b).
- particle radius determined on the basis of its volume with respect to its boundary minimum. Here, the particle boundary is obtained from image segmentation, and the minimum height value along this boundary is used as a lower boundary to measure the particle volume (see Figure 3c). A numerical correction by a factor of 0.8 is employed to remove the apparent volume below the particle due to projection. The factor of 0.8 is the ratio between sphere volume and the volume of the sphere together with its cylindrical projection to the substrate.
- particle radius determined on the basis of its volume with respect to Laplacian interpolation of its boundary. Here, the particle boundary is obtained by image segmentation, and Laplacian interpolation is run to obtain the morphology of the substrate below the particle (see Figure 3d). A numerical correction by a factor of 0.8 is employed to remove the apparent volume below particle due to projection.
- particle radius determined by radial power spectral density evaluation. Here, a 2D Fast Fourier transform is performed from the whole image, and the particle size is determined from the observed maxima in the resulting radial power spectrum, which in the ideal case of closely packed nanoparticles are directly connected with the size of the nanoparticle.

As shown in the next section, each of the algorithms has its own benefits and drawbacks with respect to the treatment of nanoparticle agglomeration, tip size, or surface roughness.

## Results and discussion

Typical examples of nanoparticle measurements are shown in Figure 1a-d, representing palladium and polymer nanoparticles of different surface coverages, deposited on a flat silicon and a rough (anodically etched) silicon surface. We can see that both substrate roughness and particle agglomeration can be easily seen on the AFM images.

We have simulated several sets of nanoparticles on rough substrates with variable roughness ($\sigma = 0 \div 10$ nm). This range was chosen in order to include typical surface morphologies observed on surfaces and thin films prepared by different technological methods [32,33]. Note that the surface root mean square value of 10 nm represents surface morphology with minimum to maximum range of some 100 nm, which is already a very high value (higher than the simulated nanoparticle size).

First, the nanoparticle coverage (ratio of sample area occupied by particles to total sample area) was varied, to include all the typical effects starting from isolated nanoparticles up to a substrate covered by several layers of nanoparticles. Secondly, the effects of relaxation and self-ordering of nanoparticles were studied, simulating the nanoparticles with same coverages but different mobility and relaxation parameters during deposition modeling.

In the following paragraphs, the effects of tip convolution on different nanoparticle processing and evaluation algorithms are discussed. For analysis, we have chosen three different AFM tips:

1. ideal tip, represented by a $\delta$-function (0 nm tip radius and slope of 90°), unavailable in practice but sometimes almost reached by carbon nanotubes - based tips [14,34].

2. sharpened tip with 10 nm tip radius and slope of 75°.

3. standard tip with 15 nm tip radius and slope of 57°.

In Table 1, results for the chosen data evaluation algorithms are presented. Values are calculated for different coverages (13, 50 and 140%), different AFM tips and different roughnesses ($\sigma$ = 0 and 10 nm). A nominal particle radius of 30 nm was used for the modeling, representing a value in the mid-range of the typical reference nanoparticles sizes. The maximum in the size distribution or in the power spectrum (determined using one of the algorithms mentioned above) was used to determine the mean nanoparticle size. Presented uncertainties are based on widths of appropriate distributions, so they do not contain any systematic error or other B-type uncertainty information [35]. We can see that for a flat substrate and an ideal tip, we get the nominal values (which could be expected); for a rough substrate or non-ideal tip values, we can see increasing differences between nominal values and results. Note that for some cases, there was no maximum observed in appropriate distribution and results could not be obtained.

We can discuss each algorithm performance more in detail separately, sorted by the amount of user influence on measurement results (which itself can affect the method reliability significantly):

• Particle projection: particle projection evaluation method is in principle only as good as the segmentation used. Even if the watershed approach is very robust itself, in the presence of voids between particles, there is a need of fine tuning of the algorithm parameters in order to get an optimum segmentation. Moreover, this algorithm is the one most influenced by tip convolution effects as the particle projection changes significantly after convolution (namely for isolated particles).

• Particle volume–boundary minimum basis: here, the influence of the tip convolution is smaller as the volume of particle changes relatively less than its projection. However, the location of the proper minimum on the particle boundary is crucial here and for densely packed particles, this algorithm fails. Here, the tip is no more able to reach the substrate at the voids between particles and detected boundary minimum is wrong, which leads to a distortion, namely for larger probes. Moreover, it can be expected that this algorithm is significantly affected by the local substrate slope (even for isolated nanoparticles) as the substrate slope is not employed in the evaluation (see Figure 3c).

• Particle volume–Laplacian boundary interpolation basis: this approach treats the substrate geometry in an optimum way for isolated particles, and it can therefore provide slightly better results for high substrate roughnesses than the previous one. However, for densely packed particles or wide tips, it also fails, as the tip does not reach the substrate, similarly as in the previous case.

• Power spectrum analysis: as for area analysis methods, this approach fails for small coverages and non-ideal tips namely. As the tip convolution increases, the apparent width of the nanoparticles increases and there is no packing effect to block this. Resulting radii are much higher than would be expected.

**Table 1 Nanoparticle radii results of nanoparticle radii simulated measurements for nanoparticles with nominal radius of 30 nm and different surface coverages.**

| | $\sigma$ = 0 nm | | | | $\sigma$ = 10 nm | | | |
|---|---|---|---|---|---|---|---|---|
| | **Pow** | **Min** | **Lap** | **Disk** | **Pow** | **Min** | **Lap** | **Disk** |
| C1, tip 1 | 32 ± 2 | 30 ± 1 | 30 ± 1 | 30 ± 1 | 33 ± 1 | 30 ± 3 | 30 ± 1 | 30 ± 1 |
| C1, tip 2 | 37 ± 7 | 34 ± 1 | 34 ± 1 | 44 ± 2 | 44 ± 20 | 33 ± 5 | 32 ± 4 | 41 ± 3 |
| C1, tip 3 | N. A. | 33 ± 3 | 33 ± 3 | 52 ± 5 | N. A. | 34 ± 6 | 34 ± 5 | 55 ± 9 |
| C2, tip 1 | 32 ± 1 | 30 ± 1 | 30 ± 1 | 29 ± 1 | 33 ± 2 | 30 ± 2 | 30 ± 1 | 30 ± 1 |
| C2, tip 2 | 38 ± 5 | 29 ± 3 | 25 ± 4 | 36 ± 3 | 38 ± 4 | 30 ± 5 | 28 ± 4 | 38 ± 6 |
| C2, tip 3 | 37 ± 6 | 28 ± 5 | 22 ± 6 | 38 ± 3 | 38 ± 8 | 26 ± 6 | 22 ± 7 | 38 ± 5 |
| C3, tip 1 | 30 ± 1 | 30 ± 1 | 30 ± 7 | 30 ± 1 | 31 ± 2 | 30 ± 2 | 28 ± 3 | 30 ± 1 |
| C3, tip 2 | 31 ± 3 | 31 ± 2 | 24 ± 6 | 34 ± 4 | 34 ± 2 | 28 ± 6 | 23 ± 7 | 34 ± 5 |
| C3, tip 3 | 34 ± 5 | 29 ± 5 | 21 ± 7 | 37 ± 5 | 33 ± 12 | 23 ± 8 | 17 ± 9 | 33 ± 7 |
| C4, tip 1 | 31 ± 1 | N. A. | 25 ± 4 | 29 ± 1 | 35 ± 5 | 29 ± 9 | 22 ± 8 | 28 ± 2 |
| C4, tip 2 | 30 ± 1 | N. A. | 19 ± 6 | 31 ± 3 | 31 ± 4 | 23 ± 12 | 18 ± 10 | 30 ± 8 |
| C4, tip 3 | 29 ± 1 | N. A. | 16 ± 5 | 36 ± 4 | 31 ± 4 | N. A. | N. A. | 30 ± 9 |

(C1: 13%, random, C2: 50%, random; C3: 50%, self-organized; C4: 140% self-organized) and different AFM tips (tip1: ideal, tip2: sharpened, tip3: standard; see text for details).

Power spectrum (pow), minimum basis volume (min), Laplacian basis volume (lap) and *xy* projection (disk) methods were used. All values are in nanometers. Total number of deposited particles was approximately 50 (C1), 180 (C2, C3) and 400 (C4)

However, for dense packing this method seems to be quite robust, even for higher surface roughness. The main benefit of this method is that is does not use any segmentation; therefore, the amount of user influence is the smallest of all the discussed approaches.

As seen from the table, generally the particle volume -based methods are only suitable for small coverages, where they produce reasonable results even for rough substrates. With higher packing of particles or smaller AFM tip side slope, the tip cannot reach the void volume between particles, which leads to a loss of information. Volume or height analysis methods are most sensitive to this effect.

For power spectrum and particle projection methods, the densely packed particles are an ideal measurand. However, even for isolated nanoparticles, these methods can be very effective if the AFM tip is sharp enough.

For all the methods based on image segmentation, the effect of the roughness can be highly suppressed by using a proper segmentation technique. Thresholding can be effective only for an extremely small roughness or substrate curvature. With a robust implementation of any more complex technique, e.g., the watershed algorithm, the effect of substrate irregularities can be highly suppressed.

As a real example, the self-organized nanoparticle film presented in Figure 1d was analyzed using all the mentioned algorithms. The nominal particle diameter of NIST traceable polymer nanoparticles was (46 ± 2) nm, i.e., the particle radius was 23 nm. They were deposited on a flat silicon substrate forming a film of unknown thickness and measured using a standard AFM tip. The resulting radii were (23 ± 3) nm for the equivalent disk radius method (particle projection), (11 ± 8) nm for the minimum basis grain volume method, (8 ± 8) nm for the Laplacean basis grain volume method and (24 ± 2) nm for the power spectrum analysis method. We can see that similarly to the modeling results, the particle projection and power spectrum method provide significantly better results for this type of sample.

## Conclusion

In this article, the results of simulated nanoparticle measurements are presented. Nanoparticles are located on rough substrates, in some cases forming self-organized structures or even several layers. In this way, we simulate typical non-ideal conditions observed at nanoparticle measurement using atomic force microscopy. To treat different tip convolution effects, nanoparticles are convolved with several typical AFM tip geometries. Results of different nanoparticle analysis algorithms are compared and discussed.

It is shown that for isolated nanoparticles, height-based algorithms can be successful if the area below the nanoparticle is properly treated, both for flat and rough substrates, providing no systematic errors and uncertainties in the range of a few percents. However, for agglomerated nanoparticles or blunt AFM tips, these algorithms provide poor results and this effect is even worse for rough surfaces; in this case, the errors are comparable to estimated values.

For agglomerated particles, methods using lateral dimensions, both power spectrum -based and particle projection -based methods are very effective, even for rough substrates. These methods can provide results with uncertainty of a few percents and no systematic errors.

The worst case was observed for non-agglomerated nanoparticles with surface coverages between 30 ÷ 80%, where all classes of algorithms provide systematic errors and uncertainties larger than 10%. Here, a combination of all the approaches must be used and results must be interpreted very carefully.

It is shown that using a simple particle deposition modeling technique, together with a tip-sample convolution algorithm, one can get relatively easily estimates of uncertainty components related to data processing methods in nanoparticle analysis. This can be also understood as a fast approach for uncertainty estimation in any particular case in practice. The method described is implemented in the open source software package for SPM data analysis Gwyddion http://gwyddion.net.

**Acknowledgements**

This work was supported by the Grant Agency of the Czech Republic under contract 203/08/1594 and by EURAMET joint research project "Traceable measurement of nanoparticle size" funded from the European Union's Seventh Framework Programme, ERA-NET Plus, under Grant Agreement No. 217257.

**Author details**

[1]Czech Metrology Institute, Okružní 31, 638 00, Brno, Czech Republic [2]Department of Physical Electronics, Faculty of Science, Masaryk University, Kotlářská 2, 611 37 Brno, Czech Republic [3]Faculty of Chemistry, Brno University of Technology, Purkyňova 118, 612 00 Brno, Czech Republic

**Authors' contributions**

PK carried out nanoparticle simulations and statistical quantities evaluation and interpretation, MV performed atomic force microscopy measurements, DN wrote software routines for nanoparticle statistical analysis, OS and PD prepared nanoparticle samples. All authors read and approved the final manuscript.

**Competing interests**

The authors declare that they have no competing interests.

Received: 15 October 2010 Accepted: 30 August 2011
Published: 30 August 2011

**References**

1. Balamurugan A, Ho KC, Chen SM: **One-pot synthesis of highly stable silver nanoparticles-conducting polymer nanocomposite and its catalytic application.** *Synth Met* 2009, **159**:2544-2549.
2. Brigger I, Dubernet C, Couvreur P: **Nanoparticles in cancer therapy and diagnosis.** *Adv Drug Deliv Rev* 2002, **54**:631-651.
3. Pradeep T, Anshup : **Noble metal nanoparticles for water purification: A critical review.** *Thin Solid Films* 2009, **517**:6441-6478.
4. Lee L, Zeng C, Cao X, Han X, Shen J, Xu G: **Polymer nanocomposite foams.** *Compos Sci Technol* 2005, **65**:2344-2363.
5. Liu W: **Nanoparticles and Their Biological and Environmental Applications.** *J Biosci Bioeng* 2006, **102**:1-7.
6. Zanetti-Ramos BG, Fritzen-Garcia MB, Schweitzer de Oliveira C, Pasa AA, Soldi V, Borsali R, Creczynski-Pasa TB: **Dynamic light scattering and atomic force microscopy techniques for size determination of polyurethane nanoparticles.** *Mat Sci Eng* 2009, **C 29**:638.
7. Bootz A, Vogel V, Schubert D, Kreuter J: **Comparison of scanning electron microscopy, dynamic light scattering and analytical ultracentrifugation for the sizing of poly(butyl cyanoacrylate) nanoparticles.** *Eur J Pharm Biopharm* 2004, **57**:369-375.
8. Brar SK, Verma M: **Measurement of nanoparticles by light-scattering techniques.** *Trends Anal Chem* 2011, **30**:4-17.
9. Yu L, Andriola A: **Quantitative gold nanoparticle analysis methods: A review.** *Talanta* 2010, **82**:869-875.
10. Henry CR: **Morphology of supported nanoparticles.** *Prog Surf Sci* 2005, **80**:92.
11. Maurya A, Chauhan P: **Structural and optical characterization of CdS/TiO2 nanocomposite.** *Mat Charact* 2011, **62**:382-390.
12. Ramallo-Lopez J, Giovanetti L, Craievich A, Vicentin F, Jose-Yacaman M, Requejo F: **XAFS, SAXS and HREM characterization of Pd nanoparticles capped with n-alkyl thiol molecules.** *Physica B* 2007, **389**:150-154.
13. Lee I, Chan KY, Phillips DL: **Atomic force microscopy of platinum nanoparticles prepared on highly oriented pyrolytic graphite.** *Ultramicroscopy* 1998, **75**:69.
14. Lacava LM, Lacava BM, Azevedo RB, Lacava ZGM, Buske N, Tronconi AL, Morais PC: **Nanoparticle sizing: a comparative study using atomic force microscopy, transmission electron microscopy, and ferromagnetic resonance.** *J Magn Magn Mat* 2001, **225**:79.
15. Binning G, Quate CF, Gerber C: **Atomic force microscope.** *Phys Rev Lett* 1986, **56(9)**:930-933.
16. Theil Hansen L, Kühle A, Sørensen AH, Bohr J, Lindelof PE: **A technique for positioning nanoparticles using an atomic force microscope.** *Nanotechnology* 1998, **9**:337.
17. Ong QK, Sokolov I: **Attachment of nanoparticles to the AFM tips for direct measurements of interaction between a single nanoparticle and surfaces.** *J Colloid Interface Sci* 2007, **310**:385.
18. Vakarelski IU, Brown SC, Moudgil BM, Higashitani K: **Nanoparticleter-minated scanning probe microscopy tips and surface samples.** *Adv Powder Technol* 2007, **18**:605.
19. Klapetek P, Nečas D, Anderson C: **Gwyddion user guide.**[http://gwyddion.net].
20. Bonet F, Delmas V, Grugeon S, Urbina RH, Silvert PY, Tekaia-Elhsissen K: **Synthesis of monodisperse Au, Pt, Pd, Ru AND Ir nanoparticles in ethylene glycol.** *NanoStruct Mat* 1999, **11(8)**:1277-1284.
21. Yang HN, Zhao YP, Chan A, Lu TM, Wang GC: **Sampling-induced hidden cycles in correlated random rough surface.** *Phys Rev B* 1997, **56**:4224.
22. Ogura H, Takahashi N: **Scattering, Radiation and Propagation Over Two-Dimensional Random Surface.** *PIER* 1996, **14**:89.
23. Ding L, Davidchack RL, Pan J: **A molecular dynamics study of sintering between nanoparticles.** *Comp Mat Sci* 2009, **45**:247.
24. Rabani E, Reichman DR, Geissler PL, Brus LE: **Drying-mediated self-assembly of nanoparticles.** *Nature* 2003, **426**:271.
25. Campbellová A, Klapetek P, Valtr M: **Tip-sample relaxation as a source of uncertainty in nanoscale scanning probe microscopy measurements.** *Meas Sci Technol* 2009, **20**:84014.
26. Yao H, Guduru P, Gao H: **Maximum strength for intermolecular adhesion of nanospheres at an optimal size.** *J R Soc Interface* 2008, **5**:1363.
27. Villarubia JS: **Algorithms for Scanned Probe Microscope Image Simulation, Surface Reconstruction, and Tip Estimation.** *J Res Natl Inst Stand Technol* 1997, **102**:425.
28. Fritzen-Garcia MB, Zanetti-Ramos BG, de Oliveira CS, Soldi V, Pasa AA, Creczynski-Pasa TB: **Atomic force microscopy imaging of polyurethane nanoparticles onto different solid substrates.** *Mat Sci Eng C* 2009, **29**:405-409.
29. Tello M, Paulo AS, Rodríguez T, Blanco M, García R: **Imaging cobalt nanoparticles by amplitude modulation atomic force microscopy: comparison between low and high amplitude solutions.** *Ultramicroscopy* 2003, **97**:171-175.
30. Klapetek P, Ohlídal I, Franta D, Montaigne-Ramil A, Bonanni A, Stifter D, Sitter H: **Atomic force microscopy characterization of ZnTe epitaxial films.** *Acta Phys Slovaca* 2003, **53**:223.
31. Gélinas V, Vidal D: **Determination of particle shape distribution of clay using an automated AFM image analysis method.** *Powder Technol* 2010, **203**:254.
32. Klapetek P, Ohlídal I, Navrátil K: **Atomic Force Microscopy Analysis of Statistical Roughness of GaAs Surfaces Originated by Thermal Oxidation.** *Microchim Acta* 2004, **147**:175-180.
33. Franta D, Ohlídal I, Klapetek P, Pokorný P: **Characterization of the boundaries of thin films of $TiO_2$ by atomic force microscopy and optical methods.** *Surf Interface Anal* 2002, **34**:759-762.
34. Oikawa K, Kim H, Watanabe N, Shigeno M, Shirakawabe Y, Yasuda K: **Measuring the sizes of nanospheres on a rough surface by using atomic force microscopy and a curvaturereconstruction method.** *Ultramicroscopy* 2007, **107**:1061.
35. *ISO/IEC Guide 98-3:2008, Uncertainty of measurement–Part 3: Guide to the expression of uncertainty in measurement (GUM:1995)* .

doi:10.1186/1556-276X-6-514
**Cite this article as:** Klapetek *et al.*: Atomic force microscopy analysis of nanoparticles in non-ideal conditions. *Nanoscale Research Letters* 2011 **6**:514.

Catalysis Today 161 (2011) 97–104

Contents lists available at ScienceDirect

Catalysis Today

journal homepage: www.elsevier.com/locate/cattod

# Physical and chemical properties of titanium dioxide printed layers

Marcela Černá, Michal Veselý, Petr Dzik*

*Brno University of Technology, Purkynova 118, 612 00 Brno, Czech Republic*

ARTICLE INFO

*Article history:*
Received 21 June 2010
Received in revised form 12 October 2010
Accepted 7 November 2010
Available online 10 December 2010

*Keywords:*
Titanium dioxide
Sol–gel
Inkjet printing
Cracking
Polyethylene glycol

ABSTRACT

This study focuses on the preparation of the $TiO_2$ thin films from alkoxide solutions containing polyethylene glycol (PEG) as an anticracking agent by the sol–gel method on soda–lime glass plates. Sol application was carried out by inkjet printing using a modified office inkjet printer equipped with piezoelectric print head. The grey level of the printed image was varied in order to control the sol loading of the resulting printed pattern. The effect of PEG addition on the precursor and prepared layer properties was studied. Also, the influence of sol loading on physical properties and on photocatalytic activity of the printed layers was investigated. The thickness of prepared layer was studied by NanoCalc 2000 and the structure of prepared layers was evaluated by optical microscopy, AFM and SEM. The hydrophilic properties of $TiO_2$ thin films were studied by examining the contact angle of water on these films. Photocatalytic activity was investigated as a rate of 2,6-dichloroindophenol (DCIP) decomposition. In all cases, we prepared transparent thin layers of $TiO_2$ with varying thickness and surface morphology. PEG proved to be an efficient agent suppressing the formation of cracks.



## 1. Introduction

Photoinduced processes are studied in a manifold ways and various applications have been developed since their first description. Despite the differences in character and utilization, all these processes have the same origin. Semiconductors can be excited by radiation of higher energy than the band gap and an energy rich electron–hole pair is formed. This energy can be utilized electrically (solar cells), chemically (photochemical catalysis), or to change the catalyst surface itself (super-hydrophilicity).[1]

We concentrate on titanium dioxide, $TiO_2$, which is one of the most important and most widely used semiconductors. $TiO_2$ has received a great deal of attention due to its chemical stability, nontoxicity, low cost, and other advantageous properties. As a result of its high refractive index, it is used as anti-reflection coating in silicon solar cells and many thin-films optical devices [2].

$TiO_2$ can be deposited on a variety of substrates, such as glass, ceramics or metal panels. During the past two decades, many synthetic methods have been proposed to obtain mesoporous titanium dioxide including the sol–gel method, template method, hydrothermal method, solvothermal method, ultrasound-induced method, ion liquid method, and evaporation-induced self-assembly method [3–10]. Particularly, it has been reported that materials prepared by the sol–gel process are more bioactive than materials of the same compositions but prepared by other methods [11]. At the same time, templating has become one of the most attractive methods used to obtain porous structure [12]. In this work we prepared thin $TiO_2$ layers by inkjet printing. This method is quite attractive since it provides a great level of control over the layer formation process and the possibility to tune the composition of deposited films [13].

The photocatalytic activity of resulted $TiO_2$ film depends strongly on the crystal phase structures, thickness and porosity of the thin films. A highly porous surface structure is very imperative among these factors because it offers a much larger number of catalytic sites than a dense surface.

Porous inorganic $TiO_2$-anatase films can be obtained using templating membranes or conventional alkoxide sol–gel route with the addition of surfactants [14]. The templates permit to retain the initial polymer morphology up to the final porous structure. Polyethylene glycol is especially suitable for modifying the porous structure of coatings [15] due to its complete decomposition at relatively low temperature [16]. To prepare porous and thicker $TiO_2$ films, Miki et al. had developed the new precursor solution comprised of aqueous $TiO_2$ sol and PEG, into which trehalose dehydrate was added as a viscous solvent [17]. In this study, PEG functioned as a pore-forming agent. Kajihara and Nakanishi prepared thicker $TiO_2$ macroporous films from a system containing PEG and poly(vinylpyrrolidone) (PVP), where PEG also played the role of pore-forming reagent and PVP having higher molecular weight was used to increase the viscosity of the solution [18]. The formation of porous structure in $TiO_2$ thin films strongly depends on the amount and the molecular weight of PEG [19].

In recent studies, several authors reported that the introduction of PEG enhances the crystallite size while it reduces density of the crystallite compared to the $TiO_2$ film of the same thickness,

* Corresponding author. Tel.: +420 541 149 411; fax: +420 541 211 697.
*E-mail address:* petr@dzik.cz (P. Dzik).

0920-5861/$ – see front matter © 2010 Elsevier B.V. All rights reserved.
doi:10.1016/j.cattod.2010.11.019

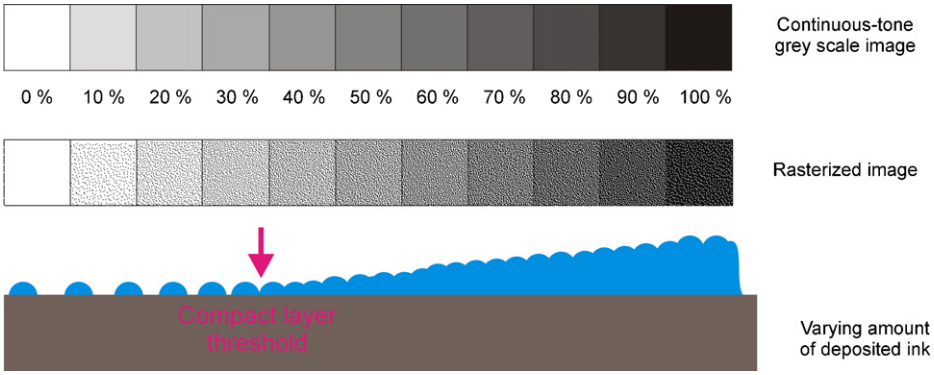


**Fig. 1.** Layer build-up for different values of sol loading.

prepared without PEG. It was also observed that PEG induced modification is a gradual change from dense, random structure to an early stage of porous network structure, where porosity and roughness increases continuously [20]. With increasing amount of added PEG also the hydroxyl group content of $TiO_2$ thin films increase and after adding suitable amount of PEG the photoinduced superhydrophilicity can be enhanced and it can caused forestalling of the conversion from the hydrophilic to the hydrophobic state [21].

However, the aim of this work was to investigate the photocatalytic activity of compact, nonporous $TiO_2$ thin films prepared with the addition of PEG as an anticracking agent.

## 2. Experimental

### 2.1. Synthesis of sol

The titanium dioxide sol was prepared using titanium(IV) isopropoxide (TTIP, p.a. purity, Fluka, Germany) as a precursor by the following route. Firstly, 40 mL of absolute ethanol (p.a., Penta, Czech Republic) was mixed with 3.8 mL of acetyl-acetone (p.a., Lachema, Czech Republic). This prepared mixture was added dropwise to TTIP under continuous stirring to control the hydrolysis and condensation reactions. This solution was maintained for a few minutes to obtain the complex chelate. Then absolute ethanol (45 $cm^3$) with 0.69 $cm^3$ of water was added drop by drop to the prepared mixture to start the hydrolysis and condensation reactions. Different amounts of PEG (p.s., Merck, Germany) with average molecular weight of 1500 were added to form the printing solutions (0, 1, 4, 16 g/L). Sol was the stored in darkness at the temperature 5 °C for a several days before it was deposited by inkjet printing.

The viscosities of prepared solutions were measured by automatic viscosimeter AVMn (Anton Paar). We observed a viscosity change as a function of the amount of present PEG. The densities were measured by densitometer DMA4500 (Anton Paar) and also in this case we observed the dependence of PEG amount on the results density. All measurements were performed at the temperature of 25 °C.

### 2.2. Coating deposition

Soda–lime glass plates with size 50 mm × 50 mm × 1.1 mm were chosen as substrates for the immobilization of $TiO_2$ thin films. Firstly, the glasses had to be pre-tread in sulphuric acid (50%, for 120 min) in order to prevent sodium ions diffusion, which would have caused a reduction of photocatalytic activity [22]. Subsequently, these plates were washed in a surfactant solution to remove of dust, grease and other residues, which might have collected during the storage of pre-treated glass plates.

Sol application was carried out by a novel innovative way utilizing a modified office inkjet printer (Epson R220). Firstly all original cartridges were removed and the ink tubing and printhead were purged by anhydrous propanol. This step is very important for removing any traces of remaining aqueous ink because if the sol came in contact with aqueous impurities the precipitated $TiO_2$ would clog the printhead nozzles.

Then the prepared sols were filtered through 0.45 μm mesh size syringe filter into the one of the ink cartridges, the other remained empty. The full cartridge was installed into the printer in the black position. After a series of head cleaning cycles a perfect nozzle check pattern was obtained. Since the sol is essentially colorless when viewed in daylight, the nozzle check printout had to be observed under a UV-A light source to prove all ink nozzles of the black channel were firing the loaded sol. Under this type of illumination, the printed sol appeared deep yellow while the paper was bright blue because of fluorescent brightening agents present in the paper [23]. Then the glass substrates were mounted into a modified CD holder, fed into the printer and printed with “black only” driver setting. It means that only the ink from the “black” cartridge (now containing titanium sol) was utilized for printing.

One of the inherent advantages of this method is that we can directly control the amount of the deposited sol (i.e. the sol loading) by changing the grey-scale level of the printed image. In Fig. 1 we can observe the creation of printed layer. The different grey levels (generally continuous tone bitmap) need to be converted into a halftone screen patter (planar distribution of dots). In the case of inkjet printing, a combination of amplitude modulation screening and frequency modulation screening is used: ink droplets of varying size are placed at different pitch. However, printing on non-porous, non-absorbing substrates results into a very high level of dot gain (the printed droplets spread on the substrate and their diameter is much larger than diameter of eject droplet which roughly corresponds to the nozzle diameter). Therefore, the printed substrate becomes completely covered by the ink at lower tonal vales (the compact layer threshold, see Fig. 1). Before this point, the substrate is covered by separate individual droplets. Beyond this point, the substrate is covered by varying amount of ink resulting into a compact layer of varying thickness.

In this work, three levels (100%, 90% and 80%) were used to give samples having three different thicknesses. Before the printing we had to also choose from three modes of the printer operation – “Slow, Medium and Rapid” [22]. Mode “Rapid” was chosen in this work. This mode means that the printhead runs very quickly above the glass surface and it prints continuously in both directions. Because the motion of the printhead and the sol deposition is very fast, the evaporation of the printed solutions takes after the printing phase is finished. Hence, in this way smooth and glossy layer of $TiO_2$ can be obtained.

Finally, the deposited layers were dried in an oven at temperature 110 °C for 30 min and consequently they were thermally treated in a calcinations furnace at 450 °C for 4 h with the ramp of 3 °C/min.

### 2.3. Characterization of prepared layers

The thickness of prepared thin films was determined by specular reflectance measurements using NanoCalc-2000 (Micropack, Germany). This method is based on the evaluation of how the film interacts with light. The main advantages of this method are accuracy, high speed, simplicity, non-destructive approach and no need of sample preparation.

The quality of prepared layers was investigated by optical microscope Nikon Eclipse E200. The records were obtained from a digital camera Nikon D70 mounted on the optical microscope. The influence of PEG and the sol loading on a cracking intensity were evaluated from the optical images.

The surface topology was studied by atomic force microscopy AFM. Veeco Di CP-II (Dymek, Japan) machine in a tapping mode was used for this purpose. SEM imaging was performed in Hitachi S4700 FESEM scanning electronic microscope.

The crystalline composition of $TiO_2$ thin films was determined by Raman spectroscopy. For this purpose we used LabRAM HR Jobin-Yvon Raman spectrometer. The argon–krypton laser RM 2018 (Spectra Physics) at 514.5 nm was used as the excitation source and laser power was kept at 1 mW.

The hydrophilic properties of prepared layers were studied by examining the contact angle of water on $TiO_2$ thin films. The determination was performed on the OCA20 (Dataphysics, Germany) by applying a sessile drop method. After the droplet deposition, its evolution was recorded by a CCD camera and the contact angle was obtained by the software processing the tangent method. Water droplets were placed at five different positions for one sample and average value was adopted as a contact angle. We investigated by this method, freshly prepared layers and also films, which were placed in the darkness for 10 days.

### 2.4. Photocatalysis

Photocatalysis experiments were performed in an aqueous solution of 2,6-dichloroindophenol (DCIP) with an initial concentration of $2 \times 10^{-5}$ mol/L. The photocatalysis reactor consists of two beakers, which were connected by a peristaltic pump. The samples were placed in one of the beaker and the other beaker was used a storehouse for DCIP. The UV irradiation was provided by high-pressure mercury lamp (OSRAM HQL 125W). This lamp had the same distance from the sample for all experiments. The intensity of UV light was 10 W/m$^2$ and it was measured by X97 Irradiance Meter with X9-7 probe.

A water cell was used to remove IR radiation. Before the reaction, each glass plate was irradiated for 10 min and then 2 mL of reaction solution was sampled every 5 min for UV–vis analysis.

## 3. Results and discussion

### 3.1. $TiO_2$ sols and films

Transparent thin films of photocatalytic $TiO_2$ were prepared using the sol–gel method. The sol was deposited onto the soda–lime glass plates by inkjet printing, gelled at 110 °C and calcinated at 450 °C. Four different concentration of PEG (0, 1, 4 and 16 g/L) denoted PEG 0, PEG 1, PEG 4, PEG 16 and three sol loadings (100%, 90% and 80%) were used.

The prepared sols were characterized by the investigation of their viscosity and density. Viscosity was measured during 17 days

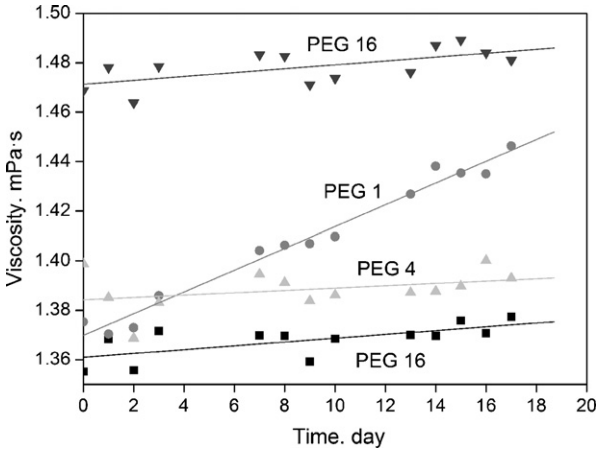


**Fig. 2.** Change of viscosity during 17 days.

**Table 1**
Density of prepared sols.

| Type of sol | Density (g/mL) |
|---|---|
| PEG 0 | 0.8193 |
| PEG 1 | 0.8196 |
| PEG 4 | 0.8208 |
| PEG 16 | 0.8263 |

because it was the maximal time for which all sols were stored before printing. We examined if the rheological properties are modified during this time. It was discovered that the viscosity was varied insignificantly (Fig. 2). From these results it was concluded that all sols can be stored for this time without change of their rheological properties.

After comparing the density of the solutions it was discovered that the density increases with increasing amount of PEG in samples. The exact values can be found in Table 1.

### 3.2. Characterization of prepared layers

We probed the dependence of PEG amount and sol loading on the final thickness of $TiO_2$ layers. It was discovered that there is not

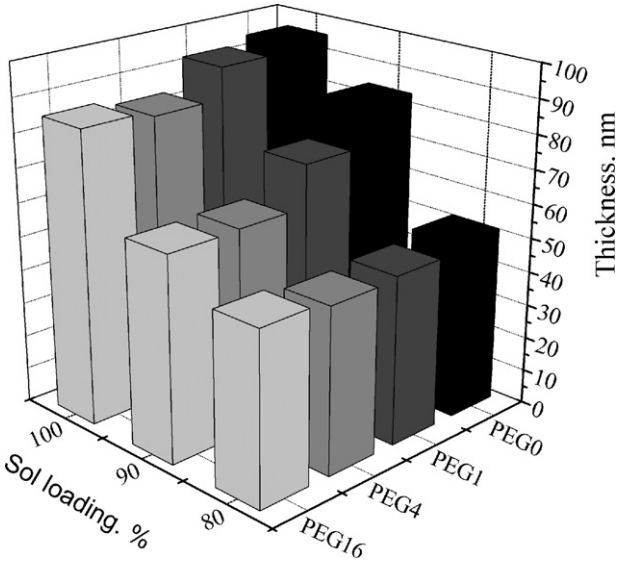


**Fig. 3.** The dependence of thickness of thin layers on the PEG amount for different sol loading.

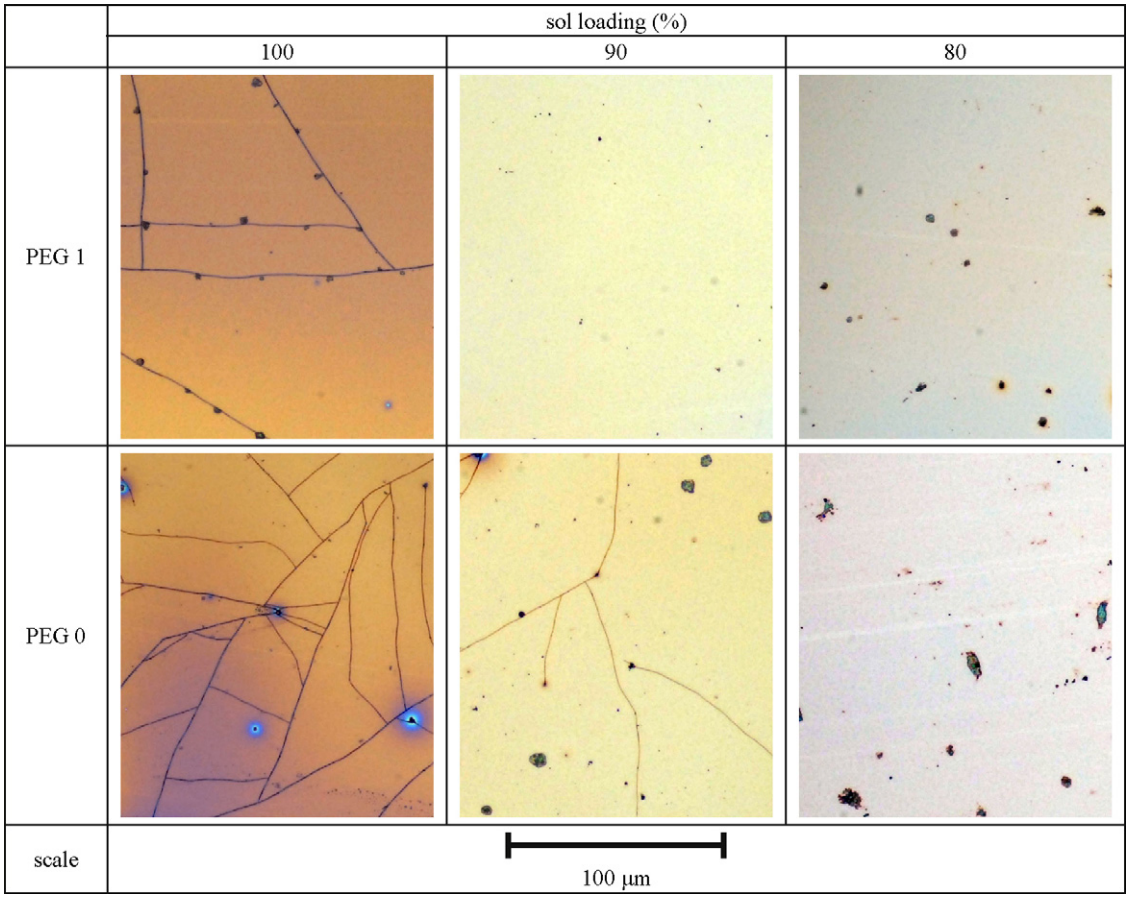


**Fig. 4.** The influence of sol loading on the cracking intensity.

a great difference between the samples PEG 0 and PEG 1. On the other side, there is a notable decreasing in the thickness for PEG 16 apparently caused by the removal of the organic matrix. With added PEG the viscosity is naturally changing. An increase of the viscosity would have a significantly influence in dip-coating and spincoating. However, based on our experience, the observed change of the viscosity does not affect the layer thickness of inkjet printed layers. Within the studied viscosity range, the droplets are formed in the same way, their amount and most important their volume is constant, so also the thickness of printed layer has to be independent on viscosity (but influenced by the organic matrix franction content). We also confirmed that with increasing sol loading the thickness of prepared $TiO_2$ layers increase. So the highest value was reached in 100% sol loading (Fig. 3).

The quality of prepared layers was investigated by optical microscopy. All samples were optically transparent and they adhered well to the glass substrate after the calcinations process. We found out that as the sol loading decreases (i.e. the layer thickness), so does the amount of cracks (Fig. 4). In case of 80% there were no cracks present. This cracking is caused by a tensile stress, which arises during the thermal treatment of layers.

When PEG was added to the sol, it induced a gradual suppression of cracking (Fig. 5). All cracks disappeared when the concentration of PEG reached 4 g/L. This was observed in all prepared samples.

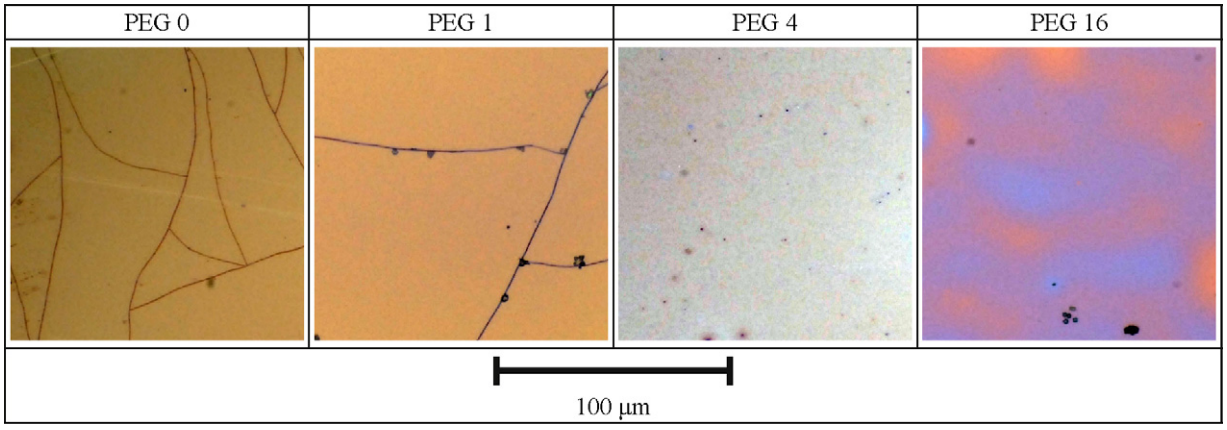


**Fig. 5.** The influence of PEG on the cracking intensity.

We believe the free volume created by PEG decomposition enables the stress-free arrangement of $TiO_2$ crystallites created during the calcinations step and in this way the formation of cracks is suppressed.

The surface topology was further studied by AFM microscopy. The influence of added PEG on the roughness of prepared films was evaluated. The results can be observed in Fig. 6. When we compare the roughness for the sample PEG 0 and PEG 16 (see the vertical scale) we can conclude that the roughness increases with increasing amount of PEG in the samples.

The SEM images (Fig. 7) give us a detailed look at appearance of the printed layer at the nanoscale. We can roughly estimate the size of primary crystallites to be approximately in the range of 30–50 nm. We can also clearly see that the way the primary cracks develop at the nanoscale is different: with the addition of PEG, the primary nanocracks are shorter and more frequent. We assume this contributes to better relaxation of tensional stresses occurring during the calcination of the layer and thus prevent the formation of larger microcracks. We also studied the thickness of the layers (Fig. 8) and we compared these results with results from specular reflectance measurement. Generally, we obtained higher values of thickness from SEM then from the optical measurement

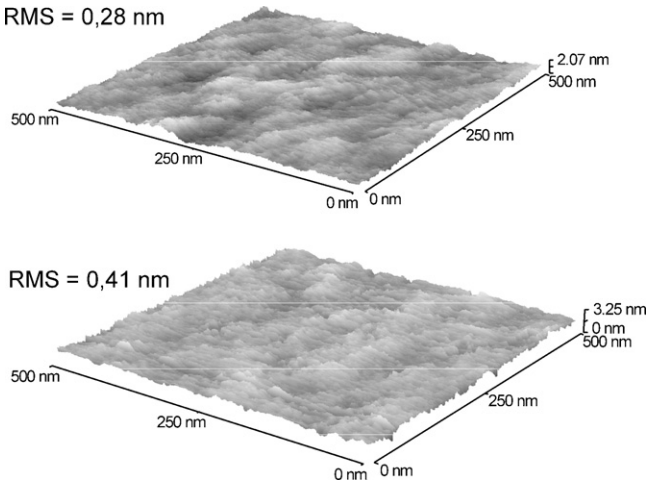


**Fig. 6.** The influence of PEG on the roughness of thin layers of PEG 0 (left) and PEG 16 (right).

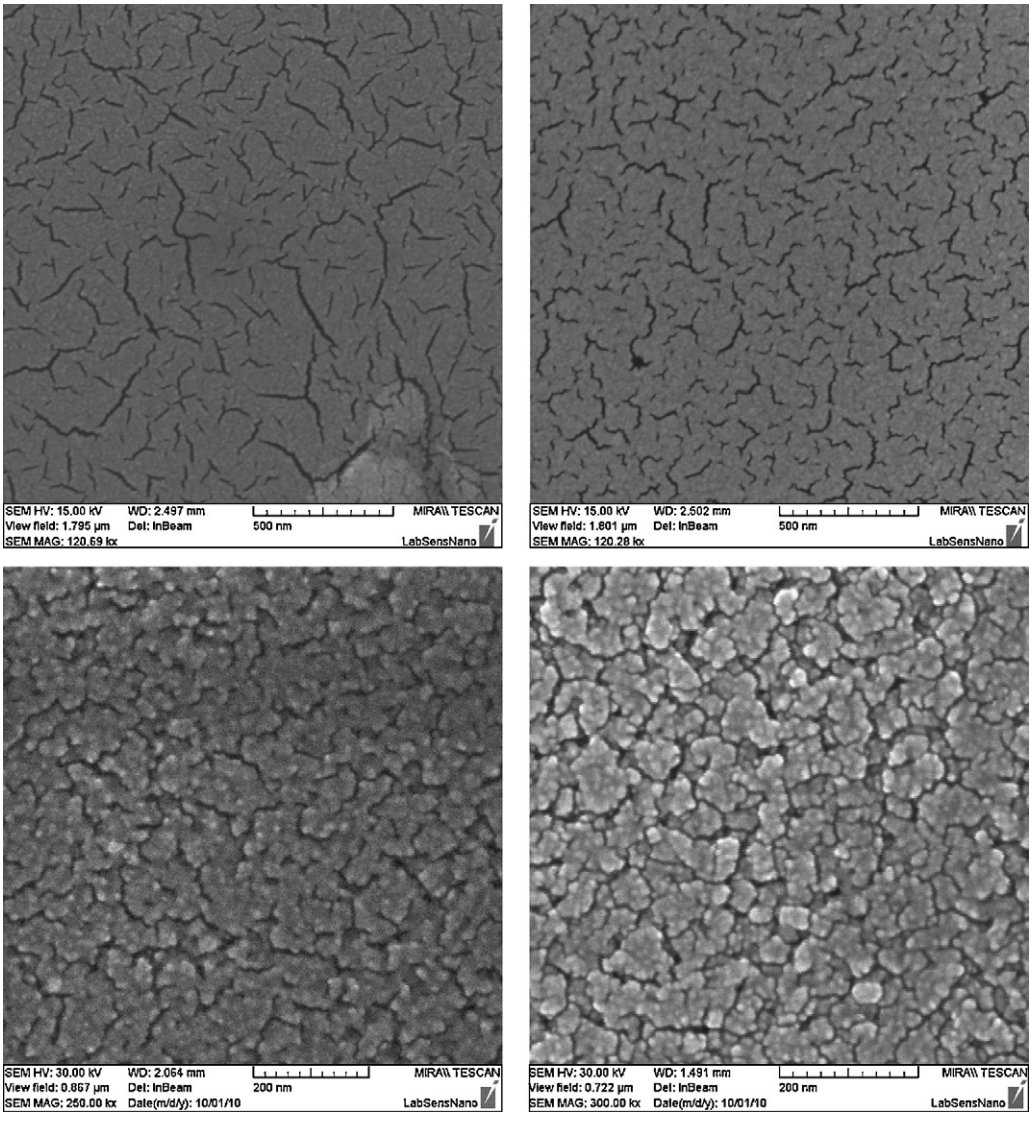


**Fig. 7.** SEM of the surface of $TiO_2$ thin films of PEG 0 (left) and PEG 16 (right).

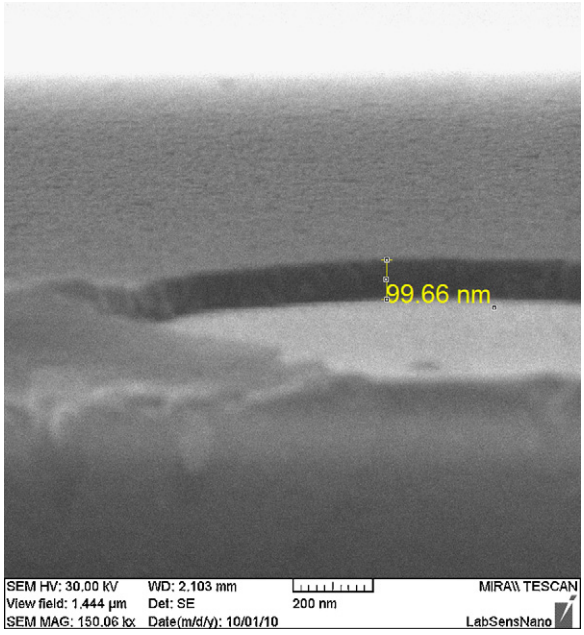


**Fig. 8.** Thickness of PEG 4 by SEM.

by NanoCalc. We believe this difference is caused by the porosity of prepared layers: Values from SEM give the real geometrical thickness of the layer, including voids, while the results from optical measurements give the net optical thickness of $TiO_2$ interacting with the probing beam. Of course, the actual refractive index porous layers will be lower then refractive index of bulk $TiO_2$. Also, other phenomena such as surface roughness may influence the results obtained from the optical method. Anyway, the optical measurement gives us a very easy way of comparing the relative thicknesses of studied layers.

Raman spectroscopy was employed to reveal the crystalline structure of prepared layers. In this particular case, the printed samples were compared to a dipcoated samples prepared using the same sol in order to see if the hydrodynamic stresses during printing have any impact on the crystalline structure of resulting $TiO_2$ (Fig. 9). It has been described that $TiO_2$ has 4 active Raman modes in rutil phase, ($A_{1g}$, $B_{1g}$, $B_{2g}$ and $E_g$), 6 for anatase ($A_{1g}$, $2B_{1g}$ and $3E_g$) and 36 for brookite (61, 62). Indeed, Raman spectra can be influenced by chemical and structural defect causing shift in Raman band positions. Recorded spectra of the sol–gel originated $TiO_2$ (both printed and dip-coated) were compared with the spectrum of Degussa P-25 as the *de-facto* industrial standard of photocatalytic

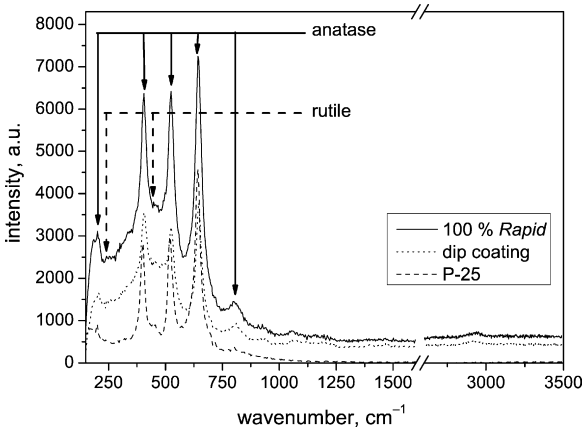


**Fig. 9.** Comparison of Raman spectra of Degussa P-25, dipcoated and printed sample.

**Table 2**
Raman bands identification.

| Phase | P-25 [cm$^{-1}$] | dip-coating, 2 layers (84 nm) [cm$^{-1}$] | 100% rapid printing [cm$^{-1}$] | Vibration mode |
|---|---|---|---|---|
| Anatase | 197 | 201 | 201 | $E_g$ |
| Rutile | – | 240 | 240 | – |
| Anatase | 401 | 401 | 401 | $B_{1g}$ |
| Rutile | 444 | 436 | 436 | $E_g$ |
| Anatase | 517 | 521 | 521 | $A_{1g}$, $B_{1g}$ |
| Anatase | 642 | 642 | 646 | $E_g$ |
| Anatase | 800 | 807 | 803 | $B_{1g}$ |

$TiO_2$. Our spectra confirmed the presence of anatase phase with a small portion of rutile [23] (Table 2).

The hydrophilic properties of prepared layers were evaluated by measuring the water contact angle as a function of the incident UV light exposure dose. All freshly prepared films showed hydrophilic properties. However, after placing these samples to the darkness for 16 days, we found out that the contact angle grew up in all studied thin films. For example, the contact angle for water on the PEG 1 grew up to 50° after 16 days in the darkness. Obviously, after the irradiation of these films by UV light with intensity of radiation of 15 W/m$^2$ all samples were converted hydrophilic nature again.

This could be explained by two ways. One of them is that by UV illumination the holes are transferred to the surface, creating oxygen vacancies most likely at the two coordinated bridging sites, which are suitable for dissociative water adsorption. Photoproduced electrons are also transferred to the surface $Ti^{4+}$, forming $Ti^{3+}$ followed by the electron transfer to adsorbed oxygen molecules. [24,25]

But on the other site, recent communication by Yates and coworkers suggest that photoproduced hydrophilic behaviour on $TiO_2$ does not involve the production of surface oxygen vacancy defect sites, enhanced surface Ti–OH coverage on defect sites, or the modified surface bonding of bridging >OH groups. They explain the hydrophilic properties as the production of the critical surface condition at the perimeter of a water droplet, which covers a hydrocarbon-coated $TiO_2$ surface. And they discovered that gas-phase $O_2$ is necessary to cause the photoinduced hydrophilicity effect. [26]

Recently, it had been found that the contact angles for water on the porous $TiO_2$ films decreased with increasing of PEG [27]. This has been confirmed by our experiment: samples PEG 0 had the greatest contact angles. It could be caused by a smaller hydroxyl group content and smaller surface roughness since in this case water could not easily enter the interior region of the thin films. Previous studies report that larger amount of the added PEG caused higher roughness so also larger surface area. The coating films with larger surface area are more easily attacked by the water vapour to produce more hydroxyl groups. Hydroxyl groups existing in the coating films are attributed to the chemically adsorbed $H_2O$ and also some $H_2O$ is physically adsorbed on the surface of $TiO_2$ coating films. Generally, with the increase of chemically adsorbed hydroxyl groups on the surface, van der Waals forces and hydrogen bonds interactions between water and hydroxyl groups will be increased. Water can easily spread across the surface and the hydrophilic character will be enhanced [27].

The rate of conversion from hydrophobic to hydrophilic character of prepared layers was studied. In order to evaluate the contact angle changes upon UV irradiation, the relative change of contact angle has been plotted as a function of the irradiation time. The relative plot has been adopted to be able to compare the samples with different PEG content which showed different values of initial contact angle.

The smallest rate was observed for the samples PEG 0. On the other side, the highest value of conversion rate was observed in

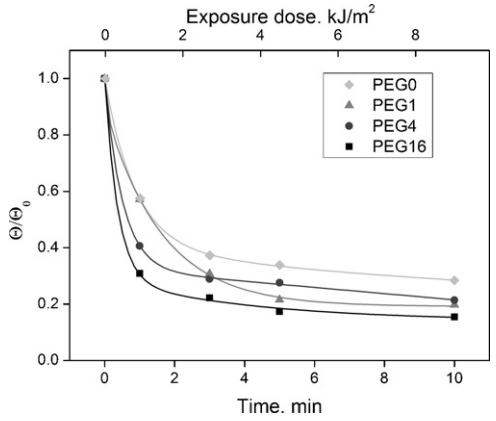


**Fig. 10.** Decreasing of water contact angle after 10 min of irradiation.

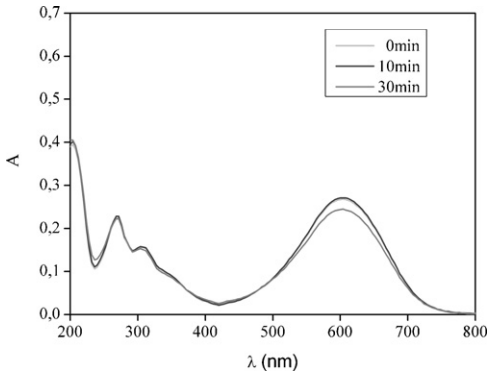


**Fig. 11.** Change of the absorption spectra of 2,6-dichloroindophenol during 30 min (blank).

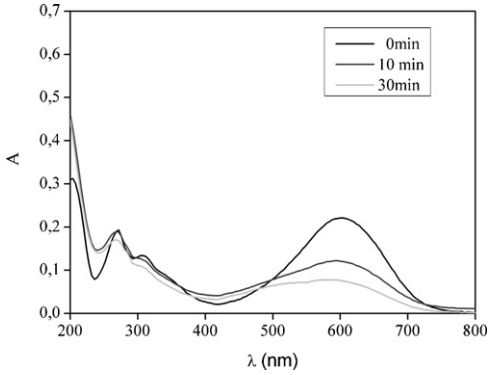


**Fig. 12.** Decreasing absorbance with irradiation time (PEG 16).

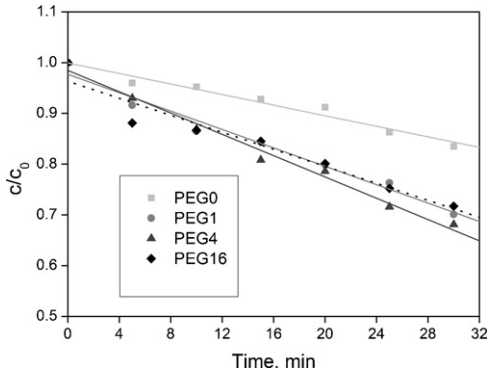


**Fig. 13.** Decreasing of 2,6-dichloroindophenol during first 30 min.

sample PEG 16 (Fig. 10). It can be explained by the different roughness of the samples, as the PEG 16 sample reached higher roughness (0.50 nm) than PEG 0 sample (0.32 nm).

### 3.3. Photocatalysis

The photocatalytic activity was evaluated as a rate of DCIP degradation realized in a batch reactor. The first step of the degradation is dechloration accompanied by discoloration. Then, the oxidation of carbon skeleton follows, leading to the creation of short carboxylic acids. Finally, these acids undergo decarboxylation and are totally cleaved. [28–30] The discoloration is naturally very easy to measure by UV–vis spectroscopy. This is very attractive from the practical point of view as inexpensive instrumentation can be used for the studying of photocatalytic efficiency. However, the authors are well conscious of the problems inherently associated with using any dye molecule for the photocatalytic testing: dye molecules can absorb photons, especially in the visible light range, and thus photoexcited electrons may be injected into the conduction band of $TiO_2$, and the dye is thereby oxidized. [31,32] From the scientific point of view, using simple molecules such as formic acid or dichloroacetic acid make much more sense [33].

Nevertheless, DCIP was chosen due to its very easy detection in the VIS range and a very low absorption at 360 nm wavelength. Moreover, an experiment with a blank (without photocatalyst) was carried out (Fig. 11). There was a little (up to 10%) decrease of absorbance of the blank due to direct photolysis. This value was subtracted from the final measured values to obtain the net photocatalytic efficiency.

DCIP has an absorbance maximum at 600 nm Fig. 12, the reduction rate of which reflects the photocatalytic reactivity of $TiO_2$ upon UV irradiation. The total reaction time for photocatalytic test was 30 min as this time was sufficient for a total decolorization of DCIP.

In Fig. 13 we can observe the profiles of the time-dependent photocatalytic reactivity of different $TiO_2$/PEG thin films. As we can observe, the absorbance of treated DCIP solution at 600 nm decreases with the irradiation time. We compared the photocatylytic efficiency of samples with and without PEG. We discovered that samples with PEG have higher photocatalytic activity than the sample without PEG. It can be accounted for the higher roughness of thin layers surface, which is created by the present of PEG.

Since the dependence of relative concentration on time is linear within the studied range, we assumed the zero order kinetics model for this part of the reaction coordinate. Therefore, the reaction rate is independent on the substrate concentration. It seems

**Table 3**
Rate constant and their standard errors.

| | 80% | | 90% | | 100% | |
|---|---|---|---|---|---|---|
| | $k$ ($\times 10^{-8}$), min$^{-1}$ | SE ($\times 10^{-8}$), min$^{-1}$ | $k$ ($\times 10^{-8}$), min$^{-1}$ | SE ($\times 10^{-8}$), min$^{-1}$ | $k$ ($\times 10^{-8}$), min$^{-1}$ | SE ($\times 10^{-8}$), min$^{-1}$ |
| PEG 0 | 0.88 | 0.13 | 0.89 | 0.07 | 0.89 | 0.07 |
| PEG 1 | 1.79 | 0.11 | 1.70 | 0.12 | 1.54 | 0.13 |
| PEG 4 | 1.41 | 0.22 | 1.64 | 0.08 | 1.82 | 0.06 |
| PEG 16 | 1.28 | 0.06 | 1.30 | 0.15 | 1.85 | 0.20 |

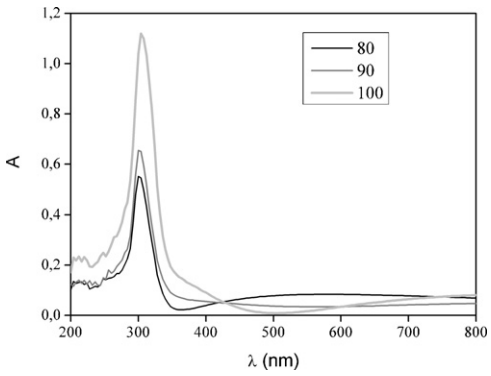


**Fig. 14.** UV–VIS absorption spectra for layers with different sol loading.

that the rate-determining step is therefore of other nature, such as the rate of electron–hole generation or the substrate delivery and/or removal from the catalyst interface. We calculated the reaction rate constants ($k$) and their standard errors (SE) for all prepared layers (Table 3).

Then we compared the influence of sol loadings on the photocatalytic reactivity of $TiO_2$ thin layers. We discovered that the samples with 100% sol loading were the most photocatalytically active. It can be explained by the effect of layers thickness, which is directly related to the value of sol loading.

Generally, when we consider a $TiO_2$ layer of sufficient thickness (100% layers), a complete absorption of incident radiation can be assumed. In this case, we can see a correlation between the initial drop spreading rate and the rate constants both as functions of PEG content: as the PEG content increases, both the rates increase as well. We assume that similarly to the situation with droplet spreading rate, the addition of PEG increases the surface RMS roughness, which also contributes to the increase in photocatalytic activity.

Such correlation was not observed in the case of thinner layers (80% and 90%). In this case, we do not see any direct influence of the PEG content or layer thickness on the reaction rate. We discovered that in this case the absorption of incident radiation is not complete (Fig. 14). Naturally, the efficiency of absorption can be influenced by other phenomena not identified in this study.

## 4. Conclusion

Transparent $TiO_2$ thin films were successfully prepared using PEG in a sol–gel system. The PEG plays a key role in stopping the generation of cracks in the layers during the annealing step at a high temperature. Sol coating on the substrate was performed in a novel way utilizing a modified office inkjet printer. This method often called “material printing” is very efficient, clean and superior to the traditional methods of spin- and dip-coating.

We discovered that the PEG concentration of 4 g/L is sufficient for suppressing the formation all cracks in the layers. When we compared the samples with and without PEG, we found out that with increasing amount of PEG the contact angle is decreasing and so is the value of its initial rate of droplet spreading. It is probably caused by increasing of the roughness with higher PEG concentration. Sample PEG 4 showed the best photocatalytic efficiency. When we compared different sol loading we discovered that the best sample is with 100% sol loading. In the case of thinner layers, the absorption of incident radiation was probably not complete and therefore no general trends were identified.

## Acknowledgements

Authors thank to Ministry of Education, Youth and Sports of Czech Republic for support by project OC10050 and the Czech Science Foundation for support through project 104/09/P165.

## References

[1] O. Crap, C.L. Huisman, A. Reller, Prog. Solid State Chem. 32 (2004) 33–177.
[2] H.A. Macleod, Thin Film Optical Filters, 2nd ed., Macmillan, New York, 1986, p. 370.
[3] R. Tan, Y. He, Y. Zhu, B. Xu, L. Cao, J. Mater. Sci. 38 (2003) 3973.
[4] C. Wang, Z. Deng, Y. Li, Inorg. Chem. 40 (2001) 5210.
[5] G.J.deA.A. Soler-Illia, A. Louis, C. Sanchez, Chem. Mater. 14 (2002) 750.
[6] J.C. Yu, L. Zhang, J. Yu, New J. Chem. 26 (2002) 416.
[7] K.S. Yoo, T.G. Lee, J. Kim, Micropor. Mesopor. Mater. 84 (2005) 211.
[8] C. Su, C.M. Tseng, L.F. Chen, B.H. You, B.C. Hsu, S.S. Chen, Thin Solid Films 498 (2006) 259.
[9] J. Jiao, Q. Xu, L. Li, J. Colloid Interface Sci. 316 (2007) 596.
[10] H.X. Li, Z.F. Bian, J. Zhu, D.Q. Zhang, G.S. Li, Y.N. Huo, H. Li, Y.F. Lu, J. Am. Chem. Soc. 129 (2007) 8406.
[11] P. Li, K. de Groot, J. Sol–Gel Sci. Technol. 2 (1994) 797.
[12] S. Bu, Ch. Cui, X. Liu, L. Bai, J. Sol–Gel Sci. Technol. 43 (2007) 151.
[13] M. Woodhouse, B.A. Parkinson, Chem. Mater. 20 (2008) 2495.
[14] N. Arconada, A. Durán, S. Suárez, R. Portela, J.M. Coronado, B. Sánchez, Y. Castro, Appl. Catal. B: Environ. 86 (2009) 1.
[15] K. Kajihara, T. Yao, J. Sol–Gel Sci. Technol. 17 (2000) 173.
[16] K. Kajihara, K. Nakanishi, K. Tanaka, K.K. Hirao, N. Soga, J. Am. Ceram. Soc. 81 (1998) 2670.
[17] T. Miki, K. Nishizawa, K. Suzuki, K. Kato, Mater. Lett. 58 (2004) 2751.
[18] K. Kajihara, K. Nakanishi, J. Mater. Res. 16 (2001) 58.
[19] S. Bu, Z. Jin, X. Liu, L. Yang, Z. Cheng, Mater. Chem. Phys. 88 (2004) 273.
[20] M. Arpi, B. Subhayan, H.M. Faruk, T. Takakazu, J. Phys. 100 (2008) 012006.
[21] J.C. Yu, J. Yu, H.Y. Tang, L. Zhang, J. Mater. Chem. 12 (2002) 81.
[22] Y. Paz, A. Heller, J. Mater. Res. 12 (10) (1997) 2759.
[23] P. Dzik, M. Veselý, J. Chomoucká, J. Adv. Oxid. Technol. 13 (2010).
[24] Y. Han, D. Chen, J. Sun, Y. Zhang, K. Xu, Acta Biomater. 4 (2008) 1518.
[25] T. Watanabe, A. Nakajima, R. Wang, M. Minabe, S. Koizumi, A. Fujishima, K. Hashimoto, Thin Solid Films 351 (1999) 260.
[26] T. Zubkov, D. Stahl, T.L. Thompson, D. Panayotov, O. Diwald, J.T. Yates Jr., J. Phys. Chem. B 109 (2005) 15454.
[27] J. Yu, X. Zhao, Q. Zhao, G. Wang, Mater. Chem. Phys. 68 (2001) 253.
[28] V. Brezova, M. Ceppan, M. Vesely, L. Lapcik, Chem. Pap. 45 (1991) 233.
[29] D.F. Ollis, Environ. Sci. Technol. 19 (1985) 480.
[30] R.W. Matthews, J. Chem. Soc. Faraday Trans. 1 85 (1989) 1291.
[31] B. Ohtani, Chem. Lett. 37 (2008) 217.
[32] H. Kisch, W. Macyk, ChemPhysChem 3 (2002) 399.
[33] J. Ryu, W. Choi, Environ. Sci. Technol. 42 (2008) 294.

# Thin Layers of Photocatalytic $TiO_2$ Prepared by Inkjet Printing of a Sol-gel Precursor

**Petr Dzik*,[1], Michal Veselý[1], and Jana Chomoucká[2]**

[1]Brno University of Technology, Faculty of Chemistry, Purkynova 118, 612 00 Brno, Czech Republic
[2]Brno University of Technology, Faculty of Electrical Engineering and Communication, Department of Microelectronics, Údolní 53, 60200 Brno, Czech Republic

## Abstract:

Transparent thin layers of photocatalytic $TiO_2$ were prepared using conventional sol-gel chemistry and a promising method of sol delivery to the substrate. Prepared sol based on tetraisopropoxy titanate and acetylacetone was loaded into a modified office inkjet printer equipped with piezoelectric print head. Sol was then printed onto pyrex glass plates, gelled at 110 °C and calcinated at 450 °C. Thus we prepared transparent thin layers of $TiO_2$ of varying thickness and surface morphology. Structure of prepared layers was studied using optical microscopy, SEM and AFM. Layer thickness and crystalline phase structure were also determined. Photocatalytic performance was evaluated by the rate of DCIP decomposition and surface properties were studied by water droplet contact angle change. In this way we were able to prepare thin layers of $TiO_2$ with excellent optical properties and photocatalytic performance comparable to dip- or spin-coated layers. Inkjet printing proved to be very elegant and clean method for sol deposition. Unlike the traditional methods of dip- and spin-coating, inkjet printing gives the user a great level of control over the deposition process, provides excellent efficiency of precursor use and easy scalability.

## Introduction

Photocatalysis on $TiO_2$ has received much attention during the last two decades. If $TiO_2$ absorbs a quantum of UV radiation of sufficient energy ($\lambda < 380$ nm) (1), an electron is excited into the conduction band and an electron-hole pair is created (2, 3). The potentials of electron and hole are strong enough to oxidize water to hydroxyl radicals and reduce molecular $O_2$. Resulting reactive oxygen species (ROS) are very powerful oxidizing agents and readily attack any organic matter in their proximity until it is totally cleaved to $CO_2$ and water (4-6). Numerous applications utilizing this process for water purification (7), toxic waste treatment (8), air purification (9, 10) and deodorizing have been proposed and some of them already successfully marketed. The same process can be applied for the design of self-cleaning (11-13) and self-disinfecting surfaces. Moreover, the oxygen vacancy creation and subsequent photo-corrosion on irradiated surfaces of $TiO_2$ convert the surface nature to superhydrophilic one, which further enhances its self-cleaning ability (14-16).

Photocatalytic systems based on slurryied powder of $TiO_2$ offer excellent performance due to their very high catalyst surface area (17). Upon immobilization, the free surface of catalyst inevitably decreases, resulting into a loss of catalytic performance due to limited mass exchange (18). Nevertheless, immobilized $TiO_2$ is the preferred form of photocatalyst for industrial application. The need of removing powder photocatalyst can prohibitively complicate any process at the industrial scale (19).

So far, several forms of immobilized $TiO_2$ were reported, featuring glass (20), quartz (21), stainless steel (22), silica gel (23), and many other materials as support. There are many methods of $TiO_2$ powder immobilization, such as suspension dip-coating, electrophoretic coating (22), spray coating (24, 25), etc. However, inferior optical and mechanical properties or resulting films restrict the use of these materials only to some type of applications, such as photocatalytic reactors.

Sol-gel technique represents a totally different approach to the preparation of $TiO_2$ thin layers. Sol-gel is one of the most successful techniques for preparing nanosized metallic oxide materials with high photocatalytic activities (26, 27). By tailoring the chemical structure of primary precursor and carefully controlling the processing parameters, nanocrystalline products with very high level of chemical purity can be achieved. In sol-gel processes, $TiO_2$ is usually prepared by the reactions of hydrolysis and polycondensation of titanium alkoxides, Ti(OR)n to form oxopolymers, which are then transformed into an tridimensional network (28, 29).

*Corresponding author; E-mail address: petr@dzik.cz

**Table 1.** Comparison of deposition techniques (adopted from (36), modified)

| | Spin | Dip | Inkjet |
|---|---|---|---|
| Precursor use efficiency | ~95 % wasted | ~95 % wasted | ~5 % wasted (print head cleaning and purging) |
| Coated area | ~ cm | ~ dm | ~ m |
| Sensitivity to surface defects | high | high | low |
| Possibility of "patterning" | none | none | excellent |

In this way, thin, compact and transparent layers of preferably photocatalytically active $TiO_2$ can be conveniently produced. Such layers find their use in the design of "smart" surfaces, such as self-cleaning glass sheets and tiles (30), mirrors with antifogging effect (31), self-disinfecting material etc (32). However, a suitable method for liquid sol application is needed in order to obtain a thin layer with excellent properties.

There are two traditional method of thin layer preparation from liquid precursors: spin-coating and dip-coating. Spin-coating method uses centrifugal force to form a film of liquid precursor: a sufficient volume of precursor is placed onto the support which is then rotated at a high speed (33). The liquid is spread by centrifugal force and a wet film of precursor is formed. The thickness of the resulting wet film depends mainly on the angular velocity of substrate rotation, precursor viscosity, precursor concentration and solvent evaporation rate (34). In contrary, dip coating is based on dipping the substrate into liquid precursor and pulling it out at constant speed (35). Again, viscosity, concentration, solvent volatility and speed of pulling influence the resulting film thickness. The faster we pull, the thicker the film is.

Both these methods are widely used, yet they are burdened by several significant disadvantages, as summarized in Table 1. Firstly, the coated area is rather limited. In the case of spin coating, this limitation is due to the centrifugal force. Substrates larger than a few centimeters simply can not be rotated at several thousands rpm. The area of dip coated substrates is usually also limited to centimeter scale, although devices handling large substrates up to meter size are known. Secondly, the efficiency of precursor use is extremely poor. In both spin- and dip-coating, most of the precursor is wasted, and only few percents are actually used to build up the film. Moreover, dip-coating gives us substrates coated from both sides, which is not always desired. Thirdly, both these methods are very sensitive to surface defects. A surface defect can produce traces and streaks and degrade large areas of coated substrate. At last, these classic methods on their own are not capable of selective deposition ("patterning"), i.e. the whole area of substrate is coated.

Because of these problems and limitations, a more robust method of liquid precursor application has been searched for. Inkjet printing is apparently a very good candidate for this task. In a conventional inkjet printer, small droplets of low viscosity ink are ejected from a print head and fall onto printed substrate (37). The movement of the print head and the substrate is precisely controlled by computer and so is the volume of ejected droplets and their loading per unit area. If we are able to replace the ink with a $TiO_2$ precursor and the printing paper with suitable substrate, we obtain a very robust device for preparation of $TiO_2$ layers.

Naturally, both the printer and precursor must fulfill certain requirements in order to be employed as a thin layer deposition tool. The printer has to be able to handle rigid media so that solid materials can be used as layer support. The precursor must be of a very low viscosity (less than 20 mPa.s) and must not damage the printer. If solid particles are present in the precursor, their diameter must be well below (preferably by two orders of magnitude) the print head nozzle diameter (50–20 μm typically) and their aggregation must be prevented. Despite these limitations, inkjet printing has been successfully used for the deposition of a wide variety of functional liquids so far, such as conducting polymers (38, 40), metallic nanoparticles dispersions (41, 42), metallic precursor solutions (43), catalyst nanoparticles dispersions (44) etc. Numerous applications of inkjet printing have been reported in the biochemical domain, such as tissue scaffolds (45, 46) or cellular patterns (47, 48). Moreover, many prototype multicomponent devices such as capacitors (49), transistors (50), electronic filter (51) and OLEDs (36) have also been successfully fabricated.

So far, a huge amount of information has been published on the photocatalytic process on $TiO_2$ and preparation of titania layers, but very little on the possibilities of inkjet printing such layers. Keat et al. reported printing aqueous mixture of $TiO_2$ sol and dissolved barium salts to prepare BaTiO3 thin ceramic films (52). Recently, Nishimoto published a five-step procedure for the preparation of a superhydrophobic-superhydrophilic pattern on a $TiO_2$ layer (53). However, in this particular example aimed to the graphic

arts application field the $TiO_2$ sol is deposited on the whole surface of substrate by dip coating and a temporary optical mask is inkjet printed onto the substrate.

Matsuo and coworkers utilized inkjet deposited sol-gel precursor for the preparation of titania layers. Their somewhat complex approach included a two-step preparation of the printing "ink" (sol based on titanium tetraisopropoxide, ethanol and nitric acid was evaporated and then re-dissolved in a mixture of ethanol and water to give 0.02 M concentration). Printing was performed by a single jet piezo device onto substrate heated to 275 °C. Printed films reached 420 nm thickness and showed broader and higher wave-number shifted Eg raman peak due to smaller crystallite size or some other defects (54).

Yoshimura and Gallage further developed the idea of "direct patterning" by utilizing inkjet printing as the precursor delivery tool. They proposed several possible pathways leading to ceramic films, distinguishing between "inkjet reaction", "inkjet deposition" and "inkjet printing" methods. However, in their illustrative example, the preparation of $TiO_2$ films still required printing onto heated substrate (55).

On contrary to the mentioned functional layers, pigment-grade titania has been *printed* for ages (56) and inkjet-printed on a massive scale for the past decade. In the field of graphic arts industry, $TiO_2$ derived pigments are used mainly in white primer coatings. The relative printing density and color brightness is often insufficient when a colored or transparent substrate is printed. In these cases, it is advantageous to print an opaque white mask first and then overprint the colored figures over this primer (57, 58). This technique is especially useful for the UV-curable inkjet, because the pigment loading is limited by viscosity requirements and white backing layer is essential for all non-white substrates (59).

In this letter, we demonstrate the benefits of using inkjet printing for the preparation of $TiO_2$ layers. By utilizing the well know sol-gel chemistry (used so far mostly for spin- and dip coated layers of $TiO_2$) together with the wide deposition possibilities offered by inkjet printer, we are able to prepare thin layers of $TiO_2$ in a very effective and clean way with minimum waste.

## Experimental

### *Sol and Substrate Preparation*

Sol-gel technique was applied for titanium dioxide thin films preparation using titanium(IV) propoxide as titanium precursors. 40 ml of ethanol was mixed with 3.8 ml acetylacetone. This mixture was then dropwise added to 10.3 ml titanium (IV) tetraisopropoxide (TTIP). Finally, 45 ml of ethanol was mixed with 0.69 ml water and this mixture was again dropwise added to the sol composition. Prepared sol was stored in an airtight bottle in darkness at 5 °C. The dynamic viscosity of prepared sol was 1.23 mPa.s.

Borosilicate glass plates of 30×30×2 mm size (Verre Equipements, France) were chosen as the substrate for immobilization of $TiO_2$ thin films. This type of glass contains only 4.2 wt.% $Na_2O$ and 0.1 wt.% of CaO. Before the application of the thin films, each glass was pre-treated in order to eliminate any dust, grease and other residues using an aqueous solution of industrial surfactant and dried under air flow.

### *Sol Application*

Sol Application was performed in a novel innovative way utilizing a modified office inkjet printer (Epson R220). Original ink cartridges were removed from the printer and the ink tubing and printhead were flushed and purged with anhydrous propanol. Flushing with anhydrous propanol is extremely important in order to remove any traces of remaining aqueous ink. If this step is omitted or performed incompletely, the titanium sol will hydrolyze upon contact with residual aqueous impurities and precipitated $TiO_2$ will clog the print head nozzles.

"Virgin empty" spongeless cartridges were supplied by MIS Associates, USA. Titanium sol was filtered through 0.2 μm mesh size syringe filter and loaded into one "virgin empty" cart. This cart was installed into the printer in the black position while the remaining positions were occupied by carts of the same type filled with a dummy ink (a mixture consisting of water, surfactant (isopropanol), humectant (DMSO) and colorant (water soluble dye)). After a series of head cleaning cycles a perfect nozzle check pattern was obtained. Since the sol is essentially colorless when viewed in daylight, the nozzle check printout had to be observed under a UV-A light source to prove all ink nozzles of the black channel were firing the loaded sol. Under this type of illumination, the printed sol appeared deep yellow while the paper was bright blue because of fluorescent brightening agents present in the paper.

Cleaned glass plates were then mounted into a modified CD holder, fed into the printer and printed with "black only" driver setting. This setting ensured that only the ink from the "black" cartridge (now containing titanium sol) was utilized for printing.

However, a suitable image had to be created to be used for printing. The amount of sol delivered to the substrate (i.e. the *sol loading* or *dot area* in the graphic arts terminology) was controlled by the intensity of

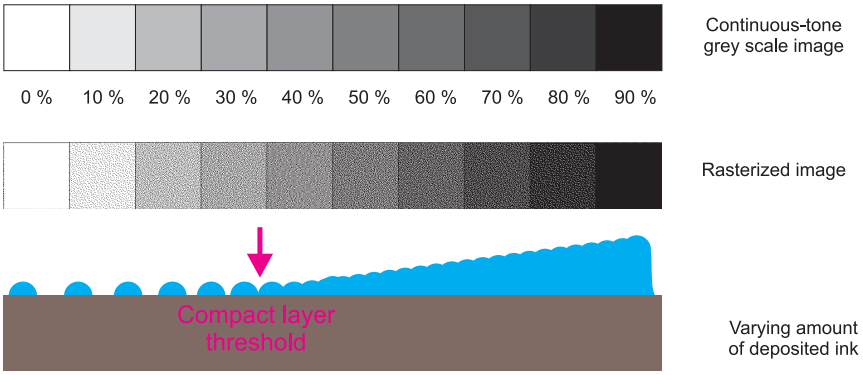


**Figure 1.** Layer build-up for different values of sol loading.

**Table 2.** Print Settings

| | Rapid | Slow |
|---|---|---|
| Media Settings | Plain paper | CD Premium Surface |
| Resolution | 360 | 720 |
| High-speed Printing | yes (= bidirectional printing) | no (= unidirectional printing) |
| Absolute Printing Speed | appr. 5 $cm^2\ s^{-1}$ | appr. 0.5 $cm^2\ s^{-1}$ |

black color of the printed image. The black color intensity was therefore varied in different levels of grey (100%, 90%, 80%, 70%, 60%) and thus glasses with corresponding relative sol loading values were printed. Sol loading of 200% and 300% was achieved by printing 100% pattern twice or three times onto the same support.

Figure 1 illustrates the printing process and layer bild-up: the different grey levels (generally a continuous-tone bitmap) needs to be converter into a halftone screen pattern (planar distribution of dots). In the case of inkjet printing, a combination of amplitude modulation screening and frequency modulation screening is used: ink droplets of varying size (i.e. AM screening) are placed at different pitch (i.e. FM screening). However, printing on non-porous, non-absorbing substrates results into a very high level of dot gain (the printed droplets spread on the surface of the substrate and their diameter is much larger than the diameter of ejected droplet which roughly corresponds to the nozzle diameter. Therefore, the printed substrate becomes completely covered by the ink at lower tonal values (the compact layer threshold). Before this point, the substrate is covered by separate individual droplets. Beyond this point, the substrate is covered by varying amount of ink resulting into a compact layer of varying thickness.

Two print setting were adopted – rapid and slow (see Table 2). The resolution, print speed and media settings were varied and their influence on the resulting $TiO_2$ layer properties was evaluated.

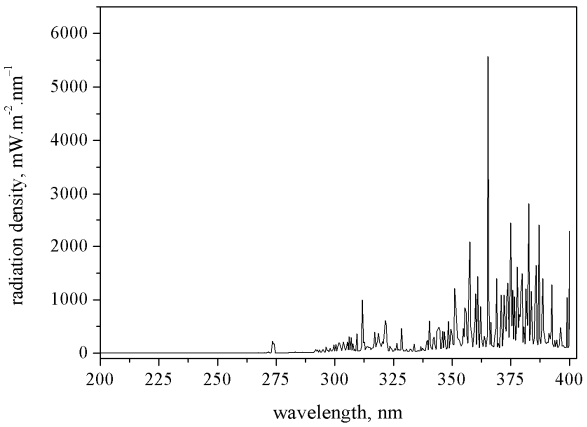


**Figure 2.** Emission spectrum of metal halogen lamp Philips HPA 400W (measured at the distance of 1 m).

## *Layer Treatment*

After being printed, the coated glass plates were dried in an oven at 110 °C for 30 min. Finally, the deposited layers were thermally treated in a calcination furnace at 450 °C for 4 hours with the heating rate of 3 $°C.min^{-1}$ to obtain transparent photocatalytically active titanium dioxide films in anatase presupposed phase.

## *Study of Printed Layers Properties*

The following methods were used for the characterization of prepared layers:

1. Optical and SEM imaging was performed in an ordinary manner on a Nikon Eclipse E200 optical microscope equipped with a Nikon D200 digital

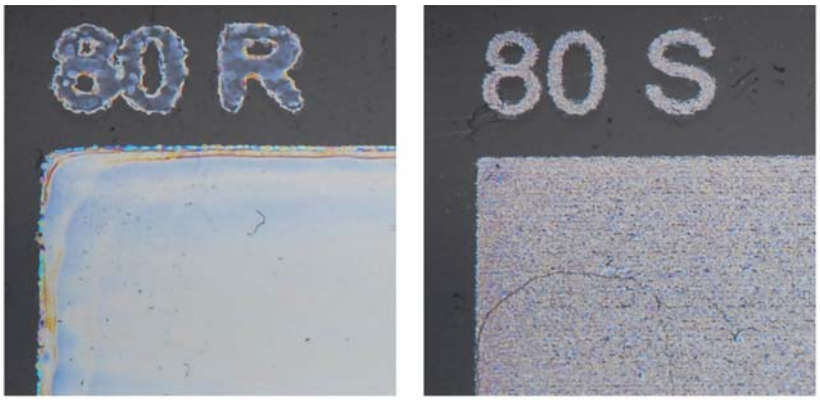


**Figure 3.** Macroscopic appearance of rapidly (left) and slowly (right) printed layers with 80% sol loading. The images cover the area of appr. 1 $cm^2$.

camera and Hitachi S4700 FESEM scanning electronic microscope. Recorded SEM images also give a general idea about the layer thickness range. Surface topology was studied by atomic force microscopy. Veeco Di CP-II machine in tapping mode was used for this purpose.

2. Layer thickness was determined from reflectance spectra by Ocean Optics NanoCalc thin film analysis system. Nanocalc measures the amount of reflected light from a thin film over a range of wavelengths and using a database of material constants calculates the film thickness.
3. Amount of deposited $TiO_2$ was determined by ICP-AES. Printed layers were dissolved in hot nitric acid, Ti concentration was determined and the amount of $TiO_2$ calculated.
4. Raman spectroscopy was performed on LabRAM HR Jobin-Yvon Raman spectrometer in order to determine the crystalline composition of $TiO_2$ thin films. The Argon-Krypton laser RM 2018 (Spectra Physics) at 514.5 nm was used as the excitation source and laser power was kept at 1 mW.
5. Surface properties were studied by evaluating the water droplet contact angle (CA). We measured the CA by OCA 20 device (DataPhysics, Germany) and utilized the sessile drop method. The deposited drop volume was 5 µl and the drop shape was recorded 15 s after its deposition. We measured the CA value at 6 different places on each sample and then the average value was calculated. Then the samples were irradiated by an UV lamp and the CA change was recorded. We used medium pressure mercury vapor lamp (Philips HPLN 125 W, without the fluorescent bulb). The integral irradiation intensity in the range 290-390 nm was 2 mW $cm^{-2}$ (determined by irradiance meter LUTRON UV 340).
6. Photocatalytic activity was confirmed by recording the dechloration rate of 2,6-dichloroindophenol (DCIP). The reaction took place in a simple single-plate reactor where the solution was circulated through a siphon by a centrifugal pump. The siphon ensured a constant level of solution over the catalyst plate during the whole reaction despite decreasing volume due to sampling. UV radiation was delivered by Philips HPA-400 W metal halogen lamp and the intensity was 2.4 mW $cm^2$. (again determined by irradiance meter LUTRON UV 340) .

We used 150 ml of 2,6-dichlorindofenolu solution of starting concentration $2\times10^{-5}$ mol $dm^{-3}$. 2 ml samples were taken at 20 minutes intervals (0, 10, 20, 40, 60, 80, 100 minutes). The DICP concentration change was determined by UV-VIS spectrophotometry at 600 nm. Formal first order kinetic model was adopted and the reaction rate constants were calculated.

## Results and Discussion

### *Sample Appearance, Layer Topology and Roughness*

Figure 3 illustrates the visual appearance of the prepared samples. Generally, we obtained transparent, homogeneous layers of $TiO_2$. However, a difference between the rapidly printed series and slowly printed series was clearly visible even by a naked eye: rapid printing resulted into poorly resolved letters but perfectly smooth, homogeneous surface of the layer giving mirror-like gloss when viewed at an angle. The slowly printed layers featured well resolved letters, but the layer surface had a pearl appearance, scattered light slightly and provided rather attenuated, semi-matt gloss.

These differences in layer appearance could be attributed to the structure and topology of the layers at

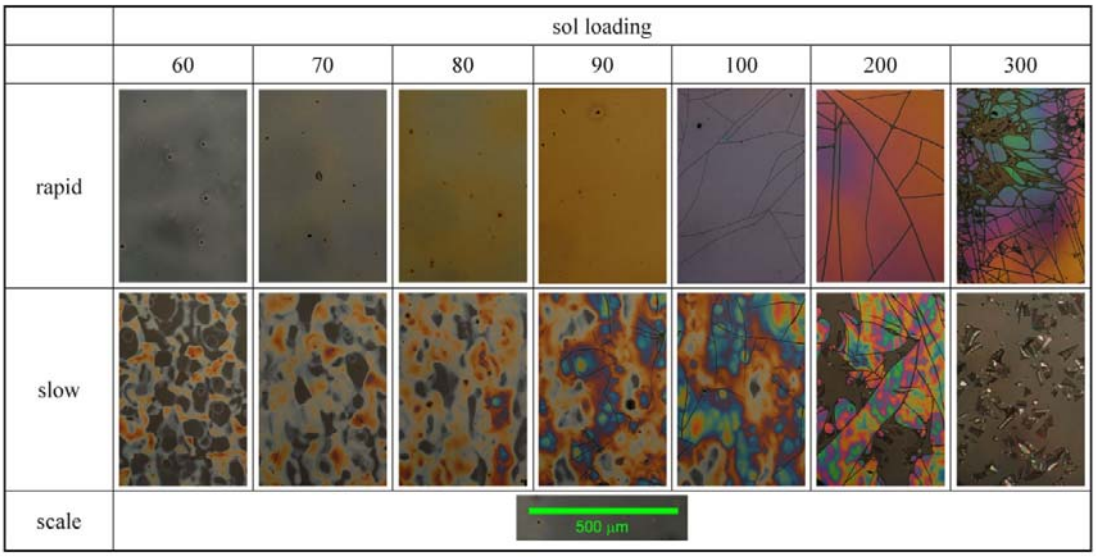


**Figure 4.** Side-by-side comparison of the slowly and rapidly printed sample series.

the micro-scale. Therefore a series of optical micrographs was recorded. Polarized light was found very useful for this, because the slightest deviations in layer thickness were clearly visualized by the vivid interference coloring. These images then clearly illustrate the principal differences between rapid and slow printed layers, no matter what the sol loading is. The rapid printed layers are very smooth and compact up to 80% of sol loading. When the sol loading value exceeds this threshold, cracking occurs, but the layer itself is still very smooth. On the other hand, the slow-printed layers show completely different structure – their surface appears to be grooved and rough. It clearly keeps the structure of individual drops forming islet-like pattern. When the sol loading value is low, we can clearly see the traces of individual drops. When the sol loading value increases, the drops overlap to much extend, but the islet-like pattern is still present and some cracing occurs in very thick regions. This islet-like structure gives the layer its pearl finish resulting into a slight scattering of both reflected and transmitted light.

The differences in the layer structure can be explained as the consequence of different speed of sol ejection: During rapid printing, the sol ejection rate is faster then solvent evaporation, and therefore a liquid film is formed on the substrate. Only then the solvent evaporates, leaving a "dry" layer of gel. However, during slow printing, the sol ejection rate is quite slow and the rate of evaporation is comparable. Therefore a solid gel is formed on the substrate already during printing and the last drops of sol are deposited onto already dried gel. Therefore the observed distinctive structure develops and the resulting layer keeps the droplet-like structure.

Optical micrographs also reveal that at higher sol loading values severe cracking occurs. Obviously, as the sol loading increases, so does the layer thickness. In thicker layers, the tension resulting from different coefficients of thermal expansion is more pronounced and these thicker layers tend to crack. The 200% and 300% layers crack so severely that layers eventually disintegrated and separated from the support. In the case of slow printed layers, cracking occurs locally at places of higher thickness.

A more detailed view at the nano-scale is provided by the SEM imaging. Here we get a closer look at the cracks and it is also possible to estimate the thickness of the layers. Figure 5 clearly illustrated that the $TiO_2$ layer partly separated from the support at the crack and bends upwards. Further, the images of greater magnification depict the crystalline structure of both the pyrex support and of the $TiO_2$ layers. According to these images, we can roughly estimate the crystalline size of $TiO_2$ to be appr. 50–30 nm. The bottom pair of high magnification SEM images also reveal that the structure of rapidly printed layer is slightly coarser – the individual crystallites seem to be more pronounced and the gaps separating them are broad and even. On the other hand, the crystallites of the slowly printed layer seem to be packed more tightly and prominent gaps are less frequent.

The surface topology was further studied by means of AFM microscopy. We focused both on the cracks topology as well as on the roughness of smooth areas between cracks. Figure 6 gives more insight into the surface topology in the microscale. We can clearly see the loose edge of the crack and its bended curvature. Naturally, the crack appear as V-shaped trenches on

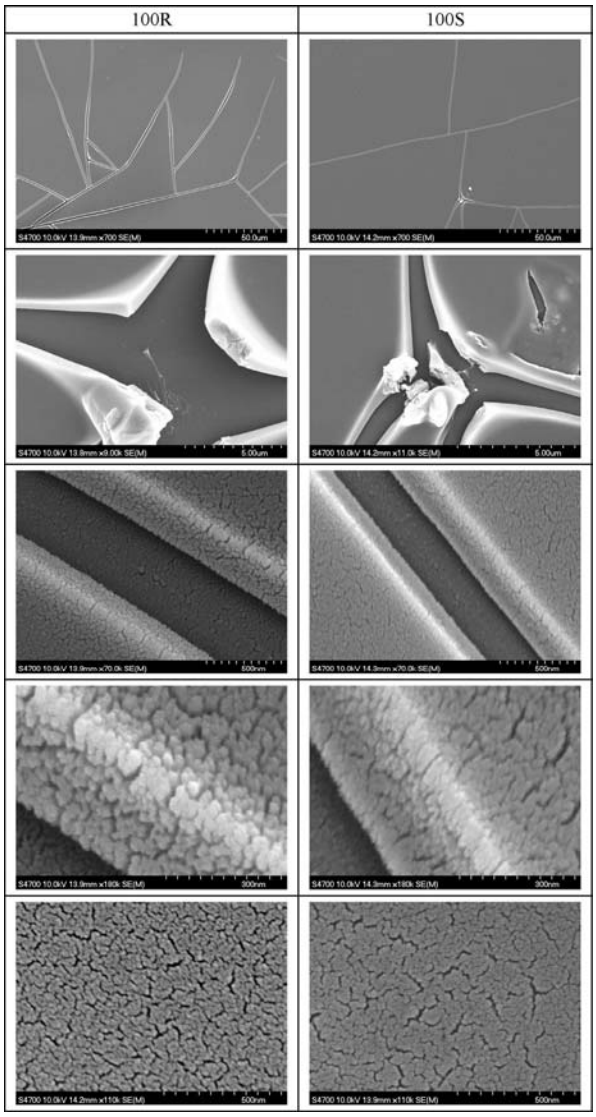


**Figure 5.** SEM images of slowly (right) and rapidly (left) printed layer having 100% sol loading.

the AFM records because the tip is scanning over the surface and can not reveal the topology below the loose edge.

While these micro-scale AFM scans show the same morphology for both the rapidly and slowly printed samples, scans recorded at higher magnification reveal some interesting differences. It seems that the slowly printer samples have an extremely smooth surface (Figure 7, bottom right). However, this smooth surface is shaped into hills and valleys up to 50 nm high and up to several micrometers wide/long (Figure 7, top right). We believe these hills and valleys are the imprints of delayed satellite droplets which have landed on a semi-dried gelling layer as the printing head repeatedly passed over the same spot during the process of slow printing. Apparently, the repeated drying and swelling

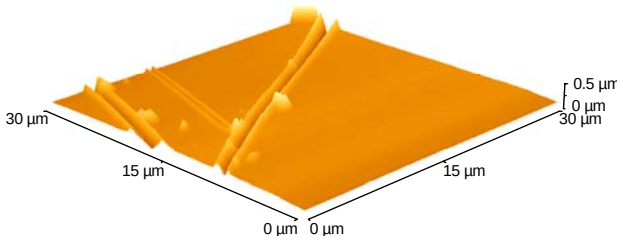


**Figure 6.** Large area AFM records of the rapidly printed sample with sol loading of 100 %.

of the layer resulted into the formation of extremely smooth layer but at the same time the casts of individual droplets shape the surface. On the other hand, the rapidly printed layers are relatively smooth when compared to slowly printed layers observed at the same scale (Figure 7, top left). However, a closer view reveals considerable roughness at the nanoscale (Figure 7, bottom left). Obviously, the at-a-blow dried layer originating from a liquid film of rapidly printed precursor cannot reflect any drop-like structure, but during the fast and single-step drying process a coarser and rougher surface is produced.

The previous verbal description of the surface topology is exactly articulated by the values of RMS roughness given in Table 3. Note that the value of RMS roughness of the rapidly printed sample is appr. 1 nm and this value is basically identical for both the 1 µm and 400 nm scans, i.e. the observed features are much smaller than the scan area. On the other hand, the RMS roughness for 1 µm scan of the slowly printed sample is 5.3 nm. This value includes the contribution of the satellite droplets imprints. The size of these imprints is comparable with the scan size. However, when we scan a smaller area not affected by these artifacts, we obtain an extremely low RMS value of appr. 0.2 nm. The RMS value of rapidly printed sample is close to published values for dip-coated layers (60), while the slowly printed samples feature surprisingly low RMS value (when droplet artifacts are excluded).

### *Amount of Deposited $TiO_2$ and Layer Thickness*

So far, the amount of deposited $TiO_2$ has been expressed as the sol loading value, measured relatively with respect to the maximum loading. However, the real absolute amount of $TiO_2$ as well as the real absolute thickness is of course of a great importance.

We measured the total Ti content by ICP-OES and then calculated the corresponding amount of $TiO_2$ per unit area. We found out that the amount of $TiO_2$ does not depend on the deposition mode (rapid or slow), i.e. the deposited amount was the same in both rapidly and slowly printed samples (see Figure 8). Quite surprisingly, the relation between the amount of $TiO_2$

**Table 3.** RMS roughness at the sub-micro and nanoscale

| | linear scale | Rms Rough (Rq) | Ave Rough (Ra) | Mean Ht | Median Ht | Surface Area | Projected Area |
|---|---|---|---|---|---|---|---|
| 100R | 1 µm | 0.9398 nm | 0.6820 nm | 2.606 nm | 2.489 nm | 1.004 µm | 1.000 µm |
| | 0.4 µm | 1.042 nm | 0.7776 nm | 4.317 nm | 4.201 nm | 0.1635 µm | 0.1600 µm |
| 100S | 1 µm | 5.268 nm | 3.053 nm | 32.48 nm | 32.21 nm | 1.025 µm | 1.000 µm |
| | 0.4 µm | 0.1980 nm | 0.1504 nm | 1.595 nm | 1.634 nm | 0.1610 µm | 0.1600 µm |

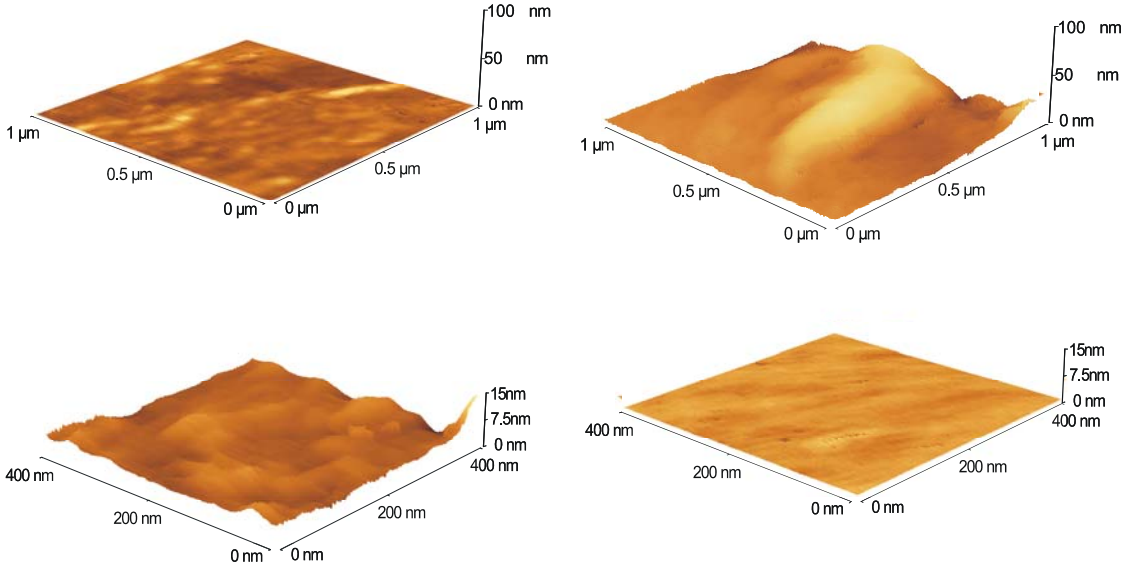


**Figure 7.** AFM records at the nanoscale. Rapidly printed sample with sol loading 100% (left) and slowly printed sample of the same sol loading (right).

per unit area and the value of relative sol loading in not linear. We believe this non-linearity is implemented into the printer driver intentionally as an internal calibration. When the printer is used for its original purpose, this calibration provides a compensation for the non-linear dependence of printed optical density on the amount of deposited ink.

A similar trend could be observed when the layer thickness has been determined by the NanoCalc system. Unfortunately, this measurement was possible only for the rapidly printed layers. The drop-like structure giving the slowly printed layer its typical pearl finish caused difficulties during reflected light measurements and therefore the thickness of slowly printed samples could not be determined.

## *Raman Spectroscopy*

Raman spectroscopy was employed to reveal the crystalline structure of prepared layers. In this particular case, the printed samples were compared to a dip-coated samples prepared using the same sol in order to see if the hydrodynamic stresses during printing have any impact on the crystalline structure of resulting $TiO_2$.

It has been described that $TiO_2$ has 4 active Raman modes in rutile modification, (A1g, B1g, B2g and Eg), 6 for anatase (A1g, 2 B1g and 3 Eg) and 36 for brookite (61, 62). Indeed, Raman spectra can be influenced by chemical and structural defects causing shifts in Raman band positions. Recorded spectra of the sol-gel originated $TiO_2$ (both printed and dip-coated) were compared with the spectrum of Degussa P-25 as the industrial standard of photocatalytic $TiO_2$. Our spectra confirmed the presence of anatase phase with a small portion of rutile.

## *Water Droplet Contact Angle*

The superhydrophilic nature of irradiated $TiO_2$ surfaces plays an important role in the self-cleaning phenomenon observed on these surfaces. We determined the water-droplet contact angle on as-prepared samples and then observed its change upon irradiation. There is no direct relation between the initial contact angle and either the sol loading or printing mode. The initial water droplet contact angle is in the range of 40–45°. Here it would be worth noting that the islet-like structure of slowly printed layers has no impact on the value of initial water droplet contact angle.

**Table 4.** Raman bands identification

| Phase | P-25 [$cm^{-1}$] | dip-coating, 2 layers (84 nm) [$cm^{-1}$] | 100 % *rapid printing* [$cm^{-1}$] | Vibration mode |
|---|---|---|---|---|
| Anatase | 197 | 201 | 201 | $E_g$ |
| Rutile | - | 240 | 240 | - |
| Anatase | 401 | 401 | 401 | $B_{1g}$ |
| Rutile | 444 | 436 | 436 | $E_g$ |
| Anatase | 517 | 521 | 521 | $A_{1g}$, $B_{1g}$ |
| Anatase | 642 | 642 | 646 | $E_g$ |
| Anatase | 800 | 807 | 803 | $B_{1g}$ |

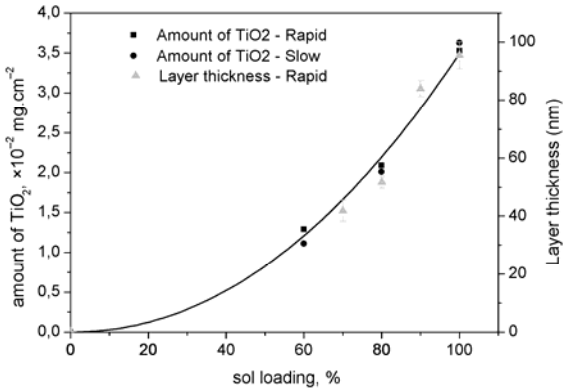


**Figure 8.** Amount of deposited $TiO_2$ as a function of sol loading.

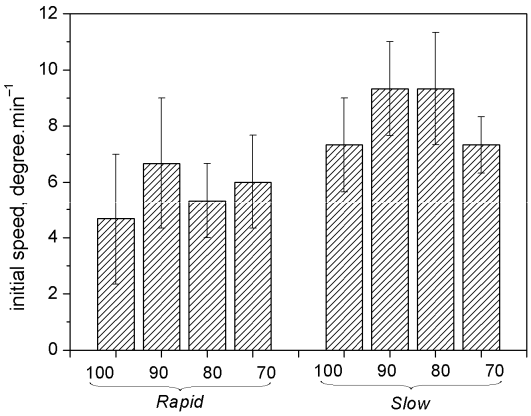


**Figure 10.** Initial rate of drop spreading.

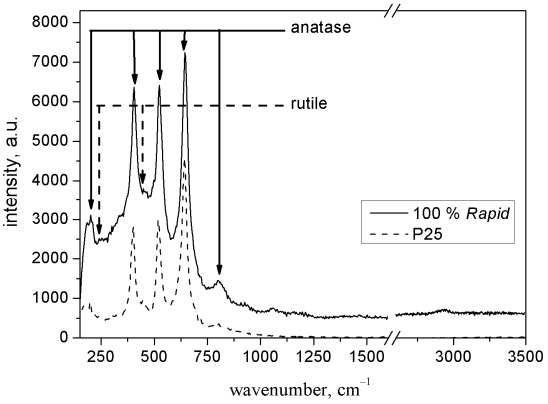


**Figure 9.** Comparison of Raman spectra of Degussa P-25, dip-coated and printed sample.

After the irradiation of the samples by UV, the contact angle quickly decreased. Within 20 minutes, its value stabilized well below 10° and the samples thus became superhydrophilic. Figure 10 illustrates the initial rate of contact angle decrease. Generally, the slow printed layers have somewhat greater initial droplet spreading rate than the rapidly printed ones but taking into account the error of measuring such low contact angle values these differences do not seem to be significant.

## *Photocatalytic Activity*

2,6-dichloroidophenol (DCIP) is one of the many dyes which can be used as a model compound for the evaluation of photocatalytic activity. The reactive oxygen species generated on the surface of irradiated titanium dioxide readily attack DCIP molecule and a series of degrading reaction takes place. The first step is dechloration accompanied by discoloration. Then the oxidation of carbon skeleton follows, leading to the formation of short carboxylic acids. Finally, these acids undergo decarboxylation and are totally cleaved.

The discoloration is naturally very easy to measure by means of UV-VIS spectrometry. This is very appealing from the practical point of view as inexpensive instrumentation can be used for the evaluation of photocatalytic activity. However, the authors are well aware of the problems inherently associated with using any dye molecule for the photocatalytic activity evaluation: dye molecules are complex systems and during their degradation many intermediates compete for oxidation by ROS. From the scientific point of view, using simple molecules such as formic acid makes much more sense.

Anyway, DCIP was used in this particular case to evaluate the photocatalytic activity of printed $TiO_2$.

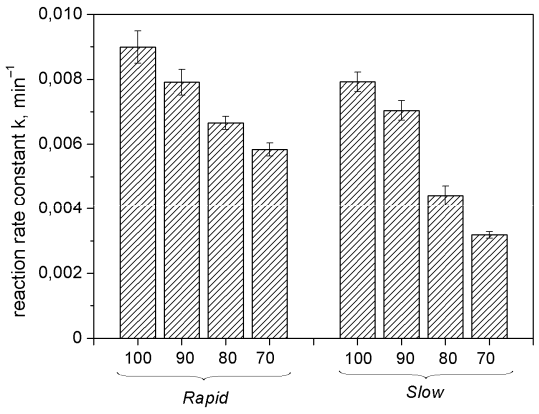


**Figure 11.** The dependance of formal 1st-order reaction rate constant on sol loading and printing mode.

We especially focused on the influence of sol loading and printing speed on the photocatalytic activity of prepared layers.

Figure 11 clearly depicts our results: The sol loading value strongly influenced the reaction rate constant and this dependence was more pronounced in the case of slowly printed layers. This is of course due to the increasing amount of deposited photocatalyst with increasing value of sol loading. Higher sol loading results into thicker layer where the absorption of incident UV radiation is more efficient.

Also, there is a slight difference between the slowly and rapidly printed layers of the same sol loading. Rapidly printed layers featured generally greater reaction rates then the slowly printed ones, despite the fact that the amount of $TiO_2$ is essentially the same. It seems that the different layer roughness influences the reaction rate – rougher layer giving greater rates. This observation is in a compliance with previously published data for dip- and doctor blade-coated layers (60), where rougher layers also resulted into greater reaction rates.

## Conclusion

In this letter, we demonstrate the benefits of using inkjet printing technology for the preparation of $TiO_2$ thin layers and report about some important properties of prepared printed layers of photocatalytically active $TiO_2$. By utilizing the well known sol-gel chemistry used so far mostly for spin- and dip coated layers of $TiO_2$, together with the wide deposition possibilities offered by inkjet printing, we are able to prepare transparent, photocatalytic layers of $TiO_2$ of variable thickness in a very effective and clean way with minimum waste.

While the previous work dealing with inkjet printed titania film focused on direct patterning of various shapes onto substrate, our work was targeted to the fabrication of smooth compact films applicable as self-cleaning surfaces. We managed to prepare samples up to 25 $cm^2$ large. The structure of prepared layers greatly depends on the printing conditions: If the sol ejection rate is faster then solvent evaporation, a smooth compact layer is produced. On the other hand, when the solvent evaporation rate is grater than sol ejection, we obtain optically rough and highly structured layer.

Slowly printed layers have a structured surface at the microscale with the "islet-like" pattern giving them a semi-opaque pearl appearance. Their photocatalytic performance is slightly lower compared to rapidly printed layers. Rapidly printed layers have better optical properties – they are perfectly smooth, even and mirror-like glossy. Their photocatalytic performance is better than the performance of the slowly printed layers probably due to greater roughness at the nanoscale, while the even thickness and smooth surface resulting into a more efficient absorption of UV radiation may also contribute.

Inkjet printing proved to be an elegant method for sol delivery to substrate. It provides a complete control over the deposition process parameters together with an excellent efficiency of precursor use. Moreover, the possibility of precise patterning and the ease of up-scaling make this type of deposition very appealing for the production of sensors, solar cells etc.

## Acknowledgement

This work has been supported by the project 104/09/P165 of the Czech Science Foundation. Authors also appreciate the help of Jiří Zita and Milan Mikula concerning the morphological characterization.

## References

(1) Blount, M. C.; Kim, D. H.; Falconer, J. L. *Environmental Science & Technology* **2001**, *35*, 2988-2994.

(2) Han, F. et al. *Applied Catalysis a-General* **2009**, *359*, 25-40.

(3) Mills, A.; LeHunte, S. *Journal of Photochemistry and Photobiology a-Chemistry* **1997**, *108*, 1-35.

(4) Litter, M. I. *Applied Catalysis B-Environmental* **1999**, *23*, 89-114.

(5) Mills, A. et al. *Journal of Photochemistry and Photobiology a-Chemistry* **2003**, *160*, 185-194.

(6) Mills, A.; Wang, J. S. *Journal of Photochemistry and Photobiology a-Chemistry* **2006**, *182*, 181-186.

(7) Bui, T. H. et al. *Research on Chemical Intermediates* **2007**, *33*, 421-431.

(8) Le-Clech, P.; Lee, E. K.; Chen, V. *Water Res.* **2006**, *40*, 323-330.

(9) Kim, S. B.; Hwang, H. T.; Hong, S. C. *Chemosphere* **2002**, *48*, 437-444.

(10) Ling, C. M.; Mohamed, A. R.; Bhatia, S. *Chemosphere* **2004**, *57*, 547-554.

(11) Chin, P.; Ollis, D. F. *Catalysis Today* **2007**, *123*, 177-188.

(12) Romeas, V. et al. *Industrial & Engineering Chemistry Research* **1999**, *38*, 3878-3885.

(13) Mills, A.; Wang, J. S.; McGrady, M. *Journal of Physical Chemistry B* **2006**, *110*, 18324-18331.

(14) Sakai, N.; Fujishima, A.; Watanabe, T.; Hashimoto, K. *Journal of Physical Chemistry B* **2001**, *105*, 3023-3026.

(15) Yu, J. C.; Yu, J. G.; Ho, W. K.; Zhao, J. C. In *1st International Conference on Semiconductor Photochemistry (SP-1)*; Glasgow, Scotland, 2001; pp 331-339.

(16) Guan, K. H. *Surface & Coatings Technology* **2005**, *191*, 155-160.

(17) Bizarro, M. et al. *Applied Surface Science* **2009**, *255*, 6274-6278.

(18) Tasbihi, M. et al. *Industrial & Engineering Chemistry Research* **2007**, *46*, 9006-9014.

(19) Yu, J. C.; Yu, J. G.; Zhao, J. C. *Applied Catalysis B-Environmental* **2002**, *36*, 31-43.

(20) Chester, G.; Anderson, M.; Read, H.; Esplugas, S. *Journal of Photochemistry and Photobiology a-Chemistry* **1993**, *71*, 291-297.

(21) Martyanov, I. N.; Klabunde, K. J. *Journal of Catalysis* **2004**, *225*, 408-416.

(22) Fernandez, A. et al. *Applied Catalysis B-Environmental* **1995**, *7*, 49-63.

(23) Bideau, M. et al. *Journal of Photochemistry and Photobiology a-Chemistry* **1995**, *91*, 137-144.

(24) Doll, T. E.; Frimmel, F. H. *Acta Hydrochimica Et Hydrobiologica* **2004**, *32*, 201-213.

(25) Byrne, J. A. et al. *Applied Catalysis B-Environmental* **1998**, *17*, 25-36.

(26) Addamo, M. et al. *Thin Solid Films* **2008**, *516*, 3802-3807.

(27) Yoon, K. H.; Noh, J. S.; Kwon, C. H.; Muhammed, M. *Materials Chemistry and Physics* **2006**, *95*, 79-83.

(28) Guo, B. et al. *Thin Solid Films* **2005**, *479*, 310-315.

(29) Attar, A. S.; Ghamsari, M. S.; Hajiesmaeilbaigi, F.; Mirdamadi, S. *Journal of Materials Science* **2008**, *43*, 1723-1729.

(30) Mills, A.; McGrady, M.; Wang, J.; Hepburn, J. *International Journal of Photoenergy* **2008**.

(31) Tazawa, M.; Okada, M.; Yoshimura, K.; Ikezawa, S. In *World Congress of the International-Solar-Energy-Society*; Gothenburg, SWEDEN, 2003; pp 159-170.

(32) Carp, O.; Huisman, C. L.; Reller, A. *Progress in Solid State Chemistry* **2004**, *32*, 33-177.

(33) Capan, R.; Chaure, N. B.; Hassan, A. K.; Ray, A. K. *Semiconductor Science and Technology* **2004**, *19*, 198-202.

(34) Schubert, D. W.; Dunkel, T. *Materials Research Innovations* **2003**, *7*, 314-321.

(35) Fretwell, R.; Douglas, P. *Journal of Photochemistry and Photobiology a-Chemistry* **2001**, *143*, 229-240.

(36) Bharathan, J.; Yang, Y. *Applied Physics Letters* **1998**, *72*, 2660-2662.

(37) Le, H. P. *Journal of Imaging Science and Technology* **1998**, *42*, 49-62.

(38) Ballarin, B. et al. *Synthetic Metals* **2004**, *146*, 201-205.

(39) Morrin, A. et al. *Electrochimica Acta* **2008**, *53*, 5092-5099.

(40) Yoshioka, Y.; Jabbour, G. E. *Synthetic Metals* **2006**, *156*, 779-783.

(41) Lee, H. H.; Chou, K. S.; Huang, K. C. *Nanotechnology* **2005**, *16*, 2436-2441.

(42) Park, B. K. et al. In *5th Symposium on Thin Films for Large Area Electronics held at the EMRS 2006 Spring Meeting*; Nice, FRANCE, 2006; pp 7706-7711.

(43) Liu, Z. C.; Su, Y.; Varahramyan, K. *Thin Solid Films* **2005**, *478*, 275-279.

(44) Taylor, A. D. et al. *Journal of Power Sources* **2007**, *171*, 101-106.

(45) Radulescu, D. et al. In *Symposium on Next Generation Biomaterals*; Pittsburgh, PA, 2005; pp 534-539.

(46) Zhang, C. H.; Wen, X. J.; Vyavahare, N. R.; Boland, T. *Biomaterials* **2008**, *29*, 3781-3791.

(47) Xu, T. et al. *Biomaterials* **2006**, *27*, 3580-3588.

(48) Xu, T. et al. *Biomaterials* **2005**, *26*, 93-99.

(49) Liu, Y.; Cui, T. H.; Varahramyan, K. *Solid-State Electronics* **2003**, *47*, 1543-1548.

(50) Kawase, T. et al. In *5th International Conference on Nano-Molecular Electronics (ICNME2002)*; Kobe, Japan, 2002; pp 279-287.

(51) Chen, B.; Cui, T. H.; Liu, Y.; Varahramyan, K. *Solid-State Electronics* **2003**, *47*, 841-847.

(52) Keat, Y. C.; Sreekantan, S.; Hutagalung, S. D.; Ahmad, Z. A. *Materials Letters* **2007**, *61*, 4536-4539.

(53) Nishimoto, S. et al. *Applied Surface Science* **2009**, *255*, 6221-6225.

(54) Matsuo, A. et al. *Journal of Electroceramics* **2006**, *16*, 533-536.

(55) Masahiro, Y.; Ruwan, G. *Journal of Solid State Electrochemistry* **2008**, *12*, 775-782.

(56) Dowling, D. G. *American ink maker* **1972**, *50*, 43-112.

(57) Suzuki, Y.; Tanno, R. Inkjet printer utilizing white ink US Patent 6,769,766, August 3, 2004.

(58) Tanabe, S. et al. Ink jet white ink and titanium dioxide slurry therefor, US Patent 6,989,054, Janurary 24, 2006.

(59) Hancock, A.; Lin, L. *Pigment & Resin Technology* **2004**, *33*, 280-286.

(60) Kontos, A. I. et al. *Thin Solid Films* **2007**, *515*, 7370-7375.

(61) Balachandran, U.; Eror, N. G. *Journal of Solid State Chemistry* **1982**, *42*, 276-282.

(62) Porkodi, K.; Arokiamary, S. D. *Materials Characterization* **2007**, *58*, 495-503.

*Received for review September 2, 2009. Revised manuscript received January 26, 2010. Accepted February 3, 2010.*

## 6.2. Posters

### P01 THE STUDY OF $TiO_2$ THIN FILMS PHOTOCATALYTIC ACTIVITY ON DEGRADATION OF YEAST AND DYE POLLUTANTS

JANA CHOMOUCKÁ, JANA DRBOHLAVOVÁ, PETR DZIK, MÁRIA VESELÁ and MICHAL VESELÝ
*Brno University of Technology, Faculty of chemistry, Institute of Physical and Applied Chemistry, Purkyňova 118, 612 00 Brno, Czech Republic,*
*chomoucka@fch.vutbr.cz*

**Introduction**

Among various oxide semiconductor photocatalysts, titanium dioxide ($TiO_2$) appears to be a promising and important prospect for use in enviromental purification, because of its strong oxidizing power, photoinduced hydrophilicity, nontoxicity and long-term photostability. $TiO_2$ shows excellent photocatalytic activity for oxidative degradation of environmental pollutants[1].

The first description of antimicrobial effect of $TiO_2$ film was published by Japanese professor Matunago and colleagues in 1985. At the beginning of the photocatalytic reaction, highly reactive groups containing oxygen atoms (ROS – reactive oxygen species) are formed. These ROS produced by photocatalysis cause different type of damage in live organisms. After a hydroxyl radical attack, the outer membrane is partially destroyed. There is no important change of cell viability during this process, but membrane permeability towards ROS is changed. At this stage, ROS can attack the cytoplasmic membrane more easily, which results in the lipid membrane peroxidation and subsequent cell death[2].

**Experimental**

Preparation of $TiO_2$ Thin Film

The substrates used as film supports were soda-lime glass plates. Boiling the glass plates in sulfuric acid removes the surface sodium ions and therefore the photoactivity of the film can be improved.

Transparent $TiO_2$ layers were immobilised on glass plates using sol-gel method with titanium tetraisopropoxide in ethanol as precursor. Depositions of thin films were realized by dip-coating method with withdrawal speed 120 mm $min^{-1}$. In the next stage, the coated substrates were dryed for 30 min. at 110 °C and then calcinated for 4 hours at 450 °C with temperature ramp of 3 °C $min^{-1}$.

Photooxidation of 2,6-dichloroindophenol

The photocatalytic activity of the $TiO_2$ films was evaluated by examining the oxidation rate of water solution 2,6-DCIP ($2 \times 10^{-5}$ mol $dm^{-3}$) upon UV irradiation (2.4 mW $cm^{-2}$, solar lamp Philips HPA-400 W) in a desk reactor. The concentration decrease of 2,6-DCIP was determinated spectrophotometrically. A photochemical dechloration of 2,6-DCIP is a reaction of first order kinetics.

Antimicrobial Efect of $TiO_2$ Thin Film

Photocatalytic killing of yeasts *Candida tropicalis* and *Candida albicans* were performed to study the antimicrobial properties of $TiO_2$ films. These yeasts belong to the class of Ascomycetes, the family of Saccharomycetaceae and the kingdom of Fungi. Generally, *Candida* is the most common cause of opportunistic mycoses (Candidiasis) worldwide. This type of endogenous infection mostly arises from overgrowth of the fungus inhabiting normal flora. *C. albicans* is the most frequently encountered medical pathogen, the second one is *C. tropicalis*.

The yeast culture for the photocatalytic test was prepared as follows: 1 ml of yeast culture cultivated for 24 h in GPY liquid nutrient media was diluted with 9 ml of deionized water and centrifuged for 5 min at 4,000 rpm. The supernatant was separated from yeast sediment and centrifugation was repeated once again with 10 ml of deionized water. After the last change of liquid, the pure yeast suspension in water was well homogenized using minishaker. 30 µl of this suspension was dropped onto 15 min pre-irradiated $TiO_2$ film on glass plate and spread for better contact of yeasts with photocatalyst surface. The sample was put in Petri dish and covered by quartz plate. The UV irradiation was provided by fluorescent lamp Sylvania Lynx-S 11 W with intensity 1.5 mW $cm^{-2}$. After exposure suspension of yeasts, 40 ml of $1.8 \times 10^{-4}$ mol $dm^{-3}$ Acridine Orange was added to the drop of irradiated sample. Nicon Eclipse 200 with epifluorescent adapter equipped with Camera Pixelink Canada was used for dead and live cell resolution and calculation. It was calculated survival ratio of yeasts.

$$SR = \frac{N_{live}}{N_{live+dead}} \quad (1)$$

**Results**

Photooxidation of 2,6-DCIP

Fig. 1. shows that the number of layers (i.e. thickness) influences the photocatalytic activity. The higher number of $TiO_2$ thin layers is, the higher the photocatalytic activity is. But in the case of 4 layers, the photocatalytic activity is smaller due to its large thickness. The layer is too thick, so the generation of electrons and holes proceed deep in the semiconductor layers, and therefore they can't get to the surface and participace the reaction. It causes the decrease of photocatalytic activity.

Antimicrobial efect of $TiO_2$ thin film

The reaction was performed only in deionized water without the nutrient compounds to avoid their influence on yeast degradation process.

The dependence of *Candida tropicalis* and *Candida albicans* survival ratio on irradiation time and $TiO_2$ layer

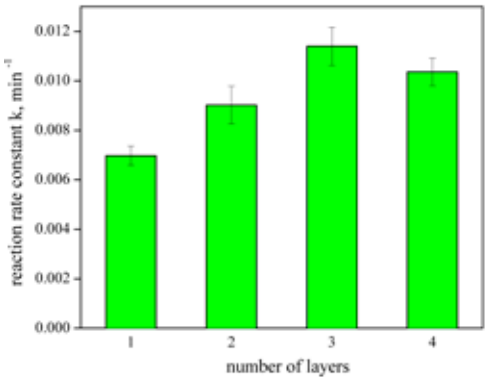


Fig. 1. **The influence of number of $TiO_2$ thin films on the photocatalytic efficiency 2,6-DCIP**

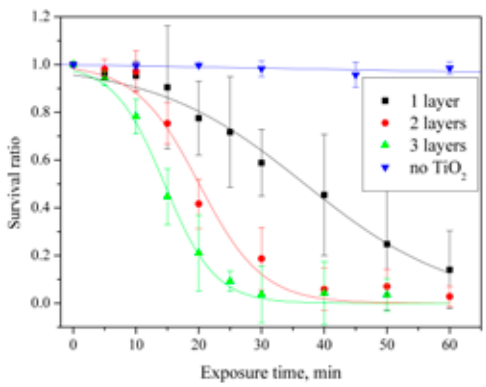


Fig. 2. **The survival ratio of *Candida tropicalis* during irradiation**

number is demonstrated at the following figures (Fig. 2. and Fig. 3.). It can be seen, there is no antimicrobial activity during UV irradiation of yeast suspension when the photocatalyst is absent.

Concerning the induction period, it is decreasing with increasing number of $TiO_2$ layer.

In the case of *Candida albicans*, we observed worse antimicrobial efficiency (Fig. 3.) therefore longer time of irradiation is necessary to kill them.

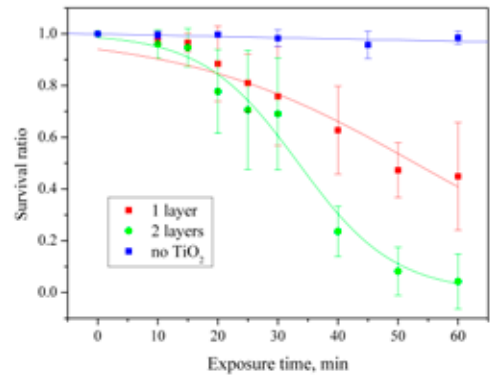


Fig. 3. **The survival ratio of *Candida albicans* during irradiation**

## Conclusions

We prepared $TiO_2$ thin films on soda-lime glass plates by dip coating method. Films are homogenous and transparent.

The photocatalytic efficiency of prepared coatings was evaluated on photocatalytic oxidation 2,6-DCIP in aqueous phase, as well as on killing of microorganisms, *Candida tropicalis* and *Candida albicans* yeasts.

We found that the number of layers (i.e thickness) positively influences the photocatalytic oxidation of 2,6-DCIP.

Concerning the microorganisms killing, *Candida tropicalis* and *Candida albicans* were selected for determination of $TiO_2$ thin film antimicrobial properties, because they represent the most frequently encountered medical pathogen, causes the opportunistic mycoses. We observed that the photocatalytic degradation rate increases with increasing $TiO_2$ film thickness.

REFERENCES

1. Carp O., Huisman C. L., Reller A.: Prog. Solid State Chem. *32*. 33 (2004).
2. Sunary K., Watanabe T., Hashimoto K.: J. Photochem. Photobiol. A: Chem. *156*, 227 (2003).

## L02 PHOTOCATALYTIC DEGRADATION OF FORMIC ACID ON $TiO_2$ THIN LAYERS

JANA CHOMOUCKÁ[a], PETR DZIK[a], MICHAL VESELÝ[a], JANA DRBOHLAVOVÁ[a], ERIC PUZENAT[b] and CHANTAL GUILLARD[b]

[a]*Brno University of Technology, Faculty of chemistry, Institute of Physical and Applied Chemistry, Purkyňova 118, 612 00 Brno, Czech Republic,*

[b]*IRCELYON UMR CNRS 5634, Université de Lyon, 2 av. Albert Einstein, Villeurbanne cedex, 69626, France, chomoucka@fch.vutbr.cz*

### Introduction

Environmental pollution is becoming more and more serious. Catalysis under UV irradiation, called photocatalysis, is attracting a great deal of attention from environmental purification point of view[1]. Titanium dioxide ($TiO_2$) photocatalysis has been focused on the elimination of toxic and hazardous organic substances and metals in wastewater, drinking water and air, which is important for the protection of the environment[2]. Heterogenous photocatalysis is a process based on the excitation of a semiconductor by light of energy equal to or higher than the bynd gap one. This excitation generates electron-hole pairs which can give rise to redox reactions with species adsorbed on the catalyst surface[3]. Among the warious semiconductors, $TiO_2$ is the most suitable photocatalyst because of its high activity, photostability and availability. Anyway, serious practical problems arise from the use of $TiO_2$ powders in the photocatalytic process – the need for post treatment separation in a slurry system. A key technology for the practical application of photocatalysis to environmental problems is the immobilization of $TiO_2$ as thin film on a solid substrate (even if normally the film-type photocatalysts have low surface areas and their intrinsic photocatalytic activity is usually smaller than of the powders).

$TiO_2$ films have been often prepared by expensive methods as pulsed laser deposition, reactive evaporation and chemical vapour deposition. Low cost preparation methods are the sol-gel process including dip-coating, spin-coating and micropiezo jet as the final step of preparation. Sol-gel method usually requires a thermal post-treatment in order to eliminate organics present in the films or to induce crystallization of the deposited material. An important requirement for improving the $TiO_2$ photocatalytic activity is to increase its specific surface area, which is certainly dependent on the crystal size. It is known that the smaller the catalyst is, the larger will be its specific surface area. Nevertheless, if the particles are very small, the charge carrier recombination is more probable. Thus the particle size must be optimized.

Formic acid (FA) was choosen because of simple mechanism of degradation: it undergoes a direct mineralisation to $CO_2$ and $H_2O$ without the formation of any stable intermediate species[4]. Moreover, it also represents a possible final step in the photodegradation of more complex organic compounds.

### Experimental

#### Preparation of $TiO_2$ Thin Films

Borosilicate glass plates (30 × 30 × 2 mm, Verre Equipements, France) were chosen as a substrate for immobilization of $TiO_2$ thin films. $TiO_2$ layers were prepared using following organometallic precursor in sol-gel process: a mixture of absolute ethanol (85 ml) and acetylacetone (3.8 ml) was added to titanium(IV) propoxide (10.3 ml) under continuous stirring, a small amount of water (0.69 ml) in ethanol was dropped at last to the previously mixed solution.

Depositions of thin films were realized by dip-coating method (withdrawal speed 120 mm $min^{-1}$) and by micropiezo jet. In the case of micropiezo jet one cartidge of desktop printer (EPSON R220) was filled with sol. The substrate was fixed into the holder for CD and it was printed by sol. It was possible to choose the area covered of substrate by sol or the quality of printing. The amount of printed precursor (i.e layer thickness) was determined by the gray level (dot area) of printed images. We used 2 printing speeds: slow at 720 DPI and rapid one at 360 DPI. These values are given by the printer driver setup. In the next stage, the coated substrates were dried for 30 min. at 110 °C and then calcinated for 4 hours at 450 °C with temperature ramp of 3 °C $min^{-1}$ which allowed us to obtain $TiO_2$ predominantly in anatase form.

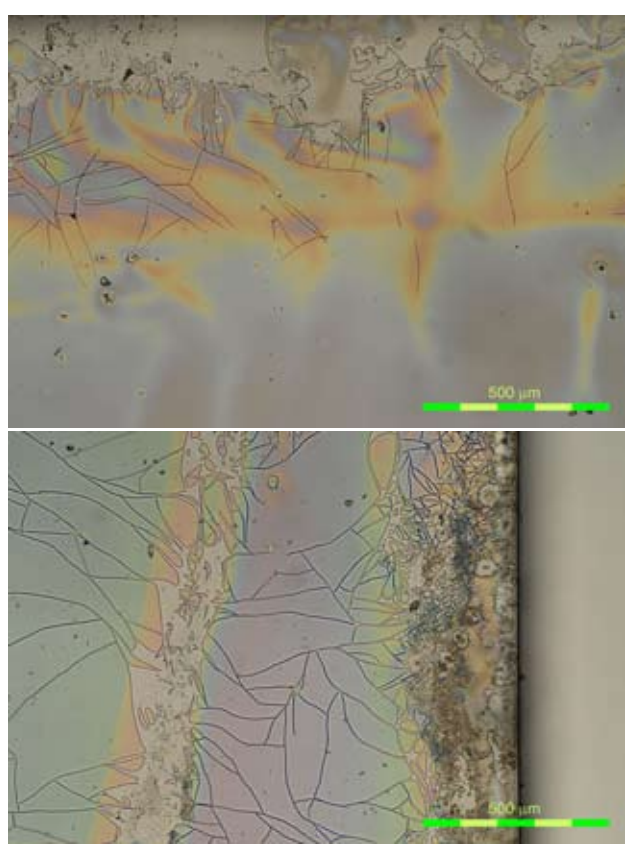


Fig. 1. **Picture from optical microscope, $TiO_2$ thin films prepared by dip coating method. 2 layers at the edge (upper) and 4 layers at the edge (down)**

### Formic Acid Photocatalytic Degradation

The formic acid reaction solution was prepared with initial concentration of 20, 50, 100, 200 and 400 mg $dm^{-3}$. The degradation process took place at ambient temperature in a Pyrex reactor (100 ml) with 30 ml of reaction solution under constant stirring. Before the reaction, the FA solution in the reactor was stirred during 30 min in obscurity to reach the solution adsorption equilibrium in contact with $TiO_2$ surface. During the FA photocatalytic oxidation with concentration ranging from 20 to 400 mg $dm^{-3}$, 0.5 ml of reaction solution was sampled every one hour for HPLC analysis. The total reaction time was 7 h. The UV irradiation was provided by high pressure mercury lamp (Philips HPK–125 W).

In order to determine the kinetic behavior of formic acid degradation on $TiO_2$ films, the initial reaction rate was estimated up to 120 min of irradiation time. The obtained values of reaction rate for various FA initial concentrations were treated using Langmuir-Hinshelwood (L-H) model.

$$r = k \cdot \theta = \frac{k \cdot K \cdot c}{1 + K \cdot c}, \text{ (per gram of photocatalyst)} \qquad (1)$$

where k is the rate constant, $\theta$ is coverage degrese of surface active sites, K is adsorption constant and $c$ is the initial concentration of reagents in the solution[5].

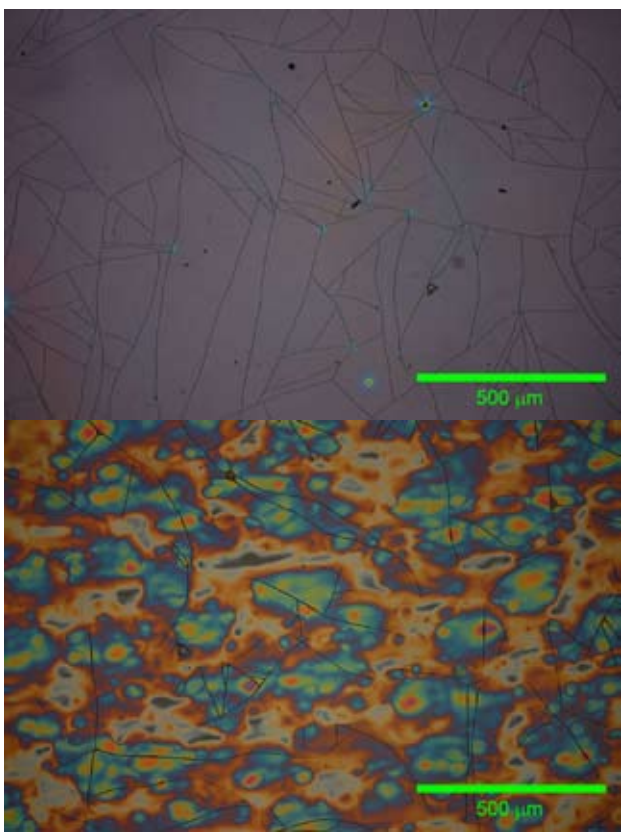


Fig. 2. **Picture from optical microscope, $TiO_2$ thin films prepared micropiezo jet by rapid (upper) and slow (down) mode**

## Results

### Characterization of $TiO_2$ Thin Films Prepared by Optical Microscope

The $TiO_2$ thin films deposited on the borosilicate glass plates were optically transparent and they adhered well to the glass substrate after the calcination process. In the case of $TiO_2$ layers prepared by dip-coating method, the layers are homogenous and without cracks in the middle of a coated surface, whereas the homogeneity gets worse towards the edge of glass. The $TiO_2$ film quality slightly decreased with increasing layer number, in the case of 4 layers some cracks is appeared in the film structure (Fig. 1.).

The second method for preparation $TiO_2$ thin films was the newly adopted picropiezo jet. Surface morfology of prepared thin film greatly depends on the print setting. The $TiO_2$ prepared by micropiezo jet by rapid mode have smooth and flat surface, cracks are observed when sol loading exceeded 90% dot area. On the other hand, the layers prepared by slow mode are uneven and discontinuous (Fig. 2.).

### Degradation of Formic Acid in Aqueous Phase

At first we will discused $TiO_2$ thin films prepared by dip-coating method. The reaction rate constants k depend strongly on $TiO_2$ layer number (i.e. layer thickness) whereas the adsorption constants decrease. The same behaviour we observed for two values of irradiance (7.7 and 4.6 mW $cm^{-2}$). The thicker $TiO_2$ film effectively absorbs the radiation, the holes can better oxidize FA (Fig. 3.).

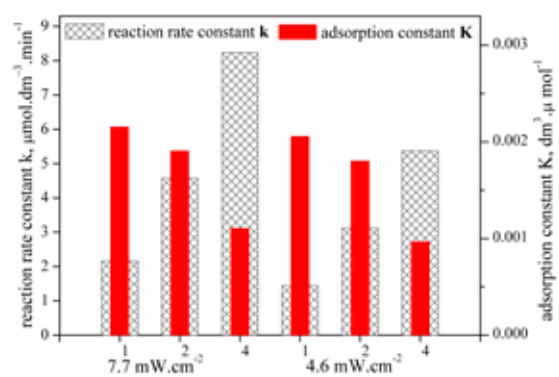


Fig. 3. **Comparison of Langmuir-Hinshelwood parameters for different intensity of irradiance**

We observed the same characteristics in the case of thin films prepared by micropiezo jet (Fig. 4.). The photocatalytic activity grows with the value of dot area. It is caused by the growing amount of deposited $TiO_2$ and the thickness of $TiO_2$ thin film. Roughness of surface has a positive influence on the adsorption of FA on the surface of $TiO_2$. We observed decrease of adsorption constant for 60 % slow mode. It could be induced by too low coverage of substrate by $TiO_2$.

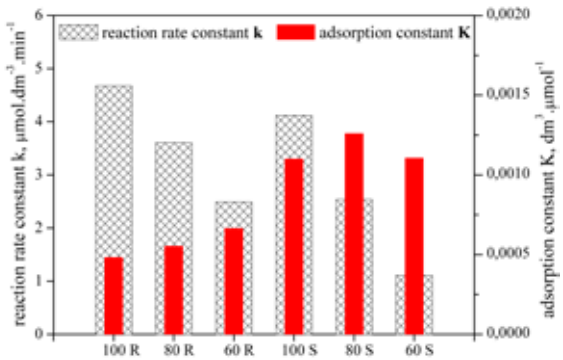


Fig. 4. **Comparison of Langmuir-Hinshelwood parameters for $TiO_2$ thin films prepared by picropiezo jet**

From the L-H model (1) we calculated the coverage of surface active sites $\theta$ by FA for different FA initial concentration (Table I and Table II). We can see that the pollutant adsorption on $TiO_2$ surface increased with increasing FA concentration. We observed a decrease in FA adsorption with increasing number of $TiO_2$ layers or sol loading. It almost achieved the value of 1 for FA initial concentration of 8.7 mmol $dm^{-3}$. That is nearly all active sites on $TiO_2$ surface were covered by FA molecules, which correlates well with obtained L-H kinetic behavior.

Table I
The coverage degree for different FA initial concentration, different iirradiance and for (1–4) $TiO_2$ layers

| c FA[mmol $dm^{-3}$] | 7.7 mW $cm^{-2}$ | | | 4.6 mW $cm^{-2}$ | | |
|---|---|---|---|---|---|---|
| | 1 | 2 | 4 | 1 | 2 | 4 |
| 8.7 | 0.95 | 0.94 | 0.91 | 0.95 | 0.93 | 0.88 |
| 4.3 | 0.90 | 0.89 | 0.83 | 0.90 | 0.86 | 0.79 |
| 2.1 | 0.82 | 0.81 | 0.71 | 0.82 | 0.76 | 0.65 |
| 1.1 | 0.70 | 0.67 | 0.55 | 0.69 | 0.61 | 0.48 |
| 0.4 | 0.48 | 0.45 | 0.32 | 0.47 | 0.39 | 0.27 |

Table II
The coverage degree for different FA initial concentration and for $TiO_2$ thin films prepared by micropiezo jet

| c FA[mmol $dm^{-3}$] | Rapid | | | Slow | | |
|---|---|---|---|---|---|---|
| | 100% | 80% | 60% | 100% | 80% | 60% |
| 8.7 | 0.81 | 0.83 | 0.85 | 0.91 | 0.92 | 0.92 |
| 4.3 | 0.68 | 0.71 | 0.74 | 0.83 | 0.85 | 0.85 |
| 2.1 | 0.51 | 0.55 | 0.59 | 0.71 | 0.73 | 0.74 |
| 1.1 | 0.34 | 0.38 | 0.42 | 0.55 | 0.58 | 0.59 |
| 0.4 | 0.17 | 0.19 | 0.22 | 0.32 | 0.35 | 0.37 |

## Conclusions

We prepared $TiO_2$ thin layers on borosilicate glass plates by dip coating method a newly by micropiezo jet. $TiO_2$ thin films prepared by dip-coating method are homogenous and transparent as well as films prepared by micropiezo jet by rapid mode. In the case of $TiO_2$ thin films prepared by slow mode, the layers are uneven and discontinuous, partial coverage of substrate with and without $TiO_2$ is observed.

The photocatalytic efficiency of prepared coatings was evaluated by the photooxidation of FA. The kinetic parameters of FA disappearance, reaction rate constant and adsorption constant, corresponded to Langmuir-Hinshelwood behavior. It was found that the photocatalytic activity grows with the value of dot area or number of layers (i.e. thickness of film).

REFERENCES

1. Kaneko M.. Okura. I.: *Photocatalysis. Science and Technology*. Kodansha-Springer. Tokyo – New York 2002.
2. Yu J. C.. Yu J.. Zhao J.: Applied Catalysis B: Environ. *36*. 31 (2002).
3. Addamo M.. et al.: Thin Solid Films *516*. 3802 (2008).
4. Mrowetz M.. Selli E.: J. Photochem. Photobiol. A: Chem. *180*, 15 (2006).
5. Carp O.. Huisman C.L.. Reller A.: Prog. Solid State Chem. *32*, 33 (2004).

## L05 THIN LAYERS OF $TiO_2$ PREPARED BY INKJET PRINTING

PETR DZIK, JANA CHOMOUCKÁ and MICHAL VESELÝ
*Faculty of Chemistry, Brno Universityof Technology, Purkyňova 118, 612 00 Brno, Czech Republic*
*petr@dzik.cz*

### Introduction

Photocatalysis on $TiO_2$ has received much attention during last two decades. If $TiO_2$ absorbs a quantum of UV radiation of sufficient energy ($\lambda < 400$ nm), an electron is excited into the valence band and an electron-hole pair is created. The potentials of electron and hole are strong enough to oxidize water to hydroxyl radicals and reduce molecular $O_2$. Resulting reactive oxygen species (ROS) are very powerful oxidizing agents and readily attack any organic matter in their proximity until it is totally cleaved to $CO_2$ and water. Numerous applications utilizing this process for water purification, toxic waste treatment, air purification and deodorizing have been proposed and some successfully marketed. The same process can be applied for the design of self-cleaning and self-disinfecting surfaces. Moreover, the oxygen vacancy creation and subsequent photo-corrosion on irradiated surfaces of $TiO_2$ convert the surface to superhydrophilic nature, which further enhances its self-cleaning ability.

Photocatalytic systems based on slurryied powder of $TiO_2$ offer excellent performance due to their very high catalyst surface area. Upon immobilization, the free surface of catalyst inevitably decreases, resulting into a loss of catalytic performance. Nevertheless, immobilized $TiO_2$ is the preferred form of photocatalyst. for industrial application. The need of removing powder photocatalyst can prohibitively complicate any process.

So far, several forms of immobilized powder $TiO_2$ were reported, featuring glass, silica gel, quartz, stainless steel, titanium, paper and many other materials as support. There are many methods of $TiO_2$ powder immobilization, such as suspension dip-coating, electrophoretic coating, spray coating, etc. However, inferior optical and mechanical properties or resulting films restrict the use of these materials only to some type of applications, such as photocatalytic reactors.

Sol-gel technique represents a totally different approach to the preparation of $TiO_2$ thin layers. Sol-gel is one of the most successful techniques for preparing nanosized metallic oxide materials with high photocatalytic activities. By tailoring the chemical structure of primary precursor and carefully controlling the processing parameters, nanocrystalline products with very high level of chemical purity can be achieved. In sol-gel processes, $TiO_2$ is usually prepared by the reactions of hydrolysis and polycondensation of titanium alkoxides, Ti(OR)n to form oxopolymers, which are then transformed into an tridimensional network.

In this way, thin, compact and transparent layers of $TiO_2$ can be conveniently produced. Such layers find their use in the design of "smart" surfaces, such as self-cleaning glass sheets and tiles, mirrors with antifogging effect, self-disinfecting material etc. However, a suitable method for liquid sol application is needed in order to obtain a thin layer with excellent properties.

There are two traditional method of thin layer preparation from liquid precursors: spin-coating and dip-coating. Spin-coating method uses centrifugal force to form a film of liquid precursor: a sufficient volume of precursor is placed onto the support which is then rotated at a high speed. The liquid is spread by centrifugal force and a wet film of precursor is formed. The thickness of the resulting wet film depends mainly on the angular velocity of substrate rotation, precursor viscosity, precursor concentration and solvent evaporation rate[1]. In contrary, dip coating is based on dipping the substrate into liquid precursor and pulling it out at constant speed. Again, viscosity, concentration, solvent volatility and speed of pulling influence the resulting film thickness. The faster we pull, the thicker the film is.

Both these methods are widely used, yet they are burdened by several significant disadvantages, as summarized in Table I. Firstly, the coated area is rather limited. In the case of spin coating, this limitation is due to the centrifugal force. Substrates larger than a few centimeters simply can not be rotated at several thousands rpm. The area of dip coated substrates is usually also limited to centimeter scale, although devices handling large substrates up to meter size are known. Secondly, the efficiency of precursor use is extremely poor. In both spin- and dip-coating, most of the precursor is wasted, and only few percents are actually used to build up the film. Moreover, dip-coating gives us substrates coated from both sides, which is not always desired. Thirdly, both these methods are very sensitive to surface defects. A surface defect can produce traces and streaks and degrade large areas of cauted substrate. At last, these classic methods on their own are not capable of selective deposition ("patterning"), i.e. the whole area of substrate is coated.

Table I
Method comparison (adopted from[2], modified by authors)

| | Spin | Dip | Inkjet |
|---|---|---|---|
| Precursor use efficiency | ~ 95 % wasted | ~ 95 % wasted | ~ 5 % wasted |
| Coated area | ~ cm | ~ dm | ~ m |
| Sensitivity to surface defects | ☹ | ☹ | ☺ |
| Possibility of "patterning" | ☹ | ☹ | ☺ |

Because of these problems and limitations, a more robust method of liquid precursor application has been searched for. Inkjet printing is apparently a very good candidate for this task. In a conventional inkjet printer, small droplets of low viscosity ink are ejected from a print head and fall onto

printed substrated[3]. The movement of the print head and the substrate is precisely controlled by computer and so is the volume of ejected droplets and their loading per unit area. If we are able to replace the ink with a liquid precursor and printing paper with suitable substrate, we obtain a very robust device for the precursor deposition.

Naturally, both the printer and precursor must fulfill certain requirements in order to be employed as a thin layer deposition tool. The printer has to be able to handle rigid media so that solid materials can be used as layer support. The precursor must be of a very low viscosity (less than 20 mPa s) and must not damage the printer. If solid particles are present in the precursor, their diameter must be well below the print head nozzle diameter (50–20 μm typically) and their aggregation must be prevented. Despite these limitations, inkjet printing has been sucessfully used for the deposition of a wide variety of liquid precursors, such as conducting polymers[4], metallic nanoparticles dispersions[5], metallic precursor solutions[6], enzymes, various catalyst nanoparticles dispersions etc.

**Experimental**

Sol and Substrate Preparation

Sol-gel technique was applied to titanium dioxide thin films preparation using titanium(IV) propoxide as titanium precursors.

40 ml of ethanol was mixed with 3.8 ml acetylacetone. This mixture was then dropwise added to 10.3 ml titanium( IV)tetraisopropoxide (TTIP). Finally, 45 ml of ethanol was mixed with 0.69 ml water and this mixture was again dropwise added to the sol composition. Prepared sol was stored in an airtight bottle in darkness at 5 °C.

Borosilicate glass plates with sizes of $30 \times 30 \times 2$ mm (Verre Equipements, France) were chosen as a substrate for immobilization of $TiO_2$ thin films. This type of glass contains only 4.2 % wt. $Na_2O$ and 0.1 % wt. of CaO. Before the preparation of the thin films, each glass was pre–treated in order to eliminate any dust, grease and other residues using an aqueous solution of industrial surfactant and dried under air flow.

Sol Application

Sol application was performed in a novel inovative way utilizing a modified office inkjet printer (Epson R220). Original ink cartridges were removed from the printer and the ink tubing and printhead were flushed and purged with anhydrous propanol. Flushing with anhydrous propanol is extremely important in order to remove any remaining aqueous ink. If this step is omitted or performed incompletely, the titanium sol will hydrolyse upon contact with residual water and precipitated $TiO_2$ will clog the print head nozzles.

"Virgin empty" spongeless carts were supplied by MIS Associates, USA. Titanium sol was filtered frough 0.2 μm mesh size syringe filter and loaded into one "virgin empty" cart. This cart was installed into the printer in the black position while the remaining positions were occupied by the same carts filled with dummy ink (a mixture consisting of water, propanol, surfactant and colorant). After a series of head cleaning cycles a perfect nozzle check pattern was obtained. Cleaned glass plates were then mounted into a modified CD holder, fed into the printer and printed with "black only" driver setting. The colour of the printed pattern was varied in different levels of grey (100%, 90%, 80%, 70%, 60%) and thus glasses with correspoding *relative sol loading value* were printed.

Two print setting were adopted – *rapid* and *slow* (see Table II). The resolution, print speed and media settings were varied and their influence on the resulting $TiO_2$ layer properties was evaluated.

Table II
Print setting

| | Rapid | Slow |
|---|---|---|
| Media Settings | Plain paper | CD Premium Surface |
| Resolution | 360 | 720 |
| Highspeed printing | yes (= bidirectional printing) | no (= unidirectional printing) |
| Absolute printing speed | appr. 1 $cm^2\ s^{-1}$ | appr. 0.05 $cm^2\ s^{-1}$ |

Layer Treatment

After the previous procedure, the coated glass plates were dried in the oven at 110 °C for 30 min. Finally, the deposited layers were thermally treated in a calcination furnace at 450 °C for 4 hours with ramp of 3 °C $min^{-1}$ to obtain the transparent photocatalytically active titanium dioxide films in anatase presupposed phase.

Study of Printed Layers Properties

**Optical and SEM imaging** was performed in an ordinary manner on a Nikon Eclipse E200 optical microscope equippend with Nikon D200 digital camera and Hitachi S4700 FESEM scanning electronic microscope. Recorded electronic images were also used to evaluate the layer thickness.

**Surface Analysis** was performed on Sanning Probe Microscopy NTegra Prima/Aura (NT-MDT).

**Photocatalytic performance** was evaluted by recording the dechloration rate of 2,6-dichloroindophenol (DCIP). The reaction took place in a simple single-plate reactor where the solution was circulated through a siphon by a centrifugal pump. The siphon ensured a constant level of solution over the catalyst plate during the whole reaction despite decreasing volume due to sampling. UV radiation was delivered by Philips HPA – 400 W metal halogen lamp and the intensity was 2.4 mW $cm^{-2}$.

The DICP concentration was determined by UV-VIS spectrophotometry at 600 nm. Samples were taken at 20 minutes intervals. Formal first order kinetic model was adopted and the reaction rate constants were calculated.

**Results**

Layer Structure and Morphology

As far as the layer morphology is concerned, we can clearly see that there are principal differences between rapid and slow printed layers, no matter what the sol loading is. The rapid printed layers are very smooth and compact up to 80 % of sol loading (see Fig. 1.). When the sol loading value exceeds this threshold, cracking occurs (See Fig. 2.).

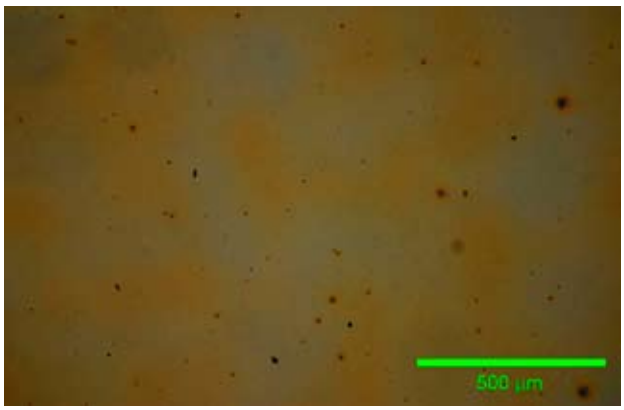


Fig. 1. **80 % sol loading, rapid printing**

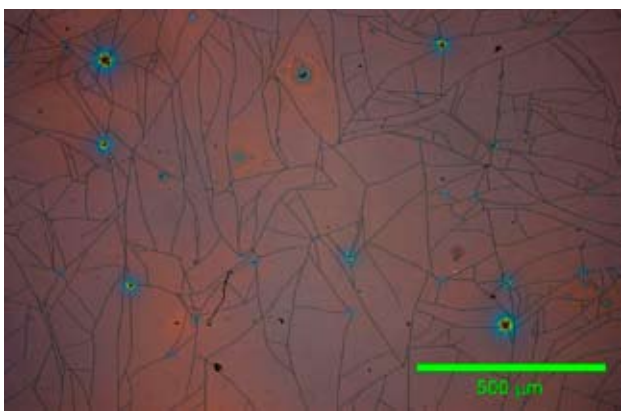


Fig. 2. **100 % sol loading, rapid printing**

On the other hand, the slow-printed layers show completely different structure – their surface is very grooved and rough. It clearly keeps the structure of individual drops. When the sol loading value is low, we can clearly see the patterns of individual drops (see Fig. 3.). When the sol loading value increases, this pattern is still present and some cracing occurs in very thick regions (Fig. 4.).

A more detailed view is provides by the SEM imaging. Here we get a closer look at the cracks and it is also possible to estimate the thickness of the layers (Fig. 6.).

The differences in the layer structure are caused by the different speed of sol ejection: During rapid printing, the sol ejection rate is faster then solvent evaporation, and therefor a liquid film is formed on the substrate. Only then the solvent evaporates, leaving a "dry" layer of gel. However, during slow printing, the sol ejection rate is very small and the rate of evaporation exceeds it. Therefore a solig gel is formed

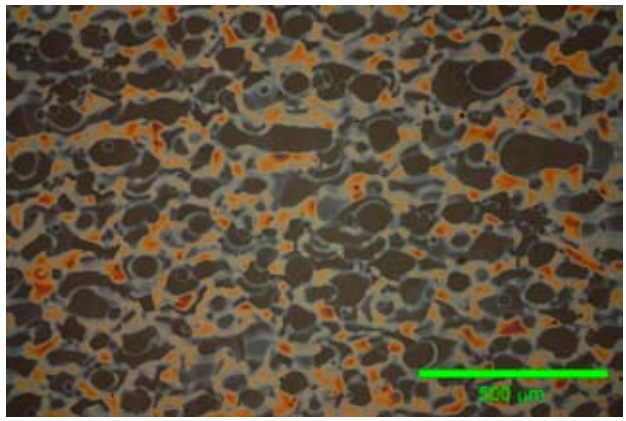


Fig. 3. **60 % sol loading, slow printing**

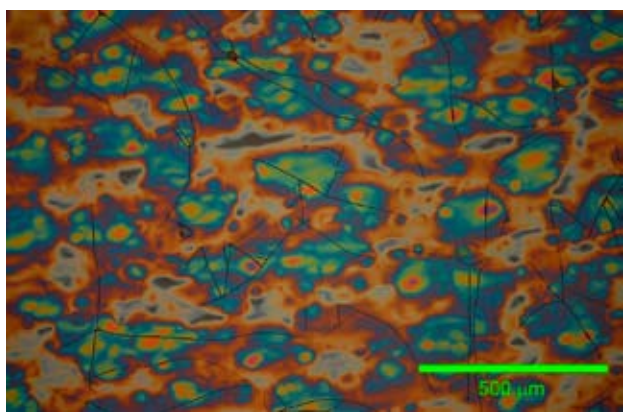


Fig. 4. **100 % sol loading, slow printing**

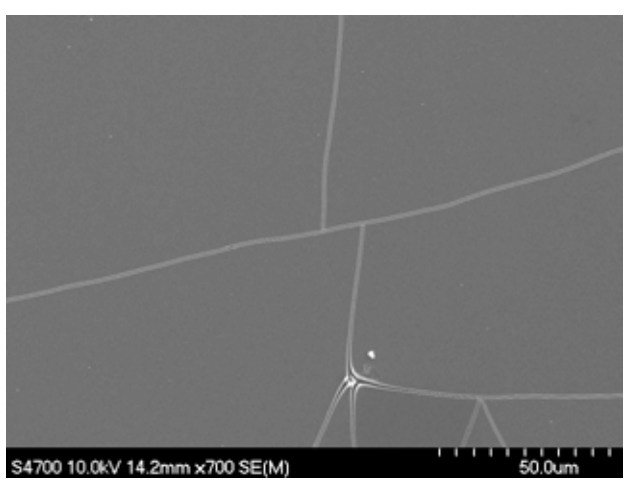


Fig. 5. **100 % sol loading, rapid printing**

on the substrate already during printing and the last drops of sol are deposited onto dried gel. Therefore a distinctive structure develops and the resulting layer is very rough.

The roughness prepared layers was in much greater detail observed by AFM. Unfortunately, the roughness of slow printed layers was too high to be observable by our device, therefore a direct comparison is not possible at the moment. The AFM record for the rapid layer reveal a very

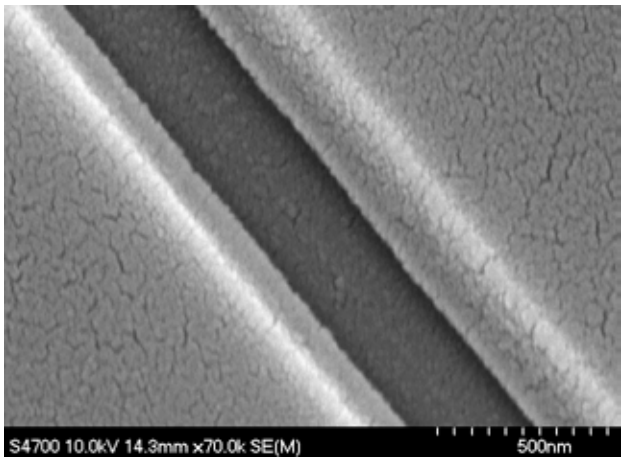


Fig. 6. **A crack detail, 100 % sol loading, rapid printing**

smooth surface whose roughness is comparable to the roughness of support glass.

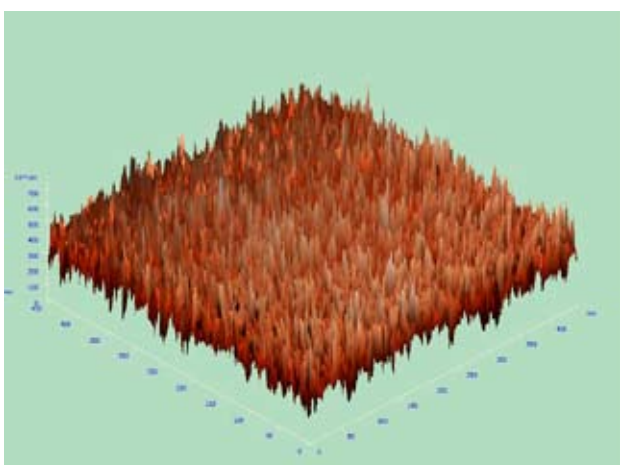

Fig. 7. **AFM record of 100% sol loading, rapid printed layer**

Photocatalytic Performance

Fig. 7 shows the overall results for the DCIP dechloration experiment. We can clearly see that the dechloration rate increases with increasing sol loading. However, the there is a difference in the slope of this dependency. We believe that this difference can be explained by the differences in layer homogeneity. While the rapidly printed layers are very smooth and compact, the slow printed layers are grooved and rough. Therefore the catalyst surface is basically constant in the case of rapid printing and only the thickness of the layer changes. On the other hand, in the case of slow printing, both the average layer thickness and interface surface increases as sol loading increases.

**Conclusion**

In this letter, we demonstrate the benefits of using inkjet printing technology for the preparation of $TiO_2$ thin layers.

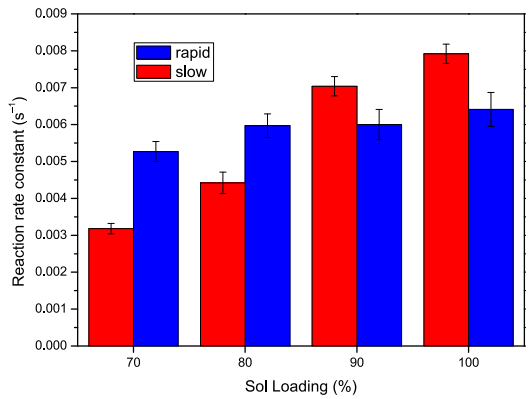


Fig. 8. **Reaction rate constant comparison**

By utilizing the well know sol-gel chemistry used so far for spin- and dip coated layers of $TiO_2$ together with the wide deposition possibilities offered by inkjet printing, we are able pro prepare thin layers of $TiO_2$ in a very effective and clean way with minimum waste. The structure of prepared layers greatly depends on the printing conditions: If the sol ejection rate is faster then solvent evaporation, a smooth compact layer is produced. On the other hand, when the solvent evaporation rate is grater than sol ejection, we obtain highly structured and porous layer.

Slowly printed layers have structured and grooved surface giving them opaque matt apperance, but their photocatalytic performance is superior compared to rapidly printed layers. We believe this is mainly due to greater catalyst interface area. On the other hand, rapidly printed layers have better optical properties – they are glossy and transparent. However, the smooth surface results into lower mass exchange rate and therefore their photocatalytic performace is lower.

*Authors would like to thank to the Czech Ministry of Education, Youth and Sports for supporting this work through project MSM0021630501.*

REFERENCES

1. Schubert D. W., Dunkel T.: Mat Res Innovat *7*, 314 (2003).
2. Bharathan J., Yang Y.: Appl. Phys. Lett. *72*, 2660(1998).
3. Hue P. Le, J. Imaging Sci. Technol. *42*, 49 (1998).
4. Liu Y. et al.: Solid-State Electron. *47*, 1543 (2003).
5. Park J.-W., Baek S.-G.: Scr. Mater. *55*, 1139 (2006).
6. Busato S.et al.: Sens. Actuators B *123*, 840 (2007).

## L18 KINETICS OF OXIDATIVE PROCESSES ON INKJET-PRINTED THIN LAYERS OF TITANIUM DIOXIDE

MICHAL VESELÝ, PETR DZIK, MÁRIA VESELÁ, JANA DRBOHLAVOVÁ AND JANA CHOMOUCKÁ
*Brno University of Technology, Faculty of Chemistry, Purkyňova 118, 612 00 Brno, Czech Republic,*
*vesely-m@fch.vutbr.cz*

**Introduction**

As the photogenerated active oxygen species are formed at the irradiated $TiO_2$ surface, this system can be utilized for microbes deactivation instead of the conventional methods such as UV irradiation, heat treatment or chemical disinfectant application.

The mechanism for bactericidal activity of photocatalytic oxidation was firstly[1] proposed by Matsunaga et al. in 1985. In this pioneer study, they showed that coenzyme A taking part in many biochemical processes is photoelectrochemically oxidized, which leads to the inhibition of cellular transpiration and eventually cell death. Most studies of photocatalytic microbe inactivation are focused on bacteria[2–16], less on viruses[17], yiest[18,19] and fungus[20,21]. As most of the bacteria-focused studies deals with *Escherichia coli*, this species was proposed as a standard microorganism for normalised testing of the photocatalytic activity of various substrates. One reason for this choice is definitely the fact that the presence of this bacteria indicates the contamination of water by feaces.

The mechanism for bactericidal effect of photocatalytic process on $TiO_2$ was in detail described on *E. coli*: Maness[22] et al. proposed, that *E. coli* was killed by the process known as lipid peroxidation. They propose that the first step is the interaction of oxidation products generated by irradiated titanium dioxide with microorganism cell wall. Here the initial oxidative damage takes place. Despite having the cell wall damaged, the cell is still viable. After the erosion of cell wall, an attack onto the cell membrane takes place. Here the peroxidation of membrane lipids takes place as the polyunsaturated phospholipids are the main components of bacterial cell membrane.

The formation of malondialdehyde was also observed, indicating the oxidative decomposition of lipids in protoplasm. This is a highly reactive compound capable of damaging proteins, nuleic acids and bases. Due to the severe erosion of membrane structures the vital biochemical processes such as respiration, semipermaeability and oxidative phosphorilation are slowed down and evetually terminated, resulting in ultimate cell death.

Sunada et al.[24] studied the destruction of *Escherichia coli* entotoxine which is an integral component of cell membrane by titanium dioxide. They proved that the cell death was accompanied by the endotoxine degradation and concluded, that the photocatalytic ptocess onto a $TiO_2$ thin film includes the destruction of outer bacterial mebrane.

Some differences in the susceptibility of various microorganisms to the photocatalityc stress can be observed. The difeerences are especially apparent between gram-positive and gram-negative bacteria. The gram-positive ones, although being less structurally complex then the gram-negative ones, are encapsulated by a thick peptidoglycanous layer. Similarly fungi and yiest are less sensitive to the photocatalitic attack because of their strong eucariotic cellular wall representing relatively strong resisting barirrier agaist the reactive oxygen radicals generate on the surface of irradiated titanium dioxide.

Electrons reduce adsorsobed oxygen to superoxide radicals ($O_2^{\bullet -}$). Electron holes exidies OH groups into hydroxyl radical $HO^{\bullet}$, which then act as the main oxidizing agents. The heterogeneous photocatalytic process then consists of a series of reactions which may be expressed by the following set of equations:

$$TiO_2 \xrightarrow{h\nu} TiO_2(e_{cb}^-, h_{vb}^+) \longrightarrow \text{recombination} \quad (1)$$

$$TiO_2(h_{vb}^+) + H_2O_{ads} \longrightarrow TiO_2 + HO_{ads}^{\bullet} + H^+ \quad (2)$$

$$TiO_2(h_{vb}^+) + HO_{ads}^- \longrightarrow TiO_2 + HO_{ads}^{\bullet} \quad (3)$$

$$TiO_2(h_{vb}^+) + D_{ads} \longrightarrow TiO_2 + D_{ads}^+ \quad (4)$$

$$HO^{\bullet} + D_{ads} \longrightarrow D_{oxid} \quad (5)$$

$$TiO_2(e_{cb}^-) + A_{ads} \longrightarrow TiO_2 + A_{ads}^- \quad (6)$$

Here, **A** stands for the electron acceptor and **D** electron donor. In most cases, a complete mineralization of organic substrate takes place and $CO_2$ a $H_2O$ are the final products. Dissolved oxygen is the usual acceptor in aqueous media, being transformed into superoxide anion-radicals ($O_2^{\bullet -}$), which can further initiate the formation of hydroxyl radical $HO^{\bullet}$:

$$TiO_2(e_{cb}^-) + O_{2_{ads}} + H^+ \longrightarrow TiO_2 + HO_2^{\bullet} \rightleftharpoons O_2^{\bullet -} + H^+ \quad (7)$$

Although the photocatalytic inactivation of microorganism is not suitable for the decompostion of a large quantity of matter in a short time, it became a highly effective measure to eliminate lower concentration of microorganisms and especially to prevent their further growth.

Generally, several different disinfection kinetic models are used in order to describe the microorganism killing[26]. The first empiric model for experimental data fitting was proposed by Chick and Watson in 1908:

$$\ln \frac{N}{N_0} = -\mathrm{k}\, c^n t \,, \quad (8)$$

where $N_0$ and $N$ corresponds to initial and remaining microorganism population, respectively, k is inactivation rate constant, $t$ is reaction time, $c$ is disinfection agent concentration and $n$ is reaction order. In most cases $n$ equals 1, causing the deactivation of microorganism to become a first-order

reaction. The Chick-Watson model was modified considering two different kinetic constants, $k_1$ describing the rate of microbial disinfection and $k_2$ taking into account the biocide concentration decrease:

$$\ln\frac{N}{N_0} = -\frac{k_1 c^n}{nk_2}\left[1-\exp\left(-nk_2 t\right)\right] \quad (9)$$

In 1972, the kinetic model of Hom was developed, which assumes a general equation for disinfection:

$$\ln\frac{N}{N_0} = -k\, c^m t^h\,, \quad (10)$$

where k is the disinfection rate constant, $c$ is the concentration of biocide, $m$ is the Hom dilution coefficient, $t$ is elapsed time and $h$ is the Hom time exponent[29]. It should be noted that if $h$ equals 1, then the equation reduces to that of the Chick-Watson model.

Some authors, who studied UV disinfection of wastewater, tried to replace the concentration of disinfectant in the previous equation (10) with the intensity $\varphi$ of UV radiation[31]. Then the expression of the rate $N/N_0$ becomes:

$$\ln\frac{N}{N_0} = -k\,\varphi^n t = -k\,H\,, \quad (11)$$

where $t$ is time of exposure and then the product $\varphi \times t$ gives the total exposure dose $H$ [J m$^{-2}$].

Horie and co-authors assumed that cell deactivation obeys a second-order reaction between cells and oxidative radicals, and the death of a cell is caused by $n$ times reactions on the basis of a series-event model. They derived complex equation for rate constant $k'$ of photocatalytic disinfection in slury of titanium dioxide taking into acount titanium dioxide concentration and incident light intensity[25].

Unfortunatelly, these equagtions doesn't obeys fully to experimental data of photocatalytic disnfection of yeasts on immobilized titanium dioxide layer.

The most popular way of titanium dioxide thin layer preparation is sol-gel method. Usually the substrates are coated by dip-coating or spin-coating method. But each of them has some drawbacks. It would be very convenient to prepare these layers by way similar to spray coating. Inkjet printing is apparently a very good candidate for this task. In a conventional inkjet printer, small droplets of low viscosity ink are ejected from a print head and fall onto printed substrate. If we are able to replace the ink with a liquid precursor and printing paper with a suitable substrate, we obtain a very robust device for the precursor deposition.

By utilizing the well know sol-gel chemistry used so far spin- and dip coated layers of $TiO_2$ with the wide deposition possibilities offered by inkjet printing, we are able to prepare photocatalytically active thin layers of $TiO_2$ in a very effective and clean way with minimum waste.

**Experimental**

Sol-gel technique was applied to titanium dioxide thin films preparation using titanium(IV) propoxide as titanium precursors. Soda lime glass plates with sizes of $50 \times 50 \times 1.5$ mm were used as a substrate for $TiO_2$ thin films after treatment for surface sodium ions leaching.

Sol application was performed in a novel innovative way utilizing a modified office inkjet printer with empty carts. Cleaned glass plates were then mounted into a modified CD holder, fed into the printer and printed with "black only" driver setting. The colour of the printed pattern was varied in different shades of grey (100%, 95%, 90%, 80%, 70%, 60%) and thus glasses with varying sol loading were printed. The resolution, print speed and media settings were also varied and their influence on the resulting $TiO_2$ layer properties was evaluated. Two way of printer setting were chosen for thin layer of $TiO_2$ preparation – slow (S) and rapid (R). The sample marked as 100 R corresponds to 100 % of sol loadings printed by rapid way.

After coating, the glass plates were dried in the oven at 110 °C for 30 min and finally at 450 °C for 4 hours.

*Photocatalytic killing* of yeast *Candida vini* and *Candida tropicalis* were performed to study the antimicrobial properties of prepared $TiO_2$ layers. The yeast cells have spherical or oval, sometimes cylindrical or elongated shape of 3.0–5.5 × 4.0–9.0 μm in size. Generally, *Candida* is the most common cause of opportunistic mycoses (Candidiasis) worldwide. This type of endogenous infection mostly arises from overgrowth of the fungus inhabiting in the normal flora.

The yeast culture for the photocatalytic test was prepared as follows: 1 ml of yeast culture cultivated for 24 h in GPY liquid nutrient media was diluted with 9 ml of deionized water and centrifuged for 5 min at 4,000 rpm. The supernatant was separated from yeast sediment and centrifugation was repeated once again with 10 ml of deionized water. After last changing of liquid, the pure yeast suspension in water was well homogenized using minishaker. 30 μl of this suspension was dropped onto 15 min pre-irradiated $TiO_2$ film on glass plate and spread by micropipette for better contact of yeasts with photocatalyst surface. The sample was then put on reflective surface in Petri dish and covered by quartz plate in order to maintain a constant humidity during reaction. The sample was irradiated by four fluorescent lamps Sylvania Lynx-S 11 W with a maximum of energy at 365 nm. Irradiance of 1 mW cm$^{-2}$ was maintained by lamp distance adjustment.

The irradiated samples were analyzed by epi-fluorescent microscopy using Acridine orange dye: 40 μl of $1.8 \times 10^{-4}$ M Acridine orange (in phosphate buffer with pH 6) was added to 30 μl drop of irradiated sample placed in Petri dish. The Acridine orange dye is capable to bind to DNA in dead cell and so in epi-fluorescence microscope this complex emits red light. Then the dead cells appear as red and live cells as green in colour. A random selection of 20 places on a sample was recorded by Pixelink PL–A662 CCD camera (Pixelink Canada) and images were processed by Lucia software. On each image, the number of live and dead cells was calculated and expressed as the survival ratio (SR), i.e. number of live cells divided by total number of cells in each image using following formula:

$$SR = \frac{N_{\text{live}}}{N_{\text{live+dead}}} \qquad (12)$$

The obtained survival ratio was averaged and processed by statistical methods.

## Results

By the described method of thin layer of titanium dioxide we prepared layers predominantly with crystaline structure proved by Raman spectroscopy (Fig. 1.). The Raman spectroscopic measurements of $TiO_2$ calcinated films revealed the anatase phase to be dominant with the small portion of rutile.

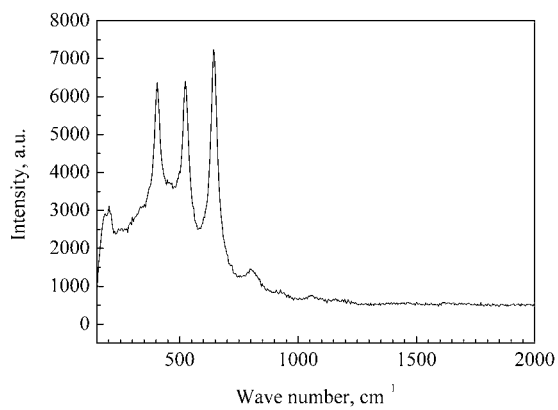


Fig. 1. **Raman spectra of printed layer of titanium dioxide 95R**

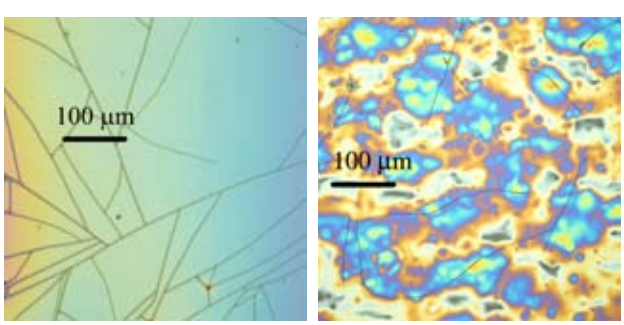


Fig. 2. **Titanium dioxide layers: Smooth surface of rapidly printed sample 95 R (left) and structured surface of slow printed sample 95 S**

The different amount of sol printed on glass surface and two different way of sol printing resulted in various surface structure, layer homogeneity and porosity. The surface structure varied from smooth surface of fast printed layers to wrinkly surface of slow printed layers (Fig. 2.). Maximum thickness was 212 nm. The smooth layer was formed by 30 nm particles of titanium dioxide. However, this smooth layer contained cracks smaller than 700 nm (Fig. 3.).

We found that process of yeast photokilling does not significantly depend on way of printing if the surface is fully covered by $TiO_2$. Generally, a damage of membrane needs

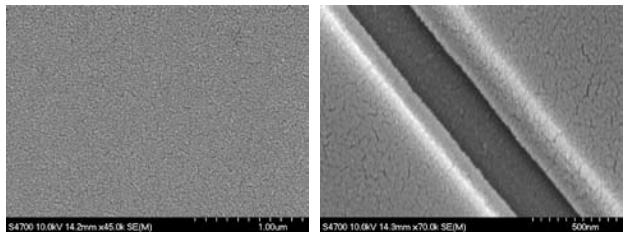

Fig. 3. **SEM microphotography of sample 95 R**

a certain time and we observed the induction period. When a membrane was perforated, the second period occurred during which the microorganism inactivation was accelerated.

The presence of plateau in the later period of reaction was found during yeast inactivation. Inner cell components present outside the cells cause the competition between these molecules and bacteria as regards the rective oxygen species. We found similar results for both used cells of *Candida tropicalis* and *Candida vini*.

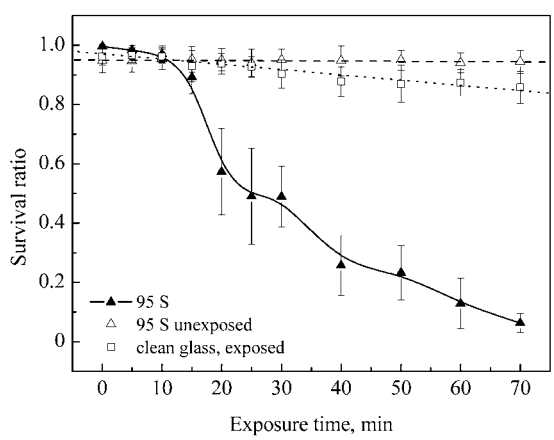


Fig. 4. **Photocatalytic inactiovation of yeast *Candida vini* on slow printed titanium dioxide layer**

## Conclusions

It was found that printed layers show photocatalytic activity. The prepared lyaers were thiner than 200 nm and transparent. Their properties were proved by phtocatalytic inactivation of yeasts. This process does not depend on the way of sol delivery by inkjet printer if the glass surface is fully covered.

*Authors thank to Ministry of Education, Youth and Sports of Czech Republic for support by project MSM0021630501.*

REFERENCES

1. Matsunaga T., Tomoda R., Nakijima T., Wake H.: FEMS Microbiol. Lett. *29*, 211 (1985).
2. Daneshvar N., Niaei A., Akbari S., Aber S., Kazemian N.: Global NEST Journal *9*, 132 (2007).
3. Byunghoon K., Dohwan K., Donglyun C., Sungyong C.: Chemosphere *52*, 277 (2003).

4. Guimaraes J. R., Barretto A. S.: Braz. J. Chem. Eng. *20*, 403 (2003).
5. Rincón A-G., Pulgarin C.: Appl. Catal. B *49*, 99 (2004).
6. Yu J. C., Tang H. Y., Yu J., Chan H. C., Zhang L., Xie Y., Wang H., Wong S. P.: J. Photochem. Photobiol. Chem. *153*, 211 (2002).
7. Kim B., Kim D., Cho D., Cho S.: Chemosphere *52*, 277 (2003).
8. Dadjour M. F., Ogino Ch., Matsumura S., Shimizu N.: Biochem. Eng. J. *25*, 243 (2005).
9. Fernández P., Blanco J, Sichel C., Malato S.: Catal. Today *101*, 345 (2005).
10. Watts R. J., Washington D., Howsawkeng J., Loge F. J., Teel A. L.: Adv. Environ. Res. *7*, 961 (2003).
11. Kühn K. P., Chaberny I. F., Massholder K., Stickler M., Benz V. W., Sonntag H-G., Erdinger L.: Chemosphere *53*, 71 (2003).
12. Nadtochenko V. A., Rincon A. G., Stanca S. E., Kiwi J.: J. Photochem. Photobiol. Chem. *169*, 131 (2005).
13. Rincón A-G., Pulgarin C.: Appl. Catal. B *51*, 283 (2004).
14. Čík G., Priesolová S., Bujdáková H., Šeršeň F., Potheová T., Krištín J.: Chemosphere *63*, 1419 (2006).
15. Kiwi J., Nadtochenko V.: Langmuir *21*, 4631 (2005).
16. McLoughlin O. A., Fernández Ibáñez P., Gernjak W., Malato Rodríguez S., Gill L., W.: Sol. Energ. *77*, 625 (2004).
17. Lee S., Nishida K., Otaki M., Ohgaki S.: Water Sci. Tech. *35*, 101 (1997).
18. Kühn K. P., Chaberny I. F., Massholder K., Stickers M., Benz V.W., Sonntag H-G., Erdinger L.: Chemosphere *53*, 71 (2003).
19. Serpone N., Salinario A., Horikoshi S., Hidaka H.: J. Photochem. Photobiol. *179*, 200 (2006).
20. Lonnen J., Kilvington S., Kehoe S. C., Al-Touati F., McGuigan K. G.: Water Res. *39*, 877 (2005).
21. Sichel C., De Cara M., Tello J., Blanco J., Fernández-Ibánez P.: Appl. Catal. Environ. *74*, 152 (2007).
22. Maness P. C., Smolinski S., Blake D. M., Huang Z., Wolfrum E. J., Jacoby W. A.: Appl. Environ. Microbiol. *65*, 4094 (1999).
23. Pal A., Pehkonen O. S., Yu L. E, Ray M. B.: J. Photochem. Photobiol. Chem. *186*, 335 (2007).
24. Sunada K., Watanabe T., Hashimito K.: J. Photochem. Photobiol. Chem. *156*, 227 (2003).
25. Horie Y., David D. A., Taya M., Setsuji T.: Ind. Eng. Chem. Res. *35*, 3920 (1996).
26. Cho M., Chung H., Choi W., Yoon J.: Water Res. *38*, 1069 (2004).
27. Salih F. M.: Water Res. *37*, 3921 (2003).
28. Cho M., Chung H., Yoon J.: Appl. Environ. Microbiol. *69*, 2284 (2003).
29. Lambert R. J. W., Johnston M. D.: J. Appl. Microbiol. *88*, 907 (2000).
30. Sellami M. H., Hassen A., Sifaoui M. S.: JQSRT *78*, 269 (2003).

## P83 FUNGICIDAL EFFECT OF PRINTED TITANIUM DIOXIDE LAYERS

MÁRIA VESELÁ, MICHAL VESELÝ, PETR DZIK, JANA CHOMOUCKÁ and LENKA ŠUPINOVÁ
*Brno University of Technology, Faculty of Chemistry, Purkyňova 118, 612 00 Brno, Czech republic,*
*vesela@fch.vutbr.cz*

### Introduction

Microorganisms are crucial and inevitable part of life on Earth. They are found basially everywhere – in air, soil, in animal and human bodies, even in places with extreme conditions. Microbial contamination is a serious issue which has to be dealt with in numerous cases of everyday life. Various sterilization and dissinfecting methods have therefore been developed so far.

Photocatalytic processes on thin layers of titanium dioxide represent a new approach to the everlasting struggle against microbial contamination. Reactive oxygen species generated on the surface of irradiated $TiO_2$ inactivate most type of microbes[1]. Apparently, titanium dioxide coated surfaces self-reducing the population of microbes to minimal level and preventing their growth would be of a great importance.

Most photodegradation reactions on organic substrates are based on the oxidative power of photoinduced electronic holes or are mediated by HO•radicals. Such reaction usually lead to a complete mineralization of organic substrate to carbon dioxide and water. However, it is necessary to provide a reducible reactant (i.e. electron acceptors) which would react with photogenerated electrones. In most cases of photocatalytic degradation reactions, oxygen is present and it acts as primary electron acceptor. Oxygen is thus transformed to superoxide radical ($O_2^{\bullet -}$) and in this way a hydroxyl radical can be produced:

$$TiO_2 \xrightarrow{h\nu} TiO_2(e^-_{cb}, h^+_{vb}) \rightarrow \text{recombination} \quad (1)$$

$$TiO_2(h^+_{vb}) + H_2O_{ads} \rightarrow TiO_2 + HO^{\bullet}_{ads} + H^+ \quad (2)$$

$$TiO_2(e^-_{cb}) + O_{2_{ads}} + H^+ \rightarrow TiO_2 + HO^{\bullet}_2 \leftrightarrow O^{\bullet -}_2 + H^+ \quad (3)$$

### Experimental

#### Material and Methods

**Sol and substrate preparation**. Sol-gel technique was applied to titanium dioxide thin films preparation using titanium(IV) propoxide as titanium precursors. A mixture of absolute ethanol and acetylacetone (ACAC) was added to titanium(IV) propoxide (TTP) under continuous stirring. Then a small amount of water in ethanol was dropped at last to the previously mixed solution. Soda lime glass plates with sizes of 50 × 50 × 1.5 mm were chosen as a substrate for immobilization of $TiO_2$ thin films. Soda lime glasses were treated in boiling 9M sulphuric acid. Before the preparation of the thin films, each glass was pre-treated in order to eliminate the dust, grease and other residues using liquid surfactants and dried under air flow.

**Sol application** was performed in a novel innovative way utilizing a modified office inkjet printer. Ink cartridges were removed from the printer and the ink tubing and printhead were flushed and purged with anhydrous propanol. "Virgin empty" spongeless carts were supplied by MIS Associates, USA. Sol was filtered through 0.2 μm mesh size syringe filter and loaded into one "virgin empty" cart. This cart was installed into the printer in the black position and after a series of head cleaning cycles a perfect nozzle check pattern was obtained. Cleaned glass plates were then mounted into a modified CD holder, fed into the printer and printed with "black only" driver setting. The colour of the printed pattern was varied in different shades of grey (100 %, 95 %, 90 %, 80 %, 70 %, 60 %) and thus glasses with varying sol loading were printed. The resolution, print speed and media settings were also varied and their influence on the resulting $TiO_2$ layer properties was evaluated. Two way of printer setting were chosen for thin layer of $TiO_2$ preparation – slow (S) and rapid (R). The sample marked as 100 R corresponds to 100 % of sol loadings printed by rapid way.

**Layer treatment**. After this procedure, the coated glass plates were dried in the oven at 110 °C for 30 min. Finally, the deposited layers were thermally treated in a calcination furnace at 450 °C for 4 hours.

#### Photocatalytic Inactivation of Yeasts

A 24-hour culture of yeast *Candida vini* CCY 29-39-3 (provided by Slovak Yeast Collection, Bratislava) was prepared at 25 °C. After the cultivation, 10 ml of culture medium was sampled into a plastic test tube, rinsed twice and centrifuged at 4,000 rpm for 6 minutes. The supernatant was discarted and the yeast sediment was diluted with 1 ml of distilled water an throroughly mixed.

A titanum dioxide coated glass plate was irradiated by UV lamp for 30 minutes in order to obtain a superhydrophilic surface. 25 μl of diluted yeast suspension was pipetted onto the glass plate and evenly spread across its surface. Then the glass plate with yeast suspension was placed in a sreaction chamber. The chamber consisted of a Petri dish with reflective aluminum foil bottom and quartz glass cover. A few drops of water were aplse placed into the reaction chamber in order to maintain the humidity.

The reaction chamber was irradiated by 4 fluorescent lamps Sylvania Lynx-S 11 W with emission maximum at 350 nm. The irradiation intensity was 1 mW $cm^{-2}$ within 290–390 nm spectral region. Irradiated samples were dyed and observed by fluorescent microscopy.

#### Survival Ratio Calculation

The exposed yeast suspension was mixed with 25 μl acridine orange solution ($1 \times 10^{-4}$ mol $dm^{-3}$) in phosphate buffer of pH = 6. After thorough mixing, the sample was observed with epi-fluorescent microscope Nikon Eclipse E200.

20 digital images of randomly chosen different places ocross the glass plate were recorded using CCD camera PixeLINK PL-A662 mounted on the Nikon microscope. At every recorded image, the number of living cells $N_L$ (green flurescence) and dead cells $N_D$ (orange fluorescence) was counted. Then, the survival ratio *SR* was calculated:

$$SR = \frac{N_L}{N_{L+D}} \quad (4)$$

## Results

After irradiating *Candida vini* suspension deposited on the 100 R glass plate a significant inactivation was observed – the SR dropped to 0.032 ± 0.023 within 70 minutes. On the other hand, the non-irradiated sample showed no inactivation within 70 minutes. These observations are in a good compliance with the results of Seven et al.[4], who also observed no inactivation of microbes on titanium dioxide in darkness. Only very small inactivation was observed on an irradiated bare glass without the catalyst layer. (Figs. 1., 2.).

These results are in agreemnet with the observations made by Kühna et al.[3], who irradiated bacteria *Pseudomonas aeruginosa* on a glass plate covered with titanium dioxide. They found out that bacreial cell inactivation takes place. This phenomenon was explained to be caused by the oxidative stress of oxygen radicals inside cells during the exposure by UV-A radiation. Once the stress rises over a certain threshold, the cell dies.

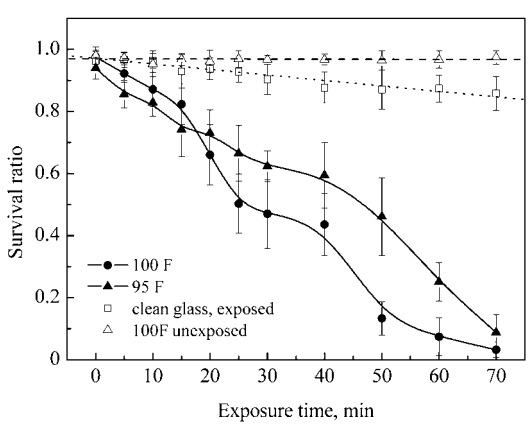


Fig. 1. **SR comparison for *Candida vini* at different conditions on R substrates**

A constant decrease of SR in a certain time from the reaction start was observed by Benabbou et al.[2] in the case of *Escherichia coli*. Cell mebrane damage resulting from photocatalytical processes leads to an increase in membrane permaebility and eventually to free outflow of cell fluids. Therefore both bacterial cells as well as molecules of intracellural organels can become the substrate of reactive oxygen species (ROS) attack. ROS react simultaneously with the cytoplasmatic membrane of living cells and with the remains of dead cells (polysycharides, lipids) at the same time. Our results also confirm this hypothesis.

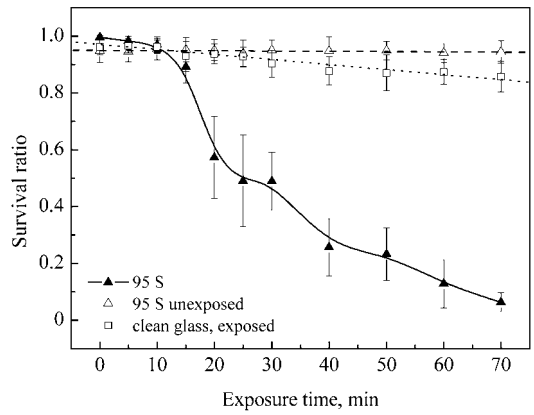


**Fig. 2. SR comparison for *Candida vini* at different conditions on S substrate**

When we compare the inactivation rates for *Candida vini* on R and S substrates (Fig. 2. and Fig. 1.) it becomes clear that the inactivation rate of *Candida vini* does not depent on the structure and topology of the catalyst layer, as long as the glass surface is well couted by titanium dioxide.

## Conclusions

When comparing the photocatylic inactivation rate of *Candida vini* on two types of immobilised catalyst (rapidly printed and slowly printed titanium dioxide layers) it is possible to conclude that significant inactivation was observed on glass plates with very high sol loading, i.e. with very well covered surface (samples 100 R, 95 R, 95 S). We also observe a certain decrease in the inactivation rate after reachicg the SR value of appr. 50 %. This might be caused by the simultaneous consuption of ROS both by the still living cells membrane as well as the organic remains of already killed cells. Almost constant SR value between 25 and 35 minutes suggest a competitive reaction pathway.

*Authors thank to Ministry of Education, Youth and Sports of Czech Republic for support by project MSM0021630501.*

REFERENCES

1. Huang N., Xiao Z., Huang D., Yuan Ch.: Supramol. Sci. *5*, 559 (1998).
2. Benabbou A. K., Derriche Z., Felix C., Lejeune P., Guillard C.: Appl. Catal. B Environ. *76*, 257 (2007).
3. Kühn K. P., Chaberny I. F., Massholder K., Stickler M., Benz V. W., Sonntag H-G., Erdinger L.: Chemosphere *53*, 71 (2003).
4. Seven O., Dindar B., Aydemir S., Metin D., Ozinel M. A., Icli S.: J. Photochem. Photobiol. Chem. *165*, 103 (2004).